Structural chemistry of transition metal dicyanometallates

Joshua A. Hill

St Catherine's College



A thesis submitted for the degree of

Doctor of Philosophy

Inorganic Chemistry Laboratory

University of Oxford

Trinity Term 2016

Structural chemistry of transition metal dicyanometallates

Joshua A. Hill, St. Catherine's College, Trinity Term 2016

A thesis submitted for the degree of Doctor of Philosophy to the Division of Mathematics, Physical, and Life Sciences at the University of Oxford

Abstract

Transition metal dicyanometallates are a family of coordination polymers characterised by their structural diversity and nanoscale separation between transition metal centres. This thesis addresses the relationships between molecular extra-framework cations and their host dicyanometallate frameworks as determinants of structure type and phase transitions. It also addresses the new tilt degrees of freedom accessible to perovskite-structured dicyanometallates and molecular perovskites more generally. A number of new dicyanometallate frameworks are reported which contain the extra-framework cations tetraethylammonium, $[NEt_4]^+$, tetra-*n*-butylammonium, $[NBu_4]^+$, and bis(triphenylphosphine)iminium, $[PPN]^+ = \{[(C_6H_5)_3P]_2N\}^+$. These new compounds are placed within the context of all known dicyanometallate frameworks of general formula $A_mB(L)X_n{\cdot}G$ where A is an extra-framework cation; B is a metal cation; X is $[Au(CN)_2]^-$, $[Ag(CN)_2]^-$, or $[Cu(CN)_2]^-$; L is a neutral ligand bound to the node metal centre (*i.e.*, not to the linker metal); and G is a non-coordinating guest molecule. They are organised according to their stoichiometry, A_mBX_n, showing the dual importance of size/shape of extra-framework cations and the coordinational preferences of the framework cation. The interdependence of degrees of freedom associated with extra-framework cations and with their host frameworks are explored in a diamondoid system and in a number of perovskite-like systems. In the diamondoid system $[NEt_4]Ag[Ag(CN)_2]_2$, coupling between $[NEt_4]^+$ conformation and lattice modes results in a second-order phase transition to an incommensurately modulated phase at low temperatures. There are few reports of incommensurability in coordination polymers; coupling of 'molecular' degrees of freedom with phonons is of fundamental interest and has been implicated in the performance of lead halide perovskites in solar cells. Dicyanometallates with perovskite(-related) structures are here shown to undergo a variety of displacive and reconstructive phase transitions as a function of temperature. In each case, the extra-framework species play a key role in determining the nature of the transitions. In molecular perovskite analogues, tilt degrees of freedom can couple at arbitrary periodicities not accessible to oxides/halides. The 'tilt tensor' is developed here as a tool for describing these tilts. This understanding of unconventional tilts is finally applied to the Prussian Blue analogue $(NH_4)_2SrFe(CN)_6$ in which such tilts can be switched on and off depending on hydration state.

Declaration of Authorship

This thesis is the result of my own work and where it draws on the work of others I acknowledge this at appropriate points in the text. This thesis has not been submitted for a degree at this, or any other, institution. The crystal structure of $[Bu_4N]_{0.5}Cd[Ag(CN)]_{2.5}$ was previously reported in a dissertation submitted for an MChem degree at this institution and some introductory material in Section 1.2 was adapted from this same document.

Joshua Hill

Acknowledgements

The work presented in this thesis would not have been possible without the assistance and support of numerous individuals and organisations. I would first and foremost like to thank Professor Andrew Goodwin for being such an inspirational, generous, and supportive supervisor. I should thank him also for giving me the freedom to spend time on all sorts of activities while a DPhil student.

For specific parts of the work presented here I would like to thank: Amber for help with single crystal refinements; Richard for assistance with CRYSTALS; Kirsten for guiding me through superspace crystallography and teaching me how to use JANA (Chapter 6); Andy Chin for performing SQUID measurements with me (Chapter 5); Arkadiy for his 3D-ΔPDF work on $[Bu_4N]Mn[Au(CN)_2]_3{\cdot}[Bu_4N]ClO_4$ (although it did not make it into this thesis); Peter Thygesen for I11 beamtime together (Chapter 5); Sam Duyker for close collaboration on his PBA system (Chapter 8); Hanna for discussions about tilts in molecular perovskites (Chapter 7); Paul Saines for encouraging me to think about tilt systems in dicyanometallate perovskites; Mark for assistance with TOPAS; Matt for sharing his pymol polyhedra script; and Chris Howard for assistance with symmetry analysis (Chapters 6 & 8). Much of this work would not have been possible without beam-time at I19 and I11, Diamond Light Source. I am grateful to all the staff at those beamlines and particularly to Claire Murray, Chiu Tang, and Dave Allan. Thanks are due to Peter, Harry, Chloe, Hanna, Emily and Ali for proof-reading parts of this thesis.

I am fortunate to have been surrounded by exceptional people while at Oxford—Goodwin group and ChemCryst members past and present. I am particularly indebted to Amber and Nick for single crystal training and advice (among many other things); Andrew C for inducting me into the world of cyanides; Matt for MOF chat, disorientating experiences, always taking an interest (in all the work going on in the group), and providing useful/'useful' suggestions; Peter my flatmate and co-conspirator; and Yue for always being around for a good chat. That is not to forget Callum, Ines, Jasper, Joe, Paul, Daiki, Mark, Chloe, Mia, Arkadiy, Ali, Phil W, Phil M, Hanna, Harry, Sam, Christoph, Laura, Emily, Sneha and numerous Part IIs; it has been a pleasure to work with you.

I am grateful for helpful email correspondence with V. A. Blatov regarding the use of TOPOS to analyse crystal structure topology and with G. Kieslich regarding his tolerance factor formulation. In addition I would like to thank all those in the Chemistry department who have helped me in my time here in particular Keith Waters, Phil Wiseman, Ashley Shepherd, Susan Davis, Aga Borkowska, and the support staff in general.

I would like to acknowledge the EPSRC for my primary funding and the ERC, the Department of Chemistry, St Catherine's College, the BCA (CCG and PCG), EPDIC, the IOP, and the Erice International School of Crystallography for further (financial) support. I am particularly lucky to have attended both the Erice crystallography school and the Durham single crystal school.

Professor Peter Battle has been omnipresent in my eight years at Oxford and St Catherine's College—first as my tutor and then as my graduate advisor/boss at

Catz. I would like to thank Peter in particular for wise advice whenever needed and for giving me the opportunity to teach at College, which I have greatly enjoyed. I am thankful for being welcomed so warmly into the SCR as a junior member and to my fantastic colleagues on the Chemistry team at Catz. I would also like to acknowledge Pascal Jerome for his years of friendship through undergraduate (and on either side)!

Finally I would like to thank Ilsa for her unerring support for the past 7 years, in particular in the latter stages of this thesis, and my family for their love and for reminding me of the world outside of Oxford. I would not have been able to do any of this without you!

For Ilsa

Contents

1 Introduction **1**

1.1 Coordination polymers outlook 3

1.2 Chemistry of dicyanometallates 8

1.3 Structural analogies 15

1.4 An aside - classification of topology 18

1.5 Perovskite-structured compounds 20

1.6 Modulated and aperiodic structures 37

1.7 Phase transitions and soft modes 46

1.8 Structural chemistry of $[PPN]^+$ 52

1.9 Structure of Thesis 53

2 Experimental methods **56**

2.1 Sample preparation 56

2.2 Diffraction 61

2.3 Other analytical techniques 72

3 New transition metal dicyanometallates **75**

3.1 Introduction 75

3.2 Results and Discussion 76

3.3 Summary 92

4 Dicyanometallates as model extended frameworks 93

4.1 Composition–structure relationships in dicyanometallates 93

4.2 Concluding remarks 98

5 Phase transitions of dicyanometallate superperovskites 100

5.1 Introduction 100

5.2 ABX_3 superperovskites 102

5.3 AB_2X_5 layered superperovskites 111

5.4 Salt-inclusion perovskite $ABX_3{\cdot}AY$ 123

5.5 Concluding remarks 136

6 Incommensurate modulation in diamondoid $[NEt_4]Ag[Ag(CN)_2]_2$ 140

6.1 Introduction 140

6.2 Results 141

6.3 Discussion 147

6.4 Conclusion 152

7 Tilts in molecular perovskite analogues 153

7.1 Further complications 162

7.2 Conclusion 164

8 Hydration-controlled unconventional tilts in the double perovskite $(NH_4)_2SrFe(CN)_6$ 166

8.1 Results 166

8.2 Discussion 168

8.3 Concluding remarks 173

9 Conclusion **175**

Bibliography **178**

Appendix A **201**

A1 PPN dicyanometallate salts: [PPN]Au(CN)$_2$ and [PPN]Ag(CN)$_2$ . . . 202

A2 [NBu$_4$]$_{0.5}$Cd[Ag(CN)$_2$]$_{2.5}$ 206

A3 Tolerance factors of superperovskites 207

A4 Thermogravimetric analysis 209

Appendix B **209**

B1 Superperovskite DSC 210

B2 Superperovskite diffraction data 211

B3 Ion-inclusion ABX$_3$·AY perovskite 215

B4 Orientation in [PPN]Mn$_2$[Ag(CN)$_2$]$_5$(EtOH)$_2$ and *R*-[PPN]Mn[Ag(CN)$_2$]$_3$ 217

Appendix C **217**

C1 Modulated structure of [NEt$_4$]Ag[Ag(CN)$_2$]$_2$ 218

Publications **218**

Abbreviations

2θ	scattering angle (diffraction)
bdc	1,4-benzenedicarboxylate
btc	1,3,5-benzenetricarboxylate
Bu	*n*-butyl, *n*-C_4H_9
DFT	density functional theory
DSC	differential scanning calorimetry
Et	ethyl, C_2H_5
G	Gauss
IUPAC	International Union of Pure and Applied Chemistry
K	Kelvin
LFSE	ligand field stabilisation energy
M	molar
Me	methyl, CH_3
MIL	Matérial Institut Lavoisier
MOF	metal–organic framework
μ_{eff}	effective magnetic moment
NLC	negative linear compressibility
NTE	negative thermal expansion
PBA	Prussian Blue analogue
PPN	bis(triphenylphosphine)iminium
PTE	positive thermal expansion
PXRD	powder x-ray diffraction
RCSR	Reticular Structure Chemistry Resource
s	second
SBU	secondary building unit
SXRD	single-crystal x-ray diffraction
TGA	thermogravimetric analysis
Z	full nuclear charge

Chapter 1

Introduction

One of the main pursuits of solid state chemistry is the understanding of relationships between composition, structure, and properties. Through detailed correlation of these aspects of solids it has been possible to optimise the properties of useful materials and understand many of the fundamental phenomena at play in the solid state.[1,2] Looking for these correlations in crystalline materials has been a preoccupation since at least Nicolas Steno's observation in 1669, using quartz crystals, of the 'Law of the constancy of interfacial angles' and early attempts at understanding the faceted nature of crystals [Figure 1.1].[3,4] Perhaps the most famous connection between the macro-structure of crystals (morphology) and properties was made by Louis Pasteur in 1847.[5] Pasteur manually sorted crystals of ammonium sodium tartrate according to their shapes - one set of crystals being a mirror image of the other. Solutions of these two sets of crystals rotated plane polarised light in opposite directions whereas an equal mixture of the spontaneously resolved crystals gave no rotation.[6] This connection between morphology and optical activity, as first observed for quartz twenty years earlier,[7] provided the foundations for understanding molecular chirality.[5,6]

Contemporary understanding of solids is rooted in the rebirth of crystallography on the basis of diffraction.[8,9] Few areas of the physical and biological sciences have been untouched by the huge successes of crystallographers in revealing the inner structures of substances. The variety of compounds whose structures were solved in

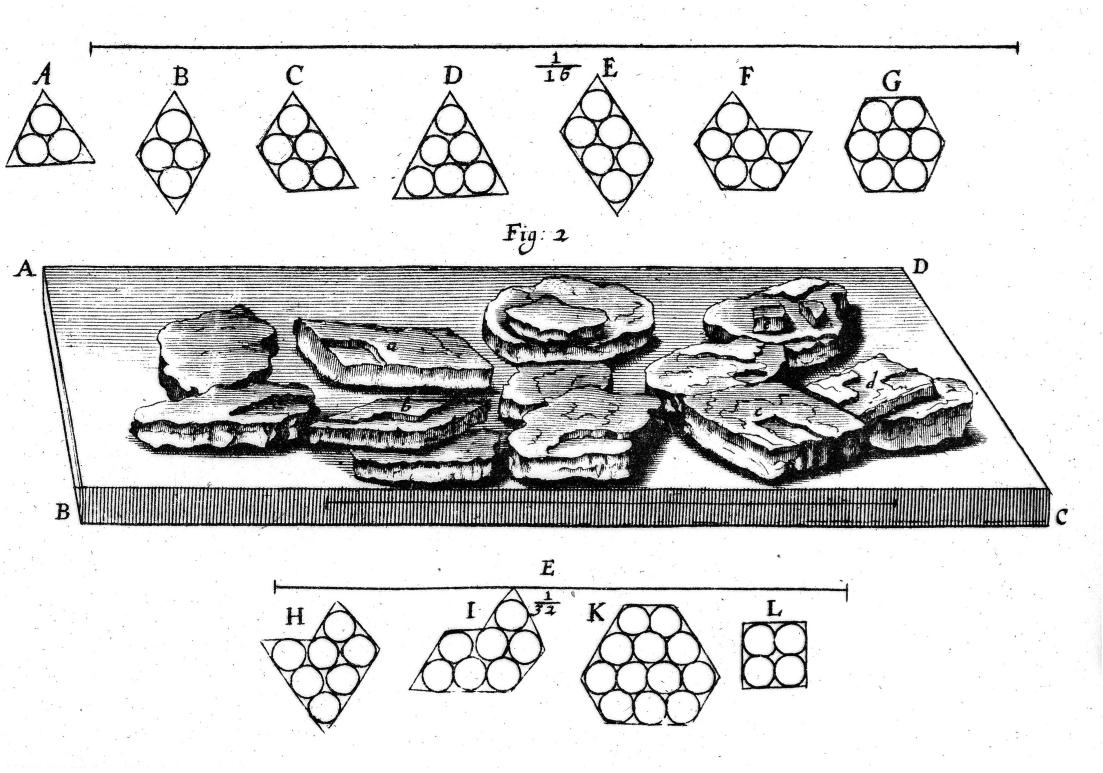

Figure 1.1: Crystals isolated from urine illustrated in Robert Hooke's *Micrographia* (1665).[4] Hooke found that he was able to reproduce the flat surfaces of the crystals by packing spheres (A–L). Reproduced under license CC BY 4.0 from Wellcome Library, London.

just the first 50 years—inorganic salts (*e.g.* sodium chloride),[10] organic molecules (*e.g.* hexamethylbenzene),[11] metalloproteins (*e.g.* vitamin b12, haemoglobin),[12,13] biological polymers (*e.g.* DNA),[14,15] and crystalline and amorphous forms of carbon[16,17]—stand as testament to this. Given the diversity of structure even within any one of these classes of compounds it is important to establish trends emerging for particular structure types. With sufficient understanding it can be possible to then develop some design rules. There have been significant successes in controlling properties by parameterising structures, *e.g.* oxide perovskites, where much predictive power regarding structure formation can be harnessed using models based on the packing of hard spheres of different sizes.[18] While packing forces are impor-

tant for all solids,[19] different chemistries and classes of compounds provide different opportunities for structural manipulation.

1.1 Coordination polymers outlook

Arguably one of the most important conceptual breakthroughs in modern structural chemistry was Robson's geometric interpretation of the structures of coordination polymers as connected nets of nodes and linkers.[20,21] The language of reticular chemistry that developed from that point has enabled the informed design of an extraordinarily large family of framework materials and coordination polymers, notably including metal–organic frameworks (MOFs)[22] and covalent organic frameworks (COFs).[23,24] The basic design approach as it is currently used reflects the realisation that specific combinations of node and linker geometries can usually lead to only a finite number of different possible structures;[25] hence control over the former (*e.g.* the choice of transition-metal elements or clusters with specific coordination geometry preferences and linkers with characteristic binding modes) enables control over the latter.[26] For example, joining the square copper paddlewheel secondary building unit (SBU) $Cu_2(–CO_2)_4$ with ditopic 1,4-benzedicarboxylate (bdc) gives the 2D square-grid Cu(bdc),[27] whereas tritopic 1,3,5-benzenetricarboxylate (btc) gives the 3D MOF $Cu_3(btc)_2{\cdot}(H_2O)_3$ (HKUST-1)[28]. A variety of other structures are accessible for this SBU with, for example, bent ditopic linkers [Figure 1.2].[26]

Metal–organic frameworks and other classes of coordination polymers have been the focus of significant attention for the past quarter of a century.[29,30] Coordination polymers have been investigated for a variety of properties, some of the most

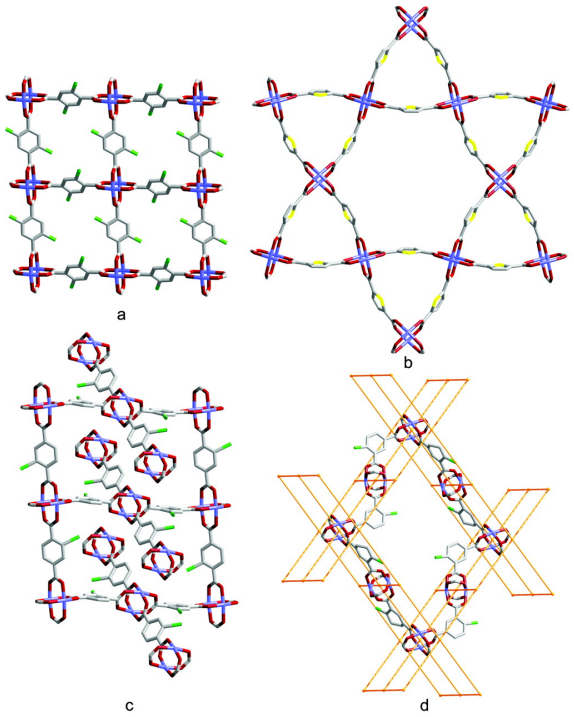

Figure 1.2: Four different structure types arising from the combination of the copper paddlewheel secondary building unit with a variety of ditopic ligands They are (a) MOF-102 with a 2D square-grid structure, (b) MOF-110 with a 2D Kagomé-like structure, (c) MOF-111 with an augmented $CdSO_4$ structure, and (d) MOF-112. Reproduced with permission from Ref. 26. Copyright (2002) National Academy of Sciences, U.S.A.

prominent being gas storage and separation,[31–33] catalysis,[29,34] unusual mechanical properties,[35] drug-delivery,[36] sensing,[37] and ion storage and transport,[38,39] with mixed success in translation to (commercially) viable functional materials.

The diversity of chemistries present in MOFs is rivalled by the number of names given to these compounds. While sometimes descriptive, *e.g.* 'ZIF' (zeolitic imidazolate framework), they are just as often institutional—UiO (Universitet i Oslo),[40] HKUST (Hong Kong University of Science and Technology),[28] and MIL (Matérial Institut Lavoisier)[41]—followed by a number. Although some guidance on nomenclature for coordination polymers has been issued by IUPAC* it remains the case that

*These guidelines, among others, explicitly advise against the use of 'hybrid inorganic–organic materials' and require that metal–organic frameworks have 'potential voids'.[42]

most coordination polymers, of which MOFs are a subset, have no IUPAC endorsed name.[42] In this context other structural descriptors can be useful for understanding how the structures of coordination polymers relate to each other. Topology descriptors have emerged as just such a useful tool for structure classification such that connections can be made between compounds of very different chemistries (*vide infra*).

While often presented as a new class of materials, it is worth noting that metal–organic frameworks and other coordination polymers have their intellectual roots in the work of Alfred Werner* and others responsible for the development of coordination chemistry in the early 20th century.[43] In the next two paragraphs I give examples of two coordination polymers that were commercially important (Prussian Blue) or 'naturally' occurring (transition metal oxalates) long before current interest, yet have important connections to contemporary concerns.

The cyanide-based coordination polymer and pigment Prussian Blue was discovered between 1704 and 1707 and once the method of its production became more widely known, the first Prussian Blue analogues (PBAs) were soon synthesised [Figure 1.3(a)].[44,45] Owing to their ability to support a range of mixed-valence states,† Prussian blue analogues continue to be of significant interest for properties such as photoswitchable magnetism [Figure 1.3(b)],[47,48] and more recently have emerged as excellent electrodes for sodium-ion batteries [Figure 1.3(c)].[49–51]

Metal–organic compounds may also be found in the environment made entirely

*The first Inorganic Chemist to receive the Nobel Prize in Chemistry (1913).

†Prussian Blue is a Class II mixed-valence in the Robin & Day classification,[46] which means that the valences are distinguishable but are not frozen in, allowing for intense intervalence charge-transfer.

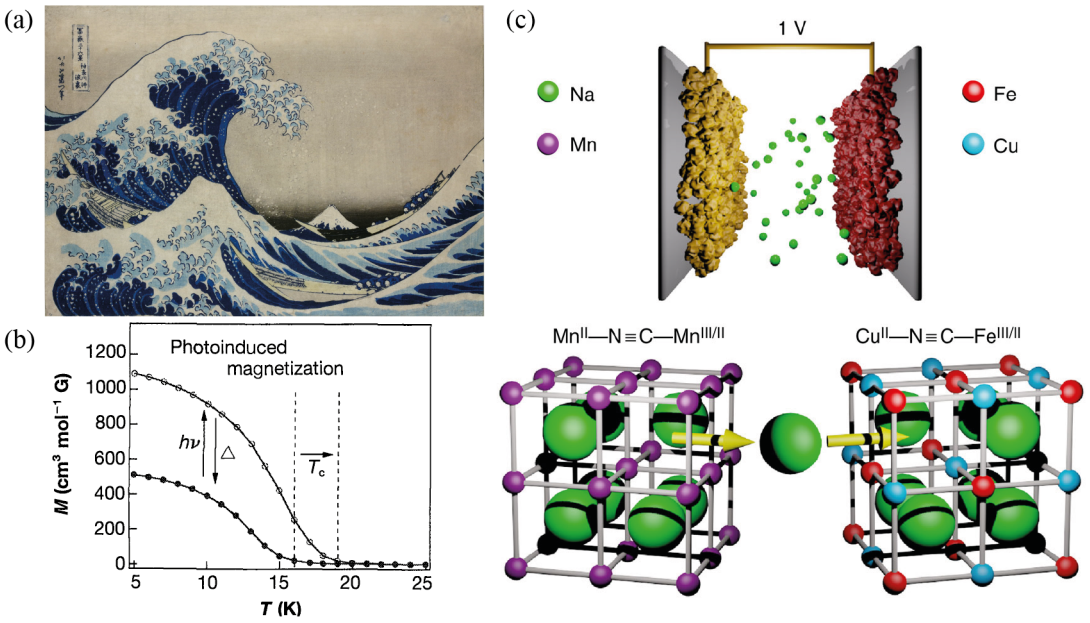

Figure 1.3: (a) *The Great Wave* by Hokusai, 1831, woodblock print. Prussian Blue fulfilled the demand for an intense, light-fast blue pigment and was used in this print. From the 1820s, Prussian Blue was available at low cost to the Japanese market from China.[52] Creative Commons (CC BY-NC-SA 4.0) © Trustees of the British Museum. (b) Photomagnetism in $K_{0.2}Co_{1.4}[Fe(CN)_6]\cdot 6.9H_2O$: the variation of field-cooled magnetization with temperature with an applied field of 5 G before (filled circles) and after (hollow circles) irradiation with red light. The light-induced magnetization enhancement can be removed by heating above 150 K. From O. Sato *et al.*, *Science*, **272**, 704-705 (1996).[47] Reprinted with permission from AAAS. (c) A Na^+ battery in which PBAs play the role of both cathode (copper hexacyanoferrate) and anode (manganese hexacyanomanganate).[50] Reprinted by permission from Macmillan Publishers Ltd: *Nature Commun.*, Ref. 50 copyright 2014.

without the involvement of humans; some microorganisms living on mineral deposits form coordination polymers, such as metal oxalates, through their metabolic activity.[53–56] Lichens, for example, can cause the 'geological biomineralisation' of Moolooite (copper(II) oxalate hydrate) from copper ores;[57] and fungi can convert many metal minerals into oxalates.[58,59] *Beauveria caledonica* for example has been shown *in vivo* to make copper, zinc, cadmium, and lead oxalates.[60] These biogeological processes have provided inspiration for the synthesis of metal-organic materials through 'accelerated ageing'.[61,62] While oxalate secondary minerals tend to be simple 1D coordination polymers,[63] 2D and 3D oxalates are also known and their

structure can be directed through templated synthesis using organoammonium and other cations.[64,65] Such compounds continue to be of interest for their magnetic and proton conducting properties,[66–68] and, being based on the simplest dicarboxylate, form an important part in the history of the development of MOFs where longer dicarboxylates are one of the most important classes of ligand.

I return now to contemporary paradigms for understanding the structures of coordination polymers. The abstraction of linker molecules to rod-like connections carries with it the implication that linker shape and chemistry bear little influence on the resulting framework structure. Certainly this is sometimes true [Figure 1.4],[69,70] but, for many coordination polymers, the packing motifs and stereochemical preferences of the organic linkers often play a defining role in directing structure. This may be as simple as linker functionalisation preventing network interpenetration but the effects can also be altogether more drastic.[71] For example, if the terephthalate linker connecting chains of corner-sharing $AlO_4(OH)_2$ octahedra in the porous 'breathing' MIL-53 (Ref. 72) is swapped for the longer and slightly-bent 4,4′-azobenzenedicarboxylate then the non-porous layered MIL-129 forms instead, where the ligands now adopt a π-π stacking motif.[73] In contrast, using 2,3,5,6-tetramethyl-bdc (Me_4-bdc) gives MIL-105 which has the same topology as MIL-53 but is non-porous: the steric bulk of the tetramethylated linkers forces a pore-blocking linker conformation to be adopted.[74] More drastically, the steric demands of Me_4-bdc prevent the formation of a tetramethylated analogue of Zn(bdc) (MOF-2) giving a structure based on tetrahedral SBUs instead of the intended paddlewheel.[75]

It is in this context that coordination polymers assembled using the dicyanometallate linker $[NC–M–CN]^-$ (M = Cu^I, Ag^I, Au^I) are particularly interesting. The

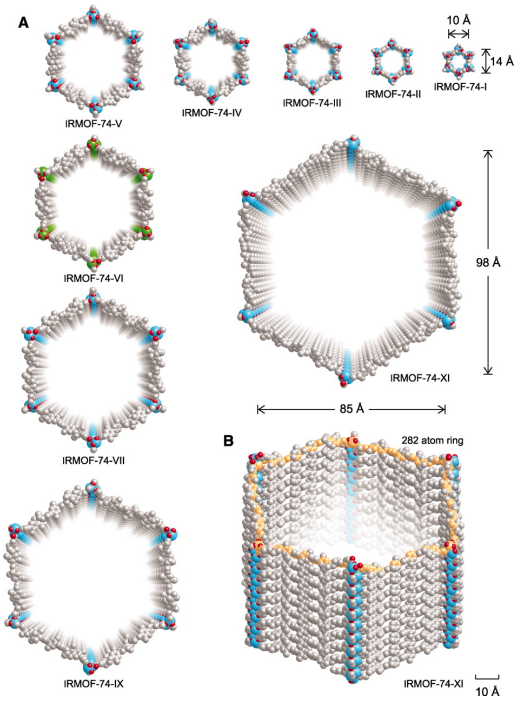

Figure 1.4: The linker of MOF-74 M_2(2,5-dioxidoterephthalate) with M = Zn^{2+} or Mg^{2+} was systematically extended yielding an 'isoreticular' series of metal–organic frameworks. Additional phenyl rings were added to extend the linker length up to a total of 11 for IRMOF-74-XI. Mg in blue, Zn in green. From H. Deng *et al.*, Science, 226, 1018–1023 (2012).[70] Reprinted with permission from AAAS.

preferred coordination mode of this linker is linear, and so it combines the nanometre scale of the organic linkers used to build MOFs with the geometric flexibility of an atomically-thin linker. In many ways, dicyanometallates can be considered a natural extension of oxide frameworks (*e.g.* perovskites) and cyanide frameworks (*e.g.* Prussian Blues) [Figure 1.5].

1.2 Chemistry of dicyanometallates

Like their oxide and cyanide cousins, dicyanometallate frameworks exhibit a variety of important functional responses. Examples include: colossal positive and negative thermal expansion in silver hexacyanocobaltate ($\equiv Co^{III}[Ag^{I}(CN)_2]_3$);[76] giant negative compressibility and guest-dependent luminescence in $Zn[Au(CN)_2]_2$;[77,78] piezo-

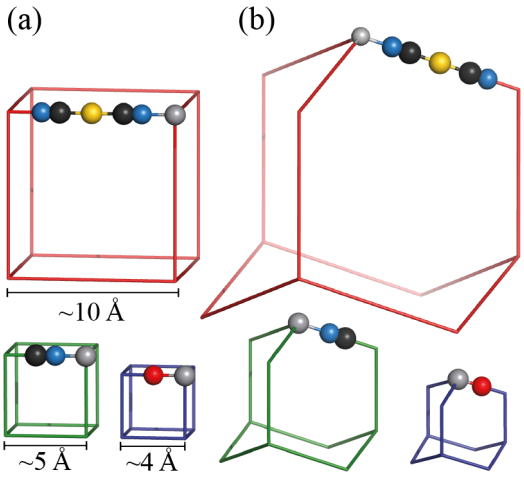

Figure 1.5: The increasing scale of oxide (blue), cyanide (green), and dicyanometallate (red) architectures illustrated with the perovskite (a) and cristobalite (b) structures. Increasing the length of the linker dramatically increases the available volume for interpenetration, extra-framework cations, and/or neutral guests. Node metal (grey), oxygen (red), nitrogen (blue), carbon (black), and linker metal (yellow).

electric behaviour in $KCo[Au(CN)_2]_3$;[79] tuneable room-temperature luminescence in $La[Au_xAg_{1-x}(CN)_2]\cdot 3H_2O$;[80] vapochromism in $Cu[Au(CN)_2]_2$;[81] heat-, light-, and pressure-induced spin-crossover in $Fe(pyz)[Ag(CN)_2]_2\cdot pyz$ (pyz = pyrazine);[82] and strain-free charge storage in $K_xFe^{II/III}[Ag(CN)_2]_3$.[83] In each of these cases, the geometric flexibility of the dicyanometallate linker plays a key role and so there is good reason to expect similarly intriguing functional responses amongst as-yet-unrealised dicyanometallate frameworks.

Thermodynamic quantities associated with the formation of dicyanoaurate and dicyanoargentate are given in Table 1.1 and it will be useful to note some aspects of their chemistry as detailed by Sharpe.[84] Gold(I) forms a stronger M–C bond than silver(I) as indicated by their force constants (280 and 180 $N\,m^{-1}$ respectively) determined from IR spectroscopy.[85–87] This small difference in CN stretching frequency indicates that the greater bond strength for dicyanoaurate is primarily due to improved σ- rather than π-bonding since back-bonding would result in occupancy of

	ΔG_f°(kJ mol^{-1})	ΔH_f°(kJ mol^{-1})	ΔS_f°(J K^{-1} mol^{-1})
$[Ag(CN)_2]^-$	117.00	138.00	67.00
$[Au(CN)_2]^-$	297.00	242.00	134.00

Table 1.1: Some thermodynamic properties of dicyanoargentate, $[Ag(CN)_2]^-$, and dicyanoaurate, $[Au(CN)_2]^-$.[84]

antibonding T_{2g} orbitals that are primarily C≡N π^* in character. However, computational studies have indicated that Au(d_π) – CN(p_π) bonding is important for the stability of $[Au(CN)_2]^-$ compared to, for example, $[Au(SCN)_2]^-$.[88] The existence of $HAu(CN)_2$ but not $HAg(CN)_2$ reflects this difference in bond strength.[89]

The dicyano anions of group 11 elements show an increased preference for linear binding and $\mu_{1,5}$-coordination down the group. The structural chemistry of dicyanoargentate shares many similarities with dicyanoaurate though the former is found in a larger range of binding modes.[90] In contrast, systems containing Cu(I) and cyanide will only occasionally give $\mu_{1,5}$-coordinated dicyanocuprate,[91–93] having a propensity to form structures featuring the bifurcated $[Cu_2(CN)_4]^{2-}$ unit, such as in $[Cu_3(2,6\text{-diaminopyrimidine}(NH_2)_2)(CN)_3]$,[94] and other motifs thus rarely fulfilling the role of simple linear linker.[90]

1.2.1 Metallophilicity

A common structural motif in dicyanometallate compounds is short M···M distances. Here, short means less than the sum of the van der Waals radii of the two atoms (<3.44 Å for Ag···Ag, <3.60 Å for Au···Au)[95,96] which is indicative of significant metallophilic interactions.*[97,98] In range of magnitudes, aurophilic in-

*Pyykkö points out that this should not be thought of as a cut-off for these interactions.[96] It is, however, a convenient marker when discussing these interactions.

teractions can best be compared to hydrogen bonds,[96] as shown with temperature dependent NMR studies of molecular systems which give interaction energies of 5–12 kJ mol^{-1}.[99–102]

Schmidbauer *et al.* coined the term aurophilicity[103] to describe the forces resulting in structures and/or conformations with short Au$\cdots$Au distances in a variety of molecular organogold(I) compounds.[99,103–105] These dispersive interactions have since been exploited in the field of crystal engineering for the rational synthesis of high-dimensional systems and to support network interpenetration.[106] Aurophilicity has also been the subject of extensive theoretical studies.[96,107,108]

More generally, closed shell $d^{10}\cdots d^{10}$ interactions have been recognised in extended structures for some time, perhaps most notably in Ag(I) containing compounds.[109] Argentophilic interactions are generally considered to be weaker than aurophilic interactions but still affect the structures and properties of molecular and extended silver(I)-containing compounds.[109,110] While most closed-shell cations will maximise their separation in a crystal structure—and thus lattice energy—ternary silver(I) compounds do not pack purely according to electrostatics and density.[109,111,112] $KAgCO_3$ exemplifies the tendency of silver(I) to form extended cationic assemblies in its compounds.[111,113] In $KAgCO_3$, Ag(I) is arranged in triangular layers with a minimum Ag$\cdots$Ag distance of 3.00 Å whereas the shortest K$\cdots$K distance is 4.04 Å [Figure 1.6].*

Why are aurophilic interactions stronger than argentophilic? The lanthanide contraction (the effect of occupying the poorly shielding 4f shell on the 6s and 6p

*This is a pertinent comparison since silver(I) is, in many respects, intermediate between sodium(I) and potassium(I).

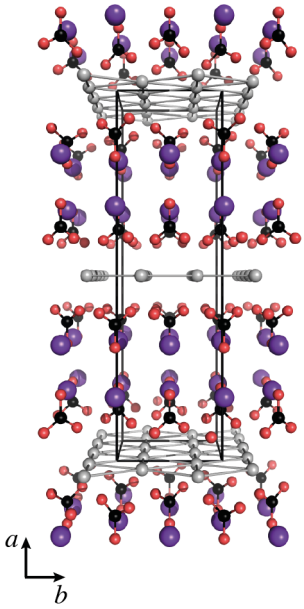

Figure 1.6: Aggregation of silver(I) ions in the crystal structure of $KAgCO_3$. The silver(I) ions form triangular layers in which the shortest Ag$\cdots$Ag distance is only 3.00 Å. These distances are found in chains running along c. The distances between the chains are alternately 3.21 Å and 3.34 Å.[113] Ag shown in grey, K in purple, C in black, and O in red.

shells) and relativistic effects are both reasonable candidates. However, Dirac-Fock level calculations reveal that relativity is almost entirely responsible for the orbital energy difference between silver and gold.[96] Relativistic contraction of 6s orbitals and indirect expansion and destabilisation of 5d orbitals in gold results in a reduced energy gap between 5d and 6s, 6p compared to non-relativistic calculations* [Figure 1.7]. While it can be convenient to think of aurophilicity in terms of hybridisation (overlap of filled 5d orbitals of one atom with the empty 6s and 6p orbitals of another) it is really a correlation effect. It is understood primarily as a dispersion phenomenon with a contribution from virtual charge-transfer.[114,115] However, σ donors do support p-participation in Au–L bonds.[96]

Theoretical models of aurophilicity give the aurophilic attraction energy, $D_e \approx$

*Gold has the largest relativistic effect of any element with atomic number less than 100.[96]

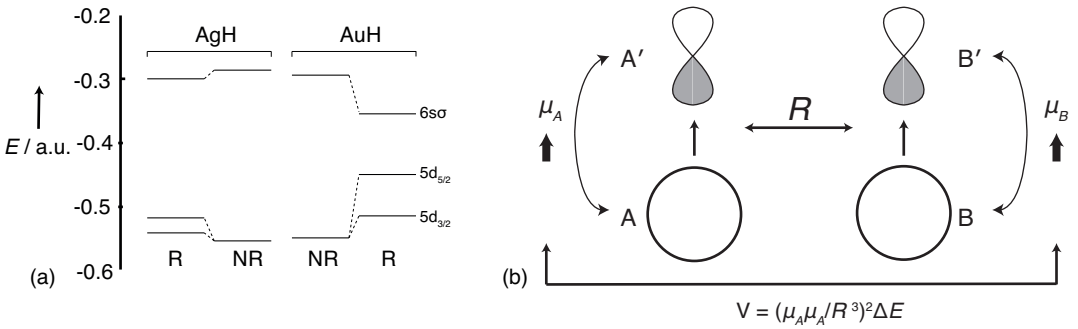

Figure 1.7: (a) Relativistic (R) and non-relativistic (NR) orbital energies for AgH and AuH molecules. Relativistic effects are more significant in determining the differences between gold and silver than the lanthanide contraction. Adapted from Reference 96 with permission from John Wiley & Sons, Inc. (b) Schematic representation of the origin of dispersion interactions: wave-functions A and B mix slightly with excited wavefunctions A′ and B′, respectively, resulting in local dipole moments. Adapted from Reference 108 with permission from The Royal Society of Chemistry.

$100\,\mathrm{kJ\,mol^{-1}}$ for an equilibrium distance $R_e = 2.73\,\text{Å}$, reducing to $D_e \approx 10\,\mathrm{kJ\,mol^{-1}}$ when $R_e = 3.48\,\text{Å}$.[114,116] Crucially, at large R_e the interaction decays as R^{-6} which is typical of dispersive interactions [Figure 1.7 (b)].[114]

Optical properties arising from metallophilic interactions

The photoluminescence of dicyanometallates has been extensively studied and is often closely linked to metallophilicity. The luminescence of the **acs**-structured $\mathrm{Ln/An[Au/Ag(CN)_2]_3{\cdot}}n\mathrm{(H_2O)}$ has been studied extensively and includes emission resulting from interaction of two emissive centres: in particular, energy transfer from $[\mathrm{Au(CN)_2}]^-$ and $\mathrm{Ln^{3+}}$.[117–122] In solution and as a dopant in alkali halide crystals dicyanoargentate and dicyanoaurate give rise to luminescence with a concentration dependence related to aggregation of the dicyanometallate units [Figure 1.8].[123–125] Emission energies are found to be inversely proportional to M$\cdots$M distance* and can be affected by the application of pressure[127] and the binding of ligands.[78]

*This correlation is similarly seen for $[\mathrm{Au(SCN)_2}]^-$.[126]

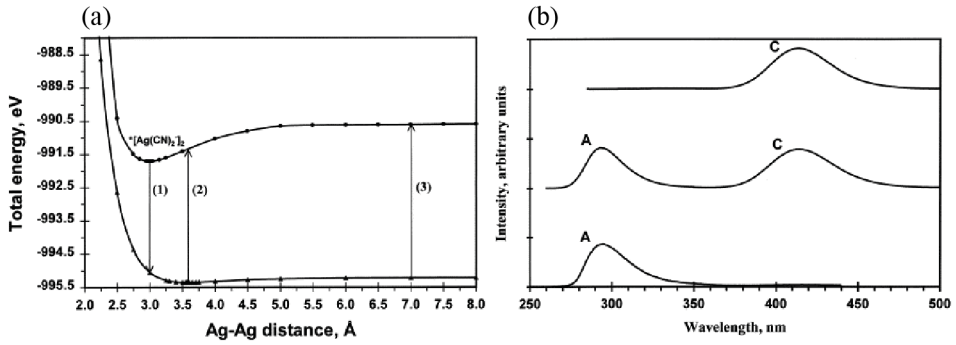

Figure 1.8: The luminescence properties of KCl crystals doped with $[Ag(CN)_2]^-$ depends on dopant concentration. (a) Emission results from excitation to an excited state involving more than one $[Ag(CN)_2]^-$ known as an excimer. Here the potential energy curve for the lowest excited state of $\{[Ag(CN)_2]^-\}_2$ is shown plotted from extended Hückel calculations. The transitions marked are (1) excimer emission (2) solid-state excitation and (3) solution absorption. (b) The emission energy of doped crystals depends on dopant concentration. From bottom to top the concentration increases (0.17, 2.7, and 4.3 % by weight). The band marked A arises from dimers $^*\{[Ag(CN)_2]^-\}_2$ whereas the band marked C arises from trimers $^*\{[Ag(CN)_2]^-\}_3$. Reprinted from H. H. Patterson, S. M. Kanan, and M. A. Omary, *Coord. Chem. Rev.*, **208**, 227–241 (2000).[125] Copyright (2000), with permission from Elsevier Science S.A.

The luminescence of $Zn[Au(CN)_2]_2$ changes on incorporation of ammonia into its structure.[78] Four polymorphs of zinc gold cyanide have been reported (denoted α–δ) and are produced through variation of synthetic conditions. Small changes are sufficient to shift the energy minimum from one polymorph to another—solvent, concentration, counterion, and/or pH can be sufficient in these cases. The α, β, and γ polymorphs are luminescent at room temperature and each show different absorption and emission maxima due to different Au$\cdots$Au distances in their crystal structures (*vide infra*). On exposure to ammonia all four polymorphs are directly (α,δ) or indirectly (β,γ) transformed to $Zn(NH_3)_2[Au(CN)_2]_2$ for which the emission maximum is shifted to a lower energy compared to $Zn[Au(CN)_2]_2$ [Figure 1.9].

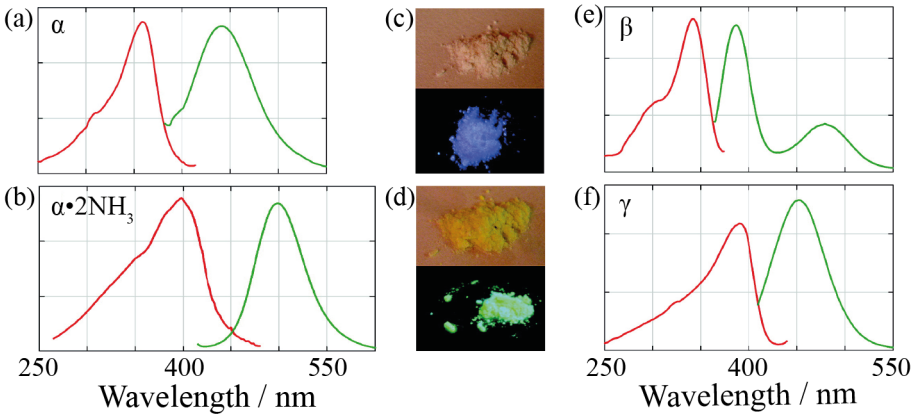

Figure 1.9: The polymorphs of $Zn[Au(CN)_2]_2$ have different luminescent properties which all change in the presence of ammonia. Excitation (red) and emission (green) spectra for (a) α-$Zn[Au(CN)_2]_2$ and (b) after exposure to ammonia yielding $Zn(NH_3)_2[Au(CN)_2]_2$. Corresponding images (c) and (d) show these compounds under visible (top) and UV light (bottom). The excitation and emission spectra of (e) β-$Zn[Au(CN)_2]_2$ and (f) γ-$Zn[Au(CN)_2]_2$ are different again. The variation in these properties arises from the different arrangements of aurophilic interactions. Copyright 2008 American Chemical Society.

1.3 Structural analogies

Many coordination polymers have structures analogous to certain oxides. Indeed we see the polymorphism of silica mirrored in that of $Zn[Au(CN)_2]_2$ despite their very different chemistries: α-$Zn[Au(CN)_2]_2$ consists of six interpenetrating β-quartz-like frameworks; β-$Zn[Au(CN)_2]_2$ has 5-fold cristobalite frameworks; and γ-$Zn[Au(CN)_2]_2$ is also based on cristobalite but is only fourfold interpenetrated due to a prolate distortion of the networks. δ-$Zn[Au(CN)_2]_2$, on the other hand, has a more unusual structure whose topology, based on bridged interwoven (6,3) nets, has been given the RCSR code **mok**.

Compared to silica, in $Zn[Au(CN)_2]_2$ the separation between tetrahedral centres is much greater and the flexibility of the dicyanoaurate linker permits a degree of bending.[77] In the case of α-$Zn[Au(CN)_2]_2$ the size of the framework voids permits

sixfold interpenetration. This interpenetration supports chains of aurophilic interactions linking the six frameworks.[128] These chains can actually be thought of as helices of weak interactions. It turns out that the combination of topology and weak interactions between interpenetrated frameworks is crucial for its structural response to temperature and pressure. While the coefficients of thermal expansion of $Zn[Au(CN)_2]_2$ are perhaps typical for these kinds of compounds—of moderate magnitude and anisotropic ($\alpha_a = +36.91(8)\,MK^{-1}$ and $\alpha_c = -57.58(8)\,MK^{-1}$)*[129]—the response to elevated pressure is more unusual. Under increasing hydrostatic pressure the structure expands in one direction while contracting in the other principal directions. This negative linear compressibility (NLC)† results from the coupling of framework hinging with the extremely compressible helices of aurophilic interactions resulting in compressibilities of $K_a = +52(6)\,TPa^{-1}$ and $K_c = -42(5)\,TPa^{-1}$ up to 1.8 GPa.‡ This 'giant' NLC is dependent on the spring-like arrangement of aurophilic interactions combining geometric and chemical compressibility to give a highly compressible direction [Figure 1.10(a-d)].[77]

In the case of $Zn[Au(CN)_2]_2$ the dicyanometallate linkers gives ∼10 Å separation between metal centres, thus permitting interpenetration of multiple networks. On going to a shorter or bulkier and bent linker the maximum degree of interpenetration is reduced. β-$Zn[Au(CN)_2]_2$ shows fivefold interpenetration of the cristobalite structure whereas $Zn(CN)_2$ and Cd(imidazolate)$_2$ are both only two-fold interpenetrated

*The coefficient of thermal expansion is used to quantify the structural response to temperature. For some arbitrary length this is $\alpha_l(T) = \frac{1}{l}\left(\frac{\partial l}{\partial T}\right)_p$.

†The property of expanding in one direction under application of hydrostatic pressure. The volume compressibility is thermodynamically required to be positive.

‡Where compressibility is defined similarly to coefficient of thermal expansion: $K_l(p) = \frac{1}{l}\left(\frac{\partial l}{\partial p}\right)_T$

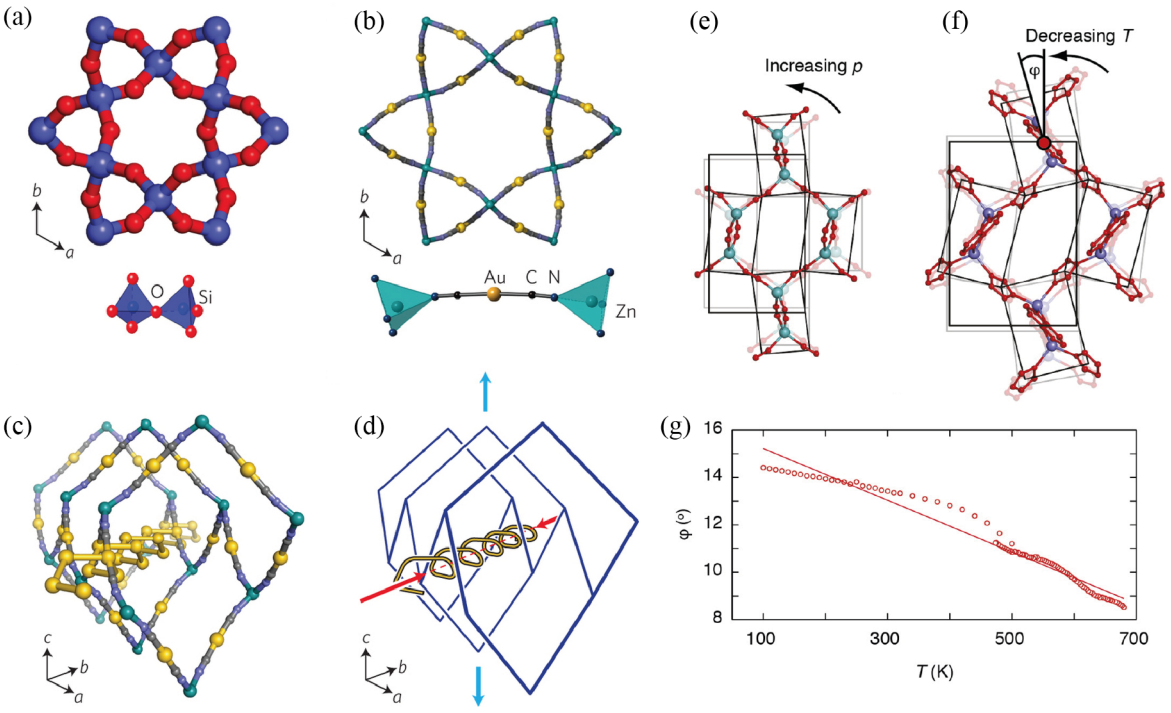

Figure 1.10: (a-d) There is a structural correspondence between quartz (a) and α-$Zn[Au(CN)_2]_2$ (b) The sixfold interpenetration of α-$Zn[Au(CN)_2]_2$ results in helices of aurophilic interactions connecting the frameworks (c). As well as being comparatively weak interactions, their spring-like arrangement makes them extremely flexible. This very compressible direction is coupled *via* framework geometry to give expansion in a perpendicular direction giving 'giant' negative linear compressibility (d). Modified by permission from Macmillan Publishers Ltd: Nature Materials, Reference 77, Copyright 2013. (e-g) The critical behaviour of $Zn(CN)_2$ and Cd(imidazolate)$_2$ is similar due to their common anticuprite topology. At ambient conditions, each net of $Zn(CN)_2$ has the β-cristobalite structure but from 1.52 GPa undergoes a transition to a distorted structure analogous to α-cristobalite (e). On the other hand, the structure of Cd(imidazolate)$_2$ is analogous to β-cristobalite under ambient conditions but the framework geometry becomes more regular (*i.e.* moves towards α-cristobalite) on heating (f) although no phase transition was observed before decomposition. The framework tilt angle decreases smoothly with increasing temperature (g). The crude linear fit was used to estimate a theoretical transition temperature of ~1500 K at which Cd(imidazolate)$_2$ would become cubic. Modified with permission from I. E. Collings *et al.*, *J. Am. Chem. Soc.*, **135**, 7610–7620 (2013). Copyright 2013 American Chemical Society.[130]

(anticuprite topology).[21,131] The shared topology of $Zn(CN)_2$ and Cd(imidazolate)$_2$ leads to similar critical behaviour despite their very different chemistries.[130] That is to say that the response of both systems to temperature/pressure is, to a significant extent, a result of the structure type [Figure 1.10(e-g)]. At ambient conditions, each net of $Zn(CN)_2$ has the β-cristobalite structure but from 1.52 GPa undergoes a transition to a distorted structure analogous to that of α-cristobalite. Conversely, under ambient conditions Cd(imidazolate)$_2$ is analogous to α-cristobalite but the framework geometry becomes more regular—moves towards β-cristobalite—on heating. This pair of compounds demonstrate that, even with rather different chemistries, structure topology can play a crucial role in determining responses to temperature and pressure.

1.4 An aside - classification of topology

Topological descriptors have become an increasingly important part of characterising the structures of coordination polymers and their usage is actively encouraged by IUPAC.[42,132,133] As well as being essential for describing particularly complex structures they can be a useful tool for mapping structure and properties across systems with very different compositional motifs (Section 1.3).[130] Topology assignment can be carried out manually for simple systems by analogy to canonical systems. There is often a trade-off between simplicity and specificity of topological descriptors, with some functioning simply as names as for the **abc** codes of the Reticular Structure Chemistry Resource (RCSR).*[132] The oldest notation applied to chemical problems

*There is not space here to discuss the interesting issue of ambiguity in topology assignment for coordination polymers.[134]

is due to A. F. Wells. Wells' notation is used for uniform nets* and is straightforward to assign but ambiguous: (n,p) where n is the number of nodes in the shortest circuit and p is the connectivity of the nodes.[135] For example there are a number of (10,3) nets—that is 3-connected nets that are based on 10-gon circuits—with the two most common denoted (10,3)-a ($SrSi_2$, **srs**) and (10,3)-b ($ThSi_2$, **ths**) [Figure 1.11].[135]

Point symbols and vertex symbols are less ambiguous for describing 3-periodic nets than Wells' notation but may still occasionally be ambiguous. Point symbols are based on shortest cycles and vertex symbols on shortest rings.[133] A cycle is a set of vertices linked by edges in which the only vertex that repeats is the first/last. A ring is a cycle that is not the sum of two smaller cycles [Figure 1.12].[133] In both cases, the symbols are defined with respect to the cycles/rings present at each angle of a vertex. Point symbols are of the form $A^a.B^b...$ where there are a angles with shortest cycles that are A-cycles and b angles with shortest cycles that are B-cycles and so on.

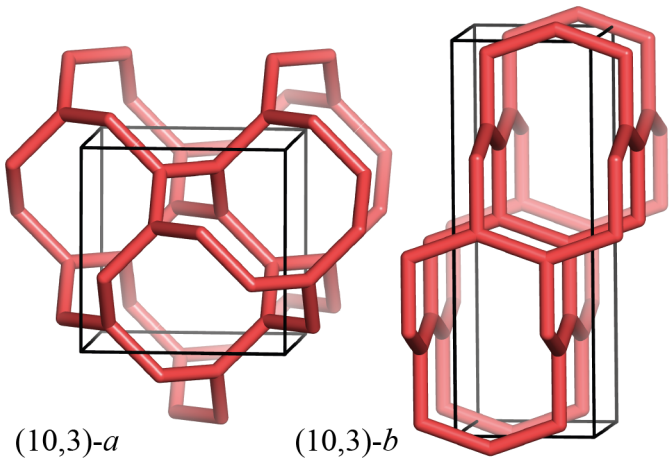

Figure 1.11: The highest symmetry embeddings of two possible (10,3) nets. The RCSR label for the chiral net (10,3)-a is **srs** and for (10,3)-b is **ths**.[132]

*Nets where all the shortest cycles at each angle at a vertex are of the same length.

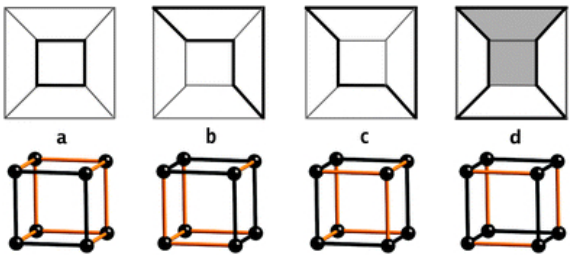

Figure 1.12: Point symbols are based on shortest cycles and vertex symbols on shortest rings. All rings are cycles but not all cycles are rings. This point can be illustrated with a cube. The cycles are illustrated in bold on the Schlegel diagrams (top) and in black on the cubes (below). (a) This 4-cycle is a strong ring (b) this 6-cycle is the sum of two 4-cycles so therefore not a ring (c) this 6-cycle is the sum of three smaller rings, but not of two, and therefore a ring (but not a strong ring) (d) this 8-cycle is not a ring as it is the sum of two smaller cycles: a 6-cycle (shaded) and a 4-cycle. For completeness, strong rings are cycles that are not the sum of any number of smaller cycles. Reproduced from Reference 133 with permission from The Royal Society of Chemistry.

This means that the net called (10,3)-a by Wells has the point symbol 10^3.[133] Vertex symbols can appear superficially similar but are quite different; Vertex symbols are of the form $A_a.B_b.C_c...$ indicating that at the first angle there are a shortest rings that are A-rings, at the second angle there are b shortest rings that are B-rings, at the third angle there are c shortest rings that are C-rings, and so on. This means that the (10,3)-a has the Vertex symbol $10_5.10_5.10_5$. In other words, there are 15 10-rings meeting at each vertex in the (10,3)-a net. Details of subtleties regarding these notations can be found in Reference 133; a mixture of topology notations will be used in this thesis depending on the familiarity of the topology in question.

1.5 Perovskite-structured compounds

The mineral Perovskite, $CaTiO_3$, lends its name to an enormous family of compounds which share a similar structure. Oxide perovskites are perhaps one of the best studied and most important classes of materials. Perovskites and perovskite-related materials support an incredible set of properties of significant academic

interest and technical importance: ferroelectricity,[136] piezoelectricity,[137] ferromagnetism,[138] colossal magnetoresitance,[139] superconductivity,[140] and ionic conductivity are some of the most important.[141] The archetypal high-symmetry perovskite $SrTiO_3$ crystallises in space group $Pm\overline{3}m$ at room temperature. This structure can be thought of as an array of corner-sharing TiO_6 octahedra with Sr^{2+} ions occupying the centre of the interstices thus formed. The deceptive simplicity of this structure belies the structural and chemical diversity that can be supported by the perovskite structure. Through judicious choice of the components in an ABX_3 perovskite it is possible to target particular modifications of the perovskite structure and, along with them, particular properties.

The perovskite structure type is also important for compounds with very different chemistries. Ammonium halide perovskites have, since mid 2012, been the focus of sustained attention due to their excellent performance as photovoltaics;[142] formate perovskites have been investigated as ferroelectrics;[143] and azide perovskites have received attention for switchable dielectric properties.[144] It is becoming increasingly apparent that the tools developed to understand the structural distortions and stability of oxide perovskites are of utility in understanding perovskites with molecular components.[145,146]

1.5.1 Tolerance factor

One of the most interesting features of the ternary perovskites, ABX_3, is their propensity to undergo structural distortions away from the ideal perovskite structure. These distortions include tilting of octahedra, displacements of the B cation(s), and changes in B—X bond lengths (*i.e.* distortion of octahedra).[147,148] Of these, oc-

tahedral tilting is the most common and occurs when the A cation is too small for the cuboctahedral site formed by the network of BX_6 octahedra. The combinations of ions which may form the perovskite structure were considered by Goldschmidt in the early 20th-century in terms of the packing of hard spheres.[18] The propensity for a perovskite structure to form was parameterised as the 'tolerance factor':

$$\alpha = \frac{(\boldsymbol{r}_{\mathrm{A}} + \boldsymbol{r}_{\mathrm{X}})}{\sqrt{2}(\boldsymbol{r}_{\mathrm{B}} + \boldsymbol{r}_{\mathrm{X}})}, \tag{1.1}$$

where $\boldsymbol{r}_i$ is the ionic radius of ion i. This semi-empirical geometric approach is rather successful, especially with better estimates of ionic radii than were available to Goldschmidt,[149] and is still used to guide the synthesis of perovskites. Almost all known oxide perovskites have tolerance factors of 0.75-1.00 with those falling below 0.9 more likely to have structures distorted by octahedral tilting. Below 0.75 a variety of other structures, such as ilmenite, become favoured. Values greater than 1, with an A cation that is too large, give hexagonal structures with columns of face sharing octahedra; the archetypal compound is $BaNiO_3$.[150]

While the tolerance factor captures the majority of perovskite phases within the range of 0.75–1.00, lying within this range is a necessary but not sufficient condition for perovskite formation. By combining the tolerance factor with the 'octahedral factor' $\mu = \boldsymbol{r}_{\mathrm{B}}/\boldsymbol{r}_{\mathrm{X}}$ the vast majority of the oxides and halides that do not behave as expected from their tolerance factor can be accounted for [Figure 1.13].[151,152] The octahedral factor is essentially a restatement of Pauling's radius ratio rules—the BX_6 octahedron as the basic building unit must, itself, pack appropriately—and it therefore fails most often for the least 'ionic' systems such as $TlPbI_3$.[152,153] Very

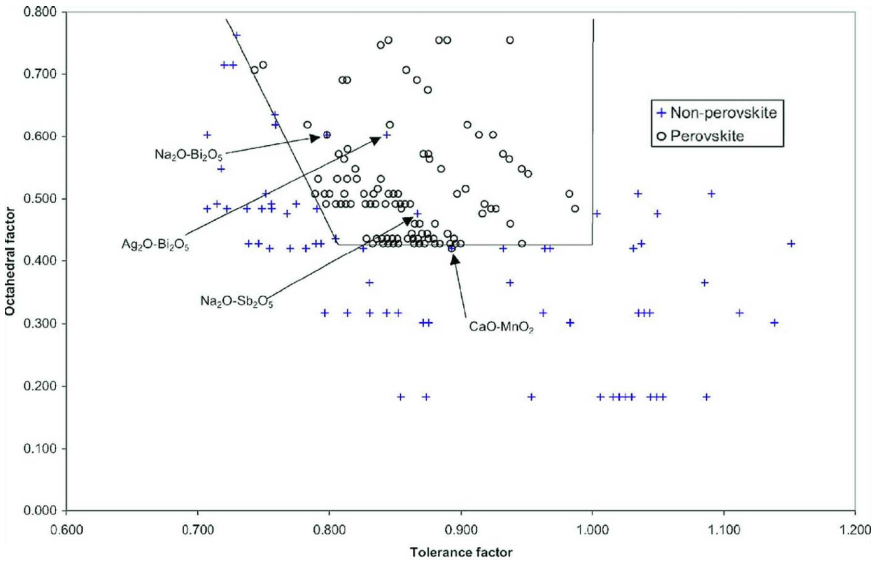

Figure 1.13: Plot of tolerance factor versus octahedral factor showing the stability region for perovskite formation for oxide perovskites.[152] The octahedral factor provides both a minimum cut-off (where the anions are too big to form octahedra with the given B cation) and a region in which perovskites can be formed with small tolerance factors as long as their octahedral factor is sufficiently large. Reproduced with permission of the International Union of Crystallography from Reference 152.

recently these cases have been accounted for by defining anion-dependent radii.[154]

The use of larger X anions has the potential to allow for chemical diversity on the A-site that is impossible for oxides. For $\alpha = 1$ and essentially the largest possible monoatomic B and X ($Pb^{2+} = 1.19\,Å$ and $I^- = 2.20\,Å$)[149] the largest A-site cation ($\boldsymbol{r}_A \sim 2.6\,Å$) equates to those with three or fewer C–C or C–N bonds.[145] While halide perovskites with small organic A cations ('inorganic-organic hybrid' perovskites) have been known since at least 1884,[155] and their structural chemistry extensively investigated,[145,156,157] they have received particular attention since 2012 due to their excellent performance in photovoltaic devices.[142]

1.5.2 Tolerance factors for molecular perovskites

With increasing size, conformational flexibility, and non-ionic interactions in molecular perovskite analogues it becomes increasingly difficult to define self-consistent,

let alone meaningful, radii. 'Thermochemical radii' have been derived for polyatomic anions from thermodynamic data for some time,[158–160] but the values for even highly symmetric cations such as NH_4^+ are heavily dependent on their anionic partner.[149] These problems have likely contributed to tolerance factors only relatively recently being applied to perovskites with molecular components.[145,146,154,161] An extended tolerance factor approach has, however, been useful in guiding syntheses of perovskites such as $[CH_3NH_3]Ca(BH_4)_3$[162] and values have been calculated for perovskites with a large range of molecular cations and X = formate, azide, cyanide, and borohydride.[161,163] In Kieslich's method,[146] Goldschmidt's tolerance factor is adapted for use with effective radii of molecular species and will now be summarised. Treating molecular species as hard spheres or rods rotating about their centre of mass, effective radii can be calculated by measuring the radius from the centre of mass of the species to the outermost atom (from crystallographic data) and then adding, to this number, the radius of the outermost atom. For example $\boldsymbol{r}_{\mathrm{A_{eff}}} = \boldsymbol{r}_{\mathrm{A_{mass}}} + \boldsymbol{r}_{\mathrm{A_{ion}}}$. Combining this approach with Goldschmidt's we have:

$$\alpha = \frac{(\boldsymbol{r}_{\mathrm{A_{eff}}} + \boldsymbol{r}_{\mathrm{X_{eff}}})}{\sqrt{2}(\boldsymbol{r}_{\mathrm{B}} + 0.5\boldsymbol{h}_{\mathrm{X_{eff}}})}, \tag{1.2}$$

where $\boldsymbol{h}_{\mathrm{X_{eff}}}$ is the length of the molecular linker, which is modelled as a rod of uniform radius [Figure 1.14(a-c)].[146]

Halide perovskites exist with a similar range of tolerance factors (0.8–1.0) as oxides. Where the A cation is too large ($\alpha > 1$) low dimensional compounds with perovskite-like building units are formed. $C_7H_7PbI_3$, for example, is a 1D material with chains of face-sharing PbI_6 octahedra separated by tropylium[164] and

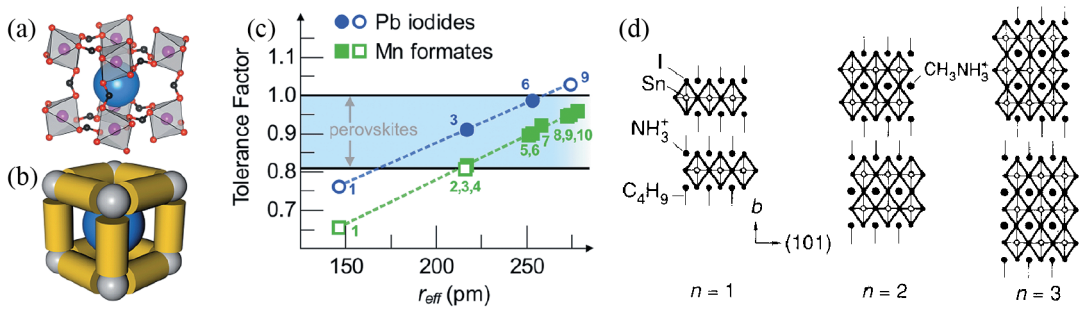

Figure 1.14: (a) A tilted formate perovskite showing the A cation as a hard sphere. (b) An example of the abstraction used for defining molecular ion radii within a molecular perovskite: the molecular linkers are shown as yellow rods where $\boldsymbol{r}_{\mathrm{A_{eff}}}$ is the radius of the rod and $\boldsymbol{h}_{\mathrm{X_{eff}}}$ half its length. (c) Tolerance factor versus A cation radius for some lead iodide and manganese formate compounds. Hollow symbols indicate non-perovskite phases. Reproduced from Reference 146 with permission from The Royal Society of Chemistry. (d) Schematic of ammonium halide analogues of Ruddlesden-Popper phases with the rocksalt layer replaced by a double layer of alkyl chains. $((C_4H_9)NH_3)_2(CH_3NH_3)_2Sn_3I_{10}$ is an example of an $n = 3$ structure. Modified by permission from Macmillan Publishers Ltd: Nature, Reference 156, copyright (1994).

$(C_2H_5NH_3)_2CuCl_4$, a magnetic multiferroic,[165] contains layers of corner-sharing $CuCl_6$ octahedra separated by ethylammonium.[166] Furthermore, replacing half of the large protonated amines with a suitably small cation gives Ruddlesden-Popper analogues such as the conductor $((C_4H_9)NH_3)_2(CH_3NH_3)_2Sn_3I_{10}$ ($n = 3$) in which blocks of $(CH_3NH_3)SnI_3$ (tolerance factor between 0.8-1.0) are separated by layers of the larger organic cation.[156] The $n = 3$ Ruddlesden-Popper phase $Sr_4Ti_3O_{10}$ is made up of alternating rocksalt and perovskite layers,[167] with n referring to the thickness of the perovskite layer. $((C_4H_9)NH_3)_2(CH_3NH_3)_2Sn_3I_{10}$ has the same stacking of perovskite blocks but the AB rocksalt layer is instead filled by a double layer of n-butylammonium chains [Figure 1.14(d)].

1.5.3 Limitations of the tolerance factor for molecular perovskite analogues

While the tolerance factor approach applied to molecular perovskite analogues is rather powerful, there are certainly confounding factors.[154] A recent example in the formate family will be illustrative of the delicate balance of interactions resulting in deviations from the structure type predicted by the tolerance factor. The compounds $NH_3NH_2B(HCOO)_3$ where B is Mn^{2+}, Zn^{2+}, Co^{2+}, or Mg^{2+} have tolerance factors between 0.81-0.85 and so would all be expected to form perovskites. However, prior to the work of Kieslich *et al.*,[168] the Mn^{2+} and Zn^{2+} compounds had been reported to form perovskite-like frameworks with $4^{12}{\cdot}6^3$ topology whereas the Co^{2+} and Mg^{2+} compounds formed a structure with hexagonal channels and $4^9{\cdot}6^3$ topology. The latter is a structure type common for analogous compounds with small A = protonated amines such as NH_4^+ and NH_3OH^+.[169,170] DFT calculations showed that the two structures lie very close in energy for $NH_3NH_2Zn(HCOO)_3$ but that the channel structure is favoured at higher temperatures.[168] The calculations suggested that the crucial factor is the increased vibrational entropy from weakened hydrogen bonding in the channel structure. This vibrational entropy is a feature of the molecular A and X components being able to support H-bonding in these perovskites and it is reasonable to expect there to be other confounding factors for molecular perovskites with different chemistries. Just as the understanding of structural and mechanical effects of H-bonding in $NH_3NH_2Zn(HCOO)_3$ have begun to be

understood by analogy to salt bridges in biological and artificial helical polymers* it seems reasonable to anticipate that other supramolecular interactions, and orderings thereof, may also be important for molecular perovskites.[172,173]

1.5.4 Octahedral tilting in perovskites and related phases with octahedral coordination

Rotation of MO_6 octahedra in oxide perovskites is a common structural distortion from the aristotype ABX_3 structure. There is renewed interest in controlling such distortions in perovskites in light of recent work exploiting symmetry relationships to engineer specific physical properties, notably polarisation.[174,175] These distortions are reflective of the inherent degrees of freedom of perovskites. The condensation of soft-phonon modes in perovskite-structured materials upon lowering temperature results in a phase transition to a structure of lower symmetry. The 'aristotype' is the phase with the highest possible symmetry and those lower symmetry phases related by removing symmetry elements (group-subgroup relation) are known as 'hettotypes'.[147] Tilting of octahedra around one or more of their symmetry axes strictly retains the corner connectivity and, to a first approximation, the regularity of the octahedra. In this way, tilting allows variation in the environment of the A-site cation at the same time as the environment of the B-cation remains essentially identical.

The combination of rotations known as a 'tilt' system can be described compactly using Glazer notation $a^{\#}b^{\#}c^{\#}$. The letters a, b, and c indicate the three

*'Salt bridges' are short-range electrostatic interactions that play an important role in stabilising entropically unfavourable conformations in proteins.[171] The amine cation in $NH_3NH_2Zn(HCOO)_3$ contributes to framework stability and mechanical properties both through hydrogen bonding and short-range electrostatic interactions.

(pseudo-)cubic axes* around which rotations may occur: [100], [010], and [001]. a, b, and c indicate tilts of different magnitudes, so where tilts are of the same magnitude then the same letter is repeated. The superscript # indicate correlation of tilts along the tilt axis and can be $+, -$, or 0. There can be positive correlation along the tilt axis ('in-phase', '+', octahedra are rotated in the same sense), negative correlation along the tilt axis ('out of phase', '$-$', octahedra are rotated in alternating sense), or no tilt ('0'). Transitions between different tilt systems are a very important aspect of the phase behaviour of perovskites. $NaTaO_3$, for example, goes through a series of phase transitions driven by octahedral tilting,[176,177]

$$\underset{(a^-a^-c^+)}{Pbnm} \overset{720\,\mathrm{K}}{\leftrightarrow} \underset{(a^0b^-c^+)}{Cmcm} \overset{835\,\mathrm{K}}{\leftrightarrow} \underset{(a^0a^0c^+)}{P4/mbm} \overset{809\,\mathrm{K}}{\leftrightarrow} \underset{(a^0a^0a^0)}{Pm\overline{3}m}.$$

A very similar series of transitions is observed for $SrZrO_3$,[178,179] $SrHfO_3$,[180] and $CaTiO_3$ which go *via* $I4/mcm$ ($a^0a^0c^-$) instead of $P4/mbm$ ($a^0a^0c^+$).[181]

There are significant constraints on the tilt systems that are possible in oxide perovskites as a consequence of the oxide anion being monoatomic: for example a rotation around **a** must be anti-correlated along **b** and **c** to avoid 'breaking' the oxide linkage.[182] Glazer originally identified 23 tilt systems but a group-theoretical approach has more recently been used to show there are only 15 possible tilt systems for 'simple' tilts—that is where those in which tilts around a particular axis have the same magnitude and the same (+) or alternating (−) signs—that are distinct in symmetry†.[184,185] The transformations between these tilt systems are shown in

*For many systems these axes will not be collinear with the unit cell axes unless a transformation is applied.

†More explicitly this means that the superposition of two tilts cannot be described by Glazer notation. This, most straightforwardly, manifests as an alternating pattern where the centre of

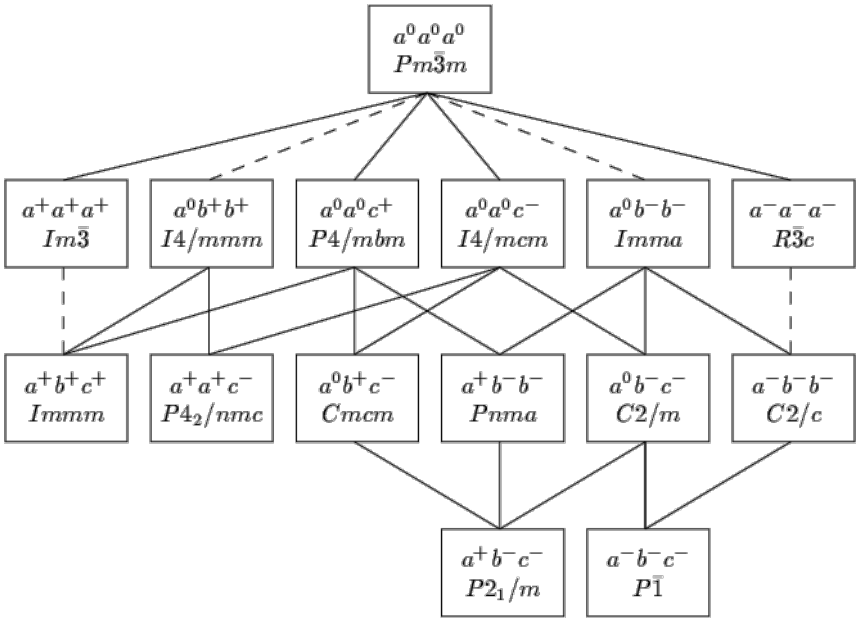

Figure 1.15: A diagram indicating group-subgroup relationships between the 15 space groups identified by Howard and Stokes[185] that can be formed by octahedral tilting alone in ABO_3 perovskites. A dashed line indicates that the corresponding transition is required to be first order by Landau theory. Reproduced with permission of the International Union of Crystallography.[185]

Figure 1.15. For tilts in oxide perovskites we can make some general statements: (i) tilting around an axis will automatically result in a doubling of the periodicity along the perpendicular axes, (ii) out of phase tilting around an axis will also result in a doubling of the periodicity along that same axis, (iii) any kind of tilting will result in a reduction in the distance between the centres of adjacent octahedra along axes perpendicular to the tilt axis, and (iv) where tilting occurs along more than one axis the crystal system of the structure will be lowered by a change in interaxial angles.[184,185]

The correlated rotation of octahedra in oxide perovskites can be explicitly described in terms of propagation wave-vectors. In principle, octahedral tilts around

mass is away from the untilted position. The alternative notation of Aleksandrov appears to be have been the first to address this.[183] The tilts along the 3 axes are denoted with a sequence of three symbols that can be 0 (no-tilt), ψ (in-phase tilt), ϕ (out of phase tilt), or Δ ($= \phi + \psi$).

the **a** axis can propagate with wave-vector $\mathbf{k}_a = [k_1, \frac{1}{2}, \frac{1}{2}]$: the sense of rotation strictly alternates within the [100] plane but rotations between neighbouring (100) planes can correlate with arbitrary periodicity along [100].* Tilts around **b** and **c** are similarly constrained to $\mathbf{k}_b = [\frac{1}{2}, k_2, \frac{1}{2}]$ and $\mathbf{k}_c = [\frac{1}{2}, \frac{1}{2}, k_3]$, respectively; to first order for small rotations these three tilt systems can operate independently. Taken together, this means that all physically realisable tilt systems of conventional perovskites can be represented by the three wave-vector components k_1, k_2, k_3 and the parameters $\epsilon_1, \epsilon_2, \epsilon_3 \in \{0, 1\}$ which represent whether a tilt axis is active ($\epsilon = 1$) or not ($\epsilon = 0$). Empirically, the overwhelming majority of tilt systems correspond to the special cases of 'in-phase' ($k_i = 0$) and 'out-of-phase' tilts ($k_i = \frac{1}{2}$), although exceptions have been known for some time.[186] The most common exception derives from a distortion with $k_2 = \frac{1}{4}$ and is seen in phases (P)-$NaNbO_3$,[187] $AgNbO_3$,[188] $Na_2MoO_{2-\delta}F_{4+\delta}$,[189] $BiFe_{0.75}Mn_{0.25}O_3$ above 6 GPa,[190] and $(Ca_{0.37}Sr_{0.63})TiO_3$.[182†] More complex cases are known such as that of (S)-$NaNbO_3$ where more than one propagation vector is active which will be discussed below.[191] Remaining with simple tilts for the moment, the '+/0/−' components of Glazer notation reflect the special cases that describe most oxide tilt systems:

$$\begin{array}{lll} + & \epsilon_i = 1 & k_i = 0 \\ 0 & \epsilon_i = 0 & \\ - & \epsilon_i = 1 & k_i = \frac{1}{2} \end{array} \quad .$$

Or, equivalently, the Glazer symbol g_i is given by $\epsilon_i \exp[2\pi \mathrm{i} k_i]$.

*A restatement of (ii) in the previous paragraph.

†This has been described as the compound tilt sequence $(a^-b^+a^-)_1^2(a^-b^-a^-)_2^3(a^-b^+a^-)_3^4$, or equivalent in relevant basis, where $(\mathbf{a}^i\mathbf{b}^j\mathbf{c}^k)_x^y$ describes the relationship between layers x and y.[184]

The case of (*S*)-$NaNbO_3$ will be used to illustrate two cases of octahedral tilting that do not fit the special periodicities implied in Glazer notation. Firstly, when periodicities above $\frac{1}{2}$ are involved, the phase of the wave-vector is ambiguous with respect to the exact active tilt system. The notation developed by Peel *et al.* has been used to resolve this ambiguity.[191*] For example in a tetragonal $2a_p \times 2a_p \times 4a_p$ supercell of a perovskite there are two possible tilt modes arising from the T_4 symmetry irreps (*i.e.* both having the same periodicity). These correspond to 'A0C0' and 'AACC' where the tilts around and along the given axis are denoted as either clockwise (C), anticlockwise (A), or zero (0) and the magnitudes of the 'A' and 'C' rotations are constrained by symmetry to be equal [Figure 1.16]. In the case of (S)-$NaNbO_3$ this ambiguity was resolved experimentally through careful analysis of peak splitting in neutron diffraction patterns.[191] The full description of the tilts turned out to be substantially more complicated and illustrates the second case that Glazer notation cannot describe—the superposition of multiple tilt correlations along the same axis—compound tilts.[183,192] (S)-$NaNbO_3$, in *Pmmn*, is found to have a tilt system $a^+b^+c^*$ where c^* corresponds to approximately '0CAC'.[†] This *compound* tilt system arises as a result of the superposition of multiple irreps along the same axis: $R_4{}^+$, $M_3{}^+$, and T_4 contributing ACAC, CCCC, and A0C0 respectively.[191]

Octahedral tilts are also important structural motifs in non-oxide perovskites and non-perovskite structured materials.[163,193–196] For perovskite related materials

*Glazer's compound tilt sequences can be used to describe some, but not all, of these tilt systems.

[†]Approximately this tilt sequence as 'A' and 'C' are here not constrained to have the same magnitude.

it can be possible to conduct the same kind of analysis as has been carried out for perovskites. ABX_4 compounds with monoatomic X, for example, have 75 possible tilt systems and the group-subgroup relationships of these have been enumerated.[193] This family with the $TlAlF_4$ structure type[197] form an important conceptual link to molecular perovskite analogues where correlations between tilts are substantially reduced by the use of long anions. Compounds such as $RbFeF_4$ consist of layers or corner-sharing FeF_6 octahedra separated by Rb cations and also undergo phase transitions involving the condensation of zone-boundary soft phonons.[198–201] In this structure some of the constraints on tilting have been lifted: the individual layers are constrained in exactly the same way as a perovskite but now the tilts of the layers are partially decoupled from one another. These layer-decoupled tilt systems can be denoted using a modified tilt system, $\mathbf{a}_u^i\mathbf{b}_v^j\mathbf{c}^k$, where u, v refer to the tilt around [100] and [010] respectively and can be parallel (p) or antiparallel (a) in alternating (001) layers.[197] This notation is not sufficient to describe the variety of tilts that are possible in the antifluorites A_2BX_6, such as ferroelastic K_2TeBr_6,[202,203] where

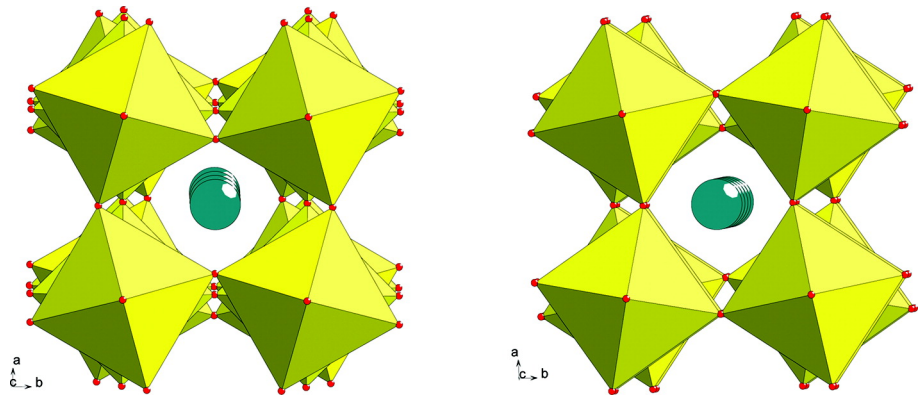

Figure 1.16: Two possible tilts modes propagating with wave-vector $\mathbf{k} =< \frac{1}{2}, \frac{1}{2}, \frac{1}{4} >$. These can be denoted 'A0C0' (left) and 'AACC' (right), In this case, (S)-$NaNbO_3$, these two tilts systems would transform as the same irreducible representation. Reprinted with permission from Peel, M. D. *et al.*, *Inorg. Chem.*, **2012**, *51*, 6876–6889. Copyright 2012 American Chemical Society.[191]

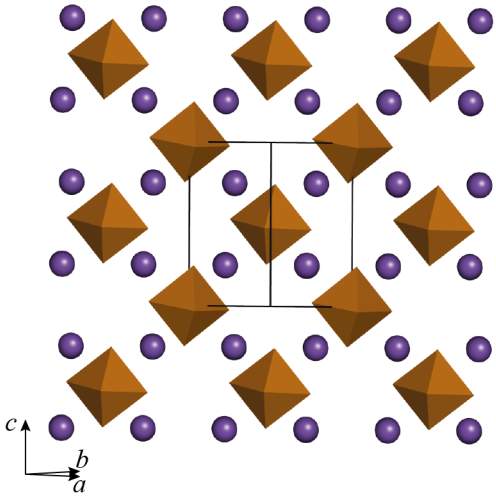

Figure 1.17: A layer of the crystal structure of $P2_1/n$ phase of K_2TeBr_6. The mechanically separated octahedra are free to tilt in the same direction within a layer as shown here where they are all tilted clockwise around the direction of view.[203]

the octahedra are isolated from one another.[204] K_2TeBr_6 has the following phase transitions,

$$P2_1/n \overset{400\,\mathrm{K}}{\leftrightarrow} P4/mnc \overset{434\,\mathrm{K}}{\leftrightarrow} Fm3m$$

in which the $P2_1/n$ phase has layers of octahedra rotated in the same direction [Figure 1.17].

Metal-Oxide Organic Layer structures, a type of metal-oxide organic framework (MOOF)* share a close conceptual link to the ABX_4 oxides: they consist of layers of corner-sharing ML_6 octahedra connected by an organic linker.[205] In this sense the tilts within the layers are constrained in exactly the same way but the correlation between layers may be decoupled. The tilts of $V^{III}{}_2(OH)_2F_3(bdc)$, or MIL-71,[206] and related MOOFs can be characterised in exactly the same way as $RbFeF_4$ [Figure 1.18]. While these compounds could, in principle, adopt a large number of tilt systems, all compounds where octahedra are linked by bdc are severely constrained

*A class of MOFs distinguished by their extended metal-oxide component.

by the small bite angle of the dicarboxylate necessitating at least one tilt; the two bridged octahedra must tilt significantly towards each other.[205] Not only does this ligand-induced tilting propagate through the layers but it is also reproduced in the next layer, thus usually only giving tilt systems that may be found in oxide perovskites.

Demonstrating the importance of extra-framework species, the evacuated (empty pore) MIL-47 (analogous to ReO_3) only shows conventional tilts whereas the as-synthesised version, MIL-47*as*, which contains guest terephthalic acid molecules

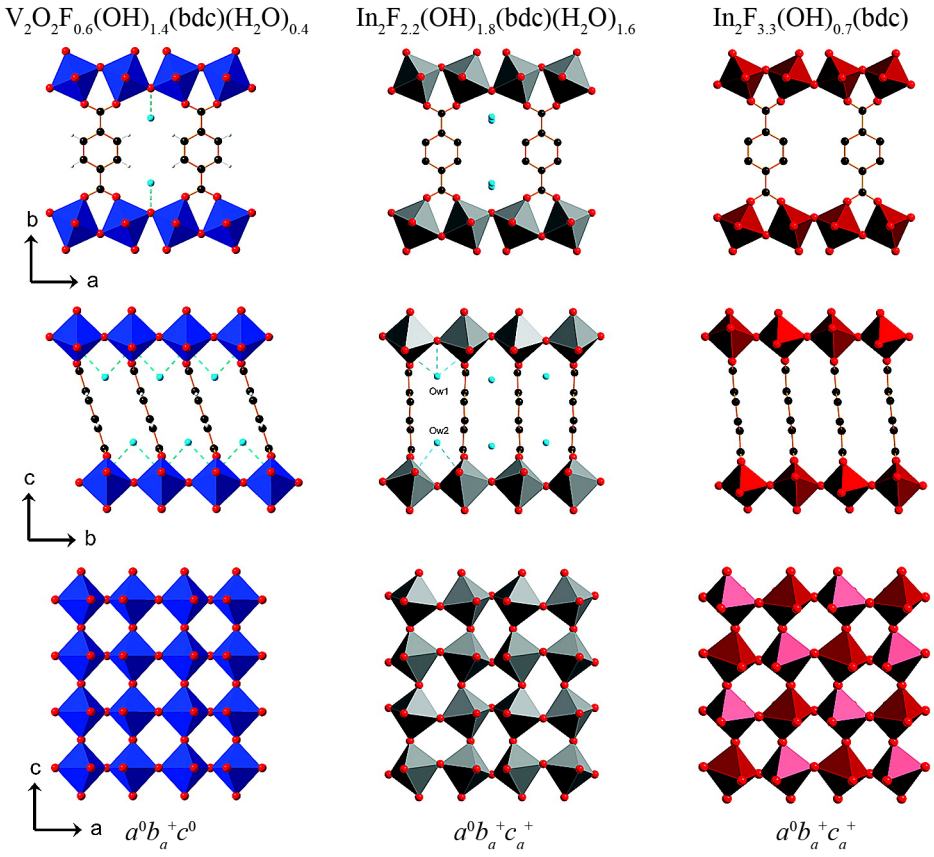

Figure 1.18: Tilt systems of some layered metal-oxide organic layer structures. While, in principle, the tilts do not need to be correlated from layer to layer the nature of the organic linker (bdc) enforces tilts analogous to those found for oxide perovskites.[205] Adapted with permission from M. Vougo-Zanda *et al. Inorganic Chemistry*, **2008**, 47, 4746–4751. Copyright 2008 American Chemical Society.

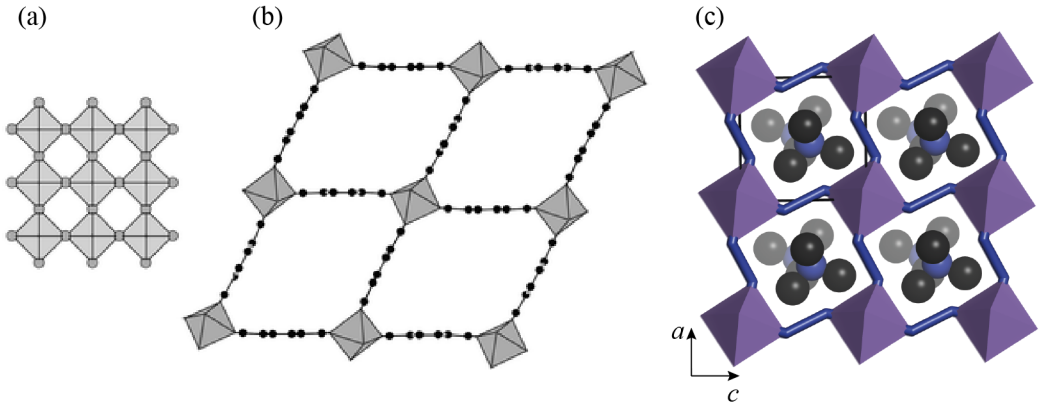

Figure 1.19: Projections of the ReO_3 structure (a) and MIL-47 (b) structures. Reproduced from Ref. 209 with permission from The Royal Society of Chemistry. (c) View of $[N(CH_3)_4]Mn(N_3)_3$ showing the in-plane in-phase tilting made possible by the molecular linkers. Mn octahedra shown in purple, N in blue, C in black.[210]

(H_2bdc), tilts in a way that would be impossible for oxides [Figure 1.19(a,b)].[207] The indium analogue of MIL-47*as*, In(OH)bdc·0.75Hbdc_2, shows the same kind of column tilts and careful single crystal work has shown it to be a 'Vernier' structure* where the two different sublattices, which have different periodicities, interact weakly through guest-framework hydrogen bonding.[208] The tendency towards conventional tilt systems in the evacuated compounds would be relieved by using a monodentate ligand or one with a larger, preferably flexible, bite angle. The restrictive effect of intra-chain bridging by dicarboxylates on possible tilts can also be seen for the analogous compounds similarly based on chains of octahedra such as the porous 'breathing' MIL-53 family.[72]

There are an increasing number of molecular perovskite analogues with unusual octahedral tilts in the literature,[144,211–213] but are only just (as of April 2016)[210] beginning to be discussed as such.[210] $[N(CH_3)_4]Mn(N_3)_3$, for example, shows that with appropriate molecular components it is possible for tilts to correlate with pe-

*Named after the Vernier scale in which measurements can be performed more accurately by the use of two offset scales.

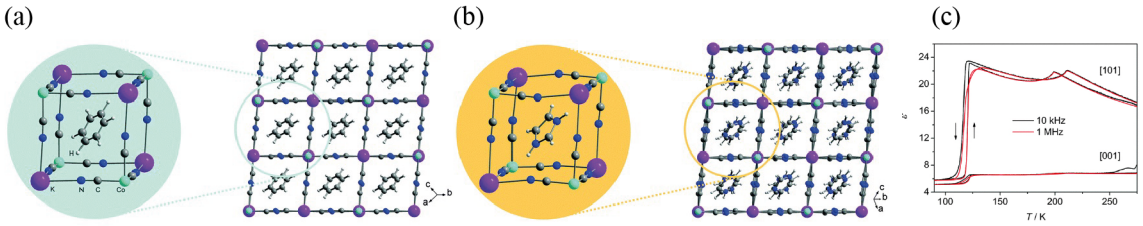

Figure 1.20: Crystal structures of $(HIm)_2[KCo(CN)_6]$ with dielectric constant. (a) High temperature $R\bar{3}c$ structure with all imidazolium ions aligned along the 3-fold rotational axis but rotationally-averaged. (b) Low temperature $C2/c$ showing ordering of imidazolium and concomitant distortion of the framework. (c) Temperature dependence of dielectric constants for different crystallographic directions. This shows that the dielectric transition occurs only in the plane perpendicular to the [001] direction in $R\bar{3}c$ (*i.e.* the 3-fold axis) in the high-T phase. The confinement of the imidazolium within the perovskite framework results in dielectric behaviour resembling a 2D liquid of polar molecules.[173] Adapted from Reference 173 with permission of The Royal Society of Chemistry.

riodicities that would be impossible for oxides [Figure 1.19(c)].[210] This compound and related azides and cyanides show rich phase behaviour involving disordering of tilts as well as cation order/disorder and displacement.[144,212] This can give rise to, for example, a switchable dielectric constant in $(HIm)_2[KCo(CN)_6]$ resulting from the order/disorder behaviour of the disk-shaped $[HIm]^+$ and concomitant framework distortion [Figure 1.20].[173]

It is becoming increasingly apparent that the interplay between molecular A-site cations and the host framework is crucial in determining the properties of many molecular perovskite analogues. To give one more example, coupling between inorganic and organic degrees of freedom in the lead halide perovskites[142] plays a crucial role in determining their band structure[214] and is implicated in the slow recombination of charge carriers.[215,216] Both of these factors are essential in their use in solar cells with over 20 % efficiency.[217] More specifically, the orientational preferences (and dynamics thereof) have been shown computationally[215] and with quasi-elastic neutron scattering[216] to be intimately coupled to framework deformations which in turn

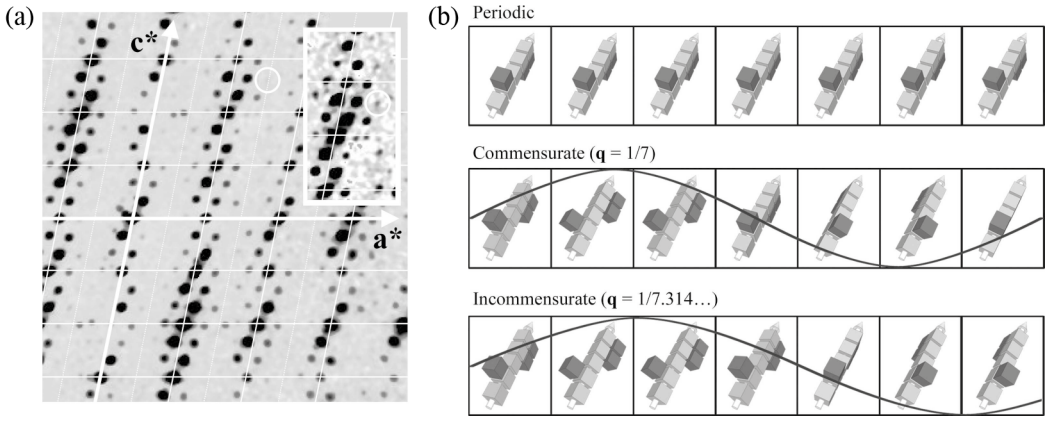

Figure 1.21: (a) A reconstruction of the ($h2l$) reciprocal plane in γ-Na_2CO_3. The white circle indicates the position of the fifth order satellite (2215), which is visible in the inset (shown at a different scale).[218] (b) Schematic representations of periodic, commensurately modulated, and incommensurately modulated crystal structures. The modulation results from rotation about the long axis of the macromolecule.[219] Both parts reproduced with permission of the International Union of Crystallography.[219]

acutely affect the band gap of the material.

1.6 Modulated and aperiodic structures

Modulated phases are crystalline but have some extra periodicity that cannot be accounted for in the parent unit cell. Experimentally this manifests as extra Bragg peaks, known as satellites, that cannot be indexed on the main cell [Figure 1.21(a)]. If these extra Bragg peaks can be indexed on fractions of integer hkl values then the modulation is 'commensurate' but if they cannot then it is 'incommensurate' and the periodicity of the unit cell and the extra periodicity will never match [Figure 1.21(b)]. Commensurate modulation can usually be thought of as an extension of the unit cell. For example, a modulated phase with peaks at $\frac{h}{4}$, $\frac{k}{4}$, $\frac{l}{4}$ could be modelled on a 4×4×4 supercell.

Incommensurately modulated structures are considered to be 'aperiodic'. Other aperiodic structure types are incommensurate composite crystals and quasicrys-

tals.[219] They are all characterised by having Bragg peaks that cannot be indexed using 3 reciprocal lattice vectors. However by extending this basis with one or more additional vectors then they can be indexed with integers. This can be described with:

$$\mathbf{H} = \sum_{j=1}^{3+d} h_j \mathbf{a}_j^*, \tag{1.3}$$

where $\mathbf{H}$ is the scattering vector for the Bragg reflection, d the number of aditional periodicities, h_j integers, and $\mathbf{a}_j^*$ the reciprocal basis vectors.[220] In this way, we consider periodicity to be recovered in aperiodic structures.

The primary focus of this section is on incommensurately modulated structures where this superspace approach, first proposed by de Wolff,[221,222] using the modulation wave-vector(s), $\mathbf{q}$, to describe the 'additional' periodicity. The wave-vector is often modelled with a variety of functions—harmonic, crenel, sawtooth, or a combination—though appropriate modelling of the modulation wavefunction can prove a significant challenge.[220] Implemented in programmes such as JANA2006, this superspace approach can be used to model complex modulation.[223]

The fundamental relationships between reciprocal and direct space allow for use of similar visualisation (*e.g.* Fourier maps) of electron density but with additional dimensionality. Superspace groups are used to describe the symmetry of these structures.[224] One interesting aspect of these space groups is that symmetry operators are not allowed to mix the coordinates in the additional direction(s) with those corresponding to 3D space.[220]

1.6.1 Incommensurate modulation

The causes of incommensurability are diverse but it usually arises from competition between conflicting structural driving forces that cannot simultaneously be satisfied. The majority of incommensurate phases reported to date are oxides,[225,226] such as $Li_{3x}Nd_{2/3-x}TiO_3$ where octahedral tilting is frustrated by antipolar Ti^{4+} off-centring.[227,228] Similarly, on doping the ferroelectric $BiFeO_3$ (tilt system $a^-a^-a^-$) with La to give paraelectric $GdFeO_3$-structured $Bi_{0.5}La_{0.5}FeO_3$ (tilt system $a^-b^+a^-$) an incommensurate intermediate phase $Bi_{0.75}La_{0.25}FeO_3$ is formed where there is competition between antipolar displacements and octahedral tilting.[229] In this case, the stereochemically active 'lone pair' of Bi^{3+} causes displacement of the Bi and some O towards each other along the $\langle 100 \rangle_p$ directions which couples to the the b^+ component of the tilt transition from $a^-a^-a^-$ to $a^-b^+a^-$ *via* lattice strain. The competition between these interactions results in regions in which either the antipolar displacements or the b^+ tilt component dominates [Figure 1.22]

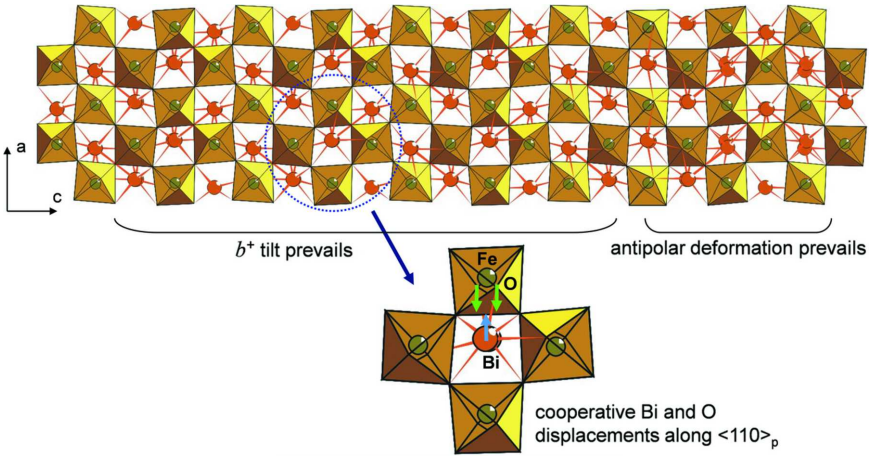

Figure 1.22: Incommensurately modulated structure of $Bi_{0.75}La_{0.25}FeO_3$ where antipolar displacements of Bi^{3+} compete with an $a^-a^-a^-$ to $a^-b^+a^-$ tilt transition giving regions in which one or the other dominates.[229] Reproduced with permission of the International Union of Crystallography.[230]

Other factors implicated in incommensuration in oxides include cation vacancy ordering (*e.g.* occupational modulation in the scheelite-related $Na_xEu_{(2-x)/3}MoO_4$ family),[231] anion vacancy ordering (*e.g.* $Sr_4Fe_6O_{13\pm\delta}$),[232] charge density waves,[230] and charge/orbital ordering (*e.g.* competing dimer/trimer formation in Fe_4O_5).[233]

Incommensurately modulated phases have similarly been observed for zeolites such as nosean[234] and the aluminophosphate VPI-5.[235] and for a small temperature range between α- and β-quartz (*vide infra*).

Incommensuration also arises in molecular systems, in particular where there is conflict between two driving forces. This occurs, perhaps most simply, in molecules such as biphenyl where the gas phase structure is preferentially bent but crystal packing favours a flat conformation [Figure 1.23]. In gaseous biphenyl its joined rings are preferentially rotated due to repulsion between the *ortho*-hydrogens. In phase I the intermolecular packing and intramolecular H$\cdots$H forces are roughly balanced leading to an average structure with a flat molecule. Understanding the two modulated phases which exist at low temperature (phase II $<\sim$40 K,[236,237] and phase III $<\sim$20 K) provides information on the dynamics of phase I. In phase III, frustrated enmeshed rotations of the linked rings results in harmonically varying rotations of amplitude $\phi \approx 5.5°$.[238,239] In 2-phenylbenzimidazole there is a similar steric clash but now N–H$\cdots$N hydrogen bonding network additionally drives towards small torsion angles.[240] These examples make it clear that significant structural complexity can arise from comparatively simple competing interactions.

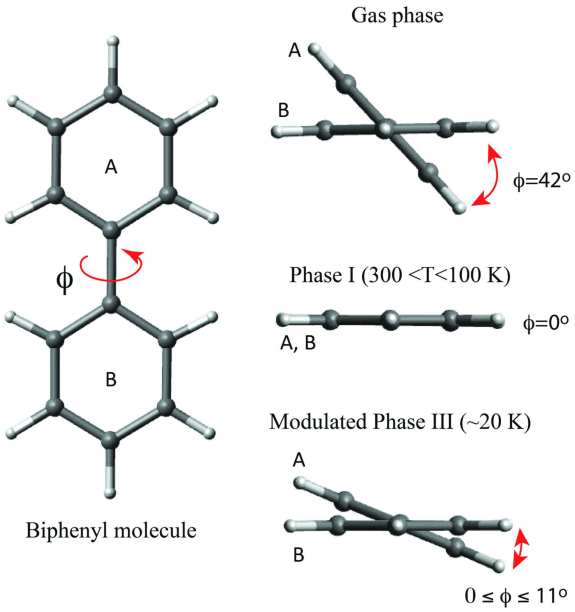

Figure 1.23: In gaseous biphenyl the rings A and B are preferentially at an angle $\phi = 42°$ due to repulsion between the *ortho*-hydrogens. In phase I the intermolecular packing and intramolecular H$\cdots$H forces are roughly balanced leading to an average structure with a flat molecule. In Phase III, frustrated enmeshed rotations of rings result in harmonically varying rotations of amplitude $\phi \approx 5.5°$.[238,239] Reproduced with permission of the International Union of Crystallography.[230]

1.6.2 Modulation in coordination polymers

Reports of both commensurately and incommensurately modulated structures remain quite rare for coordination polymers.* I give here a representative sample of the reported incommensurate coordination polymers.

The most numerous families are perovskite-related halides with organic cations. Both the perovskites $CH_3NH_3PbCl_3$ and $(CH_3)_4NGeCl_3$ have a complex series of phase transitions including a modulated phase.[241–243] More numerous are the layered perovskites $(C_3H_7NH_3)_2MCl_4$ where M = Cu^{2+},[244–246] Mn^{2+},[247–249] or Cd^{2+} which each have two incommensurate phases [Figure 1.24].[250,251] Incommensuration only occurs for $(C_nH_{3+2n}NH_3)$ when $n = 3$ for $1 \leq n \leq 10$ since in this case there is

*Structure solution and refinement for modulated phases usually requires a significant commitment of time and expertise which may, in many cases, be unavailable.

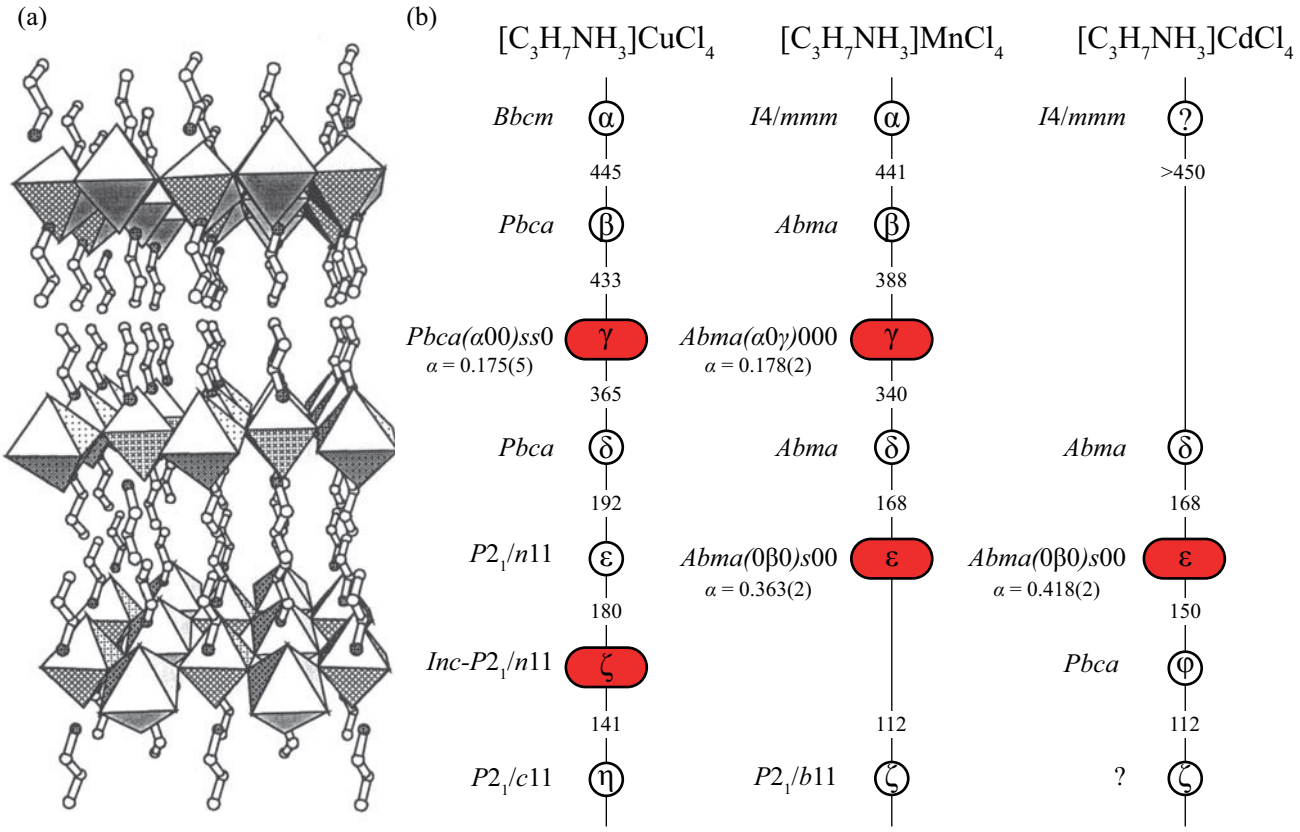

Figure 1.24: Layered hybrid perovskite family $(C_3H_7NH_3)_2MCl_4$ (a) consisting of alternating layers of corner-lined MCl_6 octahedra and $[C_3H_7NH_3]^+$. (b) Space groups and phase transitions of some members of this family. Incommensurate phases are highlighted in red with transition temperatures, in Kelvin, shown between the appropriate phases. Figures reproduced (a) and recreated (b) with permission from Reference 251.

frustration between dense packing of the alkyl chains and the relative rigidity of the layers of MCl_6 octahedra to which the cation forms hydrogen bonds.[252] The bromide $(C_3H_7NH_3)_2CuBr_4$ shows a similarly complicated set of phase transitions.[253] Lattice dynamical modelling of this family has been used to suggest that the incommensuration arises through the interaction of cation packing with the buckling/tilt instabilities of the layers of octahedra.[254] Octahedral tilting reduces the degrees of freedom of the inorganic layers compared to the untilted system and thus reduces the number of available conformations of the whole system.

Some 1D and 2D coordination polymers with incommensurate structures are

known: $[Cd(NH_3)_3Ni(CN)_4]$ where the modulation primarily manifests in changes between 4- and 6-coordinate Cd centres;[255] thermochromic [(2-Me)im]BiI_4 where the modulation results from disturbance of the arrangement of the Bi_4 chains and ordering of the 2-methylimidazolium cation;[256] and $Fe[(Hg(SCN)_3)_2](4,4'\text{-bpy})_2$ where it is induced by multi-step spin-crossover.[257]

1.6.3 Composite and host-guest structures

A subclass of modulated structures in which there are two or more mutually interpenetrating substructures with different lattices is known as composite crystal structures.[258] Examples include: minerals such as cannizzarite ($[(Pb,Bi)S]_x[(Pb,Bi)_2S_3]$ where $x \approx 1.7\text{-}1.71$ and is incommensurate); 'chimney-ladder structures' such as $[V]_{17}[Ge]_{31}$ (commensurate, superstructure >100 Å); synthetic layered inorganics such as $[PbS]_x[VS_2]$ ($x = 1.12$); and a variety of high pressure phases of metals such as Ba-IV,[259], Sr-V,[260] Rb-IV,[261] Bi-III,[262] and Sb-II.[262] Where the components have a commensurate period with respect to each other then they are often called Vernier structures. Weak satellite reflections, indicative of the effect of one substructure on the other, may or may not be observed.

Where one of these substructures is very disordered and/or a component can be removed or replaced then these are often referred to as host-guest structures—though there is no clear borderline.[226] Perhaps the most famous example of the latter are urea-inclusion compounds,[263] which have been studied for over 60 years.[264] They consist of a well-ordered framework of urea molecules connected through hydrogen bonding to give channels. These channels are occupied by organic molecules giving rise to distinctive diffuse scattering.[265] Satellite reflections are rarely observed

for these compounds, therefore the modulation wave-vectors cannot be determined well, but nonetheless it has been possible to use the superspace approach on some examples such as urea/*n*-octane.[266] In exceptional cases there can be three separate subsystems involved *e.g.* $[Hg]_x[Hg]_x[AsF_6]$ (alternatively $[Hg]_{3-\delta}[AsF_6]$).[267,268]

It is worth noting here that many porous MOFs crystallise with solvent or other molecular species from the synthesis within the pores. These molecules may be removed and in some cases replaced with others. The 'breathing' families of MILs are a noteworthy case of this as they undergo drastic structural changes on sorption/desorption of guests. The 'as-synthesised' species often contain a certain amount of Hbdc (or functionalised Hbdc) which is removed by calcining in air [Section 1.5.4]. In the case of MIL-47/MIL-53, such bdc-included species have been carefully structurally characterised. They form a number of Vernier structures resulting from the different periodicity of the chains of bdc in the pores of the framework and the framework itself: $In(OH)bdc{\cdot}(H_2bdc)_{3/4}$,[208] $VO(bdc){\cdot}(H_2bdc)_{5/7}$, $Al(OH)(bdc){\cdot}(H_2bdc)_{11/16}$, and $Ga(OH)(bdc){\cdot}(H_2bdc)_{12/17}$.[269*] For these systems, bdc$\cdots$bdc and bdc$\cdots$framework hydrogen bonding as well as π–π stacking compete and correlated disorder results in significant diffuse scattering. In the cases of $Al(OH)(bdc){\cdot}(H_2bdc)_{11/16}$ and $Ga(OH)(bdc){\cdot}(H_2bdc)_{12/17}$ the interaction between guest and framework is sufficient to result in satellite peaks in the diffraction pattern indicative of a commensurate modulated structure.[269] The structures of these compounds were refined using a supercell approach rather than a superspace (modulation wave-vector) approach.

*The proportion of guest bdc corresponds to the number of bdc/metal octahedra required for the two lattices to come into register and concurs with the values found from TGA.

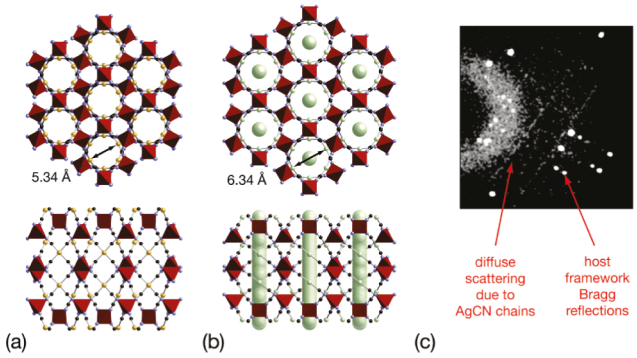

Figure 1.25: Structures of $Zn[Au(CN)_2]_2$ (a) and $Zn[Ag(CN)_2]_2{\cdot}x$AgCN (b) viewed down [001] (top) and [110] (bottom). Both are formed of 6-fold interpenetrated β-quartz nets but the Ag-analogue contains disordered chains of AgCN in its channels.[78,128,129] One consequence of this inclusion is a characteristic expansion of the ab plane and contraction along c compared to the Au-analogue. This results in the Ag-analogue having channels that are 15% wider than those in the Au-analogue. (c) The disordered AgCN chains give rise to planes of diffuse scattering in reciprocal space. Reprinted with permission from A. L. Goodwin *et al.*, Journal of the American Chemical Society, 131, 6334–6335 (2009). Copyright 2009 American Chemical Society.

Inclusion of species in host frameworks can result in changes in properties. $Zn[Ag(CN)_2]_2{\cdot}x$AgCN, like $Zn[Au(CN)_2]_2$, has a structure composed of sixfold β-quartz networks. The silver analogue also includes around 0.58 equivalents of AgCN rods in its pores, whose periodicity is incommensurate with that of the framework [Figure 1.25(a-b)].[129,270] Due to the argentophilic interactions between the framework and included AgCN, the thermal expansion of $Zn[Ag(CN)_2]_2{\cdot}x$AgCN is drastically constrained compared to the gold analogue and switches from overall positive ($\alpha_V = +15.07(12)$) to negative ($\alpha_V = -13.57(29)$) volume thermal expansion. The inclusion of AgCN gives rise to planes* of diffuse scattering but does not result in satellite reflections from the framework [Figure 1.25(c)].

Many of the above examples of incommensurability, in particular urea inclusion compounds and hybrid perovskites, demonstrate that interesting structural com-

*Since the AgCN is ordered in 1D. In contrast, 2D ordering in real space gives rise to rods of diffuse scattering in reciprocal space.

plexity can arise from the interaction of molecular and host/framework degrees of freedom.

1.7 Phase transitions and soft modes

Phase transitions in solids can be driven by a variety of parameters such as temperature,[271] pressure,[272] magnetic field,[273] electric field,[274] or chemical composition.[275] Phase transitions with temperature are perhaps the most familiar and, in most cases, the phase at higher temperature is of higher symmetry than the low-temperature phase. Phase transitions can be divided into two types: those where the change in entropy is (i) discontinuous or (ii) continuous. Discontinuous transitions are accompanied by a release of heat and associated with a discontinuity in other thermodynamic parameters such as entropy, enthalpy, and volume. These are known as first order transitions and often give a period of phase coexistence in variable temperature (or other parameter) diffraction. For transitions (ii) that are continuous across the transition temperature (or pressure, etc.) the thermodynamic quantities are continuous but their first derivative is discontinuous *i.e.* quantities such as the heat capacity and thermal expansion are discontinuous. These are also known as second-order phase transitions.

Understanding changes in symmetry associated with phase transitions is essential for understanding changes in physical properties; as exemplified in Neumann's principle "the symmetry operations of any physical property of a crystal must include the symmetry operations of the point group of the crystal"*.[276]

The transition from a high-symmetry state to a low-symmetry state can be

*Translation from IUCr Online Dictionary of Crystallography.

characterised by an order parameter. Correlated deviations from the high-symmetry structure have particular symmetries in which symmetry elements of the parent phase are broken. The overall amplitude of this symmetry breaking deviation is called the order parameter, η. These modes can be of different characters giving rise to different sorts of transitions. The two most important classes of structural transitions are (i) order-disorder phase transitions such as the ordering of metals onto different crystallographic sites (in *e.g.* the alloy Cu_3Au)[277] described in terms of a scalar mode and (ii) displacive phase transitions involving small movements of atomic positions which are usually described in terms of polar vector modes. Transitions involving atomic displacements giving rise to a structure that is not a subgroup of the parent phase (and often involving large atomic displacements) are termed reconstructive transitions.

The thermodynamics of displacive phase transitions can be considered in the context of Landau theory.[278] This phenomenological theory can be used to describe both first- and second-order phase transitions. Using the fact that the global minimum in free energy gives the equilibrium state of matter, we can consider the variation in the free energy as a function of order parameter and temperature. First- and second-order transitions show characteristic behaviour. In the former at the transitions temperature, T_c, there is a minimum in the free energy both at $\eta = 0$ and at non-zero values whereas for a second order phase transition the lone minimum switches from $\eta = 0$ to $|\eta| > 0$ [Figure 1.26(a-b)]. The variation of the order parameter with temperature for a first- and second-order phase transition is illustrated in Figure 1.26(c-d).

Importantly, the modes that drive displacive phase transitions are, in many cases,

the same phonon modes dominating the changes in dynamical behaviour with temperature. This is not an obvious result as the two phenomena occur on very different timescales—phase transitions typically in seconds and phonon frequencies[281] typically THz—but is crucial for understanding displacive transitions resulting from the 'freezing in' of soft phonon modes.[278] Soft-modes are those whose frequency falls on cooling. When the frequency of such a mode reaches zero the displacements associated with this lattice vibration freeze into the structure as static displace-

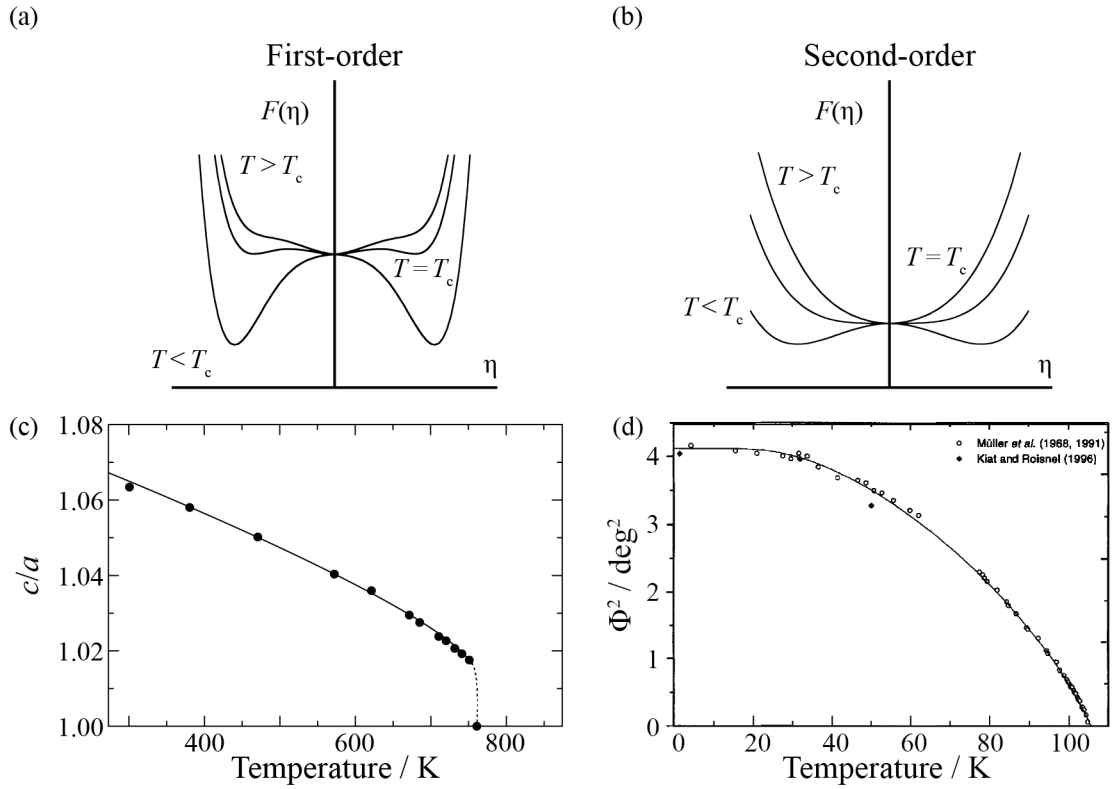

Figure 1.26: First- and second-order transitions around the transition temperature. At the transition temperature a first-order transition (a) has minima in free energy at both $\eta = 0$ and at non-zero values whereas second-order transitions (b) switches at the transition temperature from having a minimum at $\eta = 0$ to a minimum at a non-zero value.[278] Variation of order parameter with temperature for two phase transitions. (c) shows the discontinuity in ratio of lattice parameters for $PbTiO_3$ at 760 K on transformation from tetragonal to cubic.[279] (d) Continuous temperature dependence of the tilt angle in $SrTiO_3$ from EPR (open circles) and Rietveld refinement (closed circles) for the cubic to tetragonal transition.[280] Part (c) Adapted with permission from G. Shirane, S. Hoshino, and K. Suzuki, *Physical Review*, **80**, 1105–1106 (1950) Copyright (1950) by the American Physical Society. Part (d) Adapted with permission from Reference 280.

ments. Phase transitions due to the condensation of soft modes form an important class of phase transitions in functional materials and archetypal systems such as the polymorphs of silica.

Condensation of soft modes in perovskites results in rich phase transition behaviour. Group theoretical analysis (*vide infra*) along with Landau theory allows for the prediction and rationalisation of these transitions. The connections between space groups arising from tilts alone is shown in Figure 1.15 but there are many other additional possibilities resulting from displacements of the A and B cations. The ferroelectric phase transition in $PbTiO_3$, $Pm\bar{3}m \rightarrow P4mm$ at $\sim 760\,K$,[282] arises from the condensation of a soft mode at the Γ point (zone centre) involving the displacement of Ti and O in one direction along the c axis and the Pb in the opposite sense giving rise to a net polarisation [Figure 1.27].*

The condensation of soft modes can often be identified by the appearance of new peaks related to the location in the Brillouin zone at which the soft mode frequency goes to zero.[284] Using $SrZrO_3$ as an example, the second-order transition from $Pnma$ ($a^+b^-b^-$) to $Imma$ ($a^0b^-b^-$) is accompanied by the loss of peaks at the M-point owing to the loss of the frozen in displacements of oxygen atoms described as in-phase tilting (*i.e.* propagating at $\mathbf{q} =< \frac{1}{2}, \frac{1}{2}, 0 >$) [Figure 1.28].[285†]

Soft mode transitions usually involve modes with $k = 0$ or at a Brillouin zone boundary.[278] Instabilities can, however, occur at arbitrary wave-vectors giving rise to an incommensurately modulated structure [Section 1.6]. For example, between

*While long a classic example of a first order displacive phase transition the true nature of the transition has attracted controversy.[283]

†While Landau theory provides an excellent framework for understanding phase transitions, the true behaviour of order parameters can often be more complicated.[177,286]

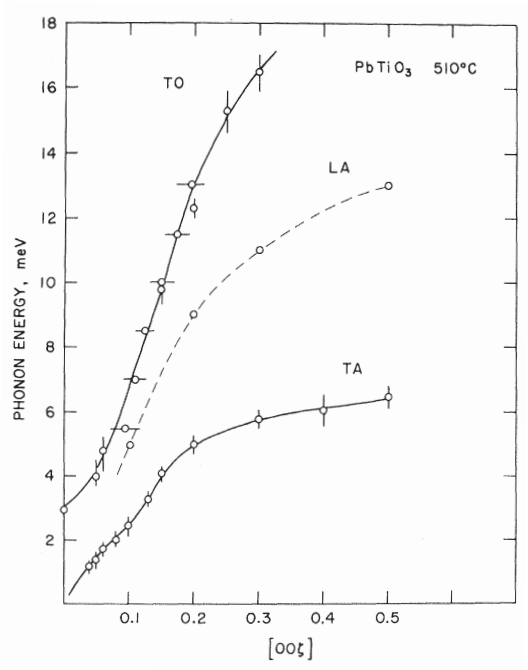

Figure 1.27: Phonon dispersion curves of $PbTiO_3$ measured using inelastic neutron scattering. Shown here are the three lowest energy branches: TO is transvere optic; LA longitudinal acoustic; TA transverse acoustic. The soft mode is the TO mode. Reprinted with permission from G. Shirane, J. D. Axe, J. Harada, and J. P. Remeika, Physical Reviews B, 2, 155 (1970). Copyright (2016) by the American Physical Society.[136]

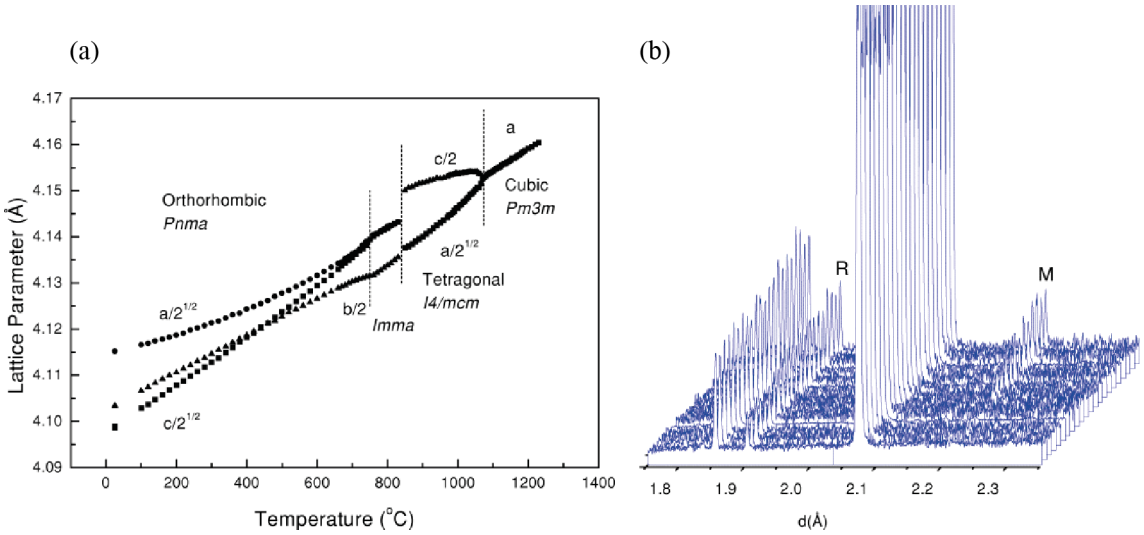

Figure 1.28: (a) Temperature dependence of lattice parameters for $SrZrO_3$. (b) Section of neutron powder diffraction patterns from 580 °C (back) to 830 °C (front). Note the disappearance of the M- point reflection at around 750 °C corresponding to the loss of in phase tilts in the *Pnma* ($a^+b^-b^-$) to *Imma* ($a^0b^-b^-$) continuous phase transition. Figures reproduced with permission from Reference 285.

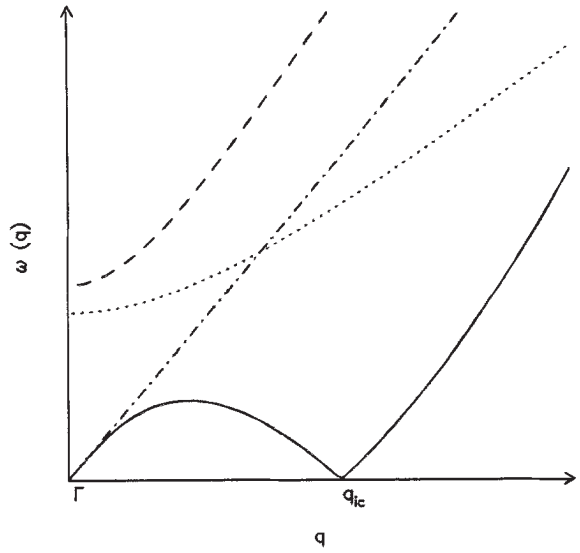

Figure 1.29: "Qualitative sketch of the level crossing between the optic and transverse acoustic modes. A dip in the lower branch at some nonzero $\mathbf{q_{ic}}$ occurs whenever the optic mode is sufficiently flat." Hypothetically, as the optic mode softens (dotted line) it will cross with the transverse acoustic mode (dash/dotted line). However, such crossing is symmetry forbidden meaning that there is an 'anti-crossing' interaction whereby the transverse acoustic mode (solid line) goes to zero at nonzero $\mathbf{q_{ic}}$ and the optic mode (dashed line) is 'repelled'.[288] Reproduced from F. S. Tautz, V. Heine, M. T. Dove, X. Chen, *Physics and Chemistry of Minerals*, **18**, 326–336 (1991) © Springer-Verlag 1991. With permission of Springer.[289]

the α- and β- phases of quartz there exists an incommensurate phase that exists over a small temperature range. This arises from the softening of an optic mode and consequent anti-crossing interaction* with an acoustic mode [Figure 1.29].[287]

The coupling of 'molecular' degrees of freedom with lattice instabilities gives rise to interesting, and surprisingly complex, phase behaviour in the alkali metal cyanides.[290] NaCN and KCN have very similar phase diagrams which will be briefly summarised.[291] On cooling from the melt they form a pseudo-NaCl-structured plastic phase (space group $Fm\overline{3}m$) in which the CN^- is orientationally disordered with the [100] then [111] directions favoured.[292] On further cooling, a first-order transition to $Immm$ is observed giving a structure in which the $(CN)^-$ are aligned along

*Modes of the same symmetry are not allowed to cross so will appear to repel each other.

the [110] direction of the cubic cell but with head-to-tail (dipolar) disorder. On approaching this transition there is a pronounced softening of the shear elastic constant c_{44},[293] accompanied by anomalous dispersion of the tranvserse acoustic phonon branch propagating along [100] of the cubic cell.[294,295] This behaviour has been identified as arising from rotovibrational coupling— that is to say coupling between the orientational degrees of freedom of $(CN)^-$ and the lattice modes.[296] This coupling is observed in INS data when the inverse of the reorientation time for the cyanide ion becomes comparable to the relevant phonon frequency.[297] On further cooling the orientational disorder is fully resolved through a second-order order-disorder transition giving an antiferroelectric ordering of CN^- in $Pmmn$.[298,299] The behaviour of these chemically simple systems—in particular the coupling of molecular rotation and lattice degrees of freedom—have important implications for the behaviour of coordination polymers with molecular extra-framework cations.

1.8 Structural chemistry of $[PPN]^+$

In this Thesis the bis(triphenylphosphane)iminium cation $\{N[P(C_6H_5)_3]_2\}^+$, $[PPN]^+$, will feature prominently as an extra-framework cation.* It will therefore be pertinent to highlight some features of the structural chemistry of this widely used cation. The CSD (V 5.37, updates 1 and 2)[301,302] contains 1528 structures with $[PPN]^+$ and REAXYS[303] lists 4601 unique substances containing this cation. Its popularity stems from a number of factors: synthetic accessibility, useful solubility properties *i.e.* soluble in most organic solvents and hot water, its fairly hydrophobic character and chemical stability in moderately forcing conditions.[304,305] Furthermore, its

*PPN is occasionally called PNP in the literature.[300]

propensity to pack closely with itself forming a variety of 1D $\pi\cdots\pi$-stacking motifs* means it is of particular utility in crystallising anionic species.[308] These supramolecular interactions have been characterised as 'phenyl embraces' and have an important effect on crystal packing. In addition, the cation has internal degrees of freedom, as might be inferred from the resonance structures [Figure 1.30(a)]. Despite the linear representation, **I**, being more commonly used in the REAXYS database and the CSD, the majority of reported structures have a non-linear P—N—P angle with a recent study finding a mean value of 143(9)° indicating that the nitrogen lone-pair is present to some degree [Figure 1.30(b)].[304] While an earlier study found there to be a low energy barrier ($<$4 kJ mol^{-1}) for bending of this angle between 130–180° with a minimum between 145–150° for the model system $[H_3PNPH_3]^+$,[308] the bent conformation is further stabilised by intramolecular hydrogen bonding between *ortho*-hydrogen of the phenyl and the nitrogen lone-pair [Figure 1.30(c)]. Overall, this means that the variation in P—N—P angle arises from the balance of intramolecular hydrogen bonding, intra/intermolecular $\pi\cdots\pi$ interactions, and packing forces in the context of a low energy barrier for bending.

1.9 Structure of Thesis

The work presented in this thesis concerns the structural chemistry of transition metal dicyanometallates $A_nB(L)X_m{\cdot}G$ where A is an extra-framework cation, B is the node metal, X is the dicyanometallate linker, L is a neutral ligand bound to the node metal centre and G is a non-coordinating guest molecule. Dicyanometallates

*The linear extension of $[PPN]^+$ means that, unlike for $[PPh_4]^+$ 2D and 3D networks are not formed.[306,307]

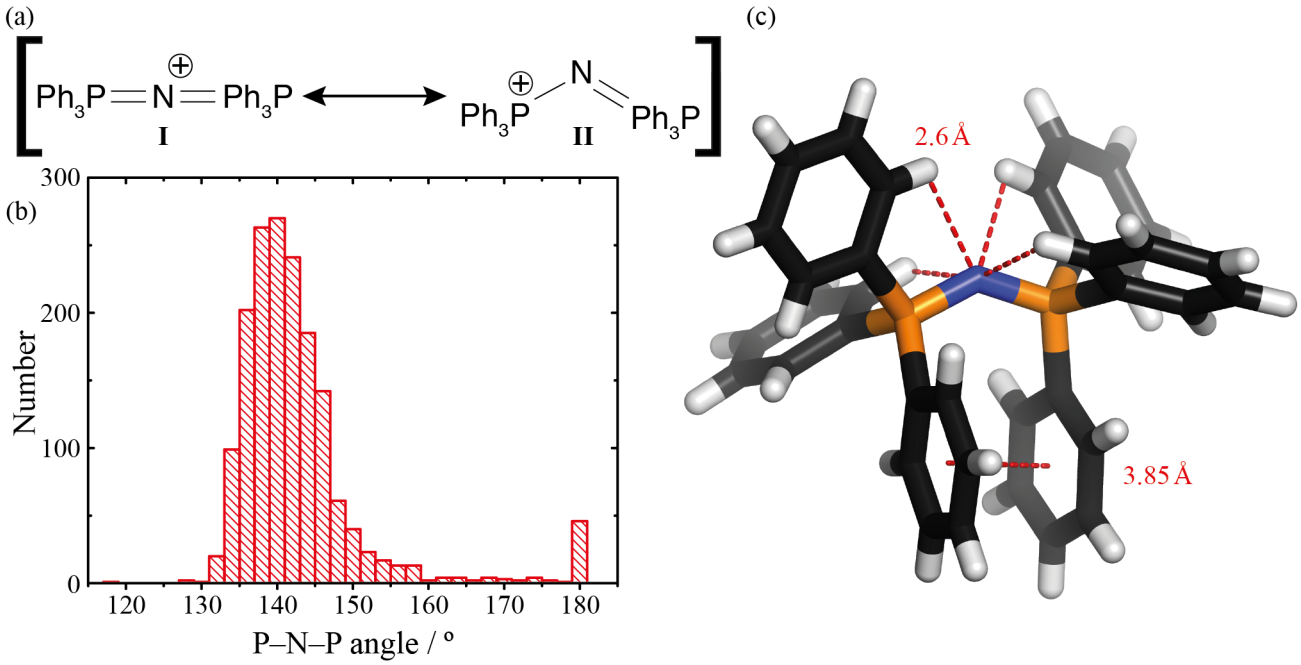

Figure 1.30: (a) Common resonance structures of $[PPN]^+$ (b) Histogram of P—N—P angles for 1404 structures with $[PPN]^+$ in the CSD with 3D coordinates (c) Conformation of $[PPN]^+$ in $[PPN][Au(CN)(CCPh)]\cdot H_2O\cdot$acetone,[309] showing four intramolecular hydrogen bonds (2.55–2.63 Å) and a short $\pi\cdots\pi$ contact.

are perhaps the simplest atomically thin linkers to provide nanoscale separation between connected metal centres making them excellent model systems for framework materials, such as MOFs, of similar dimensions. A number of new transition metal dicyanometallates are reported in Chapter 3 and their structures analysed in the context of previously reported dicyanometallates in Chapter 4. The phase transitions of the perovskite and Ruddlesden-Popper analogues are reported in Chapter 5 where a common theme is the importance of interaction between degrees of freedom of the molecular cation and those of the host framework. The importance of cation–framework coupling is explored further in Chapter 6 where the incommensurately modulated phase of triply-interpenetrated diamondoid $[N(C_2H_5)_4]Ag[Ag(CN)_2]_2$ is reported. The unusual tilt system demonstrated by one of the superperovskite dicyanometallates is used to develop an extension of Glazer tilt notation suitable for

perovskites with molecular anions, which can have significantly decoupled tilts compared to oxide perovskites (Chapter 7). An in depth understanding of the modes responsible for these unusual tilt systems is detailed for the Prussian-Blue analogue $[NH_4]_2SrFe(CN)_2{\cdot}2H_2O$ where the unconventional tilts are activated by hydration-driven distortions (Chapter 8).

Chapter 2

Experimental methods

2.1 Sample preparation

The general approach to synthesis of transition metal dicyanometallates with molecular extra-framework cations, A, was first to make the A[Au/Ag(CN)$_2$] salt. These could then be used as a reagent with transition metal salts, typically nitrates or perchlorates. For the synthesis of powders and crystals, differential solubility between starting material and products in ethanol and/or water was exploited to allow for the ready filtration and washing of the desired product.

2.1.1 Dicyanometallate precursors

[NBu$_4$]Ag(CN)$_2$·$\frac{1}{2}$H$_2$O was first prepared by adding an aqueous solution of [NBu$_4$]CN (0.5510 g in 400 mL water) to a suspension of AgCN (0.3435 g in 100 mL water) and stirring for 1 h. The excess AgCN was then removed by vacuum filtration and the volume of the filtrate reduced by rotary evaporation. The concentrated filtrate was allowed to evaporate and the resulting powder dried at 50 °C for 2.5 h then at 40 °C for 18 h. A more convenient preparation was later used after References 310 and 311. [NBu$_4$]Ag(CN)$_2$·$\frac{1}{2}$H$_2$O was precipitated from concentrated aqueous solutions of KAg(CN)$_2$ and [NBu$_4$]Cl.[311] A white precipitate formed immediately and was stirred for 1 h. The white powder was collected by vacuum filtration, washed, and dried at 50 °C overnight.

A typical synthesis of [NBu$_4$]Au(CN)$_2$·$\frac{1}{2}$H$_2$O was as follows. [NBu$_4$]Au(CN)$_2$·$\frac{1}{2}$H$_2$O

was precipitated from concentrated aqueous solutions of $KAu(CN)_2$ (1.161 g in 4 mL water) and $[NBu_4]Cl$ (1.208 g in 6 mL water).[311] A white precipitate formed immediately and was stirred for 1 h. The white powder was collected by vacuum filtration, washed, air-dried overnight and then dried under vacuum at 40 °C for 7 h. This gave 1.745 g of product (Yield: 83.5%).

$[PPN]Au(CN)_2$ was prepared by the method outlined in Reference 310. Solutions of $KAu(CN)_2$ (2.583 g in 100 mL water) and PPNCl (5.40 g in 200 mL 50:50 water:ethanol) were combined with immediate formation of a white precipitate. The reaction mixture was covered and stirred for 1 h then collected by vacuum filtration and washed with 300 mL cold water. The solid was left to air-dry overnight then dried in a vacuum oven at 40 °C for 3.5 h giving 6.80 g of product (Yield: 96.3%). Elemental analysis: Found (calculated) % C 57.74 (57.95); H 3.80 (3.84); N 5.24 (5.34).

$[PPN]Ag(CN)_2$ was prepared by a similar method to $[PPN]Au(CN)_2$. Solutions of $KAg(CN)_2$ (1.881 g in 100 mL water) and PPNCl (5.68 g in 200 mL 50:50 water:ethanol) were combined with immediate formation of a white precipitate. The reaction mixture was covered and stirred for 1 h then collected by vacuum filtration and washed with 300 mL cold water. The solid was left to air-dry overnight then dried in a vacuum oven at 40 °C for 1 week giving 5.87 g of product (Yield: 90.0%). Elemental analysis: Found (calculated) % C 65.05 (65.34); H 4.26 (4.33); N 5.88 (6.02).

2.1.2 Dicyanometallate frameworks

$[NEt_4]Ag[Ag(CN)_2]_2$ (**1**) single crystals were prepared by slow evaporation of aqueous solutions of $KAg(CN)_2$ and $[NEt_4]Cl$. Solutions of $KAg(CN)_2$ (0.2802 g, 1.411 mmol) and $[NEt_4]Cl$ (0.238 g, 1.436 mmol) were prepared with the minimum quantity of water and then mixed. The resulting colourless solution was left to evaporate slowly and crystals formed within 3 weeks. The crystals of (**1**) were manually separated from the mixture of solids formed.

$[NBu_4]_{0.5}Cd[Ag(CN)_2]_{2.5}$ (**2**) aqueous solutions of $[NBu_4]Ag(CN)_2{\cdot}\frac{1}{2}H_2O$ and $Cd(NO_3)_2{\cdot}4H_2O$ were prepared with the minimum quantity of solvent, mixed, and left to evaporate from an open petri dish. Crystals were harvested after a few days.

$[PPN]_{0.5}Cu[Au(CN)_2]_{2.5}{\cdot}EtOH$ (**3a**) single crystals were prepared by slow-diffusion in an H-shaped cell. Into one arm was placed $[PPN]Au(CN)_2$ (25 mg in 1 mL ethanol) and the other $CuCl_2{\cdot}2H_2O$ (5.4 mg in 0.142 mL ethanol). The remaining volume was carefully made up with cold ethanol with the majority of the tube surrounded by ice. Care was taken to disturb the reagent solutions as little as possible by pipetting solvent in a circular fashion down the tube walls. Each arm was first filled to just below the bridge linking the arms. The bridge was then filled by alternating small volumes ($\sim$1 mL) in either arm. Green crystals grew in the $[PPN]Au(CN)_2$ arm after 2 days.

$[PPN]_{0.5}Mn[Ag(CN)_2]_{2.5}{\cdot}EtOH$ (**3b**) was prepared by diffusion in a Schott bottle. Cold solutions of $[PPN]Ag(CN)_2$ (1.125 g in 20 mL ethanol) and $Mn(NO_3)_2{\cdot}4H_2O$ (148 mg in 6 mL ethanol) were carefully layered with a buffer of 50 mL cold ethanol separating the layers. Crystals formed overnight.

$[PPN]_{0.5}Cd[Ag(CN)_2]_{2.5}\cdot EtOH$ (**3c**) single crystals were first prepared by slow-diffusion in a vial. Cold solutions of $[PPN]Ag(CN)_2$ (101 mg in 2 mL ethanol) and $Cd(NO_3)_2\cdot 4H_2O$ (19 mg in 0.2 mL ethanol) were carefully layered with a buffer of 5 mL cold ethanol separating the layers. Crystals formed overnight. A larger scale synthesis to make the sample used for powder diffraction, TGA, and DSC was performed by diffusion in a Schott bottle. Cold solutions of $[PPN]Ag(CN)_2$ (1.108 g in 25 mL ethanol) and $Cd(NO_3)_2\cdot 4H_2O$ (184 mg in 7 mL ethanol) were carefully layered with a buffer of 50 mL cold ethanol separating the layers. Crystals formed overnight. A portion of these crystals, with mother liquor, were set aside in a sealed sample tube. The remaining product was filtered and thoroughly washed with cold ethanol then left to air-dry overnight yielding 300 mg product (Yield: 69.6 %).

$[PPN]Cd[Ag(CN)_2]_3\cdot 3EtOH\cdot nH_2O$ (**4**) crystals were selected from a small portion (roughly 3 mL) of a reaction mixture that initially yielded **3c**. Solutions of $[PPN]Ag(CN)_2$ (1.108 g in 25 mL ethanol) and $Cd(NO_3)_2\cdot 4H_2O$ (183.7 mg in 7 mL ethanol) were carefully layered with a buffer of 50 mL ethanol separating the layers in a Schott bottle. Colourless crystals formed overnight and then a portion of these crystals, with mother liquor, was set aside in a sealed sample tube. After 10 weeks a crystal of compound **4** was selected from this portion.

$[PPN]Mn[Au(CN)_2]_3$ (**5a**) was first prepared by layering ethanolic solutions of $PPNAu(CN)_2$ (50 mg in 2 mL ethanol) and $Mn(ClO_4)_2\cdot xH_2O$ (14 mg in 0.2 mL ethanol) in a small sample tube. Colourless crystals formed after 1 h. A larger scale synthesis to prepare the sample used for powder diffraction, TGA, and DSC was prepared by diffusion in a Schott bottle. Cold solutions of $[PPN]Au(CN)_2$ (1.060 g in 33 mL ethanol) and $Mn(NO_3)_2\cdot 4H_2O$ (134 mg in 4 mL ethanol) were carefully layered with

a buffer of 20 mL cold ethanol separating the layers. Crystals formed overnight. A portion of these crystals, with mother liquor, was set aside in a sealed sample tube. The remaining product was filtered and thoroughly washed with cold ethanol then left to air-dry overnight yielding 423 mg product (Yield: 70.4 %).

[PPN]Cd[Au(CN)$_2$]$_3$ (**5b**) was first prepared by layering ethanolic solutions of PPNAu(CN)$_2$ (50 mg in 2 mL ethanol) and Cd(NO$_3$)$_2$·4H$_2$O (21 mg in 0.2 mL ethanol) in a small sample tube. Colourless crystals formed after 1 h. A larger scale synthesis to prepare the sample used for powder diffraction, TGA, and DSC was was prepared by diffusion in a Schott bottle. A cold solution of [PPN]Au(CN)$_2$ (1.000 g in 30 mL ethanol) was carefully layered on top of a solution of Cd(NO$_3$)$_2$·4H$_2$O (132 mg in 4 mL ethanol). Crystals formed overnight. A portion of these crystals, with mother liquor, was set aside in a sealed sample tube. The remaining product was filtered and thoroughly washed with cold ethanol then left to air-dry overnight yielding 436 mg product (Yield: 73.6 %).

[PPN]Ni[Au(CN)$_2$]$_3$ (**5c**) was prepared by diffusion in a Schott bottle. Cold solutions of [PPN]Au(CN)$_2$ (1.09 g in 33 mL ethanol) and Ni(NO$_3$)$_2$·6H$_2$O (147 mg in 5 mL ethanol) were carefully layered with a buffer of 50 mL cold ethanol separating the layers. Crystals formed overnight. The product was filtered and thoroughly washed with cold ethanol then left to air-dry overnight yielding 492 mg product (Yield: 79.4 %).

[Bu$_4$N]Mn[Au(CN)$_2$]$_3$·[Bu$_4$N]ClO$_4$ (**6**) was first formed fortuitously in attempts to make a Mn analogue of [Bu$_4$N]Ni[Au(CN)$_2$]$_3$. A typical small-scale synthesis was as follows. Moderately sized single crystals formed overnight from a concentrated ethanolic mixture of [Bu$_4$N]Au(CN)$_2$·$\frac{1}{2}$H$_2$O (28 mg in 0.25 mL ethanol) and

$MnClO_4{\cdot}xH_2O$ (13 mg in 0.20 mL ethanol) solutions. The formula is consistent with elemental analysis found (calculated) % C 32.68 (32.92); H 5.12 (5.23); N 7.90 (8.08); Cl 2.55 (2.56). Syntheses of powder samples followed a similar procedure on an increased scale. Crystals were isolated by filtration, washed with ethanol, and dried under vacuum before being ground to a fine white powder.

2.1.3 $(NH_4)_2SrFe(CN)_6{\cdot}2H_2O$

All samples of $(NH_4)_2SrFe(CN)_6{\cdot}2H_2O$ were synthesised by Dr. S. G. Duyker.

Solutions of 2 mmol (568 mg) $(NH_4)_4Fe(CN)_6$ dissolved in 1.5 mL H_2O and 1 mmol (267 mg) $SrCl_2{\cdot}6H_2O$ dissolved in 1.0 mL H_2O were mixed and left to stand. Pale green irregular hexagonal crystals of $(NH_4)_2SrFe(CN)_6{\cdot}2H_2O$ formed within 5 min.

Anhydrous material was made either by heating in-situ on a single-crystal diffractometer or, in the case of powders, by applying a vacuum of $\sim 10^{-1}$ mbar to $(NH_4)_2SrFe(CN)_6{\cdot}2H_2O$ loaded into a 0.7 mm glass capillary at room temperature for 12 h. Powders were rehydrated by exposing the evacuated sample to water vapour in an otherwise evacuated system at room temperature for 12 h.

2.2 Diffraction

The majority of results reported in this thesis are derived from diffraction data. As such, I outline here some of the fundamental and practical aspects of X-ray diffraction. I begin by discussing the principles of diffraction and generation of X-rays. I then move on to describe some general aspects and particulars relating to this thesis of single-crystal and powder diffraction in turn.

2.2.1 Principles of diffraction

The proposal that X-rays might be diffracted by crystals was first made by Max von Laue* in 1912 and subsequently observed by Friedrich and Knipping in that same year.[312,313] W. L. Bragg was able to interpret the pattern of spots formed by this diffraction[8] and, along with his father W. H. Bragg, went on to solve the structures of some simple solids using equipment made by W. H. Bragg.[9,10,16] At the core of this understanding of the diffraction was what has become known as Bragg's Law:

$$n\lambda = 2dsin\theta, \tag{2.1}$$

where n is the order of diffraction (a positive integer), λ the wavelength of the incident radiation, d a distance between 'planes' in a crystal, and theta the angle between the lattice plane and the incident beam. W. L. Bragg's insight was based upon an analogy to reflection from an array of planes in which the X-rays 'reflected' from each parallel plane would only be in phase (*i.e.* add constructively producing a diffracted beam) when the difference in path lengths of all the diffracted beams was an integer number of wavelengths, $\Delta L = n\lambda$. The relationship between path difference for beams diffracted from adjacent planes is given by $\Delta L = 2d\sin\theta$. Combining these relationships gives the Bragg condition. This interaction of radiation (or particles) with matter where there is no exchange of energy can be formally understood on the basis of elastic scattering theory.[314] The diffraction pattern as a whole represents the transformation of the arrangement of atoms into reciprocal

*At that time Max Laue.

space, hence the mathematics of Fourier transforms is essential for relating the data to a structural model.

While the positions of peaks allow us to determine the unit cell of a crystal the information regarding the positions of atoms within the unit cell* are contained in the amplitudes and phases of diffracted beams. For each (hkl) plane the structure factors are described by

$$F_{hkl} = \sum_{j}^{N} f_j \text{exp}[2\pi \text{i}(hx_j + ky_j + lx_j)], \tag{2.2}$$

$$= \sum_{j}^{N} f_j \text{cos}[2\pi(hx_j + ky_j + lz_j)] + \text{i} \sum_{j} f_j \text{sin}[2\pi(hx_j + ky_j + lx_j)], \tag{2.3}$$

which is summed over N atoms in the asymmetric unit with, for the jth atom, scattering factor f_j fractional coordinates x_j, y_j, z_j. The scattering power for X-rays is linearly proportional to the number of electrons and decreases with increasing scattering angle. The electron density, ρ, is given by the Fourier transform of the structure factors,

$$\rho(x, y, z) = \frac{1}{V} \sum_{h,k,l} F_{h,k,l} \text{exp}[-2\pi \text{i}(hx + ky + lz)], \tag{2.4}$$

where V is the volume of the unit cell. Crucially, we generally do not have access to the complex structure factor in diffraction experiments but rather to the *intensities*. These are related to the structure factors by,

$$I(hkl) \propto |F(hkl)|^2. \tag{2.5}$$

*As well as atomic displacements, occupancies, lattice strain, etc.

This inability to access the complex component of the structure factor is known as the 'phase problem'.

2.2.2 Generation of X-rays

X-rays for use in diffraction experiments can be generated with a variety of devices. In-house instruments usually make use of closed-tube sources in which electrons are fired at a metal target producing characteristic wavelengths of light.* The electrons are generated at the cathode, typically a heated tungsten filament, and accelerated in a vacuum by action of a potential difference towards the anode. Amongst the broad 'white' radiation are sharp lines characteristic of the target metal, which Moseley showed to follow the relationship $\lambda^{-1/2} \propto Z.$[315] Bombardment with electrons ejects core electrons from the metal atoms of the target. Outer electrons subsequently fall down to this now vacant core level and release energy, in the form of light, in the process. The particular energy (wavelength) of energy produced is a function of the energy levels involved in the transition. For example, the most commonly used radiation for powder diffraction is Cu Kα_1 ($\lambda = 1.54056\,\text{Å}$) which results from the L_{III} ($2p^{2/3}$) $\rightarrow$K ($1s$) transition. The X-rays produced by the closed-tube may be passed through a monochromator to remove undesirable wavelengths of radiation.† The choice of wavelength is an important consideration for any diffraction experiment, for example Cu Kα_1 is generally unsuitable for iron-containing compounds due to fluorescence. In these, and many other cases, it may be preferable to use a synchrotron radiation source.

*Copper and molybdenum are presently the most commonly used metals.

†The intensity of closed-tube sources is limited by the ability to cool the metal target. This overheating problem can be overcome with so-called rotating anode systems and more recently by using liquid alloys of Ga or In allowing much higher power electron beams to be used.

The spectrum of synchrotron radiation spans the far infrared ($\lambda = 10^{-5}\,\mathrm{m}$) to near γ-rays ($\lambda = 10^{-12}\,\mathrm{m}$) and results from the deflection of a beam of electrons by a magnetic field. For crystallographic studies, the useful wavelengths generally lie between 0.1–2 $\times\ 10^{-10}\,\mathrm{m}$ and the choice of wavelength will be balanced by a large number of factors dictated by the nature of the sample and the information desired. For example, high energy (short wavelength) X-rays are generally more penetrative so may be useful for in-situ studies but also usually have lower detection efficiency. Synchrotron radiation is extremely bright, coherent, and spatially resolved meaning that data can, in many cases, be collected to higher resolution and in a shorter time than would be possible in-house (if the experiment were possible at all). Furthermore, the characteristics of the beam are optimised at each beamline for the particular experiments carried out there. All synchrotron experiments reported in this thesis were carried out at the UK national synchrotron, Diamond Light Source, which is third generation source operating at 3 GeV.

2.2.3 Single crystal X-ray diffraction

In single crystal diffraction the intensities of individual Bragg peaks are measured. These intensities are typically measured using 2D detectors of a variety of technologies.* The ability to collect a sufficient number and type of reflections depends on being able to relate the orientation of the crystal (unit cell) with the geometry of the instrument. This relationship is described by the orientation matrix and the Ewald sphere construction. The Ewald sphere constructions allows us to determine when particular reflections will be observed. The Ewald sphere is defined as having

*Scintillation point detectors are rarely used in contemporary single-crystal X-ray diffraction but were extensively used for a period in the transition away from film.

a radius $1/\lambda$ with origin at the centre of the crystal and the centre of reciprocal space is the point at which the incident X-ray beam leaves the sphere. When a reciprocal space point intersects with the Ewald sphere then the Bragg condition is met and it may be measured. Importantly, this relationship also means that there is a limited number of reflections can be accessed. The boundary between reflections that can and cannot be measured is described by the limiting sphere with a radius of $2/\lambda$ and centred on the origin of reciprocal space.[316] Different reflections can be accessed by rotation of the crystal. Both in-house diffractometers used here have the κ four-circle geometry but others exist.

A typical approach will first involve a short collection to determine the unit cell and orientation matrix. From the crystal system it is then possible to determine what portion of reciprocal space should be collected as a minimum. In very broad terms, after collection a peak search is performed, the peaks are fitted and then integrated. Various corrections are applied to the data (*e.g.* background, Lorentz-polarization, absorption) finally giving a list of hkl values, intensities, and errors. It is against this list that the refinement is performed but before that is possible it will be necessary to determine the space group. Not all space groups are distinguishable solely by their reflection conditions so other statistical approaches are necessary. The broadest measure of this is R_{int} which is a measure of how similar nominally equivalent reflections are,

$$R_{\text{int}} = \sum |F_{\text{o}}^2 - F_{\text{o}}^2(\text{mean})| / \sum [F_{\text{o}}^2], \tag{2.6}$$

and gives an indication of the minimum R value that can be expected in the refinement.

Structure solution is usually carried out using one of three approaches: the heavy atom method, direct methods, or charge flipping. The structural model is then refined against the data in a non-linear least squares process for which a function is minimised:

$$M = \sum w(Y_\mathrm{o} - Y_\mathrm{c})^2, \tag{2.7}$$

where 'o' and 'c' stand for observed and calculated, respectively. Y_o is typically F_o^2 although F_o was historically more common due to its use allowing significant simplifications of calculations. F_o may still occasionally be used, especially in cases where some strong reflections are poorly measured.

The quality of refinements are generally indicated using R factors with the following two formulations usually quoted:

$$R = \frac{\sum |F_\mathrm{o} - F_\mathrm{c}|}{\sum w|F_\mathrm{o}|}, \tag{2.8}$$

which is used most often and is numerically the lowest although,

$$wR = \sqrt{\frac{\sum w(F_\mathrm{o}^2 - F_\mathrm{c}^2)^2}{\sum wF_\mathrm{o}^2}}, \tag{2.9}$$

gives a better indication of the effect of adding or removing parameters from a refinement.[316]

In-house single-crystal diffraction

Single-crystal X-ray diffraction data were collected using a Nonius KappaCCD diffractometer (first collection of **2** and **5a**) or an Oxford Diffraction (Rigaku Oxford Diffraction) SuperNova diffractometer (all other in-house) fitted with an Oxford Cryosystems Cryostream 600 Series/700 Plus open-flow nitrogen cooling device.[317] DENZO/SCALEPACK[318] or CrysAlisPro[319] were used for data collection and reduction as appropriate. The structures were solved *ab initio* using SIR92[320] or SUPERFLIP.[321] All structures were refined with full-matrix least-squares on F^2 using CRYSTALS.[322,323] Hydrogen atoms were, in some cases, visible in the difference Fourier map and treated in the usual manner.[324] In the remaining cases, and particularly for disordered assemblies, hydrogen atoms were added geometrically. Full structural data are included in the Electronic Appendix.

All crystals were coated in perfluorpolyether oil and mounted on a MiTeGen loop if collected below room temperature. For collections at room temperature and above the crystal was either stuck to a glass fibre using nail varnish or, if the crystal was small and/or plate or needle in habit, coated in the minimum quantity of Paratone oil and mounted on a MiTeGen loop. The removal of ethanol in the case of [PPN]$Mn_2[Ag(CN)_2]_5(EtOH)_2$ (**5a**), for example, was performed with a crystal mounted in Paratone oil.

In the case of the modulated phase of $[NEt_4]Ag[Ag(CN)_2]_2$ (**1**) the data collection strategy was tailored to maximise the separation of main and satellite reflections. The detector was used in a 1×1 binning mode instead of the normal 2×2 and frames were collected with a width of $0.4\,^\circ$. Structure refinement was carried out

in JANA2006.[223] Further specifics relating to the refinement procedure are given in Chapter 6.

Diamond Light Source, I19

Data at 30 K were collected on compounds **1**, **3a**, and **6** at Diamond Light Source (beamline I19)[325] ($\lambda = 0.6889$ Å) fitted with an Oxford Cryosystems HeliX open-flow helium cryostat,[326] and Rigaku Saturn 724+ CCD detector. CrystalClear and CrysAlisPro[319] were used for data collection and reduction respectfully.

2.2.4 Powder X-ray diffraction

Powder diffraction generally refers to that from a polycrystalline sample of, ideally, randomly oriented crystallites. While structure solution from powder data is challenging compared to single crystal diffraction the technique has various advantages. These include: not having to make single crystals, probing the sample bulk, faster data collection and more precise lattice parameter determination. Broadly, the three main pieces of information in a powder diffraction pattern are partitioned into the peak positions, intensities, and shapes. The unit cell determines the peak positions, the atomic structure determines the intensities, and microstructure (size, strain, stress), as well as instrumental factors, determines the peak shapes. Microstructure may also have a significant effect on peak intensities in the form of preferred orientation.[327]

The diffraction of a powder is described by distribution of intensity with respect to the scattering angle, θ. The spatial averaging of the diffraction compared to a single crystal means that all equivalent reflections at a certain value of 2θ contribute to a single peak *e.g.* in a cubic system the (111), ($\bar{1}$11), ($\bar{1}\bar{1}$1), and ($\bar{1}\bar{1}\bar{1}$) reflections

all contribute to the same peak.

For an unknown powder pattern the first step in analysis is likely to be peak indexing. This process involves finding peak maxima and devising a unit cell which can account for these positions. The proposed cell can be confirmed using a Pawley refinement.[328] The Pawley refinement includes modelling of the background and peakshape but the *intensities* of the peaks are refined arbitrarily. The background and peakshape terms from Pawley refinements can usefully be carried over to Rietveld refinement which includes a structural model. For Rietveld refinement a non-linear least squares minimisation is performed but in this case the observed and calculated values refer to each data point in the powder diffraction pattern.[329,330]

In-house powder diffraction

In-house powder diffraction patterns were collected using a PANalytical Empyrean diffractometer equipped with $Cu_{K_{\alpha_1}}$ radiation ($\lambda = 1.54056\,\text{Å}$) fitted with a Ge(111) monochromator in Bragg-Brentano geometry. Soller slits of 0.04 rad were used in all cases along with a PIXcel 1D detector. When sample quantity allowed, a steel spinner sample holder was used of 10 mm diameter. In these cases, variable divergence slits with a fixed sample illumination of 10 mm was used. When there was insufficient sample, a glass flat plate was used instead with fixed 1° divergence slits.

Powder diffraction patterns in Chapter 8 were collected by Dr. S. G. Duyker using a PANalytical X'Pert Pro MPD instrument equipped with $Cu_{K_{\alpha_1}}$ radiation ($\lambda = 1.54056\,\text{Å}$) in Debye-Scherrer geometry. Patterns were typically collected for 30 min in the 10–50° 2θ range.

Diamond Light Source, I11

Variable temperature powder diffraction data were collected at Beamline I11, Diamond Light Source. Powders were finely ground and loaded into 0.5 mm borosilicate glass capillaries, which were then mounted on specially made brass pins. All capillaries with ethanol-containing material were left unsealed at one end to allow ethanol to escape and secured with quartz wool. Samples were mounted and changed with the aid of an industrial robot (Motoman HP20).[331] Data were typically collected between 140 and 580 K every 10 K with the particular temperature limits tailored for each sample guided by phase stability information from TGA and DSC. Each temperature point was allowed to stabilise before exposure rather than collecting while ramping. Temperatures up to 500 K were achieved using an Oxford Cryosystems cryostream ramping at 360 K hr^{-1} and oriented parallel to the capillary.[317] Temperatures above 500 K were achieved using a Cyberstar hot air blower ramping at 0.16 K s^{-1} (= 576 K h^{-1}) oriented perpendicular to the capillary. Data for [PPN]Mn[$Au(CN)_2$]$_3$ were only collected using the hot air blower (300 to 550 K). The nominal temperature for each collection was outputted to a log file and no internal temperature standard was used. A wavelength of 1.078265(10) Å (roughly 11.5 keV) was used for all samples.* Data were collected using the I11 position sensitive detector (PSD): a time-resolved detector which is comprised of a number of Mythen2 detector modules. A collection time of 2 s was generally used for gold containing samples and 3 s for silver-containing samples, with the resulting data being the sum of two collections offset by 0.25 ° in 2θ. This is necessary as the detector is made up

*The normal operational energy for I11 is 15 keV but this wavelength could not be used due to its proximity to the gold L I 2s, L II 2p 1/2, and L III 2p 3/2 absorption edges.

of discrete modules with small gaps between these units.

Data Analysis

Pawley and Rietveld analyses were carried out using non-linear least squares refinement as implemented in TOPAS Academic V4.1.[332] In general, a TCHZ peakshape was used. For synchrotron data, the peakshape parameters, along with the zero offset were refined from a Si standard collected at room temperature except where substantial deviations were observed.* Peak shape parameters were refined for one temperature and subsequently fixed. Lorentzian and Gaussian strain parameters were used to account for sample-specific contributions to peakshape. Peak broadening and splitting due to poor alignment for one run of PPNNi[$Au(CN)_2$]$_3$ were modelled using sample displacement and tilt parameters as implemented in TOPAS. Riteveld refinements were based on (analogous) structures determined from single crystal diffraction with a limited number of parameters refined as discussed in the main text.[128,129,310,333]

2.3 Other analytical techniques

2.3.1 TGA

Thermogravimetric analysis (except that reported in Chapter 8) was carried out using a Perkin Elmer TGA-7 Thermogravimetric Analyzer. Quantities of between 1.5 mg and 5 mg loaded into an open platinum crucible were used for each measurement. Samples were held at 40 °C for 5 min and then ramped to 1000 °C at 5 °C min^{-1}.

*The PSD is particularly sensitive to sub-optimal sample alignment.

In Chapter 8 thermogravimetric analysis was carried out by Dr. S. G. Duyker using a TA Instruments Discovery TGA thermobalance, under nitrogen flow with a heating rate of 100 K min^{-1} from 293 K to 600 K.

2.3.2 TGA/DSC

Differential Scanning Calorimetry (DSC) measurements with concurrent TGA was performed using a Mettler Toledo TGA/DSC 1 STARe System. Each sample was placed in an open alumina crucible and measurements performed under flowing dry N_2. Sample masses of between 20–50 mg were used to ensure a balance between signal amplitude and sharpness. Powders were finely ground and tamped with a Teflon rod to give a uniformly packed powder with a flat surface. As this instrument is not fitted with a cooling system there is a characteristic increase in heat flow from the sample on cooling due to the heat retained by the alumina crucible. Data were typically collected in the range 25-300 °C at 10 °C min^{-1}. This strategy was occasionally modified to perform a cycle at a lower temperature first or to go to a lower maximum temperature if the sample would decompose below 300 °C. Crucibles were cleaned between runs using 6 M HCl.

2.3.3 SQUID Magnetometry

Magnetic property measurements, as reported in Chapter 5, were carried out on using a Quantum Design MPMS-XL superconducting quantum interference device (SQUID). Microcrystalline samples were packed in gelatine capsules and inserted securely into diamagnetic plastic straws. Direct current (DC) magnetisation was measured for all samples on warming from 2 K to 300 K under an applied DC field

of 100 Oe. All samples were first measured after having been cooled in zero field and then cooled in an applied DC field of 100 Oe.

2.3.4 Elemental Analysis

All Elemental analyses were carried out by MEDAC Ltd.

Chapter 3

New transition metal dicyanometallates

3.1 Introduction

Chapters 3 and 4 are based, to a large extent, on the related publication and together expand and systematise the structural chemistry of transition metal dicyanometallates.[333] In this Chapter I report the structures of a number of new dicyanometallate frameworks which contain molecular cations. On the one hand, these are of fundamental interest in terms of their structural chemistry, but on the other hand they may prove important by virtue of their conceptual relationship to other molecular analogues of conventional ceramics, including the semiconducting lead iodide family. In Chapter 4 I move on to suggest an organisation of the structures of known dicyanometallates that helps rationalise the structural diversity of this family. In doing so I begin to develop a set of design strategies that will ultimately allow rational control over framework structure in precisely the way envisaged by Robson in his node and linker paradigm.[21]

In Table 3.1 I have collected, to the best of my knowledge, the various dicyanometallate frameworks reported to date and in this Chapter. For simplicity, I have focussed on systems expressible in the form $A_mBX_n \cdot \{guest\}$. In this representation, A denotes an extra-framework cation (if present), B is the framework

node cation, X is a dicyanometallate anion, and I allow for the presence of solvent or other neutral molecules within the structure. What is immediately clear is that the family is extremely diverse, and encompasses much of the compositional and topological complexity responsible for the rich structural chemistry of conventional ceramic frameworks. In addition, and as in the transition-metal formate "MOF perovskites",[334–336] there is the intriguing capacity to incorporate molecular cations as a means of balancing framework charge. There is strong current interest in these systems as a direct result of the recent discovery of unconventional semiconductor behaviour in the $[CH_3NH_3]PbI_3$ family of solar cell materials.[215,337,338] Ordering processes involving molecular cations can be fundamentally different from those involving spherically symmetric or dipolar cations, as in conventional oxide ceramics.[339] The relationship between molecular geometry and host framework topology remains relatively unexplored—particularly in dicyanometallates.[310] Likewise, the nanometre node separation in dicyanometallate frameworks potentially allows for the incorporation of molecular cations capable of complex supramolecular interactions. I will return to this table in Chapter 4 once I have described the new dicyanometallates, which are the subject of this chapter.

3.2 Results and Discussion

3.2.1 Structural investigation of new dicyanometallates

My starting point is to describe the various new dicyanometallates I have prepared. Motivated by the desire to introduce molecular extra-framework cations, the typical synthetic strategy was to combine a simple transition-metal salt with a specially-

Table 3.1: Summary of the structurally-characterised dicyanometallate frameworks of general formula $A_mB(L)X_n{\cdot}G$ where L is a neutral ligand bound to the node metal centre (*i.e.*, not to the linker metal), and G is a non-coordinating guest molecule. Formulae including Au/Ag indicate that both the pure gold- and silver-containing compounds are known. Newly synthesised compounds reported here are shown in red.

B^IX Coordination number = 2

Chains

Parallel

$AuCN$ [341,342]
$AgCN$ [342,346,347]
$CuCN$ [351]
$Ni(L^1)(H_2O)Ag(CN)_2$ [354]

Criss-cross

low-T $Cu(CN)$ [351]

$A_{0.5}B^IX_{1.5}$ 3

(6,3) layers

$[Cu_2(2,2'\text{-bpy})_2(CN)]_{0.5}Cu[Cu(CN)_2]_{1.5}$ [91]

AB^IX_2 4

Square grids

Wavy

$KCu[Ag(CN)_2]_2$ [365]
$RbCu[Ag(CN)_2]_2$ [365]

$CsCu[Ag(CN)_2]_2$ [365]

AB^IX_2 4

Diamondoid

Distorted

$[NEt_4]Ag[Ag(CN)_2]_2$

$B^{II}X_2$ 4

Quartz

α-$Zn[Au(CN)_2]_2$ [128]

$Co[Au(CN)_2]_2$ [376]
α-$Zn[Ag(CN)_2]_2{\cdot}xAg(CN)$ [129]

$Cd(2,2'\text{-bpy})[Au(CN)_2]_2$ [378]
$Mn(2,2'\text{-bpy})[Au(CN)_2]_2$ [380]

$B^{II}X_2$ 4

Niobium monoxide (nbo)

$Fe(3\text{-}CNpy)_2[Au/Ag(CN)_2]_2{\cdot}\frac{2}{3}H_2O$ [352,383]
$Fe(TPT)_{2/3}[Au/Ag(CN)_2]_2$ [385]

$Fe(TPT)_{2/3}[Au/Ag(CN)_2]_2{\cdot}2CH_2Cl_2$ [385]
$Fe(TPT)_{2/3}[Ag(CN)_2]_2{\cdot}MeOH$ [385]

$B^{II}X_2$ 4

Cadmium sulfate (cds)

$Fe(pmd)(H_2O)[Au(CN)_2]_2{\cdot}H_2O$ [394]

$Fe(pmd)(H_2O)[Ag(CN)_2]_2{\cdot}H_2O$ [394]
$Fe(pmd)[Au(CN)_2]_2$ [394]

$B^{II}X_2$ 4

Square grid

Regular

$Cu(py)_2[Au(CN)_2]_2$ [343]
$Fe(3\text{-}Phpy)_2[Au(CN)_2]_2$ [348]
yellow-$Fe(3\text{-}CNpy)_2[Au(CN)_2]_2$ [352]
$Fe(DEAS)_2[Au/Ag(CN)_2]_2$ [355]
$Cd(py)_2[Ag(CN)_2]_2$ [356]

$Fe(py)_2[Ag(CN)_2]_2$ [358]

$Cu(DMF)[Au(CN)_2]_2$ [81]

blue-$Cu(DMSO)_2[Au(CN)_2]_2$ [81]

$Zn(NIT4Py)_2[Au(CN)_2]_2$ [361]

$Pb(phen)_2[Au(CN)_2]_2$ [362]

$Fe(H_2O)_2[Ag(CN)_2]_2{\cdot}(2,2'\text{-bpe})$ [364]

$(\frac{1}{2},\frac{1}{2})$ offset bilayers

$Co(DMF)_2[Au(CN)_2]_2$ [366]
$Mn(3\text{-}Fpy)_2[Au(CN)_2]_2$ [367]

$Mn(H_2O)_2[Au(CN)_2]_2$ [357]

$Mn(3\text{-}Mepy)_2[Ag(CN)_2]_2$ [359]

colourless-$Fe(3\text{-}CNpy)_2[Au(CN)_2]_2H_2O$ [352]

$Fe(4\text{-}Mepy)_2[Au(CN)_2]_2$ [370]

$Fe(3\text{-}Clpy)_2[Au/Ag(CN)_2]_2$ [371,372]

$Fe(3\text{-}Brpy)_2[Au/Ag(CN)_2]_2$ [371,372]
$Fe(3\text{-}Ipy)_2[Au/Ag(CN)_2]_2$ [371,372]

$Fe(3\text{-}Ipy)_2[Au(CN)_2]_2{\cdot}\frac{1}{2}3\text{-}Ipy$ [372]

$Fe(3\text{-}Fpy)_2[Au/Ag(CN)_2]_2$ [371,372]
$Cd(3\text{-}Fpy)_2[Au(CN)_2]_2$ [377]

$Mn(bim)[Ag(CN)_2]_2[(bim)AgCN]_2{\cdot}nH_2O$ [379]

Bridged (Hofmann)

$Zn(pyz)[Au(CN)_2]_2$ [381]
$Co(pyz)[Au(CN)_2]_2$ [381]

$Cd(4,4'\text{-bpy})[Ag(CN)_2]_2$ [384]
$Mn(4,4'\text{-bpy})[Au(CN)_2]_2{\cdot}2CHCl_3$ [386]

$Cu(pyz)[Au(CN)_2]_2$ [388]
$Fe(bpmp)[Au/Ag(CN)_2]_2{\cdot}n\text{DMF}{\cdot}\frac{1}{2}\text{EtOH}{\cdot}mH_2O$ [391]

$Fe(pyz)[Au(CN)_2]_2{\cdot}(pyz)$ [82]

$B^{II}X_2$ 4

Cristoballite

β-$Zn[Au(CN)_2]_2$ [78]
γ-$Zn[Au(CN)_2]_2$ [78]

$B^{II}X_2$ 4

Interpenetrating square grid

Inclined

$Cd(NH_3)_2[Ag(CN)_2]_2$ [344]
$Cu(NH_3)_2[Ag(CN)_2]_2$ [349]
$Zn(NH_3)_2[Au(CN)_2]_2$ [78]
$Cd(py)_2[Ag(CN)_2]_2{\cdot}C_4H_5N$ [356]
$Cd(py)_2[Ag(CN)_2]_2{\cdot}C_6H_6$ [356]

$Mn(4\text{-}Mepy)_2[Ag(CN)_2]_2$ [359]

Interwoven

$Ca[Ag(CN)_2]_2{\cdot}2H_2O$ [360]

$Sr[Ag(CN)_2]_2{\cdot}2H_2O$ [360]

$Cd(4\text{-}Mepy)_2[Ag(CN)_2]{\cdot}(4\text{-}Mepy)$ [363]

$B^{II}X_2$ 4

Other

Two layer herringbone

$Cd(hydeten)[Ag(CN)_2]_2{\cdot}\frac{1}{2}H_2O$ [368]

Bifurcated chains

$Mn(NIT3Py)_2[Au(CN)_2]_2$ [369]

$Co(NIT3Py)_2[Au(CN)_2]_2$ [369]

$Zn(NIT3Py)_2[Au(CN)_2]_2$ [369]

Bridged interwoven (6,3) (mok)

δ-$Zn[Au(CN)_2]_2$ [78]

lvt

$Mn(4\text{-}CNpy)(H_2O)[Ag(CN)_2]_2$ [375]

Binodal (pts)

$Mn(py\text{-}4\text{-}aldoxime)(H_2O)[Ag(CN)_2]_2$ [375]

$A_{0.5}B^IX_{2.5}$ 5

Layered

Perovskite slabs

$[PPN]_{0.5}Cu[Au(CN)_2]_{2.5}{\cdot}EtOH$

$[PPN]_{0.5}Cd[Ag(CN)_2]_{2.5}(EtOH)$
$[PPN]_{0.5}Mn[Ag(CN)_2]_{2.5}(EtOH)$

$A_{0.5}B^IX_{2.5}$ 5

Other

Bridged interwoven (6,3) (*jah*1)

$[Bu_4N]_{0.5}Cd[Ag(CN)_2]_{2.5}$

$AB^{III}X_3$ 6

α-Po

$KCo[Au(CN)_2]_3$ [79,340]
$RbCd[Ag(CN)_2]_3$ [345]
$KNi[Au(CN)_2]_3$ [350]
$KMn[Ag(CN)_2]_3$ [353]
$KCd[Au/Ag(CN)_2]_3$ [98]
$KFe[Au/Ag(CN)_2]_3$ [83,357]

$AB^{III}X_3$ 6

Perovskite

$[PPN]Ni[Au(CN)_2]_3$ [310]

$[PPN]Co[Au(CN)_2]_3$ [310]

$[PPN]Cd[Au(CN)_2]_3$

$[PPN]Mn[Au(CN)_2]_3$

$[PPN]Cd[Ag(CN)_2]_3{\cdot}3\text{EtOH}{\cdot}xH_2O$

$AB^{III}X_3$ 6

Other

Intersecting rectangular grids (bcs)

$[Bu_4N]Ni[Au(CN)_2]_3$ [310]

$B^{III}X_3$ 6

α-Po

$Ag_3[Co(CN)_6]$ [373]

$Ag_3[Fe(CN)_6]$ [374]
$Au/Ag_3[In(CN)_6]$ [98]

$Ag_3[In(CN)_6]{\cdot}xH_2O$ [98]

$B^{III}X_3$ 6

acs

$La[Au/Ag(CN)_2]_3(H_2O)_3$ [119]
$La[Ag_{0.39}Au_{0.61}(CN)]_3(H_2O)_3$ [119]

$La[Ag_{0.83}Au_{0.17}(CN)]_3(H_2O)_3$ [119]
$Pr[Au/Ag(CN)_2]_3(H_2O)_3$ [382]

$Nd[Au/Ag(CN)_2]_3(H_2O)_3$ [121]
$Sm[Au(CN)]_3(H_2O)_3$ [387]

$Eu[Au/Ag(CN)_2]_3(H_2O)_3$ [389,390]
$Eu_{0.5}Tb_{0.5}[Au(CN)]_3(H_2O)_3$ [390]

$Gd[Au(CN)]_3(H_2O)_3$ [392]

$Tb[Au(CN)]_3(H_2O)_3$ [120,393]

$Am[Au/Ag(CN)_2]_3(H_2O)_3$ [121]

$Cm[Au/Ag(CN)_2]_3(H_2O)_3$ [382]

Abbreviations used: L^1 = N-(3-aminopropyl)-5-bromosalicylaldimine; 2,2′-bpy = 2,2′-bipyridine; Et = C_2H_5; 3-CNpy = 3-cyanopyridine; TPT = 2,4,6-tris(pridyl)triazine; Me = CH_3; pmd = pyrimidine; py = pyridine; 3-Phpy = 3-phenylpyridine; DEAS = 4′-diethylaminostilbazole; DMF = N,N′-dimethylformamide; DMSO = dimethylsulfoxide; NIT4Py = 2-(4′-pyridyl)-4,4,5,5-tetramethylimidazoline-1-oxyl-3-oxide; phen = 1,10-phenanthroline; 2,2′-bpe = 2,2′-bis(pyridyl)ethene; 3-Fpy = 3-fluoropyridine; 3-Mepy = 3-methylpyridine; 4-Mepy = 4-methylpyridine; 3-Clpy = 3-chloropyridine; 3-Brpy = 3-bromopyridine; 3-Ipy = 3-iodopyridine; bim = benzimidazolate; pyz = pyrazine; 4,4′-bpy = 4,4′-bipyridine; bpmp = 1,4-bis(pyridin-4-ylmethyl)piperazine; hydeten = N-(2-hydroxyethyl)ethylenediamine); NIT3Py = 2-(3′-pyridyl)-4,4,5,5-tetramethylimidazoline-1-oxyl-3-oxide; PPN = bis(triphenyl-phosphine)iminium cation; Bu = n-C_4H_9.

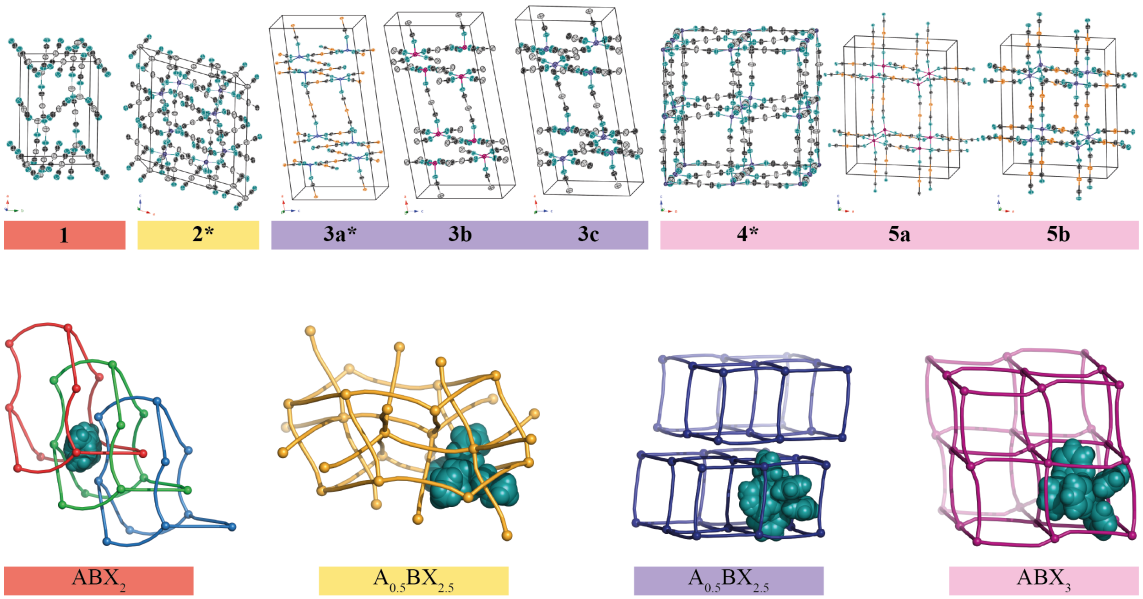

Figure 3.1: Representations of the crystal structures of the various new dicyanometallate frameworks reported in this Chapter. The top panels show structures in thermal ellipsoid representation (probability = 50%, or 90% where indicated with an asterisk). Each image is represented at the same absolute scale; extra-framework cations and solvent molecules have been omitted for clarity. The bottom panels show schematic representations of the corresponding network topologies. In each case a single extra-framework cation is shown in space-filling representation to illustrate the relationship between cation shape and network topology.

prepared molecular salt of a given dicyanometallate anion. The latter acts as the source of molecular cation in the framework that ultimately forms.* I report eight new compounds, which adopt a total of five structure types and correspond to the three fundamental compositions ABX_2, $A_{0.5}BX_{2.5}$, and ABX_3. These structures and structure types are represented together in Figure 3.1.

Diamondoid ABX_2:

The first system described was the fortuitous result of attempts to prepare $[NEt_4][Ag(CN)_2]$ as a dicyanometallate precursor for subsequent framework formation. The combination of $[NEt_4]Cl$ or $[NEt_4]Br$ with $KAg(CN)_2$ yields the same dicyanometal-

*See Appendix A1 for the structures of $PPNAu(CN)_2$ and $PPNAu(CN)_2$.

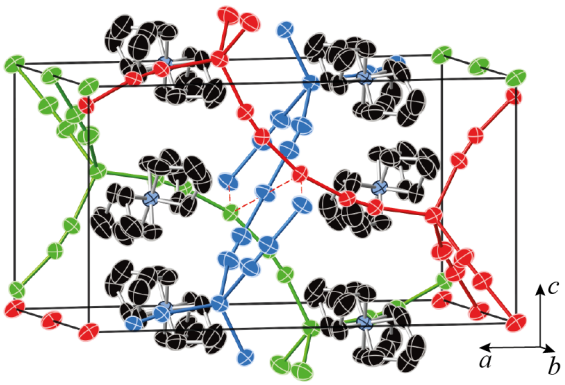

Figure 3.2: Crystal structure of $[NEt_4]Ag[Ag(CN)_2]_2$. The three diamondoid frameworks are shown in red, green, and blue. $[NEt_4]^+$ is disordered over a mirror plane. Short Ag···Ag distances illustrated in the middle of the unit cell with red dotted line. Displacement parameters drawn at 50% probability and H not shown for clarity.

late framework $[NEt_4]Ag^{I}[Ag(CN)_2]_2$ (**1**) in which silver(I) cations participate as both node and linker. The dual roles of silver(I) in this system are distinguishable by both coordination geometry and cyanide binding orientation: the node cations are tetrahedrally-coordinated by the N cyanide terminus and the linker cations are linearly-coordinated by the C cyanide terminus. The crystal structure is illustrated in Figure 3.2 and relevant crystallographic details are summarised in Table 3.2. Three distorted diamondoid networks interpenetrate, with each $[NEt_4]^+$ cation contained within a cavity formed by the combination of all three networks.

The triple interpenetration results in zig-zag chains of short Ag···Ag distances (3.042 Å) running along the *b*-direction indicative of argentophilic interactions. Similar metallophilic interactions are observed for fivefold interpenetrated β-$Zn[Au(CN)_2]_2$.[78] but here form layers of (10,3) nets.

An intriguing property of this system is the existence of a phase transition on cooling below 235 K. This transition—which will be described in detail in Chapter 6—involves the condensation of a soft phonon mode at an incommensurate wave-

Table 3.2: Crystallographic details for the new materials reported in this Chapter.

Compound	**1**	**2**	**3a**	**3b**
Empirical formula	$Ag_3N_5C_{12}H_{20}$	$Cd_2Ag_5N_{11}C_{26}H_{36}$	$Cu_2Au_5P_2N_{11}C_{50}O_2H_{42}$	$Mn_2Ag_5P_2N_{11}C_{50}O_2H_{42}$
Formula weight (g mol^{-1})	557.92	1266.79	2002.83	1540.1
Crystal System	Orthorhombic	Monoclinic	Monoclinic	Monoclinic
Space Group	*Pnma* (No. 62)	*C*2/c (No. 15)	*C*2/c (No. 15)	*C*2/c (No. 15)
Z	4	4	4	4
Radiation (Å)	Cu K$_\alpha$, $\lambda = 1.54180$	Mo K$_\alpha$, $\lambda = 0.71073$	$\lambda = 0.68890$	Cu K$_\alpha$, $\lambda = 1.54180$
Crystal colour	Pale Yellow	Colourless	Green	Colourless
Crystal size (mm)	0.05×0.11×0.12	0.06×0.14×0.16	0.01×0.01×0.01	0.09×0.22×0.27
Temperature (K)	280.2(5)	150.0(5)	30.0(3)	300.00(3)
a (Å)	16.6101(3)	16.2798(2)	27.9505(6)	28.3700(3)
b (Å)	11.2973(2)	13.9248(2)	15.0898(4)	15.6843(2)
c (Å)	9.2725(2)	18.0439(2)	13.4803(3)	13.91760(10)
V (Å^3)	1739.98(6)	3930.35(9)	5647.5(2)	6105.94(11)
β (°)	—	106.0823(5)	96.629(2)	99.6092(10)
μ (mm^{-1})	26.795	3.531	13.78	16.671
Reflections ($I > 2\sigma(I)$)	1842	4095	8549	5325
R (F_o)	0.0258	0.0220	0.0372	0.0282
R$_w$ (F_o)	0.0661	0.0493	0.0839	0.0673
GOF	0.951	1.0249	0.9932	1.0497

Compound	**3c**	**4**	**5a**	**5b**
Empirical formula	$Cd_2Ag_5P_2N_{11}C_{50}O_2H_{42}$	$Cd_1Ag_3P_2N_7C_{48}H_{48.87}O_{3.44}$	$Mn_1Au_3P_1N_6C_{24}H_{15}$	$Cd_1Au_3P_1N_6C_{24}H_{15}$
Formula weight (g mol^{-1})	1653.04	1276.78	1340.52	1398
Crystal System	Monoclinic	Cubic	Monoclinic	Monoclinic
Space Group	*C*2/c (No. 15)	$Pa\bar{3}$ (No. 205)	*I*2/a (No. 15)	*I*2/a (No. 15)
Z	4	8	4	4
Radiation (Å)	Cu K$_\alpha$, $\lambda = 1.54180$	Mo K$_\alpha$, $\lambda = 0.71073$	Mo K$_\alpha$, $\lambda = 0.71073$	Cu K$_\alpha$, $\lambda = 1.54180$
Crystal colour	Colourless	Colourless	Colourless	Colourless
Crystal size (mm)	0.04×0.10×0.23	0.19×0.34×0.39	0.06×0.08×0.10	0.02×0.02×0.10
Temperature (K)	282(8)	280.0(4)	150.0(5)	291.8(1)
a (Å)	28.5577(8)	21.7394(3)	16.7035(3)	16.8455(3)
b (Å)	15.8350(4)	21.7394(3)	12.5777(3)	12.7383(3)
c (Å)	13.9531(4)	21.7394(3)	20.6707(4)	20.8965(3)
V (Å^3)	6226.6(3)	10274.1(2)	4338.48(15)	4480.19(15)
β (°)	99.310(3)	—	92.5382(10)	92.3725(16)
μ (mm^{-1})	18.499	1.633	10.509	22.772
Reflections ($I > 2\sigma(I)$)	5585	5085	4065	4094
R (F_o)	0.0400	0.0388	0.0377	0.0226
R$_w$ (F_o)	0.1148	0.0820	0.0668	0.0525
GOF	0.958	1.0363	1.067	0.9997

vector. The study of classical soft-mode transitions in extended frameworks is a relatively unexplored field;[130,281] the purpose of drawing attention to this transition here is to highlight that the dynamics of these materials may well be of interest in their own right.

5-connected $\mathbf{A_{0.5}BX_{2.5}}$:

Reaction of $[NBu_4][Ag(CN)_2]\cdot\frac{1}{2}H_2O$ with cadmium nitrate leads to the structurally-complex phase $[NBu_4]_{0.5}Cd^{II}[Ag(CN)_2]_{2.5}$ (**2**), as illustrated in Figure 3.3(a). Key crystallographic details of **2** are again summarised in Table 3.2. In the absence of a strong coordination preference, Cd^{II} has here adopted a distorted trigonal bipyrami-

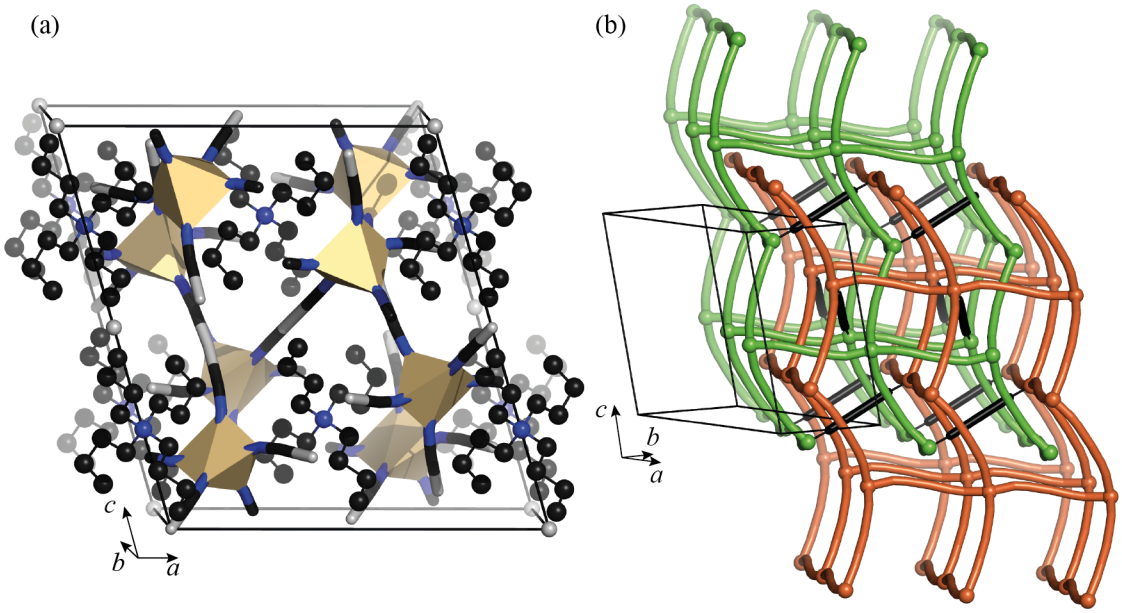

Figure 3.3: Structure of $[NBu_4]_{0.5}Cd[Ag(CN)_2]_{2.5}$ (**2**). (a) Unit cell with $[NBu_4]^+$ completed beyond cell boundary. (b) Decomposition of the *jah*1 topology adopted by **2**. The topology can be decomposed into two interpenetrating **cds** nets (green and brown) by breaking the linkers shown in black. The bonds between the black linkers and the two **cds** nets are shown with thin lines.

dal geometry. These pentacoordinate nodes connect to give a unique, self-catenating topology (TOPOS reference *jah*1*) that can be related to a linked pair of interpenetrating **cds**-type nets. **2** has a unique uninodal 5-connected topology with vertex symbol 4.4.6.6.6.6.6.6.6.6(3) (shortened to $4^2 6^8$). This self-catenating topology, *jah*1, can be decomposed, by breaking one linker, into two interpenetrating **cds** nets [Figure 3.3(b)].

Alternatively the structure can be understood by reference to another net. Looking down the *c* axis, it can be thought of as pairs of corrugated, interpenetrating (6,3) nets stacked in an *AB...* manner. These layers are connected by perpendicular struts of linear Cd–NC–Ag–CN–Cd linkages. The shortest connection between interpenetrated (6,3) nets is *via* three nodes. The additional connectivity compared

*The topology was detected with TOPOS[395,396] and deposited in the TTD[134] archive.

to the pairs of (6,3) net results in a self-catenated single network. Mindful that correlation does not necessarily imply causation, it is noted nonetheless that there is again a close match between framework cavity and molecular cation shape. This suggests that the form of the $[NBu_4]^+$ cation may be responsible for the unusual topology assumed by this material.

As in **1** and numerous other dicyanoargentate frameworks,[98,373] **2** contains a series of short $Ag^I \cdots Ag^I$ contacts generally considered indicative of $d^{10} \cdots d^{10}$ argentophilic interactions. These interactions are often strongly susceptible to changes in external conditions, such as temperature and pressure.[97,109,110,397–399] The thermal expansion behaviour of **2** was determined in order to identify any unusual thermomechanical response and shows that the primary responses are parallel and perpendicular to these argentophilic interactions. The fit to the percent change of the principal axes is shown in Figure 3.4 and the unit cells used to calculate these values can be found in Appendix A2. The coefficients of thermal expansion were found to be $\alpha_{X_1} = \alpha_{\parallel} = -83.1(1.6)\,MK^{-1}$, $\alpha_{X_2} = 4.7(1.8)\,MK^{-1}$, and $\alpha_{X_3} = \alpha_{\perp} = 138(5)\,MK^{-1}$. In terms of the unit cell axes $X_1 = \mathbf{b}$, $X_2 = -0.504\mathbf{b} + 0.864\mathbf{c}$, and $X_3 = 0.846\mathbf{b} - 0.534\mathbf{c}$ [Figure 3.5]. Coefficients of thermal expansion were calculated from single crystal diffraction data over the range 100–400 K using the webtool PASCal.[400] The NTE along X_1 arises from the geometric response of the framework to the large PTE along the argentophilic interactions (X_3) in a manner analogous to the 'wine-rack' mechanism of $Ag_3[Co(CN)_6]$.[76]

An alternative five-connected dicyanometallate structure that is more obviously related to the molecular perovskite analogues discussed above can be accessed by reaction of $[PPN]^+$ (bis(trisphenylphosphine)iminium cation) dicyanometallates with

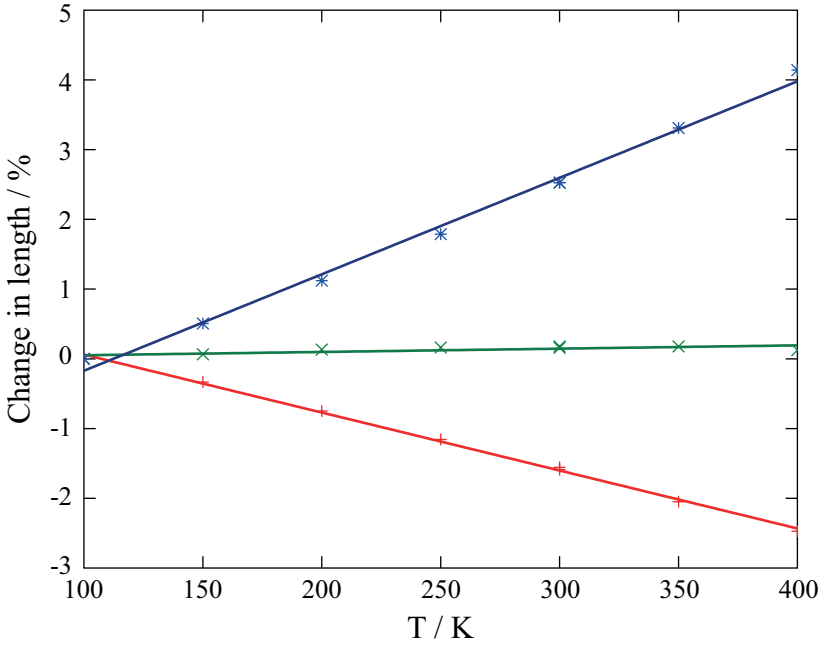

Figure 3.4: Variable temperature behaviour of $[NBu_4]_{0.5}Cd[Ag(CN)_2]_{2.5}$ (**2**) determined by single crystal diffraction. Data are plotted as percent change in principal axes of thermal expansion X_1 (red), X_2 (green), X_3 (blue) with fit shown as solid line. As **2** is monoclinic the principal axes of thermal expansion do not necessarily coincide with the crystallographic axes. Coefficients of thermal expansion were calculated using the webtool PASCal.[400]

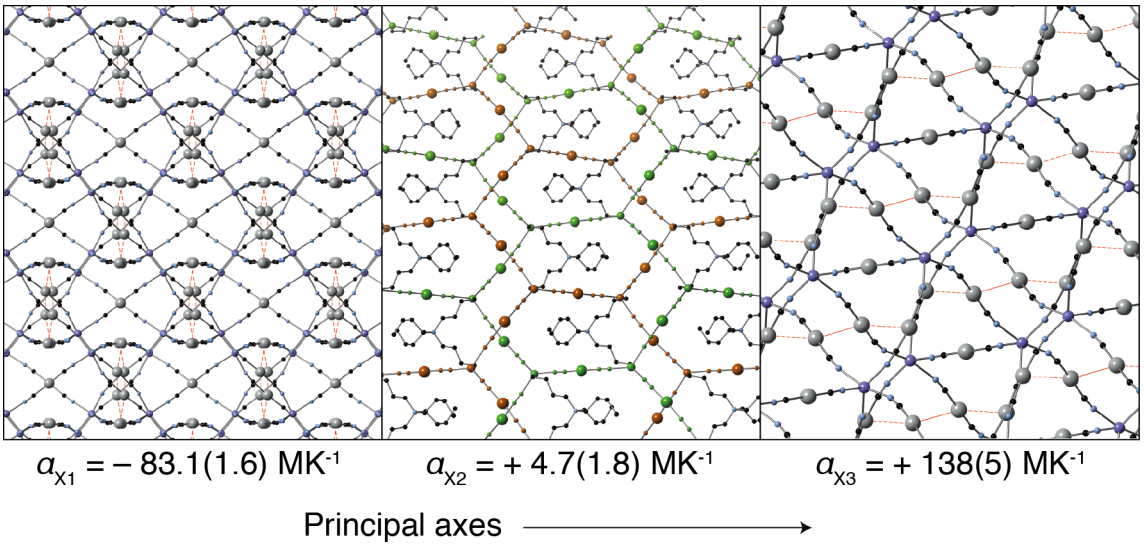

Figure 3.5: Views of the three principal axes of thermal expansion and their relationship to the crystal structure. Ag···Ag distances of less than 3.44 Å are indicated by red dashed lines. Cd (purple), Ag (grey), N (blue), C (black). In the central panel only a single pair of interwoven (6,3) nets is shown (green and brown) and the $[NBu_4]^+$ extra-framework cation is shown.

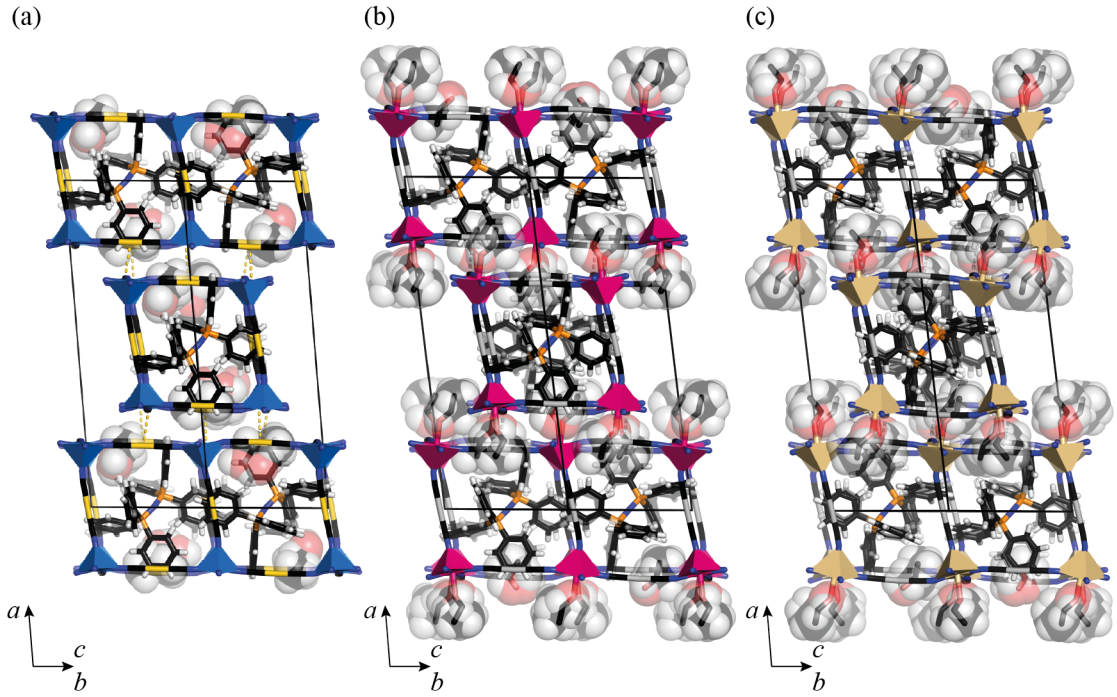

Figure 3.6: Crystal structures of (a) $[PPN]_{0.5}Cu[Au(CN)_2]_{2.5}\cdot EtOH$ (**3a**), (b) $[PPN]_{0.5}Mn[Ag(CN)_2]_{2.5}\cdot EtOH$ (**3b**), and (c) $[PPN]_{0.5}Cd[Ag(CN)_2]_{2.5}\cdot EtOH$ (**3c**). Minor disorder components of $[PPN]^+$ and EtOH shown as translucent spheres. The coordination of Jahn-Teller active Cu^{2+} is 5-coordinate (a) but those of Mn^{2+} (b) and Cd^{2+} (c) are made octahedral by a capping ethanol molecule. Interlayer Au$\cdots$Au contacts of 3.11 Å are found in (a) and Ag$\cdots$Ag contacts of 3.30 Å and 3.29 Å in (b) and (c) respectively.

transition-metal salts. The crystal structures of $[PPN]_{0.5}Cu[Au(CN)_2]_{2.5}\cdot EtOH$ (**3a**), $[PPN]_{0.5}Mn[Ag(CN)_2]_{2.5}\cdot EtOH$ (**3b**), and $[PPN]_{0.5}Cd[Ag(CN)_2]_{2.5}\cdot EtOH$ (**3c**) are shown in Figure 3.6 and key crystallographic details are again summarised in Table 3.2.

In these compounds, the dicyanometallate network forms grid-like layers of connected cubes that are then stacked on top of one another. The large molecular cations occupy the voids at the centre of each $\sim(nm)^3$ cube. Because the layers are not connected, each transition metal node is coordinated by dicyanometallate anions in a square pyramidal geometry. Whereas in the case of Cu^{2+} this coordination geometry is straightforwardly understood in terms of the d^9 electronic configura-

tion, for **3b** and **3c** the Mn^{2+} and Cd^{2+} coordination is actually octahedral and is completed by one molecule of the ethanol solvent from which the crystals were grown. The ability to incorporate octahedral node geometries *via* solvent coordination means that, in principle at least, this phase may be accessible for a range of other transition-metal dications. In practice, the balance with competing phases (discussed further below) is remarkably subtle.

In each of the compounds **3a**–**c**, successive layers are offset by one half of the cube face diagonal.* This offset has the effect of bringing Ag^+ or Au^+ cations at the cube edges into close contact, which will presumably maximise metallophilic interactions. In this sense there is a clear distinction from the structural chemistry of oxide frameworks, where there is a strong repulsion between the linker anions. In the related $n = 2$ Ruddlesden-Popper phases (*e.g.* $Sr_3Ti_2O_7$) this repulsion is relieved by presence of additional A-cations as rocksalt-type layers.[167†] In our case, the weak metallophilic forces holding neighbouring layers together may be expected to result in particularly anisotropic elastic response for this family,[402] while also allowing for the possibility of intercalation chemistry.[403–405]

Cubic ABX_3:

The analogy between dicyanometallate frameworks and perovskite oxides is clearest in the last family of compounds reported here. These again make use of the $[PPN]^+$ dicyanometallates in their synthesis. Similar conditions to those described above for **3a**–**c** allowed preparation of the ABX_3 solvate $[PPN]Cd[Ag(CN)_2]_3{\cdot}3EtOH{\cdot}nH_2O$

*The topology of $[PPN]_{0.5}BX_{2.5}{\cdot}\{EtOH\}$ corresponds to the 3-dimensional 2-periodic sphere packing (4,4)Ia.[401]

†Removal of the NaCl layers between the $n = 2$ perovskite blocks in $A_3B_2O_7$ would leave behind AB_2O_5 layers with an AB... stacking sequence exactly as found in compounds **3a**–**c**.

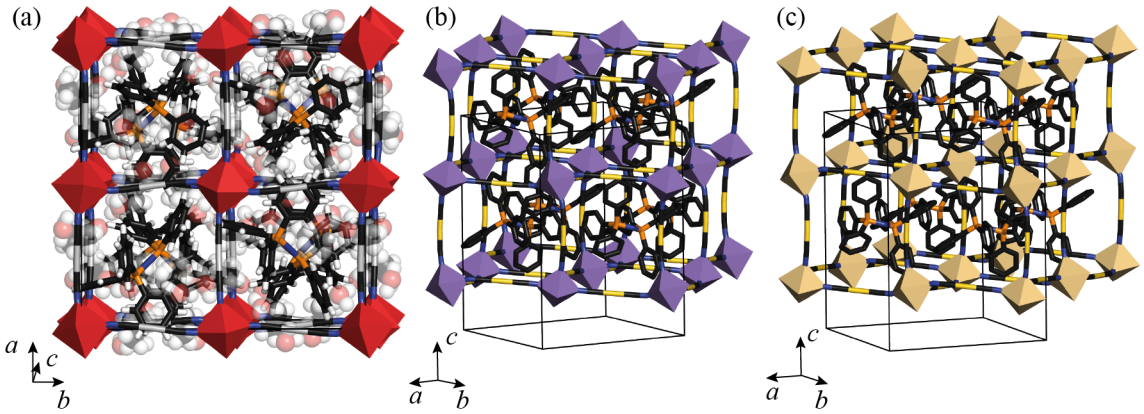

Figure 3.7: Structures of (a) [PPN]Cd[Ag(CN)$_2$]$_3$·3EtOH·nH$_2$O (**4**), (b) [PPN]Mn[Au(CN)$_2$]$_3$ (**5a**), and (c) [PPN]Cd[Au(CN)$_2$]$_3$ (**5b**). All three compounds have a perovskite structure with molecular A and X components. In the case of **4** the structure is stabilised by solvent of crystallisation (shown as translucent spheres). H atoms shown selectively for clarity.

(**4**) and the solvent-free frameworks [PPN]Mn[Au(CN)$_2$]$_3$ (**5a**) and [PPN]Cd[Au(CN)$_2$]$_3$ (**5b**). In the case of **4**, crystals grew directly from reaction mixtures that had originally formed crystals of **3c**; the relationship between these phases is discussed in more detail below. The structures of all three compounds **4**, **5a**, **5b** are clear analogues of perovskites: octahedrally-coordinated Mn^{II}/Cd^{II} centres are connected to form the characteristic cubic network, with [PPN]$^+$ cations adopting the '12-coordinate' A-cation site [Figure 3.7]. The term 'superperovskites' is used to reflect this structural correspondence and to emphasise that the B$\cdots$B separation across the perovskite cube edge is now on the nanometre scale.

Just as for other perovskite analogues, long-established geometric descriptors can be applied to these superperovskite frameworks. For example, we calculate 'tolerance factors'[18,146,163] of 1.02 (at 150 K) and 1.00 (at 300 K) for **5a** and **5b**, respectively; likewise the octahedral tilt systems active in both structures correspond to the same Glazer notation $a^-a^-c^-$.[184,195] While the tilts of compounds **5a** and **5b** can be

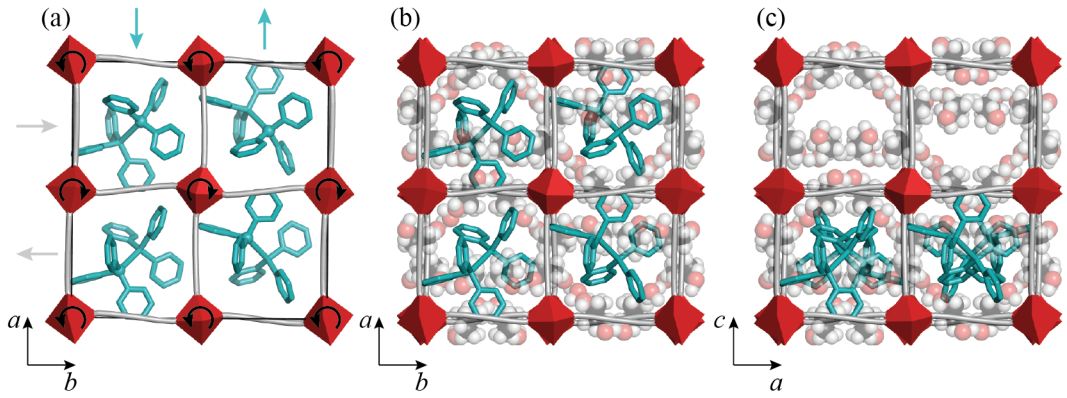

Figure 3.8: [PPN]Cd[Ag(CN)$_2$]$_3$·3EtOH·nH$_2$O (a) Front layer of octahedra to show in-phase in-plane tilting—in this plane tilting around c is correlated in-phase along b. Rows of linker displacements are indicated by grey arrows. Sheets of cation displacements are indicated with teal arrows. The 'front' P of each [PPN]$^+$ is shown as a sphere. (b) All polyhedra and front layer of [PPN]$^+$ are shown. The included solvent occupies void space allowing this system to adopt cubic symmetry. (c) Same contents as in (b) but looking down b.

described completely using Glazer notation, compound **4** shows in-phase tilting of adjacent octahedra correlated perpendicular to the rotation axis [Figure 3.8(a)]: an impossibility for perovskites, such as oxides and halides, with monoatomic anions. The tilts in compound **4** will be discussed in detail in Chapter 7 where notation to describe these unconventional tilts will be developed.

Returning to the details of the tolerance factor for molecular perovskites, it will be shown that these numbers should be used with care. The modified tolerance factor approach developed by Kieslich[146] [discussed more fully in Section 1.5.2] is followed here and formulated as,

$$\alpha = \frac{(\boldsymbol{r}_{\mathrm{A_{eff}}} + \boldsymbol{r}_{\mathrm{X_{eff}}})}{\sqrt{2}(\boldsymbol{r}_{\mathrm{B}} + 0.5\boldsymbol{h}_{\mathrm{X_{eff}}})}, \tag{3.1}$$

for which effective radii are defined from crystallographic data and $\boldsymbol{h}_{\mathrm{X_{eff}}}$ is the length of the molecular linker, which is modelled as a rod of uniform radius.[146] The effective

radii are made up of the distance from the centre of mass of the ion to the outermost atom plus the ionic radius of the outermost atom. Full details of the calculations are given in Appendix A3 and pertinent details summarised in Table 3.3. It is worth exploring here the relative importance of the terms in this equation with perovskites on the nanometre scale. This can be done by comparing **5b** with the crystallographic data from the literature for the Ni analogue, [PPN]Ni[$Au(CN)_2$]$_3$.[310] It is noteworthy that the values of $\boldsymbol{r}_{A_{eff}}$ for $[PPN]^+$ in these two systems are rather different: the $[PPN]^+$ in the monoclinic Cd^{2+} compound is 5% larger than the $[PPN]^+$ in the rhombohedral Ni^{2+} compound. This results from the conformational degrees of freedom of $[PPN]^+$ [Section 1.8]. Adding to this effect on the value of the tolerance factor is the 2% larger $\boldsymbol{r}_{X_{eff}}$ value for **5b** which results from the linker being less linear than in the Ni^{2+} analogue. The combined effect of the differences in the measured radii of the molecular components results in a variation of 0.05 in α. The difference resulting from the change in $\boldsymbol{r}_B$ for Cd^{2+} to Ni^{2+} is identical. These observations indicate two things: (i) at large length scales $\boldsymbol{r}_B$ has a comparatively small effect on the value of the tolerance factor and (ii) the internal degrees of freedom of moderately flexible molecular components can have a similar influence to changes in $\boldsymbol{r}_B$, in this case roughly 5%.

Taken together these considerations suggest that, while tolerance factors may not be as useful here as for oxides and halides, they may be useful for assessing the compatibility of, for example, molecular A cations and molecular linkers. Yet, the conformational freedom of both molecular components may be confounding factors in using tolerance factors as predictive tools.

Table 3.3: Tolerance factor calculations for real and hypothetical superperovskites. The first two entries are derived from real crystallographic data for the relevant compounds where M indicates that it is a monoclinic structure and R that it is rhombohedral. The second two entries illustrate the effect of the difference in measured radii for the molecular components in the two cases.

	$\boldsymbol{r}_{\mathrm{A_{eff}}}$ / Å	$\boldsymbol{r}_{\mathrm{X_{eff}}}$ / Å	$\boldsymbol{h}_{\mathrm{X_{eff}}}$ / Å	$\boldsymbol{r}_{\mathrm{B}}$ / Å	α
M-[PPN]Mn[Au(CN)$_2$]$_3$ **5a**	6.31	1.48	9.15	0.83	1.02
M-[PPN]Cd[Au(CN)$_2$]$_3$ **5b**	6.30	1.47	9.11	0.95	1.00
R-[PPN]Ni[Au(CN)$_2$]$_3$	6.00	1.44	9.12	0.69	1.00
'R-[PPN]Cd[Au(CN)$_2$]$_3$'	6.00	1.44	9.12	0.95	0.95
'M-[PPN]Ni[Au(CN)$_2$]$_3$'	6.30	1.47	9.11	0.69	1.05

Another aspect that should be addressed in detail is the role of cation and ligand displacements. The $[PPN]^+$ in **5a,b** all have their P$\cdots$P axis aligned along the pseudo-cubic [112] axis with the direction of the P—N—P bend angle ordered in a rocksalt fashion. The arrangement of $[PPN]^+$ in **4** is drastically different. There are 8 $[PPN]^+$ in the unit cell which can be divided into four pairs aligned along the $\langle 111 \rangle$ directions [Figure 3.9]. Within each of the pairs of cations they are displaced in opposite directions—*e.g.* in Figure 3.9(b) the green $[PPN]^+$ are aligned along the [111] but the one in the front layer is displaced in the $[\bar{1}\bar{1}\bar{1}]$ direction. The large magnitude of displacement (0.93 Å) is possible due to the presence of ethanol and water filling voids between cations as well as ligand displacement.* By comparison, displacements of 0.34 Å have been observed for the molecular perovskite $[N(CH_3)_4]Mn(N_3)_3$.[210] High temperatures would be needed to support any cubic phase with $[PPN]^+$ as the sole framework species. The combination of cation displacement, ligand displacement, and solvent inclusion suggests that $[PPN]^+$ is likely too small and of unsuitable shape to do so with the typical thermal stability of

*This displacement in $Pa\bar{3}$ is analogous to that corresponding to the $[S_2]^{2-}$ species in pyrites.[406]

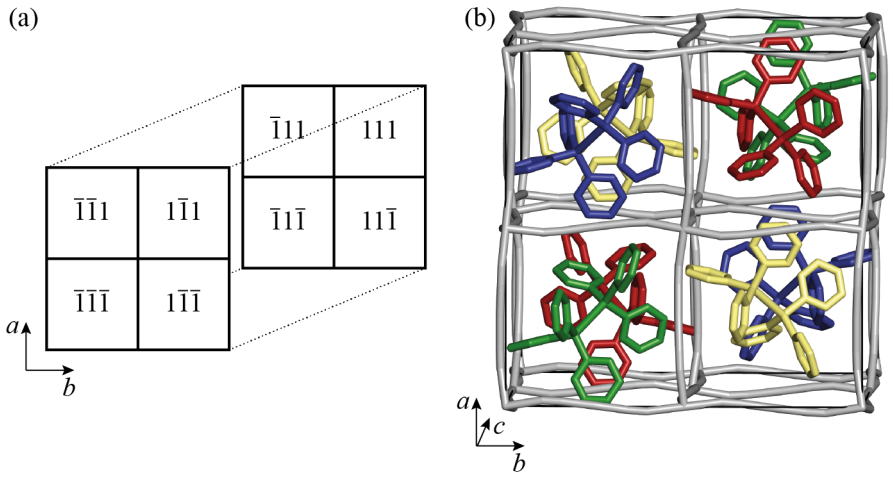

Figure 3.9: (a) Schematic showing the ordering and displacement of $[PPN]^+$ within the unit cell of $[PPN]Cd[Ag(CN)_2]_3{\cdot}3EtOH{\cdot}nH_2O$. Each $[PPN]^+$ is aligned one of the four symmetry independent $\langle 111 \rangle$ directions. For the two $[PPN]^+$ in each unit cell aligned along each of the axes, one is displaced postively and one negatively displaced along its alignment axis. (b) Representation of the ordering and displacement of $[PPN]^+$ within the unit cell. Each pair of $[PPN]^+$ are depicted in the same colour and are aligned along the same $\langle 111 \rangle$-type axis. Within a pair, the cations are displaced in the opposite direction *e.g.* the green $[PPN]^+$ are aligned along the [111] but the one in the front layer is displaced in the $[\bar{1}\bar{1}\bar{1}]$ direction.

dicyanometallate compounds [Appendix A4].[310]

Because the phenyl groups of the $[PPN]^+$ cation extend up to the perovskite cube faces in all $[PPN]^+$-containing compounds, there are direct cation–cation interactions that may influence the phase transition behaviour of these systems. In contrast to the 'simple' monopolar and/or dipolar interactions between A-site cations in oxide perovskites, these interactions are inherently multipolar, which in turn may give rise to complex ordering processes unrealisable in conventional ceramics. Indeed the $[PPN]^+$ conformations we observe in compound **3c** and its transformation product **4** are fundamentally different from those found in **5a** and **5b**: in the former the phenyl rings are oriented as if to maximise cation–π interactions with the linker Ag^+ cation, whereas in the latter intra- and inter-molecular π–π interactions dominate [Figure 3.10(a,b)]. This is entirely consistent with the diversity of $[PPN]^+ \cdots [PPN]^+$

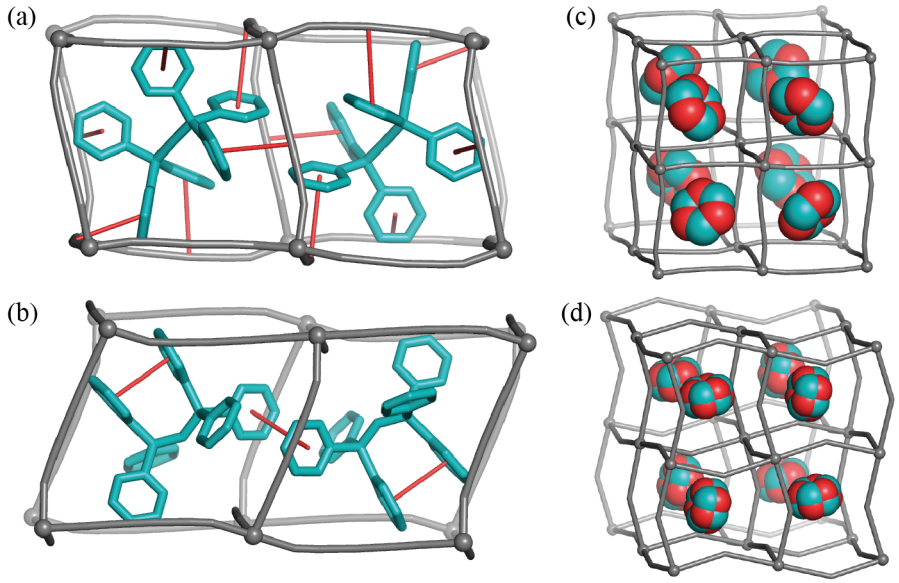

Figure 3.10: Short cation–π and π–π interactions in **3c** (a) and **5b** (b). Distances shorter than 4.2 Å are indicated by red lines. In **3c** the phenyl rings are oriented such that short cation–π distances are maximised whereas in **5b** intra- and inter-molecular π–π interactions dominate. Crucially, the latter are present between adjacent $[PPN]^+$ cations. $[PPN]^+$ cations are inherently multipolar and their packing in **4** (c) corresponds to ordered hexapoles. Such multipolar interactions are common for framework materials with molecular cations such as $[CH_3NH_3]PbI_3$ (d) where the dynamics of these interactions are implicated in slow exciton recombination (cation-ordered *Pnma* structure shown).[216,339] Framework shown in grey, cation in teal (a,b), multipoles in teal and red (c,d), H atoms not shown for clarity.

supramolecular interaction motifs known to occur in the solid state.[308] So one alternative view of the structures of **5a** and **5b** is that the anionic dicyanometallate framework acts to impose a particular geometric arrangement of the PPN^+ cations that may not necessarily be compatible with the inter-cation interactions. I suggest that exploration of this tension between complex multipolar interactions and the geometry of the lattice supporting those interactions may be a fertile playground for future research given, for example, the implication of multipolar dynamics in extending charge-carrier lifetimes in $[CH_3NH_3]PbI_3$ [Figure 3.10(c,d)].[216]

3.3 Summary

In this Chapter I have shown that the dicyanometallate linker, in combination with extra-framework cations of different shapes and sizes, can support a large range of structure types. While these are often closely related to very familiar structures—diamond, perovskite, Ruddlesden-Popper layered perovskites—they can also be much more unusual as in (**2**). The discovery of $[PPN]^+$ perovskites that crystallise in monoclinic (**5a-b**) and cubic (**4**) space groups, in the context of the rhombohedral $[PPN]Ni[Au(CN)_2]_3$ previously reported,[310] suggests that phase-transitions which retain the perovskite connectivity may be possible in this family of perovskites. In Chapter 5 I will return to investigate the phase transitions of the $[PPN]^+$-containing perovskite(-related) compounds reported here. In the next Chapter I go on to examine the structures reported here in the context of all known dicyanometalltes in order to assess the relationships between composition and structure in this large family of coordination polymers.

Chapter 4

Dicyanometallates as model extended frameworks

4.1 Composition–structure relationships in dicyanometallates

Given the diversity of known structures of dicyanometallate frameworks—*i.e.* those reported in Chapter 3 together with the exhaustive list given in Table 3.1—it is natural to ask how one might control the adoption of one architecture or another through choice of chemical composition. The approach presented here to answering this question is essentially an empirical one. I begin by organising all known dicyanometallates into compositional families of given stoichiometry A_mBX_n. Even if their structures vary, members of any one family share the same coordination number and charge state of the $B^{(n-m)+}$ cation—two aspects over which the synthetic chemist has some control. Coordination number usually fixes the value of n and so constrains the number and type of relevant network topologies. Likewise, cation charge determines the value of $n - m$ and so determines the extent of inclusion of extra-framework A^+ cations (*i.e.*, the value of m). A visual representation of this categorisation is given in Figure 4.1, and it is by interpreting the various trends that emerge from this diagram that I ultimately aim to devise design strategies linking chemical composition and framework structure.

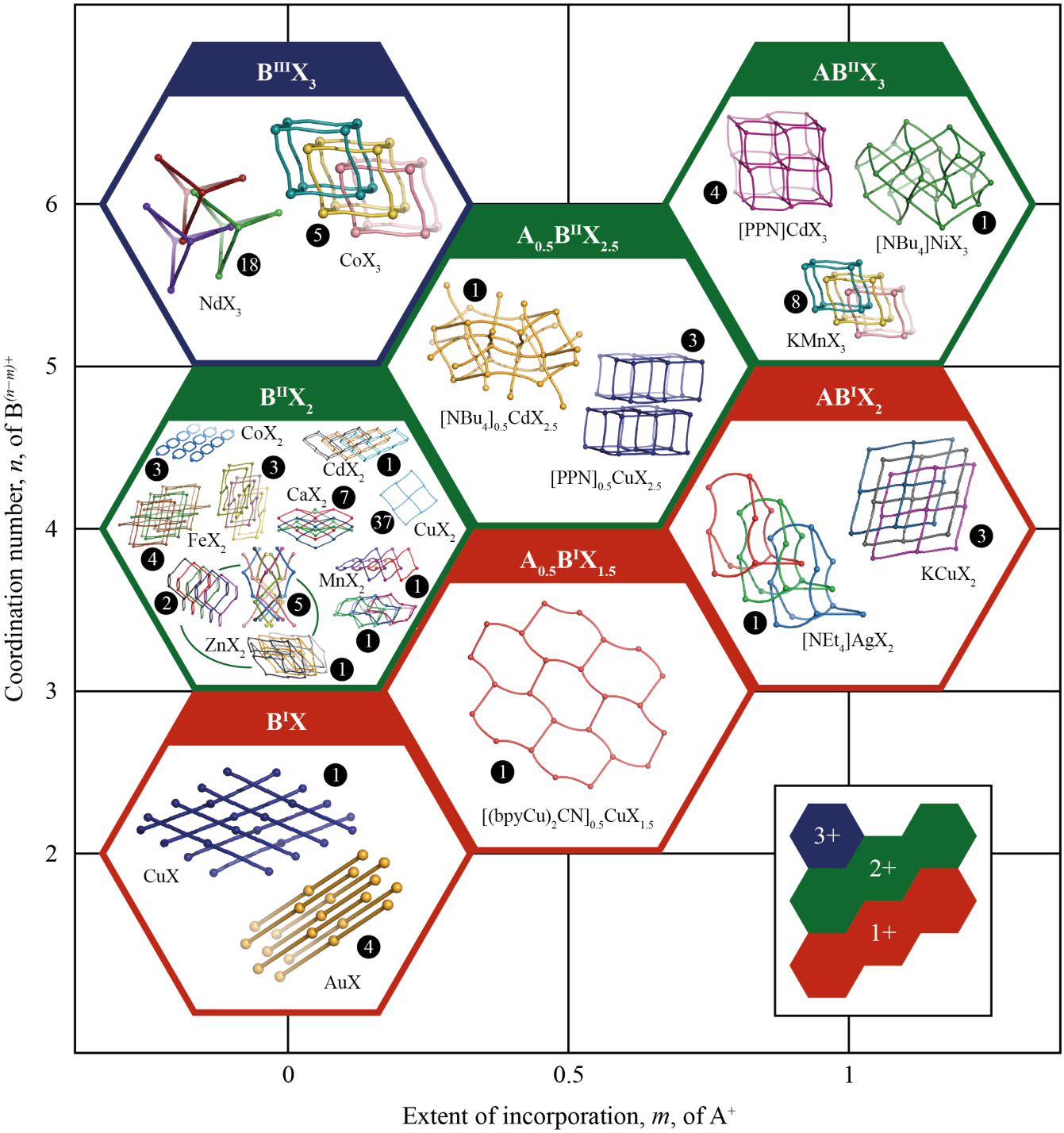

Figure 4.1: Organisation of all known dicyanometallate frameworks [enumerated in Table 3.1] according to node coordination number and extent of incorporation of extra-framework cations. The frameworks shown are representative examples of isostructural compounds; the number of such compounds known is given in the corresponding black circle. The collection of frameworks contained within a single hexagonal cell form a family with related composition A_mBX_n. The colour of the cell corresponds to the charge on the nodal cation (inset).

What is immediately obvious is that some families are considerably more populous than others. The largest and most topologically-diverse family is that with composition BX_2, consisting of a variety of structures based on four-connected nets. Fourfold connectivity is well known to favour topological diversity[135]—hence the polymorphism of *e.g.* silica, zeolites, and imidazolate MOFs.[407] In the present case, $Zn[Au(CN)_2]_2$ emerges as the most polymorphic of the BX_2 systems, crystallising in at least four different forms that include analogues of cristobalite and quartz.[78] In fact the parallel with silica is a meaningful one: the combination of tetrahedral Zn^{2+} coordination geometry and aurophilic interactions capable of bending the Zn–NC–Au–CN–Zn linkers resembles strongly the nonlinear Si–O–Si building units of SiO_2 frameworks [Figure 1.10(a)]. But one additional reason for the accessibility of these BX_2 structures will likely be the large number of divalent cations with aqueous chemistry. Even transition metals with octahedral coordination can yield four-connected frameworks if spectator ligands are present in the synthesis mixture (noting that sometimes solvent may play this role). Indeed it is the doubly-ligated octahedral [*trans*-BX_4L_2] coordination motif that yields the square grid topology—the most frequently-adopted network structure observed for this family.

In principle, any such coordinated ligands may be susceptible to exchange for dicyanometallate anions present in the reaction mixture, with concomitant incorporation of extra-framework cations:

$$\begin{aligned} BL_2X_2 + 0.5AX &\rightleftharpoons A_{0.5}BLX_{2.5} + L \\ A_{0.5}BLX_{2.5} + 0.5AX &\rightleftharpoons ABX_3 + L. \end{aligned}$$

The equilibrium position will depend on, amongst other factors, the ligand binding

strength and the stoichiometry of the AX dicyanometallate salt in the reaction mixture. So, for example, while the Cd^{2+} / $K[Ag(CN)_2]$ system forms the $B(L_2)X_2$ phase $Cd(py)_2[Ag(CN)_2]_2$ when prepared in the presence of pyridine, in the absence of pyridine the same pair of reagents yields the ABX_3 phase $KCd[Ag(CN)_2]_3$.[98,356] Likewise for the Cd^+ / $[PPN][Ag(CN)_2]$ system we obtain the five-coordinate $A_{0.5}B(L)X_{2.5}$ phase $[PPN]_{0.5}Cd(EtOH)[Ag(CN)_2]_{2.5}$ (**3c**) as a first (kinetic) product; subsequent exposure to additional $[PPN][Ag(CN)_2]$ drives formation of the superperovskite ABX_3 phase $[PPN]Cd[Ag(CN)_2]_3{\cdot}3EtOH{\cdot}nH_2O$ (**4**).

This strategy of varying B^{2+}:AX stoichiometry seems an attractive method of controlling network connectivity throughout the A_xBX_{2+x} families. The particular topology adopted for the $x \neq 0$ phases then depends on the geometry of the A^+ cation. For monoatomic A^+ (*e.g.* K^+, Na^+), the topology is usually that of the corresponding A-deficient framework; this is presumably a consequence of the much larger scale of the dicyanometallate linker. So, for example, both $KFe[Ag(CN)_2]_3$ and $Fe[Ag(CN)_2]_3$ share the same triply-interpenetrating α-Po network structure.[83] Larger, molecular cations force topological changes that reflect the cation shape. On the one hand, the cruciform conformation of $[NBu_4]^+$ helps drive the unusual topologies of $[NBu_4]_{0.5}Cd[Ag(CN)_2]_{2.5}$ and $[NBu_4]Ni[Au(CN)_2]_3$. On the other hand, the more isotropic $[PPN]^+$ cation clearly favours the cubic-type nets of $[PPN]_{0.5}Cu[Au(CN)_2]_{2.5}{\cdot}EtOH$ and $[PPN]Mn[Au(CN)_2]_3$.

Although there are far fewer examples based on monovalent B^+ cations—the need for aqueous chemistry limiting these systems to coinage metal salts—precisely these same trends are observed. Again I find that inclusion of monoatomic extra-framework cations appears to have essentially no effect on framework topology:

$KCu^{I}[Ag(CN)_2]_2$ and $Cu^{II}(DMF)[Au(CN)_2]_2$ share the same basic square-grid structures. The tetrahedral $[NEt_4]^+$ cation now favours a diamondoid topology in $[NEt_4]Ag[Ag(CN)_2]_2$; and in $[Cu_2(2,2'\text{-bpy})_2(CN)]_{0.5}Cu[Cu(CN)_2]_{1.5}$ the linear nature of the $[Cu_2(2,2'\text{-bpy})_2(CN)]^+$ cation drives a honeycomb structure with linear channels. Notable by its absence is the (10,3)-*a* or **srs** topology, a common topology for 3-connected MOFs.[25] The apparent rarity of 3-connected structures is in large part due to the propensity for Cu^+ to adopt alternative binding modes, such as bifurcated linkages,[90] though it may be possible to make a dicyanometallate framework with (10,3)-*a* topology using an octahedrally coordinated metal with meridionally disposed capping ligands.[408]

The general reliance on solution-phase synthesis—whether strictly necessary or not—is likely responsible for the relative paucity of structures known to contain B cations in the 3+ oxidation state and the complete absence of higher-valent examples. All known trivalent dicyanometallate salts adopt one of just two dense framework structures: either the triply-interpenetrating α-Po net of $Fe[Ag(CN)_2]_3$ or the triply-intepenetrating **acs** net of the lanthanide or actinide dicyanometallates $[Ln/An(OH_2)_3][Au/Ag(CN)_2]_3$. The contrast with the structural diversity of divalent BX_2 systems could hardly be clearer, and will also reflect the disparity of topological constraints associated with six- and four-connected nodes. In principle, it may be possible to access more open structure types through incorporation of extra-framework cations. Naturally, this would require coordination numbers higher than six—which is certainly feasible for the lanthanide trications. Consequently, further exploration[409] of lanthanide dicyanometallate chemistry using *molecular* AX sources may yield as-yet unrealised systems with compositions $A_{0.5}BX_{3.5}$ and/or ABX_4.

In addition to the general trends discussed here, a number of interesting comparisons can be drawn between neighbouring pairs of structural families as shown in Figure 4.1. For example, there are clear diagonal relationships which connect the topologies of higher- and lower-connected network structures. In this way, the Ruddlesden-Popper-like structure of $[PPN]_{0.5}Cu[Au(CN)_2]_{2.5}\cdot EtOH$ (an $A_{0.5}BX_{2.5}$ framework) can be seen as a natural extension of the square-grid structures of both $Cu[Ag(CN)_2]_2$ and $KCu[Ag(CN)_2]_2$ (BX_2 and ABX_2 frameworks, respectively). And then the superperovskite $[PPN]Cd[Au(CN)_2]_3$ structure emerges as a further extension on this same theme. The triad of BX / $A_{0.5}BX_{1.5}$ / ABX_2 systems $Cu[Cu(CN)_2]$ / $[Cu_2(2,2'\text{-bpy})_2(CN)]_{0.5}Cu[Cu(CN)_2]_{1.5}$ / $KCu[Cu(CN)_2]_2$ can be viewed in precisely the same terms. We anticipate there are many more such relationships, some of which may become increasingly apparent only as new dicyanometallate frameworks continue to be discovered.

4.2 Concluding remarks

While it has long been clear that a large variety of dicyanometallate frameworks can be prepared, what I have shown in this chapter is how the structures of these frameworks might be influenced rationally through variation in cation charge, coordination number, presence of coordinating ligands, and extra-framework cation size, shape and extent of incorporation. The ability to controllably explore a variety of network structures in this way reflects Robson's original vision for coordination polymer chemistry, and suggests that dicyanometallates might be considered a model family for extended framework design. In principle the diversity of structures accessible to this family also suggests a similar diversity of physical properties. More-

over, the structural flexibility imparted by the dicyanometallate linker means that these properties may be much more extreme in nature than in conventional ceramic frameworks—as is already known to be the case in a number of examples.[76,77]

But what seems to be particularly attractive about dicyanometallate framework chemistry is the ability to include complex molecular cations within a number of different framework topologies. So much of the rich structural chemistry and physics of conventional ceramic frameworks has arisen from the interplay between lattice geometry, local degrees of freedom, and nature of inter-site interactions.[2,137] Consequently, the extension of these same concepts to systems with *new* degrees of freedom (*e.g.*, molecular cation orientations and conformations), *new* lattice geometries (*e.g.*, the topology of compound **2**), and *new* types of interactions (*e.g.*, cation–π and π–π) augurs well for the discovery of new and interesting physical phenomena in this intriguing model family of framework structures.

In the next Chapter I focus on phase transitions of perovskite and perovskite-like dicyanometallates and the role of molecular extra-framework cations in determining their behaviour.

Chapter 5

Phase transitions of dicyanometallate superperovskites

5.1 Introduction

In this Chapter the phase transitions of some dicyanometallate perovskites and perovskite-related compounds are presented. In doing so I explore the relative importance of the roles of structure type and the molecular components. I contrast the behaviour found for dicyanometallates with other families of (molecular) perovskites.

The thermal behaviour of six dicyanometallates [PPN]M[$Au(CN)_2$]$_3$ where M = Mn (**5a**), Cd (**5b**), or Ni (**5c**); [PPN]M_2[$Ag(CN)_2$]$_5$($EtOH)_2$ where M = Mn (**3b**) or Cd (**3c**); and [N(n-$C_4H_9)_4$]Mn[$Au(CN)_2$]$_3$·[N(n-$C_4H_9)_4$]ClO_4 (**6**) was investigated using variable temperature powder and single-crystal X-ray diffraction, TGA, DSC, and magnetometry. The starting compounds fall into three groups: (i) ABX_3 superperovskites (**5a-c**)(ii) layered Ruddlesden-Popper $n = 2$ analogues (referred to as AB_2X_5 in this chapter) (**3b-c**) (iii) salt-inclusion ABX_3·AY superperovskites (**6**).

The results for the three groups are shown and discussed in turn with the magnetometry results for all three classes discussed together at the end. The phase transitions observed for the three groups are presented visually in Figure 5.1 and can be summarised as follows:

- Group (i) Superperovskites which crystallise in $I2/a$ transform at elevated

temperatures to $R\bar{3}c$ superperovskites. These transitions involve changes in both octahedral tilts and cation orientation/conformation. Within the temperature range studied these transformations appear to be irreversible.

- Group (ii) Layered superperovskites transform reversibly at low temperatures to a triclinic variant in a 2nd order phase transition. At elevated temperatures the ethanol crystallised within the structure is removed resulting in a reconstructive transition to a mixture of group (i) superperovskites and a sixfold

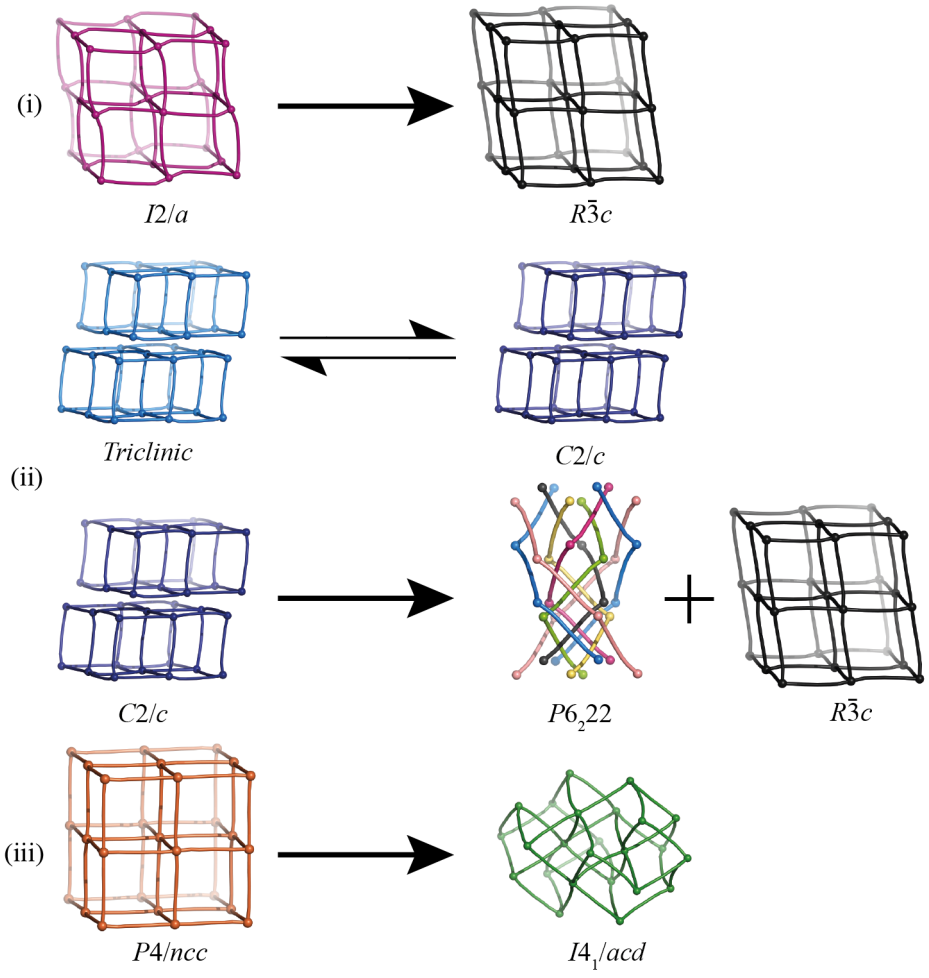

Figure 5.1: Overview of the phase transitions detailed in this Chapter. Framework of each structure type is shown (not to scale). (i) ABX_3 superperovskites, (ii) AB_2X_5 layered superperovskites, and (iii) a salt-inclusion perovskite $ABX_3{\cdot}AY$

interpenetrated quartz structured BX_2 compound.

- Group (iii), A salt-inclusion superperovskite undergoes an irreversible reconstructive transition from tetragonal perovskite-like structure to an unusual **bcs** topology.

The phase transitions of these three groups will be presented in turn, focussed primarily on evidence from variable temperature diffraction.

5.2 ABX_3 superperovskites

5.2.1 Results

The ABX_3 superperovskites [PPN]Ni[Au(CN)$_2$]$_3$ and [PPN]Co[Au(CN)$_2$]$_3$ (not studied in this Thesis) crystallise in spacegroup $R\overline{3}c$,[310] whereas [PPN]Mn[Au(CN)$_2$]$_3$ and [PPN]Cd[Au(CN)$_2$]$_3$ (compounds **5a** and **5b** in Chapter 3) crystallise in $I2/a$. I turn first to the temperature dependent diffraction of [PPN]Ni[Au(CN)$_2$]$_3$. No phase transition was seen for [PPN]Ni[Au(CN)$_2$]$_3$ in the range 100–560 K [Figure 5.2] and the DSC trace was featureless [Appendix B1]. Coefficients of thermal expansion in the range 100–300 K were found to be $\alpha_a = -10.26(10)\,\mathrm{MK}^{-1}$, $\alpha_c = +62.0(4)\,\mathrm{MK}^{-1}$, and $\alpha_V = +41.4(3)\,\mathrm{MK}^{-1}$ with some non-linearity observed at elevated temperatures [Figure 5.3(a)]. A representative Rietveld fit for 300 K data shown in Figure 5.4; corresponding refinement results are given in the Electronic Appendix. These values of thermal expansion coefficients show a slight contraction on heating of the pseudo-cubic [110] and expansion of the pseudo-cubic [111] which corresponds to the framework becoming more regular (*i.e.* towards cubic). This is consistent with the framework geometry dominating the thermal expansion in this phase. The absence

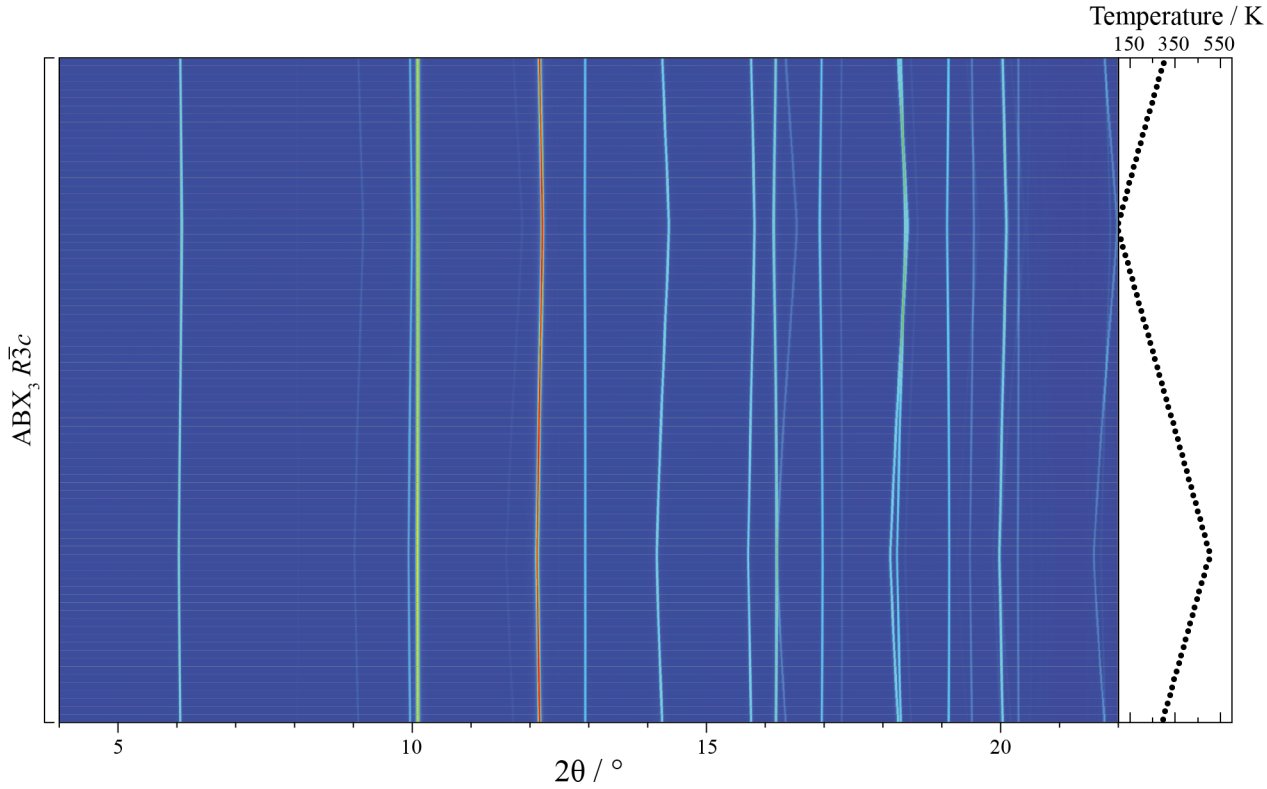

Figure 5.2: Variable temperature powder diffraction patterns of [PPN]Ni[Au(CN)$_2$]$_3$. PPN]Ni[Au(CN)$_2$]$_3$ remains in the $R\bar{3}c$ perovskite phase across all temperatures investigated (100–560 K). Data collected for temperatures above 500 K shown in Appendix B2.

of a phase transition implies that a cubic phase is not attainable within the stability range of this compound—to be expected given the [PPN]$^+$ disorder that this would require.

Both [PPN]Mn[Au(CN)$_2$]$_3$ and [PPN]Cd[Au(CN)$_2$]$_3$ were observed to transform from $I2/a$ irreversibly (on cooling back down to 450 K) to the same $R\bar{3}c$ perovskite structure of [PPN]Ni[Au(CN)$_2$]$_3$.

For [PPN]Mn[Au(CN)$_2$]$_3$ this first order transition starts at 440 K and is complete by 510 K with phase coexistence in the intermediate regime [Figure 5.5]. Coefficients of thermal expansion were calculated for each phase [see Appendix B2.2 for fits]. For the monoclinic phase these are $\alpha_{X_1} = -29.0(1.0)\,\mathrm{MK}^{-1}$, $\alpha_{X_2} = +28.6(4)\,\mathrm{MK}^{-1}$,

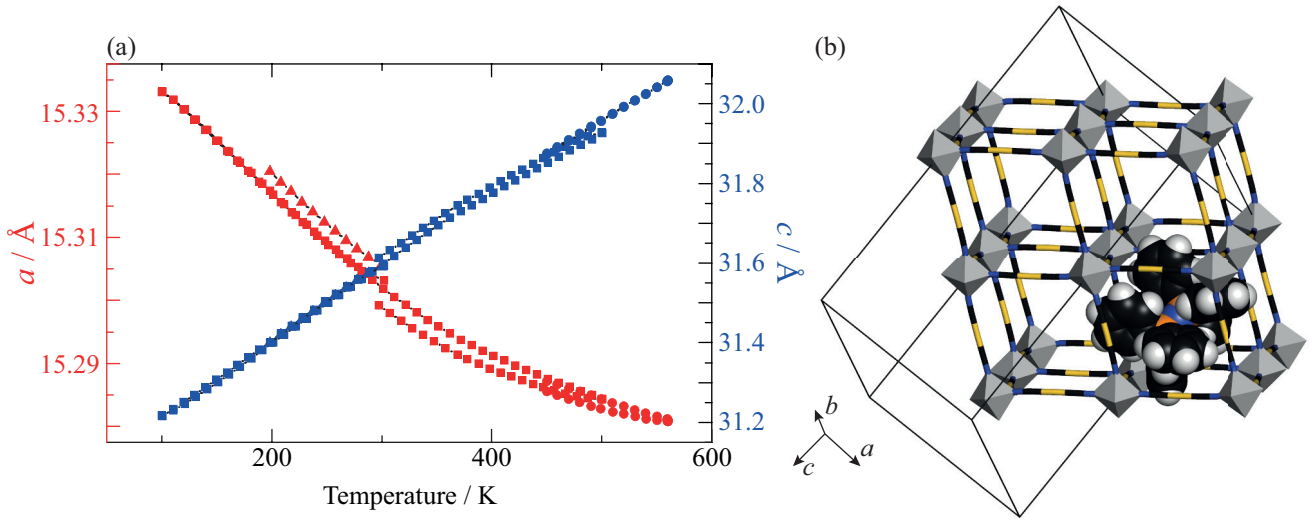

Figure 5.3: Variation in lattice parameters with temperature (a). Linear fits (100–300 K) give coefficients of thermal expansion $\alpha_a = -10.26(10)\,\mathrm{MK}^{-1}$, $\alpha_c = +62.0(4)\,\mathrm{MK}^{-1}$, $\alpha_V = +41.4(3)\,\mathrm{MK}^{-1}$. There is some non-linearity above 300 K. Errors within marker size. Square markers indicate the data shown in Figure 5.2. Triangles (cryostream) and circles (hot air blower) indicate data from another capillary. See Appendix B2.2 for fits. (b) Structure of [PPN]Ni[Au(CN)$_2$]$_3$ as reported by Lefebvre *et al.* in Reference 310 shown to emphasise the relationship to the primitive perovskite cell. Only one $[PPN]^+$ shown for clarity. The tilt system $a^-a^-a^-$ was observed as would be expected for an oxide perovskite.

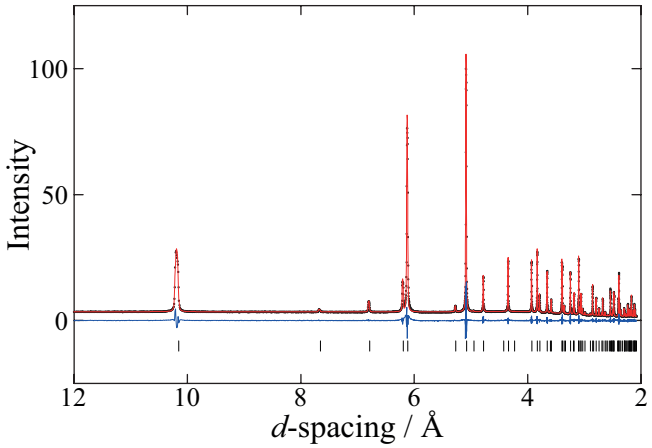

Figure 5.4: A typical Rietveld fit for *R*-[PPN]Ni[Au(CN)$_2$]$_3$ (in this case 300.03 K) $R_{wp} = 4.326\%$, $R_p = 2.252\%$, GoF = 3.876

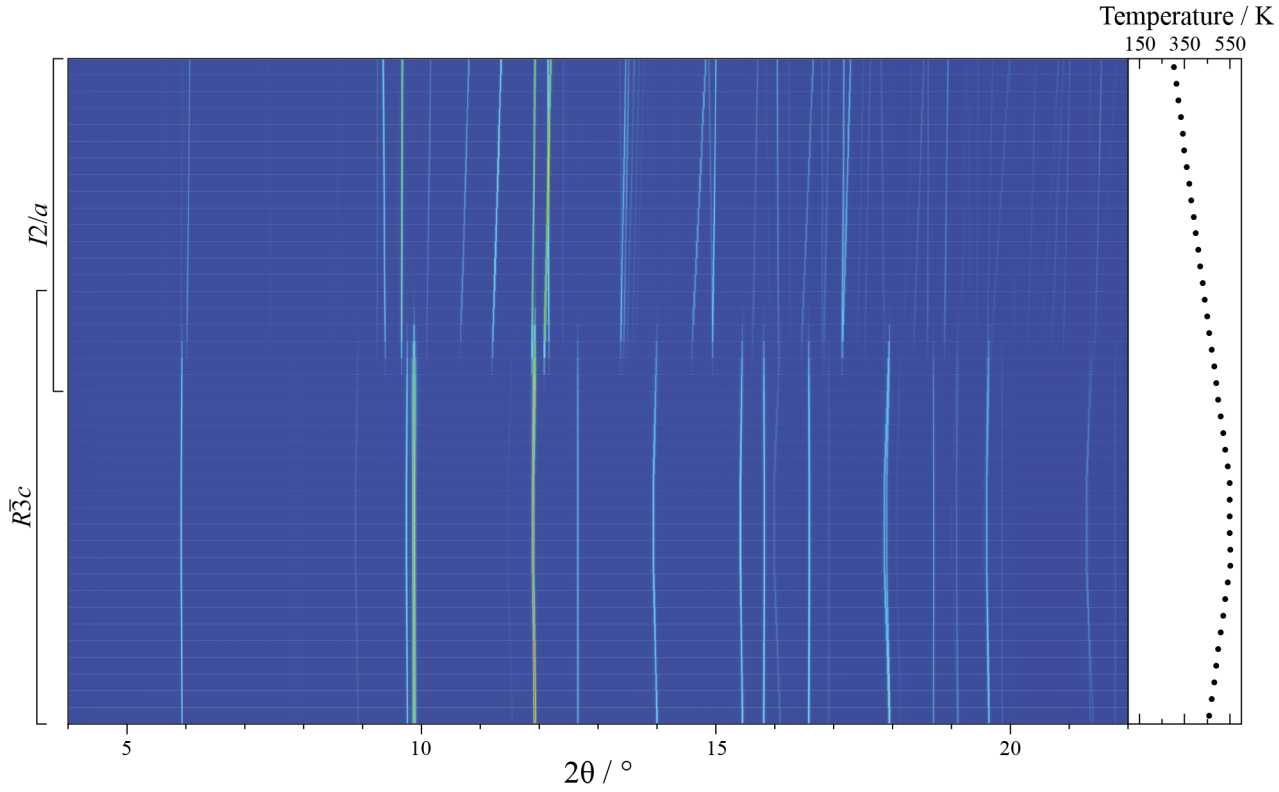

Figure 5.5: Variable temperature powder diffraction patterns of [PPN]Mn[Au(CN)$_2$]$_3$. Perovskite-structured [PPN]Mn[Au(CN)$_2$]$_3$ undergoes an irreversible first-order phase transition from the $I2/a$ to $R\overline{3}c$.

$\alpha_{X_3} = +96.0(1.2)\,\mathrm{MK}^{-1}$, and $\alpha_V = +94.6(1.2)\,\mathrm{MK}^{-1}$ where the principal directions correspond to $X_1 = 0.9773\mathbf{a} - 0.2120\mathbf{c}$; $X_2 = 0.3523\mathbf{a} + 0.9359\mathbf{c}$; $X_3 = \mathbf{b}$ and these correspond to the directions along the P$\cdots$P vector of the PPN cation (which is very close to the longest pseudocubic [112] direction), along bowed framework edges, and the shortest face-diagonal of the pseudocubic perovskite cube respectively [Figure 5.6(a)].

For the rhombohedral phase the coefficients of thermal expansion are: $\alpha_a = -7.6(3)\,\mathrm{MK}^{-1}$, $\alpha_c = +73.6(3)\,\mathrm{MK}^{-1}$, and $\alpha_V = +58.3(6)\,\mathrm{MK}^{-1}$. Again, these values show a slight contraction on heating of the pseudo-cubic [110] and expansion of the pseudo-cubic [111] which corresponds the the framework becoming more regular

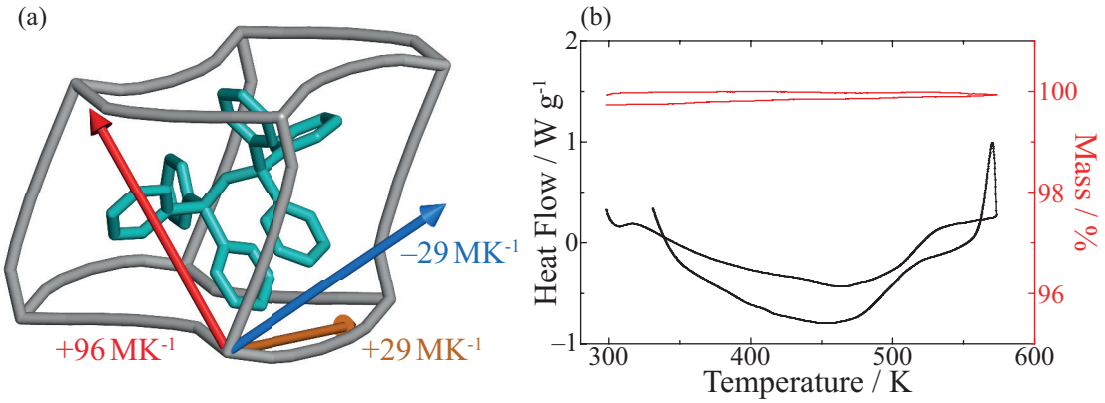

Figure 5.6: (a) Thermal expansion coefficients for M-[PPN]Mn[Au(CN)$_2$]$_3$ and the relation between principal axes and structure; $\alpha_{X_1} = -29.0(1.0)\,\mathrm{MK}^{-1}$ (blue), $\alpha_{X_2} = +28.6(4)\,\mathrm{MK}^{-1}$ (orange), $\alpha_{X_3} = +96.0(1.2)\,\mathrm{MK}^{-1}$ (red). (b) The DSC trace for [PPN]Mn[Au(CN)$_2$]$_3$ only shows very broad features.

(*i.e.* towards cubic). This is consistent with the framework geometry dominating the thermal expansion in this phase. The DSC trace was found to only show very broad features in this case [Figure 5.6(b)].* A typical Rietveld fit in the mixed-phase region and the variation in phase fraction and unit cell volume per formula unit are shown in Figure 5.7.

For [PPN]Cd[Au(CN)$_2$]$_3$ the first order transition to the rhombohedral perovskite starts at 510 K but is not quite complete at the highest temperature studied (550 K) [Figure 5.8] with ∼10 % of the monoclinic phase remaining [Figure 5.9].

Coefficients of thermal expansion were calculated for each phase. A representative Rietveld fit in the mixed phase region and phase fraction plot are shown in Figure 5.7 For the monoclinic phase these are $\alpha_{X1} = -30(4)\,\mathrm{MK}^{-1}$, $\alpha_{X2} = +23(2)\,\mathrm{MK}^{-1}$, $\alpha_{X3} = +91(4)\,\mathrm{MK}^{-1}$, and $\alpha_V = +85(2)\,\mathrm{MK}^{-1}$ where the principal directions correspond to X_1 = 0.9616**a** -0.2743**c**; X_2 = 0.4352**a** + 0.9003**c**; X_c = **b** and for the rhombohedral phase: $\alpha_a = -9.0(2)\,\mathrm{MK}^{-1}$, $\alpha_c = +92.0(1.4)\,\mathrm{MK}^{-1}$,

*The recovered DSC sample was found to be in $R\bar{3}c$ [Appendix B2.3].

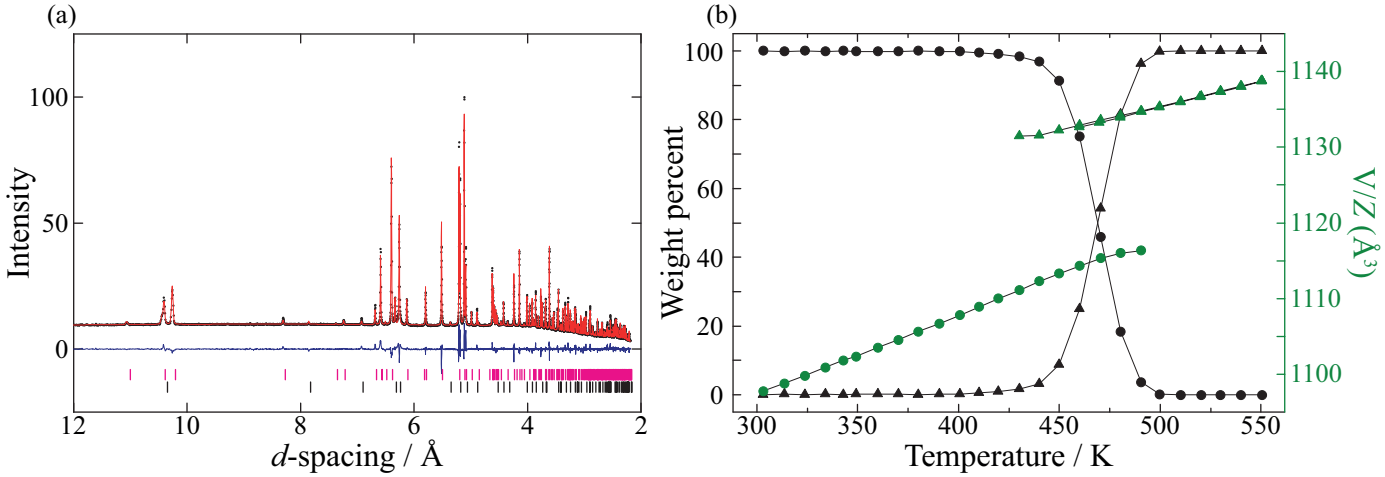

Figure 5.7: (a) A typical Rietveld fit from the region where M- and R-[PPN]Mn[Au(CN)$_2$]$_3$ coexist (in this case 460 K). Phase fractions are M- 75.14(16) % (magenta) and R 24.86(16) % (black); R_{wp} = 4.083%, R_p = 2.524%, GoF = 3.217 (b) Phase fractions of the $I2/a$ (circles) and $R\bar{3}c$ (triangles) modifications of [PPN]Mn[Au(CN)$_2$]$_3$ as a function of temperature. Variation of the volume per formula unit of the two modifications with temperature. All errors are within markers.

and $\alpha_V = +74.6(8)\,\mathrm{MK}^{-1}$. As for the monclinic Mn-analogue the principal axes of thermal expansion here correspond to the directions along the P$\cdots$P vector of the PPN cation (which is close to the longest pseudocubic [111] direction, an average of bowed framework edges, and the shortest face-diagonal of the pseudocubic perovskite cube respectively. The DSC trace of this compounds has a small feature on heating centred around 520 K, which is consistent with the appearance of the R-phase in powder diffraction [Figure 5.10].*

5.2.2 Discussion

[PPN]Mn[Au(CN)$_2$]$_3$ and [PPN]Cd[Au(CN)$_2$]$_3$ undergo a transformation from $I2/a$ to $R\bar{3}c$ at elevated temperatures that is irreversible with the temperature range studied. The transition is associated with an approximately 2 % volume increase

*Despite there being no discernible feature on cooling, the recovered sample appears to have reverted to M-[PPN]Cd[Au(CN)$_2$]$_3$ [Appendix B2.3].

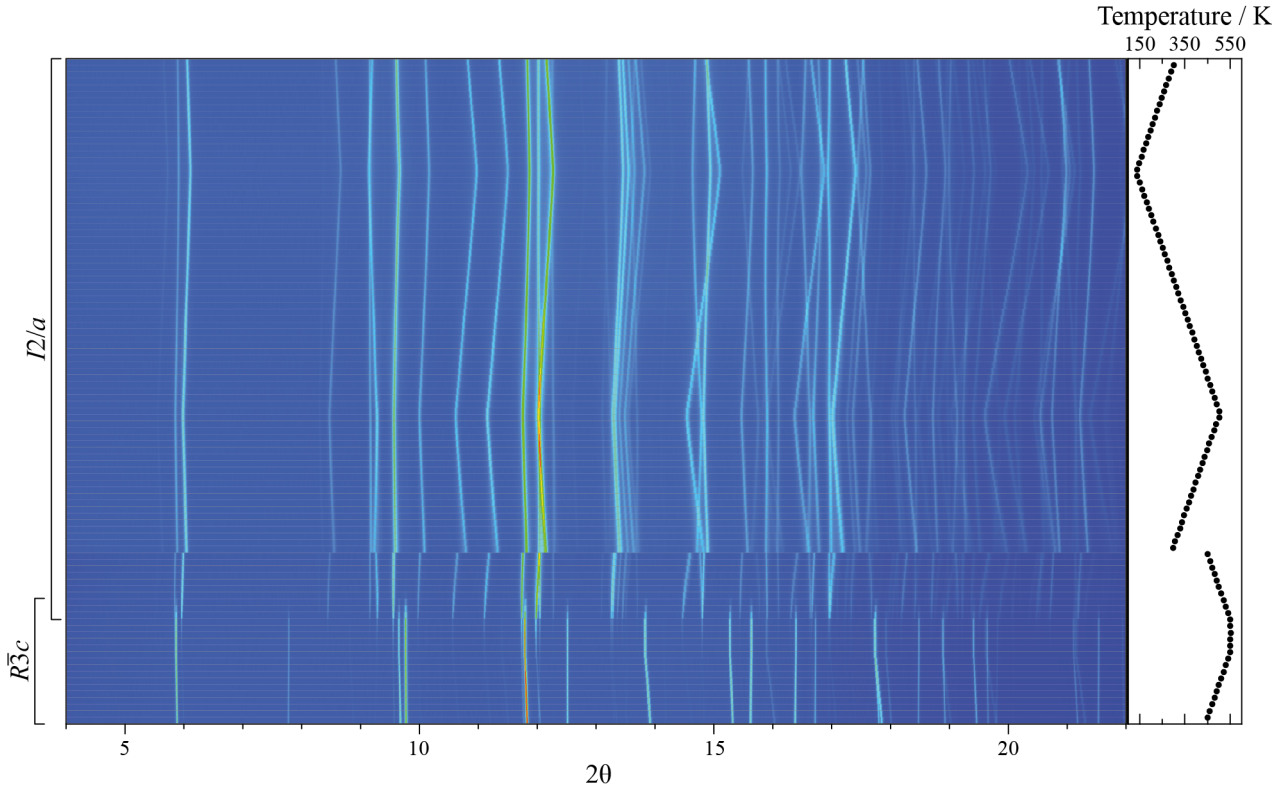

Figure 5.8: Variable temperature powder diffraction patterns of [PPN]Cd[Au(CN)$_2$]$_3$. Perovskite-structured [PPN]Cd[Au(CN)$_2$]$_3$ undergoes an irreversible first-order phase transition from the $I2/a$ to $R\overline{3}c$ that is incomplete across the temperature range investigated.

in both cases. [PPN]Ni[Au(CN)$_2$]$_3$ which is already in $R\overline{3}c$ undergoes no phase transition in the temperature range studied. The transition in the Mn and Cd analogues corresponds to a tilt transition from $a^-a^-c^-$ to $a^-a^-a^-$ but also involves reorientation of the A-site cation [PPN]$^+$. In $I2/a$ the P$\cdots$P axis is nearly aligned along the pseudocubic [112] with P—N—P bend direction ordered in a rocksalt fashion. In the $R\overline{3}c$ phase this cation lies along the 3-fold axis enforcing an average linear P—N—P angle giving an entropic stabilisation [Figure 5.11]. Furthermore, on the basis of the single crystal structures reported in Chapter 3 and by Lefebvre *et al.* in Reference 310, it seems likely that the supramolecular interactions will also change. These features may provide an explanation for the irreversible nature of the

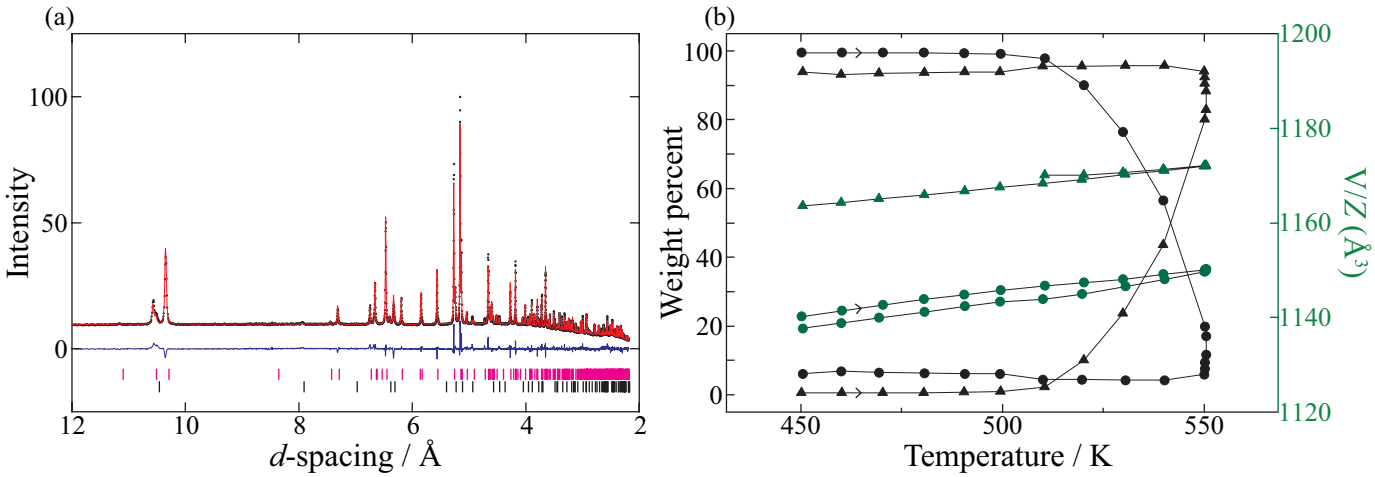

Figure 5.9: (a) A typical Rietveld fit from the region where M- (magenta) and R-[PPN]Cd[Au(CN)$_2$]$_3$ (black tickmarks) coexist (in this case 520 K). Phase fractions are M- 75.14(16)% (magenta) and R- 24.86(16)% (black); R_{wp} = 4.083%, R_p = 2.524%, GoF = 3.217 (b) Phase fractions of the $I2/a$ (circles) and $R\bar{3}c$ (triangles) modifications of [PPN]Mn[Au(CN)$_2$]$_3$. Variation of the volume per formula unit of the two modifications with temperature. Time order of data indicated with arrow. Lines are guides to the eye. All errors are within markers.

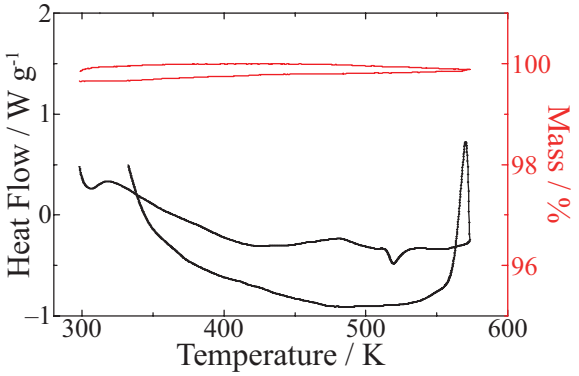

Figure 5.10: DSC of [PPN]Cd[Au(CN)$_2$]$_3$ shows a small endothermic feature on heating consistent with the monoclinic to rhombohedral transition.

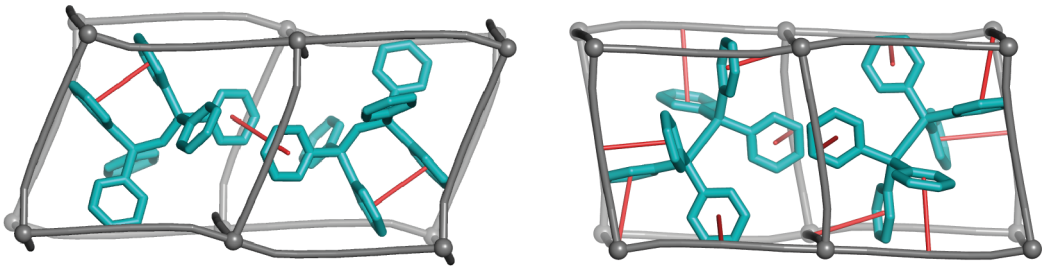

Figure 5.11: Short π–π and cation–π interactions in $M-$[PPN]B[Au(CN)$_2$]$_3$ and R-[PPN]B[Au(CN)$_2$]$_3$. In $M-$[PPN]B[Au(CN)$_2$]$_3$ the phenyl rings are oriented such that intra- and inter-molecular π–π interactions are maximised whereas in R-[PPN]B[Au(CN)$_2$]$_3$ short cation–π interactions dominate. Crucially, the latter are present between adjacent [PPN]$^+$ cations. In $M-$[PPN]B[Au(CN)$_2$]$_3$ the P—P is nearly aligned along the pseudocubic (112) with P—N—P bend direction ordered in a rocksalt fashion. In $R-$[PPN]B[Au(CN)$_2$]$_3$ it is aligned along the pseudocubic (111).

phase transition. If the transition were driven by octahedral tilting then it would be expected to be reversible. The recent demonstration that the formate perovskite [$CH_3CH_2NH_3$][Cu(HCOO)$_3$],[410] transforms to a diamondoid topology (10 % volume increase) on heating but only reverts to perovskite on application of pressure rather than on cooling, suggests that the M- to R- transition (2 % volume increase) may revert under applied pressure.

While a first-order transition between $R\bar{3}c$ and $I2/a$ is possible in atomic ternary perovskites,[185] reported instances are extremely rare. A small monoclinic distortion may be present in $LaCoO_3$ where the the structure previously reported as $R\bar{3}c$ has been reassigned as $I2/a$ in at least the range 20–300 K.[411,412] The $R\bar{3}c$ to $I2/a$ transition has been observed for the doped manganite $La_{1-x}Ba_xMnO_3$ where $x = 0.185$.[413]

Alternatively we might think of the $I2/a$ phase as a kinetic product. So why does it form for Mn^{2+} and Cd^{2+} but not Ni^{2+} or Co^{2+}?[310] While the former both

have larger ionic radii, they also lack ligand-field stabilisation energy (LFSE). This lack of LFSE will result in more rapid exchange of water for dicyanoaurate than the latter perhaps leading to suboptimal ligand organisation. Running contrary to this, the Ni analogue is found to be comparatively insoluble during synthesis. A further important factor may be stabilisation of the $R\bar{3}c$ phase due to the conformational entropy associated with disorder of the P—N—P angle along a threefold axis.

5.3 AB_2X_5 layered superperovskites

The variable-temperature diffraction behaviour of the Ruddlesden-Popper $n = 2$ analogues $[PPN]Mn_2[Ag(CN)_2]_5(EtOH)_2$ and $[PPN]Cd_2[Ag(CN)_2]_5(EtOH)_2$ is reported here. Both compounds are shown to undergo a 2nd order displacive phase transition on cooling below room temperature. The key effect of heating above room temperature is to remove ethanol, which completes the coordination sphere of Mn/Cd in the starting material. This leads to a drastic reconstructive transition which, while varying in some details between Mn and Cd, results in the formation of Ag-analogues of the perovskites in Group (i) and Mn/Cd analogues of the quartz-structured compound $Zn[Ag(CN)_2]_2{\cdot}x$AgCN.[129] The variable-temperature powder diffraction behaviour of $[PPN]Mn_2[Ag(CN)_2]_5(EtOH)_2$ is shown in Figure 5.12.

5.3.1 $[PPN]Mn_2[Ag(CN)_2]_5(EtOH)_2$

Rietveld refinement based on the single crystal structure of $[PPN]Mn_2[Ag(CN)_2]_5(EtOH)_2$ fits the initially-observed diffraction pattern well [Figure 5.13(a)]. At low temperatures there is a lowering of symmetry as indicated by reversible splitting of peaks (such as (022) at $\sim$11.8 ° / 5.2 Å) visible below 160 K [Figure 5.13(b)]. The

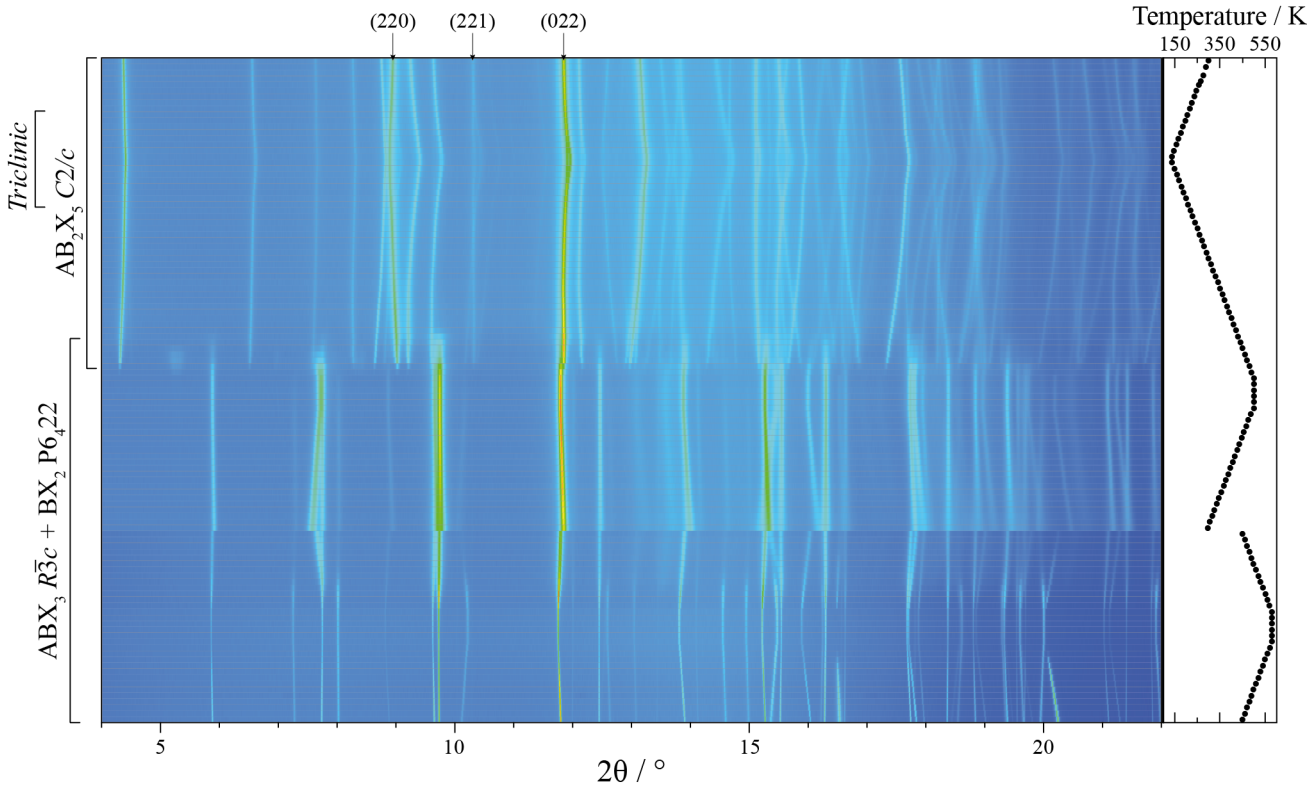

Figure 5.12: Variable temperature powder diffraction patterns of $[PPN]Mn_2[(AgCN)_2]_5(EtOH)_2$ and its transformation products.

continuous temperature dependence of the peak position/splitting and presence of only one phase is indicative of a 2nd order displacive transition. Since the ambient phase *M*-$[PPN]Mn_2[Ag(CN)_2]_5(EtOH)_2$ has $C2/c$ space group symmetry the peak splitting in the low-temperature phase requires lowering of the crystal system from monoclinic to triclinic. Hence we refer to the low-T modification as *T*-$[PPN]Mn_2[Ag(CN)_2]_5(EtOH)_2$ and note that its symmetry cannot be higher than the $C\bar{1}$ subgroup of the ambient $C2/c$ structure. Identification of the structural distortion has not been possible in the time scale of this project but may be most informatively carried out with Symmetry-mode Rietveld refinement.[414] Visual inspection of the *hkl* values of split peaks suggests that the transition could correspond to the freezing in of a phonon associated with Ag$\cdots$Ag interactions between

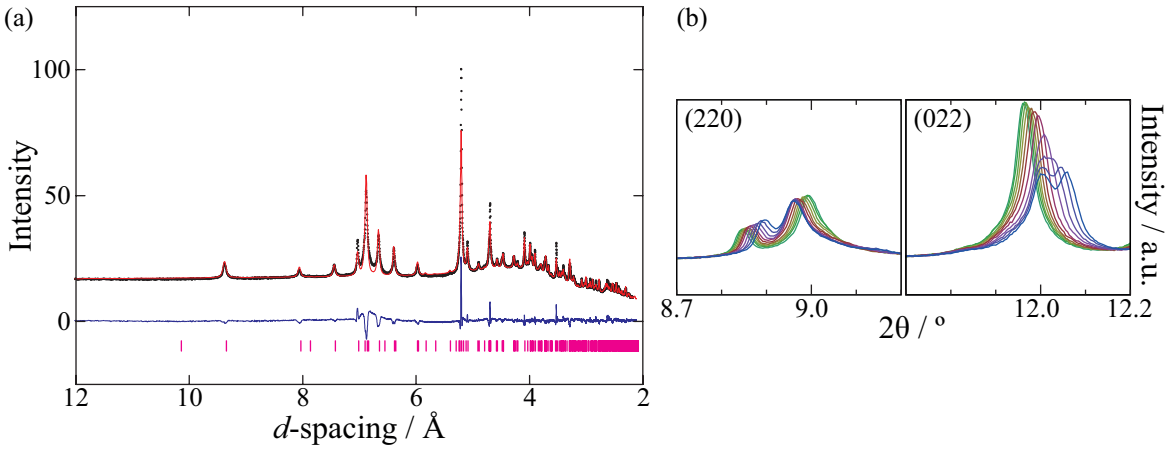

Figure 5.13: (a) Rietveld fit for M-[PPN]$Mn_2[AgCN)_2]_5(EtOH)_2$ at 300 K based on single crystal structure. $R_{wp} = 3.798\%$, $R_p = 2.486\%$, GoF = 4.785 (b) Sections of low temperature diffraction patterns of [PPN]$Mn_2[AgCN)_2]_5(EtOH)_2$ from 240 K (green) to 140 K (blue). The (220) peak does not split but the (022) does suggesting that only α and β but not γ deviate substantially from 90 ° in T-[PPN]$Mn_2[AgCN)_2]_5(EtOH)_2$ below 160 K.

perovskite blocks. There are no ($hk0$) peaks which split (*e.g.* the (220) at 8.9° / 9.0 Å) suggesting that only α should deviate substantially from 90°.

Above room temperature there are substantial structural changes. The diffraction pattern changes drastically between 420 and 490 K and on further heating with the hot air blower there is significant peak sharpening. To understand the phase transitions above room temperature it is helpful to examine the final products formed [Figure 5.14(b)]. Here I explore one possibility for the resulting mixture of compounds. In the final pattern four different phases can be identified: R-[PPN]$Mn[Ag(CN)_2]_3$, $Mn[Ag(CN)_2]_2{\cdot}x$AgCN, AgCN, and Ag. These phases were identified by indexing and subsequent refinements against known dicyanometallate structure types. R-[PPN]$Mn[Ag(CN)_2]_3$ is a direct analogue of the superperovskites discussed in the preceeding Section. $Mn[Ag(CN)_2]_2{\cdot}x$AgCN is an anlogue of $Zn[Ag(CN)_2]_2{\cdot}x$AgCN,[129] where $x \approx 0.58$. $Zn[Ag(CN)_2]_2{\cdot}x$AgCN is itself topologically identical to α-$Zn[Au(CN)_2]_2$ which crystallises in either of the pair of chiral

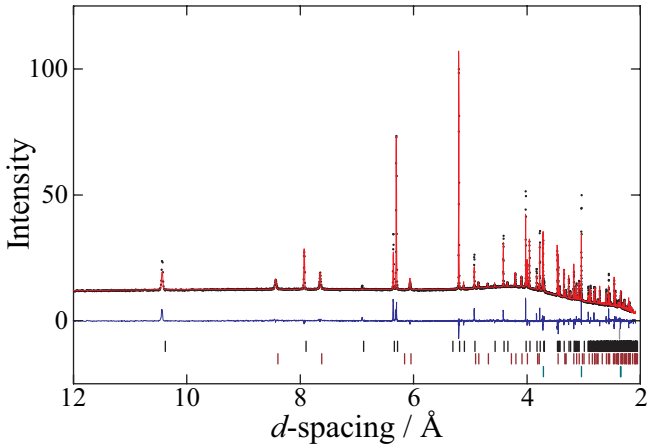

Figure 5.14: Rietveld fit to final diffraction pattern collected (450.5 K) for sample starting as $[PPN]Mn_2[Ag(CN)_2]_5(EtOH)_2$. Accounting for all peaks, four phases were refined in this fit (weight percent): Ag (0.27(3) %, grey) *R*-$[PPN]Mn[Ag(CN)_2]_3$ (68.9(3) %, black), $Mn[Ag(CN)_2]_2{\cdot}x$AgCN (19.4(3) %, dark red), and Ag(CN) (11.4(1) %, teal). R_{wp} = 4.181%, R_p = 2.063%, GoF = 3.895.

space groups $P6_422/P6_222$ with a six-fold interpenetrated quartz structure.[128] Compared to α-$Zn[Au(CN)_2]_2$, $Zn[Ag(CN)_2]_2{\cdot}x$AgCN has a larger a/c ratio giving wider channels running through the structure. These channels are occupied by chains of AgCN. The periodicity of AgCN is incommensurate with the c axis of the host lattice.[129] The presence of this 'smeared out' electron density in the channels results in a distinctive change in peak intensities compared to the empty-channel Au-analogue. The Rietveld refinement of $Mn[Ag(CN)_2]_2{\cdot}x$AgCN was based on the model reported for $Zn[Ag(CN)_2]_2{\cdot}x$AgCN with disordered chains of AgCN filling the channels [Figure 5.15(a,b)].[129,270] The maximum value of x can be determined by taking the ratio of the repeat length of AgCN and the c lattice parameter of the parent framework. Using the lattice values from this refinement this gives 0.62. A refinement with empty channels was performed. Fourier difference maps were featureless when AgCN chains were included [Figure 5.15(c)] and showed the presence of significant residual electron density when excluded from the refinement [Figure 5.15(d)].

Analysis of the phrase fractions [Table 5.1] on the assumption that all silver present in the starting material can be accounted for with the 4 phases above allows us to propose a (roughly) balanced equation for the overall reaction:

$$[\mathrm{PPN}]\mathrm{Mn_2}[\mathrm{Ag(CN)_2}]_5(\mathrm{EtOH})_2 \longrightarrow \tfrac{5}{6}[\mathrm{PPN}]\mathrm{Mn}[\mathrm{Ag(CN)_2}]_3 + \tfrac{1}{2}\mathrm{Mn}[\mathrm{Ag(CN)_2}]_2 \cdot x\,\mathrm{AgCN} + \tfrac{5}{4}\mathrm{AgCN} + \tfrac{1}{6}(\text{`[PPN]CN'} + 4\,\text{`Mn(CN)}_2\text{'}) + 2\,\mathrm{EtOH}\uparrow$$

This equation ignores the presence of ∼1.35 mole percent Ag metal seen in the diffraction pattern. Neither '[PPN]CN' nor '$\mathrm{Mn(CN)_2}$' have been identified in the

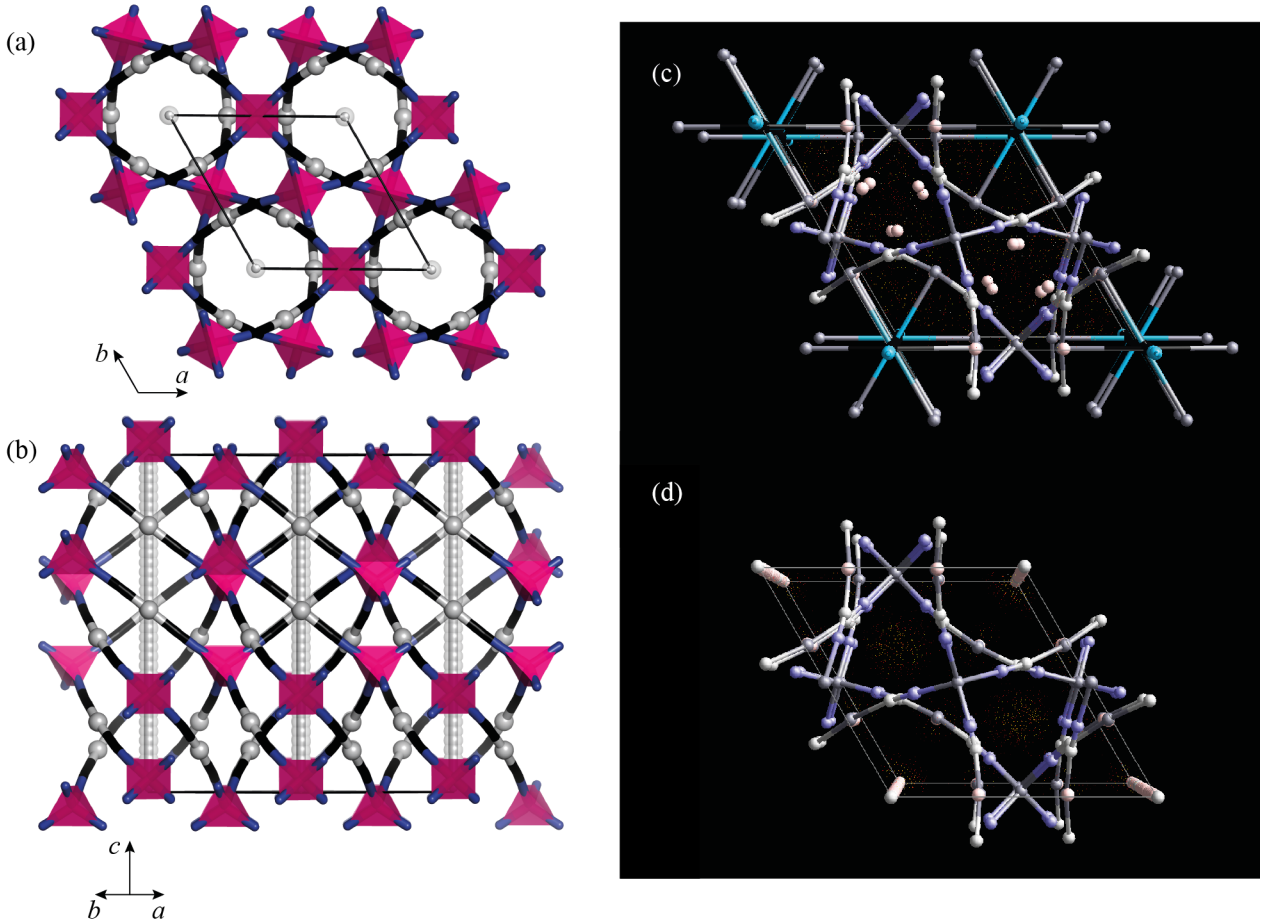

Figure 5.15: View of the structure of $\mathrm{Mn[Ag(CN)_2]_2}\cdot x\mathrm{AgCN}$ down the *c*-axis (a) and along the *ab*-direction (b). Ag shown in grey, Mn in pink, N in blue, and C in black. Channels are filled with disorded AgCN chains. When these chains are included in the Rietveld refinement (c) the Fourier difference map is featureless (difference density shown by dots and 25 pink spheres at maxima) but when the refinement is performed without them (d) there is significant residual density in the channels along *c* at the unit cell origin.

Table 5.1: Phase fractions of final decomposition products of $[PPN]Mn_2[Ag(CN)_2]_5(EtOH)_2$. Errors are a function of the fit to the data and as such underestimate the true error in weight percent.

Phase	Weight percent	Mole percent	Silver distribution / %	Calc. Silver distribution / %
R-$[PPN]Mn[Ag(CN)_2]_3$	68.9(3)	29.71(13)	48.86(7)	49.4
$Mn[Ag(CN)_2]_2{\cdot}x$AgCN	19.4(3)	23.0(4)	25.2(2)	25.9
AgCN	11.4(3)	46(1)	25.1(7)	24.7
Ag	0.27(3)	1.35(14)	0.74(7)	0

diffraction patterns but are possible decomposition products.[415] At the relevant temperatures [PPN]CN may either be a liquid or decompose (see TGA) and '$Mn(CN)_2$' may not be crystalline.[84]

Examining the intermediate region reveals phase coexistence indicating that the transition from $[PPN]Mn_2[Ag(CN)_2]_5(EtOH)_2$ to the other phases is first order and, from our structural models, it must be reconstructive rather than displacive. There are, however, some unexplained features. In the period of phase coexistence there is a very broad feature at 5.3 ° (11.6 Å). For the rest of the cryostream regime the (110) peak at around 7.8 ° (7.9 Å) has a very large shoulder peak accompanying it. After further heating this peak appears to coalesce with the (110) reflection. Splitting of the (110) peak would be incompatible with $R\bar{3}c$ symmetry; consequently it is possible that the perovskite phase is of slightly lower symmetry in this region.

These transitions are consistent with the DSC data [Figure 5.16] which show some small features at relevant temperatures.

Single crystal X-ray diffraction

The high-temperature transformation of $[PPN]Mn_2[Ag(CN)_2]_5(EtOH)_2$ was first observed as a single-crystal to single-crystal transition. Despite the drastic struc-

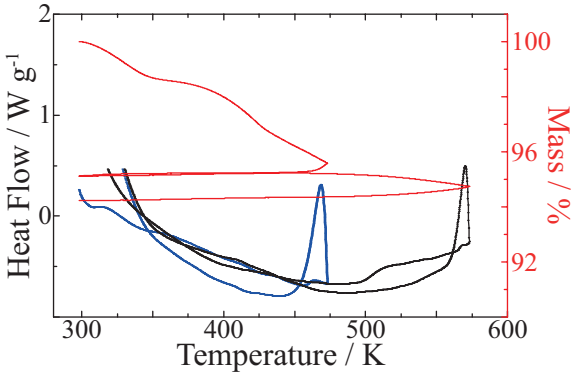

Figure 5.16: DSC and simultaneous TGA data for $[PPN]Mn_2[Ag(CN)_2]_5(EtOH)_2$. Overall 5.8 % mass is lost compared to a predicted value of 5.9 %. Heating was carried out in two stages. The turning point of the first stage (blue) coincides with a small feature seen in the second (black) stage. A further small feature is visible at 566 K which matches the temperature at which AgCN peaks disappear in the diffraction data. Features at the highest and lowest temperatures are due to instrumental factors.

tural change resulting from desolvation, it was possible to solve the structure of *R*-$[PPN]Mn[Ag(CN)_2]_3$ from the diffraction pattern at high temperature. Crystallographic details are given in Table 5.2, the unit cell of the resulting structural model is shown in Figure 5.17 along with a reconstructed slice of diffraction data. Additional powder rings, consistent with the proposed mixture of phases above, can be seen in the individual frames.

The orientation of the $[PPN]Mn_2[Ag(CN)_2]_5(EtOH)_2$ and *R*-$[PPN]Mn[Ag(CN)_2]_3$ phases in the single crystal transformation can provide some information regarding a transformation mechanism. The [001] direction in *R*-$[PPN]Mn[Ag(CN)_2]_3$ points along the P—N—P axis of $[PPN]^+$ and approximately corresponds to the [011] direction in $[PPN]Mn_2[Ag(CN)_2]_5(EtOH)_2$ which also points along the P—N—P axis. Given the similar pseudo-cubic [111] alignment of $[PPN]^+$ in both phases, this suggests that the orientation of the framework is also retained in the transition. Comparison of the two structures however, makes clear that this phase transition

Table 5.2: Crystallographic details of *R*-[PPN]Mn[Ag(CN)$_2$]$_3$ determined using single-crystal diffraction. The error in temperature is large due to failure of the cryostream during the data collection. All data logged at less than 475 K was excluded from integration and refinement. The associated .cif and .fcf files can be found in the Electronic Appendix.

Compound	*R*-[PPN]Mn[Ag(CN)$_2$]$_3$
Empirical formula	$Mn_1Ag_3P_2N_7C_{42}H_{30}$
Formula weight (g mol^{-1})	1073.23
Crystal System	Rhombohedral
Space Group	$R\bar{3}c$ (No. 167)
Z	6
Radiation (Å)	Cu K$_\alpha$, $\lambda = 1.54180$
Crystal colour	Yellow
Crystal size (mm)	0.09×0.21×0.25
Temperature (K)	475(2)
a (Å)	15.7732(4)
c (Å)	31.9203(12)
V (Å^3)	6877.6(4)
μ (mm^{-1})	13.258
Reflections ($I > 2\sigma(I)$)	1270
R (F_o)	0.0470
R$_w$ (F_o)	0.1254
GOF	0.9465

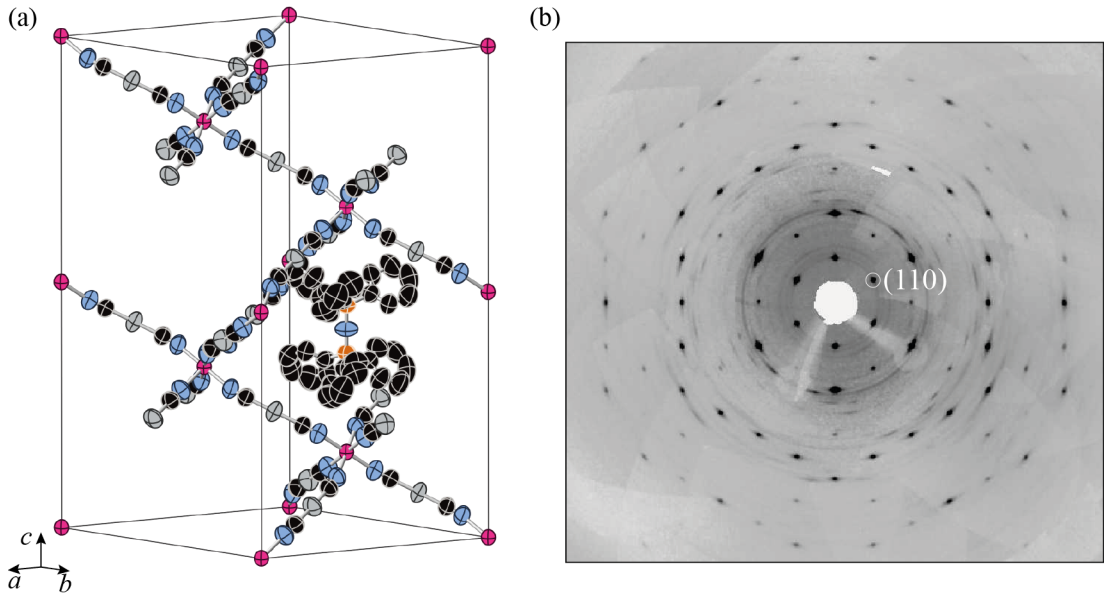

Figure 5.17: *R*-[PPN]Mn[Ag(CN)$_2$]$_3$ (a) unit cell from single-crystal diffraction. Only one [PPN]$^+$ cation and no hydrogen atoms are shown for clarity. (b) Reconstructed precession image of the ($hk0$) layer for this data collection. Additional powder rings that do not pass through the Bragg peaks are consistent with the presence of other phases as observed in the powder diffraction.

demands coordinative lability. This can reasonably be expected for high-spin Mn^{2+} given its $t_{2g}^3 e_g^2$ electronic configuration.

Alternative possibilities investigated

Taken at face value, the complexity of phases produced on heating $[PPN]Mn_2[Ag(CN)_2]_5(EtOH)_2$ may seem unlikely, and so a number of alternative possibilities were investigated.

There is no indication of the crystalline phase of $Mn(CN)_2$, which has the anticuprite structure.[415] While it is possible that ethanol molecules could remain trapped in the pores of the quartz-like phase despite using open-ended capillaries, TGA data suggest that all ethanol should be lost by the time the temperatures concerned are reached.

There is no indication of the presence of linker defects in the single crystal data for *R*-$[PPN]Mn[Ag(CN)_2]_3$. Refinements with linker atom occupancy fixed at 0.8333 give R (F_o) and R_w (F_o) of 6.84 % and 18.08 % respectively, which are roughly 2 % and 4 % higher than the final refined structure.

5.3.2 $[PPN]Cd_2[Ag(CN)_2]_5(EtOH)_2$

I now discuss the phase transitions $[PPN]Cd_2[Ag(CN)_2]_5(EtOH)_2$, a layered perovskite is which isostructural to $[PPN]Mn_2[Ag(CN)_2]_5(EtOH)_2$. The variable temperature powder diffraction behaviour of $[PPN]Cd_2[Ag(CN)_2]_5(EtOH)_2$ is shown in Figure 5.18. A broadly similar series of phase transformations is observed for $[PPN]Cd_2[Ag(CN)_2]_5(EtOH)_2$ as in the Mn-analogue already discussed. Splitting of the (022) peak below 180 K is indicative of symmetry lowering from monoclinic to triclinic giving *T*-$[PPN]Cd_2[Ag(CN)_2]_5(EtOH)_2$. In addition, there is a small pe-

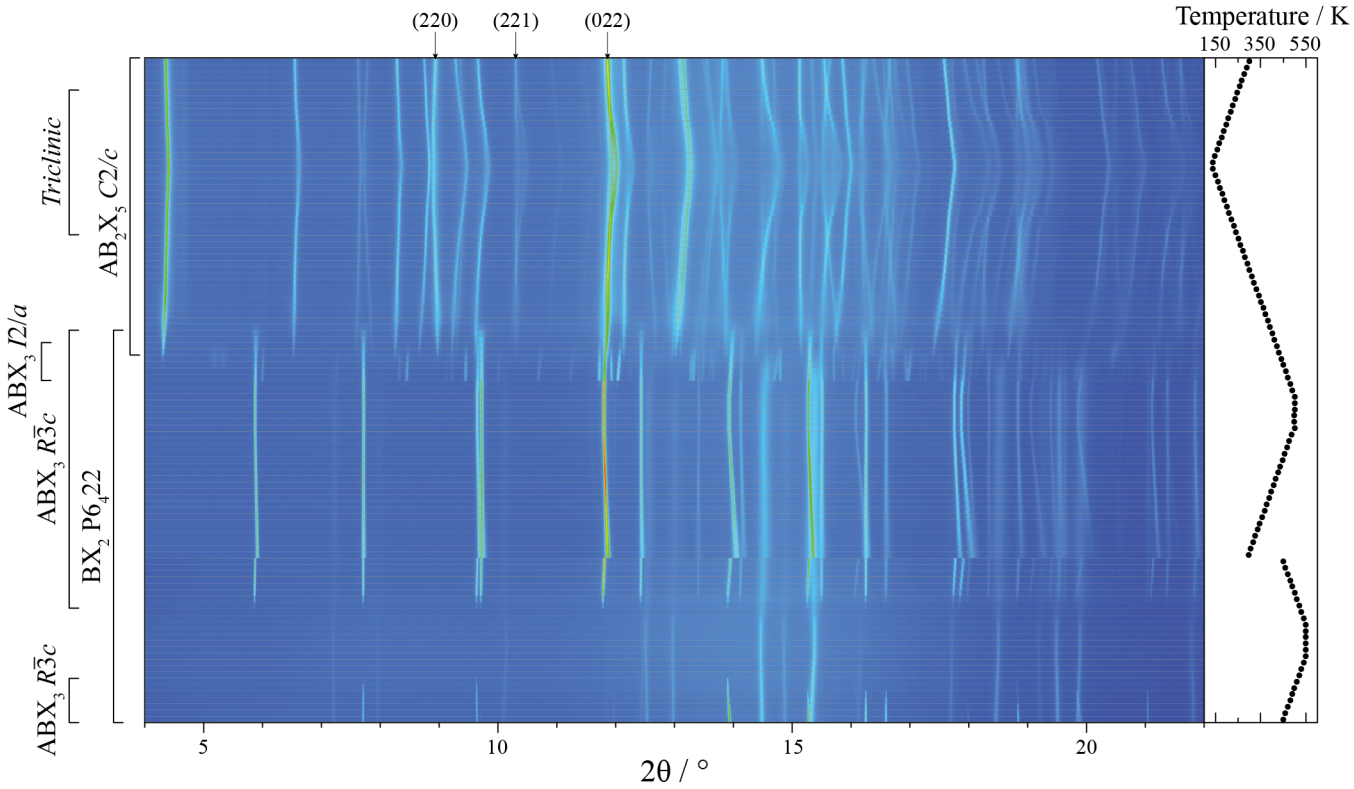

Figure 5.18: Variable temperature powder diffraction patterns of $[PPN]Cd_2[Ag(CN)_2]_5(EtOH)_2$ and its transformation products.

riod of coexistence of *M*- and *R*-$[PPN]Cd[Ag(CN)_2]_3$ phase with *R*- appearing at 390 K, which is 30 K earlier than *M*- which appears at 420 K [Figure 5.18]. The abrupt disappearance of the peaks associated with *M*-$[PPN]Cd[Ag(CN)_2]_3$ at 490 K coincides with an increase in intensity of those of *R*-$[PPN]Cd[Ag(CN)_2]_3$ suggesting that, as for the $[PPN]Cd[Au(CN)_2]_3$, *M*-$[PPN]Cd[Ag(CN)_2]_3$ transforms to *R*-$[PPN]Cd[Ag(CN)_2]_3$ at elevated temperatures. In terms of $[PPN]^+$ orientation the transient formation of the *M*- phase is surprising since in the parent compound, $[PPN]Cd_2[Ag(CN)_2]_5(EtOH)_2$, $[PPN]^+$ is aligned along the pseudocubic [111] as is the case in the *R*- phase. This suggests that there may be some reversibility in the transition, perhaps facilitated by ethanol vapour which will be present on the first heating but, presumably, not the second. Either way, this highlights the fact that

while the *M*- to *R*- transition corresponds to one which is predicted for a 'pure' tilt transition it is driven by cation reorientation.

After the disappearance of *M*-[PPN]Cd[$Ag(CN)_2$]$_3$ the only phases present are *R*-[PPN]Cd[$Ag(CN)_2$]$_3$ and Cd[$Ag(CN)_2$]$_2$·xAgCN. The peaks associated with *R*-[PPN]Cd[$Ag(CN)_2$]$_3$ disappear around 520 K with only some of the peaks returning on cooling from 510 K. Certain peaks (*e.g.* (012), (024), and (122)) disappear while others return (*e.g.* (110), (113), (116), (131), and (13$\overline{2}$)) to their previous positions. This behaviour would be consistent with preferred orientation of the phase since it regrows on cooling. While it is possible this is indicative of a phase transition it seems most likely that the disappearance of these peaks is the result of extreme preferred orientation caused by melting of *R*-[PPN]Cd[$Ag(CN)_2$]$_3$ at high temperatures. Indeed, the use of a single needle orientation (1,$\overline{1}$,0) accounts for a significant portion, but not all, of the observed peaks. This is entirely consistent with the reversible feature observed in DSC at 518/496 K [Figure 5.19] and the observation of a meniscus on the DSC sample. Furthermore, the DSC sample recovered to room temperature has a very similar diffraction pattern to that shown in Figure 5.20. It is noteworthy that, peculiarly, the (110) peak of *R*-[PPN]Cd[$Ag(CN)_2$]$_3$ is absent in the DSC-recovered sample. This is consistent with different preferred orientation of the sample measured in a flat-plate sample holder compared with in a capillary.

Compared to the Mn-analogue there is less pronounced sharpening for Cd[$Ag(CN)_2$]$_2$·xAgCN and no exsolved AgCN is observed. However, the Cd-analogue was only heated to 550 K (the Mn to 580 K) so direct comparisons may not be especially meaningful. The a/c ratio of Cd[$Ag(CN)_2$]$_2$·xAgCN is similar to that in Zn[$Ag(CN)_2$]$_2$·xAgCN suggesting that the pores are indeed occupied.[129]

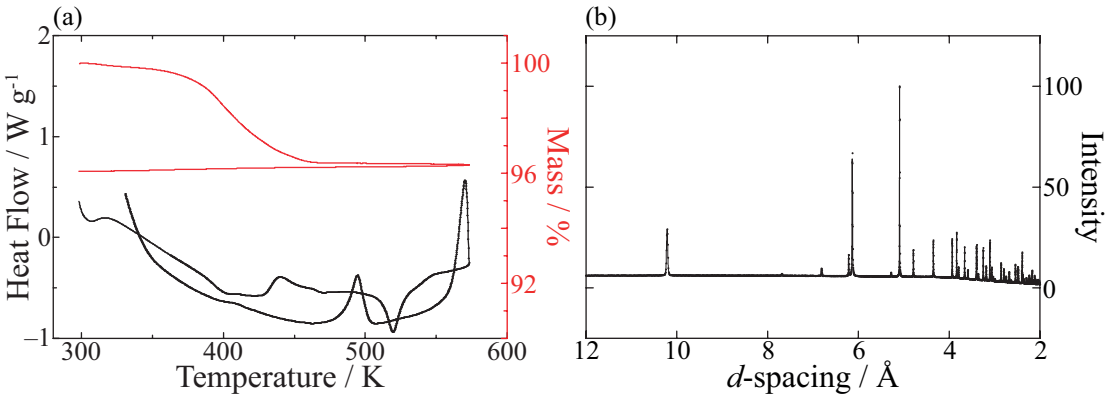

Figure 5.19: (a) DSC and simultaneous TGA data for $[PPN]Cd_2[Ag(CN)_2]_5(EtOH)_2$. Overall 3.9 % mass is lost compared to a predicted value of 5.6 %. An irreversible feature is seen with a maximum at 440 K. The asymmetric peakshape is consistent with two processes occurring as seen in the variable temperature diffraction. Large reversible features at 518/496 K are consistent with melting. Features at the highest and lowest temperatures are due to instrumental factors. (b) In-house powder diffraction of sample recovered from DSC experiment.

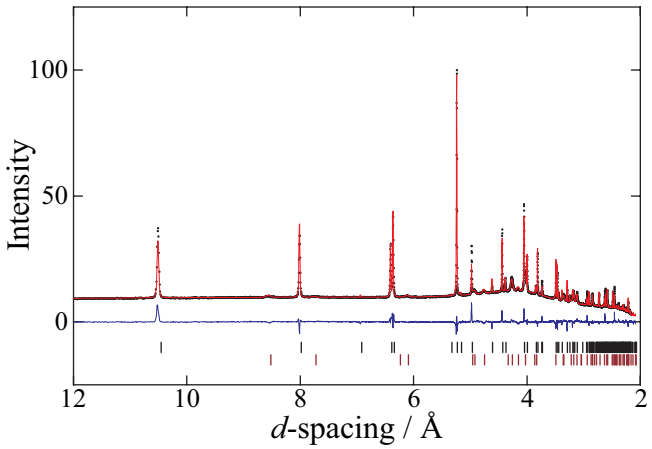

Figure 5.20: Rietveld fit to first diffraction pattern collected with hot air blower (449.9 K). Two phases were refined in this fit (weight percent): R-$[PPN]Cd[Ag(CN)_2]_3$ (74.8(2) %, black) and $Cd[Ag(CN)_2]_2{\cdot}x$AgCN (25.2(2) %, dark red). R_{wp} = 4.324%, R_p = 2.449%, GoF = 4.228.

5.4 Salt-inclusion perovskite $ABX_3{\cdot}AY$

The compound $[Bu_4N]Mn[Au(CN)_2]_3{\cdot}[Bu_4N]ClO_4$ was formed fortuitously in attempts to make a Mn analogue of the **bcs**-structured $[Bu_4N]Ni[Au(CN)_2]_3$. Moderately sized single crystals formed overnight from a concentrated ethanolic mixture of $[Bu_4N]Au(CN)_2{\cdot}\frac{1}{2}H_2O$ and $Mn(ClO_4)_2{\cdot}xH_2O$ solutions. The formula is consistent with elemental analysis found (calculated) % C 32.68 (32.92); H 5.12 (5.23); N 7.90 (8.08); Cl 2.55 (2.56).

Single-crystal X-ray diffraction

Structure solution from single crystal diffraction data proved to be a considerable challenge. I will come to show that $[Bu_4N]Mn[Au(CN)_2]_3{\cdot}[Bu_4N]ClO_4$ can be thought of as a perovskite where an extra-ion pair has been accommodated. In this case, this means that the traditional A-site—*i.e.* at $(\frac{1}{2}, \frac{1}{2}, \frac{1}{2})$ in the primitive perovskite cell—is now occupied by an anion. The two equivalents of extra-framework cations then occupy the faces, but off-set from the centre, of the perovskite cell [Figure 5.21(a)]. Presented here is a functional structural model but it is not a complete picture. The following factors have made this work challenging: scattering dominated by Au which lies on high-symmetry sites, diffuse scattering at all but the lowest temperatures [Figure 5.22 and B3.6], and a very close to metrically cubic cell. The combination of these factors means that the diffraction produced is highly pseudo-symmetric with systematically strong and weak reflections and the likelihood of twinning is significant.

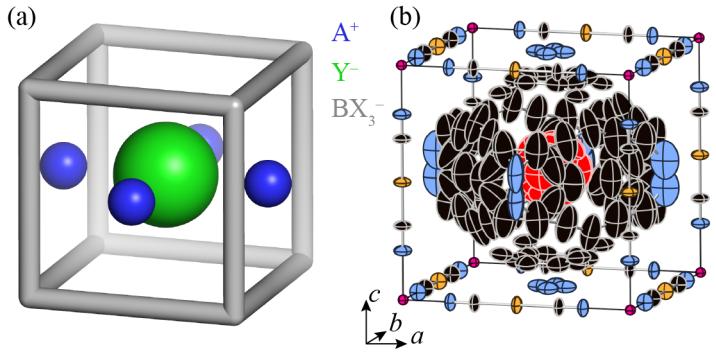

Figure 5.21: (a) Schematic representation of the $ABX_3{\cdot}AY$ structure of $[Bu_4N]Mn[Au(CN)_2]_3{\cdot}[Bu_4N]ClO_4$. BX_3^- framework shown in grey, A^+ in blue, Y^- in green. (b) Structure from single crystal diffraction based on a single perovskite cell. The extra-framework ions are heavily disordered in this collapsed cell but the framework is essentially well described in this unit cell. For reflections where $I > 2\sigma(I)$: R (F_o) = 0.040, R_w (F_o) = 0.103, GOF = 0.83. Associated .cif can be found in the Electronic Appendix.

The essentially cubic $\{Mn[Au(CN)_2]_3\}^-$ framework accounts for 51 % of the electron density in $[Bu_4N]Mn[Au(CN)_2]_3{\cdot}[Bu_4N]ClO_4$ and therefore dominates the scattering. It is however, obvious from reciprocal-space reconstructions that this system cannot be cubic due to characteristic diffuse scattering in only one set of pseudo-cubic planes [Figure 5.22(b)]. This means the model should be in a tetragonal or lower crystal system. The structural model was built up gradually in both size and complexity starting from the basic perovskite structure. Since the majority of the scattering comes from the framework, the most intense peaks can be indexed on a $\sim 10 \times 10 \times 10$ Å unit cell in $P4/mmm$ which corresponds to one perovskite cube. This ignores the weaker peaks which give a $\sim 20 \times 20 \times 20$ Å unit cell. In the $\sim 10 \times 10 \times 10$ Å unit cell the residual density within the framework was heavily disordered but it was possible to include the extra-framework ions in the refinement [Figure 5.21(b)]. After this initial insight from working with in-house data I moved on to focus primarily on data collected using the I19 instrument (Diamond Light

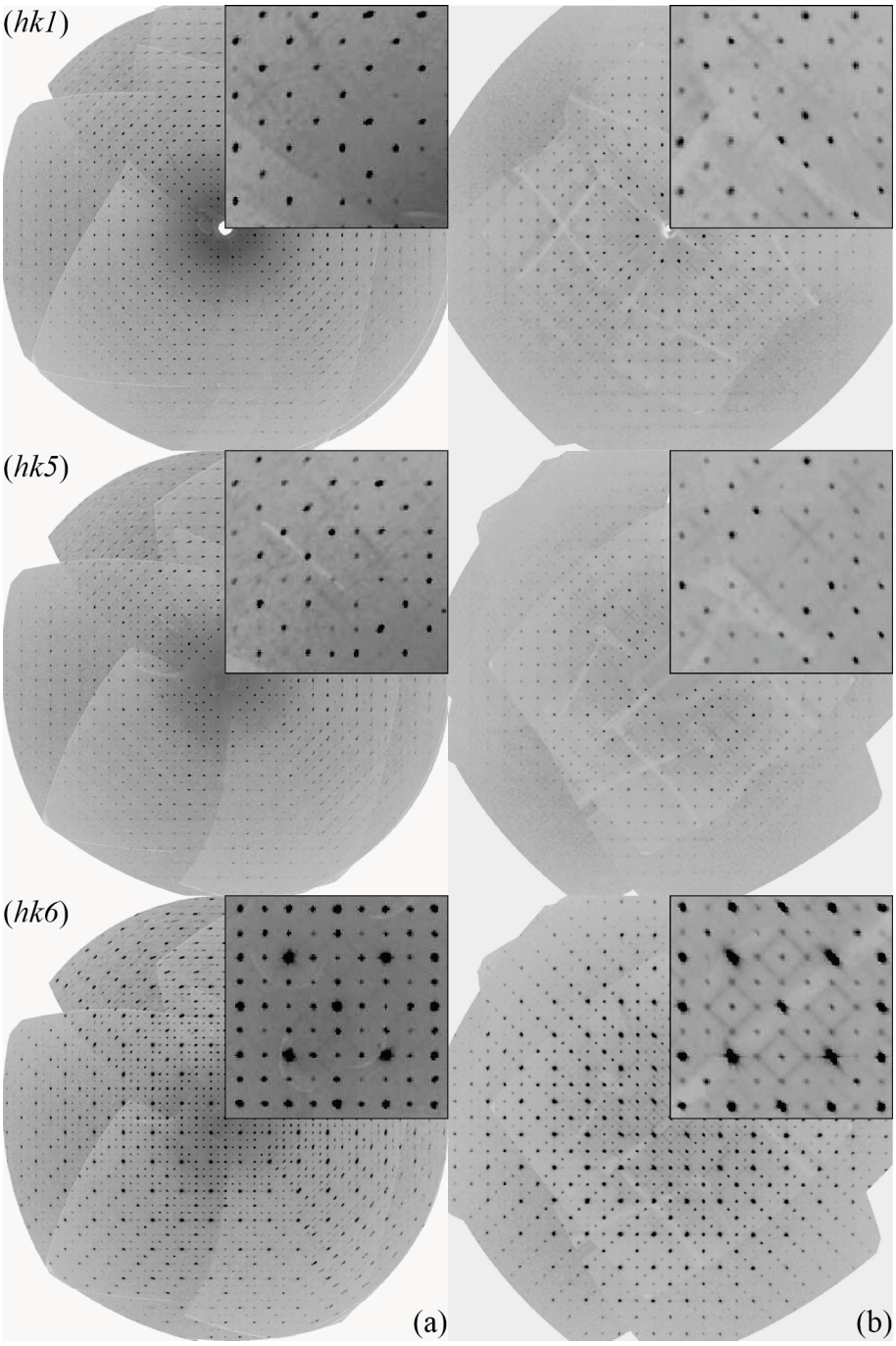

Figure 5.22: Reciprocal space reconstructions of the ($hk1$), ($hk5$), and ($hk6$) planes for data collected at 30 K on beamline I19 using $\lambda = 0.6889$ Å(a) and at 298(1) K using Cu_{K_α} (b). The diffuse scattering is substantially reduced at low temperature.

Source) at a temperature of 30 K in an attempt to reduce the apparent correlated disorder in the compound.

Building up from the $\sim 10 \times 10 \times 10$ Å model in $P4/mmm$ the corresponding $\sim 20 \times 20 \times 20$ Å (*i.e.* $2 \times 2 \times 2$ perovskite) cell should be in the maximal subgroup $I4/mcm$. As the body-centre violations in this system are fairly weak this seemed a reasonable next step. The residual electron density was, however, still very disordered indicating that the body centring should be removed. Dropping the symmetry to $P4/ncc$, which gave the highest R_{int} value of all the maximal subgroups of $I4/mcm$, allowed further progress to be made. The crucial step in coming to the present model was in recognising that both of the extra-framework species are incompatible with high symmetry sites. In this space group it cannot be avoided putting one or the other on sites with site symmetries of 2.22 and 4. By using the second origin choice of $P4/ncc$ it was possible to move $[Bu_4N]^+$ onto a low symmetry site such that the only one, ordered equivalent is in the asymmetric unit. This results in there being two $[ClO_4]^-$ units in the asymmetric unit which are centred on or near the 4*a* (2.22 symmetry) and 4*c* (4..) Wyckoff sites. The latter symmetry is clearly incompatible with the tetrahedral molecular symmetry of perchlorate. While it may be preferable to lower the symmetry to relieve the inevitable disorder across these symmetry elements, the packing of $[Bu_4N]^+$ suggests that it may be reasonable for the perchlorate ions to be disordered. In this solution the $[Bu_4N]^+$ pack to give two different pseudo-octahedral cavities [Figure 5.23] meaning that the system must accommodate a tetrahedral species within an octahedral hole.

The residual electron density around the perchlorate sites (the centres of the pseudocubic perovskite cubes) looks, necessarily, rather octahedral [Figure 5.24(a,b)].

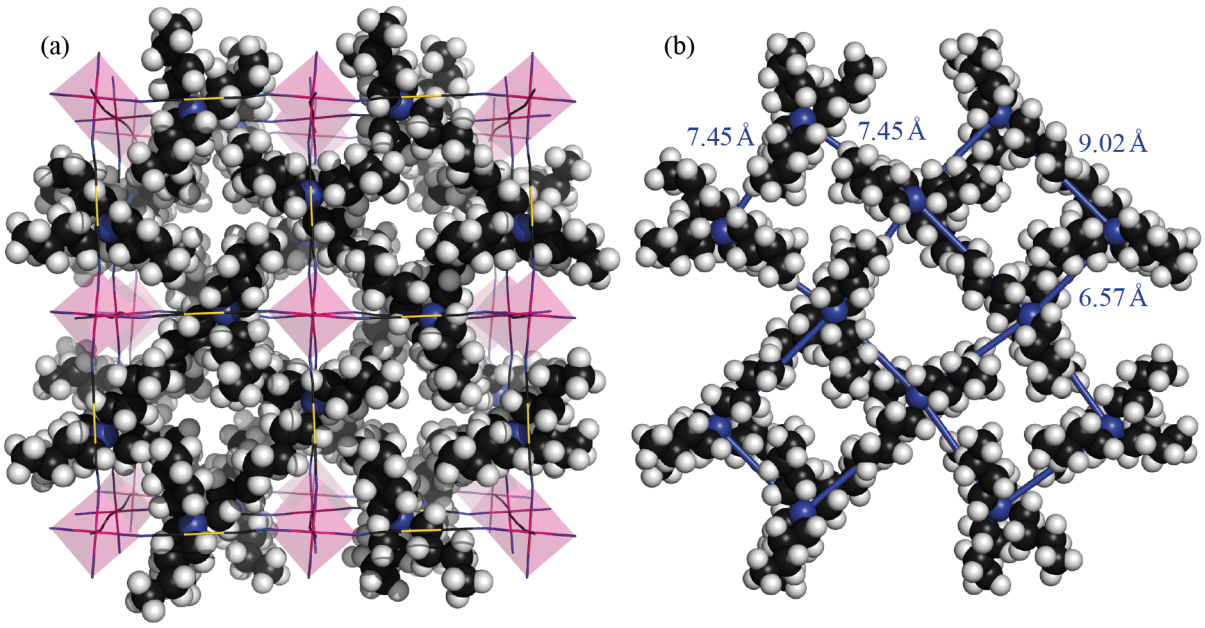

Figure 5.23: (a) In $[Bu_4N]Mn[Au(CN)_2]_3 \cdot [Bu_4N]ClO_4$ ($[ClO_4]^-$ not shown) the packing of $[Bu_4N]^+$ centred on the *ac* and *bc* faces gives two different pseudo-octahedral holes by interdigitation in the *ab* plane. The same holes lie above each other along *c* (b) The geometry of the squares formed by linking the centres of the cations indicating the N$\cdots$N distances.

Examination of this residual density suggests that a reasonable starting model would be to place three tetrahedra, each with one oxygen pointing toward the symmetry inequivalent arms of the residual density. Each tetrahedron should then be free to 'rotate' around this Cl—O bond giving a torus of electron density instead of 3 resolved oxygen atoms.* The residual density of 377 (392 ideal) electrons per unit cell when no perchlorate is included as found by PLATON SQUEEZE is consistent with the presence of 8 perchlorate anions per unit cell [See Electronic Appendix for PLATON output].[416,417] Inclusion of the disordered perchlorate (without implementing the tori) within the pseudo-octahedral sites [Figure 5.24(c,d)] gives the structural model in Figure 5.24(e) for which crystallographic details are summarised in Table

*An added complication is that at least the perchlorate on the *c* site also appears to have an off-centred component

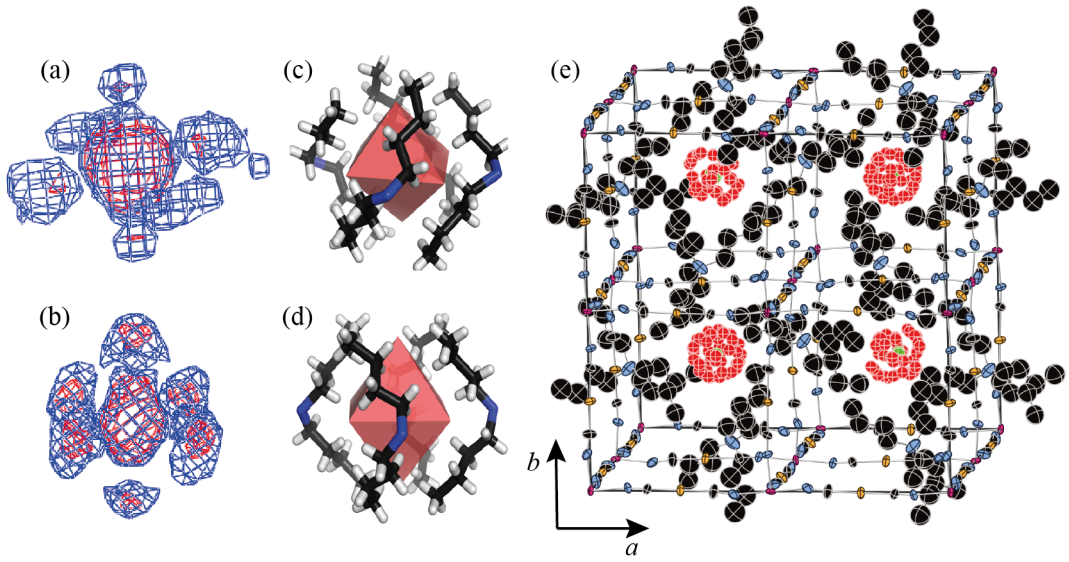

Figure 5.24: The residual density around the *a* (a) and *c* (b) Wyckoff sites. Due to the high site symmetry the residual density looks close to octahedral. Large, non-spherical density at the centre of the 'octahedra' is probably indicative of perchlorate off-centring. Pseudo-octahedral sites shown with red polyhedra at the 4*a* (c) and 4*c* (d) Wyckoff sites. A full structure solution including an disordered perchlorate (e). Only half of the extra-framework ions are shown and no hydrogen atoms are shown for clarity. Manganese in pink, gold in yellow, nitrogen in blue, carbon in black, oxygen in red, and chlorine in green.

5.3.

While caution should be used in interpreting partial structural models it seems extremely likely that the formulation of $[Bu_4N]Mn[Au(CN)_2]_3{\cdot}[Bu_4N]ClO_4$ as a perovskite which contains 2 cations and 1 anion rather than a single cation is consistent with all available evidence.* I note here the conceptually similarity to $Zn[Ag(CN)_2]_2{\cdot}x$AgCN and related phases which might reasonably be thought of as inorganic co-crystals.

*Structural models involving one cation have been explored but, for a simple-cubic framework, one $[Bu_4N]^+$ is, in any of its known conformations, too small.

Table 5.3: Crystallographic details of $[Bu_4N]Mn[Au(CN)_2]_3{\cdot}[Bu_4N]ClO_4$ derived from single-crystal diffraction. The associated .cif and .fcf files can be found in the Electronic Appendix.

Compound	$[Bu_4N]Mn[Au(CN)_2]_3{\cdot}[Bu_4N]ClO_4$
Empirical formula	$Mn_1Au_3C_{38}N_8H_{72}Cl_1O_4$
Formula weight (g mol^{-1})	1386.32
Crystal System	Tetragonal
Space Group	$P4/ncc$ (No. 130) Origin Choice 2
Z	8
Radiation (Å)	$\lambda = 0.68890$
Crystal colour	Colourless
Crystal size (mm)	0.01×0.01×0.01
Temperature (K)	30(0.5)
a (Å)	21.4048(3)
c (Å)	21.3901(2)
V (Å^3)	9800.2(2)
μ (mm^{-1})	39.93
Reflections ($I > 2\sigma(I)$)	7438
R (F_o)	0.1257
R_w (F_o)	0.1866
GOF	1.2274
Minimisation	F

Powder diffraction

Variable temperature powder diffraction data are shown in Figure 5.25. On first inspection there are two distinct regions of the diffraction data with an irreversible transition occurring at 380 K.

The powder diffraction up to 380 K is consistent with the single crystal structure of $[Bu_4N]Mn[Au(CN)_2]_3{\cdot}[Bu_4N]ClO_4$. A typical Pawley refinement fit is shown in Figure 5.26(a). Coefficients of thermal expansion for $[Bu_4N]Mn[Au(CN)_2]_3{\cdot}[Bu_4N]ClO_4$ in the range 140–380 K were found to be $\alpha_a = 23.97(9)\,MK^{-1}$, $\alpha_c = 24.65(8)\,MK^{-1}$, and $\alpha_V = 73.0(2)\,MK^{-1}$[Figure 5.26(b)].

It has not been possible to develop a full structural model of the transformation product in the time scale of this project but some pertinent information is presented here. At 380 K $[Bu_4N]Mn[Au(CN)_2]_3{\cdot}[Bu_4N]ClO_4$ transforms into a different high-

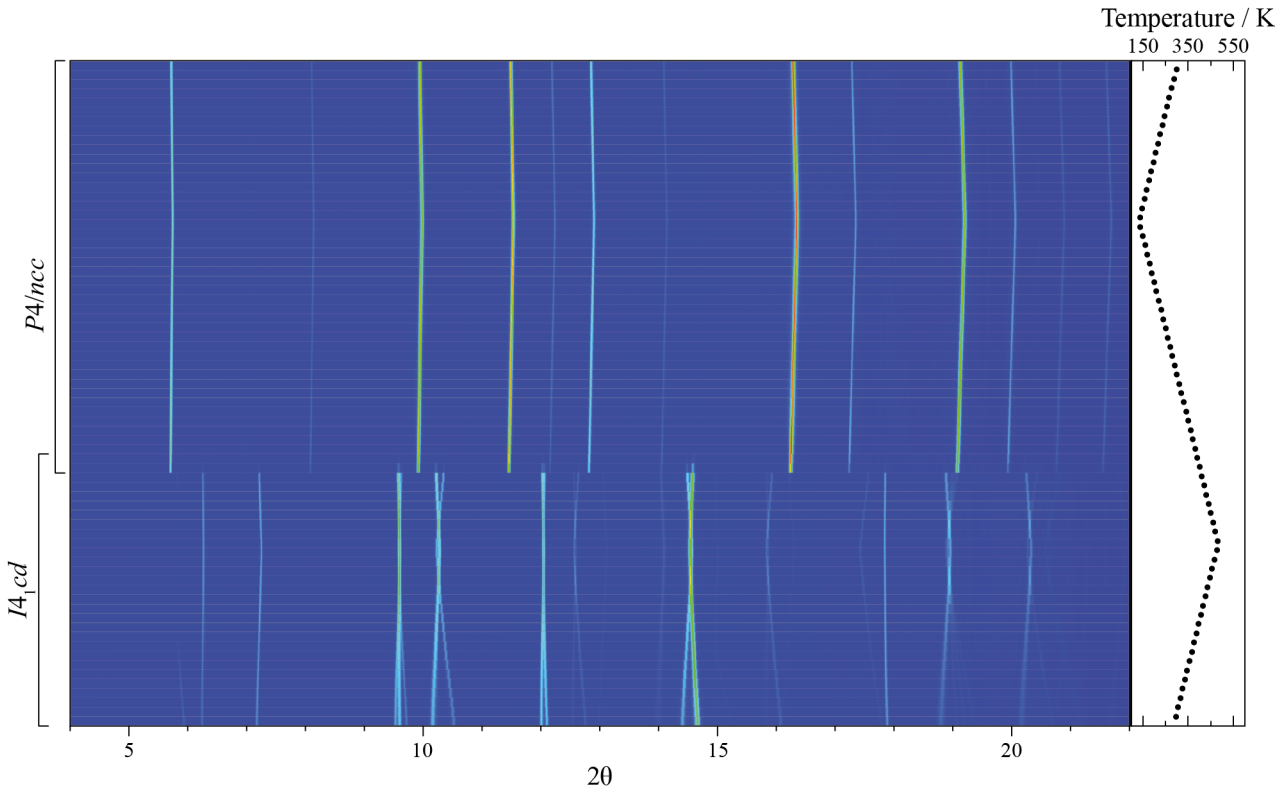

Figure 5.25: Variable temperature powder diffraction patterns of $[Bu_4N]Mn[Au(CN)_2]_3{\cdot}[Bu_4N]ClO_4$ and its transformation product.

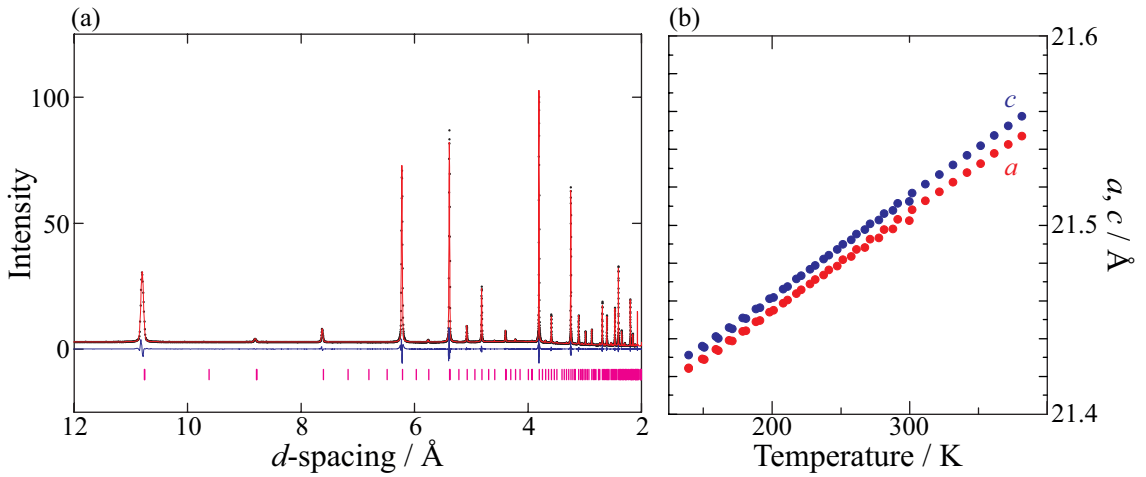

Figure 5.26: (a) Typical Pawley fit of $[Bu_4N]Mn[Au(CN)_2]_3{\cdot}[Bu_4N]ClO_4$ in $P4/ncc$. $R_{wp} = 4.203\%$, $R_p = 2.536\%$, GoF $= 4.128$. (b) Variation in lattice parameters with temperature. All errors within markers.

symmetry phase. The powder diffraction is very similar to the 6-connected structure with **bcs** topology as reported for $[Bu_4N]Ni[Au(CN)_2]_3$ [Figure 5.27(a)].[310] This compound, as determined from single-crystal data, was reported in space group $I4_1cd$. The Mn-analogue phase here, **bcs**-$[Bu_4N]Mn[Au(CN)_2]_3$, first appears at 380 K and the starting phase is absent after 410 K. A Pawley refinement based on the $[Bu_4N]Ni[Au(CN)_2]_3$ $I4_1cd$ cell accounts for the majority of peaks present with unit cell parameters $a = 24.2890(3)$ Å, $c = 23.4744(4)$ Å, $V = 13848.8(4)$ Å^3 [Figure 5.27(b)]

Transformation into the ABX_3 phase leaves an equivalent of $[Bu_4N]ClO_4$ to be accounted for. It is not clear that this equivalent of $[Bu_4N]ClO_4$ is exsolved from the structure. The highest temperature reached in this experiment was 480 K, which is just below the melting point of $[Bu_4N]ClO_4$ (484–488 K)[418] so we expect to see diffraction from this component at all temperatures. Just below 6 ° ($d \approx 10.5$ Å) is a peak which cannot be indexed on the tetragonal cell of **bcs**-$[Bu_4N]Ni[Au(CN)_2]_3$. On heating, this peak disappears from 440 K and reappears at 400 K on cooling.* This peak is at very similar d-spacing to the first, most intense peak of $[Bu_4N]ClO_4$† so it might be argued it is due to exsolved $[Bu_4N]ClO_4$ [Figure 5.27(c)].

However, it is also possible that the $[Bu_4N]ClO_4$ is included within structure of **bcs**-$[Bu_4N]Ni[Au(CN)_2]_3$. There are a few pieces of evidence in support of this view. The thermal expansion of the peak at $d \approx 10.5$ Å tracks that of the $(00l)$ peaks in the main pattern, *e.g.* (004) at 10.5 ° / $d \approx 5.9$ Å. This peak, however, cannot be indexed on the parent cell metrics even in $P1$ symmetry. This means that the

*There is also a similar, weaker peak just below 12 °.

†The crystal structure of $[Bu_4N]ClO_4$ has not been reported.

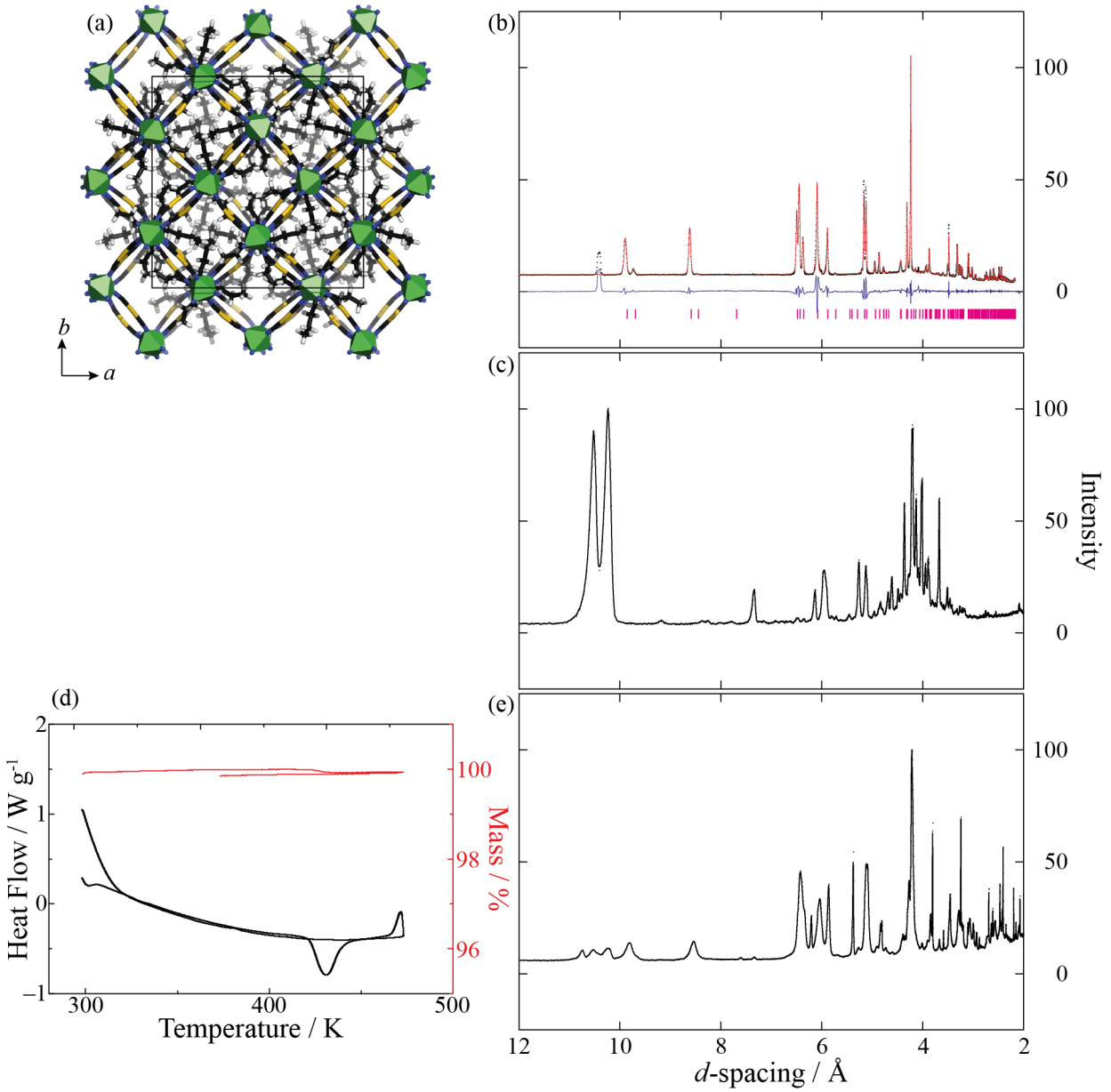

Figure 5.27: (a) Structure of $[Bu_4N]Ni[Au(CN)_2]_3$ looking down c. The structure has the unusual 6-connected **bcs** topology. Channels down c are partially filled by the arms of $[Bu_4N]^+$ (b) Pawley fit to the powder diffraction pattern of **bcs**-$[Bu_4N]Mn[Au(CN)_2]_3$ in $I4_1cd$. The unaccounted for peak at $d \approx 10.5$ Å is attributed to $[Bu_4N]ClO_4$. Lattice parameters: $a = 24.2890(3)$ Å, $c = 23.4744(4)$ Å, $V = 13848.8(4)$ Å^3 $R_{wp} = 6.103\%$, $R_p = 3.521\%$, GoF = 6.345 (c) Powder diffraction pattern of $[Bu_4N]ClO_4$. (d) DSC trace of $[Bu_4N]Mn[Au(CN)_2]_3{\cdot}[Bu_4N]ClO_4$ showing a large endothermic peak (e) Powder diffraction pattern of sample recovered from DSC. There are three peaks below 10 Å implying that a mixture of **bcs**-$[Bu_4N]Mn[Au(CN)_2]_3$ and exsolved $[Bu_4N]ClO_4$ may be present.

$[Bu_4N]ClO_4$ would be a guest with different periodicity from the main structure (c.f. $Zn[Ag(CN)_2]_2{\cdot}AgCN$[129]).

The DSC data tell a slightly different story. The only feature observed is a large, exothermic peak on heating with maximum at 430 K [Figure 5.27(d)]. This is 50 K higher than the temperature at which the variable-temperature diffraction changes. The powder diffraction pattern of the DSC sample recovered to room temperature [Figure 5.27(e)] looks similar to (b) but with additional peaks which are consistent with the positions of the most intense peaks of $[Bu_4N]ClO_4$. The temperature disparity between DSC and diffraction data means that it is difficult to draw comparison between the two.

Discussion

While the structures of $[Bu_4N]Mn[Au(CN)_2]_3{\cdot}[Bu_4N]ClO_4$ and its transformation product are not 'fully' understood, the information that has been determined raises some interesting points. $[Bu_4N]Mn[Au(CN)_2]_3{\cdot}[Bu_4N]ClO_4$ is rather unusual and could usefully be thought of as an inorganic co-crystal. The perovskite framework provides a constrained environment for a variety of molecular (rotational, conformational) degrees of freedom to interact within.

The irreversible transformation of $[Bu_4N]Mn[Au(CN)_2]_3{\cdot}[Bu_4N]ClO_4$ at high temperature appears to be a first order reconstructive phase transition due to phase coexistence. I discuss above the possibility that **bcs**-$[Bu_4N]Ni[Au(CN)_2]_3$ may have an equivalent of $[Bu_4N]ClO_4$ included within the structure. While there are a number of factors pointing towards this it seems there would need to be a significant entropic driving force to outweigh the presumed alternative gain in lattice enthalpy

resulting from $[Bu_4N]ClO_4$ being excluded from the structure.

5.4.1 Magnetometry

Magnetometry data for (**5c**), (**5a**), (**3b**), and (**6**) are shown in Figure 5.28. Inverse susceptibility plots show all compounds to be essentially paramagnetic across the temperature range studied (2–300 K) with essentially no difference between field-cooled and zero-field-cooled values. Effective magnetic moments, μ_{eff}, and Curie temperatures, θ_{C}, were extracted from linear fits to the inverse susceptibility data. The values for (**5c**) of 3.09 μ_{B} / −0.68 K are consistent with isolated Ni^{2+} centres and with previously reported data.[310] Likewise, the values for (**5a**) of 5.98 μ_{B} / −0.06 K are consistent with isolated d^5 high-spin (*i.e.* N-bound) Mn^{2+} centres. Being close to the spin-only values for 2 and 5 unpaired electrons, respectively, and extremely small negative Curie temperatures this suggests that, as would be expected, dicyanoaurate is a very poor mediator of magnetic exchange.

In contrast, the compound (**3b**) has values of 6.25 μ_{B} / −0.02 K when formulated as AB_2X_2 (with only one Mn centre this is $6.25\,\mu_{\text{B}} \div \sqrt{2} = 4.42\,\mu_{\text{B}}$). The slight downward slope of the inverse susceptibility suggests that even at 300 K the compound is not fully paramagnetic [Figure 5.28]. This is reflected in the positive gradient of the magnetic moment. The maximum in the field-cooled moment at around 30 K is reproducible and may be indicative of antiferromagnetic ordering. The magnitude of the moment is consistent with an equal mixture of high-spin and low-spin Mn^{2+} centres for which the spin only value is 6.16 μ_{B} (or 4.36 μ_{B} for one Mn^{2+} per formula unit).[420,421*] This observation is unexpected given that there is only one

*The observed moment for a compound containing isolated paramagnetic centres A_nB_m is given by $\mu_{AB} = \sqrt{n\mu_A^2 + m\mu_B^2}$.[422]

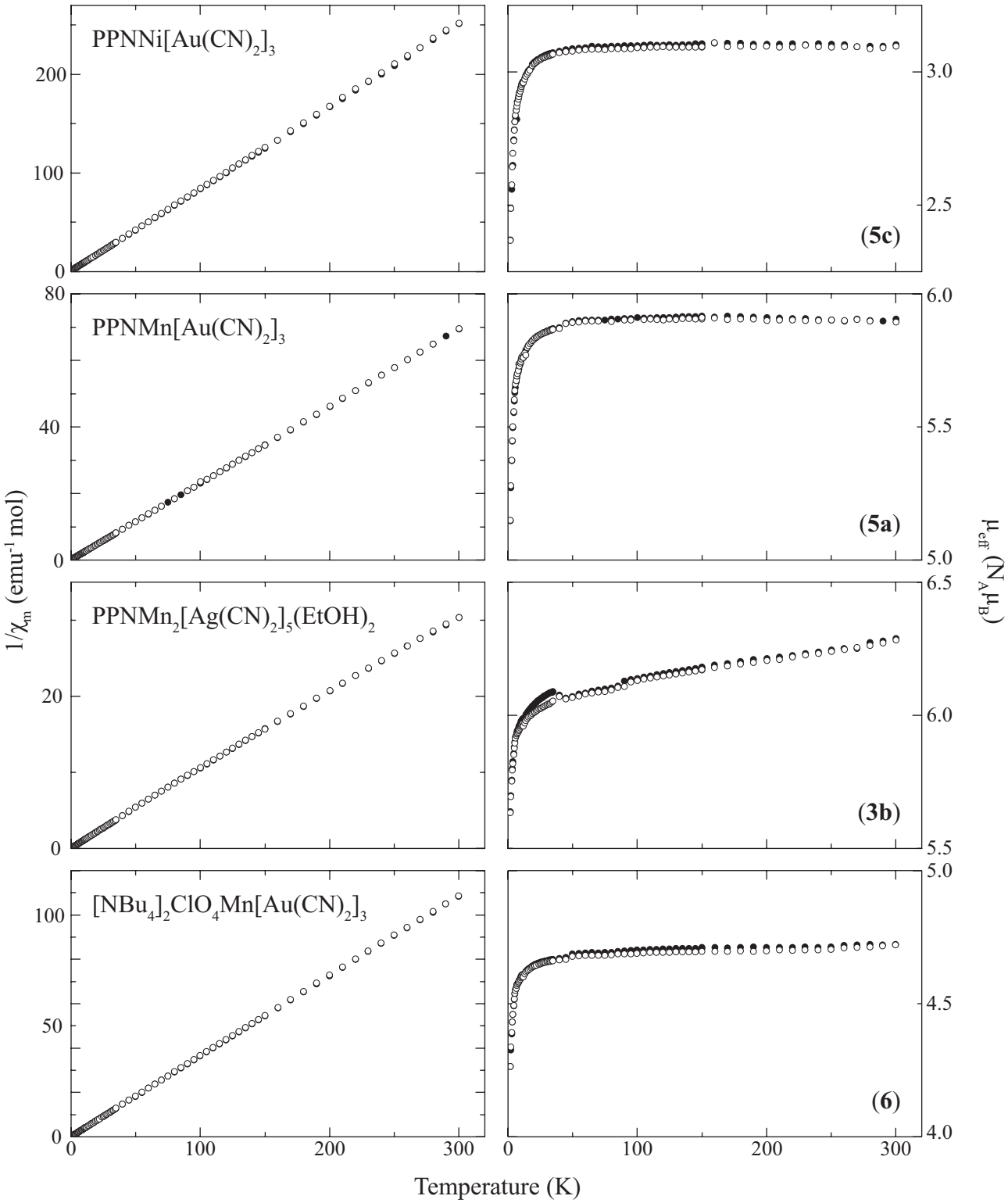

Figure 5.28: Magnetometry for selected compounds. Inverse susceptibility vs. temperature (left column) and moment vs. temperature (right column) show little, if any, interaction between magnetic sites. While (**5c**) and (**5a**) give moments consistent with isolated d^8 and d^5 high-spin ions respectively, the behaviour of (**3b**) and (**6**) is less straightforward.[419] Zero-field-cooled is shown as hollow circles and field-cooled as filled circles.

Mn^{2+} in the asymmetric unit of the crystal structure and suggests that this is not a complete picture. Low-spin electronic configurations in transition metal cyanides typically require the metal to be C-bound. This is observed for $Ag_3[Co(CN)_6]$, where all Co^{3+} centres are low spin but in this instance it would appear to require half of the cyanides to switch orientation. The exchange of one cyanide for an ethanol to complete the coordination sphere can also be expected to have an effect on the magnetism but, given that ethanol is a rather weak field ligand this is not the effect one might anticipate.

The $ABX_3{\cdot}AY$ perovskite (**6**) is paramagnetic with magnetic moment and Curie temperature of $4.70\,\mu_B$ / $-0.09\,K$. The magnitude of the magnetic moment is quite small for high-spin d^5 but also much higher than the spin-only, or Russell-Saunders coupling values for low-spin d^5 ($= 1.73\,\mu_B$ and $= 2.24\,\mu_B$).[421] The observed value would be consistent with a mixture of high-spin and low-spin Mn^{2+}. This is similar to the value of $4.53\,\mu_B$ reported for $KMn(CN)_3$ where half the Mn^{2+} is N-bound, hence high-spin, and half C-bound, hence low spin.[420] As for (**3b**), reconciling this with the structural model from diffraction is challenging. Understanding the magnetic behaviour of (**3b**) and (**6**) will require further work as both sets of data are inconsistent with the crystallographic model.

5.5 Concluding remarks

In this Chapter I have examined the thermal behaviour of three classes of perovskite(-like) dicyanometallates. The M-ABX_3 perovskites can be converted to R-ABX_3 perovskite at elevated temperatures but do not revert on cooling in the temperature range studied. While this involves a tilt transition $a^-a^-a^-$ to $a^-a^-c^-$, which

is directly analogues to an oxide tilt transition,[185] it also involves reorientation of the $[PPN]^+$ cation resulting in a prioritisation of cation–π over π–π interactions. It seems likely that these $[PPN]^+$–framework interactions and as well as packing considerations are responsible for the transition being irreversible over the temperature range investigated.

The $AB_2X_5{\cdot}(EtOH)_2$ Ruddlesden-Popper $n = 2$ analogues show a second order phase transition to a triclinic cell below room temperature. The structural details of the transition have not been fully investigated here but the observed splittings are consistent with the involvement of Ag$\cdots$Ag interactions. Removal of ethanol at elevated temperatures causes drastic structural change. While the mechanism of this reaction and the stoichiometry of the products are not well understood this process does produce an R-ABX_3 perovskite and a $BX_2{\cdot}x$AgCN analogue of $Zn[Ag(CN)_2]_2{\cdot}x$AgCN. This might be thought of as coordinative disproportionation in that a 5-coordinate network transforms to a 6- and 4-coordinate network. Furthermore, when the desolvation process was carried out on a single crystal, it was shown that the $[PPN]^+$ in $[PPN]Mn_2[Ag(CN)_2]_5(EtOH)_2$ are found in the same spatial orientation in the product R-$[PPN]Mn[Ag(CN)_2]_3$. These transformations allow for understanding the interrelated nature of perovskite-like (and quartz-like) phases.

The interrelation of the thermal behaviour of the perovskite and Ruddelsden-Popper-like classes (i) and (ii) above can be understood in one scheme [Figure 5.29]. Furthermore, this set of $[PPN]^+$-containing perovskite analogues along with $[PPN]Cd[Ag(CN)_2]_3{\cdot}3EtOH{\cdot}nH_2O$ reported in Chapter 3 collectively highlight the important role of cation orientation and internal degrees of freedom. Table 5.4 summaries the cation orientation and ordering found for these different phases.

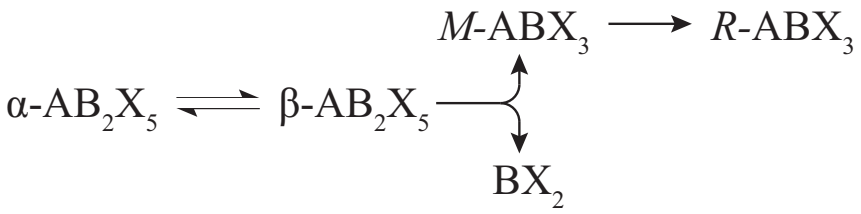

Figure 5.29: Relationship between the perovskite-like dicyanometallate phases.

Table 5.4: Summary of the orientation and P—N—P conformations found in $[PPN]^+$-continaing perovskite analogues. P$\cdots$P orientation indicates the type of pseudo-cubic perovskite direction the $[PPN]^+$ is aligned along. and No. P$\cdots$P axes indicates how many different equivalent directions $[PPN]^+$ are aligned along.

Structure family	P$\cdots$P orientation	P—N—P	P—N—P ordering	No. P$\cdots$P axes
R-[PPN]BX_3	(111)	linear*	—	1
M-[PPN]BX_3	(112)	bent	rocksalt	1
M-[PPN]$B_2X_5(EtOH)_2$	(111)	linear	—	1
[PPN]BX_3·3EtOH·$n$$H_2O$	(111)	linear	—	4†

*Constrained by symmetry.
†Ordering and displacement in columns along the four independent [111]-type directions.

Taken together, this suggests that orientation along the pseudo-cubic [111] is optimal but cubic symmetry is only achieved by inclusion of addition species as in [PPN]Cd[$Ag(CN)_2$]$_3$·3EtOH·$n$$H_2O$ which crystallises in $Pa\overline{3}$. Furthermore, the $[PPN]^+$ is displaced by 0.93 Å in intersecting columns along each of the four different $\langle 111 \rangle$ directions.

The salt-inclusion perovskite [Bu_4N]Mn[$Au(CN)_2$]$_3$·[Bu_4N]ClO_4 undergoes a reconstructive phase transition from perovskite to the unusual **bcs** topology. While a full understanding of the correlated disorder in this compound has not been achieved it is clear that the combination of packing of $[Bu_4N]^+$ to give octahedral site for the tetrahedral $[ClO_4]^-$ to sit in will give rise to significant orientational disorder. Fur-

thermore, the conformational flexibility of $[Bu_4N]^+$ and of dicyanoaurate allows for the formation of unusual structure types. While these compounds bear important similarities to familiar oxides, their thermal behaviour further demonstrates the important of molecular degrees of freedom.

Chapter 6

Incommensurate modulation in diamondoid $[NEt_4]Ag[Ag(CN)_2]_2$

6.1 Introduction

In this Chapter I report an incommensurately modulated phase of the diamondoid dicyanometallate coordination polymer $[NEt_4]Ag[Ag(CN)_2]_2$. As for the phase transitions discussed in the previous Chapter, I will show that coupling between the degrees of freedom of the molecular cation and its framework host is a central aspect of this phenomenon. Refinements were carried out with assistance from Dr. K. E. Christensen, which I gratefully acknowledge.

There is a notable lack of classical soft mode transitions reported for metal–organic frameworks (MOFs) and other coordination polymers (CPs). There are even fewer modulated phases reported for this type of material [Section 1.6.2].[208,257,269] While these phases are of substantial interest in their own right, they can also provide crucial information about the dynamical behaviour of their parent phases in the same way that, for example, tilt transitions in perovskites reflect low-energy dynamics of the high symmetry parent.[423] Furthermore, the coupling between molecular and framework degrees of freedom is increasingly being understood as important for functional materials such as the lead halide perovskites.[214–216,424]

The ambient structure of $[NEt_4]Ag[Ag(CN)_2]_2$, tetraethylammonium silver dicyanoargentate,[333] was presented in Chapter 3. It consists of three independent anionic frameworks of formula $\{Ag[Ag(CN)_2]_2\}^-$, with extra-framework cations $[NEt_4]^+$ occupying the voids thus formed [Figure 6.1]. The diamondoid topology of the $\{Ag[Ag(CN)_2]_2\}^-$ frameworks is the most common underlying structure for interpenetrating metal-organic frameworks and permits direct comparison with cristobalite.[134] The chains of short Ag$\cdots$Ag distances connecting the three networks are indicative of closed-shell 'argentophilic' interactions [Section 1.2.1].[110] In this instance, the two symmetry independent linker Ag^I are connected in zig-zag chains running along the b direction with an Ag$\cdots$Ag distance of 3.042 Å. These weak interactions are commonly associated with extreme thermal expansion and compressibility, are recognised to affect the structures of ternary silver(I) oxides, and give rise to concentration-dependent luminescence.[76,77,109,125] The low energy associated with distorting these interactions is important for the dynamical behaviour of $Ag_3[Co(CN)_6]$,[425] which features layers of argentophilic interactions in a Kagomé net.[97,373]

6.2 Results

On cooling below 235 K, a new set of reflections are observed in the diffraction pattern of $[NEt_4]Ag[Ag(CN)_2]_2$ which cannot be indexed with three lattice vectors [Figure 6.2]. However, it is possible to index these new (satellite) reflections with a modulation vector, $\mathbf{q}$, which is incommensurate with the parent cell. The value of $\mathbf{q}$ varies little with temperature and was found to be $\mathbf{q} = (0, 0, 0.12867(16))$ at 100 K [Figure 6.3(a)]. The temperature dependence of the intensity of satellite peaks is

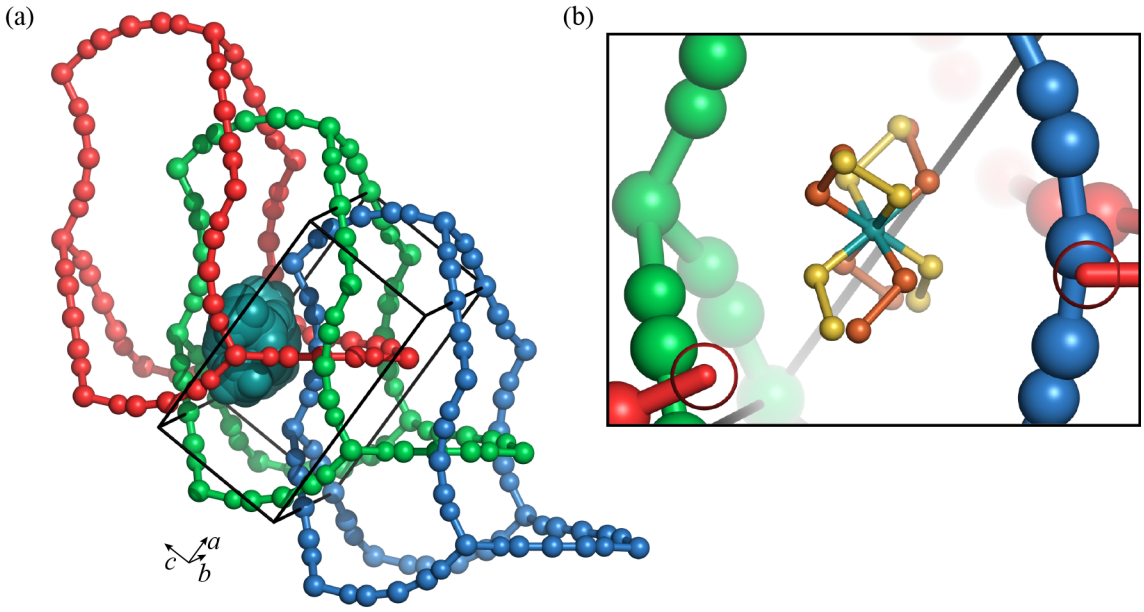

Figure 6.1: Structure of ambient phase of $[NEt_4]Ag[Ag(CN)_2]_2$. (a) It consists of three independent diamondoid networks (red, green, and blue) with $[NEt_4]^+$ (teal) filling the voids. A single 'cage' of each network is shown. Only one $[NEt_4]^+$ is shown for clarity which is disordered across a mirror plane. The *Pnma* unit cell is shown in black. (b) Close view of the two 50% occupied conformations of $[NEt_4]^+$ (yellow and orange). The nitrogen atom (teal) is common to both conformations.

consistent with a second-order phase transition since these are related to the order parameter [Figure 6.3(b-c)].[426*] The absence of a clear discontinuity in the unit cell volume across the transition temperature also supports this assignment [Appendix C1].

The observed diffraction pattern can be understood in terms of a superspace approach. The superspace group $Pnma(00\gamma)0s0$ was chosen on the basis of visual inspection of systematic absences manifested in the satellite reflections and confirmed using SUPERFLIP[321] as implemented in JANA2006.[223] Compared to the parent symmetry, this adds an extra symmetry element—an *s*-glide—a glide plane

*Additionally, a different crystal was found to be modulated on crash-cooling to 30 K with a slightly different wavevector of $\mathbf{q} = (0, 0, 0.1309(3))$. Crash-cooling refers to direct introduction of the sample into the 30 K cryostream from room temperature. Rate of cooling may play a role in determining the particular $\mathbf{q}$ observed.

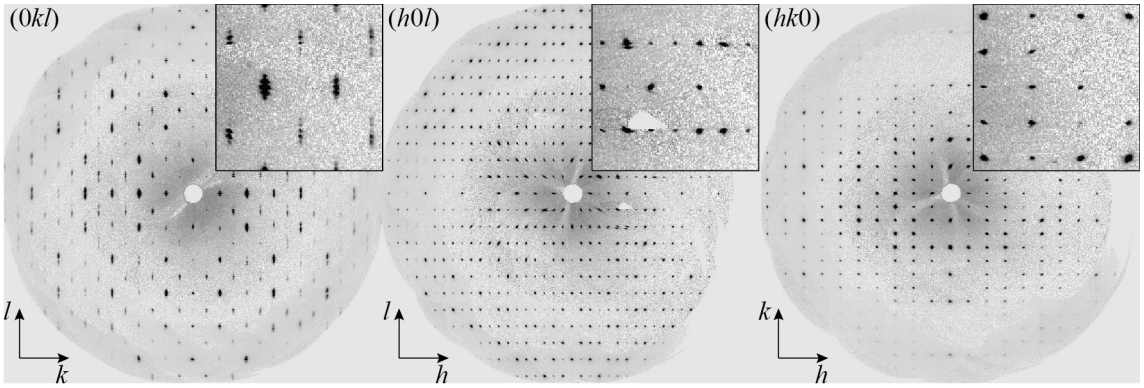

Figure 6.2: Reconstructed slices of diffraction data showing the $(0kl)$, $(h0l)$, and $(hk0)$ layers. No satellite peaks are visible in the $(h0l)$ layer due to the $h0lm$, $m = 2n$ reflection condition in space group $Pnma(00\gamma)0s0$ meaning that the first-order satellites are systematically absent. Additional planes are shown in Appendix C1.

along the 4th direction. Importantly, this glide plane acts to remove the conformational disorder of the $[NEt_4]^+$ seen in the parent $Pnma$ phase.

The modulated structure at 100 K was solved and refined against a full sphere

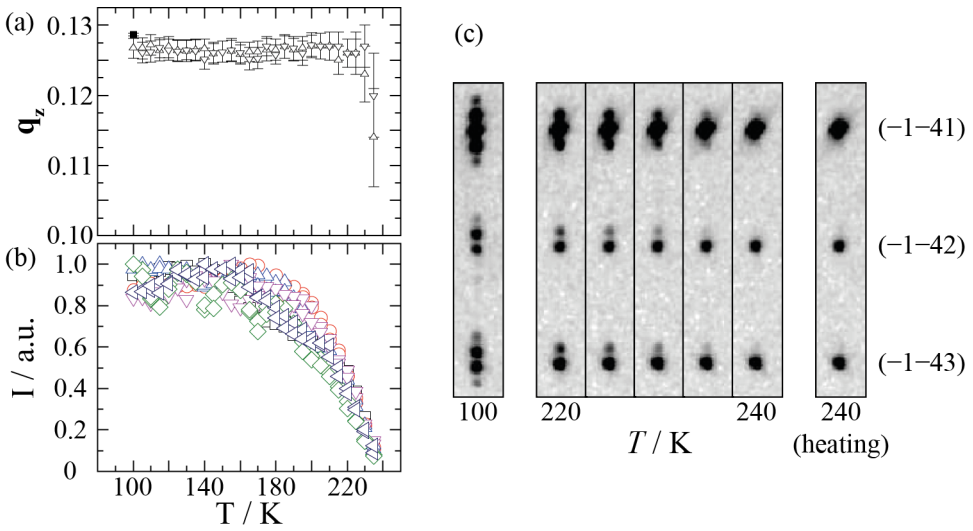

Figure 6.3: (a) z-component of modulation wave-vector derived from single-crystal diffraction. Downward hollow arrows are on cooling, upward hollow arrows on heating. Solid square from a full sphere of reciprocal space. (b) Self-normalised intensities for six first-order satellite peaks indicating continuous nature of phase transition. Peaks are $(\bar{1}721)$ black squares, $(\bar{1}72\bar{1})$ red circles, $(\bar{1}711)$ blue triangles, $(\bar{1}71\bar{1})$ magenta triangles, $(\bar{1}3\bar{3}\bar{1})$ green diamonds, and $(0\bar{5}2\bar{1})$ black triangles. (c) Evolution of satellite peaks in the $(-1,k,l)$ layer. Second-order satellites are observed for some reflections from ∼200 K. See Appendix C1 for all temperatures on heating and cooling.

Table 6.1: Crystallographic details of the modulated phase of $[NEt_4]Ag[Ag(CN)_2]_2$. Corresponding crystallographic files for the (3+1)d modulated structure and $2 \times 2 \times 8$ approximant can be found in the Electronic Appendix.

Compound	$[N(C_2H_5)_4]Ag[Ag(CN)_2]_2$
Empirical formula	$Ag_3N_5C_{12}H_{20}$
Formula weight (g mol^{-1})	557.92
Crystal System	Orthorhombic
Space Group	$Pnma(00\gamma)0s0$
Z	4
Radiation (Å)	Cu K$_\alpha$, $\lambda = 1.54180$
Crystal colour	Colourless
Crystal size (mm)	0.06×0.11×0.15
Temperature (K)	100.0(1)
a (Å)	16.5739(11)
b (Å)	11.293(14)
c (Å)	9.1495(10)
V (Å^3)	1712.5(3)
μ (mm^{-1})	27.321
Reflections (main)	1802
Reflections (satellite)	3124
Refinement on	F^2
R_{all}, wR_{all}	8.55, 22.74
R_{obs}, wR_{obs}	8.29, 22.70
Main reflections	
R_{obs}, R_{all}, wR_{all}	7.14, 7.25, 23.27
Satellite reflections	
R_{obs}, R_{all}, wR_{all}	9.49, 9.89, 22.33
GOF$_{\text{obs}}$, GOF$_{\text{all}}$	7.35, 7.08

of diffraction data using the ambient structure as starting point. Crystallographic details are summarised in Table 6.1 and crystallographic files for the modulated structure and $2 \times 2 \times 8$ approximant in $P1$ are included in the Electronic Appendix. The structure is represented as a periodic approximant in Figure 6.4. Tables of atomic positional parameters, ADP harmonic parameters, and selected interatomic distances are given in Appendix C1.*

The modulation can broadly be understood as the freezing-in of a transverse acoustic phonon propagating along c. We know this on the basis of two observa-

*H atoms are not included in this refinement due to difficulties encountered with proper identification of carbon environments within JANA2006. However, I do not anticipate that the addition of H atoms in a future refinement will result in any substantial changes to the results reported here.

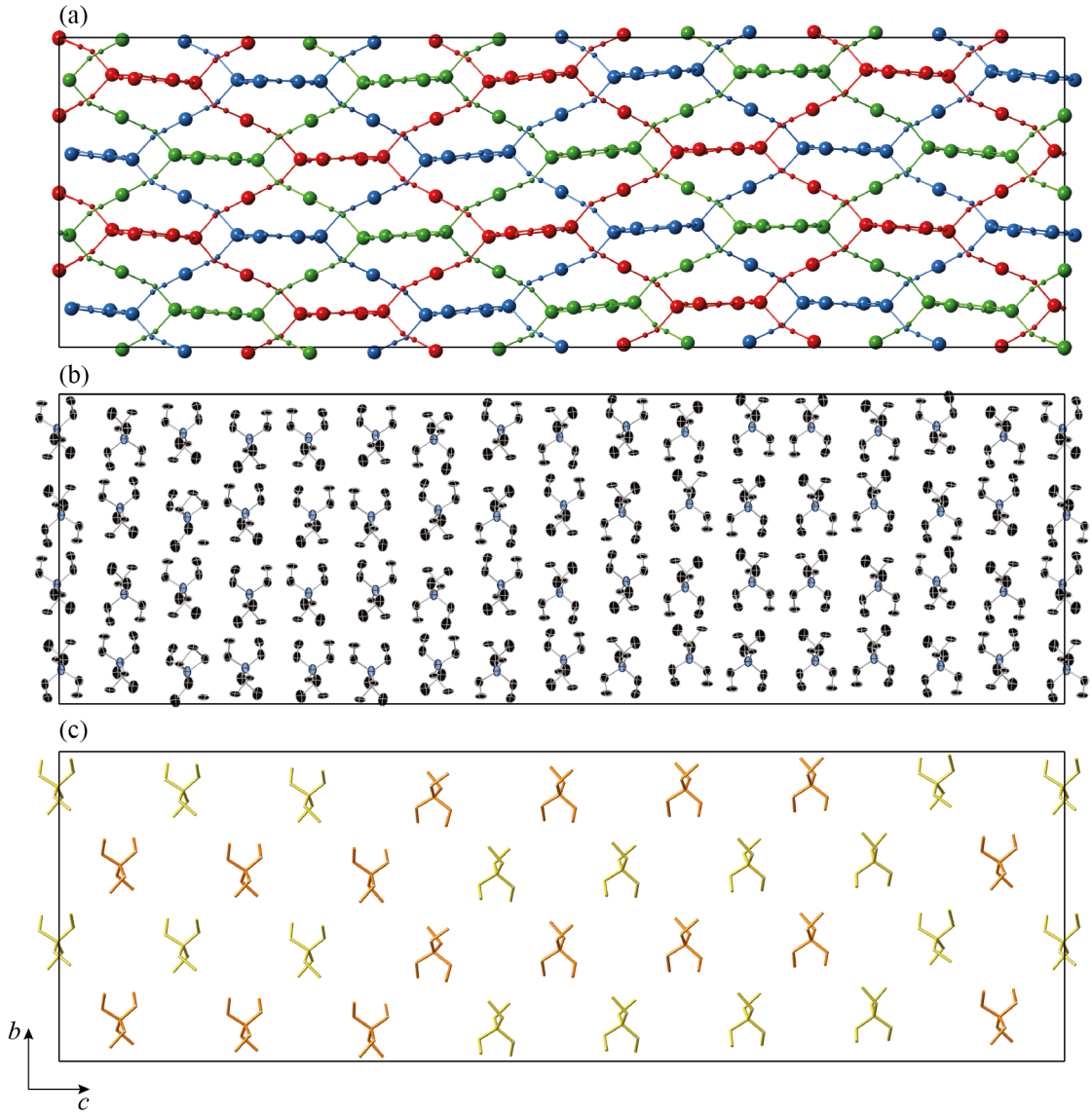

Figure 6.4: 2×2×8 periodic approximant of modulated structure. (a) Three interpenetrating diamondoid frameworks showing the long-wavelength modulation whose major feature is a sinusoidal displacement along *b* that propagates along *c*. (b) The tetraethylammonium cations show the same long sinusoidal displacement but are also conformationally modulated. This is in contrast to the parent phase in which they are conformationally disordered. (c) A layer of extra-framework cations showing the conformational resolution. Yellow and orange coloured molecules are of opposite handedness. There is a conformational flip within each chain of roughly every four molecules. N.B. Periodic approximations of aperiodic structures can be problematic towards their edges (*i.e.* occasional unphysical conformations). Displacement parameters shown at 50% probability.

tions: on the one hand, the displacements are essentially perpendicular to **q**—hence transverse phonon; on the other hand the framework modulation is largely in phase—hence acoustic mode. The largest displacements of all atoms in the structure are along y and have very similar phases and magnitudes [Figures 6.5]. Examination of Fourier maps plotted against the 4th direction reveal more details of the nature of these modulations [Figures 6.6 and 6.7]. The maps look very similar for all framework cations and for N(10), the central atom of the extra-framework cation. The carbon atoms of the extra-framework cation look quite different, with the outer carbon atoms resembling the framework more than the inner ones. The modulation of these atoms was modelled using an occupancy modulation function as well as displacement. These atoms are fully occupied where there is a brown line and unoccupied where there is no line so altogether half occupied averaged along the modulation. This occupancy variation corresponds to conformational flipping of the cation as can be seen in Figure 6.4(c). Understanding the fine details of the modulation is complicated by overlap of density in 2D Fourier maps. The maps of C(16) and C(17) look rather similar because the positions of these outer carbons is actually very similar for either conformational choice as is evident in the parent unmodulated structure [Figure 6.1(b)].

Minor displacements exist for some atoms along x and z [Figure 6.8]. In the framework only three atoms are displaced in these directions: Ag(2), N(5), and C(8) show moderate displacements in y and small displacements in z following a sinusoidal modulation. This set of atoms corresponds to one of the symmetry independent $[Ag(CN)_2]^-$ linkers. This linker forms two of the four connections for each AgN_4 tetrahedron and, therefore, these displacements will cause rotation/distortion of the

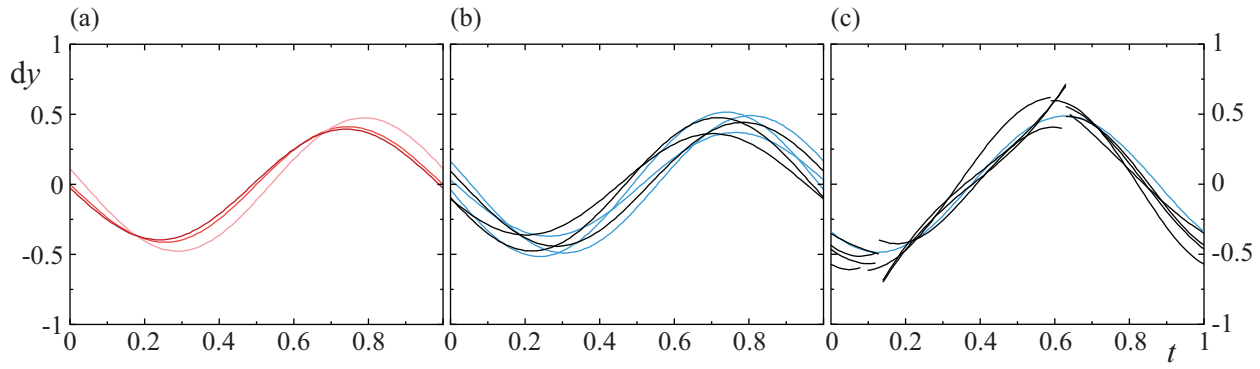

Figure 6.5: Plots of change in y position (dy) against the modulation period. (a) Ag(1), Ag(2), Ag(3) in pink to red; (b) framework C (black) and N (blue); (c) $[NEt_4]^+$ atoms N (blue), C (black).

tetrahedra. All carbon atoms of $[NEt_4]^+$ show some displacements in x and z which is consistent with conformational modulation. Fourier difference maps for x and z are shown in Appendix C1.

Looking closely at the details of Figure 6.5 we see that there is a small phase shift for the extra-framework cation compared to the framework. The similar modulation of framework and cation along with conformational resolution of the cation, which is located in a position with chiral point symmetry (2), suggests that there could be strong conformational-vibrational coupling.

Examining the variation in Ag$\cdots$Ag distances shows the maximum difference is small (0.04 Å) suggesting that we should not expect any drastic difference in optical properties between the modulated and unmodulated phases.

6.3 Discussion

The similar, but not identical, modulation of the framework and extra-framework cation suggests that there is mixing between the lattice modes associated with the framework and the molecular degrees of freedom of $[NEt_4]^+$. The nature and

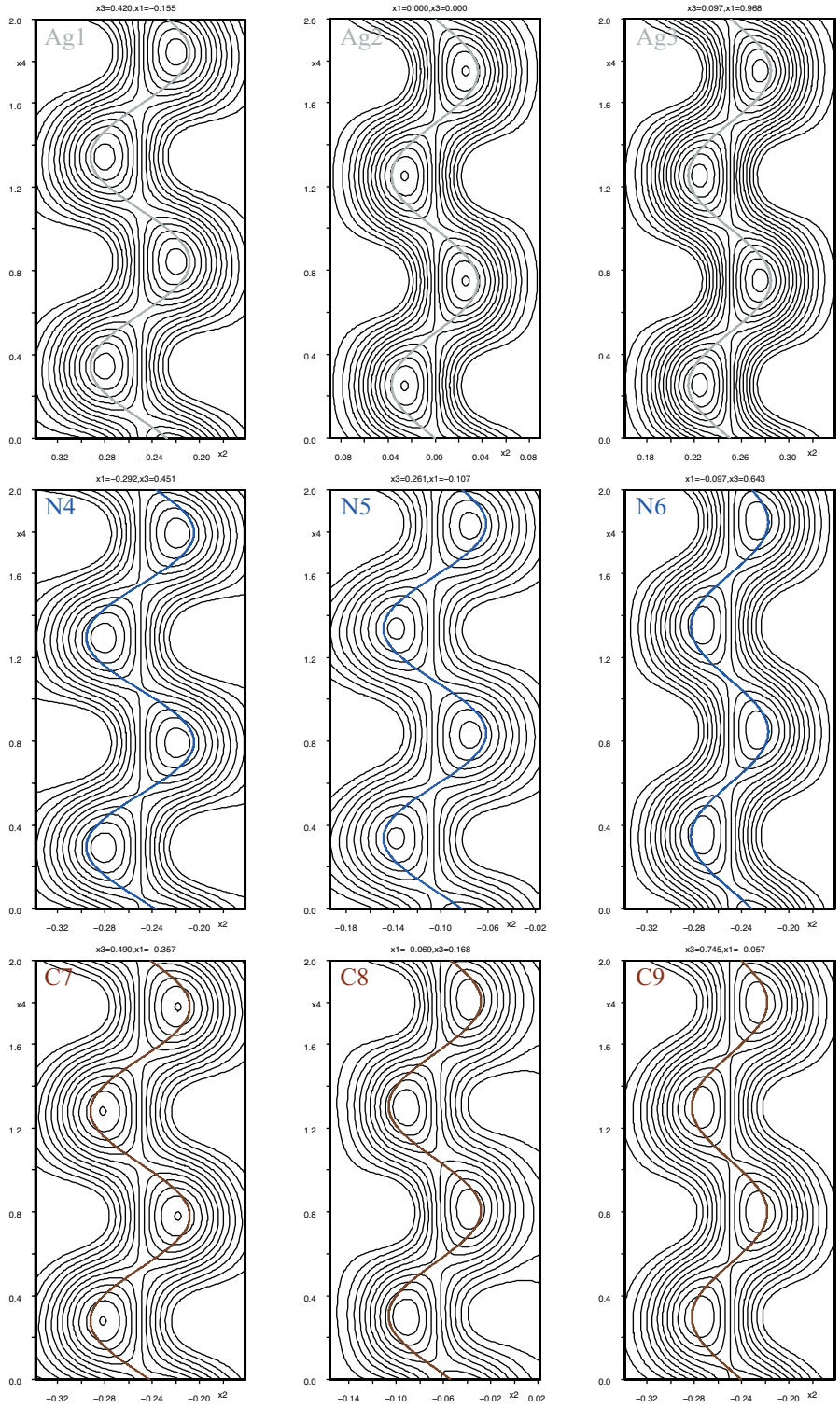

Figure 6.6: Fourier maps for the framework atoms in X2 (b) vs X4 (modulation direction) slices.

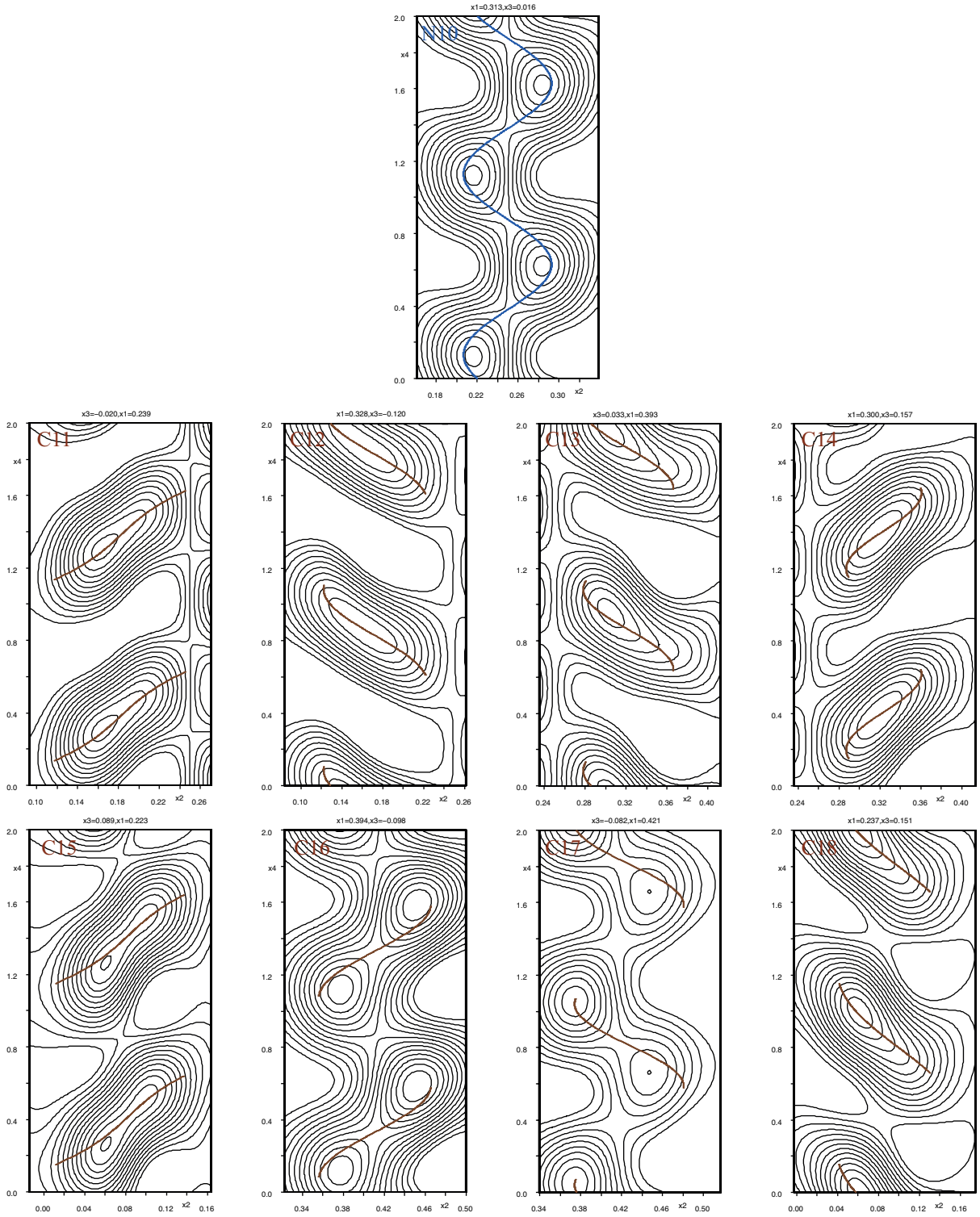

Figure 6.7: Fourier maps for the $[NEt_4]^+$ atoms in X2 (b) vs X4 (modulation direction) slices.

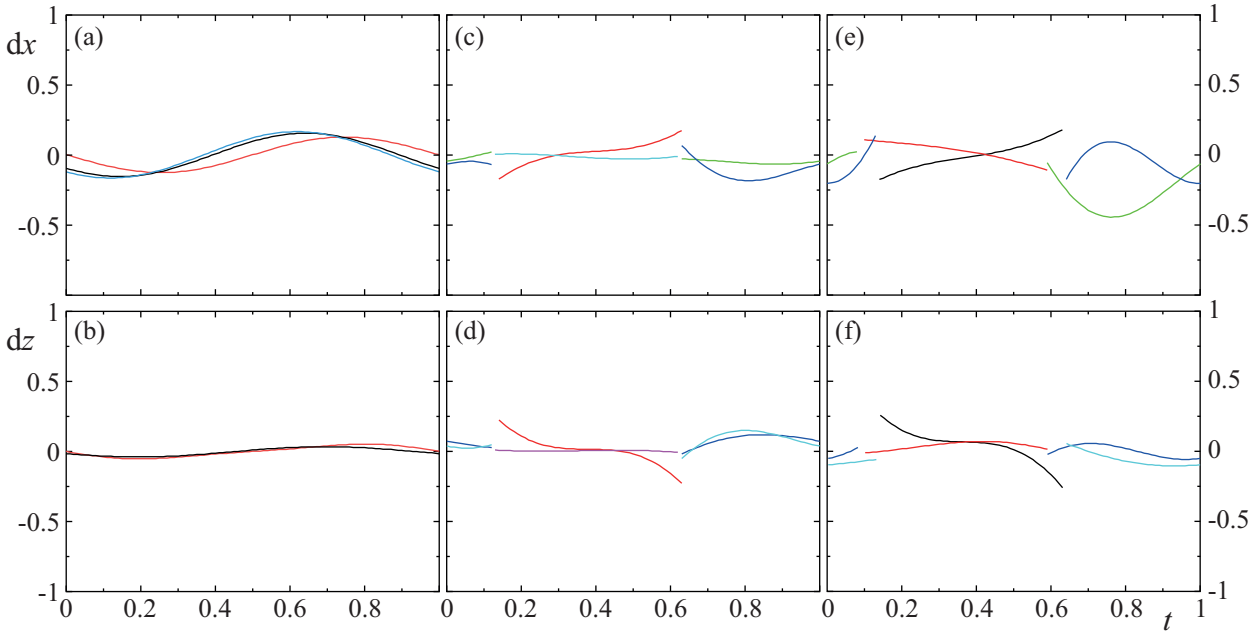

Figure 6.8: Changes in x amd z along the modulation vector. Only atoms that have non-zero displacement in x/z are shown. (a,b) Linker atoms, which are bonded to one another Ag(2) (red), N(5) (blue), C(8) (black) (c,d) carbon atoms directly bonded to nitrogen of $[NEt_4]^+$ C(11) (black), C(12) (red), C(13) (green), C(14) (blue) (e,f) outer carbon atoms of $[NEt_4]^+$ C(15) (red), C(16) (green), C(17) (blue), C(18) (cyan).

underlying symmetry of the modulation show that there is orientational ordering of $[NEt_4]^+$ in this phase. We may anticipate that understanding this coupling will have important implications for the dynamics of the parent unmodulated phase. While the underlying driving force of incommensurability remains unclear, it is possible to propose a mechanism involving two conflicting driving forces. The orientational ordering seen for $[NEt_4]^+$ is likely to favour $\mathbf{q} > 0$, for example $\mathbf{q} = \frac{1}{2}$ would equate to alternating orientations and a doubling of the unit cell along c. In contrast, the lattice flexibility will favour $\mathbf{q} \rightarrow 0$ *i.e.* translations associated with a displacive transition. The mixing between these degrees of freedom would allow for the condensation of the resulting mode at an incommensurate wave-vector. It does, however, remain surprising that $\mathbf{q}$ is so temperature-independent in the range studied.

It is worth noting the significant interest in coupling of lattice and molecular modes in conceptually related families of materials, the alkali metal cyanides, *e.g.* KCN,[291] and the methylammonium lead halide perovskite family, $[N(CH_3)H_3]PbX_3$ X=halogen.[424] The dynamics of both families have been shown to involve preferentially oriented molecular ion flipping[216,427] and significant coupling between the vibrational modes of framework and molecular ion lattices.[292,428] For $[N(CH_3)H_3]PbBr_3$, for example, the melting of orientational order of the methlyammonium has been shown to be coupled to octahedral tilting of the framework using INS,[254] and the cation ordering to have important implications for band structure.[214,429] In the alkali metal halides, the rotovibrational coupling between cyanide orientation and shear lattice modes in the high temperature plastic phase of NaCN and KCN has been the subject of extensive study and leads to unusual thermomechanical behaviour [Section 1.7].[290,292,294–296] As for these two families, valuable additional information could be obtained by experimentally and computationally probing the phonon dispersion curves (with *e.g.* inelastic neutron scattering (INS)) and molecular ion rotational dynamics (with *e.g.* solid-state NMR) of the parent phase. Indeed, such investigations will be necessary to understand how these degrees of freedom couple.

How does this modulation compare to that found in chemically related compounds? The modulation is quite different from $[Cd(NH_3)_3Ni(CN)_4]$ where the modulation is driven by competition between tetrahedral and pseudo-octahedral Cd coordination and can be described using a combination of crenel and sawtooth functions.[255] While no modulated phase has been reported for cristobalite, both quartz

[Section 1.7] and tridymite* have incommensurately modulated phases indicating that incommensurability can arise in similar networks of corner-linker tetrahedra through the coupling of rotation of tetrahedra to soft modes.[289,430]

This remains one of the few characterised examples of an incommensurately modulated phase in coordination polymers.[257]

6.4 Conclusion

The structure of an incommensurately modulated form of $[NEt_4]Ag[Ag(CN)_2]_2$ has been solved and found, to good approximation, to be consistent with the freezing-in of a transverse acoustic phonon at an incommensurate wave-vector. Further examination of the refined structure shows that strong anharmonic coupling between the framework and $[NEt_4]^+$ is present. This coupling appears to involve mixing of the framework vibrational modes and the orientational (conformational) degrees of freedom of the extra-framework cation. The phenomenology of the coupling *via* interacting phonons in the parent structure will likely be of considerable interest and extends the notion of rotovibrational coupling which has been studied intensely in systems such as KCN.

*Tridymite is a form of SiO_2 with the Lonsdaleite network *i.e.* hexagonal analogue of diamond. While the geometry of $[NEt_4]Ag[Ag(CN)_2]_2$ is quite distorted from ideal diamond it is still classified as diamond rather than Londsdaleite using TOPOS.[396]

Chapter 7

Tilts in molecular perovskite analogues

Much of the preceding discussion has focussed on the role of orientational and rotational degrees of freedom of molecular cations. In the previous Chapter, I showed that the coupling between such molecular degrees of freedom with instabilities of the host lattice can lead to unusual structural modulation. Here I focus on the degrees of freedom associated with the dicyanometallate framework itself. In particular I produce here new notation (the 'tilt tensor') for describing the octahedral tilts possible in dicyanometallate, and other molecular, perovskites.

I am grateful to Ms. H. L. B. Boström for assistance in surveying tilts in molecular perovskites and development of the shift tensor.

Octahedral rotations are one of the most important distortions—both for structure and dynamics—in oxide and halide perovskites. Being able to concisely describe the tilts found in perovskites with molecular linkers—*e.g.* formate,[143,169,431] cyanide,[432] azide,[213,433,434] thiocyanate,[435,436] dicyanamide,[437–439] and dicyanometallates—will similarly be of significant utility in understanding the structures, phase transitions, and dynamics of these compounds. In this chapter I develop notation for describing the new tilts accessible with polyatomic linkers and describe some systems in which they have been observed. In doing so I rely heavily on the various notations, in particular Glazer's,[184] that have been used to describe perovskite and perovskite-related

structures.[183]

I begin by recalling the relationship between tilt axis and propagation wave-vector in a typical oxide tilt system [Section 1.5.4].The $a^-a^-c^+$ tilt system, for example of $NaTaO_3$ below 720 K,[176,177] means that rotations propagate at $\langle\frac{1}{2},\frac{1}{2},\frac{1}{2}\rangle$ around a, $\langle\frac{1}{2},\frac{1}{2},\frac{1}{2}\rangle$ around b, and $\langle\frac{1}{2},\frac{1}{2},0\rangle$ around c. This information can be collated into a tensor,

$$\begin{bmatrix} \frac{1}{2} & \frac{1}{2} & \frac{1}{2} \\ \frac{1}{2} & \frac{1}{2} & \frac{1}{2} \\ \frac{1}{2} & \frac{1}{2} & 0 \end{bmatrix}.$$

The corner-connectivity of perovskites with monoatomic linkers (*e.g.* oxides and halides) means that *only* the diagonal terms above are free to assume arbitrary values. In contrast, for systems with molecular linkers the tilts can propagate with arbitrary wave-vector $\mathbf{k} = \langle\xi,\zeta,\eta\rangle$ hence we need nine terms in the 'tilt tensor':

$$\begin{bmatrix} \epsilon_{\xi_a}\exp\left[2\pi\mathrm{i}\cdot\xi_a\right] & \epsilon_{\zeta_a}\exp\left[2\pi\mathrm{i}\cdot\zeta_a\right] & \epsilon_{\eta_a}\exp\left[2\pi\mathrm{i}\cdot\eta_a\right] \\ \epsilon_{\xi_b}\exp\left[2\pi\mathrm{i}\cdot\xi_b\right] & \epsilon_{\zeta_b}\exp\left[2\pi\mathrm{i}\cdot\zeta_b\right] & \epsilon_{\eta_b}\exp\left[2\pi\mathrm{i}\cdot\eta_b\right] \\ \epsilon_{\xi_c}\exp\left[2\pi\mathrm{i}\cdot\xi_c\right] & \epsilon_{\zeta_c}\exp\left[2\pi\mathrm{i}\cdot\zeta_c\right] & \epsilon_{\eta_c}\exp\left[2\pi\mathrm{i}\cdot\eta_c\right] \end{bmatrix}.$$

In this tensor each of the Glazer terms $g_{ij} = \epsilon_{ij}\exp\left[2\pi\mathrm{i}\cdot k_{ij}\right]$ describe the propagation of tilts about axis i along axis j. ϵ_{ij} indicates the magnitude of the rotation and k_{ij} is the ith wave-vector component for the axis-j tilt system (i takes values of ξ, ζ, or η and j values of a, b, and c). The Glazer terms are evaluated to give the tilt tensor.

For the example of $NaTaO_3$ given above, with $a^-a^-c^+$ tilt system, this gives

$$\begin{bmatrix} - & - & - \\ - & - & - \\ - & - & + \end{bmatrix}.$$

The utility of the tilt tensor and the occurrence of unconventional tilts in molecular perovskites will now be illustrated with some examples and comparisons. Octahedral tilting occurs for most families of molecular perovskites. Bent linkers such as formate,[195,440*] and dicyanamide[437–439,441] as well as those, like thiocyanate,[435,436] with a strong preference for non-linear coordination generally show static tilt systems when the linker is ordered. On the other hand, linear linkers such as cyanide may give rise to structures with or without static tilts.[161,442–444]

The existence of unconventional tilts in molecular perovskites is highly dependent on both the nature of the linker and of the framework metal. This fact will be illustrated using the contrasting behaviour of some azide- and cyanide-based compounds.

The azide $[N(CH_3)_4]Mn(N_3)_3$ in $P2_1/m$ has the following tilt tensor,[210,211,445,446]

$$\begin{bmatrix} + & - & + \\ + & + & + \\ + & - & + \end{bmatrix},$$

but above 305 K undergoes a reversible transition to $Pm\bar{3}m$ with no tilts in which

*The tilt systems of formate perovskites are occasionally reported and tend to conform with those expected for oxides since the bent linker tends to enforce conventional in-plane tilting.[143]

both the linker and $[N(CH_3)_4]^+$ are disordered. In the $P2_1/m$ structure the azide hinges about the centre of the linker [Figure 7.1]. This is only possible due to the highly ionic interaction between azide and the d^5 Mn^{2+}.

Of the reported double perovskites $[N(CH_3)_4]BB'X_6$ where X is azide or cyanide, only those with a coordinatively flexible metal on the B-site are known, as in the two above examples. Where B is a transition metal with LFSE then B′ will be an alkali metal such as in $[N(CH_3)_4]_2KFe(N_3)_6$.[434] This compound, which crystallises in $Pa\overline{3}$, has the tilt tensor,

$$\begin{bmatrix} + & + & - \\ - & + & + \\ + & - & + \end{bmatrix},$$

whereas the cyanide analogue, $[N(CH_3)_4]_2KFe(CN)_6$ in $I4/m$,[432] is tilted in a conventional fashion ($a^0a^0c^-$) [Figure 7.2]:

$$\begin{bmatrix} 0 & 0 & 0 \\ 0 & 0 & 0 \\ - & - & - \end{bmatrix}.$$

The conventional tilts of comparatively small magnitude for cyanide are indicative of the higher energy penalty associated with distorting the linear N—C—Fe angle with this high-field ligand. Distortion of the low-spin Fe^{3+} octahedral coordination environment would lead to the loss of significant LFSE. For similar reasons, tilting is only observed for $[N(CH_3)_4]BB'(CN)_6$ where B′ has a flexible coordination environment (*i.e.* LFSE).

In ternary oxide perovskites 15 distinct 'simple' tilt systems are known but some,

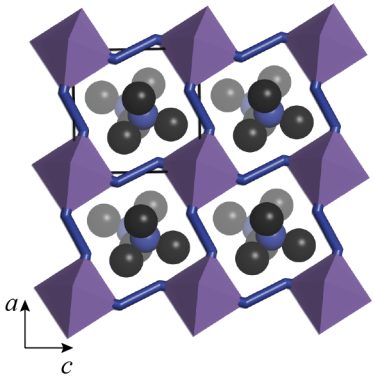

Figure 7.1: View along b axis of $[N(CH_3)_4]Mn(N_3)_3$. The tilts around b are correlated 'in-phase' in the ac plane as well as along b. Hinging at the centre of the azide linker is possible due to the highly ionic bonding with d^5 Mn^{2+}. Mn in purple and unit cell shown in black.

such as $a^-a^-c^+$ in $Pbnm$, are far more commonly found than others, such as $a^0b^-c^+$ in $Cmcm$.[185,447] Similarly, I note that simply because a tilt system is possible in a molecular perovskite this does not tell us how frequently, if at all, it will occur. Here I have given three examples of unconventional tilt systems and begun to identify the kinds of systems in which they can occur.

I move now to assess the limitations of the tilt tensor notation. I begin by

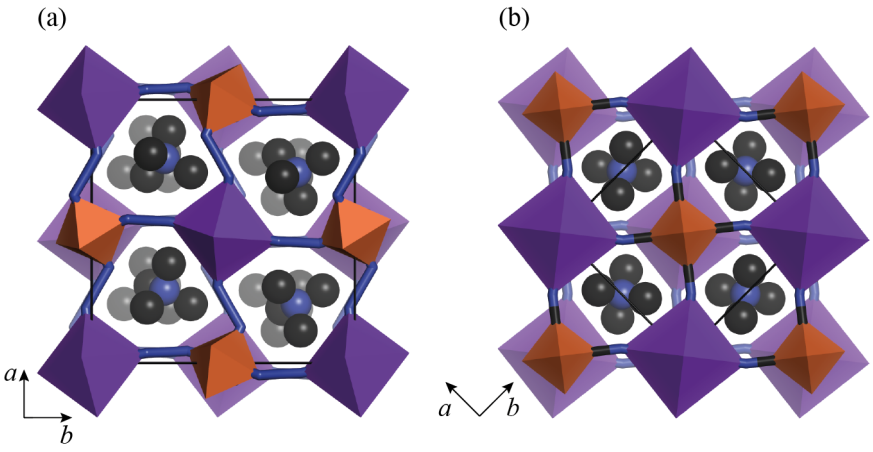

Figure 7.2: Views along c axis, (a) Unconventional tilts in $[N(CH_3)_4]_2KFe(N_3)_6$ (b) Conventional tilts in $[N(CH_3)_4]_2KFe(CN)_6$. For both parts, K in purple, Fe in orange, and unit cell shown in black.

returning to oxides and halides with unusual tilt systems then return to molecular perovskites. Whilst the vast majority of rotations in oxides/halides can be described using Glazer's notation [Section 1.5] there are two important classes of exceptions: (i) those that can be described by one wave-vector where $\mathbf{k} = \langle \xi, \frac{1}{2}, \frac{1}{2} \rangle$ but $\mathbf{k} \neq 0, \frac{1}{2}$—*e.g.* (P)-$NaNbO_3$[187]—and (ii) where the observed tilts are the result of the superposition of two or more wave-vectors (which both conform to $\mathbf{k} = \langle \xi, \frac{1}{2}, \frac{1}{2} \rangle$) resulting in *compound tilts**—*e.g.* a proposed structure of $KMnF_3$.[192] Both of these classes remain important for molecular perovskite analogues—perovskite structured materials where one or more component of ABX_3 is a molecular ion—but the tilt periodicity for molecular X is generally less restricted.

Oxides with a non- $0/\frac{1}{2}$ propagation component such as (P)-$NaNbO_3$ can be accommodated within the tilt tensor rather than using a compound tilt sequence (See Section 1.5.4):

$$\begin{bmatrix} - & - & - \\ - & \mathrm{i} & - \\ - & - & - \end{bmatrix}.$$

However, it is worth noting that above periodicities of $\frac{1}{2}$ the tilt tensor is ambiguous with respect to the exact active tilt system. The notation developed by Peel *et al.* has been used to resolve these ambiguities [Section 1.5.4] for tilt propagation along the axis of rotation and could be used in combination with the tilt tensor.[191] Furthermore, a single tensor alone cannot be used to describe tilt systems with more

*Strictly, compound tilts should arise from the action of two irreps with conflicting symmetries *i.e.* not those arising as secondary, symmetry compatible tilt components.[185,448] However, whether arising from compound tilts or symmetry-allowed secondary tilts these structural distortions, it is important to be able to describe these distortions fully.

than one propagation vector active along a given axis, as is found in the $P4/mbm$ structure of $KMnF_3$ proposed by Hidaka *et al.*[192*] In this relatively simple case, tilts only exist along the c axis but are, in Peel's notation, of the form 'A0' or 'C0' [Figure 7.3(a)].[†] This can be thought of as the result of combining $-$ and $+$ tilts of the same magnitude along c so that on alternate octahedra they cancel out or reinforce each other. Using the tilt tensor notation this could be described as the sum of two tensors,

$$\begin{bmatrix} 0 & 0 & 0 \\ 0 & 0 & 0 \\ - & - & - \end{bmatrix} + \begin{bmatrix} 0 & 0 & 0 \\ 0 & 0 & 0 \\ - & - & + \end{bmatrix},$$

though clearly this approach would rapidly become cumbersome with an increasing number of wave-vectors.

I note here that the tilt tensor could be formulated slightly differently to give information on which tilts are required to be of the same magnitude by symmetry (*e.g.* $a^-a^-a^-$ vs. $a^-a^-c^-$) as is contained in Glazer. This could be done by explicitly showing the ϵ_{ij} terms (*e.g.* '-1' and '-0.8' instead of $-$) or by including letters, which for $a^-a^-c^+$ would look like:

$$\begin{bmatrix} -a & -a & -a \\ -a & -a & -a \\ -c & -c & +c \end{bmatrix}.$$

*While this structure appears to have been incorrectly assigned, and more recent diffraction and Raman work suggest the true spacegroup to be $Cmcm$,[449,450] this structural model is a useful example for illustrating the tilt tensor.

[†]To retain corner connectivity the columns must alternate in their sense of rotation. In the language of mechanics, the compatibility criterion is thus satisfied.

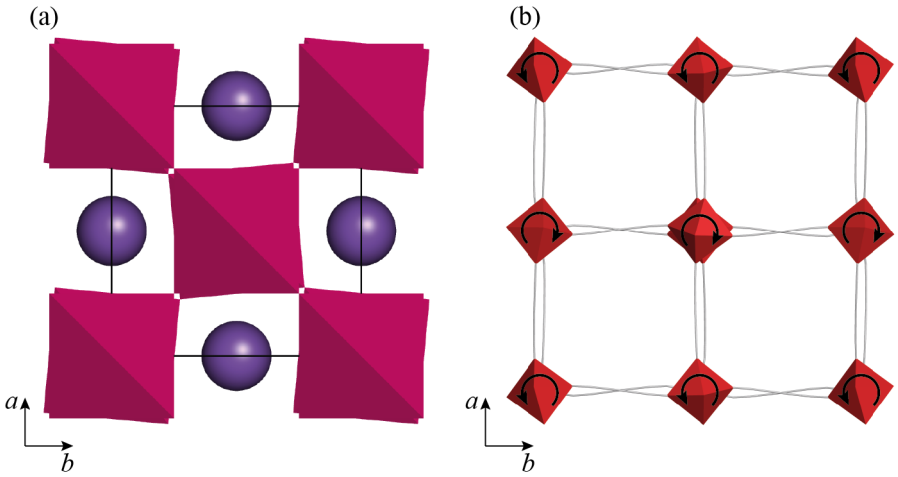

Figure 7.3: (a) Compound tilt system in $KMnF_3$. The tilts along c are of the form 'A0' or 'C0' as they are the result of combining − and + tilt systems of the same magnitude. (b) One layer of octahedra of [PPN]Cd[Ag(CN)$_2$]$_3$·3EtOH·nH$_2$O (**4**). Sense of rotation along c is indicated with arrows. The octahedra all rotate around c in the same sense along b but alternate along a. Behind the central octahedron is shown the next octahedron along c, which is out of phase with the first.

I now return to consider the presence of unconventional tilts in dicyanometallates. The superperovskite [PPN]Cd[Ag(CN)$_2$]$_3$·3EtOH·nH$_2$O (**4**), reported in Chapter 3, shows in-phase tilting of adjacent octahedra correlated perpendicular to the rotation axis—*i.e.* unconventional tilts [Figure 7.3(b)]. The primary tilt system of **4** is described by the following tilt tensor:

$$\begin{bmatrix} - & - & + \\ + & - & - \\ - & + & - \end{bmatrix}.$$

Since there are two Cd in the asymmetric unit of this compound the tilts at these two sites will necessarily be different. The remaining tilts of small magnitude can

be described with a supplementary tilt tensor,

$$\begin{bmatrix} + & 0 & - \\ - & + & 0 \\ 0 & - & + \end{bmatrix}.$$

These tensors have been assigned visually by assessment of the crystal structure. Through symmetry analysis it is possible to determine how significant the octahedral tilts are in determining the structure formed. Do the tilts or the extra-framework cation drive the structure? The first approach is to assess the symmetry impact of the $[PPN]^+$ alignment and displacement along {111}-type directions which are discussed in Section 3.2.1. This is achieved by taking just the N and P positions in $[PPN]^+$ (these lie along the threefold axis) from the crystal structure and assessing their symmetry with FINDSYM.[451,452] This shows that the pattern of $[PPN]^+$ displacements alone, which involve a displacement of ∼1 Å from the centre of the cavity, gives $Pa\overline{3}$ symmetry. This demonstrates that the tilt modes cannot be the only primary 'order parameter' for the imagined transition from the perovskite aristotype. Input and output can be found in the Electronic Appendix.

The second, related, approach is to focus instead on assessing the pattern of tilts using other parts of the ISOTROPY suite, for which I am grateful to Prof. C. J. Howard.[414,451] The general approach is to assess the structure of **4** in relation to the archetypal $Pm\overline{3}m$ structure with the B site at the origin. Assessing the 'transition' of $Pm\overline{3}m$ to $Pa\overline{3}$ with a $2 \times 2 \times 2$ cell with COPL gives a list of possible order parameters for a phase transition.[453,454] There is only one irreducible representation (irrep) that reduces the symmetry to $Pa\overline{3}$. However, assessment of the tilt pattern

formed by this X_5^+ irrep indicates that it does not reproduce the observed tilt pattern (it is, however, closely related and propagates with wave-vectors $\langle 0, 0, \frac{1}{2}\rangle$, $\langle 0, \frac{1}{2}, 0\rangle$, and $\langle \frac{1}{2}, 0, 0\rangle$).

The next lowest symmetry given by this analysis is $Ia\overline{3}$ arising from the M_5^+ irrep. This irrep produces the primary (large magnitude) tilts observed but clearly does not account for the observed symmetry. Now we can use COPL again to assess possible active irreps for a transition from the $2 \times 2 \times 2$ $Ia\overline{3}$ to $Pa\overline{3}$. The only possible order parameter to go down to $Pa\overline{3}$ is H_1^+. This irrep should be equivalent to adding the X_5^+ irrep to the smaller cell along with M_5^+. Indeed, looking at the distortions arising from these irreps in ISODISTORT we can see that the X_5^+ gives the (111) displacements of an A-site atom that is required to reproduce the pattern of $[PPN]^+$ displacements. In addition, it seems that X_5^+ may give rise to the secondary, supplementary tilts described above. Taken together this implies a picture of symmetry lowering which is driven by the cation ordering from the X_5^+ irrep which then allows the M_5^+ to be active giving the main tilt components. This example suggests that molecular extra-framework cation-induced symmetry lowering may play a role in allowing complex tilt systems to arise, which should perhaps not be surprising given the crucial role of cation–cavity size mismatch in driving tilt instabilities in oxide perovskites.

7.1 Further complications

While the tilt tensor can usefully be applied to a number of known molecular perovskite systems there are two significant complicating factors. Firstly, compound tilts seem to be common in molecular perovskites. Given the limited sense in which

tilt systems in molecular perovskites are currently discussed, it is hoped that the tilt tensor will still find use in such cases where it is only approximate. A full understanding of compound tilt systems will, in each case, require a mode decomposition to be performed since a larger mode amplitude does not necessarily imply that it is the mode responsible for symmetry breaking.[414,451]

The second common complicating factor is the presence of shifts—that is to say *displacements* of columns or layers of octahedra. An illustrative example is $[N(CH_3)_4]Ca(N_3)_3$ [Figure 7.4] in which columns of octahedra, along with their linkers, are displaced along the c-axis in a checkerboard pattern.[455] While relatively simple to describe in this instance, those found for all members of the families $[N(CH_3)_xH_{4-x}]B[N_3]_3$ where $1 \leq x \leq 3$ and B is Mn or Cd are more difficult to describe but do decrease in magnitude with increasing x.[144,213,446] A shift tensor can be described by analogy with the tilt tensor,

$$\begin{bmatrix} \epsilon_{\xi_a} \exp\left[2\pi \mathrm{i} \cdot \xi_a\right] & \epsilon_{\zeta_a} \exp\left[2\pi \mathrm{i} \cdot \zeta_a\right] & \epsilon_{\eta_a} \exp\left[2\pi \mathrm{i} \cdot \eta_a\right] \\ \epsilon_{\xi_b} \exp\left[2\pi \mathrm{i} \cdot \xi_b\right] & \epsilon_{\zeta_b} \exp\left[2\pi \mathrm{i} \cdot \zeta_b\right] & \epsilon_{\eta_b} \exp\left[2\pi \mathrm{i} \cdot \eta_b\right] \\ \epsilon_{\xi_c} \exp\left[2\pi \mathrm{i} \cdot \xi_c\right] & \epsilon_{\zeta_c} \exp\left[2\pi \mathrm{i} \cdot \zeta_c\right] & \epsilon_{\eta_c} \exp\left[2\pi \mathrm{i} \cdot \eta_c\right] \end{bmatrix},$$

but in this case the diagonal terms will always be 0 if the shift is inactive in that direction or + if it is active. Each off diagonal term corresponds to the correlation between columnar displacements in the a, b, or c directions in the two perpendicular

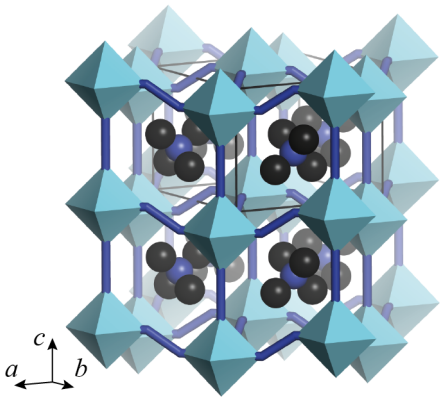

Figure 7.4: Columnar shifts along c in $[N(CH_3)_4]Ca(N_3)_3$. The shifts have a checkerboard ordering. Ca shown in blue, unit cell in black.

directions. So, for example the shifts in $[N(CH_3)_4]Ca(N_3)_3$ would be described as

$$\begin{bmatrix} 0 & 0 & 0 \\ 0 & 0 & 0 \\ - & - & + \end{bmatrix}.$$

While not developed further here, understanding the coupling between these shifts, octahedral tilting, and ordering/displacement of A-cations will be essential for understanding the structure and dynamics of these compounds. Shear modes in MOF-5, for example, make a significant contribution to the negative thermal expansion observed for this WO_3 analogue.[456,457]

7.2 Conclusion

In this chapter I have developed notation for describing tilt systems where the restriction for $\mathbf{k} = \langle \xi, \frac{1}{2}, \frac{1}{2} \rangle$ found in oxide and halide perovskites is lifted. While a single 'tilt tensor' cannot be used to fully describe the periodicity of the octahedral rotations in a large proportion of molecular perovskites, I hope that it will prove

useful in classifying the unusual tilt systems that are important in these systems. The tilt degrees of freedom in molecular perovskites usually operate at a significantly reduced energy scale compared to those in oxides. This means that coupling between tilts and other degrees of freedom—whether derived from molecular components or the perovskite architecture—is crucial for determining the structure and properties of these compounds.

Chapter 8

Hydration-controlled unconventional tilts in the double perovskite $(NH_4)_2SrFe(CN)_6$

The work in this Chapter was carried out in close collaboration with Dr. S. G. Duyker (Sydney) while he was a visitor in Oxford. While not a dicyanometallate, our discovery of an unconventional tilt system in hydrated $(NH_4)_2SrFe(CN)_6{\cdot}2H_2O$ provided an important example of the unusual tilts that are possible for molecular perovskite analogues as discussed in Chapter 7. In this Chapter, a new polymorph of $(NH_4)_2SrFe(CN)_6{\cdot}2H_2O$ with an unconventional tilt system is reported. On removal of water, in single crystals and powders, a transition to a conventional tilt system is observed. The transition is shown to be reversible in powders with the original polymorph being formed. This shows that the coupling of tilt degrees of freedom at periodicities forbidden for oxides, *i.e.* other than $\langle \frac{1}{2}, \frac{1}{2}, \xi \rangle$, can be chemically activated. The distortion induced by hydration is decomposed into its underlying symmetry modes.

8.1 Results

The structures of $(NH_4)_2SrFe(CN)_6{\cdot}2H_2O$ and $(NH_4)_2SrFe(CN)_6$ were determined from single crystal diffraction. Representations of their structures are shown in

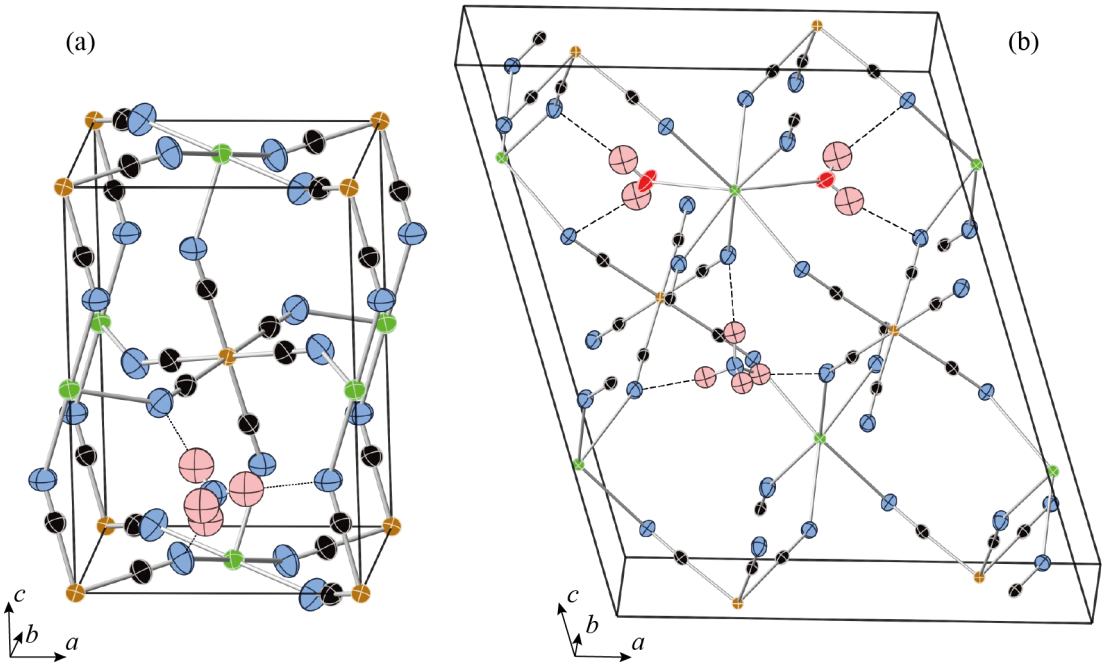

Figure 8.1: Crystal structures of (a) $(NH_4)_2SrFe(CN)_6$ and (b) $(NH_4)_2SrFe(CN)_6{\cdot}2H_2O$. Unit cell contents shown except only one ammonium and two waters are shown for clarity. Hydrogen bonding indicated by dotted lines. Thermal ellipsoids are shown at the 50 % level. Sr in green, Fe in brown, C in black, N in blue, O in red, and H in pink.

Figure 8.1 and crystallographic details summarised in Table 8.1. Both structures are made up of $Fe(CN)_6$ octahedra connected into a perovskite type network through bonding to Sr^{2+}. In both cases, three short $NH_4\cdots NC$ distances per $[NH_4]^+$ are indicative of hydrogen bonding to the framework cyanides. The hydrogen atoms were located in a Fourier difference map. The anhydrous material was formed by in-situ single-crystal dehydration at 300 K under flowing dry nitrogen, indicating that the water is quite weakly bound in the dihydrate. The water in the dihydrate modifies the structure by binding to Sr^{2+} and lies in two of the perovskite cube faces. Additionally, the hydrogen atoms, which were located in a Fourier difference map, also lie in this plane. The $O\cdots NC$ distances suggest that the water molecules also form hydrogen bonds to the framework.

Table 8.1: Crystallographic details of $(NH_4)_2SrFe(CN)_6$ and $(NH_4)_2SrFe(CN)_6{\cdot}2H_2O$. Corresponding .cif and .fcf files can be found in the Electronic Appendix.

Compound	$(NH_4)_2SrFe(CN)_6$	$(NH_4)_2SrFe(CN)_6{\cdot}2H_2O$
Empirical formula	$C_6H_8Fe_1N_8Sr_1$	$C_6H_{12}\ Fe_1N_8O_2Sr_1$
Formula weight (g mol^{-1})	335.65	371.68
Crystal System	Monoclinic	Monoclinic
Space Group	$P2_1/n$ (No. 14)	$C2/c$ (No. 15)
Z	2	4
Radiation (Å)	Cu K$_\alpha$, $\lambda = 1.54180$	Cu K$_\alpha$, $\lambda = 1.54180$
Crystal colour	Colourless	Colourless
Crystal size (mm)	0.05×0.08×0.09	0.05×0.06×0.09
Temperature (K)	300.0(1)	150.0(1)
a (Å)	7.4087(4)	12.2629(6)
b (Å)	7.5926(4)	7.4837(3)
c (Å)	10.7605(6)	15.1106(7)
β (°)	90.336(5)	106.601(5)
V (Å^3)	605.28(6)	1328.93(11)
μ (mm^{-1})	15.341	14.139
Reflections ($I > 2\sigma(I)$)	6734	1274
R (F_o)	0.0374	0.0207
R_w (F_o)	0.0989	0.0576
GOF	1.0151	1.0021

8.2 Discussion

The anhydrous material, which is made by dehydration of the dihydrate, is a cyanide analogue of a double perovskite which may also be called a cyanoelpasolite.[458] The $P2_1/n$ structure adopted can be accounted for purely by the $a^-a^-c^+$ tilt system and does not require ordering of ammonium [See Electronic Appendix for symmetry decomposition]. This is one of the most common structures among ordered oxide and cyanide double perovskites[459] such as Sr_2NdBiO_6 and $Cs_2LiCr(CN)_6$.[460,461]

The dihydrate crystallises in $C2/c$ as a result of the ordered hydration pattern of the now 8-coordinate Sr^{2+} with point symmetry C_2. The relationship between the dihydrate and anhydrate is shown in Figure 8.2. While the Sr is no longer octahedral, the geometry and retained topology of the structure allows for us to consider the hydrated structure just as we would an ordinary perovskite. Examination of the

rotation of the FeC_6 octahedra reveals that the rotations propagate at a periodicity of $\mathbf{k} = \langle \frac{1}{4}, \frac{1}{4}, \frac{1}{4} \rangle$. The periodicity is illustrated in 1D in Figure 8.2(b-c). The simplified tilt tensor is:

$$\begin{bmatrix} \mathrm{i} & \mathrm{i} & \mathrm{i} \\ \mathrm{i} & \mathrm{i} & \mathrm{i} \\ \mathrm{i}c & \mathrm{i}c & \mathrm{i}c \end{bmatrix}.$$

where c indicates a different magnitude of tilt. There are, in fact, combined tilts along all three axes.

Symmetry analysis using ISODISTORT,[414] part of the ISOTROPY software suite,[451] allows for a better understanding of this structural distortion. It is convenient to consider the hydration pattern of $(NH_4)_2SrFe(CN)_6{\cdot}2H_2O$ as a correlated distortion of the B-site coordination environment. This distortion is described by the Λ_3 irrep at $\mathbf{k} = \langle \frac{1}{4}, \frac{1}{4}, \frac{1}{4} \rangle$ and, importantly, accounts entirely for the observed space group symmetry [Figure 8.3(a)]. This same analysis accounts for the coupling between hydration-induced distortions and octahedral tilts. There are two different tilt systems of the correct symmetry to couple to the Λ_3 hydration pattern. The first corresponds to tilts around axes parallel and antiparallel to [100] of the monoclinic cell and is also associated with the Λ_3 irrep; the other involves an inclination of the tilt axis towards [103] and is associated with the Λ_2 irrep. Both of these tilt systems couple at $\mathbf{k} = \langle \frac{1}{4}, \frac{1}{4}, \frac{1}{4} \rangle$. It is this Λ_2 that gives the largest amplitude of tilt.* †

*Λ_3 is the only single order parameter that can act as primary order parameter and is a factual description of both symmetry-breaking hydration and tilt mechanisms. Coupling to Λ_2 and a variety of Γ and R irreps is fully allowed by symmetry.

†The mode decomposition also showed that while the $[NH_4]^+$ ordering has the same periodicity it is not required to generate the $C2/c$ space group observed.

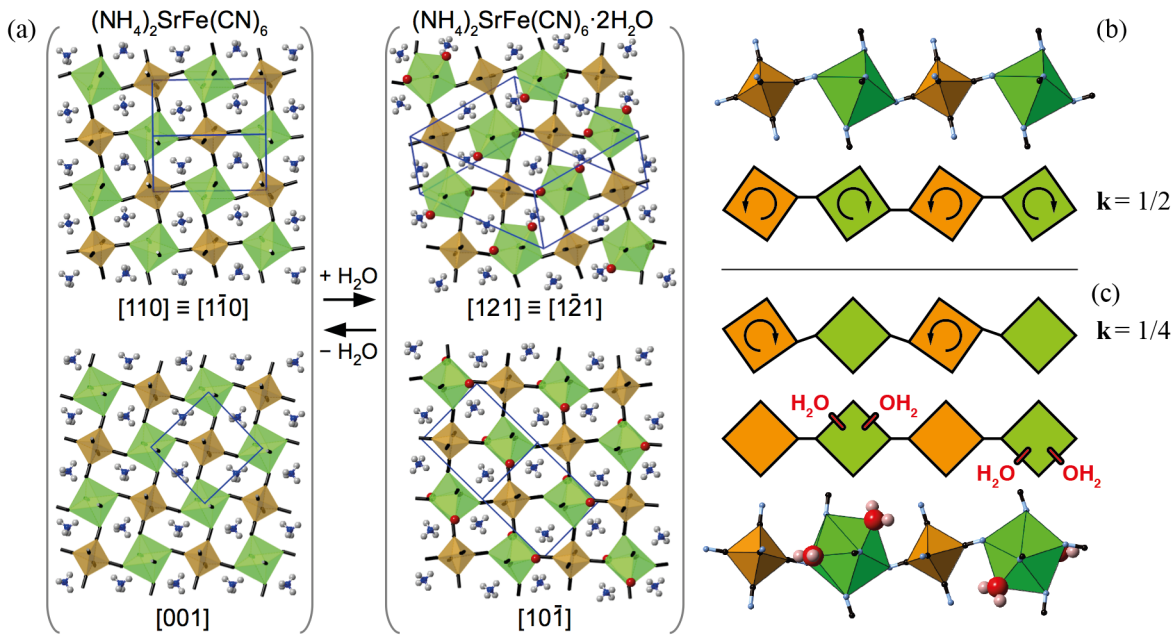

Figure 8.2: (a) Single layers of the $(NH_4)_2SrFe(CN)_6$ and $(NH_4)_2SrFe(CN)_6{\cdot}2H_2O$ crystal structures, viewed along the two unique pseudo-cubic perovskite axes of each structure (directions given in terms of the observed unit cells). For the anhydrous compound the in-plane tilts are conventional—the tilt of each Fe octahedron is the same as that preceding it (b). In the dihydrate, the rotation of Fe octahedra alternates from one to the next along pseudocubic axes, just as the disposition of the waters coordinated to Sr does (c). Sr in green, Fe in brown. The view directions in terms of the monoclinic unit cells are shown underneath each image.

The pattern of hydration does not result in a net polarisation but gives polar chains running along the b axis [Figure 8.3(b)]. Indeed, the asymmetric distortion induced by hydration is analogous to a second-order Jahn-Teller distortion (SOJT) with the distinction here being the chemical origin of the distortion and the ability to switch it on and off. This SOJT-like distortion is applicable to a much wider range of ions since it is not dependent on particular electronic configurations (*i.e.* d^0 such as Ti^{4+} or s^2d^10 ions such as Pb^{2+}). The reversibility of this transition was demonstrated in powders [Figure 8.4] and, importantly, shows that the unconventional tilts can be switched on and off.

Interestingly, the related compound $(NH_4)_2BaFe(CN)_6{\cdot}3H_2O$ shows remarkable

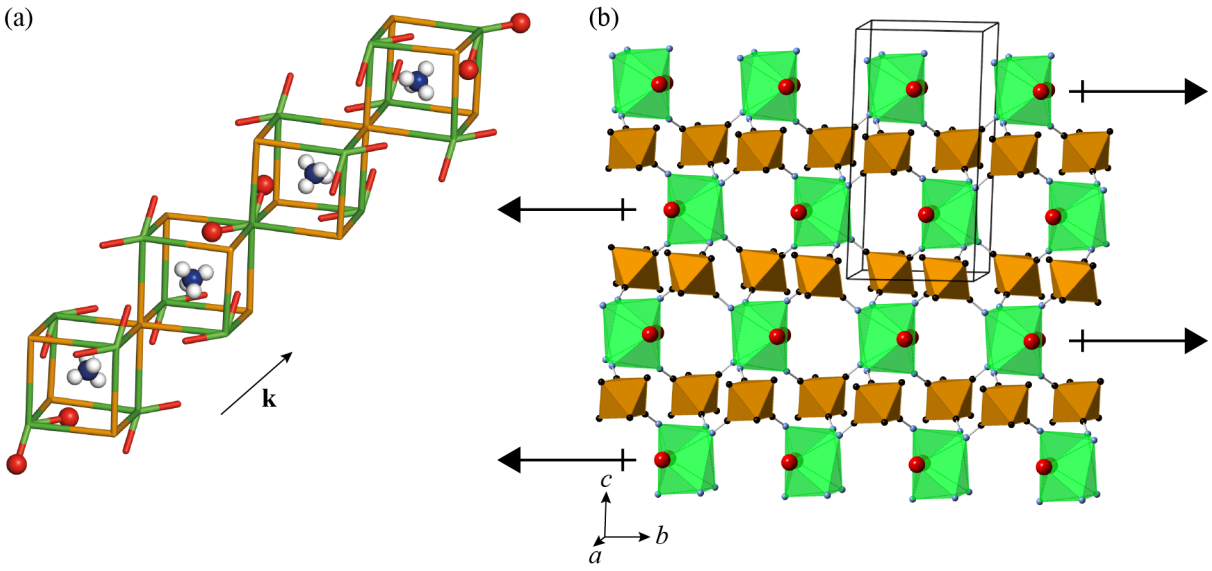

Figure 8.3: (a) Representation of the hydration pattern of $(NH_4)_2SrFe(CN)_6{\cdot}2H_2O$. The hydration pattern orders along the pseudo-cubic [111] direction repeating every other Sr centre *i.e.* $\mathbf{k} = \langle\frac{1}{4},\frac{1}{4},\frac{1}{4}\rangle$. This is highlighted by the oxygen atoms shown as spheres. (b) While there is no overall polarisation in $(NH_4)_2SrFe(CN)_6{\cdot}2H_2O$, the hydration results in polar chains along the b axis. Sr in green, Fe in brown, O in red, N in blue, H in white. H on water not shown for clarity.

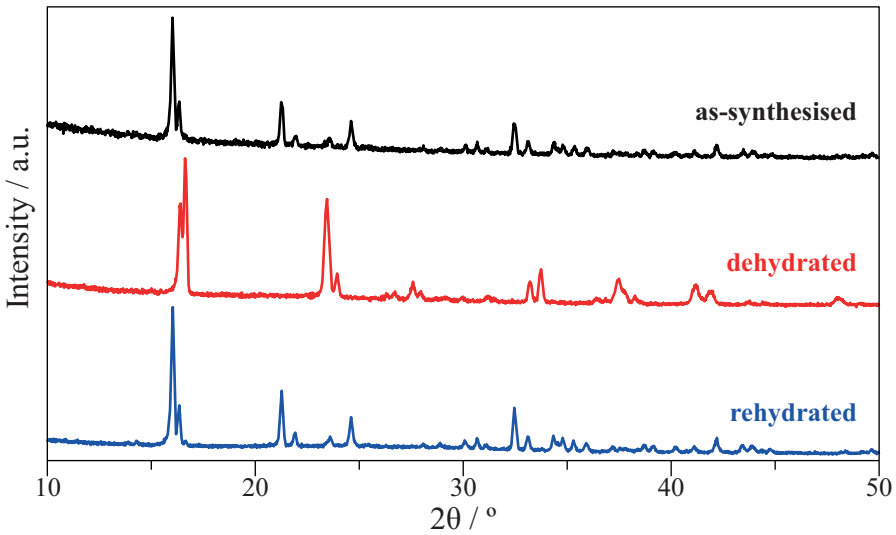

Figure 8.4: Powder diffraction patterns ($\lambda = 1.54056\,\text{Å}$) of the as-synthesised (black), dehydrated (red), and rehydrated (blue) material. The dehydration is fully reversible.

structural similarities to the hydrate discussed here [Figure 8.5].[462] The larger alkaline-earth Ba instead of Sr allows for the binding of a third molecule of water. Crystallising in $R\bar{3}c$, its tilt system can be described by the same primary tilt tensor as noted above. Group theoretical analysis shows that this tilt system arises from exactly the Λ_2 irrep at $\mathbf{k} = \langle\frac{1}{4},\frac{1}{4},\frac{1}{4}\rangle$ discussed above. As the Λ_3 irrep is inconsistent with a Λ_2 primary order parameter, in this case the Λ_3 tilt system is not activated by hydration. The tilt system, in this case, results from a different but qualitatively similar hydration pattern that gives Ba^{2+} in an irregular tricapped trigonal prism with D_3 site symmetry. In consequence, there is no local polarisation at the Ba site but, nevertheless, the Ba coordination is axially distorted in a conceptually similar fashion to a first-order Jahn-Teller distortion. The similarity of this hydration pattern can be seen by the location of the water molecules in the pseudo-cubic faces and their hydrogen bonding the the nitrogen binding the next Ba^{2+} along this [110] direction. TGA has been reported for this compound and shows that the first step is loss of water.[462] As such, it would be worth investigating whether a similar structural transition occurs for $(NH_4)_2BaFe(CN)_6{\cdot}3H_2O$.

The dihydrate $(NH_4)_2SrFe(CN)_6{\cdot}2H_2O$ reported here is distinct from the orthorhombic polymorph reported by Medina Córdoba *et al.*.[463] Due to different patterns of both water coordination to the strontium (site symmetry C_s) and of hydrogen bonding this has a structure more akin to $KLuFe(CN)_6{\cdot}3.5H_2O$.[464] While only one hydrogen atom per water could be located reliably in the orthorhombic polymorph, there is a short NH$\cdots$O hydrogen bonding contact between ammonium and water (N—O <3 Å) in the orthorhombic polymorph which is absent from the monoclinic one reported here. While the TGA reported in Reference 463 suggests

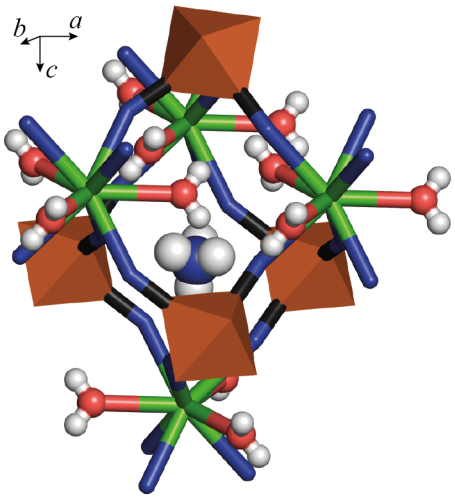

Figure 8.5: The water in $(NH_4)_2BaFe(CN)_6{\cdot}3H_2O$ is bound to Ba and located in a similar place to those in $(NH_4)_2SrFe(CN)_6{\cdot}2H_2O$. They occupy three of the faces of each perovskite cube (top half) rather than two in the Sr analogue [Figure 8.1] giving distortions transforming as the Λ_2 irrep rather than Λ_3. Nine-coordinate Ba here has D_3 symmetry and therefore no polarity.

that dehydration would be possible, it remains an open question whether the dehydrated product is the same and whether it would return to the same hydrated polymorph on rehydration. The orthorhombic polymorph was formed using a different set of reagents ($Na_4Fe(CN)_6$+$SrCl_2$+NH_4Cl). Of the analogous compounds known $(NH_4)_2BaCo(CN)_6{\cdot}4H_2O$, which crystallises in $P6/m$, has a somewhat similar structure to the orthorhombic polymorph. The Ba^{2+} sits in a regular tricapped trigonal prism and one water of crystallisation is apparently included in the structure, disordered across the same site as $[NH_4]^+$.[465]

8.3 Concluding remarks

The study of $(NH_4)_2SrFe(CN)_6{\cdot}2H_2O$ and $(NH_4)_2SrFe(CN)_6$ has shown that unconventional tilts can be switched on and off through binding of guest molecules in molecular perovskite analogues. The symmetry-reducing role of hydration has been understood in detail through mode decomposition and represents a degree of

symmetry control across a much broader set of **k**-points than is encountered in non-molecular perovskites. The hydrogen bonding network formed by the guest water appears to be important for the formation of the monoclinic structure reported here rather than the orthorhombic polymorph previously reported.[463] The role of hydrogen bonding could be further explored by, for example, the use of other small ammonium cations like $[NH_3(CH_3)]^+$ to induce different ordering patterns. Further exploration[462,465] of the role of the size of the alkaline earth cation may lead to the discovery of other interesting structural distortions. Excitingly, this work points towards the possibility of using guest molecules in perovskites to induce second-order Jahn-Teller distortions that, in oxides, would ordinarily only be possible with particular electronic configurations. Furthermore, the hydration induced tilts might be combined with other distortions to drive polarisation in a similar way to the inducement of polarisation in hybrid improper ferroelectrics by the action of multiple octahedral tilt modes in *e.g.* $Ca_3Ti_2O_7$.[174,466,467]

Chapter 9

Conclusion

The structural chemistry of transition metal dicyanometallates encompasses familiar structures as well as unique structure types. Here, whilst significantly extending the number of known compounds, I have shown that the dicyanometallate family can be thought of as a model family for extended frameworks more generally. These atomically thin linkers give nanometre separation between metal centres, which is of the same order of magnitude as found in canonical metal–organic frameworks. As such, they can be thought of as a natural extension of the series oxides/halides/cyanides/formates/azides and bridge to the length-scale of metal–organic frameworks. Their symmetrical nature (c.f. cyanide) and atomic thickness means they are an excellent embodiment of the abstraction of bridging ligands to rod-like linkers, which has proven so useful in developing design rules for coordination polymers.[20,21,468]

The compounds and structures reported in Chapters 3 and 5 correspond both to canonical structure types, such as perovskite [PPN]M[Au/Ag$(CN)_2]_3$, and rather more unusual structure types such as topologically unique $[Bu_4N]Cd_2[Au(CN)_2]_5$. In Chapter 4 I place these and other new compounds in the context of all known 'simple' dicyanometallates and establish an overview of this structural family. Organising these compounds into fundamental formulae A_nBX_m allows an understanding of the diversity of structures found for given compositions. Drawing attention to these structure–composition relationships highlights the interplay of driving forces

that result in the formation of one structure type rather than another. One of the most intriguing features to emerge from this chemistry is the huge potential for supramolecular-type interactions to play a role in the structures and dynamics of these dicyanometallates. Just as hydrogen bonding has proved so important to the properties of ammonium metal formates and multipolar cation ordering to the lead halide perovskites, the broad potential for chemical diversity and mutual interaction of extra-framework cations in dicyanometallates frameworks cannot fail to affect their structure, dynamics, and mechanical properties.

In Chapter 5 the phase transitions of some superperovskites are examined. The compounds examined show a range of displacive and reconstructive transitions arising from loss of included solvent and from complex interactions between extra-framework species. While some of the transitions bear significant resemblance to those seen in oxide perovskites, *e.g.* $R\bar{3}c$ to $I2/a$ tilt transitions, the reorientation and internal degrees of freedom of molecular extra-framework cations play a central role in driving these transitions.

In Chapter 6 the incommensurately modulated phase of an ABX_2 diamondoid dicyanometallate was described. Understanding this comparatively unusual, yet mercifully simple, phase provides us with information regarding the dynamical behaviour of the parent phase. Here, again, the interaction between extra-framework cation and framework is crucial. The incommensuration is associated with orientational ordering of the extra-framework cation along the fourth direction. It is exactly such cation-lattice rotovibrational coupling that is emerging as important for the exceptional properties of the lead halide perovskites, for example.

Returning to perovskite structured materials, in Chapter 7 I develop an extension

of the Glazer tilt system for describing the unconventional tilts found in molecular perovskite analogues. While in oxides and halides octahedral rotations are restricted to propagating at $\mathbf{k} = \langle \xi, \frac{1}{2}, \frac{1}{2} \rangle$, the tilts in molecular perovskites can propagate at arbitrary wave-vectors. Tilt systems which would be impossible for an oxide perovskite are observed in [PPN]Cd[$Ag(CN)_2$]$_3$·3EtOH·$n$$H_2O$ and have been reported in a variety of other molecular perovskite systems. The 'tilt tensor' described in Chapter 7 is a first step towards a systematic understanding of such tilt systems.

In Chapter 8 I apply the understanding of unconventional tilts developed in the preceding Chapter to a cyanide double perovskite. In $(NH_4)_2SrFe(CN)_6·2H_2O$ these unconventional tilts are shown by symmetry analysis to be switched on and off by the hydration pattern. Binding of two water molecules to each Sr^{2+} induces a tilt mode of the same periodicity.

Overall, I hope I have shown that the dicyanometallate family can be considered a model family of extended frameworks with its own interesting features. I have shown that the spaces available within dicyanometallate frameworks can be filled with large organic counterions and that the interaction between these can result in both unusual and familiar structures as well as interesting dynamical properties. Furthermore I have sought to understand the unconventional tilt systems that can be achieved for molecular perovskite analogues more generally. Together this work shows the importance of understanding the coupling between molecular and lattice degrees of freedom. A fuller understanding of these systems could be achieved by experimentally and computationally probing the phonon dispersion curves (with *e.g.* inelastic neutron scattering (INS)) and molecular ion rotational dynamics (with *e.g.* solid-state NMR). While this coupling is of significant interest in its own right, it

may also point towards approaches for inducing polarity in coordination polymers more generally.

Bibliography

[1] Cox, P. A. *Transition Metal Oxides: An introduction to their electronic structure and properties*; Clarendon Press: Oxford, UK, 2010.

[2] Bruce, D. W., O'Hare, D., Walton, R. I., Eds. *Functional Oxides*; John Wiley & Sons, Ltd.: Chichester, UK, 2010.

[3] Stenonis, N. *De solido intra solidum naturaliter contento*; Florence, 1669.

[4] Hooke, R. *Micrographia: or some physiological descriptions of minute bodies made by magnifying glasses. With observations and inquiries thereupon*; J. Martyn and J. Allestry, 1665.

[5] Derewenda, Z. S. *Acta Crystallogr. Sect. A*, **2008**, *64*, 246–258.

[6] Flack, H. D. *Acta Crystallogr. Sect. A*, **2009**, *65*, 371–389.

[7] Herschel, J. *Camb. Philos. Soc. Trans.*, **1822**, *1*, 43–52.

[8] Bragg, W. L. *Proc. Camb. Philos. Soc.*, **1912**, *XVII*, 43–57.

[9] Bragg, W. H.; Bragg, W. L. *Proc. Royal Soc. Lond. A: Math. Phys. Eng. Sci.*, **1913**, *88*, 428–438.

[10] Bragg, W. L. *Proc. Royal Soc. Lond. A: Math. Phys. Eng. Sci.*, **1913**, *89*, 248–277.

[11] Lonsdale, K. *Proc. Royal Soc. Lond. A: Math. Phys. Eng. Sci.*, **1929**, *123*, 494–515.

[12] Hodgkin, D. C.; Pickworth, J.; Robertson, J. H.; Trueblood, K. N.; Prosen, R. J.; White, J. G. *Nature*, **1955**, *176*, 325–328.

[13] Perutz, M. F.; Rossmann, M. G.; Cullis, A. F.; Muirhead, H.; Will, G.; North, A. C. T. *Nature*, **1960**, *185*, 416–422.

[14] Watson, J. D.; Crick, F. H. C. *Nature*, **1953**, *171*, 737–738.

[15] Franklin, R. E.; Gosling, R. G. *Nature*, **1953**, *171*, 740–741.

[16] Bragg, W. H.; Bragg, W. L. *Proc. Royal Soc. Lond. A: Math. Phys. Eng. Sci.*, **1913**, *89*, 277–291.

[17] Franklin, R. E. *Acta Crystallogr.*, **1950**, *3*, 107–121.

[18] Goldschmidt, V. M. *Naturwissenschaften*, **1926**, *14*, 477–485.

[19] Damasceno, P. F.; Engel, M.; Glotzer, S. C. *Science*, **2012**, *337*, 453–457.

[20] Hoskins, B. F.; Robson, R. *J. Am. Chem. Soc.*, **1989**, *111*, 5962–5964.

[21] Hoskins, B. F.; Robson, R. *J. Am. Chem. Soc.*, **1990**, *112*, 1546–1554.

[22] Yaghi, O. M.; O'Keeffe, M.; Ockwig, N. W.; Chae, H. K.; Eddaoudi, M.; Kim, J. *Nature*, **2003**, *423*, 705–714.

[23] Côté, A. P.; El-Kaderi, H. M.; Furukawa, H.; Hunt, J. R.; Yaghi, O. M. *J. Am. Chem. Soc.*, **2007**, *129*, 12914–12915.

[24] Feng, X.; Ding, X.; Jiang, D. *Chem. Soc. Rev.*, **2012**, *41*, 6010–6022.

[25] Ockwig, N. W.; Delgado-Friedrichs, O.; O'Keeffe, M.; ; Yaghi, O. M. *Acc. Chem. Res.*, **2005**, *38*, 176–182.

[26] Eddaoudi, M.; Kim, J.; Vodak, D.; Sudik, A.; Wachter, J.; O'Keeffe, M.; Yaghi, O. M. *Proc. Natl. Acad. Sci. USA*, **2002**, *99*, 4900–4904.

[27] Carson, C. G.; Brunnello, G.; Lee, S. G.; Jang, S. S.; Gerhardt, R. A.; Tannenbaum, R. *Eur. J. Inorg. Chem.*, **2014**, *2014*, 2140–2145.

[28] Chui, S. S.-Y.; Lo, S. M.-F.; Charmant, J. P. H.; Orpen, A. G.; Williams, I. D. *Science*, **1999**, *283*, 1148–1150.

[29] Lee, J.; Farha, O. K.; Roberts, J.; Scheidt, K. A.; Nguyen, S. T.; Hupp, J. T. *Chem. Soc. Rev.*, **2009**, *38*, 1450–1459.

[30] Long, J. R.; Yaghi, O. M. *Chem. Soc. Rev.*, **2009**, *38*, 1213–1214.

[31] Rosi, N. L.; Eckert, J.; Eddaoudi, M.; Vodak, D. T.; Kim, J.; O'Keeffe, M.; Yaghi, O. M. *Science*, **2003**, *300*, 1127–1129.

[32] Farha, O. K.; Eryazici, I.; Jeong, N. C.; Hauser, B. G.; Wilmer, C. E.; Sarjeant, A. A.; Snurr, R. Q.; Nguyen, S. T.; Yazaydın, A. Ö.; Hupp, J. T. *J. Am. Chem. Soc.*, **2012**, *134*, 15016–15021.

[33] He, Y.; Zhou, W.; Qian, G.; Chen, B. *Chem. Soc. Rev.*, **2014**, *43*, 5657–5678.

[34] Liu, J.; Chen, L.; Cui, H.; Zhang, J.; Zhang, L.; Su, C.-Y. *Chem. Soc. Rev.*, **2014**, *43*, 6011–6061.

[35] Tan, J. C.; Cheetham, A. K. *Chem. Soc. Rev.*, **2011**, *40*, 1059–1080.

[36] Horcajada, P.; Gref, R.; Baati, T.; Allan, P. K.; Maurin, G.; Couvreur, P.; Férey, G.; Morris, R. E.; Serre, C. *Chem. Rev.*, **2012**, *112*, 1232–1268.

[37] Hu, Z.; Deibert, B. J.; Li, J. *Chem. Soc. Rev.*, **2014**, *43*, 5815–5840.

[38] Morozan, A.; Jaouen, F. *Energy & Environ. Sci.*, **2012**, *5*, 9269–9290.

[39] Wang, L.; Han, Y.; Feng, X.; Zhou, J.; Qi, P.; Wang, B. *Coord. Chem. Rev.*, **2016**, *307*, 361–381.

[40] Cavka, J. H.; Jakobsen, S.; Olsbye, U.; Guillou, N.; Lamberti, C.; Bordiga, S.; Lillerud, K. P. *J. Am. Chem. Soc.*, **2008**, *130*, 13850–13851.

[41] Serre, C.; Millange, F.; Thouvenot, C.; Noguès, M.; Marsolier, G.; Louër, D.; Férey, G. *J. Am. Chem. Soc.*, **2002**, *124*, 13519–13526.

[42] Batten, S. R.; Champness, N. R.; Chen, X.-M.; Garcia-Martinez, J.; Kitagawa, S.; Óhrström, L.; O'Keeffe, M.; Suh, M. P.; Reedijk, J. *Pure Appl. Chem.*, **2013**, *85*, 1715–1724.

[43] Werner, H. *Angew. Chem. Int. Ed.*, **2013**, *52*, 6146–6153.

[44] Kraft, A. *Bulletin for the History of Chemistry*, **2008**, *3*, 61–67.

[45] Brown, J. *Philos. Trans.*, **1724**, *33*, 17–24.

[46] Robin, M. B.; Day, P. In *Mixed Valence Chemistry-A Survey and Classification*; Emeléus, H. J., Sharpe, A. G., Eds.; Advances in Inorganic Chemistry and Radiochemistry; Academic Press, 1968; Vol. 10; pp 247–422.

[47] Sato, O.; Iyoda, T.; Fujishima, A.; Hashimoto, K. *Science*, **1996**, *272*, 704–705.

[48] Aguila, D.; Prado, Y.; Koumousi, E. S.; Mathoniere, C.; Clerac, R. *Chem. Soc. Rev.*, **2016**, *45*, 203–224.

[49] Wessells, C. D.; Huggins, R. A.; Cui, Y. *Nature Commun.*, **2011**, *2*, 550.

[50] Pasta, M.; Wessells, C. D.; Liu, N.; Nelson, J.; McDowell, M. T.; Huggins, R. A.; Toney, M. F.; Cui, Y. *Nature Commun.*, **2014**, *5*, 3007.

[51] Wang, L.; Song, J.; Qiao, R.; Wray, L. A.; Hossain, M. A.; Chuang, Y.-D.; Yang, W.; Lu, Y.; Evans, D.; Lee, J.-J.; Vail, S.; Zhao, X.; Nishijima, M.; Kakimoto, S.; Goodenough, J. B. *J. Am. Chem. Soc.*, **2015**, *137*, 2548–2554.

[52] `http://www.britishmuseum.org/research/collection_online/collection_object_details.aspx?objectId=8808&partId=1`, Last accessed 07/06/2016.

[53] Echigo, T.; Kimata, M. *Can. Mineral.*, **2010**, *48*, 1329–1357.

[54] Gadd, G. M.; Rhee, Y. J.; Stephenson, K.; Wei, Z. *Environ. Microbiol. Reports*, **2012**, *4*, 270–96.

[55] Adamo, P.; Violante, P. *Appl. Clay Sci.*, **2000**, *16*, 229–256.

[56] Purvis, O. W.; Halls, C. *Lichenol.*, **1996**, *28*, 571–601.

[57] Chisholm, J. E.; Jones, G. C.; Purvis, O. W. *Mineral. Mag.*, **1987**, *51*, 715–718.

[58] Sayer, J. A.; Kierans, M.; Gadd, G. M. *FEMS Microbiol. Lett.*, **1997**, *154*, 29–35.

[59] Wei, Z.; Hillier, S.; Gadd, G. M. *Environ. Microbiol.*, **2012**, *14*, 1744–1753.

[60] Fomina, M.; Hillier, S.; Charnock, J. M.; Melville, K.; Alexander, I. J.; Gadd, G. M. *Appl. Environ. Microbiol.*, **2005**, *71*, 371–381.

[61] Cliffe, M. J.; Mottillo, C.; Stein, R. S.; Bučar, D.-K.; Friščić, T. *Chem. Sci.*, **2012**, *3*, 2495–2500.

[62] Qi, F.; Stein, R. S.; Friščić, T. *Green Chem.*, **2014**, *16*, 121–132.

[63] Decurtins, S.; Pellaux, R.; Antorrena, G.; Palacio, F. *Coord. Chem. Rev.*, **1999**, *190-192*, 841–854.

[64] Ayyappan, S.; Cheetham, A. K.; Natarajan, S.; Rao, C. N. R. *Chem. Mater.*, **1998**, *10*, 3746–3755.

[65] Pointillart, F.; Train, C.; Gruselle, M.; Villain, F.; Schmalle, H. W.; Talbot, D.; Gredin, P.; Decurtins, S.; Verdaguer, M. *Chem. Mater.*, **2004**, *16*, 832–841.

[66] Pellaux, R.; Schmalle, H. W.; Huber, R.; Fischer, P.; Hauss, T.; Ouladdiaf, B.; Decurtins, S. *Inorg. Chem.*, **1997**, *36*, 2301–2308.

[67] Sadakiyo, M.; Yamada, T.; Kitagawa, H. *J. Am. Chem. Soc.*, **2009**, *131*, 9906–9907.

[68] Sadakiyo, M.; Ōkawa, H.; Shigematsu, A.; Ohba, M.; Yamada, T.; Kitagawa, H. *J. Am. Chem. Soc.*, **2012**, *134*, 5472–5475.

[69] Sonnauer, A.; Hoffmann, F.; Fröba, M.; Kienle, L.; Duppel, V.; Thommes, M.; Serre, C.; Férey, G.; Stock, N. *Angew. Chem. Int. Ed.*, **2009**, *48*, 3791–3794.

[70] Deng, H.; Grunder, S.; Cordova, K. E.; Valente, C.; Furukawa, H.; Hmadeh, M.; Gándara, F.; Whalley, A. C.; Liu, Z.; Asahina, S.; Kazumori, H.; O'Keeffe, M.; Terasaki, O.; Stoddart, J. F.; Yaghi, O. M. *Science*, **2012**, *336*, 1018–1023.

[71] Farha, O. K.; Malliakas, C. D.; Kanatzidis, M. G.; Hupp, J. T. *J. Am. Chem. Soc.*, **2010**, *132*, 950–952.

[72] Loiseau, T.; Serre, C.; Huguenard, C.; Fink, G.; Taulelle, F.; Henry, M.; Bataille, T.; Férey, G. *Chem. Eur. J.*, **2004**, *10*, 1373–1382.

[73] Volkringer, C.; Loiseau, T.; Devic, T.; Férey, G.; Popov, D.; Burghammer, M.; Riekel, C. *CrystEngComm*, **2010**, *12*, 3225–3228.

[74] Serre, C.; Millange, F.; Devic, T.; Audebrand, N.; Beek, W. V. *Mater. Res. Bull.*, **2006**, *41*, 1550–1557.

[75] Braun, M. E.; Steffek, C. D.; Kim, J.; Rasmussen, P. G.; Yaghi, O. M. *Chem. Commun.*, **2001**, 2532–2533.

[76] Goodwin, A. L.; Calleja, M.; Conterio, M. J.; Dove, M. T.; Evans, J. S. O.; Keen, D. A.; Peters, L.; Tucker, M. G. *Science*, **2008**, *319*, 794–797.

[77] Cairns, A. B.; Catafesta, J.; Levelut, C.; Rouquette, J.; van der Lee, A.; Peters, L.; Thompson, A. L.; Dmitriev, V.; Haines, J.; Goodwin, A. L. *Nature Mater.*, **2013**, *12*, 212–216.

[78] Katz, M. J.; Ramnial, T.; Yu, H.-Z.; Leznoff, D. B. *J. Am. Chem. Soc.*, **2008**, *130*, 10662–10673.

[79] Abrahams, S. C.; Bernstein, J. L.; Liminga, R.; Eisenmann, E. T. *J. Chem. Phys.*, **1980**, *73*, 4585–4590.

[80] Colis, J. C. F.; Larochelle, C.; Fernández, E. J.; López-de Luzuriaga, J. M.; Monge, M.; Laguna, A.; Tripp, C.; Patterson, H. *J. Phys. Chem. B*, **2005**, *109*, 4317–4323.

[81] Lefebvre, J.; Batchelor, R. J.; Leznoff, D. B. *J. Am. Chem. Soc.*, **2004**, *126*, 16117–16125.

[82] Niel, V.; Muñoz, M. C.; Gaspar, A. B.; Galet, A.; Levchenko, G.; Real, J. A. *Chem. Eur. J.*, **2002**, *8*, 2446–2453.

[83] Hill, J. A.; Cairns, A. B.; Lim, J. J. K.; Cassidy, S. J.; Clarke, S. J.; Goodwin, A. L. *CrystEngComm*, **2015**, *17*, 2925–2928.

[84] Sharpe, A. G. *The Chemistry of Cyano Complexes of the Transition Metals*; Academic Press: London, UK, 1976.

[85] Jones, L. H. *J. Chem. Phys.*, **1953**, *21*, 1891–1892.

[86] Jones, L. H.; Penneman, R. A. *J. Chem. Phys.*, **1954**, *22*, 965–970.

[87] Jones, L. H. *J. Chem. Phys.*, **1954**, *22*, 1135–1136.

[88] Schwerdtfeger, P.; Boyd, P. D. W.; Burrell, A. K.; Robinson, W. T.; Taylor, M. J. *Inorg. Chem.*, **1990**, *29*, 3593–3607.

[89] Penneman, R. A.; Staritzky, E.; Jones, L. H. *J. Am. Chem. Soc.*, **1956**, *78*, 62–62.

[90] Alexandrov, E. V.; Virovets, A. V.; Blatov, V. A.; Peresypkina, E. V. *Chem. Rev.*, **2015**, *115*, 12286–12319.

[91] Chesnut, D. J.; Zubieta, J. *Chem. Commun.*, **1998**, 1707–1708.

[92] Chesnut, D. J.; Kusnetzow, A.; Zubieta, J. *J. Chem. Soc., Dalton. Trans.*, **1998**, 4081–4084.

[93] Bowmaker, G. A.; Hartl, H.; Urban, V. *Inorg. Chem.*, **2000**, *39*, 4548–4554.

[94] Tronic, T. A.; deKrafft, K. E.; Lim, M. J.; Ley, A. N.; Pike, R. D. *Inorg. Chem.*, **2007**, *46*, 8897–8912.

[95] Bondi, A. *J. Phys. Chem.*, **1964**, *68*, 441–451.

[96] Pyykkö, P. *Angew. Chem. Int. Ed.*, **2004**, *43*, 4412–4456.

[97] Goodwin, A. L.; Keen, D. A.; Tucker, M. G.; Dove, M. T.; Peters, L.; Evans, J. S. O. *J. Am. Chem. Soc.*, **2008**, *130*, 9660–9661.

[98] Korčok, J. L.; Katz, M. J.; Leznoff, D. B. *J. Am. Chem. Soc.*, **2009**, *131*, 4866–4871.

[99] Schmidbaur, H.; Graf, W.; Müller, G. *Angew. Chem. Int. Ed. Engl.*, **1988**, *27*, 417–419.

[100] Schmidbaur, H.; Dziwok, K.; Grohmann, A.; Müller, G. *Chem. Ber.*, **1989**, *122*, 893–895.

[101] Harwell, D. E.; Mortimer, M. D.; Knobler, C. B.; Anet, F. A. L.; Hawthorne, M. F. *J. Am. Chem. Soc.*, **1996**, *118*, 2679–2685.

[102] Schmidbaur, H. *Gold Bull.*, **2000**, *33*, 3–10.

[103] Scherbaum, F.; Grohmann, A.; Huber, B.; Krüger, C.; Schmidbaur, H. *Angew. Chem. Int. Ed. Engl.*, **1988**, *27*, 1544–1546.

[104] Smyslova, E. I.; Perevalova, E. G.; Dyadchenko, V. P.; Grandberg, K. I.; Slovokhotov, Yu. L.; Struchkov, Yu. T. *J. Organomet. Chem.*, **1981**, *215*, 269–279.

[105] Scherbaum, F.; Huber, B.; Müller, G.; Schmidbaur, H. *Angew. Chem. Int. Ed. Engl.*, **1988**, *27*, 1542–1544.

[106] Katz, M. J.; Sakai, K.; Leznoff, D. B. *Chem. Soc. Rev.*, **2008**, *37*, 1884–1895.

[107] Pyykkö, P. *Inorg. Chim. Acta*, **2005**, *358*, 4113–4130.

[108] Pyykkö, P. *Chem. Soc. Rev.*, **2008**, *37*, 1967–1997.

[109] Jansen, M. *Angew. Chem. Int. Ed. Engl.*, **1987**, *26*, 1098–1110.

[110] Schmidbaur, H.; Schier, A. *Angew. Chem. Int. Ed.*, **2015**, *54*, 746–784.

[111] Jansen, M. *J. Less Common Met.*, **1980**, *76*, 285–292.

[112] Jansen, M.; Linke, C. *Angew. Chem. Int. Ed. Engl.*, **1992**, *31*, 653–654.

[113] Barclay, G. A.; Hoskins, B. F. *J. Chem. Soc. (Resumed)*, **1963**, 2807–2812.

[114] Pyykkö, P.; Mendizabal, F. *Chem. Eur. J.*, **1997**, *3*, 1458–1465.

[115] Pyykkö, P.; Runeberg, N.; Mendizabal, F. *Chem. Eur. J.*, **1997**, *3*, 1451–1457.

[116] Schwerdtfeger, P.; Bruce, A. E.; Bruce, M. R. M. *J. Am. Chem. Soc.*, **1998**, *120*, 6587–6597.

[117] Assefa, Z.; Patterson, H. H. *Inorg. Chem.*, **1994**, *33*, 2187–2195.

[118] Yersin, H.; Trümbach, D.; Strasser, J. *Inorg. Chem.*, **1998**, *37*, 3209–3216.

[119] Colis, J. C. F.; Larochelle, C.; Staples, R.; Herbst-Irmer, R.; Patterson, H. *Dalton Trans.*, **2005**, 675–679.

[120] Tanner, P.; Zhou, X.; Wong, W.-T.; Kratzer, C.; Yersin, H. *J. Phys. Chem. B*, **2005**, *109*, 13083–13090.

[121] Assefa, Z.; Kalachinkova, K.; Haire, R. G.; Sykora, R. E. *J. Solid State Chem.*, **2007**, *180*, 3121–3129.

[122] Larochelle, C. L.; Krebs, J. K. *Opt. Mater.*, **2008**, *30*, 1446–1450.

[123] Rawashdeh-Omary, M. A.; Omary, M. A.; Patterson, H. H. *J. Am. Chem. Soc.*, **2000**, *122*, 10371–10380.

[124] Rawashdeh-Omary, M. A.; Omary, M. A.; Patterson, H. H.; Fackler, J. P. *J. Am. Chem. Soc.*, **2001**, *123*, 11237–11247.

[125] Patterson, H. H.; Kanan, S. M.; Omary, M. A. *Coord. Chem. Rev.*, **2000**, *208*, 227–241.

[126] Coker, N. L.; Bauer, J. A. K.; Elder, R. C. *J. Am. Chem. Soc.*, **2004**, *126*, 12–13.

[127] Yersin, H.; Riedl, U. *Inorg. Chem.*, **1995**, *34*, 1642–1645.

[128] Hoskins, B. F.; Robson, R.; Scarlett, N. V. Y. *Angew. Chem. Int. Ed. Engl.*, **1995**, *34*, 1203–1204.

[129] Goodwin, A. L.; Kennedy, B. J.; Kepert, C. J. *J. Am. Chem. Soc.*, **2009**, *131*, 6334–6335.

[130] Collings, I. E.; Cairns, A. B.; Thompson, A. L.; Parker, J. E.; Tang, C. C.; Tucker, M. G.; Catafesta, J.; Levelut, C.; Haines, J.; Dmitriev, V.; Pattison, P.; Goodwin, A. L. *J. Am. Chem. Soc.*, **2013**, *135*, 7610–7620.

[131] Tian, Y.-Q.; Xu, L.; Cai, C.-X.; Wei, J.-C.; Li, Y.-Z.; You, X.-Z. *Eur. J. Inorg. Chem.*, **2004**, 1039–1044.

[132] O'Keeffe, M.; Peskov, M. A.; Ramsden, S. J.; Yaghi, O. M. *Acc. Chem. Res.*, **2008**, *41*, 1782–1789.

[133] Blatov, V. A.; O'Keeffe, M.; Proserpio, D. M. *CrystEngComm*, **2010**, *12*, 44–48.

[134] Alexandrov, E. V.; Blatov, V. A.; Kochetkov, A. V.; Proserpio, D. M. *CrystEngComm*, **2011**, *13*, 3947–3958.

[135] Wells, A. F. *Structural Inorganic Chemistry*, 5th ed.; Clarendon Press: Oxford, UK, 1984.

[136] Shirane, G.; Axe, J. D.; Harada, J.; Remeika, J. P. *Phys. Rev. B*, **1970**, *2*, 155–159.

[137] Newnham, R. E.; Ruschau, G. R. *J. Am. Ceram. Soc.*, **1991**, *74*, 463–480.

[138] Jonker, G. H.; Van Santen, J. H. *Physica*, **1950**, *16*, 337–349.

[139] Cava, R. J.; van Dover, R. B.; Batlogg, B.; Rietman, E. A. *Phys. Rev. Lett.*, **1987**, *58*, 408–410.

[140] David, W. I. F.; Harrison, W. T. A.; Gunn, J. M. F.; Moze, O.; Soper, A. K.; Day, P.; Jorgensen, J. D.; Hinks, D. G.; Beno, M. A.; Soderholm, L.; Capone II, D. W.; Schuller, I. K.; Segre, C. U.; Zhang, K.; Grace, J. D. *Nature*, **1987**, *327*, 310–312.

[141] Li, M.; Pietrowski, M. J.; De Souza, R. A.; Zhang, H.; Reaney, I. M.; Cook, S. N.; Kilner, J. A.; Sinclair, D. C. *Nature Mater.*, **2014**, *13*, 31–35.

[142] Green, M. A.; Ho-Baillie, A.; Snaith, H. J. *Nature Photonics*, **2014**, *8*, 506–514.

[143] Lawler, J. M. M.; Manuel, P.; Thompson, A. L.; Saines, P. J. *Dalton Trans.*, **2015**, *44*, 11613–11620.

[144] Du, Z.-Y.; Xu, T.-T.; Huang, B.; Su, Y.-J.; Xue, W.; He, C.-T.; Zhang, W.-X.; Chen, X.-M. *Angew. Chem. Int. Ed.*, **2015**, *54*, 914–918.

[145] Mitzi, D. B. *J. Chem. Soc., Dalton. Trans.*, **2001**, 1–12.

[146] Kieslich, G.; Sun, S.; Cheetham, A. K. *Chem. Sci.*, **2014**, *5*, 4712–4715.

[147] Megaw, H. D. *Crystal Structures. A Working Approach*; Saunders: Philadelphia, USA, 1973.

[148] Megaw, H. D.; Darlington, C. N. W. *Acta Crystallogr. Sect. A*, **1975**, *31*, 161–173.

[149] Shannon, R. D. *Acta Crystallogr. Sect. A*, **1976**, *32*, 751–767.

[150] Lander, J. J. *Acta Crystallogr.*, **1951**, *4*, 148–156.

[151] Li, C.; Soh, K. C. K.; Wu, P. *J. Alloy. Compd.*, **2004**, *372*, 40–48.

[152] Li, C.; Lu, X.; Ding, W.; Feng, L.; Gao, Y.; Guo, Z. *Acta Crystallogr. Sect. B*, **2008**, *64*, 702–707.

[153] Pauling, L. *J. Am. Chem. Soc.*, **1929**, *51*, 1010–1026.

[154] Travis, W.; Glover, E. N. K.; Bronstein, H.; Scanlon, D. O.; Palgrave, R. *Chem. Sci.*, **2016**, *7*, 4548–4556.

[155] Topsöe, H. *Z. Krist.*, **1884**, *8*, 246–296.

[156] Mitzi, D. B.; Feild, C. A.; Harrison, W. T. A.; Guloy, A. M. *Nature*, **1994**, *369*, 467–469.

[157] Saparov, B.; Mitzi, D. B. *Chem. Rev.*, **2016**, *116*, 4558–4596.

[158] Kapustinskii, A. F. *Q. Rev. Chem. Soc.*, **1956**, *10*, 283–294.

[159] Jenkins, H. D. B.; Thakur, K. P. *J. Chem. Educ.*, **1979**, *56*, 576–577.

[160] Roobottom, H. K.; Jenkins, H. D. B.; Passmore, J.; Glasser, L. *J. Chem. Educ.*, **1999**, *76*, 1570–1573.

[161] Schwarten, M.; Babel, D. *Z. Anorg. Allg. Chem.*, **2000**, *626*, 1921–1928.

[162] Schouwink, P.; Ley, M. B.; Tissot, A.; Hagemann, H.; Jensen, T. R.; Smrčok, Ľ.; Černý, R. *Nature Commun.*, **2014**, *5*, 5706.

[163] Kieslich, G.; Sun, S.; Cheetham, A. K. *Chem. Sci.*, **2015**, *6*, 3430–3433.

[164] Maughan, A. E.; Kurzman, J. A.; Neilson, J. R. *Inorg. Chem.*, **2015**, *54*, 370–378.

[165] Kundys, B.; Lappas, A.; Viret, M.; Kapustianyk, V.; Rudyk, V.; Semak, S.; Simon, C.; Bakaimi, I. *Phys. Rev. B*, **2010**, *81*, 224434.

[166] Steadman, J. P.; Willett, R. D. *Inorg. Chim. Acta*, **1970**, *4*, 367–371.

[167] Ruddlesden, S. N.; Popper, P. *Acta Crystallogr.*, **1958**, *11*, 54–55.

[168] Kieslich, G.; Kumagai, S.; Butler, K. T.; Okamura, T.; Hendon, C. H.; Sun, S.; Yamashita, M.; Walsh, A.; Cheetham, A. K. *Chem. Commun.*, **2015**, *51*, 15538–15541.

[169] Xu, G.-C.; Ma, X.-M.; Zhang, L.; Wang, Z.-M.; Gao, S. *J. Am. Chem. Soc.*, **2010**, *132*, 9588–9590.

[170] Liu, B.; Shang, R.; Hu, K.-L.; Wang, Z.-M.; Gao, S. *Inorg. Chem.*, **2012**, *51*, 13363–13372.

[171] Kumar, S.; Nussinov, R. *ChemBioChem*, **2002**, *3*, 604–617.

[172] Zhang, W.; Cai, Y.; Xiong, R.-G.; Yoshikawa, H.; Awaga, K. *Angew. Chem. Int. Ed.*, **2010**, *49*, 6608–6610.

[173] Zhang, X.; Shao, X.-D.; Li, S.-C.; Cai, Y.; Yao, Y.-F.; Xiong, R.-G.; Zhang, W. *Chem. Commun.*, **2015**, *51*, 4568–4571.

[174] Stroppa, A.; Barone, P.; Jain, P.; Perez-Mato, J. M.; Picozzi, S. *Adv. Mater.*, **2013**, *25*, 2284–2290.

[175] Pitcher, M. J.; Mandal, P.; Dyer, M. S.; Alaria, J.; Borisov, P.; Niu, H.; Claridge, J. B.; Rosseinsky, M. J. *Science*, **2015**, *347*, 420–424.

[176] Darlington, C. N. W.; Knight, K. S. *Acta Crystallogr. Sect. B*, **1999**, *55*, 24–30.

[177] Kennedy, B. J.; Prodjosantoso, A. K.; Howard, C. J. *J. Phys.: Condens. Matter*, **1999**, *11*, 6319–6327.

[178] Ahtee, M.; Glazer, A. M.; Hewat, A. W. *Acta Crystallogr. Sect. B*, **1978**, *34*, 752–758.

[179] Kennedy, B. J.; Howard, C. J.; Chakoumakos, B. C. *Phys. Rev. B*, **1999**, *59*, 4023–4027.

[180] Kennedy, B. J.; Howard, C. J.; Chakoumakos, B. C. *Phys. Rev. B*, **1999**, *60*, 2972–2975.

[181] Kennedy, B. J.; Howard, C. J.; Chakoumakos, B. C. *J. Phys.: Condens. Matter*, **1999**, *11*, 1479–1488.

[182] Howard, C. J.; Withers, R. L.; Knight, K. S.; Zhang, Z. *J. Phys.: Condens. Matter*, **2008**, *20*, 135202.

[183] Aleksandrov, K. S. *Ferroelectrics*, **1976**, *14*, 801–805.

[184] Glazer, A. M. *Acta Crystallogr. Sect. B*, **1972**, *28*, 3384–3392.

[185] Howard, C. J.; Stokes, H. T. *Acta Crystallogr. Sect. B*, **1998**, *54*, 782–789.

[186] Francombe, M. H.; Lewis, B. *Acta Crystallogr.*, **1958**, *11*, 175–178.

[187] Sakowski-Cowley, A. C.; Łukaszewicz, K.; Megaw, H. D. *Acta Crystallogr. Sect. B*, **1969**, *25*, 851–865.

[188] Fábry, J.; Zikmund, Z.; Kania, A.; Petříček, V. *Acta Crystallogr. Sect. C*, **2000**, *56*, 916–918.

[189] Ishikawa, H.; Munao, I.; Bode, B. E.; Hiroi, Z.; Lightfoot, P. *Chem. Commun.*, **2015**, *51*, 15469–15471.

[190] Belik, A. A.; Abakumov, A. M.; Tsirlin, A. A.; Hadermann, J.; Kim, J.; Tendeloo, G. V.; Takayama-Muromachi, E. *Chem. Mater.*, **2011**, *23*, 4505–4514.

[191] Peel, M. D.; Thompson, S. P.; Daoud-Aladine, A.; Ashbrook, S. E.; Lightfoot, P. *Inorg. Chem.*, **2012**, *51*, 6876–6889.

[192] Hidaka, M. *J. Phys. Soc. Jpn.*, **1975**, *39*, 180–186.

[193] Deblieck, R.; Van Tendeloo, G.; Van Landuyt, J.; Amelinckx, S. *Acta Crystallogr. Sect. B*, **1985**, *41*, 319–329.

[194] Flerov, I.; Gorev, M.; Aleksandrov, K.; Tressaud, A.; Grannec, J.; Couzi, M. *Mater. Sci. Eng. R: Reports*, **1998**, *24*, 81–151.

[195] Bovill, S. M.; Saines, P. J. *CrystEngComm*, **2015**, *17*, 8319–8326.

[196] Young, J.; Rondinelli, J. M. *J. Phys. Chem. Lett.*, **2016**, *7*, 918–922.

[197] Bulou, A.; Fourquet, J. L.; Leble, A.; Nouet, J.; Pape, R. D.; Plet, F. In *Solid State Chemistry. Proc. 2nd Eur. Conf.*; Metselaar, E., Heijligers, H. J., Schoonman, J., Eds.; Elsevier Scientific: Amsterdam, Netherlands, 1983; pp 679–682.

[198] Abrahams, S. C.; Bernstein, J. L. *Mater. Res. Bull.*, **1972**, *7*, 715–720.

[199] Hidaka, M.; Wood, I. G.; Wanklyn, B. M.; Garrard, B. J. *J. Phys. C: Solid State Phys.*, **1979**, *12*, 1799.

[200] Moron, M. C.; Bulou, A.; Pique, C.; Vourquet, J. L. *J. Phys.: Condens. Matter*, **1990**, *2*, 8269–8275.

[201] Pique, C.; Bulou, A.; Moron, M. C.; Burriel, R.; Fourquet, J. L.; Rousseau, M. *J. Phys.: Condens. Matter*, **1990**, *2*, 8277–8292.

[202] Ihringer, J.; Abrahams, S. C. *Phys. Rev. B*, **1984**, *30*, 6540–6548.

[203] Abrahams, S. C.; Ihringer, J.; Marsh, P.; Nassau, K. *J. Chem. Phys.*, **1984**, *81*, 2082–2087.

[204] Burns, G.; Glazer, A. M. *Space groups for solid state scientists*; Elsevier : Academic Press: Amsterdam, Netherlands, 2013.

[205] Vougo-Zanda, M.; Anokhina, E. V.; Duhovic, S.; Liu, L.; Wang, X.; Oloba, O. A.; Albright, T. A.; Jacobson, A. J. *Inorg. Chem.*, **2008**, *47*, 4746–4751.

[206] Barthelet, K.; Adil, K.; Millange, F.; Serre, C.; Riou, D.; Férey, G. *J. Mater. Chem.*, **2003**, *13*, 2208–2212.

[207] Barthelet, K.; Marrot, J.; Riou, D.; Férey, G. *Angew. Chem. Int. Ed.*, **2002**, *41*, 281–284.

[208] Anokhina, E. V.; Vougo-Zanda, M.; Wang, X.; Jacobson, A. J. *J. Am. Chem. Soc.*, **2005**, *127*, 15000–15001.

[209] Barthelet, K.; Marrot, J.; Férey, G.; Riou, D. *Chem. Commun.*, **2004**, 520–521.

[210] Gómez-Aguirre, L. C.; Pato-Doldán, B.; Stroppa, A.; Yang, L.-M.; Frauenheim, T.; Mira, J.; Yáñez-Vilar, S.; Artiaga, R.; Castro-García, S.; Sánchez-Andújar, M.; Señarís-Rodríguez, M. A. *Chem. Eur. J.*, **2016**, *22*, 7863–7870.

[211] Mautner, F. A.; Cortés, R.; Lezama, L.; Rojo, T. *Angew. Chem. Int. Ed. Engl.*, **1996**, *35*, 78–80.

[212] Zhang, W.; Ye, H.-Y.; Graf, R.; Spiess, H. W.; Yao, Y.-F.; Zhu, R.-Q.; Xiong, R.-G. *J. Am. Chem. Soc.*, **2013**, *135*, 5230–5233.

[213] Du, Z.-Y.; Sun, Y.-Z.; Chen, S.-L.; Huang, B.; Su, Y.-J.; Xu, T.-T.; Zhang, W.-X.; Chen, X.-M. *Chem. Commun.*, **2015**, *51*, 15641–15644.

[214] Etienne, T.; Mosconi, E.; De Angelis, F. *J. Phys. Chem. Lett.*, **2016**, *7*, 1638–1645.

[215] Motta, C.; El-Mellouhi, F.; Kais, S.; Tabet, N.; Alharbi, F.; Sanvito, S. *Nature Commun.*, **2015**, *6*, 7026.

[216] Leguy, A. M. A.; Frost, J. M.; McMahon, A. P.; Sakai, V. G.; Kockelmann, W.; Law, C.; Li, X.; Foglia, F.; Walsh, A.; O'Regan, B. C.; Nelson, J.; Cabral, J. T.; Barnes, P. R. F. *Nature Commun.*, **2015**, *6*, 7124.

[217] Yang, W. S.; Noh, J. H.; Jeon, N. J.; Kim, Y. C.; Ryu, S.; Seo, J.; Seok, S. I. *Science*, **2015**, *348*, 1234–1237.

[218] Dusek, M.; Chapuis, G.; Meyer, M.; Petricek, V. *Acta Crystallogr. Sect. B*, **2003**, *59*, 337–352.

[219] Lovelace, J. J.; Simone, P. D.; Petříček, V.; Borgstahl, G. E. O. *Acta Crystallogr. Sect. D*, **2013**, *69*, 1062–1072.

[220] van Smaalen, S. *Z. Krist. - Cryst. Mater.*, **2004**, *219*, 681–691.

[221] de Wolff, P. M. *Acta Crystallogr. Sect. A*, **1974**, *30*, 777–785.

[222] de Wolff, P. M. *Acta Crystallogr. Sect. A*, **1977**, *33*, 493–497.

[223] Petříček, V.; Dušek, M.; Palatinus, L. *Z. Krist. - Cryst. Mater.*, **2014**, *229*, 345.

[224] Stokes, H. T.; Campbell, B. J.; van Smaalen, S. *Acta Crystallogr. Sect. A*, **2011**, *67*, 45–55.

[225] Aroyo, M. I.; Perez-Mato, J. M.; Capillas, C.; Kroumova, E.; Ivantchev, S.; Madariaga, G.; Kirov, A.; Wondratschek, H. *Z. Krist. - Cryst. Mater.*, **2006**, *221*, 15–27.

[226] Van Smaalen, S. *Incommensurate Crystallography*; Oxford University Press: Oxford, UK, 2007.

[227] Abakumov, A. M.; Erni, R.; Tsirlin, A. A.; Rossell, M. D.; Batuk, D.; Nénert, G.; Tendeloo, G. V. *Chem. Mater.*, **2013**, *25*, 2670–2683.

[228] Erni, R.; Abakumov, A. M.; Rossell, M. D.; Batuk, D.; Tsirlin, A. A.; Nenert, G.; Van Tendeloo, G. *Nature Mater.*, **2014**, *13*, 216–217.

[229] Rusakov, D. A.; Abakumov, A. M.; Yamaura, K.; Belik, A. A.; Tendeloo, G. V.; Takayama-Muromachi, E. *Chem. Mater.*, **2011**, *23*, 285–292.

[230] Pinheiro, C. B.; Abakumov, A. M. *IUCrJ*, **2015**, *2*, 137–154.

[231] Arakcheeva, A.; Logvinovich, D.; Chapuis, G.; Morozov, V.; Eliseeva, S. V.; Bunzli, J.-C. G.; Pattison, P. *Chem. Sci.*, **2012**, *3*, 384–390.

[232] Pérez, O.; Mellenne, B.; Retoux, R.; Raveau, B.; Hervieu, M. *Solid State Sci.*, **2006**, *8*, 431–433.

[233] Ovsyannikov, S. V. et al. *Nature Chem.*, **2016**, *8*, 501–508.

[234] Hassan, I.; Buseck, P. R. *Am. Mineral.*, **1989**, *74*, 394–410.

[235] de Oñate Martínez, J.; McCusker, L. B.; Baerlocher, C. *Microporous Mesoporous Mater.*, **2000**, *34*, 99–113.

[236] Benkert, C.; Heine, V. *J. Phys. C: Solid State Phys.*, **1987**, *20*, 3355–3367.

[237] Launois, P.; Moussa, F.; Lemée-Cailleau, M. H.; Cailleau, H. *Phys. Rev. B*, **1989**, *40*, 5042–5055.

[238] Baudour, J. L.; Sanquer, M. *Acta Crystallogr. Sect. B*, **1983**, *39*, 75–84.

[239] Heine, V.; Price, S. L. *J. Phys. C: Solid State Phys.*, **1985**, *18*, 5259.

[240] Zúñiga, F. J.; Palatinus, L.; CabildoI, P.; Claramunt, R. M.; Elguero, J. *Z. Krist. - Cryst. Mater.*, **2006**, *221*, 281–287.

[241] Kawamura, Y.; Mashiyama, H. *J. Korean Phys. Soc.*, **1999**, *35*, S1437–S1440.

[242] Fütterer, K.; Depmeier, W.; Petříček, V. *Acta Crystallogr. Sect. B*, **1995**, *51*, 768–779.

[243] Futterer, K.; Withers, R. L.; Welberry, T. R.; Depmeier, W. *J. Phys.: Condens. Matter*, **1995**, *7*, 4983.

[244] Etxebarria, J.; Ruiz-Larrea, I.; Tello, M. J.; López-Echarri, A. *J. Phys. C: Solid State Phys.*, **1988**, *21*, 1717.

[245] Doudin, B.; Chapuis, G. *Acta Crystallogr. Sect. B*, **1990**, *46*, 180–186.

[246] Jahn, I. R.; Schwab, K.; Knorr, K.; Holocher, K. *J. Phys.: Condens. Matter*, **1994**, *6*, 10839–10853.

[247] Muralt, P.; Kind, R.; Bührer, W. *Phys. Rev. B*, **1988**, *38*, 666–679.

[248] Muralt, P. *J. Phys. C: Solid State Phys.*, **1986**, *19*, 1689.

[249] Harris, P.; Larsen, F. K.; Lebech, B.; Achiwa, N. *Acta Crystallogr. Sect. B*, **1994**, *50*, 676–684.

[250] Doudin, B.; Chapuis, G. *Acta Crystallogr. Sect. B*, **1988**, *44*, 495–502.

[251] Chapuis, G. *Crystallogr. Rev.*, **1996**, *5*, 109–128.

[252] Depmeier, W. *Z. für Krist. - Cryst. Mater.*, **2009**, *224*, 287–294.

[253] Jahn, I. R.; Ritter, H.; Schwab, K.; Knorr, K. *Ferroelectrics*, **1998**, *205*, 119–132.

[254] Swainson, I. P.; Stock, C.; Parker, S. F.; Van Eijck, L.; Russina, M.; Taylor, J. W. *Phys. Rev. B*, **2015**, *92*, 100303.

[255] Petříček, V.; Dušek, M.; Černák, J. *Acta Crystallogr. Sect. B*, **2005**, *61*, 280–286.

[256] Gągor, A.; Węcławik, M.; Bondzior, B.; Jakubas, R. *CrystEngComm*, **2015**, *17*, 3286–3296.

[257] Trzop, E.; Zhang, D.; Piñeiro-Lopez, L.; Valverde-Muñoz, F. J.; Carmen Muñoz, M.; Palatinus, L.; Guerin, L.; Cailleau, H.; Real, J. A.; Collet, E. *Angew. Chem. Int. Ed.*, **2016**, *55*, 8675–8679.

[258] Yamamoto, A. *Acta Crystallogr. Sect. A*, **1993**, *49*, 831–846.

[259] Nelmes, R. J.; Allan, D. R.; McMahon, M. I.; Belmonte, S. A. *Phys. Rev. Lett.*, **1999**, *83*, 4081–4084.

[260] McMahon, M. I.; Bovornratanaraks, T.; Allan, D. R.; Belmonte, S. A.; Nelmes, R. J. *Phys. Rev. B*, **2000**, *61*, 3135–3138.

[261] McMahon, M. I.; Rekhi, S.; Nelmes, R. J. *Phys. Rev. Lett.*, **2001**, *87*, 055501.

[262] McMahon, M. I.; Degtyareva, O.; Nelmes, R. J. *Phys. Rev. Lett.*, **2000**, *85*, 4896–4899.

[263] Harris, K. D. M.; Thomas, J. M. *J. Chem. Soc. Faraday Trans.*, **1990**, *86*, 2985–2996.

[264] Smith, A. E. *Acta Crystallogr.*, **1952**, *5*, 224–235.

[265] Forst, R.; Jagodzinski, H.; Boysen, H.; Frey, F. *Acta Crystallogr. Sect. B*, **1987**, *43*, 187–197.

[266] Peral, I.; Madariaga, G.; Petricek, V.; Breczewski, T. *Acta Crystallogr. Sect. B*, **2001**, *57*, 378–385.

[267] Brown, D.; Cutforth, B. D.; Davies, C. G.; Gillespie, R. J.; Ireland, P. R.; Vekris, J. E. *Can. J. Chem.*, **1974**, *52*, 791–793.

[268] Tun, Z.; Brown, I. D. *Acta Crystallogr. Sect. B*, **1986**, *42*, 209–213.

[269] Wang, X.; Jacobson, A. J. *J. Solid State Chem.*, **2015**, *236*, 230–235.

[270] Goodwin, A. L. Negative thermal expansion behaviour in cyanide-bridged molecular framework materials. Ph.D. thesis, Department of Chemistry, University of Sydney, 2003.

[271] Hatch, D. M.; Ghose, S. *Phys. Chem. Miner.*, **1991**, *17*, 554–562.

[272] Lee, Y.; Mitzi, D. B.; Barnes, P. W.; Vogt, T. *Phys. Rev. B*, **2003**, *68*, 020103.

[273] Kemper, J. B.; Vafek, O.; Betts, J. B.; Balakirev, F. F.; Hardy, W. N.; Liang, R.; Bonn, D. A.; Boebinger, G. S. *Nature Phys.*, **2016**, *12*, 47–51.

[274] Wooldridge, J.; Stewart, M.; Vecchini, C.; Cain, M. G.; Gutmann, M.; Reece, M. *J. Am. Ceram. Soc.*, **2014**, *97*, 2111–2115.

[275] Shirane, G.; Suzuki, K.; Takeda, A. *J. Phys. Soc. Jpn.*, **1952**, *7*, 12–18.

[276] Neumann, F. E. In *Vorlesungen über die Theorie der Elastizität der festen Körper und des Lichtäthers*; Meyer, O. E., Ed.; Leipzig, B. G. Teubner-Verlag, 1885.

[277] Chipman, D.; Warren, B. E. *J. Appl. Phys.*, **1950**, *21*, 696–697.

[278] Dove, M. T. *Structure and Dynamics: An atomic view of materials*; Oxford University Press: Oxford, UK, 2003.

[279] Shirane, G.; Hoshino, S.; Suzuki, K. *Phys. Rev.*, **1950**, *80*, 1105–1106.

[280] Hayward, S. A.; Salje, E. K. H. *Phase Transit.*, **1999**, *68*, 501–522.

[281] Ryder, M. R.; Civalleri, B.; Bennett, T. D.; Henke, S.; Rudić, S.; Cinque, G.; Fernandez-Alonso, F.; Tan, J.-C. *Phys. Rev. Lett.*, **2014**, *113*, 215502.

[282] Glazer, A. M.; Mabud, S. A. *Acta Crystallogr. Sect. B*, **1978**, *34*, 1065–1070.

[283] Ravel, B.; Stern, E. A.; Yacobi, Y.; Dogan, F. *Jpn. J. Appl. Phys.*, **1993**, *32*, 782–784.

[284] Glazer, A. M. *Acta Crystallogr. Sect. A*, **1975**, *31*, 756–762.

[285] Howard, C. J.; Knight, K. S.; Kennedy, B. J.; Kisi, E. H. *J. Phys.: Condens. Matter*, **2000**, *12*, L677–L683.

[286] Howard, C. J.; Kennedy, B. J.; Chakoumakos, B. C. *J. Phys.: Condens. Matter*, **2000**, *12*, 349.

[287] Berge, B.; Dolino, G.; Vallade, M.; Boissier, M.; Vacher, R. *J. Phys. France*, **1984**, *45*, 715–724.

[288] Dove, M. T.; Giddy, A. P.; Heine, V. *Ferroelectrics*, **1992**, *136*, 33–49.

[289] Tautz, F. S.; Heine, V.; Dove, M. T.; Chen, X. *Phys. Chem. Miner.*, **1991**, *18*, 326–336.

[290] Bounds, D. G.; Klein, M. L.; McDonald, I. R. *Phys. Rev. Lett.*, **1981**, *46*, 1682–1685.

[291] Dultz, W.; Krause, H. *Phys. Rev. B*, **1978**, *18*, 394–400.

[292] Chelli, R.; Cardini, G.; Califano, S. *J. Chem. Phys.*, **1997**, *107*, 8041–8050.

[293] Haussühl, S. *Solid State Commun.*, **1973**, *13*, 147–151.

[294] Rowe, J. M.; Rush, J. J.; Vagelatos, N.; Price, D. L.; Hinks, D. G.; Susman, S. *J. Chem. Phys.*, **1975**, *62*, 4551–4554.

[295] Rowe, J. M.; Rush, J. J.; Prince, E.; Chesser, N. J. *Ferroelectrics*, **1977**, *16*, 107–109.

[296] De Raedt, B.; Michel, K. H. *Faraday Discuss. Chem. Soc.*, **1980**, *69*, 88–97.

[297] Rowe, J. M.; Rush, J. J.; Chesser, N. J.; Michel, K. H.; Naudts, J. *Phys. Rev. B*, **1978**, *40*, 455–458.

[298] Rowe, J. M.; Rush, J. J.; Prince, E. *J. Chem. Phys.*, **1977**, *66*, 5147–5149.

[299] dos Santos, R. R.; Koiller, B.; von der Weid, J. P.; Ribeiro, S. C.; Chaves, A. S.; Barreto, F. C. S. *J. Phys. C: Solid State Phys.*, **1978**, *11*, 4557.

[300] Carter, S. J.; Foxman, B. M.; Stuhl, L. S. *J. Am. Chem. Soc.*, **1984**, *106*, 4265–4266.

[301] Bruno, I. J.; Cole, J. C.; Edgington, P. R.; Kessler, M.; Macrae, C. F.; McCabe, P.; Pearson, J.; Taylor, R. *Acta Crystallogr. Sect. B*, **2002**, *58*, 389–397.

[302] Allen, F. H. *Acta Crystallogr. Sect. B*, **2002**, *58*, 380–388.

[303] REAXYS, version 2.20770.1, *Elsevier Information Systems GmbH*, **2016**,

[304] Bauzá, A.; Frontera, A.; Mooibroek, T. J.; Reedijk, J. *CrystEngComm*, **2015**, *17*, 3768–3771.

[305] Martinsen, A.; Songstad, J. *Acta Chem. Scand.*, **1977**, *A31*, 645–650.

[306] Scudder, M.; Dance, I. *J. Chem. Soc., Dalton. Trans.*, **1998**, 3155–3166.

[307] Scudder, M.; Dance, I. *J. Chem. Soc., Dalton Trans.*, **1998**, 3167–3176.

[308] Lewis, G. R.; Dance, I. *J. Chem. Soc., Dalton. Trans.*, **2000**, 299–306.

[309] Alsalme, A.; Jaafar, M.; Liu, X.; Dielmann, F.; Hahn, F. E.; Al-farhan, K.; Reedijk, J. *Polyhedron*, **2015**, *88*, 1–5.

[310] Lefebvre, J.; Chartrand, D.; Leznoff, D. B. *Polyhedron*, **2007**, *26*, 2189–2199.

[311] Mason, W. R. *J. Am. Chem. Soc.*, **1973**, *95*, 3573–3581.

[312] Friedrich, W.; Knipping, P.; M, L. *Bayerische Akad. d. Wiss. zu München, Sitzungsber. math.-phys. Kl.*, **1912**, 303–322.

[313] Forman, P. *Arch. for Hist. Exact Sci.*, **1969**, *6*, 38–71.

[314] Sivia, D. S. *Elementary Scattering Theory For X-ray and Neutron Users*; Oxford University Press: Oxford, UK, 2011.

[315] Moseley, H. G. J. *Philos. Mag. Ser. 6*, **1913**, *26*, 1024–1034.

[316] The 14th BCA/CCG Intensive Teaching School in X-ray Structure Analysis. Course notes, 2013.

[317] Cosier, J.; Glazer, A. M. *J. Appl. Crystallogr.*, **1986**, *19*, 105–107.

[318] Otwinowski, Z.; Minor, W. *Methods Enzymol.*, **1997**, *276*, 307–326.

[319] *CrysalisPro*; Rigaku Oxford Diffraction, 2015.

[320] Altomare, A.; Cascarano, G.; Giacovazzo, C.; Guagliardi, A.; Burla, M. C.; Polidori, G.; Camalli, M. *J. Appl. Crystallogr.*, **1994**, *27*, 435–435.

[321] Palatinus, L.; Chapuis, G. *J. Appl. Crystallogr.*, **2007**, *40*, 786–790.

[322] Betteridge, P. W.; Carruthers, J. R.; Cooper, R. I.; Prout, K.; Watkin, D. J. *J. Appl. Crystallogr.*, **2003**, *36*, 1487–1487.

[323] Parois, P.; Cooper, R. I.; Thompson, A. L. *Chem. Cent. J.*, **2015**, *9*, 30.

[324] Cooper, R. I.; Thompson, A. L.; Watkin, D. J. *J. Appl. Crystallogr.*, **2010**, *43*, 1100–1107.

[325] Nowell, H.; Barnett, S. A.; Christensen, K. E.; Teat, S. J.; Allan, D. R. *J. Synchrotron Radiat.*, **2012**, *19*, 435–441.

[326] Goeta, A. E.; Thompson, L. K.; Sheppard, C. L.; Tandon, S. S.; Lehmann, C. W.; Cosier, J.; Webster, C.; Howard, J. A. K. *Acta Crystallogr. Sect. C*, **1999**, *55*, 1243–1246.

[327] Wenk, H.-R.; Van Houtte, P. *Reports on Prog. Phys.*, **2004**, *67*, 1367.

[328] Pawley, G. S. *J. Appl. Crystallogr.*, **1981**, *14*, 357–361.

[329] Rietveld, H. M. *Acta Crystallogr.*, **1967**, *22*, 151–152.

[330] Rietveld, H. M. *J. Appl. Crystallogr.*, **1969**, *2*, 65–71.

[331] Parker, J. E.; Thompson, S. P.; Cobb, T. M.; Yuan, F.; Potter, J.; Lennie, A. R.; Alexander, S.; Tighe, C. J.; Darr, J. A.; Cockcroft, J. C.; Tang, C. C. *J. Appl. Crystallogr.*, **2011**, *44*, 102–110.

[332] Coelho, A. A. *TOPAS-Academic, V4.1*, **2007**, Coelho Software.

[333] Hill, J. A.; Thompson, A. L.; Goodwin, A. L. *J. Am. Chem. Soc.*, **2016**, *138*, 5886–5896.

[334] Wang, Z.; Zhang, B.; Otsuka, T.; Inoue, K.; Kobayashi, H.; Kurmoo, M. *Dalton Trans.*, **2004**, 2209–2216.

[335] Hu, K.-L.; Kurmoo, M.; Wang, Z.; Gao, S. *Chem. Eur. J.*, **2009**, *15*, 12050–12064.

[336] Collings, I. E.; Hill, J. A.; Cairns, A. B.; Cooper, R. I.; Thompson, A. L.; Parker, J. E.; Tang, C. C.; Goodwin, A. L. *Dalton Trans.*, **2016**, *45*, 4169–4178.

[337] Lee, M. M.; Teuscher, J.; Miyasaka, T.; Murakami, T. N.; Snaith, H. J. *Science*, **2012**, *338*, 643–647.

[338] Stoumpos, C. C.; Malliakas, C. D.; Kanatzidis, M. G. *Inorg. Chem.*, **2013**, *52*, 9019–9038.

[339] Weller, M. T.; Weber, O. J.; Henry, P. F.; Di Pumpo, A. M.; Hansen, T. C. *Chem. Commun.*, **2015**, *51*, 4180–4183.

[340] Eisenmann, E. T. *J. Electrochem. Soc.*, **1977**, *124*, 1957–1958.

[341] Zhdanov, G. S.; Shugam, E. A. *Acta Physicochimica U.R.S.S*, **1945**, *20*, 253.

[342] Bowmaker, G. A.; Kennedy, B. J.; Reid, J. C. *Inorg. Chem.*, **1998**, *37*, 3968–3974.

[343] Lefebvre, J.; Korčok, J. L.; Katz, M. J.; Leznoff, D. B. *Sensors*, **2012**, *12*, 3669–3692.

[344] Soma, T.; Iwamoto, T. *Chem. Lett.*, **1995**, *24*, 271–272.

[345] Hoskins, B. F.; Robson, R.; Scharlett, N. V. Y. *J. Chem. Soc., Chem. Commun.*, **1994**, *1994*, 2025–2026.

[346] West, C. D. *Z. Krist. Krist. Krist. Krist.*, **1934**, *88*, 173–175.

[347] West, C. D. *Z. Krist. Krist. Krist. Krist.*, **1935**, *90*, 555–558.

[348] Yoshida, K.; Kosone, T.; Kanadani, C.; Saito, T.; Kitazawa, T. *Polyhedron*, **2011**, *30*, 3062–3066.

[349] Vlček, A.; Orendáč, M.; Orendáčová, A.; Kajňaková, M.; Papageorgiou, T.; Chomič, J.; Černák, J.; Massa, W.; Feher, A. *Solid State Sci.*, **2007**, *9*, 116–125.

[350] Lefebvre, J.; Trudel, S.; Hill, R. H.; Leznoff, D. B. *Chem. Eur. J.*, **2008**, *14*, 7156–7167.

[351] Hibble, S. J.; Cheyne, S. M.; Hannon, A. C.; Eversfield, S. G. *Inorg. Chem.*, **2002**, *41*, 4990–4992.

[352] Galet, A.; Muñoz, M. C.; Martínez, V.; Real, J. A. *Chem. Commun.*, **2004**, 2268–2269.

[353] Geiser, U.; Schlueter, J. A. *Acta Crystallogr. Sect. C*, **2003**, *59*, i21–i23.

[354] Chakraborty, J.; Nandi, M.; Mayer-Figge, H.; Sheldrick, W. S.; Sorace, L.; Bhaumik, A.; Banerjee, P. *Eur. J. Inorg. Chem.*, **2007**, 5033–5044.

[355] Agustí, G.; Gaspar, A. B.; Muñoz, M. C.; Lacroix, P. G.; Real, J. A. *Aust. J. Chem.*, **2009**, *62*, 1155–1165.

[356] Soma, T.; Iwamoto, T. *J. Inclus. Phenom. Mol.*, **1996**, *26*, 161–173.

[357] Dong, W.; Zhu, L.-N.; Sun, Y.-Q.; Liang, M.; Liu, Z.-Q.; Liao, D.-Z.; Jiang, Z.-H.; Yan, S.-P.; Cheng, P. *Chem. Commun.*, **2003**, 2544–2545.

[358] Rodríguez-Velamazán, J. A.; Castro, M.; Palacios, E.; Burriel, R.; Kitazawa, T.; Kawasaki, T. *J. Phys. Chem. B*, **2007**, *111*, 1256–1261.

[359] Kosone, T.; Suzuki, Y.; Kanadani, C.; Saito, T.; Kitazawa, T. *Bull. Chem. Soc. Jpn.*, **2009**, *82*, 347–351.

[360] Range, K.-J.; Zabel, M.; Meyer, H.; Fischer, H. *Z. Naturforsch. B*, **1985**, *40*, 1618–1621.

[361] Wang, S.-P.; Chen, J.; Gao, D.-Z.; Song, Y.; Wang, Q.-M.; Liao, D.-Z.; Jiang, Z.-H.; Yan, S.-P. *J. Coord. Chem.*, **2005**, *58*, 1695–1702.

[362] Katz, M. J.; Michaelis, V. K.; Aguiar, P. M.; Yson, R.; Lu, H.; Kaluarachchi, H.; Batcherlor, R. J.; Schreckenbach, G.; Kroeker, S.; Patterson, H. H.; Leznoff, D. B. *Inorg. Chem.*, **2008**, *47*, 6353–6363.

[363] Soma, T.; Iwamoto, T. *Chem. Lett.*, **1994**, *23*, 821–824.

[364] Othong, J.; Wannarit, N.; Pakawatchai, C.; Youngme, S. *Acta Crystallogr. Sect. E*, **2014**, *70*, 107–110.

[365] Chippindale, A. M.; Cheyne, S. M.; Hibble, S. J. *Angew. Chem. Int. Ed.*, **2005**, *44*, 7942–7946.

[366] Colacio, E.; Lloret, F.; Kivekäs, R.; Ruiz, J.; Suárez-Varela, J.; Sundberg, M. R. *Chem. Commun.*, **2002**, 592–593.

[367] Kosone, T.; Kanadani, C.; Saito, T.; Kitazawa, T. *Polyhedron*, **2009**, *28*, 1930–1934.

[368] Korkmaz, N.; Karadağ, A.; Aydın, A.; Yanar, Y.; Karaman, I.; Tekin, Ş. *New J. Chem.*, **2014**, *38*, 4760–4773.

[369] Wang, S.-P.; Gao, D.-Z.; Song, Y.; Liu, Z.-Q.; Liao, D.-Z.; Jiang, Z.-H.; Yan, S.-P. *Inorg. Chim. Acta*, **2006**, *359*, 505–510.

[370] Kosone, T.; Tomori, I.; Kanadani, C.; Saito, T.; Mochida, T.; Kitazawa, T. *Dalton Trans.*, **2010**, *39*, 1719–1721.

[371] Muñoz, M. C.; Gaspar, A. B.; Galet, A.; Real, J. A. *Inorg. Chem.*, **2007**, *46*, 8182–8192.

[372] Agustí, G.; Muñoz, M. C.; Gaspar, A. B.; Real, J. A. *Inorg. Chem.*, **2008**, *47*, 2552–2561.

[373] Ludi, A.; Güdel, H. U.; Dvořák, V. *Helv. Chim. Acta*, **1967**, *50*, 2035–2039.

[374] Schröder, U.; Scholz, F. *Inorg. Chem.*, **2000**, *39*, 1006–1015.

[375] Kawasaki, T.; Kachi-Terajima, C.; Saito, T.; Kitazawa, T. *Bull. Chem. Soc. Jpn.*, **2008**, *81*, 268–273.

[376] Abrahams, S. C.; Zyontz, L. E.; Bernstein, J. L. *J. Chem. Phys.*, **1982**, *76*, 5458–5462.

[377] Kitazawa, T.; Hiruma, K.; Sato, H.; Tamura, K.; Yamagishi, A. *Dalton Trans.*, **2013**, *42*, 16680–16682.

[378] Guo, Y.; Liu, Z.-Q.; Zhao, B.; Feng, Y.-H.; Xu, G.-F.; Yan, S.-P.; Cheng, P.; Wang, Q.-L.; Liao, D.-Z. *CrystEngComm*, **2009**, *11*, 61–66.

[379] Wannarit, N.; Hahnvajanawong, V.; Pakawatchai, C.; Youngme, S. *Transit. Met. Chem.*, **2012**, *37*, 79–84.

[380] Theppitak, C.; Chainok, K. *Acta Crystallogr. Sect. E: Crystallogr. Commun.*, **2015**, *71*, m179–m180.

[381] Ovens, J. S.; Leznoff, D. B. *Dalton Trans.*, **2011**, *40*, 4140–4146.

[382] Assefa, Z.; Haire, R. G.; Sykora, R. E. *J. Solid State Chem.*, **2008**, *181*, 382–391.

[383] Galet, A.; Niel, V.; Muñoz, M. C.; Real, J. A. *J. Am. Chem. Soc.*, **2003**, *125*, 14224–14225.

[384] Soma, T.; Yuge, H.; Iwamoto, T. *Angew. Chem. Int. Ed. Engl.*, **1994**, *33*, 1665–1666.

[385] Arcís-Castillo, Z.; Muñoz, M. C.; Molnár, G.; Bousseksou, A.; Real, J. A. *Chem. Eur. J.*, **2013**, *19*, 6851–6861.

[386] Yoshida, K.; Akahoshi, D.; Kawasaki, T.; Saito, T.; Kitazawa, T. *Polyhedron*, **2013**, *66*, 252–256.

[387] Stier, A.; Range, K.-J. *Z. Krist.*, **1997**, *212*, 51.

[388] Yeung, W.-F.; Wong, W.-T.; Zuo, J.-L.; Lau, T.-C. *J. Chem. Soc., Dalton. Trans.*, **2000**, 629–631.

[389] Assefa, Z.; Staples, R. J.; Fackler, J. P., Jr. *Acta Crystallogr. Sect. C*, **1995**, *51*, 2527–2529.

[390] Ahern, J. C.; Roberts, R. J.; Follansbee, P.; McLaughlin, J.; Leznoff, D. B.; Patterson, H. H. *Inorg. Chem.*, **2014**, *53*, 7571–7579.

[391] Li, J.-Y.; Ni, Z.-P.; Yan, Z.; Zhang, Z.-M.; Chen, Y.-C.; Liu, W.; Tong, M.-L. *CrystEngComm*, **2014**, *16*, 6444–6449.

[392] Stier, A.; Range, K.-J. *Z. Naturforsch. B Chem. Sci.*, **1996**, *51*, 698–702.

[393] Kalachnikova, K.; Assefa, Z.; Sykora, R. E. *Acta Crystallogr. Sect. E*, **2007**, *63*, i162.

[394] Niel, V.; Thompson, A. L.; Muñoz, M. C.; Galet, A.; Goeta, A. E.; Real, J. A. *Angew. Chem. Int. Ed.*, **2003**, *42*, 3760–3763.

[395] Blatov, V. A. *Struct. Chem.*, **2012**, *23*, 955–963.

[396] Blatov, V. A.; Shevchenko, A. P.; Proserpio, D. M. *Cryst. Growth Des.*, **2014**, *14*, 3576–3586.

[397] Pyykkö, P. *Chem. Rev.*, **1997**, *97*, 597–636.

[398] Omary, M. A.; Webb, T. R.; Assefa, Z.; Shankle, G. E.; Patterson, H. H. *Inorg. Chem.*, **1998**, *37*, 1380–1386.

[399] Goodwin, A. L.; Keen, D. A.; Tucker, M. G. *Proc. Natl. Acad. Sci. USA*, **2008**, *105*, 18708–18713.

[400] Cliffe, M. J.; Goodwin, A. L. *J. Appl. Crystallogr.*, **2012**, *45*, 1321–1329.

[401] Koch, E.; Fisher, W. *Z. Krist.*, **1978**, *148*, 107–152.

[402] Ortiz, A. U.; Boutin, A.; Fuchs, A. H.; Coudert, F.-X. *Phys. Rev. Lett.*, **2012**, *109*, 195502.

[403] Hofmann, K. A.; Küspert, F. A. *Z. Anorg. Allg. Chem.*, **1897**, *15*, 204–207.

[404] Powell, H. M.; Rayner, J. H. *Nature*, **1949**, *163*, 566–567.

[405] Walker, G. F.; Hawthorne, D. G. *Trans. Faraday Soc.*, **1967**, *63*, 166–174.

[406] Finklea III, S. L.; Cathey, L.; Amma, E. L. *Acta Crystallogr. Sect. A*, **1976**, *32*, 529–537.

[407] Banerjee, R.; Phan, A.; Wang, B.; Knobler, C.; Furukawa, H.; O'Keeffe, M.; Yaghi, O. M. *Science*, **2008**, *319*, 939–943.

[408] Kostakis, G. E.; Powell, A. K. *Dalton Trans.*, **2010**, *39*, 2449–2450.

[409] Roberts, R. J.; Li, X.; Lacey, T. F.; Pan, Z.; Patterson, H. H.; Leznoff, D. B. *Dalton Trans.*, **2012**, *41*, 6992–6997.

[410] Shang, R.; Chen, S.; Wang, B.-W.; Wang, Z.-M.; Gao, S. *Angew. Chem. Int. Ed.*, **2016**, *55*, 2097–2100.

[411] Maris, G.; Ren, Y.; Volotchaev, V.; Zobel, C.; Lorenz, T.; Palstra, T. T. M. *Phys. Rev. B*, **2003**, *67*, 224423.

[412] Thornton, G.; Tofield, B. C.; Hewat, A. W. *J. Solid State Chem.*, **1986**, *61*, 301–307.

[413] Rotiroti, N.; Tamazyan, R.; Smaalen, S. v.; Mukovskii, Y. *Acta Crystallogr. Sect. C*, **2005**, *61*, i83–i85.

[414] Campbell, B. J.; Stokes, H. T.; Tanner, D. E.; Hatch, D. M. *J. Appl. Crystallogr.*, **2006**, *39*, 607–614.

[415] Kareis, C. M.; Lapidus, S. H.; Stephens, P. W.; Miller, J. S. *Inorg. Chem.*, **2012**, *51*, 3046–3050.

[416] Spek, A. L. *J. Appl. Crystallogr.*, **2003**, *36*, 7–13.

[417] van der Sluis, P.; Spek, A. L. *Acta Crystallogr. Sect. A*, **1990**, *46*, 194–201.

[418] Hervert, K. L. *Encyclopedia of Reagents for Organic Synthesis*; John Wiley & Sons, Ltd: London, UK, 2001.

[419] Goldenberg, N. *Trans. Faraday Soc.*, **1940**, *36*, 847–854.

[420] Qureshi, A. M.; Sharpe, A. G. *J. Inorg. Nucl. Chem.*, **1968**, *30*, 2269–2270.

[421] Entley, W. R.; Girolami, G. S. *Inorg. Chem.*, **1994**, *33*, 5165–5166.

[422] Chester, A. W.; Schweizer, A. E. *Inorg. Nucl. Chem. Lett.*, **1971**, *7*, 451 – 454.

[423] Tomeno, I.; Tsunoda, Y.; Oka, K.; Matsuura, M.; Nishi, M. *Phys. Rev. B*, **2009**, *80*, 104101.

[424] Leguy, A.; Goni, A. R.; Frost, J. M.; Skelton, J.; Brivio, F.; Rodriguez-Martinez, X.; Weber, O. J.; Pallipurath, A. R.; Alonso, M. I.; Campoy-Quiles, M.; Weller, M. T.; Nelson, J.; Walsh, A.; Barnes, P. R. F. *Phys. Chem. Chem. Phys.*, **2016**, DOI:10.1039/C6CP03474H.

[425] Conterio, M. J.; Goodwin, A. L.; Tucker, M. G.; Keen, D. A.; Dove, M. T.; Peters, L.; Evens, J. S. O. *J. Phys.: Condens. Matter*, **2008**, *20*.

[426] Adamson, J.; Funnell, N. P.; Thompson, A. L.; Goodwin, A. L. *Phys. Chem. Chem. Phys.*, **2014**, *16*, 2654–2659.

[427] Wasylishen, R. E.; Knop, O.; Macdonald, J. B. *Solid State Commun.*, **1985**, *56*, 581–582.

[428] Brivio, F.; Frost, J. M.; Skelton, J. M.; Jackson, A. J.; Weber, O. J.; Weller, M. T.; Goñi, A. R.; Leguy, A. M. A.; Barnes, P. R. F.; Walsh, A. *Phys. Rev. B*, **2015**, *92*, 144308.

[429] Quarti, C.; Mosconi, E.; De Angelis, F. *Chem. Mater.*, **2014**, *26*, 6557–6569.

[430] Graetsch, H. A. *Acta Crystallogr. Sect. B*, **2009**, *65*, 543–550.

[431] Chen, S.; Shang, R.; Hu, K.-L.; Wang, Z.-M.; Gao, S. *Inorg. Chem. Front.*, **2014**, *1*, 83–98.

[432] Xu, W.-J.; Chen, S.-L.; Hu, Z.-T.; Lin, R.-B.; Su, Y.-J.; Zhang, W.-X.; Chen, X.-M. *Dalton Trans.*, **2016**, *45*, 4224–4229.

[433] Du, Z.-Y.; Zhao, Y.-P.; Zhang, W.-X.; Zhou, H.-L.; He, C.-T.; Xue, W.; Wang, B.-Y.; Chen, X.-M. *Chem. Commun.*, **2014**, *50*, 1989–1991.

[434] Du, Z.-Y.; Zhao, Y.-P.; He, C.-T.; Wang, B.-Y.; Xue, W.; Zhou, H.-L.; Bai, J.; Huang, B.; Zhang, W.-X.; Chen, X.-M. *Cryst. Growth Des.*, **2014**, *14*, 3903–3909.

[435] Thiele, V. G.; Messer, D. *Z. Anorg. Allg. Chem.*, **1980**, *464*, 255–267.

[436] Xie, K.-P.; Xu, W.-J.; He, C.-T.; Huang, B.; Du, Z.-Y.; Su, Y.-J.; Zhang, W.-X.; Chen, X.-M. *CrystEngComm*, **2016**, *18*, 4495–4498.

[437] Schlueter, J. A.; Manson, J. L.; Hyzer, K. A.; Geiser, U. *Inorg. Chem.*, **2004**, *43*, 4100–4102.

[438] Bermúdez-García, J. M.; Sánchez-Andújar, M.; Yáñez-Vilar, S.; Castro-García, S.; Artiaga, R.; López-Beceiro, J.; Botana, L.; Alegría, Á.; Señarís-Rodríguez, M. A. *Inorg. Chem.*, **2015**, *54*, 11680–11687.

[439] Bermudez-Garcia, J. M.; Sanchez-Andujar, M.; Yanez-Vilar, S.; Castro-Garcia, S.; Artiaga, R.; Lopez-Beceiro, J.; Botana, L.; Allegria, A.; Senaris-Rodriguez, M. A. *J. Mater. Chem. C*, **2016**, *4*, 4889–4898.

[440] Li, W.; Thirumurugan, A.; Barton, P. T.; Lin, Z.; Henke, S.; Yeung, H. H.-M.; Wharmby, M. T.; Bithell, E. G.; Howard, C. J.; Cheetham, A. K. *J. Am. Chem. Soc.*, **2014**, *136*, 7801–7804.

[441] Tong, M.-L.; Ru, J.; Wu, Y.-M.; Chen, X.-M.; Chang, H.-C.; Mochizuki, K.; Kitagawa, S. *New J. Chem.*, **2003**, *27*, 779–782.

[442] Ziegler, B.; Witzel, M.; Babel, D. *Z. Anorg. Allg. Chem.*, **1991**, *600*, 239–248.

[443] Her, J.-H.; Stephens, P. W.; Kareis, C. M.; Moore, J. G.; Min, K. S.; Park, J.-W.; Bali, G.; Kennon, B. S.; Miller, J. S. *Inorg. Chem.*, **2010**, *49*, 1524–1534.

[444] Chapman, K. W.; Chupas, P. J.; Kepert, C. J. *J. Am. Chem. Soc.*, **2006**, *128*, 7009–7014.

[445] Mautner, F. A.; Hanna, S.; Cortés, R.; Lezama, L.; Barandika, M. G.; Rojo, T. *Inorg. Chem.*, **1999**, *38*, 4647–4652.

[446] Zhao, X.-H.; Huang, X.-C.; Zhang, S.-L.; Shao, D.; Wei, H.-Y.; Wang, X.-Y. *J. Am. Chem. Soc.*, **2013**, *135*, 16006–16009.

[447] Saines, P. J. Structural Studies of Lanthanide Double Perovskites. Ph.D. thesis, Department of Chemistry, University of Sydney, 2008.

[448] Howard, C. J. Private Communication, **2016**.

[449] Aleksandrov, K. S.; Bartolomé, J. *Phase Transit.*, **2001**, *74*, 255–335.

[450] Carpenter, M. A.; Salje, E. K. H.; Howard, C. J. *Phys. Rev. B*, **2012**, *85*, 224430.

[451] ISOTROPY Software Suite, iso.byu.edu.

[452] Stokes, H. T.; Hatch, D. M. *J. Appl. Crystallogr.*, **2005**, *38*, 237–238.

[453] Stokes, H. T.; Hatch, D. M. *J. Appl. Crystallogr.*, **2002**, *35*, 379.

[454] Hatch, D. M.; Stokes, H. T. *Phys. Rev. B*, **2001**, *65*, 014113.

[455] Mautner, F. A.; Krischner, H.; Kratky, C. *Monatsh.Chem.*, **1988**, *119*, 1245–1249.

[456] Wu, Y.; Kobayashi, A.; Halder, G. J.; Peterson, V. K.; Chapman, K. W.; Lock, N.; Southon, P. D.; Kepert, C. J. *Angew. Chem. Int. Ed.*, **2008**, *120*, 9061–9064.

[457] Rimmer, L. H. N.; Dove, M. T.; Goodwin, A. L.; Palmer, D. C. *Phys. Chem. Chem. Phys.*, **2014**, *16*, 21144–21152.

[458] Babel, D. *Z. Naturforsch. B*, **1982**, *37*, 1534.

[459] Anderson, M. T.; Greenwood, K. B.; Taylor, G. A.; Poeppelmeier, K. R. *Prog. Solid State Chem.*, **1993**, *22*, 197–233.

[460] Lenz, A.; Múller-Buschbaum, H. *J. Less Common Met.*, **1990**, *161*, 141–146.

[461] Ryan, R. R.; Swanson, B. I. *Acta Crystallogr. Sect. B*, **1978**, *34*, 1398–1399.

[462] Medina Córdoba, L.; Echeverría, G. A.; Piro, O. E.; Gómez, M. I. *J. Therm. Analysis Calorim.*, **2015**, *120*, 1827–1834.

[463] Medina Córdoba, L.; Morán, J. A.; Santos, S.; Piro, O. E.; Gómez, M. I. *J. Chem. Crystallogr.*, **2011**, *41*, 1280–1284.

[464] Duyker, S. G.; Halder, G. J.; Southon, P. D.; Price, D. J.; Edwards, A. J.; Peterson, V. K.; Kepert, C. J. *Chem. Sci.*, **2014**, *5*, 3409–3417.

[465] Gil, D. M.; Santo, A. D.; Pomiro, F.; Echeverría, G. A.; Piro, O. E.; Carbonio, R. E.; Altabef, A. B. *Polyhedron*, **2014**, *73*, 51–58.

[466] Benedek, N. A.; Fennie, C. J. *Phys. Rev. Lett.*, **2011**, *106*, 107204.

[467] Oh, Y. S.; Luo, X.; Huang, F.-T.; Wang, Y.; Cheong, S.-W. *Nature Mater.*, **2015**, *14*, 407–413.

[468] Robson, R. *J. Chem. Soc., Dalton. Trans.*, **2000**, 3735–3744.

[469] Cordero, B.; Gomez, V.; Platero-Prats, A. E.; Reves, M.; Echeverria, J.; Cremades, E.; Barragan, F.; Alvarez, S. *Dalton Trans.*, **2008**, 2832–2838.

Appendix A

A1 PPN dicyanometallate salts: [PPN]Au(CN)$_2$ and [PPN]Ag(CN)$_2$

A1.1 Single crystal x-ray diffraction

Single-crystal X-ray diffraction data of starting materials [PPN]Au(CN)$_2$ (**S1**) and [PPN]Ag(CN)$_2$ (**S2**) were collected using an Oxford Diffraction (Rigaku Oxford Diffraction) SuperNova diffractometer fitted with an Oxford Cryosystems Cryostream 700 Plus open-flow nitrogen cooling device.[317] CrysAlisPro was used for data collection and reduction.[319] The structures were solved *ab initio* using SIR92.[320] All structures were refined with full-matrix least-squares on F^2 using CRYSTALS.[322,323] Hydrogen atoms were visible in the difference Fourier map and treated in the usual manner.[324] Key crystallographic details can be found in Table A1.1. Associated .cif and .fcf files can be found in the Electronic Appendix. The crystal structures are represented in Figure A1.1.

A1.2 Powder x-ray diffraction

Table A1.1: Crystallographic details of [PPN]Au(CN)$_2$ and [PPN]Ag(CN)$_2$.

Compound	[PPN]Au(CN)$_2$	[PPN]Ag(CN)$_2$
Empirical formula	$Au_1P_2N_3C_{38}H_{30}$	$Ag_1P_2N_3C_{38}H_{30}$
Formula weight (g mol^{-1})	787.59	698.49
Crystal System	Triclinc	Triclinc
Space Group	$P\bar{1}$ (No. 2)	$P\bar{1}$ (No. 2)
Z	2	2
Radiation (Å)	Cu K$_\alpha$, $\lambda = 1.54180$	Cu K$_\alpha$, $\lambda = 1.54180$
Crystal colour	Colourless	Colourless
Crystal size (mm)	0.02×0.01×0.15	0.04×0.01×0.13
Temperature (K)	280.0(2)	280.0(4)
a (Å)	9.7335(3)	9.7325(10)
b (Å)	11.0381(5)	10.9975(14)
c (Å)	17.0129(5)	17.099(2)
α (°)	73.058(3)	73.500(11)
β (°)	81.926(2)	82.138(9)
γ (°)	79.666(3)	80.190(10)
V (Å^3)	1712.60(11)	1721.5(4)
μ (mm^{-1})	9.167	5.81
Reflections ($I > 2\sigma(I)$)	6734	7229
R (F_o)	0.0207	0.0333
R$_w$ (F_o)	0.0524	0.0803
GOF	0.9995	0.7792

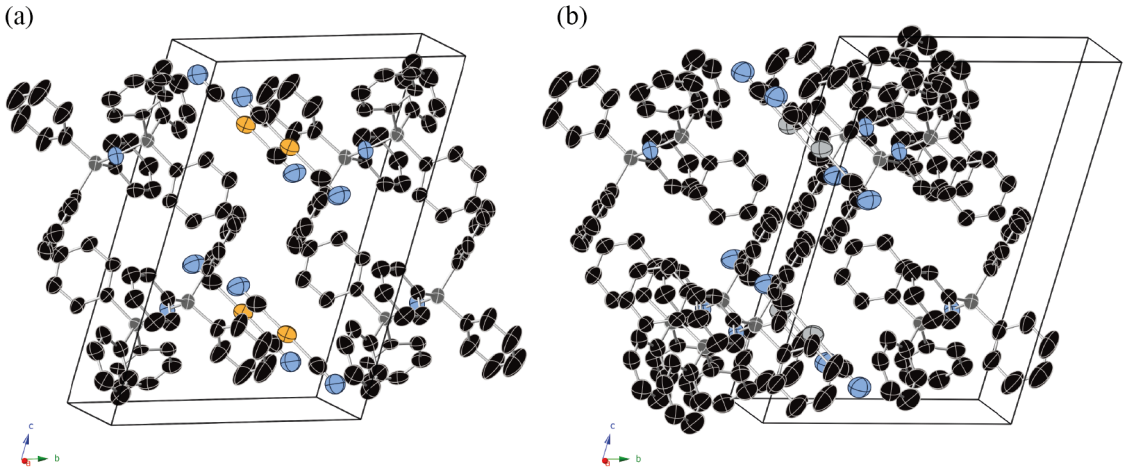

Figure A1.1: Representations of the crystal structures of (a) [PPN]Au(CN)$_2$ and (b) [PPN]Ag(CN)$_2$. Second disordered component of each phenyl ring not shown for clarity. Hydrogen not shown for clarity.

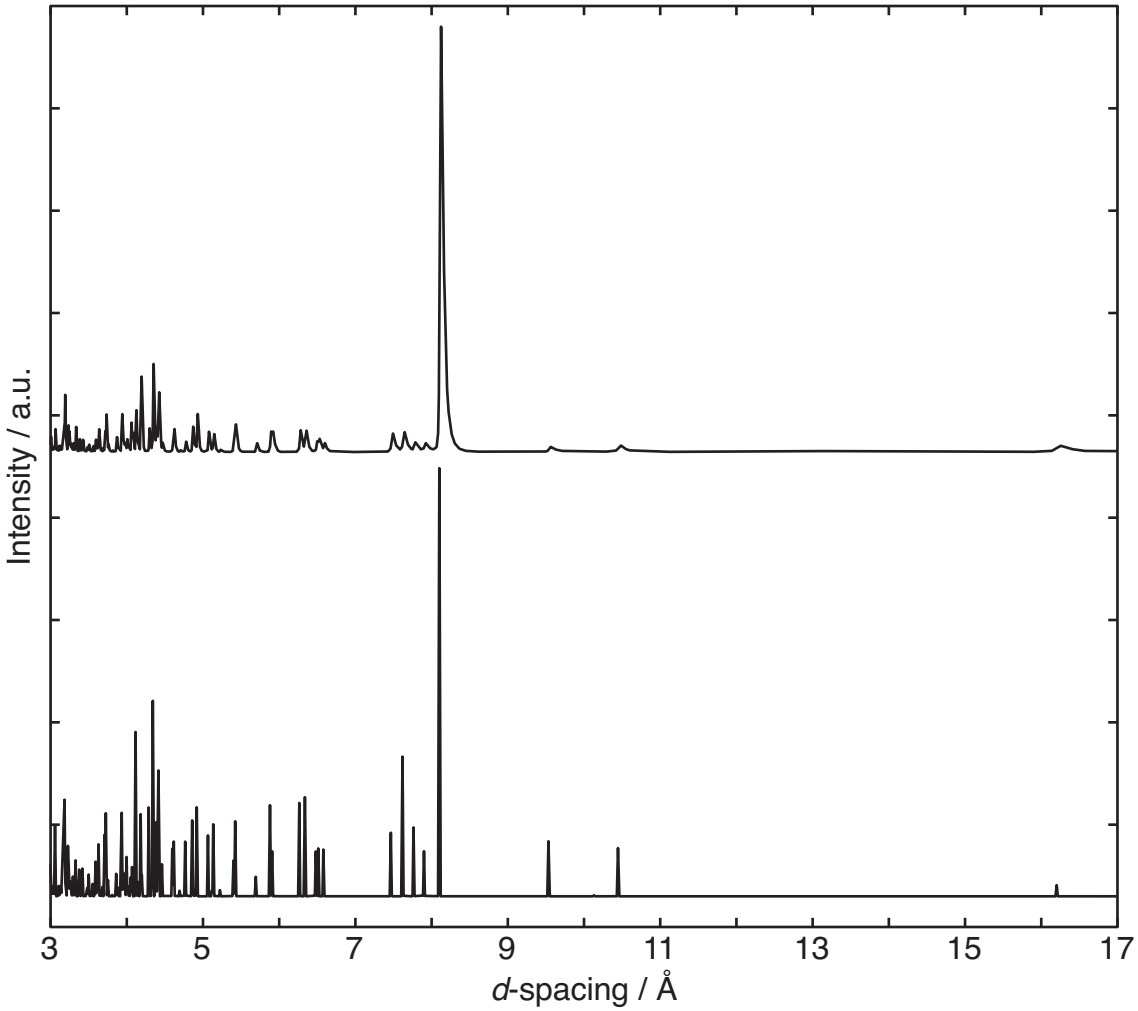

Figure A1.2: Experimental (top) and predicted (bottom) powder patterns for [PPN]Au(CN)$_2$.

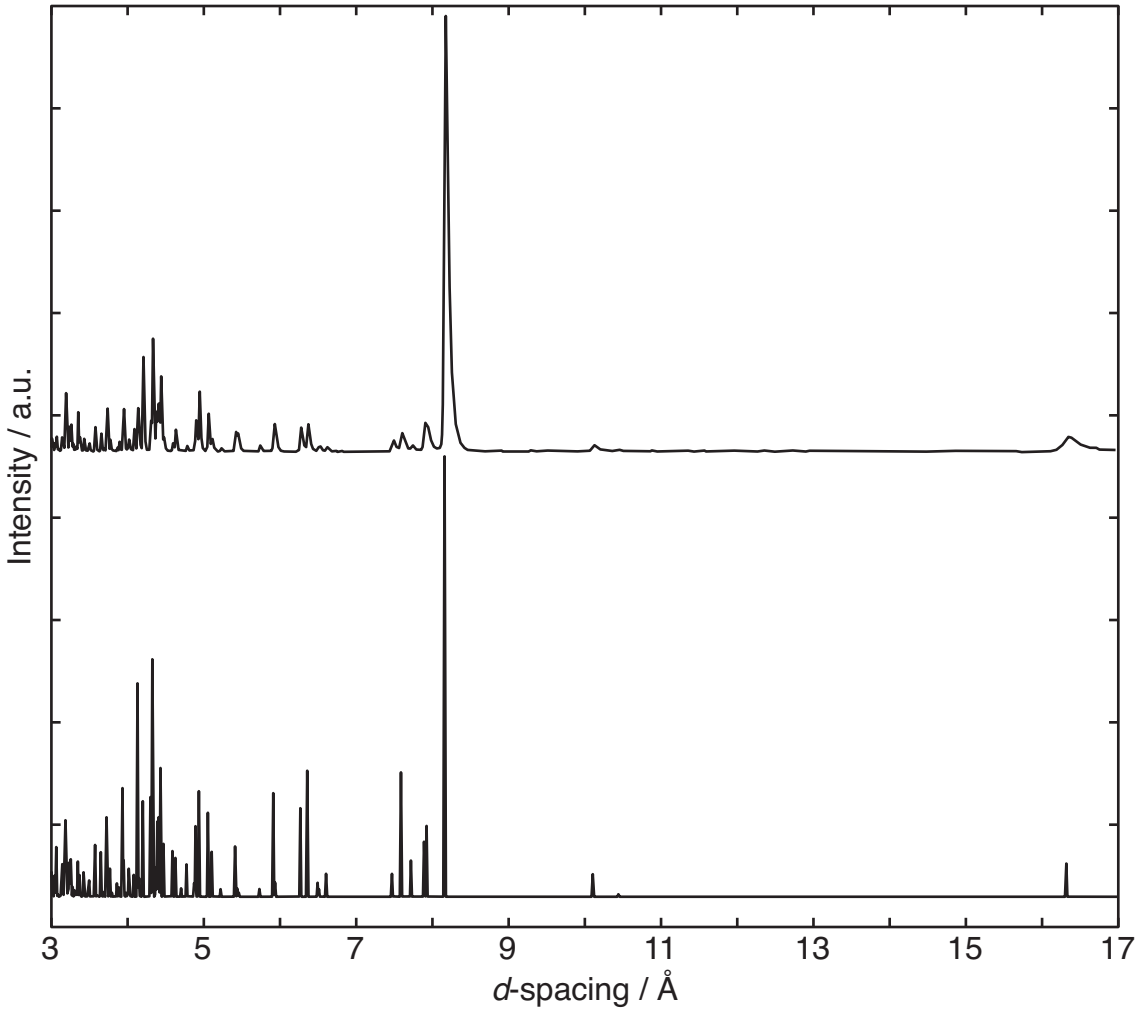

Figure A1.3: Experimental (top) and predicted (bottom) powder patterns for $[PPN]Ag(CN)_2$.

A2 $[NBu_4]_{0.5}Cd[Ag(CN)_2]_{2.5}$

Variable temperature unit cell parameters determined by single crystal diffraction are given in Table A2.2.

Table A2.2: Variable temperature unit cell parameters of $[NBu_4]_{0.5}Cd^{II}[Ag(CN)_2]_{2.5}$ (**2**) determined from single crystal diffraction.

Run	T / K	a / Å	b / Å	c / Å	β / °	V / Å^3
1	300	16.4746(10)	13.7363(7)	18.1177(10)	105.035(6)	3959.7(4)
2	100	16.2218(5)	13.9534(3)	18.0142(5)	106.186(3)	3915.186(3)
3	150	16.2725(3)	13.9069(2)	18.0406(3)	105.9628(17)	3925.17(11)
4	200	16.3346(3)	13.849(19)	18.0701(3)	105.691(17)	3935.47(11)
5	250	16.4028(3)	13.7921(2)	18.0929(3)	105.3864(19)	3946.43(12)
6	300	16.4766(4)	13.7317(3)	18.1122(4)	105.035(2)	3957.61(15)
7	350	16.5585(9)	13.6675(6)	18.1352(9)	104.682(6)	3970.2(4)
8	400	16.6326(14)	13.6086(9)	18.1559(13)	104.248(9)	3983.1(5)

A3 Tolerance factors of superperovskites

Tolerance factors, α for various 'superperovskites' were calculated using a method adapted from Ref. 146. As detailed in that paper, Goldschmidt's tolerance factor (eqn. A3.1):

$$\alpha = (\boldsymbol{r}_{\mathrm{A}} + \boldsymbol{r}_{\mathrm{X}})/\sqrt{2}(\boldsymbol{r}_{\mathrm{B}} + \boldsymbol{r}_{\mathrm{X}}), \tag{A3.1}$$

where $\boldsymbol{r}_{\mathrm{i}}$ are the ionic radii for the species in a perovskite ABX_3, can be adapted for systems with molecular A and X species. Effective radii for A and X must be defined. This is done by measuring the radius from the centre of mass of the species to the outermost atom (from crystallographic data) and, to this number, adding the radius of the outermost atom. For example $\boldsymbol{r}_{\mathrm{A_{eff}}} = \boldsymbol{r}_{\mathrm{A_{mass}}} + \boldsymbol{r}_{\mathrm{A_{ion}}}$. Combining this approach with Goldschmidt's we have:

$$\alpha = (\boldsymbol{r}_{\mathrm{A_{eff}}} + \boldsymbol{r}_{\mathrm{X_{eff}}})/\sqrt{2}(\boldsymbol{r}_{\mathrm{B}} + 0.5\boldsymbol{h}_{\mathrm{X_{eff}}}), \tag{A3.2}$$

where $\boldsymbol{h}_{\mathrm{X_{eff}}}$ is the length of the molecular linker. Values of $\boldsymbol{r}_{\mathrm{A_{mass}}}$ and $\boldsymbol{r}_{\mathrm{X_{mass}}}$ were measured from single crystal data and combined with tabulated data for ionic radii and covalent radii.[149,469]. Where there are crystallographical distinct X both were measured and a mean taken. In the case of disordered crystal structures a mean position was used. Numerical values are listed in Table A3.3.

While these PPN systems lack hydrogen bonding it is important to treat these tolerance factors rather cautiously. Given the flexibility of dicyanometallate linkers, the variety of conformations known for $[PPN]^+$, and problems with defining

Table A3.3: Tolerance factor calculations for some PPN superperovskites. COM stands for centre of mass. All distances in Å.

Compound	$r_{A_{eff}}$	$r_{X_{eff}}$	r_B	$h_{X_{eff}}$	α	A COM to edge	r(outer elem)
PPNMn[Au(CN)$_2$]$_3$ (**5b**)	6.31	1.482	0.83	9.148	1.020	5.58	0.73
PPNCd[Au(CN)$_2$]$_3$ (**5c**)	6.30	1.467	0.95	9.111	0.998	5.57	0.73
PPNNi[Au(CN)$_2$]$_3$ [310]	5.99	1.437	0.69	9.12	1.001	5.26	0.73

Compound	X COM to central atom	central atom	r(central atom)	X COM to end	r(end atom)	Temperature / K
PPNMn[Au(CN)$_2$]$_3$ (**5b**)	0.112	Au	1.37	3.114	1.46	150
PPNCd[Au(CN)$_2$]$_3$ (**5c**)	0.097	Au	1.37	3.096	1.46	300
PPNNi[Au(CN)$_2$]$_3$ [310]	0.067	Au	1.370	3.1	1.46	293

appropriate sets of radii. However, they could be extremely useful for identifying the interactions that cause the tolerance factor concept to breakdown in these, and other,[168] systems.

A4 Thermogravimetric analysis

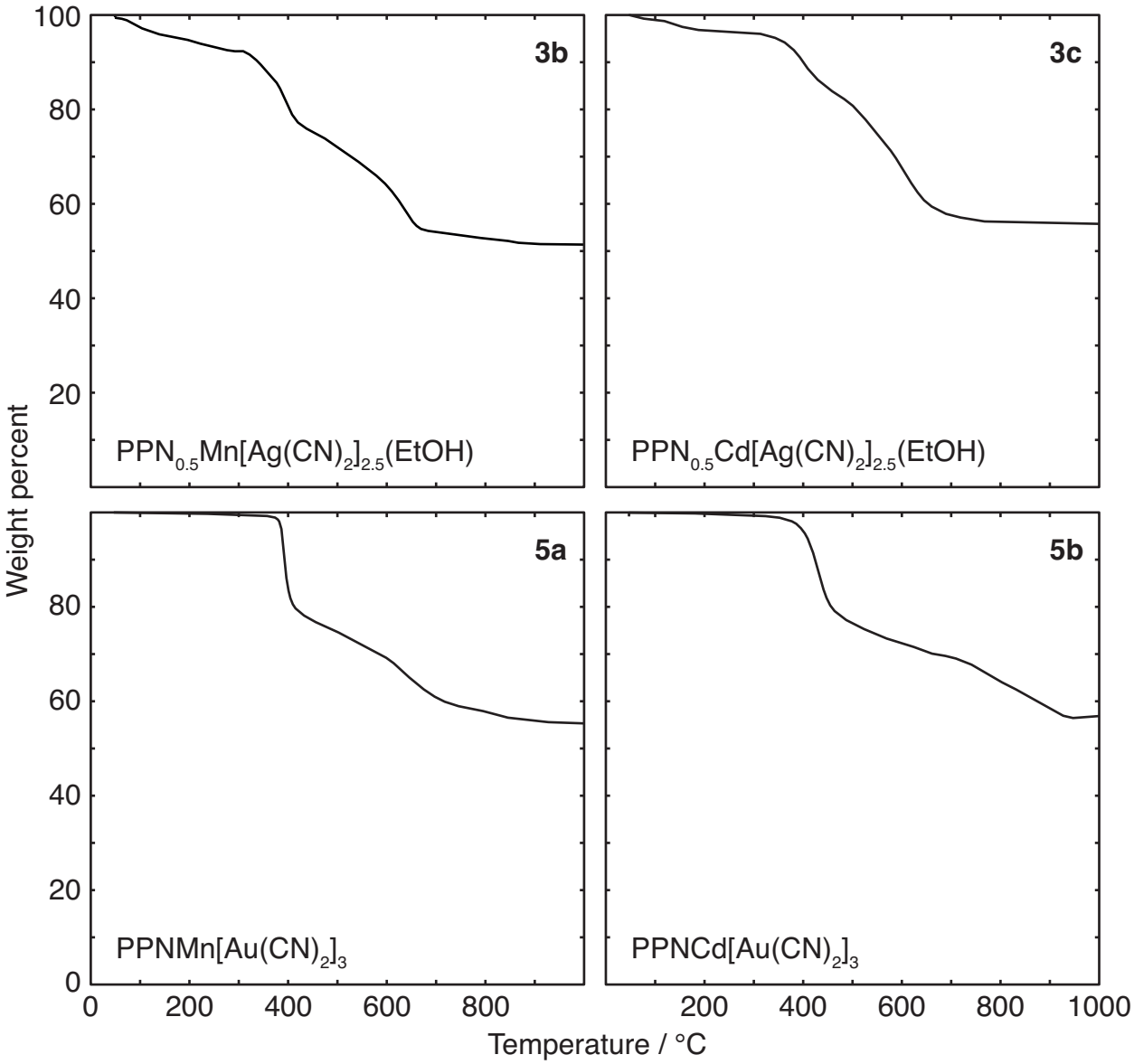

Figure A4.4: Thermogravimetric analysis for samples **3b**, **3c**, **5a**, and **5c**. Loss of ethanol prior to decomposition is evident for **3b** and **3c**.

Appendix B

B1 Superperovskite DSC

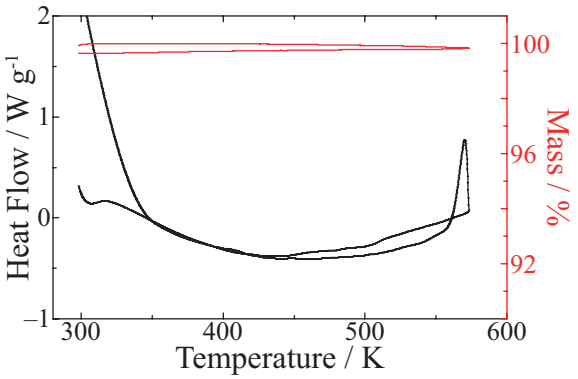

Figure B1.1: DSC and simultaneous TGA data for $[PPN]Ni[AuCN)_2]_3$. Negligible mass loss was observed. Features at the highest and lowest temperatures are due to instrumental factors.

B2 Superperovskite diffraction data

B2.1 I11

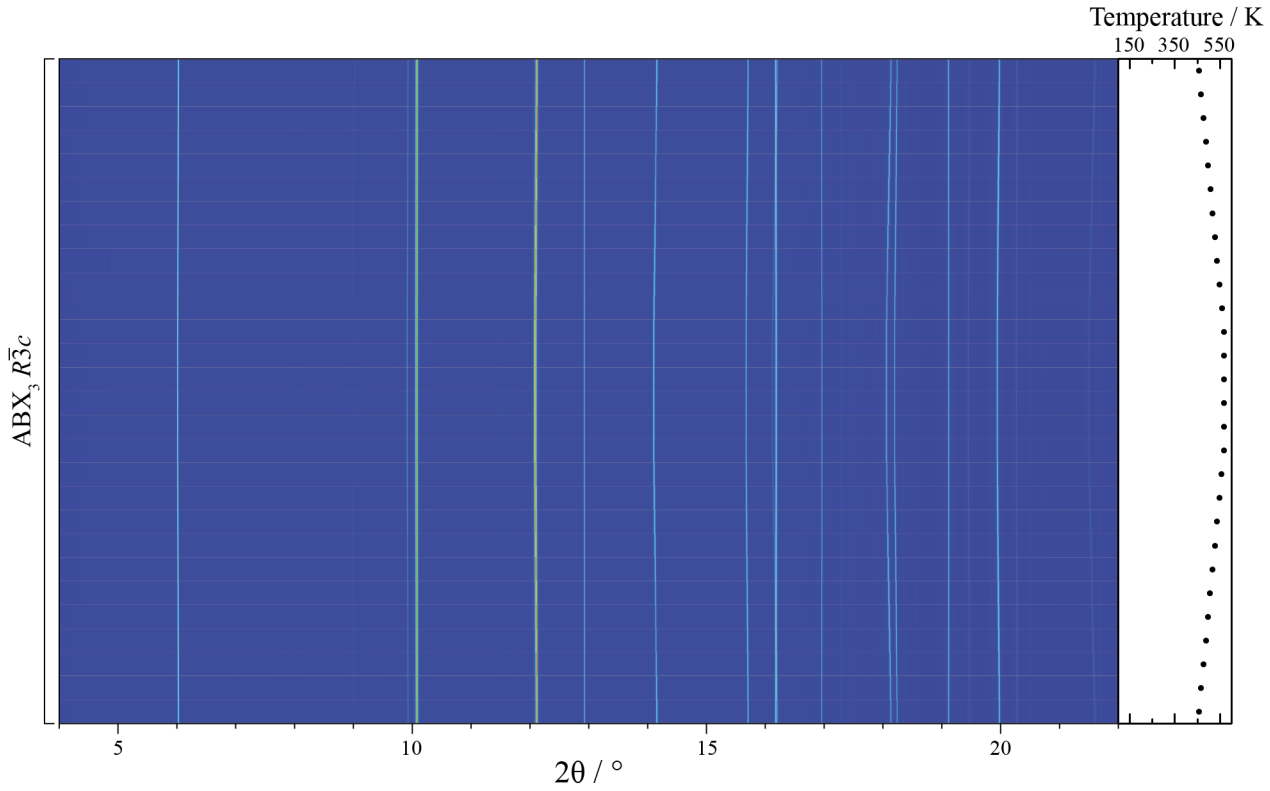

Figure B2.2: High temperature powder diffraction for [PPN]Ni[Au(CN)$_2$]$_3$.

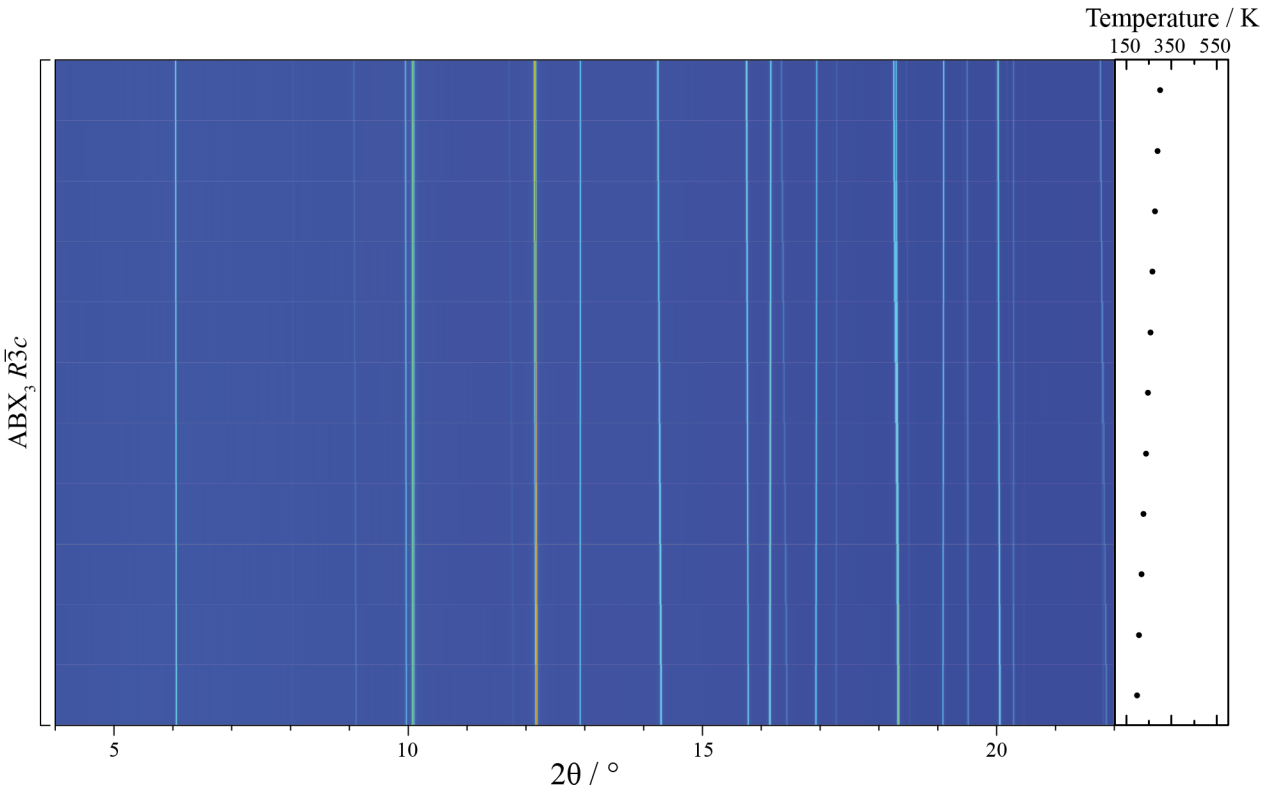

Figure B2.3: Repeated low temperature powder diffraction for [PPN]Ni[Au(CN)$_2$]$_3$

B2.2 Thermal expansion

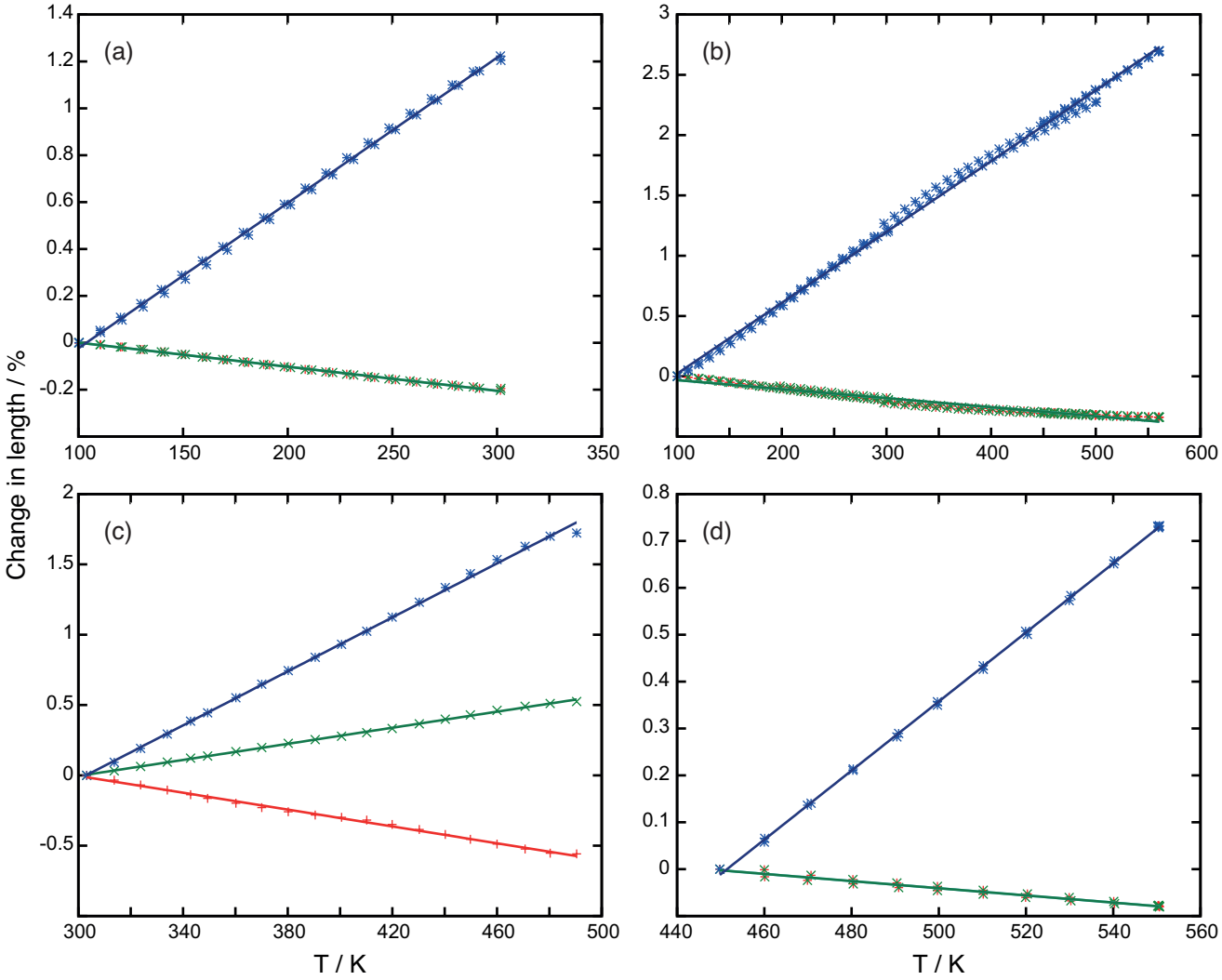

Figure B2.4: Fits to variable temperature diffraction data of some dicyanometallate perovskites. X_1 (red), X_2 (green), X_3 (blue) with fits shown as solid lines. (a) [PPN]Ni[Au(CN)$_2$]$_3$ linear range; $\alpha_{X_1} = \alpha_{X_2} = \alpha_a = -10.26(10)\,\mathrm{MK}^{-1}$, $\alpha_{X_3} = \alpha_c = +62.0(4)\,\mathrm{MK}^{-1}$, and $\alpha_V = +41.4(3)\,\mathrm{MK}^{-1}$ (b) [PPN]Ni[Au(CN)$_2$]$_3$ full range; $\alpha_{X_1} = \alpha_{X_2} = \alpha_a = -7.48(15)\,\mathrm{MK}^{-1}$, $\alpha_{X_3} = \alpha_c = +58.8(2)\,\mathrm{MK}^{-1}$, and $\alpha_V = +43.49(20)\,\mathrm{MK}^{-1}$ (c) *M*-[PPN]Mn[Au(CN)$_2$]$_3$; $\alpha_{X_1} = -29.0(1.0)\,\mathrm{MK}^{-1}$, $\alpha_{X_2} = +28.6(4)\,\mathrm{MK}^{-1}$, $\alpha_{X_3} = +96.0(1.2)\,\mathrm{MK}^{-1}$, and $\alpha_V = +94.6(1.2)\,\mathrm{MK}^{-1}$ where the principal directions correspond to $X_1 = 0.9773\mathbf{a} - 0.2120\mathbf{c}$; $X_2 = 0.3523\mathbf{a} + 0.9359\mathbf{c}$; $X_3 = \mathbf{b}$ (d) *R*-[PPN]Mn[Au(CN)$_2$]$_3$; $\alpha_{X_1} = \alpha_{X_2} = \alpha_a = -7.6(3)\,\mathrm{MK}^{-1}$, $\alpha_{X_3} = \alpha_c = +73.6(3)\,\mathrm{MK}^{-1}$, and $\alpha_V = +58.3(6)\,\mathrm{MK}^{-1}$

B2.3 In-house

DSC-recovered samples

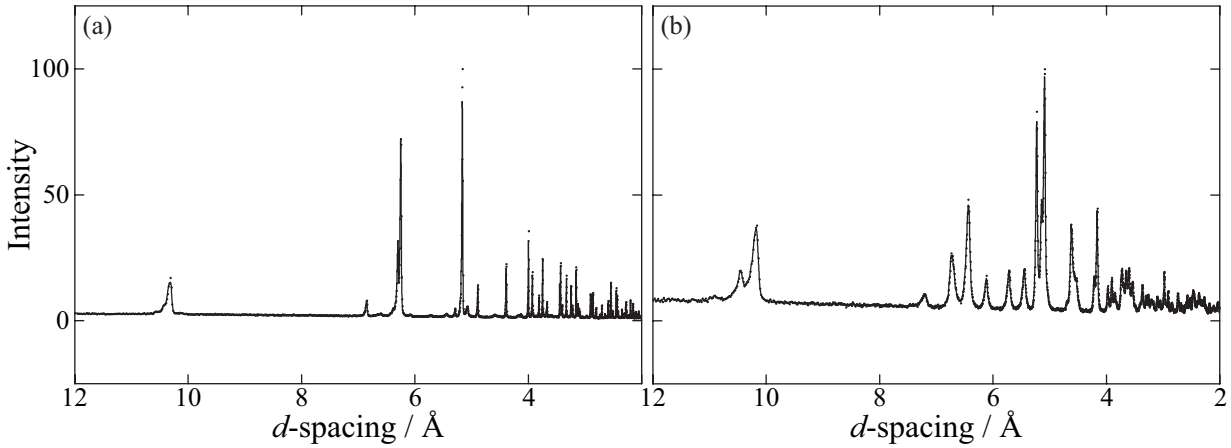

Figure B2.5: Powder diffraction patterns of superperovskites recovered from DSC experiment (a) [PPN]Mn[Au(CN)$_2$]$_3$ (b) [PPN]Cd[Au(CN)$_2$]$_3$. [PPN]Mn[Au(CN)$_2$]$_3$ appears to be purely rhombohedral whereas [PPN]Cd[Au(CN)$_2$]$_3$ returns to the monoclinic form.

B3 Ion-inclusion $ABX_3 \cdot AY$ perovskite

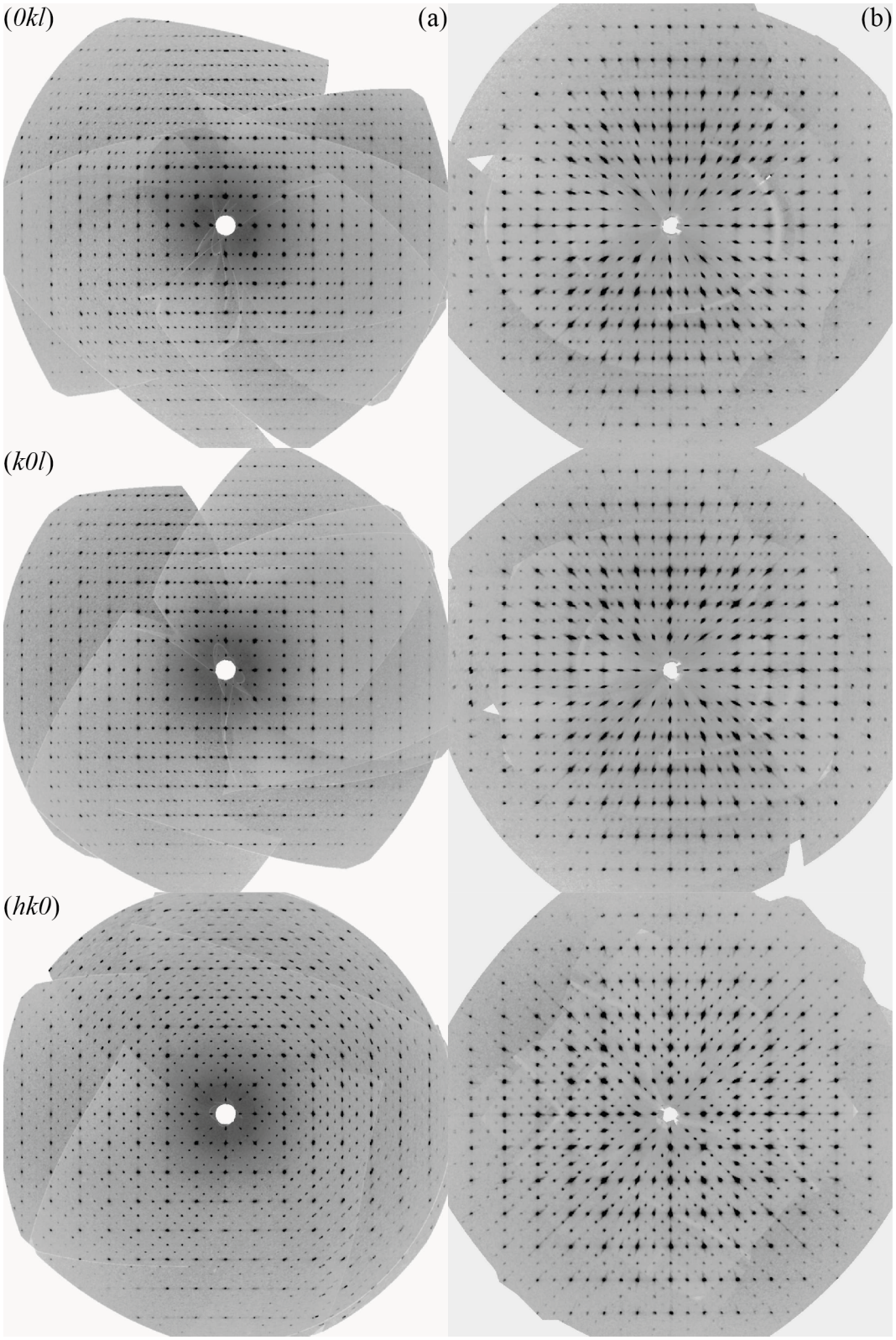

Figure B3.6: Reciprocal space reconstructions of the $0kl$, $h0l$, and $hk0$ planes for data collected at 30 K on beamline I19 using $\lambda = 0.6889$ Å(a) and at 298(1) K using Cu_{K_α} (b).

B4 Orientation in $[PPN]Mn_2[Ag(CN)_2]_5(EtOH)_2$ and R-$[PPN]Mn[Ag(CN)_2]_3$

Ethanol was removed from $[PPN]Mn_2[Ag(CN)_2]_5(EtOH)_2$ in a single-crystal to single-crystal fashion. The orientation matrices for the same crystal before (300 K) and after (475 K) desolvation were superimposed to allow comparison of the physical orientations of the two crystal structures. The unit cells are shown overlapped in Figure B4.7.

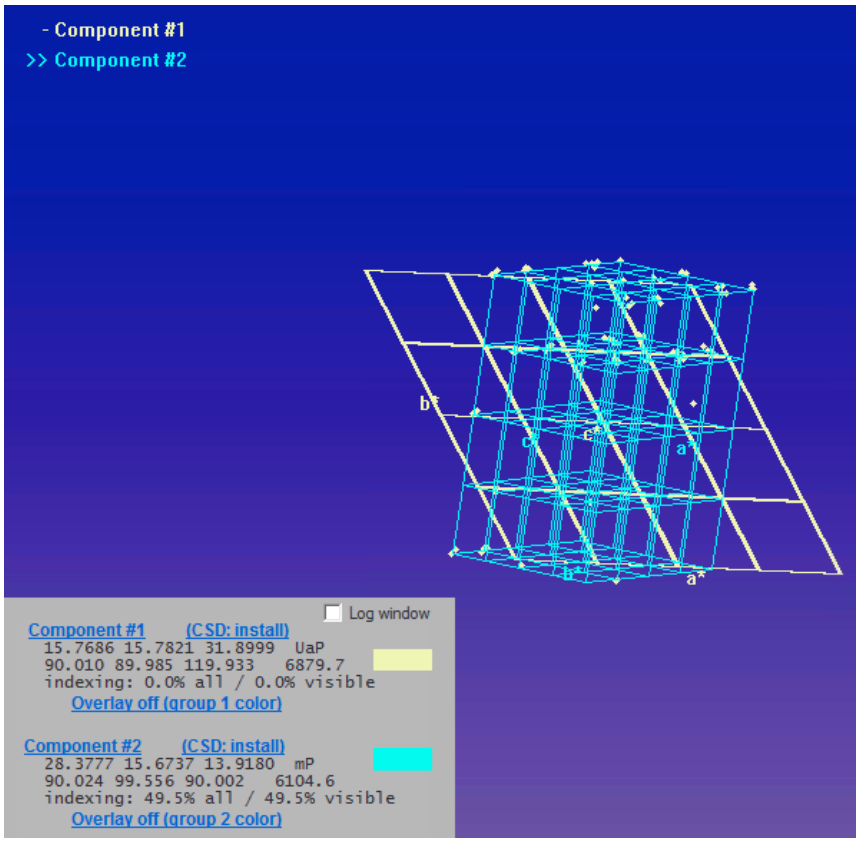

Figure B4.7: Orientation of the unit cells of $[PPN]Mn_2[Ag(CN)_2]_5(EtOH)_2$ and R-$[PPN]Mn[Ag(CN)_2]_3$ shown looking down c^* of the perovskite phase.

Appendix C

C1 Modulated structure of $[NEt_4]Ag[Ag(CN)_2]_2$

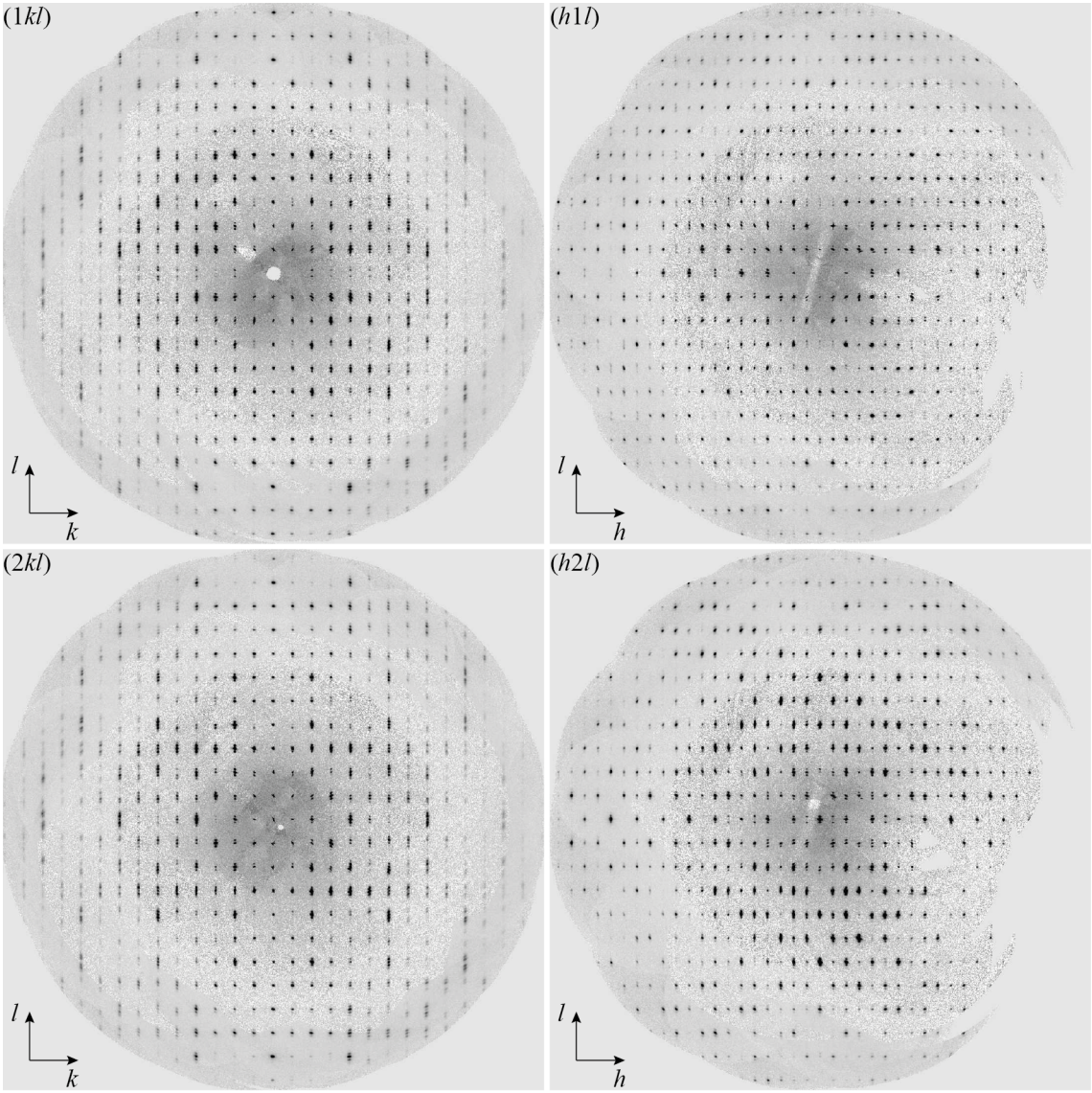

Figure C1.1: Reciprocal space reconstructions of diffraction data for $[NEt_4]Ag[Ag(CN)_2]_2$. Satellite peaks are observed along the l direction.

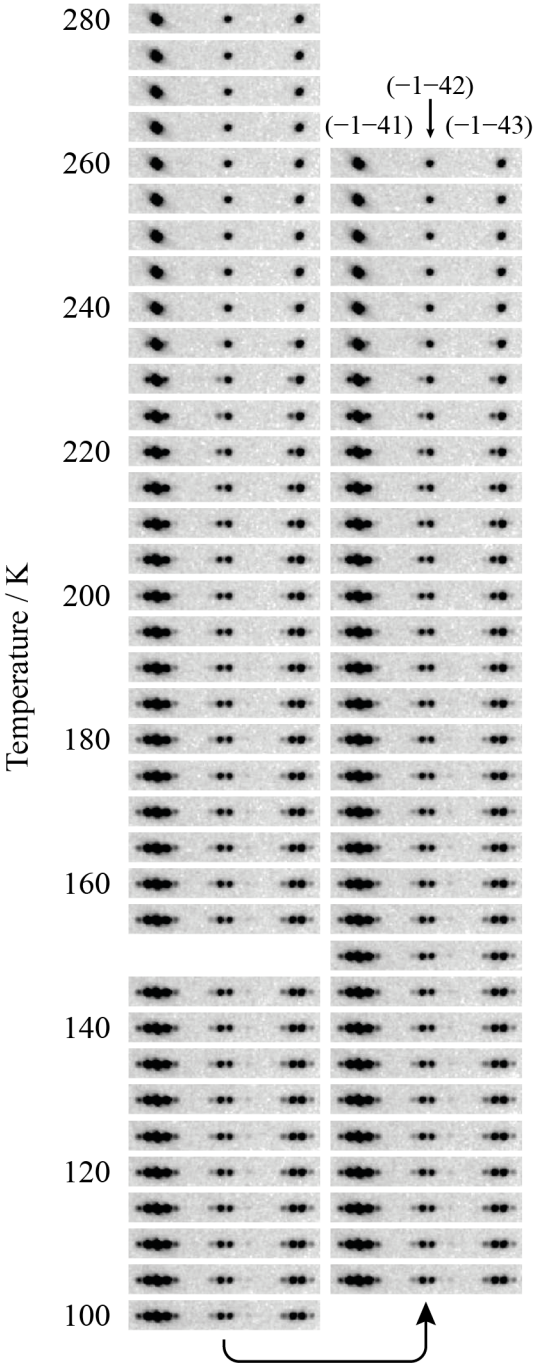

Figure C1.2: Evolution of some satellite peaks in the $-1kl$ layer of reciprocal space for a crystal of $[NEt_4]Ag[Ag(CN)_2]_2$. The hkl values of the main reflections are indicated at the top right.

Table C1.1: Single crystal unit cells from identical short collections for $[NEt_4]Ag[Ag(CN)_2]_2$.

T / K	a / Å	b / Å	c / Å	α / °	β / °	γ / °	V / Å^3	No. peaks Main	No. peaks 1st satellite	No. peaks 2nd peaks	$\mathbf{q_x}$	$\mathbf{q_y}$	$\mathbf{q_z}$
280	16.613(9)	11.311(5)	9.265(5)	89.93(4)	90.08(4)	90.17(4)	1741(1)	73	0	0	-	-	-
275	16.604(9)	11.306(5)	9.266(5)	89.91(4)	90.07(4)	90.10(4)	1739(2)	74	0	0	-	-	-
270	16.616(9)	11.303(5)	9.261(5)	89.91(4)	89.90(4)	89.87(4)	1739(2)	76	0	0	-	-	-
265	16.614(8)	11.299(5)	9.259(5)	89.92(4)	90.08(4)	90.11(4)	1738(1)	76	0	0	-	-	-
260	16.607(8)	11.293(6)	9.258(5)	89.93(4)	90.08(4)	90.11(4)	1736(2)	76	0	0	-	-	-
255	16.602(9)	11.294(5)	9.257(5)	89.91(4)	90.09(4)	90.10(4)	1736(2)	78	0	0	-	-	-
250	16.593(9)	11.291(5)	9.257(5)	89.89(4)	90.08(4)	90.09(4)	1734(2)	77	0	0	-	-	-
245	16.594(8)	11.288(5)	9.252(4)	89.93(4)	90.08(4)	90.10(4)	1733(1)	77	0	0	-	-	-
240	16.596(9)	11.282(5)	9.246(5)	89.91(4)	90.11(4)	90.09(4)	1731(2)	79	0	0	-	-	-
235	16.599(9)	11.281(5)	9.244(5)	89.96(4)	90.06(4)	90.06(4)	1731(1)	83	6	0	0(0.012)	0(0.006)	0.114(7)
230	16.593(9)	11.277(5)	9.233(5)	90.01(4)	90.03(4)	90.01(4)	1728(1)	80	29	0	0(0.006)	0(0.003)	0.123(4)
225	16.586(8)	11.272(4)	9.219(4)	90.16(4)	89.98(4)	89.99(4)	1724(1)	79	43	0	0(0.004)	0(0.002)	0.126(3)
220	16.586(9)	11.244(7)	9.206(5)	90.51(5)	89.88(5)	89.97(5)	1717(2)	80	56	0	0(0.004)	0(0.002)	0.126(2)
215	16.582(11)	11.250(9)	9.208(6)	90.49(6)	89.91(5)	90.07(7)	1718(2)	77	63	0	0(0.004)	0(0.0018)	0.125(2)
210	16.572(12)	11.285(11)	9.201(7)	89.97(7)	90.09(6)	90.04(7)	1721(2)	80	72	1	0(0.003)	0(0.0018)	0.127(2)
205	16.570(14)	11.286(11)	9.191(8)	89.97(8)	90.09(7)	90.04(8)	1719(2)	77	77	1	0(0.003)	0(0.0016)	0.1270(18)
200	16.576(14)	11.247(10)	9.197(8)	90.44(8)	89.90(7)	89.95(8)	1715(3)	79	80	2	0(0.003)	0(0.0014)	0.1270(16)
195	16.565(14)	11.286(10)	9.185(9)	89.92(9)	90.05(7)	90.01(8)	1717(3)	80	81	4	0(0.003)	0(0.0015)	0.1267(17)
190	16.563(8)	11.246(6)	9.187(4)	90.05(5)	89.94(4)	89.84(5)	1711(1)	81	83	7	0(0.003)	0(0.0015)	0.1265(16)
185	16.562(11)	11.232(10)	9.179(6)	90.35(7)	89.81(5)	89.74(7)	1708(2)	80	86	9	0(0.003)	0(0.0014)	0.1269(16)
180	16.549(13)	11.225(9)	9.171(7)	90.43(7)	89.85(6)	89.71(7)	1703(2)	79	86	9	0(0.003)	0(0.0014)	0.1265(15)
175	16.554(14)	11.241(9)	9.172(8)	90.43(8)	89.80(7)	89.76(8)	1707(2)	81	89	11	0(0.003)	0(0.0014)	0.1265(16)
170	16.552(14)	11.240(11)	9.171(8)	90.49(8)	89.74(7)	89.75(8)	1706(3)	81	91	13	0(0.003)	0(0.0013)	0.1262(15)
165	16.541(14)	11.229(13)	9.161(8)	90.49(9)	89.81(7)	89.66(8)	1701(3)	79	90	15	0(0.002)	0(0.0013)	0.1262(14)
160	16.552(11)	11.286(8)	9.153(6)	89.91(6)	90.06(6)	90.00(6)	1710(2)	80	92	16	0(0.002)	0(0.0012)	0.1258(14)
155	16.550(13)	11.286(9)	9.152(7)	89.91(7)	90.03(6)	89.97(7)	1709(2)	81	95	14	0(0.002)	0(0.0013)	0.1263(15)
145	16.534(13)	11.218(13)	9.161(8)	90.29(8)	89.90(6)	89.67(8)	1699(3)	81	92	18	0(0.002)	0(0.0013)	0.1259(15)
140	16.548(16)	11.219(15)	9.169(10)	90.37(11)	89.85(8)	89.80(10)	1702(3)	81	96	20	0(0.002)	-0.0015(13)	0.1266(14)
135	16.56(2)	11.230(18)	9.144(12)	90.51(13)	89.74(10)	89.86(13)	1701(4)	81	91	19	0(0.003)	0(0.0014)	0.1265(15)
130	16.523(13)	11.208(10)	9.157(7)	90.39(8)	89.72(6)	89.57(8)	1696(2)	80	92	23	0(0.003)	0(0.0013)	0.1263(15)
125	16.514(12)	11.218(9)	9.182(7)	90.14(7)	89.72(6)	89.59(7)	1701(2)	78	95	20	0(0.003)	-0.0013(14)	0.1264(15)
120	16.514(13)	11.219(10)	9.184(8)	90.13(8)	89.71(6)	89.60(8)	1702(2)	83	96	21	0(0.003)	-0.0013(14)	0.1269(15)
115	16.511(12)	11.209(11)	9.181(7)	90.19(7)	89.66(6)	89.57(7)	1699(2)	83	99	22	0(0.003)	-0.0013(14)	0.1264(15)
110	16.54(2)	11.203(19)	9.158(12)	90.42(13)	89.78(10)	89.86(13)	1697(4)	79	96	22	0(0.003)	-0.0012(14)	0.1272(15)
105	16.519(14)	11.215(12)	9.192(8)	90.29(8)	89.50(7)	89.66(9)	1703(3)	80	98	19	0(0.003)	-0.0016(14)	0.1267(15)
100	16.526(19)	11.210(14)	9.197(10)	90.15(11)	89.61(9)	89.74(11)	1704(3)	82	99	24	0(0.002)	-0.0013(13)	0.1267(14)
105	16.507(12)	11.205(10)	9.169(7)	90.29(8)	89.63(6)	89.58(7)	1696(2)	84	97	23	0(0.003)	-0.0011(14)	0.1261(15)
110	16.510(14)	11.213(9)	9.173(8)	90.29(8)	89.56(7)	89.56(8)	1698(2)	81	99	21	0(0.003)	-0.0013(14)	0.1262(15)
115	16.517(14)	11.222(13)	9.182(8)	90.22(9)	89.59(7)	89.61(9)	1702(3)	77	97	19	0(0.002)	0(0.0013)	0.1268(14)
120	16.512(12)	11.216(8)	9.181(7)	90.22(7)	89.60(6)	89.56(7)	1700(2)	78	96	21	0(0.003)	-0.0015(14)	0.1265(15)
125	16.517(12)	11.227(9)	9.176(7)	90.20(7)	89.74(6)	89.65(7)	1701(2)	79	96	22	0(0.003)	-0.0015(14)	0.1263(15)
130	16.533(14)	11.224(10)	9.171(8)	90.35(9)	89.69(7)	89.67(8)	1702(3)	80	98	22	0(0.002)	-0.0015(13)	0.1265(14)
135	16.524(11)	11.225(8)	9.167(6)	90.29(6)	89.76(6)	89.63(7)	1700(2)	82	90	19	0(0.002)	-0.0013(13)	0.1264(15)
140	16.526(9)	11.227(10)	9.145(5)	89.98(6)	90.02(5)	89.67(6)	1697(2)	77	94	17	0(0.003)	-0.0013(14)	0.1252(15)
145	16.537(12)	11.232(11)	9.163(7)	90.29(8)	89.85(6)	89.73(7)	1702(2)	79	96	15	0(0.003)	0(0.0014)	0.1261(15)
150	16.542(13)	11.233(13)	9.167(8)	90.40(8)	89.83(7)	89.78(8)	1703(3)	80	95	15	0(0.003)	-0.0011(14)	0.1262(15)
155	16.548(12)	11.240(11)	9.169(7)	90.37(8)	89.81(6)	89.77(7)	1705(2)	83	93	14	0(0.003)	0(0.0014)	0.1265(16)
160	16.544(13)	11.239(13)	9.158(8)	90.60(9)	89.79(7)	89.77(8)	1703(3)	83	95	16	0(0.003)	0(0.0014)	0.1261(15)
165	16.556(12)	11.248(11)	9.158(7)	90.46(7)	89.82(6)	89.78(7)	1705(2)	84	93	13	0(0.003)	0(0.0014)	0.1252(16)
170	16.558(12)	11.257(11)	9.156(7)	90.38(7)	89.87(6)	89.83(7)	1706(2)	82	87	14	0(0.003)	0(0.0014)	0.1253(15)
175	16.559(10)	11.249(11)	9.160(6)	90.38(7)	89.89(5)	89.83(7)	1706(2)	82	86	12	0(0.002)	0(0.0013)	0.1270(14)
180	16.565(12)	11.245(8)	9.166(7)	90.44(7)	89.82(6)	89.79(7)	1707(2)	78	86	11	0(0.002)	0(0.0013)	0.1258(14)
185	16.573(15)	11.239(11)	9.172(9)	90.44(9)	89.93(8)	89.85(9)	1708(3)	80	90	8	0(0.003)	0(0.0015)	0.1270(17)
190	16.563(10)	11.248(8)	9.173(6)	90.45(6)	89.89(5)	89.85(6)	1709(2)	82	82	5	0(0.003)	0(0.0015)	0.1267(17)
195	16.574(10)	11.262(8)	9.182(6)	90.30(6)	89.93(5)	89.94(6)	1714(2)	83	83	3	0(0.003)	0(0.0015)	0.1260(17)
200	16.571(10)	11.254(9)	9.189(6)	90.33(6)	89.93(5)	89.92(6)	1714(2)	79	79	2	0(0.003)	0(0.0015)	0.1272(17)
205	16.579(10)	11.257(7)	9.186(5)	90.43(6)	89.87(5)	89.98(6)	1714(2)	78	77	1	0(0.003)	0(0.0016)	0.1270(18)
210	16.577(10)	11.250(9)	9.194(6)	90.50(6)	89.84(5)	89.96(6)	1715(2)	80	70	1	0(0.003)	0(0.0018)	0.127(2)
215	16.581(9)	11.254(6)	9.197(5)	90.42(5)	89.91(4)	90.03(5)	1716(2)	80	62	0	0(0.004)	0(0.0019)	0.127(2)
220	16.582(9)	11.246(6)	9.202(5)	90.41(5)	89.96(4)	89.97(5)	1716(2)	80	56	0	0(0.004)	0(0.002)	0.126(2)
225	16.584(8)	11.287(6)	9.225(5)	89.93(5)	90.08(4)	90.05(5)	1727(1)	77	47	0	0(0.004)	0(0.002)	0.126(2)
230	16.584(8)	11.281(6)	9.231(5)	90.01(4)	90.03(4)	90.00(4)	1727(2)	80	30	1	0(0.006)	0(0.003)	0.127(3)
235	16.594(9)	11.284(5)	9.242(5)	89.95(4)	90.01(4)	89.98(4)	1730(2)	83	8	0	0(0.011)	0(0.005)	0.120(6)
240	16.605(9)	11.286(5)	9.244(5)	89.96(4)	90.06(4)	90.08(4)	1732(1)	82	1	0	0(0.03)	0(0.014)	0.118(17)
245	16.601(9)	11.289(5)	9.249(5)	89.92(4)	90.04(4)	90.04(4)	1733(2)	80	0	0	-	-	-
250	16.601(9)	11.295(5)	9.250(5)	89.92(4)	90.05(4)	90.06(4)	1734(1)	79	0	0	-	-	-
255	16.595(9)	11.296(5)	9.257(5)	89.90(4)	90.05(5)	90.02(4)	1735(2)	77	0	0	-	-	-
260	16.614(9)	11.302(6)	9.251(5)	89.95(4)	90.09(4)	90.13(4)	1737(2)	78	0	0	-	-	-

Table C1.2: Self-normalised intensities for a selection of satellite peaks in $[NEt_4]Ag[Ag(CN)_2]_2$. Peak maxima were identified by integration of single frames so shows systematic errors according to the movement of the peak maxima to angular values between frames.

T / K	$\mathbf{q_z}$	$\sigma(\mathbf{q_x})$	I($1\bar{7}21$)	I($1\bar{7}2\bar{1}$)	I($1\bar{7}11$)	I($1\bar{7}1\bar{1}$)	I($\bar{1}33\bar{1}$)	I($0\bar{5}2\bar{1}$)	mean(I)
235	0.114	0.0070	0.114785	0.108094	0.109149	0.149685	0.079973	0.090397	0.10868
230	0.123	0.0040	0.261826	0.221415	0.210135	0.214618	0.15393	0.191312	0.208873
225	0.126	0.0030	0.385011	0.356414	0.343477	0.35725	0.245275	0.309158	0.332764
220	0.126	0.0020	0.484792	0.462946	0.440962	0.489401	0.339167	0.399394	0.43611
215	0.125	0.0020	0.549452	0.584465	0.500647	0.540465	0.407738	0.500818	0.513931
210	0.127	0.0020	0.615822	0.678953	0.583463	0.642238	0.474744	0.608549	0.600628
205	0.127	0.0018	0.661402	0.743037	0.609299	0.700709	0.54284	0.60981	0.644516
200	0.127	0.0016	0.659489	0.815318	0.673199	0.797991	0.558801	0.640023	0.690803
195	0.1267	0.0017	0.673148	0.858045	0.785235	0.833846	0.624407	0.685503	0.743364
190	0.1265	0.0016	0.706165	0.892701	0.836176	0.8474	0.7169	0.718962	0.786384
185	0.1269	0.0016	0.700365	0.902055	0.912687	0.855162	0.788563	0.751295	0.818354
180	0.1265	0.0015	0.715062	0.948407	0.910082	0.883255	0.811126	0.791301	0.843205
175	0.1265	0.0016	0.73011	0.907492	0.941659	0.89279	0.796243	0.838391	0.851114
170	0.1262	0.0015	0.802951	0.995135	0.949175	0.895272	0.725391	0.841557	0.868247
165	0.1262	0.0014	0.851118	1	0.945143	0.936407	0.770476	0.966031	0.911529
160	0.1258	0.0014	0.881373	0.982909	0.96985	0.874941	0.882622	0.970753	0.927075
155	0.1263	0.0015	0.92656	0.991078	0.917914	1	0.927134	0.998095	0.96013
145	0.1259	0.0015	0.968955	0.920149	0.914313	0.974074	0.856757	0.974295	0.934757
140	0.1266	0.0014	1	0.892087	0.888478	0.968203	0.78045	1	0.921536
135	0.1265	0.0015	0.95721	0.900535	0.923556	0.94409	0.922545	0.954305	0.933707
130	0.1263	0.0015	0.956903	0.898138	0.949291	0.927029	0.952607	0.947061	0.938505
125	0.1264	0.0015	0.97439	0.894485	0.975459	0.911742	0.976541	0.948322	0.946823
120	0.1269	0.0015	0.97889	0.903379	0.976571	0.860402	0.90215	0.910569	0.921993
115	0.1264	0.0015	0.97569	0.888212	1	0.868913	0.811504	0.918297	0.910436
110	0.1272	0.0015	0.945683	0.906795	0.963512	0.811545	0.834334	0.874158	0.889338
105	0.1267	0.0015	0.948882	0.899643	0.99781	0.866391	0.972918	0.877405	0.927175
100	0.1267	0.0014	0.948809	0.875777	0.976338	0.835855	1	0.864391	0.916862
105	0.1261	0.0015	0.936421	0.89896	0.976869	0.838377	0.942479	0.867638	0.910124
110	0.1262	0.0015	0.941329	0.907324	0.972273	0.828448	0.842559	0.895275	0.897868
115	0.1268	0.0014	0.968955	0.902431	0.979773	0.793459	0.793403	0.861923	0.883324
120	0.1265	0.0015	0.986545	0.878802	0.976654	0.849803	0.881531	0.904478	0.912969
125	0.1263	0.0015	0.982148	0.912789	0.948993	0.886249	0.958818	0.973088	0.943681
130	0.1265	0.0014	0.990562	0.89666	0.97443	0.83156	0.960636	0.950254	0.934017
135	0.1264	0.0015	0.96393	0.910726	0.941775	0.924035	0.915607	0.925166	0.930206
140	0.1252	0.0015	0.960584	0.907004	0.89991	0.928054	0.801153	0.934584	0.905215
145	0.1261	0.0015	0.956917	0.930437	0.904274	0.92037	0.788087	0.975019	0.912518
150	0.1262	0.0015	0.925741	0.929573	0.912189	0.866036	0.902374	0.975073	0.918498
155	0.1265	0.0016	0.891351	0.975298	0.926907	0.810008	0.911872	0.9297	0.907523
160	0.1261	0.0015	0.819562	0.957287	0.902167	0.791371	0.872508	0.935255	0.879692
165	0.1252	0.0016	0.786954	0.95921	0.915973	0.829945	0.77947	0.888299	0.859975
170	0.1253	0.0015	0.740745	0.912873	0.896459	0.848385	0.67541	0.840538	0.819068
175	0.127	0.0014	0.724587	0.878398	0.873577	0.764933	0.757662	0.822855	0.803669
180	0.1258	0.0014	0.711191	0.878844	0.864517	0.798936	0.769245	0.741367	0.794017
185	0.127	0.0017	0.722177	0.851953	0.866757	0.753822	0.727433	0.689796	0.768656
190	0.1267	0.0017	0.660745	0.824407	0.8195	0.80595	0.687594	0.663581	0.743629
195	0.126	0.0017	0.64786	0.842083	0.784389	0.762687	0.580301	0.639432	0.709459
200	0.1272	0.0017	0.597619	0.791772	0.69467	0.720134	0.539105	0.617376	0.660113
205	0.127	0.0018	0.610636	0.710151	0.594481	0.673759	0.512373	0.618369	0.619961
210	0.127	0.0020	0.574112	0.638721	0.523595	0.600512	0.458195	0.551209	0.557724
215	0.127	0.0020	0.513192	0.567611	0.481515	0.52238	0.392351	0.457646	0.489116
220	0.126	0.0020	0.41889	0.460841	0.405519	0.455004	0.303636	0.375916	0.403301
225	0.126	0.0020	0.342235	0.332562	0.313128	0.385776	0.240379	0.297996	0.318679
230	0.127	0.0030	0.22653	0.22918	0.222066	0.229827	0.145425	0.202018	0.209174
235	0.12	0.0060	0.120278	0.118312	0.125676	0.134358	0.07572	0.123373	0.116286

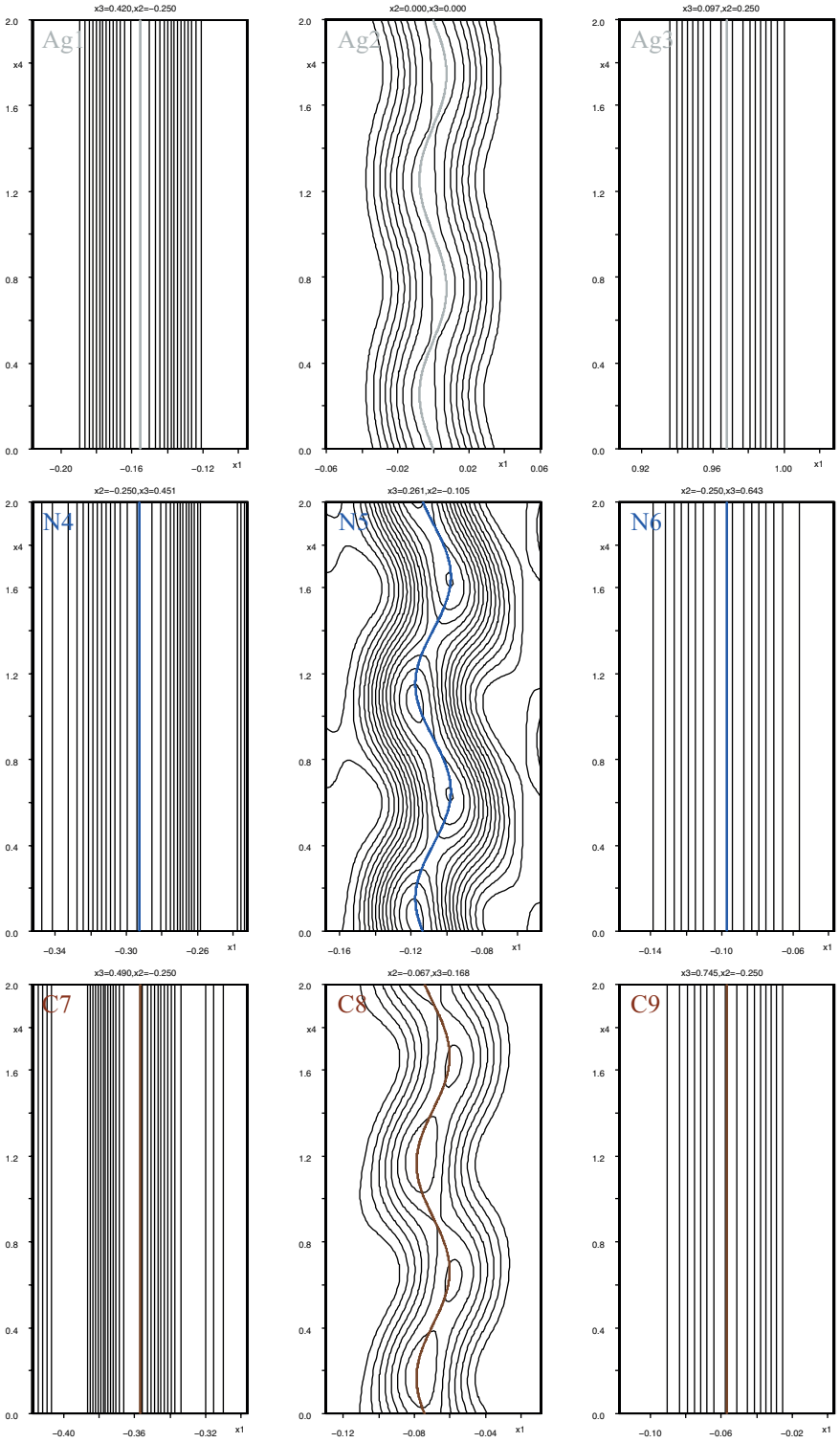

Figure C1.3: Fourier maps for the framework atoms in X1 (a) vs X4 (modulation direction) slices.

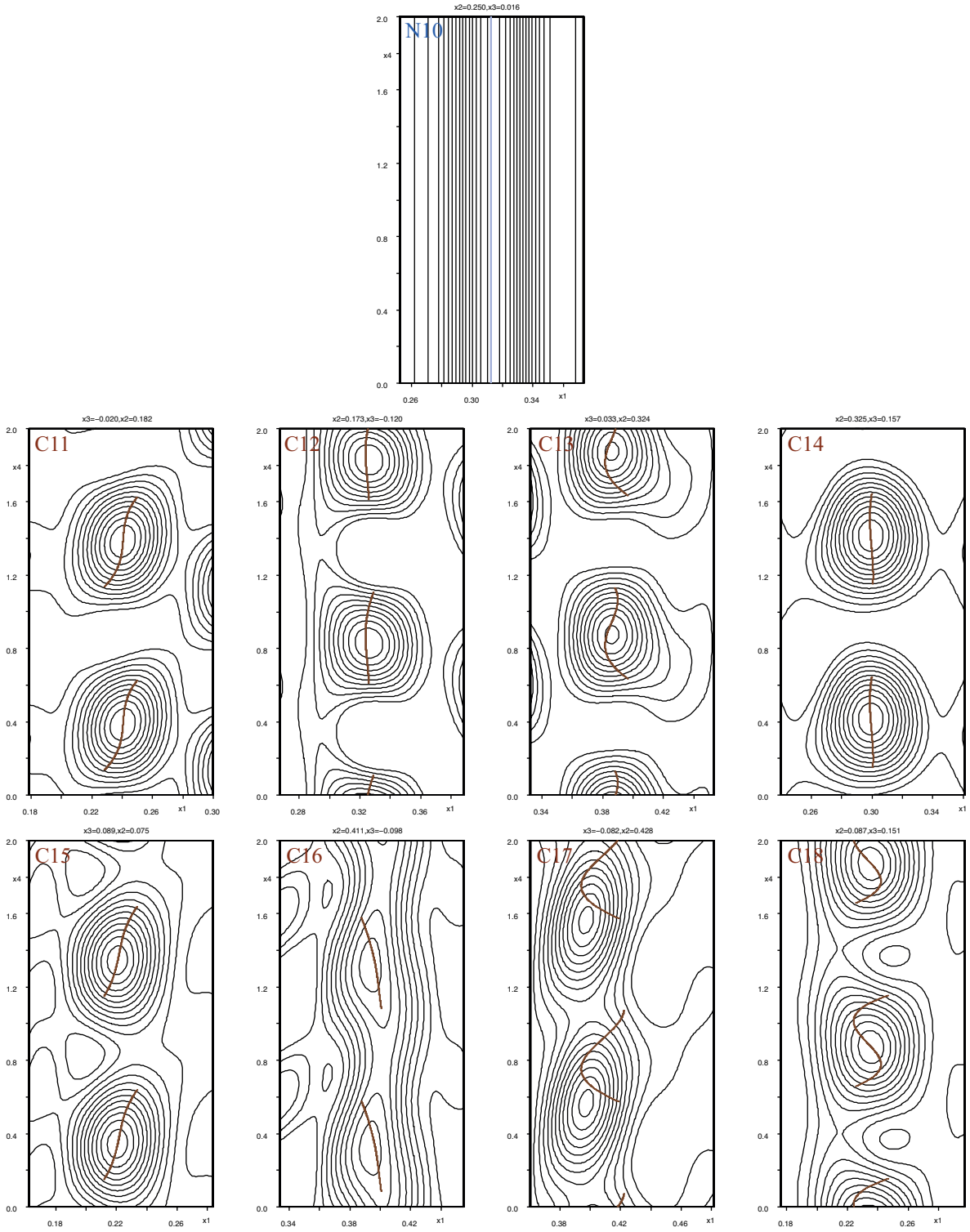

Figure C1.4: Fourier maps for the $[NEt_4]^+$ atoms in X1 (a) vs X4 (modulation direction) slices.

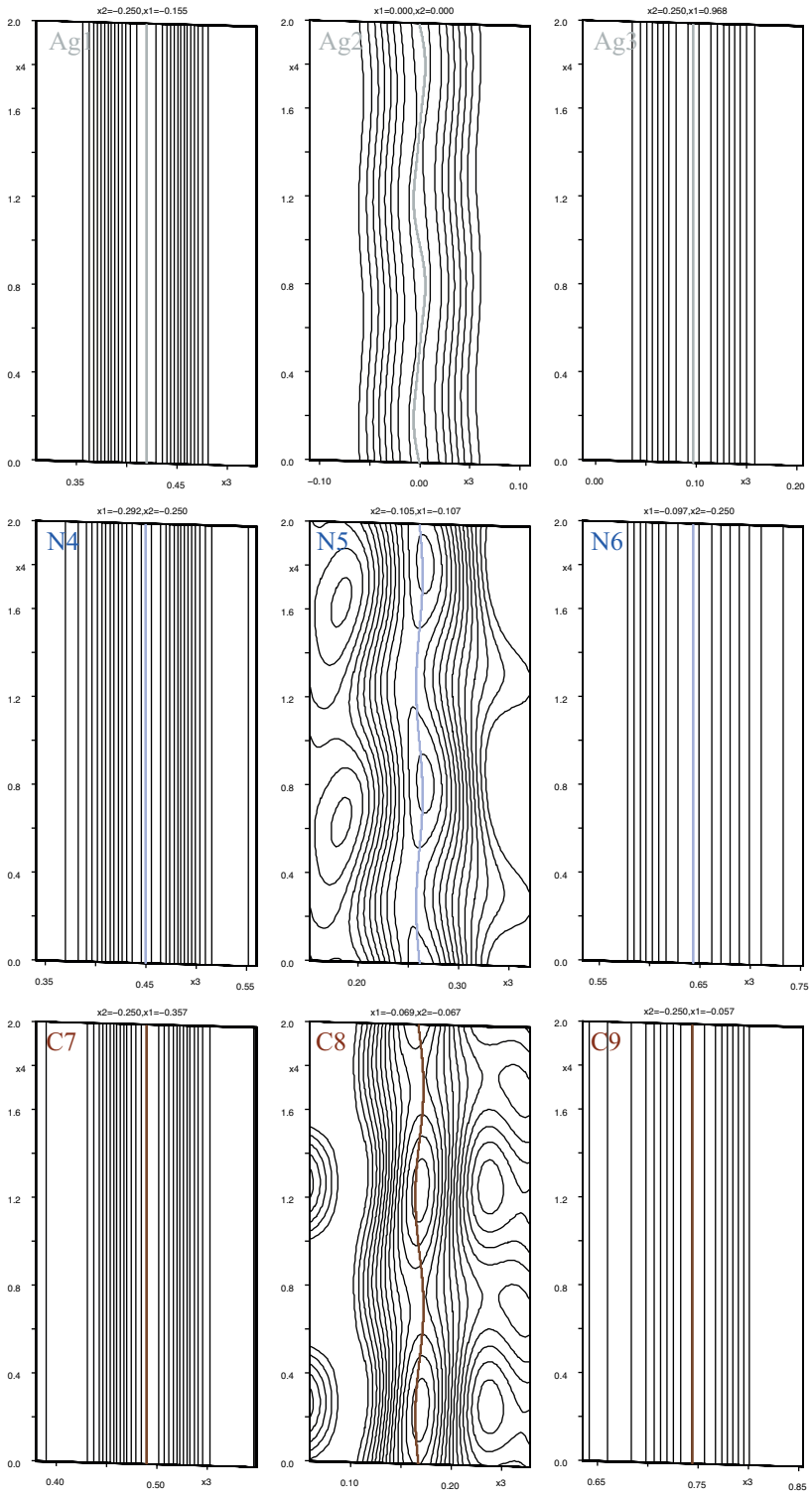

Figure C1.5: Fourier maps for the framework atoms in X3 (c) vs X4 (modulation direction) slices.

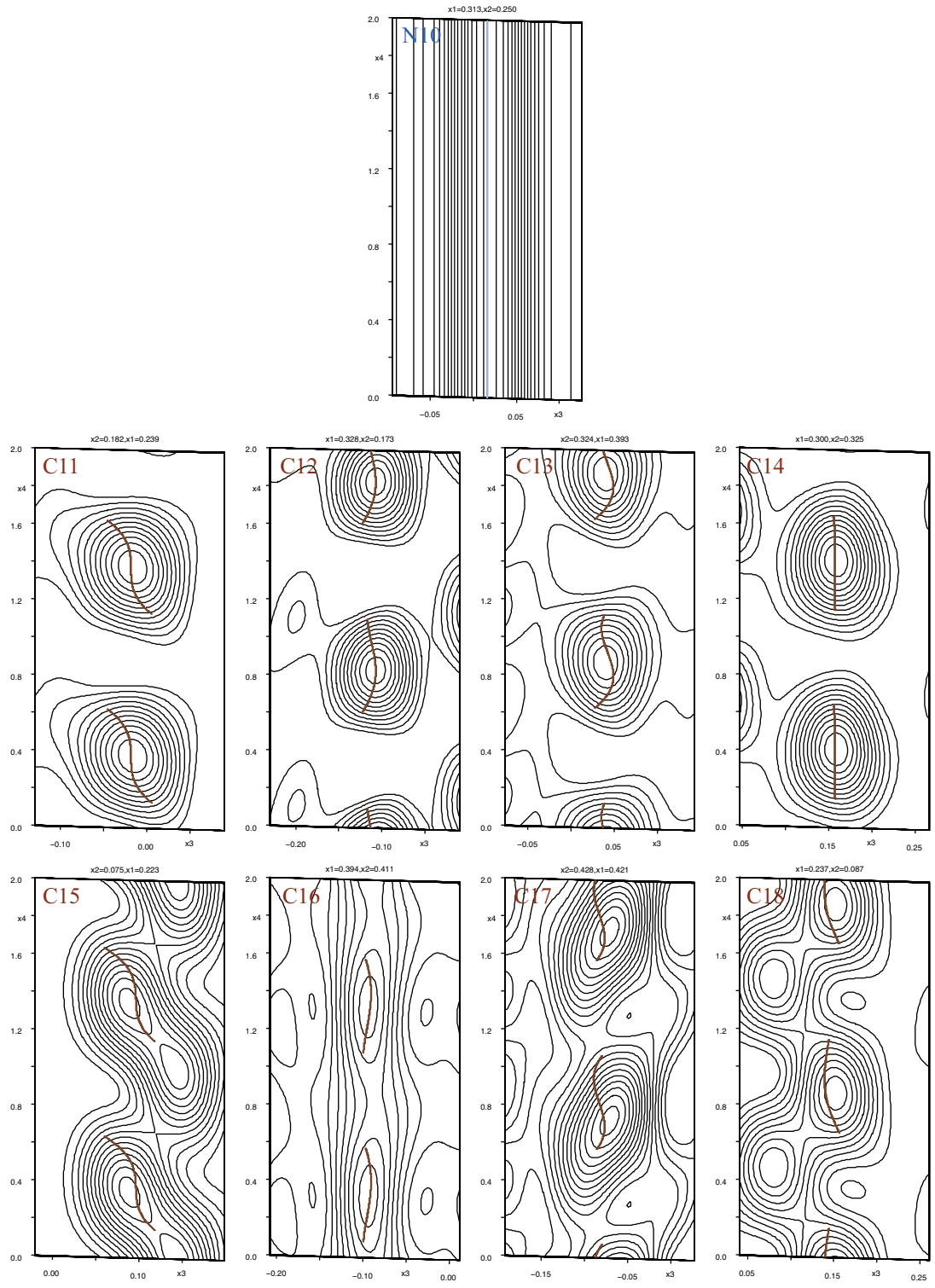

Figure C1.6: Fourier maps for the $[NEt_4]^+$ atoms in X3 (c) vs X4 (modulation direction) slices.

Table C1.3: Selected interatomic distances for the modulated structure of $[NEt_4]Ag[Ag(CN)_2]_2$

	Average / Å	Minimal / Å	Maximal / Å
Ag1-N4	2.289(9)	2.286(9)	2.291(9)
Ag1-N6	2.265(8)	2.264(8)	2.267(8)
Ag2-C8	2.069(13)	2.050(14)	2.097(14)
Ag2-C8^{v}	2.069(13)	2.050(14)	2.097(14)
Ag3-Ag2^{i}	3.0082(19)	2.982(2)	3.034(2)
Ag3-Ag2^{ii}	3.0087(19)	2.982(2)	3.034(2)
Ag3-C7^{iv}	2.084(11)	2.082(11)	2.086(11)
Ag3-C9^{iii}	2.072(9)	2.069(9)	2.076(9)
N4-C7	1.130(14)	1.128(14)	1.131(14)
N5-C8	1.143(18)	1.131(19)	1.155(19)
N6-C9	1.150(12)	1.146(12)	1.155(12)
N10-C11	1.5(3)	1.3(6)	1.7(6)
N10-C11^{vi}	1.5(3)	1.3(6)	1.7(6)
N10-C12	1.5(3)	1.5(6)	1.6(6)
N10-C12^{vi}	1.5(3)	1.5(6)	1.6(6)
N10-C13	1.5(5)	1.4(8)	1.6(8)
N10-C13^{vi}	1.5(5)	1.4(8)	1.6(8)
N10-C14	1.5(4)	1.5(6)	1.6(6)
N10-C14^{vi}	1.5(4)	1.5(6)	1.6(6)
C11-C12	1.5(9)	1.5(9)	1.5(9)
C12-C16^{vi}	1.5(4)	1.4(7)	1.5(7)
C13-C16	1.5(7)	1.5(8)	1.5(8)
C14-C18^{vi}	1.6(7)	1.5(13)	1.6(13)

Symmetry codes: (i) $x+1, y, z$; (ii) $-x+1, y+1/2, -z$; (iii) $-x+1, y+1/2, -z+1$; (iv) $-x+1/2, -y, z-1/2$; (v) $-x, -y, -z$; (vi) $x, -y+1/2, z$

Table C1.4: Final coordinates, equivalent isotropic displacement parameters and Fourier amplitudes of the displacive modulation functions (s for sine, c for cosine) for the modulated structure of $[NEt_4]Ag[Ag(CN)_2]_2$

.

	Wave	x	y	z	U_{eq} / Å^2
Ag3		0.96770(4)	0.25	0.09678(6)	0.0322(2)
	s,1	0	-0.03492(11)	0	
	c,1	0	0.00045(11)	0	
Ag2		0	0	0	0.0352(2)
	s,1	-0.00763(6)	-0.03644(12)	-0.00532(10)	
	c,1	0	0	0	
	s,2	0.00013(13)	0.00044(13)	-0.0012(2)	
	c,2	0	0	0	
Ag1		-0.15548(5)	-0.25	0.41960(7)	0.0406(3)
	s,1	0	-0.03524(14)	0	
	c,1	0	0.02292(14)	0	
N6		-0.0973(5)	-0.25	0.6435(8)	0.037(2)
	s,1	0	-0.0270(13)	0	
	c,1	0	0.0186(13)	0	
N4		-0.2923(5)	-0.25	0.4505(9)	0.041(3)
	s,1	0	-0.0436(15)	0	
	c,1	0	0.0131(17)	0	
N5		-0.1074(4)	-0.1049(7)	0.2614(7)	0.043(2)
	s,1	-0.0081(6)	-0.0369(11)	-0.0032(9)	
	c,1	-0.0058(6)	0.0228(12)	0.0003(10)	
C8		-0.0694(5)	-0.0671(8)	0.1684(7)	0.039(2)
	s,1	-0.0080(7)	-0.0368(11)	-0.0039(11)	
	c,1	-0.0047(7)	0.0133(13)	-0.0009(11)	
C9		-0.0570(6)	-0.25	0.7452(10)	0.033(3)
	s,1	0	-0.0305(14)	0	
	c,1	0	0.0097(15)	0	
C7		-0.3569(7)	-0.25	0.4896(10)	0.036(3)
	s,1	0	-0.0414(16)	0	
	c,1	0	0.0081(18)	0	
N10		0.3128(5)	0.25	0.0163(8)	0.038(3)
	s,1	0	-0.0313(16)	0	
	c,1	0	-0.0295(15)	0	
C11		0.239(3)	0.182(4)	-0.020(5)	0.033(5)
	s,1	0.012(13)	0.022(14)	-0.03(2)	
	c,1	0.009(13)	0.020(13)	-0.03(2)	
	s,2	0.03(2)	0.09(3)	-0.07(4)	
	c,2	0.381(9)	0.5	0.001	
C12		0.328(3)	0.173(4)	-0.120(5)	0.048(6)
	s,1	0.001(15)	-0.021(9)	-0.02(2)	
	c,1	-0.005(18)	-0.041(9)	0.00(3)	
	s,2	0.00(3)	-0.005(15)	0.01(5)	
	c,2	0.859(8)	0.5	0.0031	
C13		0.393(4)	0.324(6)	0.033(7)	0.056(6)
	s,1	0.03(2)	-0.038(19)	-0.04(3)	
	c,1	0.01(2)	-0.05(2)	-0.02(3)	
	s,2	-0.03(3)	0.02(3)	0.05(6)	
	c,2	0.882(10)	0.5	0.001	
C14		0.300(4)	0.325(5)	0.157(5)	0.051(5)
	s,1	0.00(2)	-0.048(18)	0.00(3)	
	c,1	0.003(16)	-0.032(15)	0.00(2)	
	s,2	0.00(3)	-0.02(3)	-0.01(5)	
	c,2	0.398(8)	0.5	0.0072	
C15		0.223(3)	0.075(4)	0.089(7)	0.042(7)
	s,1	0.007(15)	0.025(17)	-0.03(3)	
	c,1	0.006(12)	0.014(13)	-0.03(2)	
	s,2	0.02(2)	0.09(3)	-0.08(5)	
	c,2	0.395(11)	0.5	-0.0486	
C16		0.394(4)	0.411(5)	-0.098(6)	0.048(7)
	s,1	0.001(8)	-0.024(8)	0.002(9)	
	c,1	-0.002(12)	-0.044(8)	-0.010(11)	
	s,2	-0.008(17)	0.004(11)	-0.007(15)	
	c,2	0.331(19)	0.5	0	
C17		0.421(6)	0.428(8)	-0.082(9)	0.063(10)
	s,1	0.036(13)	-0.026(16)	-0.02(2)	
	c,1	0.02(2)	-0.06(3)	-0.03(4)	
	s,2	-0.03(3)	0.02(4)	0.04(6)	
	c,2	-0.18(2)	0.5	0	
C18		0.237(5)	0.087(5)	0.151(9)	0.048(6)
	s,1	-0.06(3)	-0.01(3)	0.01(6)	
	c,1	-0.04(2)	-0.02(2)	-0.01(4)	
	s,2	0.08(4)	-0.03(4)	-0.01(9)	
	c,2	-0.093(12)	0.5	0	

Table C1.5: Displacement parameters for the average structure of $[NEt_4]Ag[Ag(CN)_2]_2$

.

	U^{11}	U^{22}	U^{33}	U^{12}	U^{13}	U^{23}
Ag1	0.0303(4)	0.0604(7)	0.0311(3)	0	0.0031(2)	0
Ag2	0.0363(4)	0.0367(5)	0.0327(3)	0.0016(3)	0.0079(2)	0.0023(2)
Ag3	0.0261(4)	0.0384(4)	0.0323(3)	0	-0.0042(2)	0
N4	0.023(4)	0.065(8)	0.035(4)	0	0.005(3)	0
N5	0.039(4)	0.052(5)	0.037(3)	-0.003(3)	0.005(2)	0.004(3)
N6	0.033(4)	0.051(5)	0.028(3)	0	-0.004(3)	0
C7	0.034(5)	0.040(7)	0.033(4)	0	-0.001(3)	0
C8	0.038(4)	0.044(5)	0.036(3)	0.003(3)	0.006(3)	0.001(3)
C9	0.023(4)	0.038(5)	0.038(4)	0	0.001(3)	0
N10	0.027(4)	0.057(7)	0.029(3)	0	-0.005(3)	0
C11	0.030(6)	0.022(14)	0.046(6)	-0.011(7)	-0.006(5)	0.001(7)
C12	0.037(7)	0.071(15)	0.034(5)	0.015(8)	-0.001(4)	-0.003(6)
C13	0.027(7)	0.092(16)	0.050(7)	-0.011(8)	-0.008(6)	-0.003(8)
C14	0.054(8)	0.059(12)	0.040(5)	-0.020(7)	-0.004(5)	-0.001(6)
C15	0.034(7)	0.021(17)	0.071(9)	-0.001(8)	0.005(6)	0.006(9)
C16	0.041(9)	0.050(18)	0.052(7)	-0.030(10)	-0.001(6)	0.007(9)
C17	0.034(13)	0.10(3)	0.060(8)	-0.033(14)	0.008(8)	0.010(12)
C18	0.039(11)	0.028(13)	0.077(9)	-0.013(7)	0.027(8)	0.001(7)

Publications

Articles arising from this thesis are listed below along with the location of the work on which they are based. In addition, articles relating to work carried out during this same time period, but not included in this thesis, are listed.

- *Guest-activated forbidden tilts in a molecular perovskite analogue*
  S. G. Duyker, **J. A. Hill**, C. J. Howard, and A. L. Goodwin, *submitted*
  Chapter 8

- *Dicyanometallates as model extended frameworks*
  J. A. Hill, A. L. Thompson, and A. L. Goodwin *J. Am. Chem. Soc.* **138** 5886–5896 (2016)
  Chapters 3 & 4

- *Chemical Control of Mesoscale Polarisation* via *Geometric Frustration in Supramolecular Crystals*
  C. S. Zehe, **J. A. Hill**, N. P. Funnell, K. Kreger, A. L. Goodwin, H.-W. Schmidt, J. Senker, *submitted*

- *Zero-strain reductive intercalation in a molecular framework.*
  J. A. Hill, A. B. Cairns, J. J. K. Lim, S. J. Cassidy, S. J. Clarke, and A. L. Goodwin *CrystEngComm* **17** 2925–2928 (2015)

- *Flexibility transition and guest-driven reconstruction in a ferroelastic metal–organic framework*
  S. J. Hunt, M. J. Cliffe, **J. A. Hill**, A. B. Cairns, N. P. Funnell, and A. L. Goodwin *CrystEngComm* **17** 361–369 (2015)

- *Glass formation* via *structural fragmentation of a 2D coordination network*
  D. Umeyama, N. P. Funnell, M. J. Cliffe, **J. A. Hill**, A. L. Goodwin, Y. Hijikata, T. Itakura, T. Okubo, S. Horike, and S. Kitagawa *Chem. Commun.* **51** 12728–12731 (2015)

- *Defect-dependent colossal negative thermal expansion in UiO-66(Hf) metal–organic framework*
  M. J. Cliffe, **J. A. Hill**, C. A. Murray, F.-X. Coudert, and A. L. Goodwin *Phys. Chem. Chem. Phys.* **17** 11586–11592 (2015)

- *Compositional dependence of anomalous thermal expansion in perovskite-like ABX_3 formates.*
  I. E. Collings, **J. A. Hill**, A. B. Cairns, R. I. Cooper, A. L. Thompson, J. E. Parker, C. C. Tang, and A. L. Goodwin *Dalton Transactions* **45** 4169–4178 (2016)

Guest-activated forbidden tilts in a molecular perovskite analogue

Samuel G. Duyker,*[a,b] Joshua A. Hill,[a] Christopher J. Howard,[c] and Andrew L. Goodwin*[a]

[a] *Department of Chemistry, University of Oxford, Inorganic Chemistry Laboratory, South Parks Road, Oxford, OX1 3QR, UK*

[b] *School of Chemistry, The University of Sydney, Sydney, NSW 2006, Australia*

[c] *School of Engineering, University of Newcastle, Callaghan, NSW 2308, Australia*

Supporting Information Available

ABSTRACT: The manipulation of distortions in perovskite structures is critical to tailoring the properties of these materials for a variety of applications. Here we demonstrate a violation of traditional tilt rules in the double perovskite analogue $(NH_4)_2SrFe(CN)_6{\cdot}2H_2O$. The forbidden tilt pattern we observe arises through coupling to hydration-driven Jahn-Teller-like distortions of the Sr coordination environment. Access to novel distortion mechanisms and the ability to switch these distortions on and off through chemical modification fundamentally expands the toolbox of techniques available for engineering symmetry-breaking processes in solid materials.

Symmetry-breaking processes have long played a central role in the design of functional materials. An important example is the ferroelectric instability of perovskite ceramics such as $BaTiO_3$ and $PbZr_xTi_{1-x}O_3$, which is responsible for their switchable polarisation, dielectric and piezoelectric responses.[1-3] The ABX_3 perovskite structure is also famously susceptible to symmetry-lowering *via* correlated tilts of corner-sharing $[BX_6]$ octahedra.[4] One of the most exciting recent developments in the field has been the realisation that clever combinations of different tilt instabilities can be exploited in the design of new classes of functional ceramics,[5] including multiferroics and negative thermal expansion materials.[6,7] The development of so-called "tilt engineering" strategies relies on a deep collective understanding of the different possible symmetry-breaking processes accessible through octahedral tilt mechanisms and their various combinations.[8]

In this context there is an important conceptual difference between "conventional" perovskites and their contemporary molecular analogues—systems in which the X anion connecting neighbouring coordination octahedra is molecular rather than monoatomic. Whereas an intrinsic limitation for oxide perovskites is that tilt directions (clockwise/anticlockwise) must alternate for neighbouring octahedra if network connectivity is to be retained,[8-10] the use of molecular spacers allows for new ("forbidden") tilt patterns where this strict alternation is no longer observed.[11,12] Formally this distinction is captured by the associated distortion periodicities **k**, given relative to the simple cubic ABX_3 aristotype: conventional tilts must couple at $\mathbf{k} = \langle ½,½,ξ \rangle$, but forbidden tilts can be associated with arbitrary **k** and hence result in symmetry-lowering processes inaccessible to oxide perovskites. Examples of such distortions are now known for both azide[13,14] and dicyanometallate[15] perovskites, with the same degrees of freedom accessible to formate perovskites[16] and Prussian Blue analogues.[17] So, in principle, there is enormous scope for tilt engineering strategies in molecular perovskites. What remains to be shown is the extent to which there exists genuine chemical control over the activation and nature of these forbidden tilts.

Here we study the structural chemistry of ammonium strontium ferrocyanide, $(NH_4)_2SrFe(CN)_6$, a molecular analogue of well-known double perovskites such as Sr_2FeMoO_6.[18] We show that simple (de)hydration of this material is sufficient to switch on and off forbidden tilt systems. The underlying mechanism involves coupling of tilts to the specific pattern of Sr–OH_2 bonds formed during hydration. A similar mechanism is observed in the related Ba-containing framework (first reported in Ref. 19) except that the increase in cation radius drives a different hydration pattern, in turn affecting the symmetry of the forbidden tilt systems activated. So not only do we show how to access unconventional tilt order for these molecular perovskites, but we also establish a methodology through which simple chemical modification might eventually be used to manipulate physical properties that depend on the nature of activated tilts.

Mixing aqueous solutions of $(NH_4)_4Fe(CN)_6$ and $SrCl_2$ in a 2:1 stoichiometric ratio yields crystals of $(NH_4)_2SrFe(CN)_6{\cdot}2H_2O$ (**1**$\cdot 2H_2O$). Upon heating to around 300 K under dry N_2, water is eliminated from the structure in a single-crystal-to-single-crystal transformation, yielding the dehydrated framework $(NH_4)_2SrFe(CN)_6$ (**1**). This transformation is entirely reversible on rehydration (see Supporting Information). The structures of **1** and **1**$\cdot 2H_2O$ were determined using single-crystal X-ray diffraction, and the reversibility of hydration assessed using powder X-ray diffraction (see Supporting Information for further details).

Compound **1** crystallises with a double perovskite structure consisting of octahedrally-coordinated Sr^{2+} and $Fe(CN)_6^{4-}$ ions that alternate in three dimensions [Fig. 1(a)]. Each NH_4^+ cation—analogous to the perovskite A-site cation—occupies a pseudo-cubic cavity. The structure has $P2_1/n$ symmetry, which is actually very common for oxide double perovskites.[20,21] This particular symmetry results from a combination of rocksalt-type cation order with activation of the (conventional) $a^-a^-c^+$ Glazer octahedral tilt

system.[9] The presence of octahedral tilts in **1** can be rationalized in terms of tolerance factor arguments.[22] Hydrogen-bonding interactions between NH_4^+ ions and the N-terminus of neighbouring cyanide bridges induce bending of the Fe–CN–Sr linkages at the N atom, distorting the framework away from a conventional Prussian blue structure to give Fe–N–Sr angles of 140–145°.

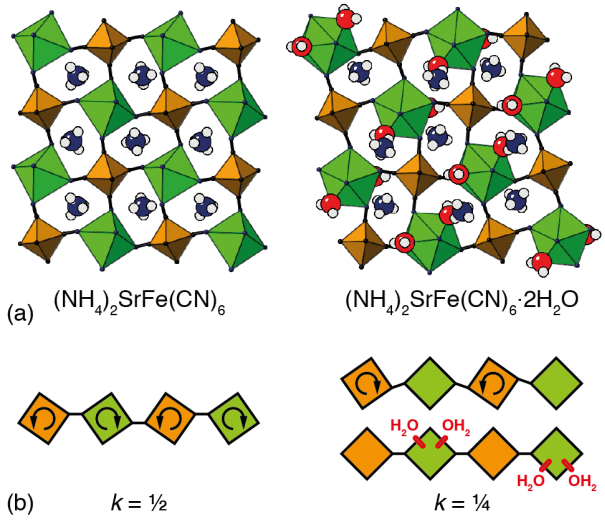

Figure 1. (a) Representations of single layers of the **1** (left) and **1**·2H_2O (right) crystal structures, viewed along a unique perovskite axis of each structure. Sr polyhedra are shown in green, Fe in orange, cyanide bridges in black, NH_4^+ in blue and white, and H_2O in red and white. See Figure S1 for images showing multiple layers. (b) The structure of **1** is that of a conventional double perovskite, with octahedra of the same type tilted in phase with respect to each other (left). Forbidden tilt systems appear in **1**·2H_2O due to the distortive effect of the H_2O molecules on the Sr geometry, with each Fe tilted out of phase with respect to the neighboring Fe in each repeating Sr···Fe··· chain (right).

The hydrated phase **1**·2H_2O has a structure with the same basic framework connectivity as **1** but in which the coordination number of Sr^{2+} has increased from six to eight in order to accommodate two additional H_2O molecules. The particular H_2O arrangements we observe are different from those in the orthorhombic modification[23] of $(NH_4)_2SrFe(CN)_6{\cdot}2H_2O$ (accessed via an alternative synthetic route, and having a different framework connectivity related to the $KLnFe(CN)_6{\cdot}nH_2O$ phases[24]), and lead instead to a monoclinic structure with $C2/c$ symmetry. For our study it is convenient to consider the hydration pattern in **1**·2H_2O in terms of a correlated distortion of B-site coordination environments of the underlying perovskite-like lattice. Analysis using the ISOTROPY software suite[25] gives that this distortion, when couched in group theoretical terms, is described by the Λ_3 irreducible representation (irrep[26]) at **k** = [¼,¼,¼] with reference to the parent cubic structure. Importantly, activation of a distortion with this particular irrep accounts entirely for the space group symmetry of **1**·2H_2O; in other words, it is the primary order parameter.

This same group theoretical analysis also accounts for the coupling between hydration-induced distortions and octahedral tilts. In particular, there are two forbidden tilt systems of the correct symmetry to couple to the Λ_3 hydration pattern: one corresponds to tilts around axes parallel and antiparallel to [100] of the monoclinic cell and is also associated with the Λ_3 irrep; the other involves an inclination of the tilt axis towards [103] and reflects are dominant Λ_2 component to the experimental crystal structure. Both tilt systems couple at **k** = [¼,¼,¼]. If the Sr ions are treated as having zero tilt, the result of the ¼-component **k**-vector is that along the parent perovskite axes of **1**·2H_2O, the senses of the tilts in the repeating $(Sr^{\cdots}Fe^{\cdots})_n$ chains are given by 0 + 0 – 0 + 0 –. In other words, the tilt of each Fe octahedron is opposite to that of the Fe preceding it. This is in contrast to the conventional double perovskite with uniform octahedra and **k** = [½,½,½], where these Fe tilts would be in phase with respect to each other [Fig. 1(b)].

The hydration-induced distortion of Sr^{2+} coordination geometries is analogous to a second-order Jahn-Teller (SOJT) effect, with the key distinction here being the chemical origin of the distortion and the ability to switch it on and off through (de)sorption.[27] The point symmetry (C_2) of the distorted Sr^{2+} environment allows a finite local polarisation in the same way that stereoactive lone-pair formation drives polarisation in conventional SOJT perovskites such as $BiFeO_3$.[28] In **1**·2H_2O the polarisation direction tends to alternate throughout the Sr sublattice, which requires quadrupling of the parent ABX_3 cell; hence **k** = [¼,¼,¼] [Fig. 2].

An interesting comparison can be drawn to the Ba-containing analogue $(NH_4)_2BaFe(CN)_6{\cdot}3H_2O$ (**2**·3H_2O), first described in Ref. 19. In this structurally related compound, the larger Ba^{2+} cation coordinates three H_2O molecules to give a total coordination number of nine and a coordination geometry with D_3 point symmetry. Consequently, there is no longer any local polarization at the Ba site, but the Ba coordination is nevertheless axially distorted in a conceptually similar fashion to the first-order Jahn-Teller (FOJT) effect observed in *e.g.* $LaMnO_3$.[29] A similar group theoretical analysis of the hydration pattern in **2**·3H_2O reveals it to be described entirely by the Λ_2 irrep at **k** = [¼,¼,¼] [Fig. 2]. This accounts for the corresponding space group symmetry (here, $R\bar{3}c$) and also explains the activation of the same Λ_2 forbidden tilt system that is dominant in **1**·2H_2O. As the Λ_3 irrep is inconsistent with a Λ_2 primary order parameter, in this case the Λ_3 tilt system is *not* activated by hydration. Hence there is scope for chemical control over the particular forbidden tilt systems activated by hydration in these double perovskite analogues.

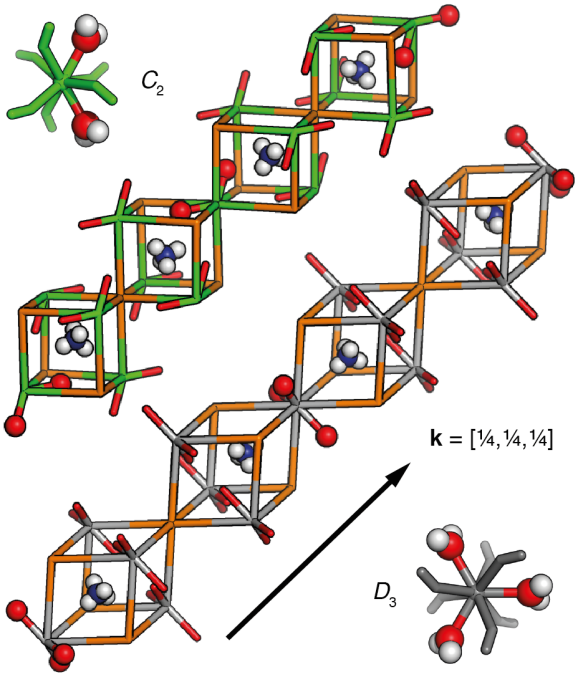

Figure 2. Simplified representations of the **1**·2H_2O (top) and **2**·3H_2O (bottom) structures in terms of the cubic parent perovskite, with Sr shown in green, Ba in grey, and Fe in orange. The ordering of the coordinated H_2O molecules (red) and NH_4^+ ions (blue/white) with ¼ components along the [111] perovskite direction, is evident. The local distortions induced by hydration at Sr and Ba sites are illustrated in the insets.

So we have shown that hydration of molecular perovskite analogues can activate unconventional symmetry-breaking processes that are altogether unrealizable in oxide perovskites. The key implication is that the diversity of distortion mechanisms exploitable in tilt engineering strategies will be substantially greater for molecular perovskites, for which $\mathbf{k} \neq \langle ½,½,\xi \rangle$ systems are no longer forbidden. Moreover, the ability to switch on and off a specific set of symmetry-lowering distortions *via* host-guest interactions (here, hydration) offers an extraordinary opportunity to develop *e.g.* guest-responsive ferroelectric or piezoelectric devices.

While we have focused on a small subset of perovskite-like Prussian blue analogues, there is clear opportunity for exploration of a wide range of chemically related systems. For example, the extent to which $NH_4^{+}\cdots H_2O$ interactions are responsible for controlling hydration patterns may be elucidated by substituting different cavity ions (*e.g.* $NMeH_3^{+}$); likewise, the nature of the B-site cations might also be varied to explore effects of charge state, polarizability, and size. And, finally, there is scope for investigating the effect of incorporating a range of guests other than H_2O. In all cases, by establishing the phenomenology of unconventional symmetry-breaking mechanisms in molecular perovskite analogues we might now hope to develop increasingly sophisticated design strategies for realisations of new classes of advanced functional materials.

ASSOCIATED CONTENT

Supporting Information

Experimental details. This material is available free of charge via the Internet at http://pubs.acs.org.

AUTHOR INFORMATION

Corresponding Author

samuel.duyker@sydney.edu.au or
andrew.goodwin@chem.ox.ac.uk

Notes

The authors declare no competing financial interests.

ACKNOWLEDGMENT

S.G.D. acknowledges an Endeavour Fellowship funded by the Australian Government. S.G.D. thanks C. J. Kepert (Sydney) for access to the powder diffractometer and thermogravimetric analyzer. J.A.H. and A.L.G. gratefully acknowledge funding from the EPSRC and the ERC (Grant 279705).

REFERENCES

(1) Megaw, H. D. *Proc. R. Soc. London, A* **1947**, *189*, 261.
(2) Cochran, W. *Adv. Phys.* **1960**, *9*, 387.
(3) Laulhé, C.; Hippert, F.; Bellissent, R.; Simon, A.; Cuello, G. J. *Phys. Rev. B* **2009**, *79*, 064104.
(4) Cowley, R. A. *Phys. Rev. Lett.* **1962**, *9*, 159.
(5) Benedek, N. A.; Fennie, C. J. *Phys. Rev. Lett.* **2011**, *106*, 107204.
(6) Pitcher, M. J.; Mandal, P.; Dyer, M. S.; Alaria, J.; Borisov, P.; Niu, H.; Claridge, J. B.; Rosseinsky, M. J. *Science* **2015**, *347*, 420.
(7) Senn, M. S.; Bombardi, A.; Murray, C. A.; Vecchini, C.; Scherillo, A.; Luo, X.; Cheong, S. W. *Phys. Rev. Lett.* **2015**, *114*, 035701.
(8) Howard, C. J.; Stokes, H. T. *Acta Cryst. B.* **1998**, *54*, 782.
(9) Howard, C. J.; Kennedy, B. J.; Woodward, P. M. *Acta Cryst. B.* **2003**, *59*, 463.
(10) Howard, C. J.; Withers, R. L.; Knight, K. S.; Zhang, Z. *J. Phys.: Condens. Matter* **2008**, *20*, 135202.
(11) Goodwin, A. L.; Kepert, C. J. *Phys. Rev. B* **2005**, *71*, 140301.
(12) Goodwin, A. L. *Phys. Rev. B* **2006**, *74*, 134302.
(13) Du, Z.-Y.; Zhao, Y.-P.; He, C.-T.; Wang, B.-Y.; Xue, W.; Zhou, H.-L.; Bai, J.; Huang, B.; Zhang, W.-X.; Chen, X.-M. *Cryst. Growth Des.* **2014**, *14*, 3903.
(14) Du, Z.-Y.; Zhao, Y.-P.; Zhang, W.-X.; Zhou, H.-L.; He, C.-T.; Xue, W.; Wang, B.-Y.; Chen, X.-M. *Chem. Commun.* **2014**, *50*, 1989.
(15) Hill, J. A.; Thompson, A. L.; Goodwin, A. L. *J. Am. Chem. Soc.* **2016**, *138*, 5886.
(16) Bovill, S. M.; Saines, P. J. *CrystEngComm* **2015**, *17*, 8319.
(17) Kareis, C. M.; Lapidus, S. H.; Her, J.-H.; Stephens, P. W.; Miller, J. S. *J. Am. Chem. Soc.* **2012**, *134*, 2246.
(18) Patterson, F. K.; Moeller, C. W.; Ward, R. *Inorg. Chem.* **1963**, *2*, 196.
(19) Córdoba, L. M.; Echeverría, G. A.; Piro, O. E.; Gómez, M. I. *J. Therm. Anal. Calorim.* **2015**, *120*, 1827.
(20) Anderson, M. T.; Greenwood, K. B.; Taylor, G. A.; Poeppelmeier, K. R. *Prog. Solid State Chem.* **1993**, *22*, 197.
(21) Lenz, A.; Müller-Buschbaum, H. *J. Less Common Met.* **1990**, *161*, 141.
(22) Kieslich, G.; Sun, S.; Cheetham, A. K. *Chem. Sci.* **2015**, *6*, 3430.
(23) Medina Córdoba, L.; Morán, J. A.; Santos, S.; Piro, O. E.; Gómez, M. I. *J. Chem. Crystallogr.* **2011**, *41*, 1280.
(24) Duyker, S. G.; Halder, G. J.; Southon, P. D.; Price, D. J.; Edwards, A. J.; Peterson, V. K.; Kepert, C. J. *Chem. Sci.* **2014**, *5*, 3409.
(25) ISOTROPY Software Suite, iso.byu.edu.
(26) Miller, S. C.; Love, W. F. *Tables of irreducible representations of space groups and co-representations of magnetic space groups*; Pruett Press, 1967.
(27) Ra, H.-S.; Ok, K. M.; Halasyamani, P. S. *J. Am. Chem. Soc.* **2003**, *125*, 7764.
(28) Kubel, F.; Schmid, H. *Acta Cryst. B.* **1990**, *46*, 698.
(29) Goodenough, J. B. *Annu. Rev. Mater. Sci.* **1998**, *28*, 1.

JACS
JOURNAL OF THE AMERICAN CHEMICAL SOCIETY

Article

pubs.acs.org/JACS

Dicyanometallates as Model Extended Frameworks

Joshua A. Hill, Amber L. Thompson, and Andrew L. Goodwin*

Inorganic Chemistry Laboratory, Department of Chemistry, University of Oxford, South Parks Road, Oxford OX1 3QR, U.K.

Supporting Information

ABSTRACT: We report the structures of eight new dicyanometallate frameworks containing molecular extra-framework cations. These systems include a number of hybrid inorganic−organic analogues of conventional ceramics, such as Ruddlesden−Popper phases and perovskites. The structure types adopted are rationalized in the broader context of all known dicyanometallate framework structures. We show that the structural diversity of this family can be understood in terms of (i) the charge and coordination preferences of the particular metal cation acting as framework node, and (ii) the size, shape, and extent of incorporation of extra-framework cations. In this way, we suggest that dicyanometallates form a particularly attractive model family of extended frameworks in which to explore the interplay between molecular degrees of freedom, framework topology, and supramolecular interactions.

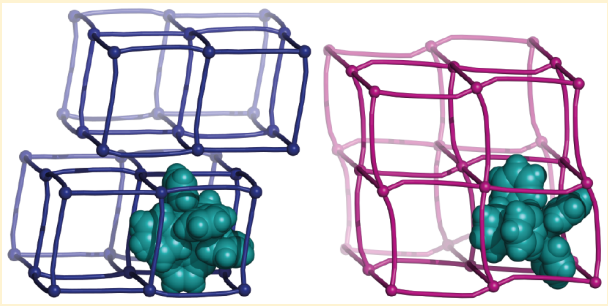

INTRODUCTION

Arguably one of the most important conceptual breakthroughs in modern structural chemistry was Robson's geometric interpretation of the structures of coordination polymers as connected nets of nodes and linkers.[1] The language of reticular chemistry that developed from that point has enabled the informed design of an extraordinarily large family of framework materials and coordination polymers, notably including metal−organic frameworks (MOFs)[2] and covalent organic frameworks (COFs).[3,4] The basic design approach as it is currently used reflects the realization that specific combinations of node and linker geometries can usually lead to only a finite number of different possible structures;[5] hence, control over the former (e.g., the choice of transition-metal elements or clusters with specific coordination geometry preferences and linkers with characteristic binding modes) enables control over the latter.[6]

The abstraction of linker molecules to rodlike connections carries with it the implication that linker shape and chemistry bear little influence on the resulting framework structure. Certainly this is sometimes true,[7,8] but for many coordination polymers the packing motifs and stereochemical preferences of the organic linkers often play a defining role in directing structure. This may be as simple as linker functionalization preventing network interpenetration but the effects can also be altogether more drastic.[9] For example, if the terephthalate linker connecting chains of corner-sharing $AlO_4(OH)_2$ octahedra in the porous "breathing" MIL-53 (ref 10) is swapped for the longer and slightly bent 4,4′-azobenzenedicarboxylate then the nonporous layered MIL-129 forms instead, where the ligands now adopt a $\pi-\pi$ stacking motif.[11]

It is in this context that we have developed a particular interest in coordination polymers assembled using the dicyanometallate linker $[NC-M-CN]^-$ (M = Cu^I, Ag^I, Au^I). The preferred coordination mode of this linker is linear, and so it combines the nanometre scale of the organic linkers used to build MOFs with the geometric flexibility of an atomically thin linker. In many ways, dicyanometallates can be considered the natural extension of oxide frameworks (e.g., perovskites) and cyanide frameworks (e.g., Prussian Blues) [Figure 1].

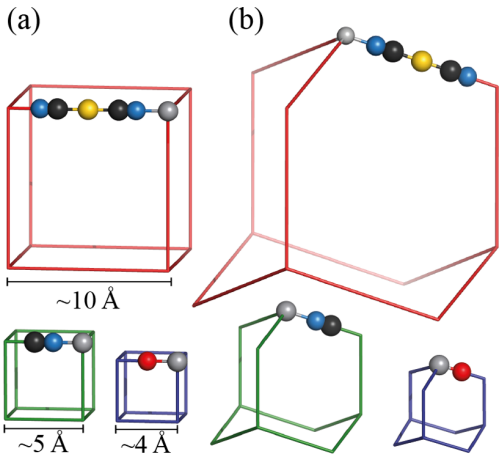

Figure 1. Increasing scale of oxide (blue), cyanide (green), and dicyanometallate (red) architectures illustrated with the perovskite (a) and cristobalite (b) structures. Increasing the length of the linker dramatically increases the available volume for interpenetration, extra-framework cations, and/or neutral guests. Node metal (gray), oxygen (red), nitrogen (blue), carbon (black), and linker metal (yellow).

Received: December 24, 2015

ACS Publications © XXXX American Chemical Society

DOI: 10.1021/jacs.5b13446
J. Am. Chem. Soc. XXXX, XXX, XXX−XXX

Table 1. Summary of the Structurally Characterized Dicyanometallate Frameworks of General Formula $A_nB(L)X_m{\cdot}G$, Where L Is a Neutral Ligand Bound to the Node Metal Center (i.e., Not to the Linker Metal) and G Is a Non-coordinating Guest Molecule[a]

B^IX Coordination number = 2	
Chains	
Parallel	
AuCN [34,35]	
AgCN [35,39,40]	
CuCN [44]	
$Ni(L^1)(H_2O)Ag(CN)_2$ [47]	
Criss-cross	
low-T Cu(CN) [44]	
$A_{0.5}B^IX_{1.5}$	3
(6,3) layers	
$[Cu_2(2,2'\text{-bpy})_2(CN)]_{0.5}Cu[Cu(CN)_2]_{1.5}$ [55]	
AB^IX_2	4
Square grids	
Wavy	
$KCu[Ag(CN)_2]_2$ [60]	
$RbCu[Ag(CN)_2]_2$ [60]	
$CsCu[Ag(CN)_2]_2$ [60]	
AB^IX_2	4
Diamondoid	
Distorted	
$[NEt_4]Ag[Ag(CN)_2]_2$*	
$B^{II}X_2$	4
Quartz	
α-$Zn[Au(CN)_2]_2$ [70]	
$Co[Au(CN)_2]_2$ [72]	
α-$Zn[Ag(CN)_2]_2{\cdot}xAg(CN)$ [73]	
$Cd(2,2'\text{-bpy})[Au(CN)_2]_2$ [75]	
$Mn(2,2'\text{-bpy})[Au(CN)_2]_2$ [78]	
$B^{II}X_2$	4
Niobium monoxide (nbo)	
$Fe(3\text{-CNpy})_2[Au/Ag(CN)_2]_2{\cdot}\frac{2}{3}H_2O$ [45,81]	
$Fe(TPT)_{2/3}[Au/Ag(CN)_2]_2$ [84]	
$Fe(TPT)_{2/3}[Au/Ag(CN)_2]_2{\cdot}2CH_2Cl_2$ [84]	
$Fe(TPT)_{2/3}[Ag(CN)_2]_2{\cdot}MeOH$ [84]	
$B^{II}X_2$	4
Cadmium sulfate (cds)	
$Fe(pmd)(H_2O)[Au(CN)_2]_2{\cdot}H_2O$ [94]	
$Fe(pmd)(H_2O)[Ag(CN)_2]_2{\cdot}H_2O$ [94]	
$Fe(pmd)[Au(CN)_2]_2$ [94]	

$B^{II}X_2$	4
Square grid	
Regular	
$Cu(py)_2[Au(CN)_2]_2$ [36]	
$Fe(3\text{-Phpy})_2[Au(CN)_2]_2$ [41]	
$yellow\text{-}Fe(3\text{-CNpy})_2[Au(CN)_2]_2$ [45]	
$Fe(DEAS)_2[Au/Ag(CN)_2]_2$ [48]	
$Cd(py)_2[Ag(CN)_2]_2$ [49]	
$Fe(py)_2[Ag(CN)_2]_2$ [52]	
$Cu(DMF)[Au(CN)_2]_2$ [17]	
$blue\text{-}Cu(DMSO)_2[Au(CN)_2]_2$ [17]	
$Zn(NIT4Py)_2[Au(CN)_2]_2$ [56]	
$Pb(phen)_2[Au(CN)_2]_2$ [57]	
$Fe(H_2O)_2[Ag(CN)_2]_2{\cdot}(2,2'\text{-bpe})$ [59]	
$(\frac{1}{2},\frac{1}{2})$ **offset bilayers**	
$Co(DMF)_2[Au(CN)_2]_2$ [61]	
$Mn(3\text{-Fpy})_2[Au(CN)_2]_2$ [62]	
$Mn(H_2O)_2[Au(CN)_2]_2$ [51]	
$Mn(3\text{-Mepy})_2[Ag(CN)_2]_2$ [53]	
$colourless\text{-}Fe(3\text{-CNpy})_2[Au(CN)_2]_2H_2O$ [45]	
$Fe(4\text{-Mepy})_2[Au(CN)_2]_2$ [65]	
$Fe(3\text{-Clpy})_2[Au/Ag(CN)_2]_2$ [66,67]	
$Fe(3\text{-Brpy})_2[Au/Ag(CN)_2]_2$ [66,67]	
$Fe(3\text{-Ipy})_2[Au/Ag(CN)_2]_2$ [66,67]	
$Fe(3\text{-Ipy})_2[Au(CN)_2]_2{\cdot}\frac{1}{2}3\text{-Ipy}$ [67]	
$Fe(3\text{-Fpy})_2[Au/Ag(CN)_2]_2$ [66,67]	
$Cd(3\text{-Fpy})_2[Au(CN)_2]_2$ [74]	
$Mn(bim)[Ag(CN)_2]_2[(bim)AgCN]_2{\cdot}nH_2O$ [76]	
Bridged (Hofmann)	
$Zn(pyz)[Au(CN)_2]_2$ [79]	
$Co(pyz)[Au(CN)_2]_2$ [79]	
$Cd(4,4'\text{-bpy})[Ag(CN)_2]_2$ [82]	
$Mn(4,4'\text{-bpy})[Au(CN)_2]_2{\cdot}2CHCl_3$ [85]	
$Cu(pyz)[Au(CN)_2]_2$ [87]	
$Fe(bpmp)[Au/Ag(CN)_2]_2{\cdot}n\text{DMF}{\cdot}\frac{1}{2}\text{EtOH}{\cdot}mH_2O$ [90]	
$Fe(pyz)[Au(CN)_2]_2{\cdot}(pyz)$ [18]	
$B^{II}X_2$	4
Cristoballite	
β-$Zn[Au(CN)_2]_2$ [14]	
γ-$Zn[Au(CN)_2]_2$ [14]	

$B^{II}X_2$	4
Interpenetrating square grid	
Inclined	
$Cd(NH_3)_2[Ag(CN)_2]_2$ [37]	
$Cu(NH_3)_2[Ag(CN)_2]_2$ [42]	
$Zn(NH_3)_2[Au(CN)_2]_2$ [14]	
$Cd(py)_2[Ag(CN)_2]_2{\cdot}C_4H_5N$ [49]	
$Cd(py)_2[Ag(CN)_2]_2{\cdot}C_6H_6$ [49]	
$Mn(4\text{-Mepy})_2[Ag(CN)_2]_2$ [53]	
Interwoven	
$Ca[Ag(CN)_2]_2{\cdot}2H_2O$ [54]	
$Sr[Ag(CN)_2]_2{\cdot}2H_2O$ [54]	
$Cd(4\text{-Mepy})_2[Ag(CN)_2]{\cdot}(4\text{-Mepy})$ [58]	
$B^{II}X_2$	4
Other	
Two layer herringbone	
$Cd(hydeten)[Ag(CN)_2]_2{\cdot}\frac{1}{2}H_2O$ [63]	
Bifurcated chains	
$Mn(NIT3Py)_2[Au(CN)_2]_2$ [64]	
$Co(NIT3Py)_2[Au(CN)_2]_2$ [64]	
$Zn(NIT3Py)_2[Au(CN)_2]_2$ [64]	
Bridged interwoven (6,3) (mok)	
δ-$Zn[Au(CN)_2]_2$ [14]	
lvt	
$Mn(4\text{-CNpy})(H_2O)[Ag(CN)_2]_2$ [71]	
Binodal (pts)	
$Mn(py\text{-}4\text{-aldoxime})(H_2O)[Ag(CN)_2]_2$ [71]	
$A_{0.5}B^IX_{2.5}$	5
Layered	
Perovskite slabs	
$[PPN]_{0.5}Cu[Au(CN)_2]_{2.5}{\cdot}EtOH$*	
$[PPN]_{0.5}Cd[Ag(CN)_2]_{2.5}(EtOH)$*	
$[PPN]_{0.5}Mn[Ag(CN)_2]_{2.5}(EtOH)$*	
$A_{0.5}B^IX_{2.5}$	5
Other	
Bridged interwoven (6,3) (*jah*1)	
$[Bu_4N]_{0.5}Cd[Ag(CN)_2]_{2.5}$*	

$AB^{III}X_3$	6
α-Po	
$KCo[Au(CN)_2]_3$ [15,33]	
$RbCd[Ag(CN)_2]_3$ [38]	
$KNi[Au(CN)_2]_3$ [43]	
$KMn[Ag(CN)_2]_3$ [46]	
$KCd[Au/Ag(CN)_2]_3$ [50]	
$KFe[Au/Ag(CN)_2]_3$ [19,51]	
$AB^{III}X_3$	6
Perovskite	
$[PPN]Ni[Au(CN)_2]_3$ [32]	
$[PPN]Co[Au(CN)_2]_3$ [32]	
$[PPN]Cd[Au(CN)_2]_3$*	
$[PPN]Mn[Au(CN)_2]_3$*	
$[PPN]Cd[Ag(CN)_2]_3{\cdot}3EtOH{\cdot}xH_2O$*	
$AB^{III}X_3$	6
Other	
Intersecting rectangular grids (bcs)	
$[Bu_4N]Ni[Au(CN)_2]_3$ [32]	
$B^{III}X_3$	6
α-Po	
$Ag_3[Co(CN)_6]$ [68]	
$Ag_3[Fe(CN)_6]$ [69]	
$Au/Ag_3[In(CN)_6]$ [50]	
$Ag_3[In(CN)_6]{\cdot}xH_2O$ [50]	
$B^{III}X_3$	6
acs	
$La[Au/Ag(CN)_2]_3(H_2O)_3$ [77]	
$La[Ag_{0.39}Au_{0.61}(CN)]_3(H_2O)_3$ [77]	
$La[Ag_{0.83}Au_{0.17}(CN)]_3(H_2O)_3$ [77]	
$Pr[Au/Ag(CN)_2]_3(H_2O)_3$ [80]	
$Nd[Au/Ag(CN)_2]_3(H_2O)_3$ [83]	
$Sm[Au(CN)]_3(H_2O)_3$ [86]	
$Eu[Au/Ag(CN)_2]_3(H_2O)_3$ [88,89]	
$Eu_{0.5}Tb_{0.5}[Au(CN)]_3(H_2O)_3$ [89]	
$Gd[Au(CN)]_3(H_2O)_3$ [91]	
$Tb[Au(CN)]_3(H_2O)_3$ [92,93]	
$Am[Au/Ag(CN)_2]_3(H_2O)_3$ [83]	
$Cm[Au/Ag(CN)_2]_3(H_2O)_3$ [80]	

[a]Formulae including Au/Ag indicate that both the pure gold- and silver-containing compounds are known. Newly synthesized compounds reported as part of our study are indicated by an asterisk. Abbreviations used: L^1 = *N*-(3-aminopropyl)-5-bromosalicylaldimine; 2,2′-bpy = 2,2′-bipyridine; Et = C_2H_5; 3-CNpy = 3-cyanopyridine; TPT = 2,4,6-tris(pridyl)triazine; Me = CH_3; pmd = pyrimidine; py = pyridine; 3-Phpy = 3-phenylpyridine; DEAS = 4′-diethylaminostilbazole; DMF = *N*,*N*′-dimethylformamide; DMSO = dimethyl sulfoxide; NIT4Py = 2-(4′-pyridyl)-4,4,5,5-tetramethylimidazoline-1-oxyl-3-oxide; phen = 1,10-phenanthroline; 2,2′-bpe = 2,2′-bis(pyridyl)ethene; 3-Fpy = 3-fluoropyridine; 3-Mepy = 3-methylpyridine; 4-Mepy = 4-methylpyridine; 3-Clpy = 3-chloropyridine; 3-Brpy = 3-bromopyridine; 3-Ipy = 3-iodopyridine; bim = benzimidazolate; pyz = pyrazine; 4,4′-bpy = 4,4′-bipyridine; bpmp = 1,4-bis(pyridin-4-ylmethyl)piperazine; hydeten = *N*-(2-hydroxyethyl)ethylenediamine); NIT3Py = 2-(3′-pyridyl)-4,4,5,5-tetramethylimidazoline-1-oxyl-3-oxide; PPN = bis(triphenylphosphine)iminium cation; Bu = *n*-C_4H_9.

Like their oxide and cyanide cousins, dicyanometallate frameworks exhibit a variety of important functional responses. Examples include colossal positive and negative thermal expansion in silver hexacyanocobaltate (≡ $Co^{III}[Ag^I(CN)_2]_3$);[12] giant negative compressibility and guest-dependent luminescence in $Zn[Au(CN)_2]_2$;[13,14] piezoelectric behavior in $KCo[Au(CN)_2]_3$;[15] tunable room-temperature luminescence in $La[Au_xAg_{1-x}(CN)_2]{\cdot}3H_2O$;[16] vapochromism in $Cu[Au(CN)_2]_2$;[17] heat-, light-, and pressure-induced spin-crossover in $Fe(pyz)[Ag(CN)_2]_2{\cdot}pyz$ (pyz = pyrazine);[18] and strain-free charge storage in $K_xFe^{II/III}[Ag(CN)_2]_3$.[19] In each of these cases, the geometric flexibility of the dicyanometallate linker plays a key role and so there is good reason to expect similarly intriguing functional responses among as-yet-unrealised dicyanometallate frameworks. Yet, in this context of developing new functional dicyanometallates, what is con-

DOI: 10.1021/jacs.5b13446
J. Am. Chem. Soc. XXXX, XXX, XXX−XXX

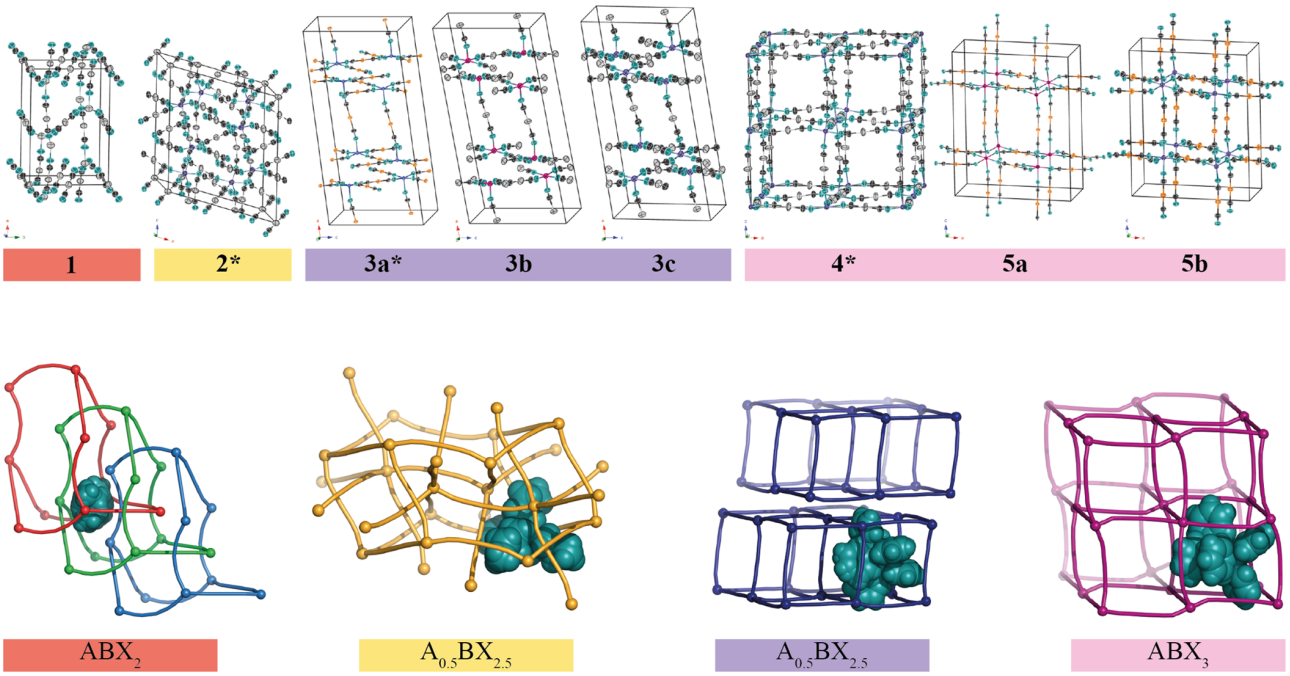

Figure 2. Representations of the crystal structures of the various new dicyanometallate frameworks reported in this study. The top panels show structures in thermal ellipsoid representation (probability = 50%, or 90% where indicated with an asterisk). Each image is represented at the same absolute scale; extra-framework cations and solvent molecules have been omitted for clarity. The bottom panels show schematic representations of the corresponding network topologies. In each case a single extra-framework cation is shown in space-filling representation to illustrate the relationship between cation shape and network topology. More detailed representations are given as SI.

spicuously absent is an overview of the structural chemistry of the family of the sort that has been so enabling in, e.g., oxide[20,21] and cyanide[22−24] framework chemistry.

Table 1 summarizes, to the best of our knowledge, the various dicyanometallate frameworks reported to date. For simplicity, we have focused on systems expressible in the form $A_mBX_n{\cdot}\{guest\}$. In this representation, A denotes an extra-framework cation (if present), B is the framework node cation, X is a dicyanometallate anion, and we allow for the presence of solvent or other neutral molecules within the structure. What is immediately clear is that the family is extremely diverse, and encompasses much of the compositional and topological complexity responsible for the rich structural chemistry of conventional ceramic frameworks. In addition, and as in the transition-metal formate "MOF perovskites",[25−27] there is the intriguing capacity to incorporate molecular cations as a means of balancing framework charge. There is strong current interest in these systems as a direct result of the recent discovery of unconventional semiconductor behavior in the $[CH_3NH_3]PbI_3$ family of solar cell materials.[28−30] Ordering processes involving molecular cations can be fundamentally different from those involving spherically symmetric or dipolar cations, as in conventional oxide ceramics.[31] The relationship between molecular geometry and host framework topology remains relatively unexplored—particularly in dicyanometallates.[32] Likewise, the nanometre node separation in dicyanometallate frameworks potentially allows for the incorporation of molecular cations capable of complex supramolecular interactions.

Our paper has two principal objectives. The first aim is to report the structures of a number of new dicyanometallate frameworks which contain molecular cations. On the one hand, these are of fundamental interest in terms of their structural chemistry, but on the other hand they may prove important by virtue of their conceptual relationship to other molecular analogues of conventional ceramics, including the semiconducting lead iodide family. The second—and ultimately more important—aim of our study is to suggest an organization of the structures of known dicyanometallates that helps rationalize the structural diversity of this family. In doing so we begin to develop a set of design strategies that will ultimately allow rational control over framework structure in precisely the way envisaged by Robson's original study.[1]

RESULTS AND DISCUSSION

Structural Investigation of New Dicyanometallates. Our starting point is to describe the various new dicyanometallates we have prepared. Motivated by the desire to introduce molecular extra-framework cations, our typical synthetic strategy was to combine a simple transition-metal salt with a specially prepared molecular salt of a given dicyanometallate anion. The latter acts as the source of molecular cation in the framework that ultimately forms. We report eight new compounds, which adopt a total of five structure types and correspond to the three fundamental compositions ABX_2, $A_{0.5}BX_{2.5}$, and ABX_3.

Diamondoid ABX_2. The first system we describe was actually the fortuitous result of our attempts to prepare $[NEt_4][Ag(CN)_2]$ as a dicyanometallate precursor for subsequent framework formation. The combination of $[NEt_4]Cl$ or $[NEt_4]Br$ with $KAg(CN)_2$ yields the same dicyanometallate framework $[NEt_4]Ag^I[Ag(CN)_2]_2$ (**1**) in which silver(I) cations participate as both node and linker. The dual roles of silver(I) in this system are distinguishable by both coordination

DOI: 10.1021/jacs.5b13446
J. Am. Chem. Soc. XXXX, XXX, XXX−XXX

Table 2. Crystallographic Details for the New Materials Reported in This Study

Compound	1	2	3a	3b
Empirical formula	$Ag_3N_5C_{12}H_{20}$	$Cd_2Ag_5N_{11}C_{26}H_{36}$	$Cu_2Au_5P_2N_{11}C_{46}H_{30}$	$Mn_2Ag_5P_2N_{11}C_{46}H_{30}$
Formula weight (g mol^{-1})	557.92	1266.79	2002.83	1540.1
Crystal System	Orthorhombic	Monoclinic	Monoclinic	Monoclinic
Space Group	*Pnma* (No. 62)	*C*2/c (No. 15)	*C*2/c (No. 15)	*C*2/c (No. 15)
Z	4	4	4	4
Radiation (Å)	Cu K$_\alpha$, $\lambda = 1.54180$	Mo K$_\alpha$, $\lambda = 0.71073$	$\lambda = 0.68890$	Cu K$_\alpha$, $\lambda = 1.54180$
Crystal colour	Pale Yellow	Colourless	Green	Colourless
Crystal size (mm)	0.05×0.11×0.12	0.06×0.14×0.16	0.01×0.01×0.01	0.09×0.22×0.27
Temperature (K)	280.2(5)	150.0(5)	30.0(3)	300.00(3)
a (Å)	16.6101(3)	16.2798(2)	27.9505(6)	28.3700(3)
b (Å)	11.2973(2)	13.9248(2)	15.0898(4)	15.6843(2)
c (Å)	9.2725(2)	18.0439(2)	13.4803(3)	13.91760(10)
V (Å^3)	1739.98(6)	3930.35(9)	5647.5(2)	6105.94(11)
β (°)	—	106.0823(5)	96.629(2)	99.6092(10)
μ (mm^{-1})	26.795	3.531	13.78	16.671
Reflections ($I > 2\sigma(I)$)	1842	4095	8549	5325
R (F_o)	0.0258	0.0220	0.0372	0.0282
R$_w$ (F_o)	0.0661	0.0493	0.0839	0.0673
GOF	0.951	1.0249	0.9932	1.0497

Compound	3c	4	5a	5b
Empirical formula	$Cd_2Ag_5P_2N_{11}C_{46}H_{30}$	$Cd_1Ag_3P_2N_7C_{48}H_{48.87}O_{3.44}$	$Mn_1Au_3P_1N_6C_{24}H_{15}$	$Cd_1Au_3P_1N_6C_{24}H_{15}$
Formula weight (g mol^{-1})	1653.04	1276.78	1340.52	1398
Crystal System	Monoclinic	Cubic	Monoclinic	Monoclinic
Space Group	*C*2/c (No. 15)	*Pa*$\bar{3}$ (No. 205)	*I*2/a (No. 15)	*I*2/a (No. 15)
Z	4	8	4	4
Radiation (Å)	Cu K$_\alpha$, $\lambda = 1.54180$	Mo K$_\alpha$, $\lambda = 0.71073$	Mo K$_\alpha$, $\lambda = 0.71073$	Cu K$_\alpha$, $\lambda = 1.54180$
Crystal colour	Colourless	Colourless	Colourless	Colourless
Crystal size (mm)	0.04×0.10×0.23	0.19×0.34×0.39	0.06×0.08×0.10	0.02×0.02×0.10
Temperature (K)	282(8)	280.0(4)	150.0(5)	291.8(1)
a (Å)	28.5577(8)	21.7394(3)	16.7035(3)	16.8455(3)
b (Å)	15.8350(4)	21.7394(3)	12.5777(3)	12.7383(3)
c (Å)	13.9531(4)	21.7394(3)	20.6707(4)	20.8965(3)
V (Å^3)	6226.6(3)	10274.1(2)	4338.48(15)	4480.19(15)
β (°)	99.310(3)	—	92.5382(10)	92.3725(16)
μ (mm^{-1})	18.499	1.633	10.509	22.772
Reflections ($I > 2\sigma(I)$)	5585	5085	4065	4094
R (F_o)	0.0400	0.0388	0.0377	0.0226
R$_w$ (F_o)	0.1148	0.0820	0.0668	0.0525
GOF	0.958	1.0363	1.067	0.9997

geometry and cyanide binding orientation: the node cations are tetrahedrally coordinated by the N cyanide terminus and the linker cations are linearly coordinated by the C cyanide terminus. The crystal structure is illustrated in Figure 2, and relevant crystallographic details are summarized in Table 2. Three distorted diamondoid networks interpenetrate, with each $[NEt_4]^+$ cation contained within a cavity formed by the combination of all three networks.

An intriguing property of this system is the existence of a phase transition on cooling below 235 K. This transition—which will be described in detail elsewhere—involves the condensation of a soft phonon mode at an incommensurate wave-vector. The study of classical soft-mode transitions in extended frameworks is a relatively unexplored field;[95,96] the purpose of drawing attention to this transition here is simply to highlight that the dynamical properties of these materials may, in due course, be of interest in their own right.

Five-Connected $A_{0.5}BX_{2.5}$. Reaction of $[NBu_4][Ag(CN)]\cdot 0.5H_2O$ with cadmium nitrate leads to the structurally complex phase $[NBu_4]_{0.5}Cd^{II}[Ag(CN)_2]_{2.5}$ (**2**), as illustrated in Figure 2. Key crystallographic details of **2** are again summarized in Table 2. In the absence of a strong coordination preference, Cd^{II} has here adopted a distorted trigonal bipyramidal geometry. These pentacoordinate nodes connect to give a unique, self-catenating topology (TOPOS reference *jah*1; the topology was detected with TOPOS[97,98] and deposited in the TTD[99] archive) that can be related to a linked pair of interpentrating **cds**-type nets (see Supporting Information (SI)). Mindful that correlation does not necessarily imply causation, we note nonetheless that there is again a close match between framework cavity and molecular cation shape. This suggests that the form of the $[NBu_4]^+$ cation may be responsible for the unusual topology assumed by this material.

As in **1** and numerous other dicyanoargentate frameworks, **2** contains a series of short $Ag^I\cdots Ag^I$ contacts generally considered indicative of $d^{10}\cdots d^{10}$ argentophilic interactions. These interactions are often strongly susceptible to changes in external conditions, such as temperature and pressure.[100−105] We determined the thermal expansion behavior of **2** in order to identify any unusual thermomechanical response, and found moderately strong positive and negative thermal expansion in directions that are respectively parallel and perpendicular to these argentophilic interactions ($\alpha_{\|}$ = +138(5) MK^{-1}, $\alpha_{\perp}$ = −83.1(1.6) MK^{-1}; see SI for further discussion).[106]

An alternative five-connected dicyanometallate structure that is more obviously related to the molecular perovskite analogues

DOI: 10.1021/jacs.5b13446
J. Am. Chem. Soc. XXXX, XXX, XXX−XXX

discussed above can be accessed by reaction of $[PPN]^+$ dicyanometallates with transition-metal salts ($[PPN]^+$ = bis(trisphenylphosphine)iminium cation). The crystal structures of $[PPN]_{0.5}Cu[Au(CN)_2]_{2.5}$·EtOH (**3a**), $[PPN]_{0.5}Mn[Ag(CN)_2]_{2.5}(EtOH)$ (**3b**), and $[PPN]_{0.5}Cd[Ag(CN)_2]_{2.5}(EtOH)$ (**3c**) are shown in Figure 2, and key crystallographic details are again summarized in Table 2. In these compounds, the dicyanometallate network forms grid-like layers of connected cubes that are then stacked on top of one another. The large molecular cations occupy the voids at the center of each ~$(nm)^3$ cube. Because the layers are not connected, each transition metal node is coordinated by dicyanometallate anions in a square pyramidal geometry. Whereas in the case of Cu^{2+} this coordination geometry is straightforwardly understood in terms of the d^9 electronic configuration, for **3b** and **3c** the Mn^{2+} and Cd^{2+} coordination is actually octahedral and is completed by one molecule of the ethanol solvent from which the crystals were grown. The ability to incorporate octahedral node geometries via solvent coordination means that, in principle at least, this phase may be accessible for a range of other transition-metal dications. In practice, the balance with competing phases (discussed further below) is remarkably subtle.

In each of the compounds **3a**–**c**, successive layers are offset by one-half of the cube face diagonal. This offset has the effect of bringing Ag^+ or Au^+ cations at the cube edges into close contact, which will presumably maximize metallophilic interactions. In this sense there is a clear distinction from the structural chemistry of oxide frameworks, where there is a strong repulsion between the linker anions. In the related $n = 2$ Ruddlesden–Popper phases (e.g., $Sr_3Ti_2O_7$) this repulsion is relieved by presence of additional A-cations as rocksalt-type layers.[107] In our case, the weak metallophilic forces holding neighboring layers together may be expected to result in particularly anisotropic elastic response for this family,[108] while also allowing for the possibility of intercalation chemistry.[109−111]

Cubic ABX_3. The analogy between dicyanometallate frameworks and perovskite oxides is clearest in the last family of compounds we report. These again make use of the $[PPN]^+$ dicyanometallates in their synthesis. Similar conditions to those described above for **3a**–**c** allowed preparation of the ABX_3 solvate $[PPN]Cd[Ag(CN)_2]_3$·3EtOH (**4**) and the solvent-free frameworks $[PPN]Mn[Au(CN)_2]_3$ (**5a**) and $[PPN]Cd[Au(CN)_2]_3$ (**5b**). In the case of **4**, crystals grew directly from reaction mixtures that had originally formed crystals of **3c**; the relationship between these phases is discussed in more detail below. The structures of all three compounds **4**, **5a**, **5b** are clear analogues of perovskites: octahedrally coordinated Mn^{II}/Cd^{II} centers are connected to form the characteristic cubic network, with $[PPN]^+$ cations adopting the "12-coordinate" A-cation site [Figure 2]. We use the term "super-perovskites" to reflect this structural correspondence and to emphasize that the B···B separation across the perovskite cube edge is now on the nanometre scale.

Just as for other perovskite analogues, long-established geometric descriptors can be applied to these superperovskite frameworks. For example, we calculate "tolerance factors" of 1.02 (at 150 K) and 1.00 (at 300 K) for **5a** and **5b**, respectively (see SI);[112−114] likewise the octahedral tilt systems active in both structures correspond to the same Glazer notation $a^-a^-c^-$.[115,116] While the tilts of compounds **5a** and **5b** can be described completely using Glazer notation, compound **4** shows in-phase tilting of adjacent octahedra correlated perpendicular to the rotation axis: an impossibility for perovskites, such as oxides and halides, with monatomic anions. The tilt system of **4** is described by the following tilt tensor (see SI for discussion of this notation):

$$\begin{bmatrix} - & - & + \\ + & - & - \\ - & + & - \end{bmatrix}.$$

Because the phenyl groups of the PPN^+ cation extend up to the perovskite cube faces, there are direct cation–cation interactions that may influence the phase transition behavior of these systems. In contrast to the simple monopolar and/or dipolar interactions between A-site cations in oxide perovskites, these interactions are inherently multipolar, which in turn may give rise to complex ordering processes unrealisable in conventional ceramics. Indeed the PPN^+ conformations we observe in compound **3c** and its transformation product **4** are fundamentally different from those found in **5a** and **5b**: in the former the phenyl rings are oriented as if to maximize cation–π interactions with the linker Ag^+ cation, whereas in the latter intra- and inter-molecular π–π interactions dominate (Figure 3a,b). This is entirely consistent with the diversity of $PPN^+\cdots PPN^+$ supramolecular interaction motifs known to occur in the solid state.[117] So one alternative view of the structures of **5a** and **5b** is that the anionic dicyanometallate framework acts to impose a particular geometric arrangement of the PPN^+ cations that may not necessarily be compatible with the inter-cation interactions. We suggest that exploration of this tension between complex multipolar interactions and the geometry of the lattice supporting those interactions may be a fertile playground for future research given, for example, the implication of multipolar dynamics in extending charge-carrier lifetimes in $[CH_3NH_3]PbI_3$ (Figure 3c,d).[118]

Composition–Structure Relationships in Dicyanometalates. Given the diversity of known structures of dicyanometallate frameworks—i.e., those reported in the preceding section together with the exhaustive list given in Table 1—it is natural to ask how one might control the adoption of one architecture or another through choice of chemical composition. Our approach to answering this question is essentially an empirical one. We begin by organizing all known dicyanometallates into compositional families of given stoichiometry A_mBX_n. Even if their structures vary, members of any one family share the same coordination number and charge state of the $B^{(n-m)+}$ cation—two aspects over which the synthetic chemist has some control. Coordination number usually fixes the value of n and so constrains the number and type of relevant network topologies. Likewise, cation charge determines the value of $n - m$ and so determines the extent of inclusion of extra-framework A^+ cations (i.e., the value of m). A visual representation of our categorization is given in Figure 4, and it is by interpreting the various trends that emerge from this diagram that we ultimately aim to devise design strategies linking chemical composition and framework structure.

What is immediately obvious is that some families are considerably more populous than others. The largest and most topologically diverse family is that with composition BX_2, consisting of a variety of structures based on four-connected nets. Four-fold connectivity is well known[119] to favor topological diversity—hence the polymorphism of, e.g., silica, zeolites, and imidazolate MOFs.[120] In the present case,

DOI: 10.1021/jacs.5b13446
J. Am. Chem. Soc. XXXX, XXX, XXX–XXX

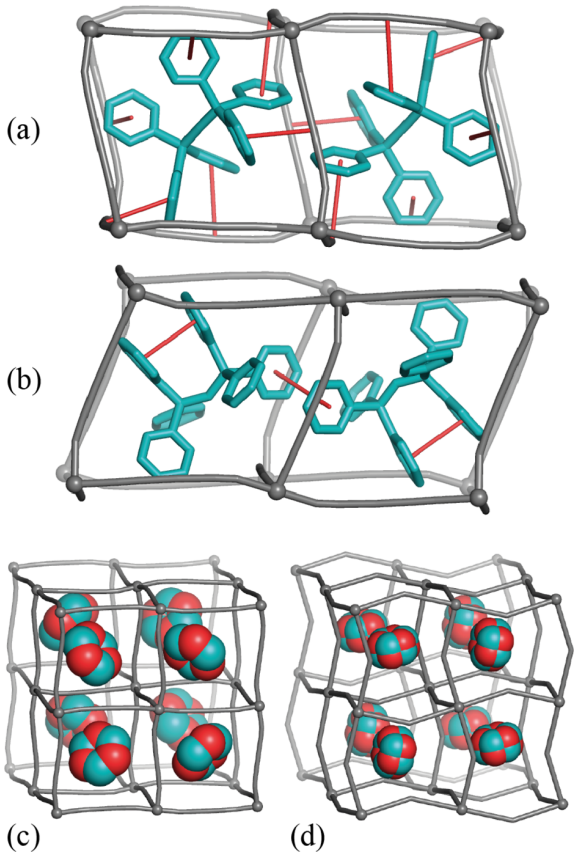

Figure 3. Short cation–π and π–π interactions in **3c** (a) and **5b** (b). Distances shorter than 4.2 Å are indicated by red lines. In **3c** the phenyl rings are oriented such that short cation–π distances are maximized, whereas in **5b** intra- and inter-molecular π–π interactions dominate. Crucially, the latter are present between adjacent $[PPN]^+$ cations. $[PPN]^+$ cations are inherently multipolar and their packing in **4** (c) corresponds to ordered hexapoles. Such multipolar interactions are common for framework materials with molecular cations such as $[CH_3NH_3]PbI_3$ (d) where the dynamics of these interactions are implicated in slow exciton recombination (cation-ordered *Pnma* structure shown).[31,118] Framework shown in gray, cation in teal (a,b), and multipoles in teal and red (c,d); H atoms not shown for clarity.

$Zn[Au(CN)_2]_2$ emerges as the most polymorphic of the BX_2 systems, crystallizing in at least four different forms that include analogues of cristobalite and quartz.[14] In fact the parallel with silica is a meaningful one: the combination of tetrahedral Zn^{2+} coordination geometry and aurophilic interactions capable of bending the Zn–NC–Au–CN–Zn linkers resembles strongly the nonlinear Si–O–Si building units of SiO_2 frameworks. But one additional reason for the accessibility of these BX_2 structures will likely be the large number of divalent cations with aqueous chemistry. Even transition metals with octahedral coordination can yield four-connected frameworks if spectator ligands are present in the synthesis mixture (noting that sometimes solvent itself may play this role). Indeed it is the doubly ligated octahedral [*trans*-BX_4L_2] coordination motif that yields the square grid topology—the most frequently adopted network structure observed for this family.

In principle, any such coordinated ligands may be susceptible to exchange for dicyanometallate anions present in the reaction mixture, with concomitant incorporation of extra-framework cations:

$$BL_2X_2 + 0.5AX \rightleftharpoons A_{0.5}BLX_{2.5} + L$$
$$A_{0.5}BLX_{2.5} + 0.5AX \rightleftharpoons ABX_3 + L$$

The equilibrium position will depend on, among other factors, the ligand binding strength and the stoichiometry of AX dicyanometallate salt in the reaction mixture. So, for example, while the $Cd^{2+}/K[Ag(CN)_2]$ system forms the $B(L_2)X_2$ phase $Cd(py)_2[Ag(CN)_2]_2$ when prepared in the presence of pyridine, in the absence of pyridine the same pair of reagents yields the ABX_3 phase $KCd[Ag(CN)_2]_3$. Likewise for the $Cd^+/[PPN][Ag(CN)_2]$ system we obtain the five-coordinate $A_{0.5}B(L)X_{2.5}$ phase $[PPN]_{0.5}Cd(EtOH)[Ag(CN)_2]_{2.5}$ (**3c**) as a first (kinetic) product; subsequent exposure to additional $[PPN][Ag(CN)_2]$ drives formation of the superperovskite ABX_3 phase $[PPN]Cd[Ag(CN)_2]_3{\cdot}3EtOH{\cdot}nH_2O$ (**4**).

This strategy of varying B^{2+}:AX stoichiometry seems an attractive method of controlling network connectivity throughout the A_xBX_{2+x} families. The particular topology adopted for the $x \neq 0$ phases then depends on the geometry of the A^+ cation. For monatomic A^+ (e.g., K^+, Na^+), the topology is usually that of the corresponding A-deficient framework: this is presumably a consequence of the much larger scale of the dicyanometallate linker. So, for example, both $KFe[Ag(CN)_2]_3$ and $Fe[Ag(CN)_2]_3$ share the same triply interpenetrating α-Po network structure. Larger, molecular cations force topological changes that reflect the cation shape. On the one hand, the cruciform conformation of $[NBu_4]^+$ helps drive the unusual topologies of $[NBu_4]_{0.5}Cd[Ag(CN)_2]_{2.5}$ and $[NBu_4]Ni[Au(CN)_2]_3$. On the other hand, the more isotropic $[PPN]^+$ cation clearly favors the cubic-type nets of $[PPN]_{0.5}Cu[Au(CN)_2]_{2.5}{\cdot}EtOH$ and $[PPN]Mn[Au(CN)_2]_3$.

Although there are far fewer examples based on monovalent B^+ cations—the need for aqueous chemistry limiting these systems to coinage metal salts—precisely these same trends are observed. Again we find that inclusion of monatomic extra-framework cations appears to have essentially no effect on framework topology: $KCu^I[Ag(CN)_2]_2$ and $Cu^{II}(DMF)[Au(CN)_2]_2$ share the same basic square-grid structures. The tetrahedral $[NEt_4]^+$ cation now favors a diamondoid topology in $[NEt_4]Ag[Ag(CN)_2]_2$; and in $[Cu_2(2,2'\text{-bpy})_2(CN)]_{0.5}Cu[Cu(CN)_2]_{1.5}$ the linear nature of the $[Cu_2(2,2'\text{-bpy})_2(CN)]^+$ cation drives a honeycomb structure with linear channels. Notable by its absence is the (10,3)-*a* or **srs** topology, a common topology for 3-connected MOFs.[5] The apparent rarity of 3-connected structures is in large part due to the propensity for Cu^+ to adopt alternative binding modes, such as bifurcated linkages,[24] though it may be possible to make a dicyanometallate framework with (10,3)-*a* topology using an octahedrally coordinated metal with meridionally disposed capping ligands.[121]

The general reliance on solution-phase synthesis—whether strictly necessary or not—is likely responsible for the relative paucity of structures known to contain B cations in the 3+ oxidation state and the complete absence of higher-valent examples. All known trivalent dicyanometallate salts adopt one of just two dense framework structures: either the triply interpenetrating α-Po net of $Fe[Ag(CN)_2]_3$ or the triply interpenetrating **acs** net of the lanthanide salts $[Ln(OH_2)_3][Au/Ag(CN)_2]_3$. The contrast with the structural diversity of divalent BX_2 systems could hardly be clearer, and will reflect

DOI: 10.1021/jacs.5b13446
J. Am. Chem. Soc. XXXX, XXX, XXX–XXX

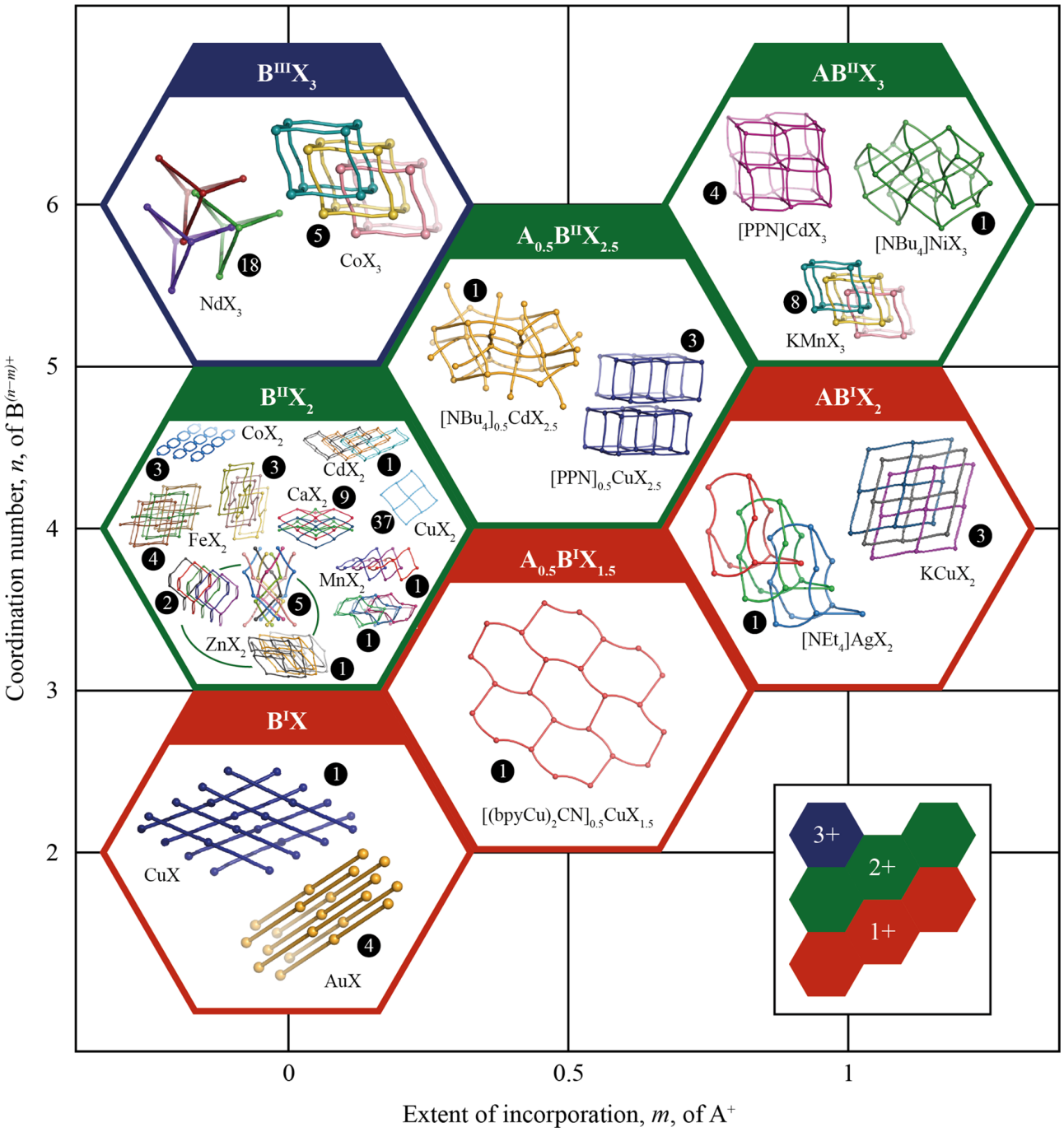

Figure 4. Organization of all known dicyanometallate frameworks according to node coordination number and extent of incorporation of extra-framework cations. The frameworks shown are representative examples of isostructural compounds; the number of such compounds known is given in the corresponding black circle. The collection of frameworks contained within a single hexagonal cell form a family with related composition A_mBX_n. The color of the cell corresponds to the charge on the nodal cation (inset).

also the disparity of topological constraints associated with six- and four-connected nodes. In principle, it may be possible to access more open structure types through incorporation of extra-framework cations. Naturally, this would require coordination numbers higher than six—which is certainly feasible for the lanthanide trications. Consequently, further exploration[122] of lanthanide dicyanometallate chemistry using *molecular* AX sources may yield as-yet unrealised systems with compositions $A_{0.5}BX_{3.5}$ and/or ABX_4.

In addition to the general trends we discuss here, a number of interesting comparisons can be drawn between neighboring pairs of structural families as shown in Figure 4. For example, there are clear diagonal relationships which connect the topologies of higher- and lower-connected network structures. In this way, the Ruddlesden−Popper-like structure of

DOI: 10.1021/jacs.5b13446
J. Am. Chem. Soc. XXXX, XXX, XXX−XXX

$[PPN]_{0.5}Cu[Au(CN)_2]_{2.5}$·EtOH (an $A_{0.5}BX_{2.5}$ framework) can be seen as a natural extension of the square-grid structures of both $Cu[Ag(CN)_2]_2$ and $KCu[Ag(CN)_2]_2$ (BX_2 and ABX_2 frameworks, respectively). And then the superperovskite $[PPN]Cd[Au(CN)_2]_3$ structure emerges as a further extension on this same theme. The triad of $BX/A_{0.5}BX_{1.5}/ABX_2$ systems $Cu[Cu(CN)_2]/[Cu_2(2,2'\text{-bpy})_2(CN)]_{0.5}Cu[Cu(CN)_2]_{1.5}/KCu[Cu(CN)_2]_2$ can be viewed in precisely the same terms. We anticipate there are many more such relationships, some of which may become increasingly apparent only as new dicyanometallate frameworks continue to be discovered.

CONCLUSIONS

While it has long been clear that a large variety of dicyanometallate frameworks can be prepared, what we have shown here is how the structures of these frameworks might be influenced rationally through variation in cation charge, coordination number, presence of coordinating ligands, and extra-framework cation size, shape and extent of incorporation. The ability to controllably explore a variety of network structures in this way reflects Robson's original vision for coordination polymer chemistry, and suggests that dicyanometalates might be considered a model family for extended framework design. In principle the diversity of structures accessible to this family also suggests a similar diversity of physical properties. Moreover, the structural flexibility imparted by the dicyanometallate linker means that these properties may be much more extreme in nature than in conventional ceramic frameworks—as is already known to be the case in a number of examples.[12,13]

But what we see as particularly attractive about dicyanometalate framework chemistry is the ability to include complex molecular cations within a number of different framework topologies. So much of the rich structural chemistry and physics of conventional ceramic frameworks has arisen from the interplay between lattice geometry, local degrees of freedom, and nature of intersite interactions. Consequently the extension of these same concepts to systems with *new* degrees of freedom (e.g., molecular cation orientations and conformations), *new* lattice geometries (e.g., the topology of compound **2**), and *new* types of interactions (e.g., cation−π and $\pi-\pi$) augurs well for the discovery of new and interesting physical phenomena in this intriguing model family of framework structures.

METHODS

Sample Preparation. *Dicyanometallate Precursors.* $[NBu_4]Ag(CN)]_2{\cdot}0.5H_2O$ was prepared by adding an aqueous solution of $[NBu_4]CN$ (0.5510 g in 400 mL water) to a suspension of AgCN (0.3435 g in 100 mL water) and stirring for 1 h. The excess AgCN was then removed by vacuum filtration and the volume of the filtrate reduced by rotary evaporation. The concentrated filtrate was allowed to evaporate, and the resulting powder was dried at 50 °C for 2.5 h and then at 40 °C for 18 h.

$[PPN]Au(CN)_2$ was prepared by the method outlined in ref 32. Solutions of $KAu(CN)_2$ (2.583 g in 100 mL water) and PPNCl (5.40 g in 200 mL 50:50 water:ethanol) were combined with immediate formation of a white precipitate. The reaction mixture was covered and stirred for 1 h then collected by vacuum filtration and washed with 300 mL cold water. The solid was left to air-dry overnight then dried in a vacuum oven at 40 °C for 3.5 h giving 6.80 g of product (Yield: 96.3%). Elemental analysis: Found (calculated)% C 57.74 (57.95); H 3.80 (3.84); N 5.24 (5.34).

$[PPN]Ag(CN)_2$ was prepared by a similar method to $[PPN]Au(CN)_2$. Solutions of $KAg(CN)_2$ (1.881 g in 100 mL water) and PPNCl (5.68 g in 200 mL 50:50 water:ethanol) were combined with immediate formation of a white precipitate. The reaction mixture was covered and stirred for 1 h then collected by vacuum filtration and washed with 300 mL cold water. The solid was left to air-dry overnight then dried in a vacuum oven at 40 °C for 1 week giving 5.87 g of product (Yield: 90.0%). Elemental analysis: Found (calculated)% C 65.05 (65.34); H 4.26 (4.33); N 5.88 (6.02).

Dicyanometallate Frameworks. $[NEt_4]Ag[Ag(CN)_2]_2$ (**1**) single crystals were prepared by slow evaporation of aqueous solutions of $KAg(CN)_2$ and $[NEt_4]Cl$. Solutions of $KAg(CN)_2$ (0.2802 g, 1.411 mmol) and $[N(C_2H_5)_4]Cl$ (0.2380 g, 1.436 mmol) were prepared with the minimum quantity of water and then mixed. The resulting colorless solution was left to evaporate slowly and crystals formed within 3 weeks.

$[NBu_4]_{0.5}Cd[Ag(CN)_2]_{2.5}$ (**2**) Aqueous solutions of $[NBu_4]Ag(CN)_2{\cdot}0.5H_2O$ and $Cd(NO_3)_2{\cdot}4H_2O$ were prepared with the minimum quantity of solvent, mixed, and left to evaporate from an open Petri dish. Crystals were harvested after a few days.

$[PPN]_{0.5}Cu[Au(CN)_2]_{2.5}$· EtOH (**3a**) single crystals were prepared by slow-diffusion in an H-cell. Into one arm was placed $[PPN]Au(CN)_2$ (25 mg in 1 mL of ethanol) and the other $CuCl_2{\cdot}2H_2O$ (5.4 mg in 0.142 mL of ethanol). The remaining volume was carefully made up with cold ethanol. Green crystals grew in the $[PPN]Au(CN)_2$ arm after 2 days.

$[PPN]_{0.5}Mn[Ag(CN)_2]_{2.5}(EtOH)$ (**3b**) was prepared by diffusion in a Schott bottle. Cold solutions of $[PPN]Ag(CN)_2$ (1.125 g in 20 mL of ethanol) and $Mn(NO_3)_2{\cdot}4H_2O$ (148 mg in 6 mL of ethanol) were carefully layered with a buffer of 50 mL cold ethanol separating the layers. Crystals formed overnight.

$[PPN]_{0.5}Cd[Ag(CN)_2]_{2.5}$·EtOH (**3c**) single crystals were prepared by slow-diffusion in a vial. Cold solutions of $[PPN]Ag(CN)_2$ (101 mg in 2 mL of ethanol) and $Cd(NO_3)_2{\cdot}4H_2O$ (19 mg in 0.2 mL of ethanol) were carefully layered with a buffer of 5 mL of cold ethanol separating the layers. Crystals formed overnight.

For $[PPN]Cd[Ag(CN)_2]_3{\cdot}3EtOH{\cdot}nH_2O$ (**4**), a crystal was selected from a small portion (roughly 3 mL) of a reaction mixture that initially yielded **3c**. Solutions of $[PPN]Ag(CN)_2$ (1.108 g in 25 mL of ethanol) and $Cd(NO_3)_2{\cdot}4H_2O$ (183.7 mg in 7 mL of ethanol) with a buffer of 50 mL of ethanol separating the layers in a Schott bottle. Colorless crystals formed overnight and then a portion of these crystals, with mother liquor, were set aside in a sealed sample tube. After 10 weeks a crystal of compound **4** was selected from this portion.

$[PPN]Mn[Au(CN)_2]_3$ (**5a**) was prepared by layering ethanolic solutions of $PPNAu(CN)_2$ (50 mg in 2 mL of ethanol) and $Mn(ClO_4)_2{\cdot}xH_2O$ (14 mg in 0.2 mL of ethanol) in a small sample tube. Colorless crystals formed after 1 h.

$[PPN]Cd[Au(CN)_2]_3$ (**5b**) was prepared by layering ethanolic solutions of $PPNAu(CN)_2$ (50 mg in 2 mL of ethanol) and $Cd(NO_3)_2{\cdot}4H_2O$ (21 mg in 0.2 mL of ethanol) in a small sample tube. Colorless crystals formed after 1 h.

Single-Crystal X-ray Diffraction. Single-crystal X-ray diffraction data were collected using a Nonius KappaCCD diffractometer (**2** and **5a**) or an Oxford Diffraction (Rigaku Oxford Diffraction) SuperNova diffractometer (**1**, **3b**, **3c**, **4**, **5b**) fitted with an Oxford Cryosystems Cryostream 600 Series/700 Plus open-flow nitrogen cooling device.[123] Data for **3a** were collected at Diamond Light Source (beamline I19)[124] fitted with an Oxford Cryosystems HeliX open-flow helium cryostat.[125] DENZO/SCALEPACK,[126] CrysAlisPro,[127] or CrystalClear were used for data collection and reduction as appropriate. The structures were solved *ab initio* using SIR92[128] or SUPERFLIP.[129] All structures were refined with full-matrix least-squares on F^2 using CRYSTALS.[130,131] Hydrogen atoms were, in some cases, visible in the difference Fourier map and treated in the usual manner.[132] In the remaining cases, and particularly for disordered assemblies, hydrogen atoms were added geometrically. Full structural data are included in the SI, including CIF files, and have been submitted to the CCDC as numbers 1444134−1444141. These data can also be obtained free of charge from The Cambridge Crystallographic Data Centre via http://www.ccdc.cam.ac.uk/data_request/cif.

DOI: 10.1021/jacs.5b13446
J. Am. Chem. Soc. XXXX, XXX, XXX−XXX

■ ASSOCIATED CONTENT

Supporting Information

The Supporting Information is available free of charge on the ACS Publications website at DOI: 10.1021/jacs.5b13446.

X-ray crystallographic data for **1**, **2**, **3a**, **3b**, **3c**, **4**, **5a**, **5b**, **S1**, and **S2** (CIF)

Single-crystal X-ray structural information and methods for [PPN]Au/Ag(CN)$_2$, variable-temperature single-crystal X-ray diffraction studies, powder diffraction data, TGA data, tolerance factor calculations, and topology decomposition of **2** (PDF)

■ AUTHOR INFORMATION

Corresponding Author

*andrew.goodwin@chem.ox.ac.uk

Notes

The authors declare no competing financial interest.

■ ACKNOWLEDGMENTS

The authors gratefully acknowledge financial support from the ERC (Grant 279705) and the EPSRC (Grant EP/G004528/2). We are extremely grateful for the award of beamtime to the Block Allocation Group (MT9981) used to collect the single crystal synchrotron X-ray diffraction data on the I19 beamline at the Diamond Light Source. J.A.H. thanks G. Kieslich for helpful conversations regarding tolerance factors and V. A. Blatov for comments on the topology of compound **2**.

■ REFERENCES

(1) Hoskins, B. F.; Robson, R. *J. Am. Chem. Soc.* **1990**, *112*, 1546−1554.

(2) Yaghi, O. M.; O'Keeffe, M.; Ockwig, N. W.; Chae, H. K.; Eddaoudi, M.; Kim, J. *Nature* **2003**, *423*, 705−714.

(3) Côté, A. P.; El-Kaderi, H. M.; Furukawa, H.; Hunt, J. R.; Yaghi, O. M. *J. Am. Chem. Soc.* **2007**, *129*, 12914−12915.

(4) Feng, X.; Ding, X.; Jiang, D. *Chem. Soc. Rev.* **2012**, *41*, 6010−6022.

(5) Ockwig, N. W.; Delgado-Friedrichs, O.; O'Keeffe, M.; Yaghi, O. M. *Acc. Chem. Res.* **2005**, *38*, 176−182.

(6) Eddaoudi, M.; Kim, J.; Vodak, D.; Sudik, A.; Wachter, J.; O'Keeffe, M.; Yaghi, O. M. *Proc. Natl. Acad. Sci. USA* **2002**, *99*, 4900−4904.

(7) Sonnauer, A.; Hoffmann, F.; Fröba, M.; Kienle, L.; Duppel, V.; Thommes, M.; Serre, C.; Férey, G.; Stock, N. *Angew. Chem., Int. Ed.* **2009**, *48*, 3791−3794.

(8) Deng, H.; Grunder, S.; Cordova, K. E.; Valente, C.; Furukawa, H.; Hmadeh, M.; Gándara, F.; Whalley, A. C.; Liu, Z.; Asahina, S.; Kazumori, H.; O'Keeffe, M.; Terasaki, O.; Stoddart, J. F.; Yaghi, O. M. *Science* **2012**, *336*, 1018−1023.

(9) Farha, O. K.; Malliakas, C. D.; Kanatzidis, M. G.; Hupp, J. T. *J. Am. Chem. Soc.* **2010**, *132*, 950−952.

(10) Loiseau, T.; Serre, C.; Huguenard, C.; Fink, G.; Taulelle, F.; Henry, M.; Bataille, T.; Férey, G. *Chem.−Eur. J.* **2004**, *10*, 1373−1382.

(11) Volkringer, C.; Loiseau, T.; Devic, T.; Férey, G.; Popov, D.; Burghammer, M.; Riekel, C. *CrystEngComm* **2010**, *12*, 3225−3228.

(12) Goodwin, A. L.; Calleja, M.; Conterio, M. J.; Dove, M. T.; Evans, J. S. O.; Keen, D. A.; Peters, L.; Tucker, M. G. *Science* **2008**, *319*, 794−797.

(13) Cairns, A. B.; Catafesta, J.; Levelut, C.; Rouquette, J.; van der Lee, A.; Peters, L.; Thompson, A. L.; Dmitriev, V.; Haines, J.; Goodwin, A. L. *Nat. Mater.* **2013**, *12*, 212−216.

(14) Katz, M. J.; Ramnial, T.; Yu, H.-Z.; Leznoff, D. B. *J. Am. Chem. Soc.* **2008**, *130*, 10662−10673.

(15) Abrahams, S. C.; Bernstein, J. L.; Liminga, R.; Eisenmann, E. T. *J. Chem. Phys.* **1980**, *73*, 4585−4590.

(16) Colis, J. C. F.; Larochelle, C.; Fernández, E. J.; López-de Luzuriaga, J. M.; Monge, M.; Laguna, A.; Tripp, C.; Patterson, H. *J. Phys. Chem. B* **2005**, *109*, 4317−4323.

(17) Lefebvre, J.; Batchelor, R. J.; Leznoff, D. B. *J. Am. Chem. Soc.* **2004**, *126*, 16117−16125.

(18) Niel, V.; Muñoz, M. C.; Gaspar, A. B.; Galet, A.; Levchenko, G.; Real, J. A. *Chem.−Eur. J.* **2002**, *8*, 2446−2453.

(19) Hill, J. A.; Cairns, A. B.; Lim, J. J. K.; Cassidy, S. J.; Clarke, S. J.; Goodwin, A. L. *CrystEngComm* **2015**, *17*, 2925−2928.

(20) Rao, C. N. R. *Annu. Rev. Phys. Chem.* **1989**, *40*, 291−326.

(21) Cox, P. A. *Transition Metal Oxides: An Introduction to Their Electronic Structure and Properties*; Clarendon Press: Oxford, UK, 2010.

(22) Sharpe, A. G. *The Chemistry of Cyano Complexes of the Transition Metals*; Academic Press: London, 1976.

(23) Dunbar, K. R., Heintz, R. A. *Progress in Inorganic Chemistry*; John Wiley & Sons, Inc.: Hoboken, NJ, USA, 2007; pp 283−391.

(24) Alexandrov, E. V.; Virovets, A. V.; Blatov, V. A.; Peresypkina, E. V. *Chem. Rev.* **2015**, *115*, 12286−12319.

(25) Wang, Z.; Zhang, B.; Otsuka, T.; Inoue, K.; Kobayashi, H.; Kurmoo, M. *Dalton Trans.* **2004**, 2209−2216.

(26) Hu, K.-L.; Kurmoo, M.; Wang, Z.; Gao, S. *Chem.−Eur. J.* **2009**, *15*, 12050−12064.

(27) Collings, I. E.; Hill, J. A.; Cairns, A. B.; Cooper, R. I.; Thompson, A. L.; Parker, J. E.; Tang, C. C.; Goodwin, A. L. *Dalton Trans.* **2016**, *45*, 4169−4178.

(28) Lee, M. M.; Teuscher, J.; Miyasaka, T.; Murakami, T. N.; Snaith, H. J. *Science* **2012**, *338*, 643−647.

(29) Stoumpos, C. C.; Malliakas, C. D.; Kanatzidis, M. G. *Inorg. Chem.* **2013**, *52*, 9019−9038.

(30) Motta, C.; El-Mellouhi, F.; Kais, S.; Tabet, N.; Alharbi, F.; Sanvito, S. *Nat. Commun.* **2015**, *6*, 7026.

(31) Weller, M. T.; Weber, O. J.; Henry, P. F.; Di Pumpo, A. M.; Hansen, T. C. *Chem. Commun.* **2015**, *51*, 4180−4183.

(32) Lefebvre, J.; Chartrand, D.; Leznoff, D. B. *Polyhedron* **2007**, *26*, 2189−2199.

(33) Eisenmann, E. T. *J. Electrochem. Soc.* **1977**, *124*, 1957−1958.

(34) Zhdanov, G. S.; Shugam, E. A. *Acta Physicochimica U.R.S.S.* **1945**, *20*, 253.

(35) Bowmaker, G. A.; Kennedy, B. J.; Reid, J. C. *Inorg. Chem.* **1998**, *37*, 3968−3974.

(36) Lefebvre, J.; Korčok, J. L.; Katz, M. J.; Leznoff, D. B. *Sensors* **2012**, *12*, 3669−3692.

(37) Soma, T.; Iwamoto, T. *Chem. Lett.* **1995**, *24*, 271−272.

(38) Hoskins, B. F.; Robson, R.; Scarlett, N. V. Y. *J. Chem. Soc., Chem. Commun.* **1994**, *1994*, 2025−2026.

(39) West, C. D. *Z. Kristallogr. Krist.* **1934**, *88*, 173−175.

(40) West, C. D. *Z. Kristallogr. Krist.* **1935**, *90*, 555−558.

(41) Yoshida, K.; Kosone, T.; Kanadani, C.; Saito, T.; Kitazawa, T. *Polyhedron* **2011**, *30*, 3062−3066.

(42) Vlček, A.; Orendáč, M.; Orendáčová, A.; Kajňaková, M.; Papageorgiou, T.; Chomič, J.; Černák, J.; Massa, W.; Feher, A. *Solid State Sci.* **2007**, *9*, 116−125.

(43) Lefebvre, J.; Trudel, S.; Hill, R. H.; Leznoff, D. B. *Chem. - Eur. J.* **2008**, *14*, 7156−7167.

(44) Hibble, S. J.; Cheyne, S. M.; Hannon, A. C.; Eversfield, S. G. *Inorg. Chem.* **2002**, *41*, 4990−4992.

(45) Galet, A.; Muñoz, M. C.; Martínez, V.; Real, J. A. *Chem. Commun.* **2004**, 2268−2269.

(46) Geiser, U.; Schlueter, J. A. *Acta Crystallogr., Sect. C: Cryst. Struct. Commun.* **2003**, *59*, i21−i23.

(47) Chakraborty, J.; Nandi, M.; Mayer-Figge, H.; Sheldrick, W. S.; Sorace, L.; Bhaumik, A.; Banerjee, P. *Eur. J. Inorg. Chem.* **2007**, *2007*, 5033−5044.

(48) Agustí, G.; Gaspar, A. B.; Muñoz, M. C.; Lacroix, P. G.; Real, J. A. *Aust. J. Chem.* **2009**, *62*, 1155−1165.

(49) Soma, T.; Iwamoto, T. *J. Inclusion Phenom. Mol. Recognit. Chem.* **1996**, *26*, 161−173.

(50) Korčok, J. L.; Katz, M. J.; Leznoff, D. B. *J. Am. Chem. Soc.* **2009**, *131*, 4866−4871.

DOI: 10.1021/jacs.5b13446
J. Am. Chem. Soc. XXXX, XXX, XXX−XXX

(51) Dong, W.; Zhu, L.-N.; Sun, Y.-Q.; Liang, M.; Liu, Z.-Q.; Liao, D.-Z.; Jiang, Z.-H.; Yan, S.-P.; Cheng, P. *Chem. Commun.* **2003**, *2003*, 2544−2545.
(52) Rodríguez-Velamazán, J. A.; Castro, M.; Palacios, E.; Burriel, R.; Kitazawa, T.; Kawasaki, T. *J. Phys. Chem. B* **2007**, *111*, 1256−1261.
(53) Kosone, T.; Suzuki, Y.; Kanadani, C.; Saito, T.; Kitazawa, T. *Bull. Chem. Soc. Jpn.* **2009**, *82*, 347−351.
(54) Range, K.-J.; Zabel, M.; Meyer, H.; Fischer, H. *Z. Naturforsch. B* **1985**, *40*, 1618−1621.
(55) Chesnut, D. J.; Zubieta, J. *Chem. Commun.* **1998**, 1707−1708.
(56) Wang, S.-P.; Chen, J.; Gao, D.-Z.; Song, Y.; Wang, Q.-M.; Liao, D.-Z.; Jiang, Z.-H.; Yan, S.-P. *J. Coord. Chem.* **2005**, *58*, 1695−1702.
(57) Katz, M. J.; Michaelis, V. K.; Aguiar, P. M.; Yson, R.; Lu, H.; Kaluarachchi, H.; Batchelor, R. J.; Schreckenbach, G.; Kroeker, S.; Patterson, H. H.; Leznoff, D. B. *Inorg. Chem.* **2008**, *47*, 6353−6363.
(58) Soma, T.; Iwamoto, T. *Chem. Lett.* **1994**, *23*, 821−824.
(59) Othong, J.; Wannarit, N.; Pakawatchai, C.; Youngme, S. *Acta Crystallogr., Sect. E: Struct. Rep. Online* **2014**, *70*, 107−110.
(60) Chippindale, A. M.; Cheyne, S. M.; Hibble, S. J. *Angew. Chem., Int. Ed.* **2005**, *44*, 7942−7946.
(61) Colacio, E.; Lloret, F.; Kivekäs, R.; Ruiz, J.; Suárez-Varela, J.; Sundberg, M. R. *Chem. Commun.* **2002**, 592−593.
(62) Kosone, T.; Kanadani, C.; Saito, T.; Kitazawa, T. *Polyhedron* **2009**, *28*, 1930−1934.
(63) Korkmaz, N.; Karadağ, A.; Aydın, A.; Yanar, Y.; Karaman, I.; Tekin, Ş. *New J. Chem.* **2014**, *38*, 4760−4773.
(64) Wang, S.-P.; Gao, D.-Z.; Song, Y.; Liu, Z.-Q.; Liao, D.-Z.; Jiang, Z.-H.; Yan, S.-P. *Inorg. Chim. Acta* **2006**, *359*, 505−510.
(65) Kosone, T.; Tomori, I.; Kanadani, C.; Saito, T.; Mochida, T.; Kitazawa, T. *Dalton Trans.* **2010**, *39*, 1719−1721.
(66) Muñoz, M. C.; Gaspar, A. B.; Galet, A.; Real, J. A. *Inorg. Chem.* **2007**, *46*, 8182−8192.
(67) Agustí, G.; Muñoz, M. C.; Gaspar, A. B.; Real, J. A. *Inorg. Chem.* **2008**, *47*, 2552−2561.
(68) Ludi, A.; Güdel, H. U.; Dvořák, V. *Helv. Chim. Acta* **1967**, *50*, 2035−2039.
(69) Schröder, U.; Scholz, F. *Inorg. Chem.* **2000**, *39*, 1006−1015.
(70) Hoskins, B. F.; Robson, R.; Scarlett, N. V. Y. *Angew. Chem., Int. Ed. Engl.* **1995**, *34*, 1203−1204.
(71) Kawasaki, T.; Kachi-Terajima, C.; Saito, T.; Kitazawa, T. *Bull. Chem. Soc. Jpn.* **2008**, *81*, 268−273.
(72) Abrahams, S. C.; Zyontz, L. E.; Bernstein, J. L. *J. Chem. Phys.* **1982**, *76*, 5458−5462.
(73) Goodwin, A. L.; Kennedy, B. J.; Kepert, C. J. *J. Am. Chem. Soc.* **2009**, *131*, 6334−6335.
(74) Kitazawa, T.; Hiruma, K.; Sato, H.; Tamura, K.; Yamagishi, A. *Dalton Trans.* **2013**, *42*, 16680−16682.
(75) Guo, Y.; Liu, Z.-Q.; Zhao, B.; Feng, Y.-H.; Xu, G.-F.; Yan, S.-P.; Cheng, P.; Wang, Q.-L.; Liao, D.-Z. *CrystEngComm* **2009**, *11*, 61−66.
(76) Wannarit, N.; Hahnvajanawong, V.; Pakawatchai, C.; Youngme, S. *Transition Met. Chem.* **2012**, *37*, 79−84.
(77) Colis, J. C. F.; Larochelle, C.; Staples, R.; Herbst-Irmer, R.; Patterson, H. *Dalton Trans.* **2005**, *2005*, 675−679.
(78) Theppitak, C.; Chainok, K. *Acta Crystallogr. E: Crystallogr. Commun.* **2015**, *71*, m179−m180.
(79) Ovens, J. S.; Leznoff, D. B. *Dalton Trans.* **2011**, *40*, 4140−4146.
(80) Assefa, Z.; Haire, R. G.; Sykora, R. E. *J. Solid State Chem.* **2008**, *181*, 382−391.
(81) Galet, A.; Niel, V.; Muñoz, M. C.; Real, J. A. *J. Am. Chem. Soc.* **2003**, *125*, 14224−14225.
(82) Soma, T.; Yuge, H.; Iwamoto, T. *Angew. Chem., Int. Ed. Engl.* **1994**, *33*, 1665−1666.
(83) Assefa, Z.; Kalachnikova, K.; Haire, R. G.; Sykora, R. E. *J. Solid State Chem.* **2007**, *180*, 3121−3129.
(84) Arcís-Castillo, Z.; Muñoz, M. C.; Molnár, G.; Bousseksou, A.; Real, J. A. *Chem. - Eur. J.* **2013**, *19*, 6851−6861.
(85) Yoshida, K.; Akahoshi, D.; Kawasaki, T.; Saito, T.; Kitazawa, T. *Polyhedron* **2013**, *66*, 252−256.
(86) Stier, A.; Range, K.-J. *Z. Kristallogr.* **1997**, *212*, 51−51.
(87) Yeung, W.-F.; Wong, W.-T.; Zuo, J.-L.; Lau, T.-C. *J. Chem. Soc., Dalton Trans.* **2000**, 629−631.
(88) Assefa, Z.; Staples, R.; Fackler, J. P., Jr. *Acta Crystallogr., Sect. C: Cryst. Struct. Commun.* **1995**, *51*, 2527−2529.
(89) Ahern, J. C.; Roberts, R. J.; Follansbee, P.; McLaughlin, J.; Leznoff, D. B.; Patterson, H. H. *Inorg. Chem.* **2014**, *53*, 7571−7579.
(90) Li, J.-Y.; Ni, Z.-P.; Yan, Z.; Zhang, Z.-M.; Chen, Y.-C.; Liu, W.; Tong, M.-L. *CrystEngComm* **2014**, *16*, 6444−6449.
(91) Stier, A.; Range, K.-J. *Z. Naturforsch., B: J. Chem. Sci.* **1996**, *51*, 698−702.
(92) Tanner, P. A.; Zhou, X.; Wong, W.-T.; Kratzer, C.; Yersin, H. *J. Phys. Chem. B* **2005**, *109*, 13083−13090.
(93) Kalachnikova, K.; Assefa, Z.; Sykora, R. E. *Acta Crystallogr., Sect. E: Struct. Rep. Online* **2007**, *63*, i162.
(94) Niel, V.; Thompson, A. L.; Muñoz, M. C.; Galet, A.; Goeta, A. E.; Real, J. A. *Angew. Chem., Int. Ed.* **2003**, *42*, 3760−3763.
(95) Collings, I. E.; Cairns, A. B.; Thompson, A. L.; Parker, J. E.; Tang, C. C.; Tucker, M. G.; Catafesta, J.; Levelut, C.; Haines, J.; Dmitriev, V.; Pattison, P.; Goodwin, A. L. *J. Am. Chem. Soc.* **2013**, *135*, 7610−7620.
(96) Ryder, M. R.; Civalleri, B.; Bennett, T. D.; Henke, S.; Rudić, S.; Cinque, G.; Fernandez-Alonso, F.; Tan, J.-C. *Phys. Rev. Lett.* **2014**, *113*, 215502.
(97) Blatov, V. A. *Struct. Chem.* **2012**, *23*, 955−963.
(98) Blatov, V. A.; Shevchenko, A. P.; Proserpio, D. M. *Cryst. Growth Des.* **2014**, *14*, 3576−3586.
(99) Alexandrov, E. V.; Blatov, V. A.; Kochetkov, A. V.; Proserpio, D. M. *CrystEngComm* **2011**, *13*, 3947−3958.
(100) Pyykkö, P. *Chem. Rev.* **1997**, *97*, 597−636.
(101) Omary, M. A.; Webb, T. R.; Assefa, Z.; Shankle, G. E.; Patterson, H. H. *Inorg. Chem.* **1998**, *37*, 1380−1386.
(102) Goodwin, A. L.; Keen, D. A.; Tucker, M. G. *Proc. Natl. Acad. Sci. USA* **2008**, *105*, 18708−18713.
(103) Goodwin, A. L.; Keen, D. A.; Tucker, M. G.; Dove, M. T.; Peters, L.; Evans, J. S. O. *J. Am. Chem. Soc.* **2008**, *130*, 9660−9661.
(104) Schmidbaur, H.; Schier, A. *Angew. Chem., Int. Ed.* **2015**, *54*, 746−784.
(105) Jansen, M. *Angew. Chem., Int. Ed. Engl.* **1987**, *26*, 1098−1110.
(106) Cliffe, M. J.; Goodwin, A. L. *J. Appl. Crystallogr.* **2012**, *45*, 1321−1329.
(107) Ruddlesden, S. N.; Popper, P. *Acta Crystallogr.* **1958**, *11*, 54−55.
(108) Ortiz, A. U.; Boutin, A.; Fuchs, A. H.; Coudert, F.-X. *Phys. Rev. Lett.* **2012**, *109*, 195502.
(109) Hofmann, K. A.; Küspert, F. *Z. Anorg. Allg. Chem.* **1897**, *15*, 204−207.
(110) Powell, H. M.; Rayner, J. H. *Nature* **1949**, *163*, 566−567.
(111) Walker, G. F.; Hawthorne, D. G. *Trans. Faraday Soc.* **1967**, *63*, 166−174.
(112) Goldschmidt, V. M. *Naturwissenschaften* **1926**, *14*, 477−485.
(113) Kieslich, G.; Sun, S.; Cheetham, A. K. *Chem. Sci.* **2014**, *5*, 4712−4715.
(114) Kieslich, G.; Sun, S.; Cheetham, A. K. *Chem. Sci.* **2015**, *6*, 3430−3433.
(115) Glazer, A. M. *Acta Crystallogr., Sect. B: Struct. Crystallogr. Cryst. Chem.* **1972**, *28*, 3384−3392.
(116) Bovill, S. M.; Saines, P. J. *CrystEngComm* **2015**, *17*, 8319−8326.
(117) Lewis, G. R.; Dance, I. *J. Chem. Soc., Dalton Trans.* **2000**, 299−306.
(118) Leguy, A. M. A.; Frost, J. M.; McMahon, A. P.; Sakai, V. G.; Kochelmann, W.; Law, C.; Li, X.; Foglia, F.; Walsh, A.; O'Regan, B. C.; Nelson, J.; Cabral, J. T.; Barnes, P. R. F. *Nat. Commun.* **2015**, *6*, 7124.
(119) Wells, A. F. *Structural Inorganic Chemistry*, 5th ed.; Clarendon Press: Oxford, UK, 1984.
(120) Banerjee, R.; Phan, A.; Wang, B.; Knobler, C.; Furukawa, H.; O'Keeffe, M.; Yaghi, O. M. *Science* **2008**, *319*, 939−943.
(121) Kostakis, G. E.; Powell, A. K. *Dalton Trans.* **2010**, *39*, 2449−2450.

DOI: 10.1021/jacs.5b13446
J. Am. Chem. Soc. XXXX, XXX, XXX−XXX

(122) Roberts, R. J.; Li, X.; Lacey, T. F.; Pan, Z.; Patterson, H. H.; Leznoff, D. B. *Dalton Trans.* **2012**, *41*, 6992−6997.
(123) Glazer, J.; Cosier, A. M. *J. Appl. Crystallogr.* **1986**, *19*, 105−107.
(124) Nowell, H.; Barnett, S. A.; Christensen, K. E.; Teat, S. J.; Allan, D. R. *J. Synchrotron Radiat.* **2012**, *19*, 435−441.
(125) Goeta, A. E.; Thompson, L. K.; Sheppard, C. L.; Tandon, S. S.; Lehmann, C. W.; Cosier, J.; Webster, C.; Howard, J. A. K. *Acta Crystallogr., Sect. C: Cryst. Struct. Commun.* **1999**, *55*, 1243−1246.
(126) Otwinowski, Z.; Minor, W. *Methods Enzymol.* **1997**, *276*, 307−326.
(127) *Crysalis PRO*; Agilent Technologies: Yarnton, England, 2010.
(128) Altomare, A.; Cascarano, G.; Giacovazzo, C.; Guagliardi, A.; Burla, M. C.; Polidori, G.; Camalli, M. *J. Appl. Crystallogr.* **1994**, *27*, 435.
(129) Palatinus, L.; Chapuis, G. *J. Appl. Crystallogr.* **2007**, *40*, 786−790.
(130) Betteridge, P. W.; Carruthers, J. R.; Cooper, R. I.; Prout, K.; Watkin, D. J. *J. Appl. Crystallogr.* **2003**, *36*, 1487.
(131) Parois, P.; Cooper, R. I.; Thompson, A. L. *Chem. Cent. J.* **2015**, *9*, 30.
(132) Cooper, R. I.; Thompson, A. L.; Watkin, D. J. *J. Appl. Crystallogr.* **2010**, *43*, 1100−1107.

DOI: 10.1021/jacs.5b13446
J. Am. Chem. Soc. XXXX, XXX, XXX−XXX

Chemical Control of Mesoscale Polarisation *via* Geometric Frustration in Supramolecular Crystals

Christoph S. Zehe[1], Joshua A. Hill[2], Nicholas P. Funnell[2,3], Klaus Kreger[4], Andrew L. Goodwin[2]*, Hans-Werner Schmidt[4]*, Jürgen Senker[1]*

[1]Inorganic Chemistry III, Universitätsstrasse 30, University of Bayreuth, 95447, Bayreuth, Germany,

[2]Department of Chemistry, University of Oxford, Inorganic Chemistry Laboratory, South Parks Road, Oxford OX1 3QR, UK,

[3]Current address: ISIS, Rutherford Appleton Laboratory, Chilton, Didcot OX11 0QX, UK,

[4]Macromolecular Chemistry I, Universitätsstrasse 30, University of Bayreuth, 95447, Bayreuth, Germany.

*To whom correspondence should be addressed;

Email: juergen.senker@uni-bayreuth.de, andrew.goodwin@chem.ox.ac.uk, hans-werner.schmidt@uni-bayreuth.de.

For the development of ultrahigh density memories, columnar supramolecular phases with polarisation along the columnar axis have gained increasing interest since every column might ultimately function as an individual memory element. If these columns aggregate in hexagonal rod packings, the intercolumnar dipole-dipole interactions frustrate. Here, we show that this geometric frustration allows for the formation of mesoscale domains exhibiting spontaneous polarisation. The frustration suppresses conventional antiferroelectric dipole order, which heightens the sensitivity towards secondary intercolumnar packing effects, altering the effective intercolumnar interactions. By investigating the disordered structures of several benzene-1,3,5-trisamides, which form columnar supramolecular assemblies *via* triple helical hydrogen bonding, we develop a strategy to control the emergence of polarisation and the domain sizes by chemical design of the molecular synthons. Our results demonstrate how a concept typically applied to the physics of triangular antiferromagnets can be exploited to develop a new route to organic ferroelectric materials.

Organic materials featuring ferroelectric polarisation[1] are attractive candidates for easily processable, low-cost electric sensors[2], electro-optics[3] and non-volatile memory devices[4,5]. The fundamental requirements for these materials are spontaneous and switchable polarisation, which are generally induced in supramolecular solids[1,3] and liquid crystalline (LC) phases[6] by ordering either permanent molecular dipoles or supramolecular dipole moments generated or enhanced through the assembly[7]. Examples include aligning molecules which exhibit polar bonds[8,9], forming extended hydrogen bond networks[7,10,11], and creating charge transfer complexes[12–15]. While the rigidity of solid assemblies allows for stable ferroelectric ordering, it can restrict molecular reorientation and hence hamper switching of polarisation. In contrast, LC phases provide sufficient molecular mobility while maintaining residual orientational order[6,16,17]. In the earliest and most prominent examples - tilted chiral smectic C phases (SmC*)[18] - chirality induces layers with electric polarisation. The helical superstructure formed by these layers, nevertheless, prevents the emergence of macroscopic polarisation and leads to an apolar material. To induce ferroelectricity, this structure needs to be unwound using e.g. surface interactions[19].

Recently, the first example of an intrinsically ferroelectric LC with polarisation along the columnar axis (referred to as axially polar) was realised based on columnar stacking of a phthalonitrile derivative[17]. Its remnant polarisation (1.7 μC/cm^2) is of the same order of magnitude as polyvinylidene fluoride (7 μC/cm^2), which is the most common solid organic ferroelectric material[20]. Due to the complex molecular design, as well as the liquid crystalline nature of the resulting supramolecular phases, however, establishing structure-property

relations remain difficult since similar derivatives exhibit either switchable but volatile or nonvolatile but nonswitchable polarisation[17]. The most challenging problem is hereby to control ferroelectric ordering of neighbouring columns in the rod packing by overcoming intercolumnar dipole-dipole interactions, which favour macrodipole anti-alignment[3] resulting in apolar paralectric phases[17]. Such axially polar ferroelectric materials, however, have gained increasing interest for the development of ultrahigh density memories, since every column might ultimately function as an individual memory element[21,22].

Another versatile class of supramolecular synthons assembling into columnar phases with axial polarity are benzene-1,3,5-tricarboxamides[23] (BTAs). BTAs are easily accessible and allow to control the solid/LC phase behaviour *via* the molecular design \cite[24]. In thin films of oriented LCs of BTAs with long aliphatic side groups, polarisation is induced and switched by electric fields, while simply freezing the LC state yields a remnant polarisation[23,25] of up to 2 μC/cm^2; however, experimental evidence for the existence of spontaneous polarisation is missing. Generally, possible ordering schemes and ordering mechanisms of the macrodipoles leading to spontaneous polarisation in such columnar phases remain unclear[17,21,22,26–28]. In particular, the question arises how inherent antiferroelectric interactions between macrodipoles of neighbouring columns may be overcome to induce spontaneous polarisation on mesoscopic and macroscopic length scales. Here, we demonstrate that the complex interplay of electrostatic and steric interactions between supramolecular columns of BTAs with axial polarity may induce spontaneous mesoscale polarisation in frustrated (pseudo-)hexagonal rod packings.

Results and Discussion

Columnar assemblies of BTAs. BTAs are based on a benzene core, which is linked to peripheral groups *via* three amide bonds in 1,3,5 positions (Fig. 1a). The formation of threefold intermolecular hydrogen bonds in a helical arrangement drives the molecular self-assembly into well-ordered columns (Fig. 1b, left), aligning all carbonyl bonds in one direction and all NH bonds in the opposite direction. As a result, the dipole moments of the individual amide units reinforce to give to macrodipoles[23] along the columnar axis (Fig. 1b, left). At the same time, the side groups on the outside of the stacks give rise to a corrugated surface topography (Fig. 1b, right). The macrodipoles of neighbouring columns prefer an anti-alignment due to the interactions of their electric fields in a side-by-side arrangement (Fig. 1c). Since van der Waals forces require neighbouring columns to pack as densely as possible, a hexagonal rod packing[29] results (Fig. 1d). Hereby, the surface topography (Fig. 1c) imposes steric restraints, favouring either parallel or antiparallel arrangements depending on subtle structural details of the peripheral groups. In such a triangular lattice, however, the macrodipole interactions between neighbouring columns become frustrated, as it is not

possible to simultaneously align all of them antiparallel relative to their nearest neighbours (Fig. 1d). The frustration reduces the contribution of the macrodipole interactions to the total energy of the rod packing. Examples from the field of frustrated antiferromagnetism show that this heightens the sensitivity towards secondary interactions and increases the propensity for complex phase behaviour[30].

Single crystal Bragg structure solutions. We study a series of four selected BTAs (Fig. 2a) using single-crystal X-ray diffraction measurements and analyse the structured diffuse scattering patterns we observe in terms of a simple statistical mechanical model developed for triangular Ising antiferromagnets[31]. Compounds **1** and **2** differ in terms of the connectivity of the amide units (Fig. 2a). The higher torsional flexibility of the amide linkage with respect to the benzene ring[32] in the case of **1** allows the C=O bonds to orient more directly along the columnar axis. This enhances the macrodipole moment compared to **2** but retains a similar intercolumnar separation. The longer branched side groups in compound **3** merely increase the distance (Fig. 2a) between macrodipoles with respect to **1** and **2**. In **4**, a polar C-F bond is introduced[33] in order to reduce the macrodipole moment.

The columnar packing arrangements of **1** and **2** were recently determined experimentally[32,34]; refinement reveals a similar packing of the molecules for **3** and **4** (Fig. 2b; see sections 1 and 2 of Supplementary Information for crystallographic details). For **1** (ref. 34), **2** and **3** each stack in the conventional Bragg (average structure) solution appears as a superposition of two columns with opposite macrodipole orientations situated on so-called split sites (Supplementary Fig. S2). Since Bragg diffraction arises from spatially averaged electron density, this split-site model reflects the disorder of the macrodipole orientations in different unit cells within the coherence length of the X-ray beam[35]. The occupancies for each of the sets of split sites are exactly 50% for **1**, leading to a centrosymmetric average electron density distribution. In contrast, the occupancies vary between 65-80% and 70-80% for the major component in **2** and **3**, respectively (Fig. 2c). This major component of the structure of compound **2** shows a stripe-type (along the crystallographic *a* direction) macrodipole pattern in a pseudo-triangular arrangement with neighbouring stripes having antiparallel macrodipole directions, thus lowering the space-group symmetry (Fig. 2b and 2c; Supplementary Fig. S3 explains relation to ref. 32). The unit cell of **3** consists of three stacks, where the macrodipoles of two stacks are predominantly pointing ‘up’ and the macrodipole of the remaining stack is pointing ‘down’, leading to a honeycomb-like pattern (Fig. 2c). The same honeycomb pattern is observed for **4** without disorder in the macrodipole orientations. As a result, the unit cells of **1** and **2** contain no net macrodipole moment since an equal part of up- and down-oriented columns are present. For compounds **3** and **4**, however, the unit cells contain an excess of one orientation leading to a net polarisation along the direction of the columnar axis.

Modelling of structured diffuse scattering. We also observed that for **1**, **2** and **3** selected layers of the reciprocal space, reconstructed from the single crystal X-ray diffraction experiments, exhibit intense structured diffuse scattering (Fig. 3a). Such scattering arises from correlated disorder within the coherence length of the X-ray beam and its shape contains crucial information about the origin of the disorder[35]. In order to understand the origin of both the disorder and the ordering schemes observed from Bragg scattering we applied a two-dimensional Ising model. The superstructures observed for **2**-**4** cannot emerge from a model that considers only nearest neighbour (n.n.) column interactions[31] J_1. To keep the model as simple as possible, however, we include (effective) couplings J_2 to the next-nearest neighbour (n.n.n.) columns. We interpret the physical origin of J_1 and J_2 as a combination of dipolar and steric interactions between neighbouring columns. The key point is then that the balance of these interactions is influenced by small variations of the chemical structure of the molecules, which in turn drives the emergence and controls the length scale of polarisation. We treated J_1 and J_2 as possibly ferroelectric or antiferroelectric effective pairwise interactions and equilibrated the system in a Monte-Carlo simulation using an energy E defined by summation over all interactions for a given ensemble (with Ising state σ = +1 or –1 for a column pointing up and down, respectively):

$$E = J_1 \sum_{\langle i,j \rangle} \sigma_i \sigma_j + J_2 \sum_{\langle\langle i,j \rangle\rangle} \sigma_i \sigma_j \ , \qquad (1)$$

where single brackets denote a sum over n.n. and double brackets a sum over n.n.n. interactions. For these models we optimised the coupling constants (given in Fig. 3b) in an iterative empirical approach until the best qualitative match between simulated and experimental diffraction patterns (Fig. 3a) is reached. The fact that in all four cases J_1 adopts a positive value (normalised to $J_1/kT = 1$) indicates that antiferroelectric interactions dominate between n.n. The crucial difference between compounds **1** and **2** with respect to **3** and **4** becomes evident in the effective n.n.n. interactions. J_2 is positive for **1** and **2** and negative for **3** and **4**. This reveals antiferroelectric couplings between n.n.n. columns for compounds **1** and **2** and ferroelectric interactions for **3** and **4**. Recalling that the X-ray beam averages within its coherence length over different unit cells, the models (Fig. 3c) not only reproduce qualitatively the diffuse scattering but also reflect the average Bragg structure shown in Figs. 2b and 2c. **1** and **2** both exhibit disorder on a local scale with preferred antiferroelectric arrangement between neighbouring columns. For **3** and **4** the negative sign of J_2 induces mesoscale domains with a honeycomb structure leading to spontaneous polarisation, where **4** exhibits significantly larger domains. Similar ordering schemes have been proposed for frustrated macrodipoles in triangular lattices[17,21,22,26,36]; however, no experimental evidence has yet been provided.

Role of macrodipole moments. To rationalise the ratios of the coupling constants, we estimate the magnitude of the macrodipoles of **1** to **4** based on quantum chemical calculations. On DFT level, the average dipole moment per molecule for a stack containing up to six molecules in crystal structure geometry increases steadily with increasing number of molecules (Fig. 4a) due to cooperative effects[37]. Convergence can be reached only using semiempirical calculations; however, the magnitude of the dipole moments differs markedly for both techniques. Therefore, we scaled the less precise AM1 results to the more accurate PBE1PBE calculations (Fig. 4a) and extended them until convergence is reached, i.e. to the limit of an infinite stack. This results in average molecular dipole moments of 12.2 D, 10.8 D and 6.6 D for **1**, **2** and **4**, respectively. The smaller value of **2** compared to **1** is caused by the enhanced conjugation of the amide bond's π-system with the benzene ring in **2**, restraining the tilt of the CO bond into the stacking direction[32]. The average dipole moment of **4** is only about 62 % of that of **2**, which is a result of the anti-alignment of the C-F bonds with respect to the carbonyl groups due to weak intramolecular NH···F contacts (Fig. 4b). For **3**, where the number of atoms per molecules does not allow for extensive calculations, we expect similar values as for **1**, since the conjugation of the amide bond with the benzene core, and hence the torsional flexibility, is similar to **1**. Interestingly, the apolar structures of **1** and **2** exhibit large average dipole moments with short intercolumnar distances of $r_{\mathrm{col}} = 14.1$ Å and 14.5 Å (averaged over the different directions), respectively. Increasing the intercolumnar distance in **3** to $r_{\mathrm{col}} = 17.1$ Å while maintaining the large average dipole moments of **1** (12.2 D), or reducing the average dipole moment to 6.6 D as in **4** with $r_{\mathrm{col}} = 13.9$ Å, results in domains of spontaneous polarisation. With these values, we can estimate the polarisation within each domain to 1.6 μC/cm^2 and 1.4 μC/cm^2 for **3** and **4**.

These findings are understood by recalling that the particular phase adopted depends not only on the electrostatic interactions of macrodipoles but also the steric requirements of a dense columnar packing. On the one hand, the macrodipole interactions decrease due to their $1/r^3_{\mathrm{col}}$-dependence from the n.n. to the n.n.n.. On the other hand, in a collective ensemble, cooperative packing effects can introduce effective n.n.n. ferroelectric interactions[38], i.e. negative J_2 values, due to interdependencies between column packing and polarisation. Varying either r_{col} by longer side groups (as in **3**) or decreasing the macrodipole moment of each column (as in **4**), decreases the contribution of the macrodipole interactions to the effective coupling constants and increases the sensitivity towards packing effects, leading to negative J_2. This allows us to move between non-polar stripe phases as in **1** and **2** and polar honeycomb phases in the Ising phase diagram[31] as in **3** and **4** by chemical modification of the molecular synthons (Fig. 5).

Conclusion

Our models indicate that, in contrast to established approaches where supramolecular interactions between molecules are used to create ferroelectric order[3], polarisation emerges here from weak interactions between self-assembled supramolecular columns. Since these interactions are encoded in the molecular structure, the latter controls the dipole ordering and the length scale of domain formation. This finding illustrates an application of emerging complexity in supramolecular systems[39] and constitutes an interesting example of introducing hierarchical order in supramolecular systems[40].

We have shown that with small but systematic chemical modifications of the molecular synthons, a broad range of J_1/J_2 values is accessible and consequently antiferroelectric and ferroelectric domain structures are formed. Counterintuitively, mesoscale polarisation is maximised for systems where dipolar interactions are reduced. The phase behaviour we observed resembles that of frustrated antiferromagnets, where chemical variation leads to different J values and hence varying degrees of simple[41] or complex[30] magnetic order. Future development of relations - analogous to the Goodenough-Kanamori[41,42] rules - between the chemical structure of synthons and the values of J_1/J_2 will allow the prediction of macrodipole organisation in axially polar triangular columnar phases. Investigation of other columnar phases based on hexagonal and on alternative, e.g. orthorhombic, lattices may lead to the development of a wide variety of new axially polar columnar ferroelectric materials, both solid and liquid crystalline.

Methods

Synthesis. All compounds were synthesised according to the procedures reported in the literature[33,43]. Single crystals of **1**, **2** and **3** were obtained by slow solvent evaporation of a saturated solution using N,N-dimethylformamide under ambient conditions. Single crystals of **4** were grown by sublimation of 0.5 g in a closed glass vessel at 160° C for 3 days.

Structural characterisation. Single crystal X-ray diffraction experiments were carried out using an Oxford Diffraction diffractometer (CuKα_1 radiation) under Oxford Cryosystems 700 Plus open-flow nitrogen cryostream[44] at 150 K for **3** and **4** and on a STOE IPDS II instrument (Mo-Kα radiation) under ambient conditions in case of **2**. For structure solution and refinement the program CRYSTALS[45] was used. See Supplementary Information section 1 and 2 for details.

Quantum chemical calculations. Structures obtained from single crystal structure solution were geometry optimised on the DFT level with the software package CASTEP[46] using the PBE functional and the Tkatchenko-Scheffler dispersion correction scheme[47]. An electronic cut off energy of 900 eV and a Monkhorst k point grid spacing of 0.07 Å^{-1} was used. Dipole moments were calculated for clusters of molecules extracted from the geometry optimised crystal structures while keeping the

geometry fixed. For this, the software package GAUSSIAN09[48] with either the PBE1PBE functional on the DFT level and a 6-311++G** basis set or the semiempirical AM1 method was used. The dipole moments $\delta_{AM1}(n_{mol})$ obtained for the AM1 method as a function of the stack size n_{mol} were first fitted to those of the PBE functional $\delta_{PBE}(n_{mol})$ for stacks consisting of up to six molecules ($n_{mol} \leq 6$) by a least-squares refinement of the coefficients c_1 and c_2 in the equation $c_1 \cdot \delta_{AM1}(n_{mol}) + c_2$. Subsequently, the obtained coefficients were used to correct the AM1 results $\delta_{AM1}(n_{mol})$ of stacks containing more than six molecules ($n_{mol} > 6$).

Model generation. Two-dimensional Ising models were generated with a custom Monte Carlo code. The energy was defined by

$$E = J_1 \sum_{\langle i,j \rangle} \sigma_i \sigma_j + J_2 \sum_{\langle\langle i,j \rangle\rangle} \sigma_i \sigma_j \,,$$

where single brackets denote a sum over nearest neighbours, double brackets a sum over next nearest neighbours and σ_i = 1 and –1 for columns pointing up and down, respectively. The energy was equilibrated for systems containing 100 x 100 spins with periodic boundary conditions using the Metropolis algorithm[49] with $J_1/kT = 1$, where k denotes the Boltzmann constant and T the simulation temperature. For compound **2**, where the underlying rod packing is pseudo-hexagonal, the coupling constants were allowed to differ in the different crystallographic directions of the two-dimensional lattice (Supplementary Fig. S5). The entire code is available upon request.

Simulation of X-Ray Diffraction Patterns. The calculation of powder and single crystal diffraction intensities was facilitated with the programs CrystalDiffract[50] and SingleCrystal[51], respectively. For all models, the basic shape of single crystal diffuse scattering was first inspected using test models being generated by populating the 100 x 100 models with carbon in case of $\sigma_i = 1$ and voids otherwise. The shape and intensity of diffuse scattering showed sensitivity towards changes in the coupling constants of about $kT/20$, in particular in the region around $J_2 = 0$ or $J_2 = 0$. Subsequently, 36 x 36 subensembles were randomly chosen from the 100 x 100 models and populated with stacks obtained from the single-crystal structure solutions. Different subensembles were tested and, by comparing the diffuse scattering with that of the reference models, it was ensured that the decrease of model size does not affect the diffraction pattern. Scattering from these models is identical to that of the test models up to a scale factor. Comparisons of the simulations of powder diffraction patterns using those models with experimental data obtained from ground single crystals show excellent accordance (see Supplementary Figs. S6-S9).

References

1. Horiuchi, S. & Tokura, Y. Organic ferroelectrics. *Nature Mater.* **7,** 357–366 (2008).
2. Scott, J. F. Applications of modern ferroelectrics. *Science* **315,** 954–959 (2007).
3. Tayi, A. S., Kaeser, A., Matsumoto, M., Aida, T. & Stupp, S. I. Supramolecular ferroelectrics. *Nature Chem.* **7,** 281–294 (2015).
4. Naber, R. C. G. *et al.* High-performance solution-processed polymer ferroelectric field-effect transistors. *Nature Mater.* **4,** 243–248 (2005).
5. Asadi, K., de Leeuw, D. M., de Boer, B. & Blom, P. W. M. Organic non-volatile memories from ferroelectric phase-separated blends. *Nature Mater.* **7,** 547–550 (2008).
6. Lagerwall, S. T. Ferroelectric and antiferroelectric liquid crystals. *Ferroelectrics* **301,** 15–45 (2004).
7. Horiuchi, S. *et al.* Ferroelectricity near room temperature in co-crystals of nonpolar organic molecules. *Nature Mater.* **4,** 163–166 (2005).
8. Lovinger, A. J. Ferroelectric polymers. *Science* **220,** 1115–1121 (1983).
9. Fu, D.-W. *et al.* Diisopropylammonium bromide is a high-temperature molecular ferroelectric crystal. *Science* **339,** 425–428 (2013).
10. Horiuchi, S. *et al.* Above-room-temperature ferroelectricity in a single-component molecular crystal. *Nature* **463,** 789–792 (2010).
11. Horiuchi, S. *et al.* Above-room-temperature ferroelectricity and antiferroelectricity in benzimidazoles. *Nature Commun.* **3,** 1308 (2012).
12. Horiuchi, S., Okimoto, Y., Kumai, R. & Tokura, Y. Quantum phase transition in organic charge-transfer complexes. *Science* **299,** 229–232 (2003).
13. Collet, E. *et al.* Laser-induced ferroelectric structural order in an organic charge-transfer crystal. *Science* **300,** 612–615 (2003).
14. Kagawa, F., Horiuchi, S., Tokunaga, M., Fujioka, J. & Tokura, Y. Ferroelectricity in a one-dimensional organic quantum magnet. *Nature Phys.* **6,** 169–172 (2010).
15. Tayi, A. S. *et al.* Room-temperature ferroelectricity in supramolecular networks of charge-transfer complexes. *Nature* **488,** 485–489 (2012).
16. Reddy, R. A. *et al.* Spontaneous ferroelectric order in a bent-core smectic liquid crystal of fluid orthorhombic layers. *Science* **332,** 72–77 (2011).
17. Miyajima, D. *et al.* Ferroelectric columnar liquid crystal featuring confined polar groups within core-shell architecture. *Science* **336,** 209–213 (2012).
18. Meyer, R. B., Liebert, L., Strzelecki, L. & Keller, P. Ferroelectric liquid crystals. *J. Phys. Lett. (Paris)* **36,** 69–71 (1975).
19. Clark, N. A. & Lagerwall, S. T. Submicrosecond bistable electro-optic switching in liquid crystals. *Appl. Phys. Lett.* **36,** 899–901 (1980).
20. Furukawa, T., Date, M. & Fukada, E. Hysteresis phenomena in polyvinylidene fluoride under high electric field. *J. Appl. Phys.* **51,** 1135–1141 (1980).
21. Kishikawa, K., Nakahara, S., Nishikawa, Y., Kohmoto, S. & Yamamoto, M. A ferroelectrically switchable columnar liquid crystal phase with achiral molecules: superstructures and properties of liquid crystalline ureas. *J. Am. Chem. Soc.* **127,** 2565–2571 (2005).
22. Takezoe, H., Kishikawa, K. & Gorecka, E. Switchable columnar phases. *J. Mater. Chem.* **16,** 2412–2416 (2006).

23. Fitié, C. F. C., Roelofs, W. S. C., Kemerink, M. & Sijbesma, R. P. Remnant polarization in thin films from a columnar liquid crystal. *J. Am. Chem. Soc.* **132,** 6892–6893 (2010).

24. Cantekin, S., de Greef, T. F. A. & Palmans, A. R. A. Benzene-1,3,5-tricarboxamide: a versatile ordering moiety for supramolecular chemistry. *Chem. Soc. Rev.* **41,** 6125–6137 (2012).

25. Sugita, A., Suzuki, K. & Tasaka, S. Electrical properties in disk-like phenylene derivative in crystalline state. *Chem. Phys. Lett.* **396,** 131–135 (2004).

26. Zimmermann, H., Poupko, R., Luz, Z. & Billard, J. Pyramidic mesophases. *Z. Naturforsch.* **40,** 149–160 (1985).

27. Tschierske, C. Materials chemistry: liquid crystals stack up. *Nature* **419,** 681–683 (2002).

28. Pleiner, H., Brand, H. R. & Cladis, P. E. Polar columnar and tetrahedratic phases. *Mol. Cryst. Liq. Cryst.* **396,** 169–176 (2003).

29. O'Keeffe, M. & Andersson, S. Rod packings and crystal chemistry. *Acta Crystallogr. A* **33,** 914–923 (1977).

30. Moessner, R. & Ramirez, A. P. Geometrical frustration. *Phys. Today* **59,** 24–29 (2006).

31. Brandt, U. & Stolze, J. Ground states of the Triangular Ising model with two-and three-spin interactions. *Z. Phys. B Con. Mat.* **64,** 481–490 (1986).

32. Schmidt, M. *et al.* Crystal structure of a highly efficient clarifying agent for isotactic polypropylene. *Cryst. Growth Des.* **12,** 2543–2551 (2012).

33. Zehe, C. *et al.* Influence of fluorine side-group substitution on the crystal structure formation of benzene-1,3,5-trisamides. *CrystEngComm* **16,** 9273–9283 (2014).

34. Kristiansen, M. *et al.* Structural aspects of 1,3,5-benzenetrisamides−a new family of nucleating agents. *Cryst. Growth Des.* **9,** 2556–2558 (2009).

35. Keen, D. A. & Goodwin, A. L. The crystallography of correlated disorder. *Nature* **521,** 303–309 (2015).

36. Gorecka, E. *et al.* Axially polar columnar phase made of polycatenar bent-shaped molecules. *J. Am. Chem. Soc.* **126,** 15946–15947 (2004).

37. Filot, I. A. W. *et al.* Understanding cooperativity in hydrogen-bond-induced supramolecular polymerization: a density functional theory study. *J. Phys. Chem. B* **114,** 13667–13674 (2010).

38. Welberry, T. R., Heerdegen, A. P., Goldstone, D. C. & Taylor, I. A. Diffuse scattering resulting from macromolecular frustration. *Acta Crystallogr. B* **67,** 516–524 (2011).

39. Cairns, A. B. *et al.* Encoding complexity within supramolecular analogues of frustrated magnets. *Nature Chem.* **8,** 442–447 (2016).

40. Aida, T., Meijer, E. W. & Stupp, S. I. Functional supramolecular polymers. *Science* **335,** 813–817 (2012).

41. Goodenough, J. B. Theory of the role of covalence in the perovskite-type manganites [La, M(II)]MnO_3. *Phys. Rev.* **100,** 564–573 (1955).

42. Kanamori, J. Superexchange interaction and symmetry properties of electron orbitals. *J. Phys. Chem. Solids* **10,** 87–98 (1959).

43. Abraham, F., Ganzleben, S., Hanft, D., Smith, P. & Schmidt, H.-W. Synthesis and structure-efficiency relations of 1,3,5-benzenetrisamides as nucleating agents and clarifiers for isotactic poly(propylene). *Macromol. Chem. Phys.* **211,** 171–181 (2010).

44. Cosier, J. & Glazer, A. M. A nitrogen-gas-stream cryostat for general X-ray diffraction studies. *J. Appl. Crystallogr.* **19,** 105–107 (1986).

45. Betteridge, P. W., Carruthers, J. R., Cooper, R. I., Prout, K. & Watkin, D. J. CRYSTALS version 12. Software for guided crystal structure analysis. *J. Appl. Crystallogr.* **36,** 1487 (2003).
46. Clark, S. J. *et al.* First principles methods using CASTEP. *Z. Kristallogr.* **220,** 567–570 (2005).
47. McNellis, E. R., Meyer, J. & Reuter, K. Azobenzene at coinage metal surfaces. Role of dispersive van der Waals interactions. *Phys. Rev. B* **80,** 205414 (2009).
48. Frisch, M. J. *et al. Gaussian09; Revision C.01* (Gaussian Inc., Wallingford, Conneticut, US, 2010).
49. Metropolis, N., Rosenbluth, A. W., Rosenbluth, M. N., Teller, A. H. & Teller, E. Equation of state calculations by fast computing machines. *J. Chem. Phys.* **21,** 1087–1092 (1953).
50. Palmer, D. C. *CrystalDiffract 6* (CrystalMaker Software Ltd, Begbroke, Oxfordshire, England, 2013).
51. Palmer, D. C. *SingleCrystal 2* (CrystalMaker Software Ltd, Begbroke, Oxfordshire, England, 2010).

Acknowledgments

C.S.Z., H.W.S. and J.S. gratefully acknowledge financial support from the German Research Foundation (SFB840). C.S.Z. acknowledges the Hanns-Seidel-Foundation and the Elite Network Bavaria for financial and other support. All authors thank Thomas Weber (ETH Zürich) for the crystal structure data of **1** and Sandra Ganzleben for her support with the syntheses of the compounds. A.L.G., J.A.H., and N.P.F. gratefully acknowledge financial support from the ERC (Grant 279705) and the EPSRC (Grant EP/G004528/2).

Author Contributions

C.S.Z., A.L.G., H.W.S. and J.S. conceived the study; K.K. was involved with the synthesis of the compounds and C.S.Z. performed the crystallisation experiments; C.S.Z. and J.A.H. performed the single-crystal diffraction experiments; C.S.Z., J.S. and A.L.G. conceived and conducted the simulations; All authors analysed and interpreted the data; C.S.Z., J.S., H.W.S. and A.L.G. prepared the manuscript. All authors discussed the results and commented on the manuscript.

Additional Information

Supplementary Information is available in the online version of the paper. Reprints and permissions information is available at www.nature.com/reprints. Correspondence and requests for materials and data should be addressed to J.S. on behalf of all authors.

Competing financial interests

The authors declare no competing financial interests.

Figure 1 | Macrodipoles created in a columnar stacking of BTA molecules by triple-helical hydrogen bonds on a frustrated triangular lattice. a, Basic design scheme of BTAs consisting of a central benzene core linked by amide bonds in 1,3,5-position to peripheral groups (denoted as R), e.g. *tert*-butyl groups. **b**, Side-view of a columnar stack of six BTA molecules highlighting the alignment of all N-H upwards and all C=O bonds downwards (left side), where the hydrogen bonds are indicated as dotted lines; all non-NH protons are omitted for clarity. The macrodipole is indicated as grey arrow. A space-filling model of the same structure illustrates the surface topography of the column (right side). **c**, Side view of two columns in antiparallel orientation illustrating a favourable alignment of the macrodipoles and an optimal close packing. The direction of the macrodipole is symbolised from here on by a black and white hexagon for up- and down-orientation, respectively. **d**, Top view on an ensemble of seven stacks in a hexagonal rod packing. The macrodipole interaction, favouring antiparallel arrangements of neighbouring dipoles, becomes frustrated (indicated by the grey hexagon) on such a triangular lattice.

Figure 2 | Varying the molecular structures of BTAs influences the disorder and average crystal structures found by single-crystal structure solution. a, Molecular structures of the four different BTAs investigated in this study. **b**, Single crystal structure solutions from Bragg reflections viewed along the direction of molecular stacks, which coincides with the direction of the polar axis of the indicated space groups. Molecules with black bonds are located behind molecules with grey bonds. **c**, Schematic representation of **b**, where the amount of black and white in each hexagon symbolises the refined occupancies of up- and down-oriented columns at the respective position (cf. Fig. 1c). The dashed blue line indicates the unit cell corresponding to the underlying hexagonal or pseudo-hexagonal (in case of **2**) lattice, whereas the black solid lines illustrate the superstructures observed for compounds **2** to **4**.

Figure 3 | The combination of frustrated macrodipole interactions with packing effects leads to ordered and disordered macrodipole arrangements and manifests in diffuse X-ray scattering. The ratios of the intercolumnar coupling constants J_1 and J_2 are given for **1** - **4**; for compound **2,** average constants are calculated (see Supplementary Fig. S5). All constants are normalised according to $J_1/kT = 1$, where T is the simulation temperature and k the Boltzmann constant. For **1**, **3** and **4** the hk2 planes and for **2** the h2k plane of the reciprocal space reconstruction are compared with the simulations and selected directions are indicated (experimental picture taken from ref. 34). **c**, Cutout of the Ising model simulations containing approximately 70 x 70 columns for every compound. The red boxes contain magnifications of the local structure, where the triangular unit cells from Fig. 2b and 2c are indicated in yellow. The blue lines emphasise domains exhibiting net polarisation for **3** and **4** and the scale bars in the top left corners correspond to distance of 10 nm.

Figure 4 | The macrodipoles of individual columns can be altered introducing polar groups. a, Average dipole moment per molecule for stacks of varying sizes isolated from the crystal structure without geometry optimisation. The filled circles correspond to calculations using the PBE1PBE functional and are limited to six molecules due to calculation time. To estimate the average dipole moment per molecule in the limit of an infinite stack, values $\delta_{AM1}(n_{mol})$ obtained by the semiempirical AM1 method are scaled by the equation $c_1 \cdot \delta_{AM1}(n_{mol}) + c_2$ (open circles), where the displayed c_1 and c_2 values are constants for each compound and n_{mol} demarks the number of molecules in the stack. **b**, The C-F bond (green) in the crystal structure of **4** points in the same direction as the N-H bond (blue), forming a weak intramolecular hydrogen bond. This introduces a dipole moment opposing that of the C=O bond (red) and hence reduces the overall macrodipole μ in the stacking direction. All non-NH protons are omitted for clarity.

Figure 5 | Varying the magnitude of the macrodipoles and packing effects by chemical modifications of the molecular synthons leads to different Ising phases. The ground state phase diagram[31] of the simple two-dimensional Ising model exhibiting antiferroelectric nearest ($J_1 > 0$) and varying next-nearest neighbour interactions can be divided into two regions: for antiferroelectric n.n.n. interactions ($J_2 > 0$) a local stripe-like pattern (white background) as observed for **1** and **2** and for ferroelectric n.n.n. interactions ($J_2 < 0$) a honeycomb-like pattern (grey background) with permanent polarisation for each domain as found for **3** and **4** are the ground states, respectively (cf. Fig. 2c). Note that for the case $J_1 > 0$ the models exhibit no phase transition as a function of the temperature.

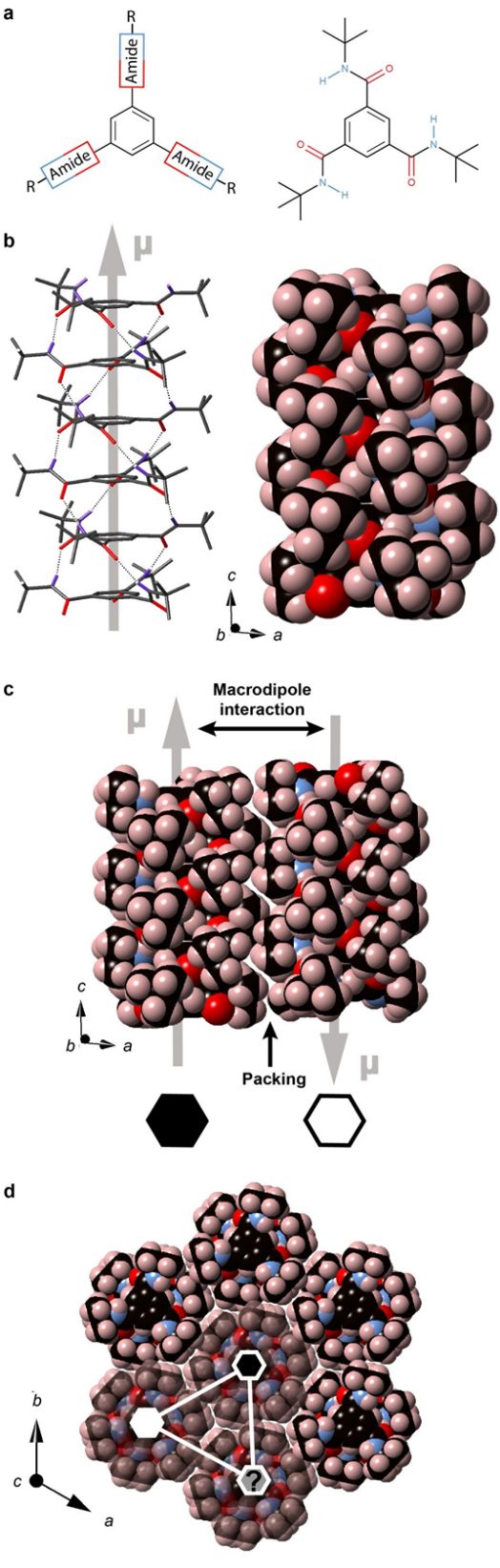
a
R
Amide
R
Amide
Amide
R
b
μ
c
b
a
c
Macrodipole
interaction
μ
c
b
a
Packing
μ
d
b
c
a
?

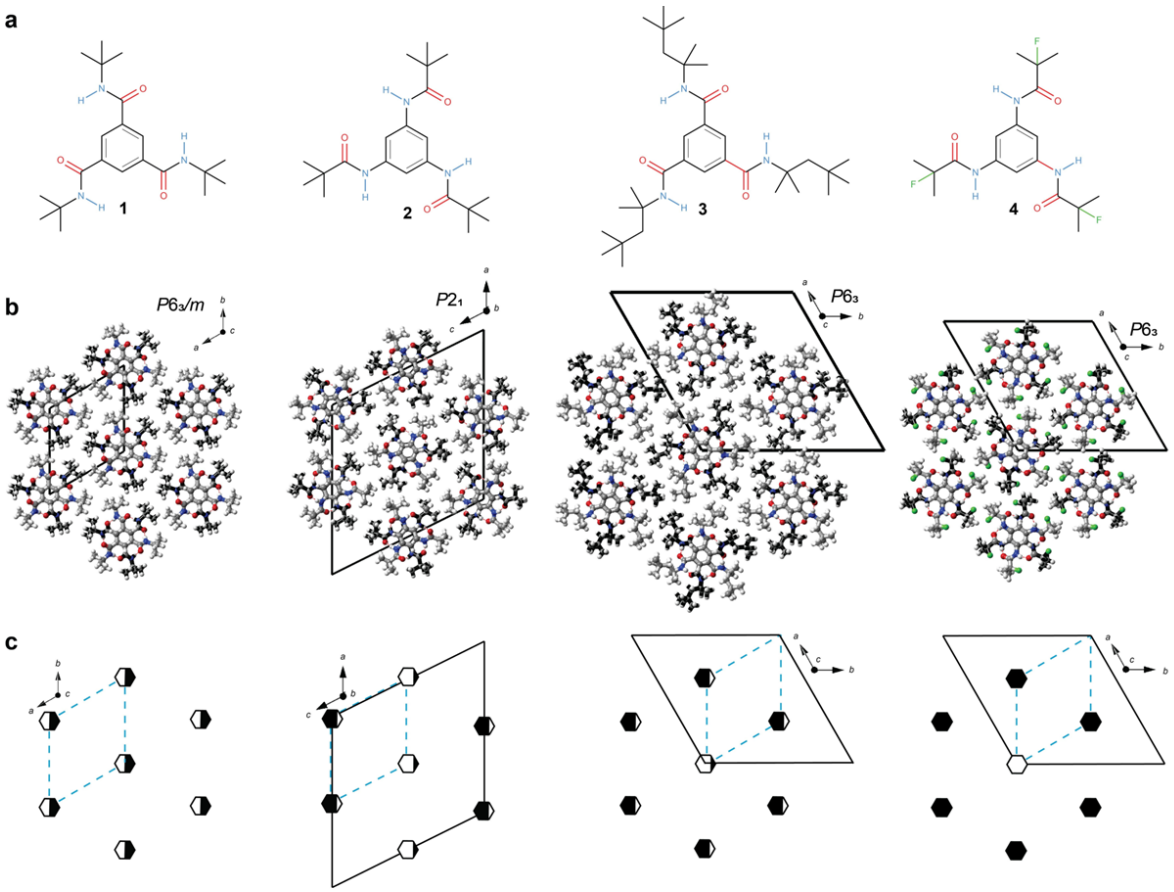
a
1
2
3
4
b
P6₃/m
P2₁
P6₃
P6₃
c

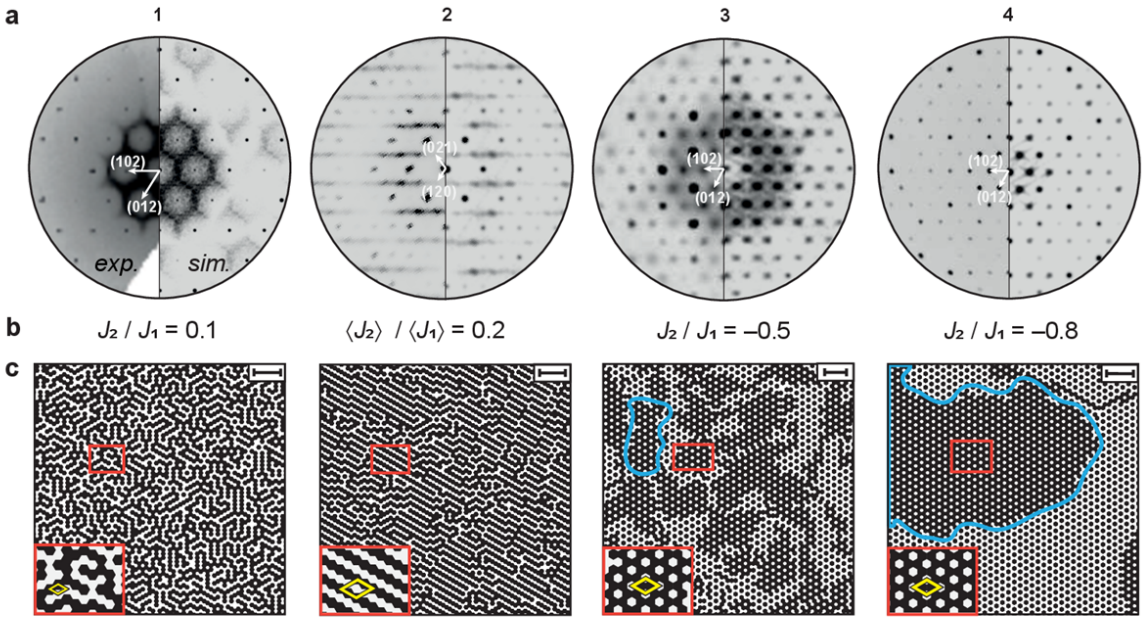
a
1
2
3
4
(102)
(012)
exp.
sim.
(021)
(120)
b
$J_2 / J_1 = 0.1$
$\langle J_2 \rangle / \langle J_1 \rangle = 0.2$
$J_2 / J_1 = -0.5$
$J_2 / J_1 = -0.8$
c

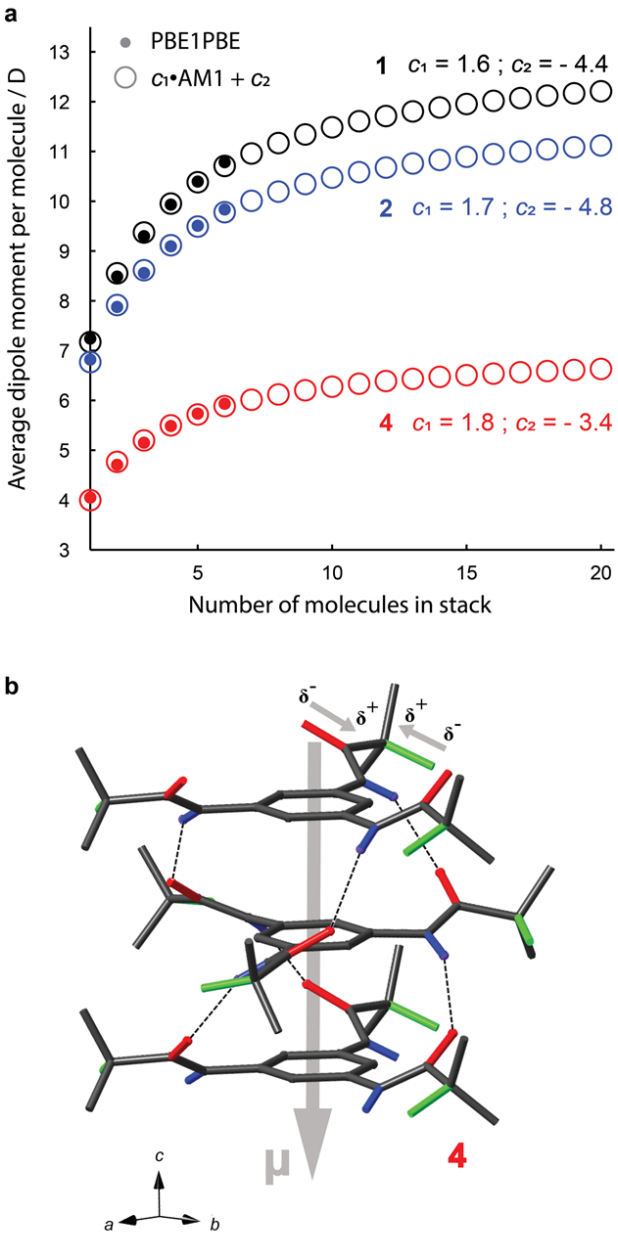
a
PBE1PBE
c1•AM1 + c2
1 c1 = 1.6 ; c2 = - 4.4
2 c1 = 1.7 ; c2 = - 4.8
4 c1 = 1.8 ; c2 = - 3.4
Average dipole moment per molecule / D
Number of molecules in stack
b
δ-
δ+
δ+
δ-
μ
4
c
a
b

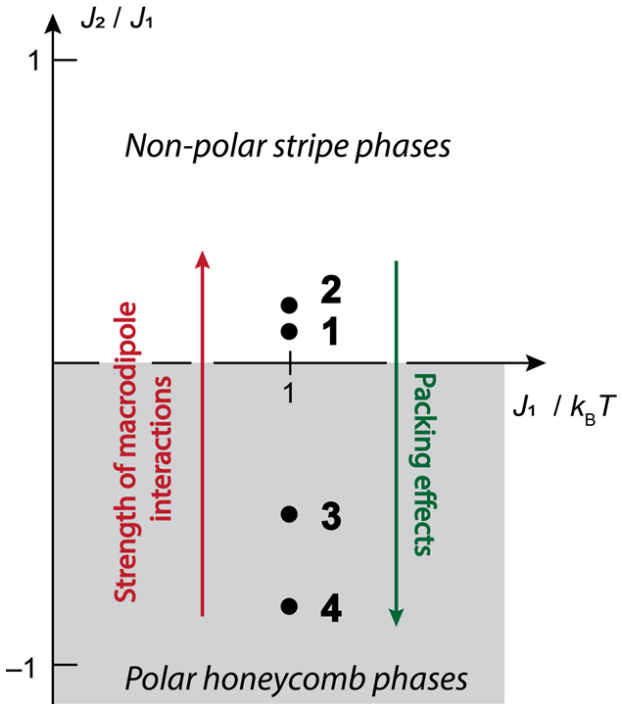
J₂ / J₁
1
Non-polar stripe phases
2
1
1
J₁ / k_B T
Strength of macrodipole interactions
Packing effects
3
4
–1
Polar honeycomb phases

Volume 17 | Number 15 | 21 April 2015 | Pages 2905–3042

CrystEngComm

www.rsc.org/crystengcomm

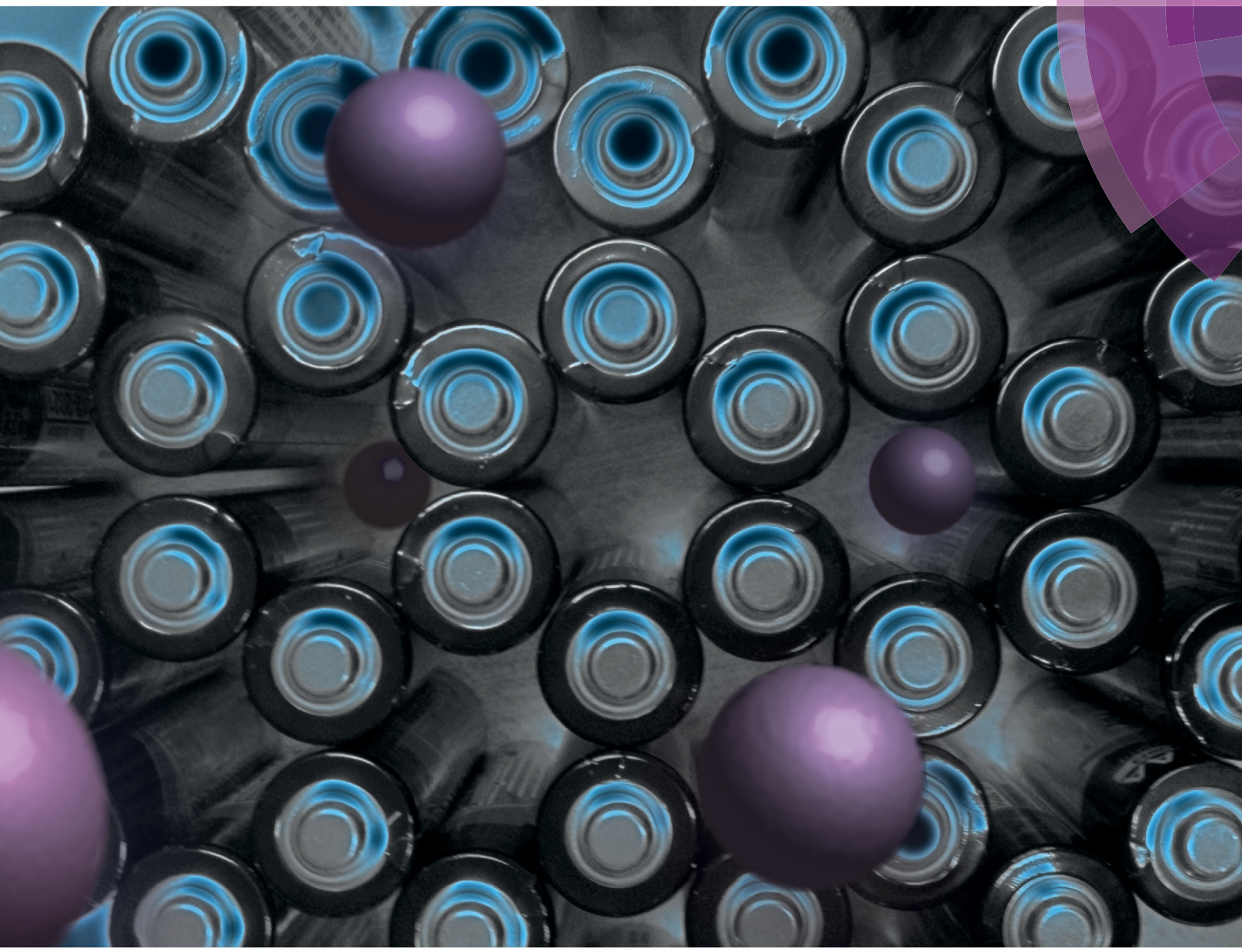

ROYAL SOCIETY OF CHEMISTRY

COMMUNICATION

Andrew L. Goodwin *et al.*

Zero-strain reductive intercalation in a molecular framework

CrystEngComm

COMMUNICATION

View Article Online
View Journal | View Issue

Open Access Article. Published on 08 January 2015. Downloaded on 04/04/2016 18:17:01.
This article is licensed under a Creative Commons Attribution 3.0 Unported Licence.

Cite this: *CrystEngComm*, 2015, **17**, 2925

Received 29th November 2014,
Accepted 22nd December 2014

DOI: 10.1039/c4ce02364a

www.rsc.org/crystengcomm

Zero-strain reductive intercalation in a molecular framework†

Joshua A. Hill, Andrew B. Cairns, Jared J. K. Lim, Simon J. Cassidy, Simon J. Clarke and Andrew L. Goodwin*

Reductive intercalation of potassium within the molecular framework $Ag_3[Fe(CN)_6]$ gives rise to a volume strain that is an order of magnitude smaller than is typical for common ion-storage materials. We suggest that framework flexibility might be exploited as a general strategy for reducing cycling strain in battery and ion-storage materials.

One of the central considerations in the development of ion-storage materials is the effect of mass transport on bulk physical properties of the host material.[1] The existence of large structural changes on charge or discharge increases the propensity for dislodging, cracking and degradation—all of which reduce battery life and long-term storage capacity.[2–4] Upon intercalation most ion-storage media undergo molar volume expansions of between 1 and 10%:[4] a response equivalent to a temperature increase of *ca.* 2000 K.[5] The practical consequences of such a large 'electrochemical shock' are so severe that much of the field has focussed on developing inventive work-arounds to accommodate volume strain. So, for example, one strategy is that of nanofabrication: by preparing battery materials in the form of nanowires or thin-films it is possible to sustain much larger volume strains, albeit at the expense of storage density.[6,7]

Ion-storage media that can accommodate Na^+ or K^+ are increasingly sought-after as battery electrode materials.[8,9] These earth-abundant elements could be used in place of lithium for large, static batteries where energy density is much less important compared to mobile applications. One of the challenges in developing electrodes for such batteries is accommodating these much larger ions without drastic volume changes.

Department of Chemistry, University of Oxford, Inorganic Chemistry Laboratory, South Parks Road, Oxford, OX1 3QR, UK.
E-mail: andrew.goodwin@chem.ox.ac.uk; Fax: +44 (0)1865 274690;
Tel: +44 (0)1865 272137

† Electronic supplementary information (ESI) available: Synthesis, experimental methods, and sample characterisation; X-ray powder diffraction refinement details. See DOI: 10.1039/c4ce02364a

We were intrigued by the possibility of exploiting structural flexibility in molecular framework materials as a means of engineering systems with much-reduced *intrinsic* volume strains. Our particular focus on molecular frameworks has been motivated by the increasingly-apparent predisposition of such materials to anomalous temperature- and pressure-dependent strain behaviour. For example, negative thermal expansion (NTE, volume reduction on heating) is rarely observed in conventional engineering materials[10] but is not at all uncommon amongst molecular frameworks;[11–13] moreover this NTE effect can be tensioned against the more usual positive thermal expansion contributions of other structural motifs to produce materials with near-zero coefficients of thermal expansion.[14] Negative and near-zero compressibilities are also achievable in similar systems.[15–17] Such unconventional mechanical responses are rationalised in terms of geometric flexibility: the ease with which molecular frameworks can vary their lattice geometries allows behaviour not observed in conventional materials.[18] Given that thermal and pressure-induced strains can be ameliorated by framework flexibility, our hope was that electrochemical strain might also be fundamentally reduced in suitably-chosen molecular frameworks.

Perhaps the key difficulty faced in developing molecular-framework-based ion-storage materials is that redox chemistry is surprisingly rare for these systems.[19] The few molecular frameworks for which bulk insertion has actually been demonstrated include MIL-53(Fe),[20,21] lithium isopropoxide-modified magnesium 2,5-dioxido-1,4-benzenedicarboxylate,[22] $Zn_{0.5}Co_{0.5}(HCOO)_3$,[23] and the Prussian Blue analogue $K_2Cu[Fe(CN)_6]$.[24] Unfortunately, for each of these systems electrochemical strain is not especially reduced relative to "traditional" ion-storage materials such as Li_xCoO_2, and in some cases is actually much larger.[25] Encouraged both by a voltammetric study of the $[Fe^{II/III}(CN)_6]^{4-/3-}$ couple[26] and by the discovery of extreme flexibility in silver(I)/gold(I) hexacyanometallates,[27] we have chosen to focus on reductive intercalation in silver(I) hexacyanoferrate(III), $Ag_3[Fe(CN)_6]$

Open Access Article. Published on 08 January 2015. Downloaded on 04/04/2016 18:17:01.
This article is licensed under a Creative Commons Attribution 3.0 Unported Licence.

[Fig. 1(a)]. Our X-ray powder diffraction measurements, which are discussed below, reveal that the intrinsic volume strain associated with potassium intercalation in this system is an order of magnitude smaller than for typical ion-storage materials. This ranks $Ag_3[Fe(CN)_6]$ amongst the few known "zero-strain" insertion compounds ($Li_4Ti_5O_{12}$,[28] 2,6-napth-$(COOLi)_2$,[29] and $Na_{0.84}Ni[Fe(CN)_6]_{0.71}$ (ref. 30)) in spite of the relatively large ionic radius of potassium [$r(K^+)$ = 1.52 Å *cf.* $r(Li^+)$ = 0.90 Å and $r(Na^+)$ = 1.16 Å].[31]

The crystal structure of $Ag_3[Fe(CN)_6]$ has been reported previously:[26,27] octahedral Fe^{3+} centres are connected *via* almost-linear dicyanoargentate ions to form three interpenetrating cubic nets [Fig. 1(a)]. The structure has $P\bar{3}1m$ crystal symmetry, and includes a set of small vacant channels that run parallel to the trigonal *c* crystal axis. X-ray powder diffraction patterns for $KAg_3[Fe(CN)_6]$ have twice been reported,[26,32] but to the best of our knowledge its crystal structure has not yet been determined. In contrast, the structure of the Mn analogue $KAg_3[Mn(CN)_6]$ is known: it is closely related to that of $Ag_3[Fe(CN)_6]$ except with one half of the channels occupied by K^+ cations, lowering the crystal symmetry to $P312$.[16] This close structural similarity suggests that cation insertion within $Ag_3[Fe(CN)_6]$ framework might be possible *via* straightforward inclusion of K^+ ions within these same channels.

A sample of $Ag_3[Fe(CN)_6]$, prepared as described previously,[27] was reacted at 0 °C with stoichiometric quantities of potassium naphthalenide, using dried THF as solvent and working under a dinitrogen atmosphere on a Schlenk line. The solid product obtained is air-stable and exhibits a qualitatively similar X-ray powder diffraction pattern to the parent $Ag_3[Fe(CN)_6]$ (as noted in ref. 26) [Fig. 2(a)]. On close inspection, small but meaningful shifts in the Bragg reflection positions and intensities are evident; we note that the difference between the diffraction patterns attributed to $Ag_3[Fe(CN)_6]$ and $KAg_3[Fe(CN)_6]$ in ref. 26 map quantitatively onto to those observed here. Rietveld refinement of our powder diffraction data (performed using TOPAS[46]) using a structural model for $KAg_3[Fe(CN)_6]$ based on published coordinates for $KAg_3[Mn(CN)_6]$ (ref. 16) gave an acceptable fit [Fig. 2(a)] and a physically-sensible set of refined parameters (see ESI† for full details). Our refinements indicated a small but significant variation in the lattice parameters (a = 7.0279(5) Å, c = 7.2546(5) Å for the vacant framework and a = 7.06984(23) Å, c = 7.1836(3) Å after intercalation), together with a K-site occupancy of 0.920(13). Infrared absorption spectra measured for starting material and product also reveal the redshift in CN stretching frequencies characteristic of Fe^{III}/Fe^{II} reduction [Fig. 2(b)].[33,34] The presence of a small quantity of remnant Fe^{III} is suggested by a weak feature in the infrared absorption spectrum near 2170 cm^{-1} [Fig. 2(b)] and will likely include contributions both from intercalated product (since the K-site occupancy is slightly less than unity) and a small fraction of unreacted $Ag_3[Fe(CN)_6]$ also evident in the diffraction data (see ESI†). Nevertheless the dominant product is consistent with the formulation $K_{0.92}Ag_3[Fe(CN)_6]$ (we use $KAg_3[Fe(CN)_6]$ hereafter for convenience) and with a structural model in which K^+ ions are incorporated within one half of the initially-vacant framework channels.

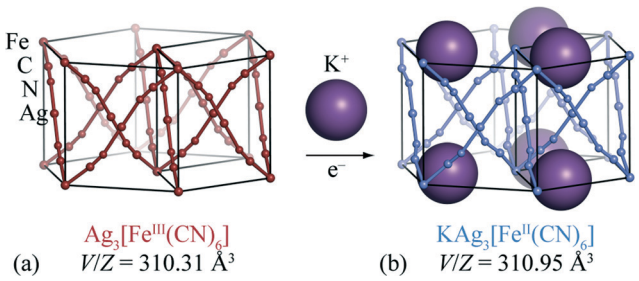

Fig. 1 (a) The trigonal structure of $Ag_3[Fe(CN)_6]$ consists of three interpenetrating α-Po cubic nets. (b) Reductive intercalation of K^+ ions within this structure gives rise to the structurally-related phase $KAg_3[Fe(CN)_6]$. The K^+ ions occupy one-dimensional channels which run parallel to the *c* crystallographic axis (vertical).

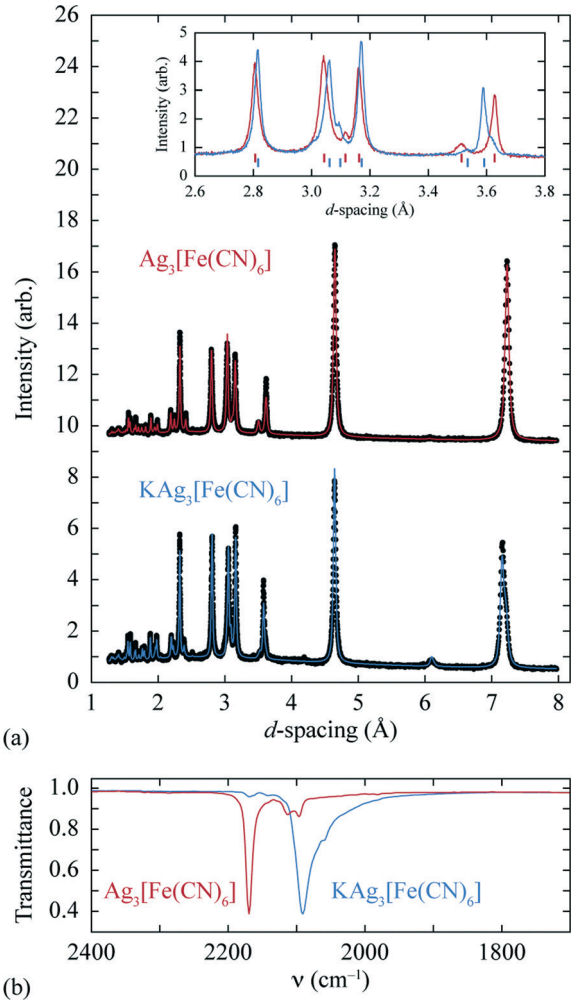

Fig. 2 (a) Powder X-ray diffraction patterns and Rietveld fits for the empty (top, $Ag_3[Fe(CN)_6]$) and intercalated (bottom, $KAg_3[Fe(CN)_6]$) frameworks. A representative section of the diffraction pattern, highlighting the small shifts in peak positions and intensities, is shown in the inset. (b) The change in CN stretching frequencies on intercalation is as expected for Fe^{III}/Fe^{II} reduction.[33,34]

 This journal is © The Royal Society of Chemistry 2015

Open Access Article. Published on 08 January 2015. Downloaded on 04/04/2016 18:17:01.
This article is licensed under a Creative Commons Attribution 3.0 Unported Licence.

The volume strain associated with potassium ion intercalation is determined straightforwardly by the variation in lattice constants. We find V = 310.31(5) Å^3 for the vacant framework and V = 310.95(3) Å^3 after intercalation, corresponding to a volume strain $\Delta V/V$ = +0.206(18)%. Table 1 places this value in the context of volume strains measured for a range of topical and well-known ion storage compounds; these data are represented graphically in Fig. 3, where they are distributed according to stored charge density. While this density is (understandably) lower for $KAg_3[Fe(CN)_6]$ than most Li- and Na-based systems, the volume strain of intercalation is essentially identical to that of the "zero-strain" Li-ion storage material $Li_{2.33}Ti_{1.67}O_4$.[37]

The small intercalation strain of $KAg_3[Fe(CN)_6]$ is explained by the compensating changes in lattice parameters during K^+ insertion. On intercalation, the framework expands modestly along the a and b crystal axes in order to widen the channels and accommodate the extra-framework cations. The crucial point is that expansion of the framework in one set of directions results in a contraction along the c axis—the framework behaves much like a three-dimensional "wine-rack" by simply flexing whilst maintaining its basic framework dimensions. So the Fe···Fe separation across connected Fe–CN–Ag–NC–Fe linkages ($=\sqrt{a^2+c^2}$) changes by just 0.2% on intercalation, whereas the angle between adjacent linkages (given by $2\tan^{-1}\left(\frac{c}{a}\right)$) changes by 1.0% and hence accounts for most of the (small) strain observed. This behaviour contrasts with the responses observed in ion-storage materials based on layered or dense framework structures. In the former instance (*e.g.* TiS_2), intercalation simply results in increasing interlayer separation; and in the latter (*e.g.* $LiFePO_4$), the whole lattice expands to accommodate the intercalant. For both types of system the volume strain is inherently large and positive because each of the linear strains is positive. The key advantage offered by molecular frameworks as ion-storage media is that their mechanical responses—whether to variations in temperature or pressure, or to guest inclusion—can be tailored to ensure an expansion in one or more directions is counteracted by a contraction in other directions.[13,16,47] Whereas the linear strains induced by changes in temperature and/or pressure can be anomalously large, here we find that the strains can be much smaller than those observed in conventional systems; for example, the linear strain anisotropy $\Delta\varepsilon = \varepsilon_{max} - \varepsilon_{min}$ in the "zero strain" material $Li_2[2,6\text{-napth(COOLi)}_2]$ is 22.70%, but is only 1.58% for $KAg_3[Fe(CN)_6]$.[29]

In order for this "zero-strain" property of $Ag_3[Fe(CN)_6]$ to find practical application, it remains to demonstrate the reversibility of the ion storage mechanism we explore here. Similarly, the use of other alkali metals (*e.g.* Li) and fine-tuning of the redox potentials by substitution at the Fe site are avenues for future work. The key result of this preliminary investigation is to demonstrate how the crucially important problem of intercalation strain might, in principle, be overcome by exploiting geometric flexibility whether such an approach is based on hexacyanometallate chemistry or otherwise.

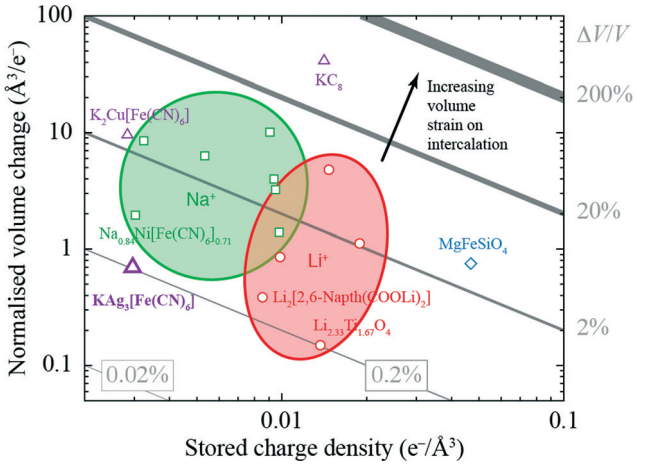

Fig. 3 Ashby-type diagram for the ion-storage compounds of Table 1, with data points coloured by intercalant (Mg – blue, Li – red, Na – green, K – purple). The diagonal lines connect points of constant intercalation volume strain $\varepsilon_V = \Delta V/V$. Different applications place different demands on stored charge density (*e.g.* portability *vs.* cost), yet in all cases it is desirable to minimise intercalation strain.

Table 1 Intercalation volume strains for some topical and canonical ion-storage compounds. The intercalated ion is indicated in bold

Compound	Normalised intercalation volume change (Å^3/e$^-$)	Stored charge density (×10^{-3} e$^-$/Å^3)	Intercalation strain, $\varepsilon_V = \lvert\Delta V/V\rvert$ (%)	Ref.
MgFeSiO$_4$	0.75	46.86	3.53	35
LiCoO$_2$	0.86	9.87	0.85	25
LiFePO$_4$	−4.80	14.71	7.06	36
Li$_{2.33}$Ti$_{1.67}$O$_4$	0.15	13.69	0.20	37
Li$_2$[2,6-napth(COOLi)$_2$]	−0.39	8.55	0.33	29
LiC$_6$	1.12	18.90	2.12	38
Na$_3$Mn$_2$(CN)$_6$	−1.39	9.78	1.36	39
Na$_{1.5}$VP$_{4.8}$F$_{0.7}$	−3.23	9.50	3.07	40
Na$_2$FePO$_4$F	3.99	9.39	3.75	41
Na$_{0.84}$Ni[Fe(CN)$_6$]$_{0.71}$	−1.95	3.02	0.59	30
Na$_2$FeP$_2$O$_7$	−6.32	5.34	3.37	42
Na$_3$V$_2$(PO$_4$)$_3$	−10.08	9.08	9.15	43, 44
Na$_2$Mn$_2$(CN)$_6$	8.50	3.24	2.75	39
K$_2$Cu[Fe(CN)$_6$]	−9.55	2.84	2.71	24
K$_{0.92}$Ag$_3$Fe(CN)$_6$	−0.70	2.96	0.21	This work
KC$_8$	−41.24	14.13	58.28	45

Acknowledgements

The authors gratefully acknowledge financial support from the E.P.S.R.C. (EP/G004528/2) and the E.R.C. (grant ref.: 279705) to J.A.H., A.B.C., and A.L.G., and from the Diamond Light Source to S.J.C. (Cassidy).

Open Access Article. Published on 08 January 2015. Downloaded on 04/04/2016 18:17:01.
This article is licensed under a Creative Commons Attribution 3.0 Unported Licence.

References

1 Y.-M. Chiang, *Science*, 2010, **330**, 1485–1486.
2 F. Cheng, J. Liang, Z. Tao and J. Chen, *Adv. Mater.*, 2011, **23**, 1695–1715.
3 F. Yang, *J. Power Sources*, 2011, **196**, 465–469.
4 W. H. Woodford, W. C. Carter and Y.-M. Chiang, *Energy Environ. Sci.*, 2012, **5**, 8014–8024.
5 *Thermal Expansion of Crystals*, ed. R. Krishnan, Pergamon Press, Oxford, 1979, vol. 22.
6 K. T. Nam, D.-W. Kim, P. J. Yoo, C.-Y. Chiang, N. Meethong, P. T. Hammond, Y.-M. Chiang and A. M. Belcher, *Science*, 2006, **312**, 885–888.
7 A. Magasinski, P. Dixon, B. Hertzberg, A. Kvit, J. Ayala and G. Yushin, *Nat. Mater.*, 2010, **9**, 353–358.
8 N. Yabuuchi, K. Kubota, M. Dahbi and S. Komaba, *Chem. Rev.*, 2014, **114**, 11636–11682.
9 M. Pasta, C. D. Wessells, N. Liu, J. Nelson, M. T. McDowell, R. A. Huggins, M. F. Toney and Y. Cui, *Nat. Commun.*, 2014, **5**, 3001, DOI: 10.1038/ncomms4007.
10 G. D. Barrera, J. A. O. Bruno, T. H. K. Barron and N. L. Allan, *J. Phys.: Condens. Matter*, 2005, **17**, R217–R252.
11 J. L. C. Roswell, E. C. Spencer, J. Eckert, J. A. K. Howard and O. M. Yaghi, *Science*, 2005, **309**, 1350–1354.
12 Y. Wu, A. Kobayashi, G. J. Halder, V. K. Peterson, K. W. Chapman, N. Lock, P. D. Southon and C. J. Kepert, *Angew. Chem.*, 2008, **120**, 9061–9064.
13 A. L. Goodwin, M. Calleja, M. J. Conterio, M. T. Dove, J. S. O. Evans, D. A. Keen, L. Peters and M. G. Tucker, *Science*, 2008, **319**, 794–797.
14 A. E. Phillips, G. J. Halder, K. W. Chapman, A. L. Goodwin and C. J. Kepert, *J. Am. Chem. Soc.*, 2010, **132**, 10–11.
15 A. L. Goodwin, D. A. Keen and M. G. Tucker, *Proc. Natl. Acad. Sci. U. S. A.*, 2008, **105**, 18708–18713.
16 A. B. Cairns, A. L. Thompson, M. G. Tucker, J. Haines and A. L. Goodwin, *J. Am. Chem. Soc.*, 2012, **134**, 4454–4456.
17 W. Li, M. R. Probert, M. Kosa, T. D. Bennett, A. Thirumurugan, R. P. Burwood, M. Parinello, J. A. K. Howard and A. K. Cheetham, *J. Am. Chem. Soc.*, 2012, **134**, 11940–11943.
18 C. Serre, C. Mellot-Draznieks, S. Surblé, N. Audebrand, Y. Filinchuk and G. Férey, *Science*, 2007, **315**, 1828–1831.
19 C. Combelles, M. B. Yahia, L. Pedesseau and M.-L. Doublet, *J. Phys. Chem. C*, 2010, **114**, 9518–9527.
20 G. Férey, F. Millange, M. Morcrette, C. Serre, M.-L. Doublet, J.-M. Grenèche and J.-M. Tarascon, *Angew. Chem.*, 2007, **119**, 3323–3327.
21 G. de Combarieu, M. Morcrette, F. Millange, N. Guillou, J. Cabana, C. P. Grey, I. Margiolaki, G. Férey and J.-M. Tarascon, *Chem. Mater.*, 2009, **21**, 1602–1611.
22 B. M. Wiers, M.-L. Foo, N. P. Balsara and J. R. Long, *J. Am. Chem. Soc.*, 2011, **133**, 14522–14525.
23 K. Saravanan, M. Nagarathinam, P. Balaya and J. J. Vittal, *J. Mater. Chem.*, 2010, **20**, 8329–8335.
24 C. D. Wessells, R. A. Huggins and Y. Cui, *Nat. Commun.*, 2011, **2**, 550.
25 Y. Takahashi, N. Kijima, K. Dokko, M. Nishizawa, I. Uchida and J. Akimoto, *J. Solid State Chem.*, 2007, **180**, 313–321.
26 U. Schröder and F. Scholz, *Inorg. Chem.*, 2000, **39**, 1006–1015.
27 A. L. Goodwin, D. A. Keen, M. G. Tucker, M. T. Dove, L. Peters and J. S. O. Evans, *J. Am. Chem. Soc.*, 2008, **130**, 9660–9661.
28 T. Ohzuku, A. Ueda and N. Yamamoto, *J. Electrochem. Soc.*, 1995, **142**, 1431–1435.
29 N. Ogihara, T. Yasuda, Y. Kishida, T. Ohsuna, K. Miyamoto and N. Ohba, *Angew. Chem., Int. Ed.*, 2014, **53**, 11467–11472.
30 Y. You, X.-L. Wu, Y.-X. Yin and Y.-G. Guo, *J. Mater. Chem. A*, 2013, **1**, 14061–14065.
31 R. D. Shannon, *Acta Crystallogr., Sect. A: Cryst. Phys., Diffr., Theor. Gen. Crystallogr.*, 1976, **32**, 751–767.
32 H. Kahlert, *Ph.D. thesis*, Humboldt-Universität, Berlin, Germany, 1998.
33 A. G. Sharpe, *The Chemistry of Cyano Complexes of the Transition Metals*, Academic Press, London, 1976.
34 S. B. Moon, A. Xidis and V. D. Neff, *J. Phys. Chem.*, 1993, **97**, 1634–1638.
35 Y. Orikasa, T. Masese, Y. Koyama, T. Mori, M. Hattori, K. Yamamoto, T. Okado, Z.-D. Huang, T. Minato, C. Tassel, J. Kim, Y. Kobayashi, T. Abe, H. Kageyama and Y. Uchimoto, *Sci. Rep.*, 2014, **4**, 5622.
36 A. Yamada, H. Koizumi, N. Sonoyama and R. Kanno, *Electrochem. Solid-State Lett.*, 2005, **8**, A409–A413.
37 S. Scharner, W. Weppner and P. Schmid-Beurmann, *J. Electrochem. Soc.*, 1999, **146**, 857–861.
38 X.-L. Wang, K. An, L. Cai, Z. Feng, S. E. Nagler, C. Daniel, K. J. Rhodes, A. D. Stoica, H. D. Skorpenske, C. Liang, W. Zhang, J. Kim, Y. Qi and S. J. Harris, *Sci. Rep.*, 2012, **2**, 747.
39 H.-W. Lee, R. Y. Wang, M. Pasta, S. Woo Lee, N. Liu and Y. Cui, *Nat. Commun.*, 2014, **5**, 5280, DOI: 10.1038/ncomms6280.
40 Y.-U. Park, D.-H. Seo, H.-S. Kwon, B. Kim, J. Kim, H. Kim, I. Kim, H.-I. Yoo and K. Kang, *J. Am. Chem. Soc.*, 2013, **135**, 13870–13878.
41 B. L. Ellis, W. R. M. Makahnouk, Y. Makimura, K. Toghill and L. F. Nazar, *Nat. Mater.*, 2007, **6**, 749–753.
42 P. Barpanda, G. Liu, C. D. Ling, M. Tamaru, M. Avdeev, S.-C. Chung, Y. Yamada and A. Yamada, *Chem. Mater.*, 2013, **25**, 3480–3487.
43 Z. Jian, L. Zhao, H. Pan, Y.-S. Hu, H. Li, W. Chen and L. Chen, *Electrochem. Commun.*, 2012, **14**, 86–89.
44 Z. Jian, W. Han, X. Lu, H. Yang, Y.-S. Hu, J. Zhou, Z. Zhou, J. Li, W. Chen, D. Chen and L. Chen, *Adv. Energy Mater.*, 2013, **3**, 156–160.
45 P. Lagrange, D. Guerard and A. Herold, *Ann. Chim.*, 1978, **3**, 143–159.
46 A. A. Coelho, *TOPAS-Academic V4.1*, Brisbane, 2007.
47 A. L. Goodwin, B. J. Kennedy and C. J. Kepert, *J. Am. Chem. Soc.*, 2009, **131**, 6334–6335.

 This journal is © The Royal Society of Chemistry 2015

CrystEngComm

PAPER

View Article Online
View Journal | View Issue

CrossMark click for updates

Cite this: *CrystEngComm*, 2015, **17**, 361

Flexibility transition and guest-driven reconstruction in a ferroelastic metal–organic framework†

Sarah J. Hunt, Matthew J. Cliffe, Joshua A. Hill, Andrew B. Cairns, Nicholas P. Funnell and Andrew L. Goodwin*

Received 29th July 2014,
Accepted 1st October 2014

DOI: 10.1039/c4ce01572j

www.rsc.org/crystengcomm

The metal–organic framework copper(I) tricyanomethanide, Cu(tcm), undergoes a ferroelastic transition on cooling below T_f = 240 K. Thermal expansion measurements reveal an order-of-magnitude variation in framework flexibility across T_f. The low-temperature phase α-Cu(tcm) exhibits colossal positive and negative thermal expansion that is the strongest ever reported for a framework material. On exposure to acetonitrile, Cu(tcm) undergoes a reconstructive solid-phase transition to acetonitrilocopper(I) tricyanomethanide. This transition can be reversed by heating under vacuum. Infrared spectroscopy measurements are sensitive to the phase change, suggesting that Cu(tcm) may find application in solid-phase acetonitrile sensing.

Open Access Article. Published on 02 October 2014. Downloaded on 04/04/2016 18:20:24.
This article is licensed under a Creative Commons Attribution 3.0 Unported Licence.

1. Introduction

Framework materials with the wine-rack topology have emerged as an important class of materials because their characteristic low-energy 'breathing' mode allows for extreme mechanical responses to external stimuli.[1–3] Examples include sorption- and temperature-driven breathing in the so-called MIL family of metal–organic frameworks (MOFs),[4,5] and colossal positive/negative thermal expansion (PTE/NTE) and negative linear compressibility (NLC) in the transition-metal dicyanometallates.[6–8] In all cases framework breathing couples expansion in one direction to contraction in a perpendicular direction, with the framework angle θ approaching 90° for increased framework volumes [Fig. 1]. While it is usually symmetry-allowed for these systems to adopt arbitrary geometries (*i.e.* values of θ), in some cases the θ = 90° limit actually corresponds to a higher space group symmetry.[9] For this square geometry, framework breathing is symmetry forbidden, resulting in a fundamental increase in rigidity. So the existence of a 'flexibility transition' between low- and high-symmetry geometries would allow wine-rack frameworks to be switched between compliant (low-symmetry, $\theta \neq 90°$) and rigid (high-symmetry, θ = 90°) states.

Such transitions are well established in the field of conventional ceramics, where they are usually discussed in the context of ferroelasticity.[10–13] The magnitude of symmetry-breaking strain ε [= $(b - a)/(a + b)$ for a tetragonal–orthorhombic transition] acts as an order parameter just as magnetisation does for ferromagnets and polarisation for ferroelectrics. In this way, the rigid high-symmetry 'paraelastic' state of Fig. 1 corresponds to ε = 0 and the flexible low-symmetry 'ferroelastic' state to $\varepsilon > 0$. The crucial difference between MOF-type systems and conventional ceramics is that the extreme mechanical flexibilities of the former allow, in principle, for very much larger strains to develop across a ferroelastic

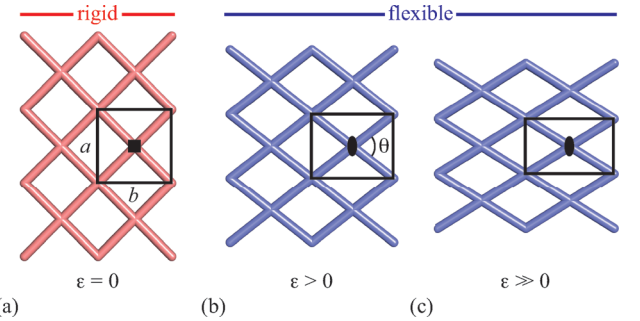

Fig. 1 The dominant low-energy deformation mode of 'wine-rack' framework materials involves 'breathing' *via* changes in the framework angle θ. For the ideal square geometry in (a) this deformation is forbidden by the presence of fourfold rotation axes. Consequently the change in angle from square (a) to rectangular (b) geometries represents a symmetry-breaking ferroelastic phase transition, for which the deviation of the angle θ from 90° is related to the order parameter $\varepsilon = (b - a)/(a + b)$. Breathing of the lower-symmetry rectangular geometry is allowed by the remaining symmetry elements (such as the diads shown here), such that the progression from geometries (b) to (c), for example, is continuous in all respects.

Department of Chemistry, University of Oxford, Inorganic Chemistry Laboratory, South Parks Road, Oxford, OX1 3QR, UK.
E-mail: andrew.goodwin@chem.ox.ac.uk

† Electronic supplementary information (ESI) available: Atomic coordinates and lattice parameter data. CCDC 1016797. For ESI and crystallographic data in CIF or other electronic format see DOI: 10.1039/c4ce01572j

Open Access Article. Published on 02 October 2014. Downloaded on 04/04/2016 18:20:24.
This article is licensed under a Creative Commons Attribution 3.0 Unported Licence.

transition. Consequently the flexibilities of paraelastic and ferroelastic states may be substantially more different for these materials than is the case for conventional inorganics. While there are a handful of very recent studies of ferroelastic transitions in MOFs,[14,15] and indeed switching between 'narrow pore' and 'large pore' states of pillared MOFs might be interpretable in terms of an improper ferroelastic response,[9] there remains a clear need to establish a model system in which ferroelasticity drives a fundamental change in framework flexibility.

Here we show that the previously-unreported framework material copper(I) tricyanomethanide, Cu(tcm), exhibits a ferroelastic transition at a critical temperature T_f = 240 K. Under ambient conditions, this system adopts a tetragonal wine-rack topology, for which breathing is symmetry forbidden. On cooling below 240 K the crystal symmetry lowers to an orthorhombic subgroup, for which breathing is symmetry allowed. Measurement of the coefficients of thermal expansion α allows quantification of the flexibility of both high- and low-temperature phases; we find that values of α within the ferroelastic phase are more than an order of magnitude larger than within the paraelastic phase. In fact the NTE effect we observe, $\alpha = -407(28)$ MK^{-1} ($20 < T < 240$ K), is many times larger than the most extreme sustained NTE behaviour ever reported: $\alpha \simeq -170$ MK^{-1} for FMOF-1,[16] $\alpha = -130$ MK^{-1} for $Ag_3[Co(CN)_6]$,[6] and $\alpha = -80(12)$ MK^{-1} for the pillared zinc/terephthalate MOF of ref. 9. Consequently, T_f signifies not only the emergence of symmetry-breaking strain, but also a fundamental shift in the degree of framework flexibility.

In an attempt to explore the extent to which a similar transition might be brought about by guest uptake, we find that Cu(tcm) is reversibly convertible into a topologically-distinct solvate [Cu(MeCN)(tcm)] upon exposure to acetonitrile. Involving reconstruction between triply-interpenetrating (10,3)-*b* and interdigitated (6,3) nets, this solid–solid transformation highlights the extreme coordinative lability of Cu^+ ions in the parent system. The two frameworks are distinguished not only by their network topology but also by their spectroscopic behaviour, suggesting that Cu(tcm) might find application as a solid-phase acetonitrile sensor.

2. Methods

All reagents were obtained from commercial suppliers and used as received.

2.1. Copper(I) tricyanomethanide

Synthesis of copper(I) tricyanomethanide followed the reduction protocol reported elsewhere for the related binuclear compound bis-(tricyanomethanido)-tetrakis-(triphenylphosphine) dicopper(I).[17] A saturated aqueous solution of copper(II) sulfate (Sigma Aldrich, 99%; 0.3991 g) was reduced by dropwise addition of a concentrated aqueous solution of excess sodium hydrogen sulfite (Sigma Aldrich, 0.3587 g). The resulting mint-green solution was stirred for 30 min, after which time an aqueous solution of a stoichiometric quantity of potassium tricyanomethanide (Alfa Aesar; 0.3229 g) was added dropwise. A fine, off-white precipitate formed immediately. After further stirring for 2 h, the precipitate was filtered, washed with H_2O, and dried under vacuum to afford a polycrystalline sample of copper(I) tricyanomethanide.

Copper(I) tricyanomethanide could also be obtained by heating the acetonitrile complex (see below) under vacuum at 473 K for 12 h.

2.2. Acetonitrilocopper(I) tricyanomethanide

Polycrystalline samples of acetontrilocopper(I) tricyanomethanide were prepared by mixing acetonitrile solutions containing stoichiometric quantities of tetrakis(acetonitrilo)-copper(I) triflate (Sigma Aldrich, 0.9421 g) and potassium tricyanomethanide (Alfa Aesar, 0.3229 g). The reaction mixture was stirred for 2 h and the off-white precipitate filtered and then dried under vacuum to afford acetonitrilocopper(I) tricyanomethanide in quantitative yield.

Single crystal samples of acetonitrilocopper(I) tricyanomethanide could be obtained using slow-diffusion techniques. To separate arms of a glass H-tube were placed chilled acetonitrile solutions of potassium tricyanomethanide (Alfa Aesar, 47.18 mg) and tetrakis(acetonitrilo)copper(I) tetrafluoroborate (Sigma Aldrich, 320.0 mg). Further chilled acetonitrile was then carefully added until the cross-bar was filled. After a period of 14 d, small colourless single crystals suitable for single-crystal X-ray diffraction measurements had formed.

Acetonitrilocopper(I) tricyanomethanide could also be made by exposing dry copper(I) tricyanomethanide to a few drops of acetonitrile and leaving for 12 h, then filtering and drying at 50 °C under vacuum.

2.3. Single-crystal X-ray diffraction

Single-crystal X-ray diffraction data were collected for acetonitrilocopper(I) tricyanomethanide using an Agilent Technologies SuperNova diffractometer (Cu Kα radiation, λ = 1.5418 Å) at 100 K using an Oxford Cryosystems cryostream,[18] scanning about the ω and ϕ circles. The data were integrated and corrected for absorption using CrysAlisPro, the structure was solved in *Pbca* using SIR92 (ref 19) and refined using CRYSTALS.[20] All non-hydrogen atoms were refined anisotropically; hydrogen atom positions were refined against the low angle data, according to the procedure described in ref. 21, and were then constrained to ride on their host atoms. A final *R*-factor of 1.99% was obtained. Crystal structure refinement details are given in Table 1.

2.4. Powder X-ray diffraction

All samples were assessed for crystallinity and purity *via* their X-ray powder diffraction patterns, measured using a Philips PW1730 diffractometer (Cu Kα radiation, λ = 1.541 Å) over the angular (2θ) range 10–70° using a step size of 0.05°. Higher-quality diffraction patterns were collected using a PANalytical X'Pert PRO diffractometer (monochromated Cu Kα_1 radiation, λ = 1.54060 Å) using the same angular range and a step size of 0.008°.

 This journal is © The Royal Society of Chemistry 2015

Open Access Article. Published on 02 October 2014. Downloaded on 04/04/2016 18:20:24.
This article is licensed under a Creative Commons Attribution 3.0 Unported Licence.

Table 1 Single-crystal X-ray diffraction data collection and refinement details for [Cu(MeCN)(tcm)] at T = 100 K

Formula	$CuC_6N_4H_3$
Crystal size (mm)	0.033 × 0.034 × 0.039
Crystal symmetry	Orthorhombic
Space group	*Pbca*
a (Å)	12.9802(3)
b (Å)	8.14490(18)
c (Å)	14.5848(3)
V (Å^3)	1541.94(5)
Z	8
No. of measured reflns.	14 516
No. of independent reflns.	1620
No. of observed rflns. [$I > 2\sigma(I)$]	1480
No. of parameters	100
R_{int}	0.025
R ($I/\sigma > 2.0$)	0.0199
wR	0.0524
$\Delta\rho_{max}$, $\Delta\rho_{min}$ (e Å^{-3})	0.26, −0.29

Variable-temperature powder X-ray diffraction patterns were measured on a Siemens D5000 X-ray diffractometer (Cu Kα radiation, λ = 1.5418 Å) fitted with an Oxford Cryosystems PheniX cryostat. For temperatures below 300 K the copper(I) tricyanomethanide sample was combined with vaseline and then loaded into the sample holder. Data collections were carried out every 10 K on heating from 20 to 290 K. Scans were ~5 h long and were carried out over the angular range $5° < 2\theta < 120°$ using a step size of 0.02°. Four minute intervals between data collections allowed for temperature equilibration of the sample.

All fits to X-ray powder diffraction data were carried out using TOPAS Academic;[22] in general a modified Thompson–Cox–Hastings pseudo-Voigt (TCHZ) peak shape with a simple axial divergence correction was used and the large anisotropic strain found in this system was accounted for by using a Stephens anisotropic peak broadening term.[23] Rietveld refinement of the room and low-temperature (20 K) structures of α- and β-Cu(tcm) were carried out. For the room temperature structure all atom positions were refined with appropriate bond distance (Cu–N, C–N and C–C) and bond angle restraints; the Cu isotropic atomic displacement parameter was refined freely and all atoms within the tcm moiety were constrained to have equal isotropic displacement parameters. A fourth-order spherical harmonic correction was used to account for preferred orientation. At low temperature, the tcm group was refined as a rigid body and all thermal parameters were fixed. Sample environment peaks were identified by their persistence across the α–β transition and were fitted using the Pawley method. Variable-temperature lattice parameters were determined by using sequential (seed-batch) Pawley fits to data in *Fdd*2 and $I4_1md$, where the starting lattice parameters for each temperature were those found for the previous temperature.

2.5. Thermogravimetric analysis

Thermogravimetric measurements were carried out using a Perkin Elmer TGA 7, with Perkin Elmer TAC 7/DX thermal analysis controller, from 30 to 600 °C at a rate of 10 °C min^{-1} under flowing nitrogen.

2.6. Infrared spectroscopy

Infrared spectra were measured using a Bruker Tensor 27 FT-IR spectrometer fitted with an attenuated total reflectance diamond. A small amount of powdered sample was pressed onto the diamond surface and spectra were measured over the range 4000–600 cm^{-1}. Background scans were recorded before each measurement. Absolute transmittance values were normalised to the tricyanomethanide C–N stretch (2200 cm^{-1}) for each measurement.

3. Results and discussion

Copper(I) tricyanomethanide structure

Having prepared a sample of Cu(tcm), its crystal structure was determined using powder X-ray diffraction methods. The ambient-temperature powder X-ray diffraction pattern—shown in Fig. 2(a)—could be indexed according to a tetragonal cell with lattice parameters a = 7.539(2) Å and c = 9.034(3) Å. A Pawley fit confirmed the space group assignment $I4_1md$. Based on the cell metric and space group symmetry, a structural model was proposed in which both Cu atoms and tcm groups were centred on the 4*a* Wyckoff positions, with z = 0

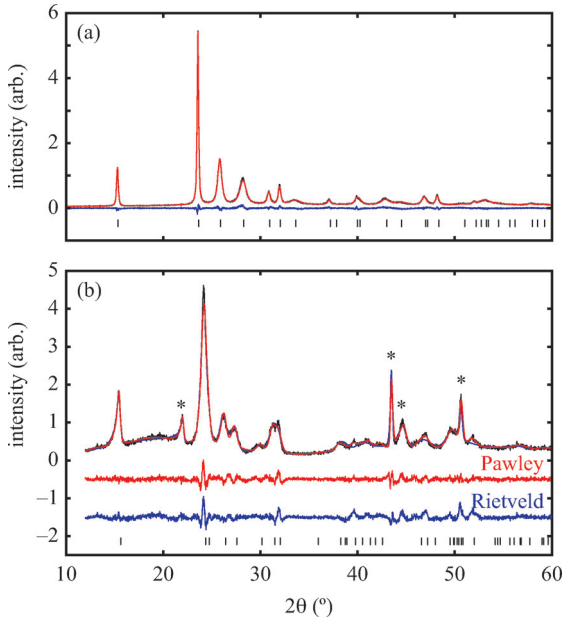

Fig. 2 Powder X-ray diffraction data measured using Cu Kα radiation (black lines), with reflection positions indicated by vertical tick marks. (a) β-Cu(tcm), measured at 298 K; Rietveld fit (red lines), and difference (data – fit, blue lines). (b) α-Cu(tcm), measured at 20 K. Impurity peaks from the low-temperature sample environment are indicated by asterisks; both Pawley (red lines) and Rietveld (blue lines) fit and difference curves are shown, with the latter shifted vertically by 0.5 and 1.5 units. Pawley fits were used to extract thermal lattice parameter variations. The quality of the Rietveld fit is low as a result of severe anisotropic peak broadening and the large number of coupled positional degrees of freedom, but is sufficient to demonstrate the displacive nature of the phase transition.

Open Access Article. Published on 02 October 2014. Downloaded on 04/04/2016 18:20:24.
This article is licensed under a Creative Commons Attribution 3.0 Unported Licence.

for the former and $z \simeq \frac{1}{2}$ for the latter. Using this initial model as a starting point, Rietveld refinement gave a satisfactory fit to data [Fig. 2(a)]. The corresponding atomic coordinates and atomic displacement parameters are given in Table 2, and the crystal structure is illustrated in Fig. 3(a–c). In this structure, both Cu^+ and tcm^- ions are three-coordinate and connect to form a three-dimensional network with the (10,3)-*b* topology (Schläfli symbol 10^3). This network is sufficiently open that three such nets interpenetrate to give a structure related to that of the MOF Δ-[Cr(Hbiim)(H_2biim$_2$)]SO_4·H_2O (biim = biimidazole).[24,25]

The established structural chemistry of copper(I) tricyanomethanides is limited to ternary and quaternary systems of the form [Cu(tcm)(N-donor)]·{guest}.[26] This is perhaps surprising, given that the analogous silver(I) complex Ag(tcm) has been known for some time.[27] The stronger preference for tetrahedral coordination over trigonal coordination for Cu^+ relative to Ag^+ may be an important factor at play in determining the different accessibilities of these two phases. It now seems that both Cu(tcm) and Ag(tcm) adopt polar crystal structures based on three-coordinate M(I)/tcm geometries, but in contrast to the three-dimensional topology of Cu(tcm) the structure of Ag(tcm) is described by stacked, pairwise-interwoven (6,3)-net layers.[27,28] Despite our reliance here on powder diffraction methods for structure solution and refinement, the relatively small number of structural parameters and the good quality of fit-to-data give us confidence in the structural model we have determined for Cu(tcm). There is no risk of confusion with the Ag(tcm) structure, which would predict a very different powder diffraction pattern to that observed in our measurements. For completeness, we note that the Cu–N bond lengths and N–Cu–N bond angles we obtain (d(Cu–N) = 2.025, 2.036 Å; ∠(N–Cu–N) = 122.8, 114.5°) are fully consistent with the values reported elsewhere for [Cu(tcm)(hmt)], [Cu(tcm)(bipy)], and [Cu(tcm)(bpe)]·0.25bpe·0.5MeCN (hmt = hexamethylenetetramine; bipy = 4,4'-bipyridine; bpe = 1,2-bis(4-pyridyl)ethene): 1.92 < d(Cu–N) <2.22 Å and 103.3< ∠N–Cu–N <129.8°.[26] Good consistency is of course expected given our use of soft Cu–N bond length restraints.

Variable-temperature behaviour

Powder X-ray diffraction patterns collected over the temperature range 20 < T < 290 K reveal a second-order phase transition near T_f = 240 K that involves splitting of a number of diffraction peaks in a manner consistent with a reduction from tetragonal to orthorhombic symmetry [Fig. 4(a)]. There are two maximal subgroups of $I4_1md$ with orthorhombic symmetry: namely, *Fdd*2 and *Imm*2. The reflection conditions differ between these two cases, and we found that our data were consistent only with the former. Making use of the appropriate cell transform

$$\begin{bmatrix}\mathbf{a}\\ \mathbf{b}\\ \mathbf{c}\end{bmatrix}_{Fdd2} = \begin{bmatrix}1 & 1 & 0\\ -1 & 1 & 0\\ 0 & 0 & 1\end{bmatrix}\begin{bmatrix}\mathbf{a}\\ \mathbf{b}\\ \mathbf{c}\end{bmatrix}_{I4_1md}, \quad (1)$$

Table 2 Structural parameters for β-Cu(tcm) as determined by Rietveld refinement against powder X-ray diffraction data collected at 298 K. Space group: $I4_1md$. Lattice parameters: a = 7.5510(4) Å, c = 9.0436(5) Å

Atom	x	y	z	B_{iso} (Å^2)
Cu	0	0	0	4.30(7)
C1	0	0	0.4873(7)	1.44(9)
C2	0	0	0.3554(7)	1.44(9)
C3	0.1560(4)	0	0.56396(25)	1.44(9)
N1	0	0	0.2267(8)	1.44(9)
N2	0.2727(6)	0	0.6277(4)	1.44(9)

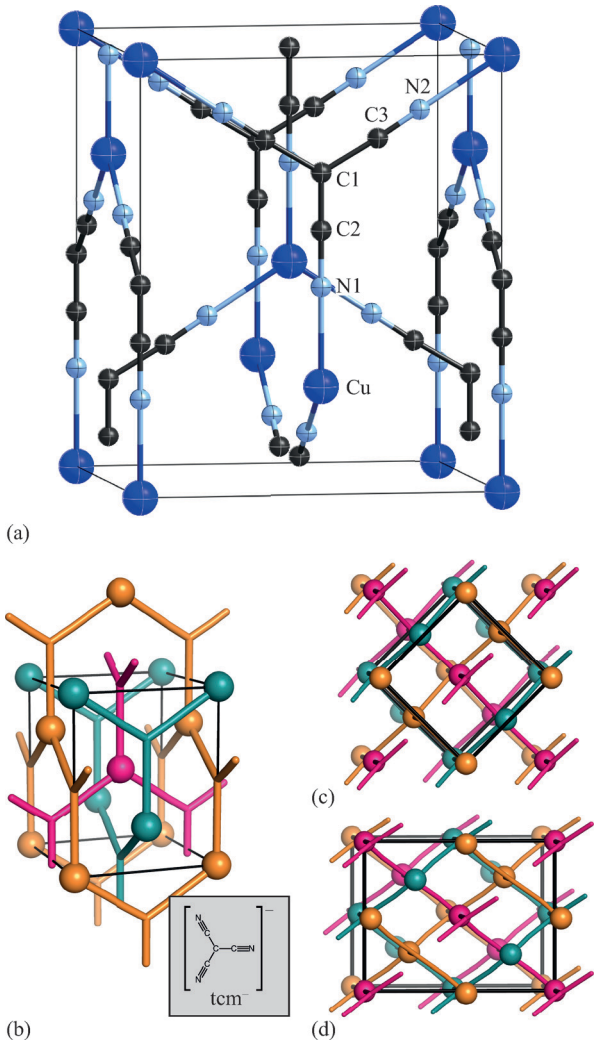

Fig. 3 (a) Representation of the crystal structure of β-Cu(tcm), viewed with the tetragonal *c* axis oriented vertically. Thermal ellipsoids are represented at 50% probability. (b) Topological representation of the same framework, where Cu atoms are shown as large spheres, tcm moieties in stick representation, and the unit cell in black. The three mutually-interpenetrating (10,3)-*b* frameworks are coloured differently. The inset shows the chemical structure of the tricyanomethanide anion. (c) The same framework, viewed slightly away from *c*, illustrating its square wine-rack geometry with θ = 90°. (d) The low-temperature α-Cu(tcm) phase—shown here in terms of the structural model determined using powder X-ray diffraction data collected at 20 K—has the same network connectivity, but the loss of tetragonal symmetry allows θ to deviate from 90°. The *Fdd*2 unit cell, shown here in black, has twice the volume of the $I4_1md$ cell of β-Cu(tcm).

This journal is © The Royal Society of Chemistry 2015

Open Access Article. Published on 02 October 2014. Downloaded on 04/04/2016 18:20:24.
This article is licensed under a Creative Commons Attribution 3.0 Unported Licence.

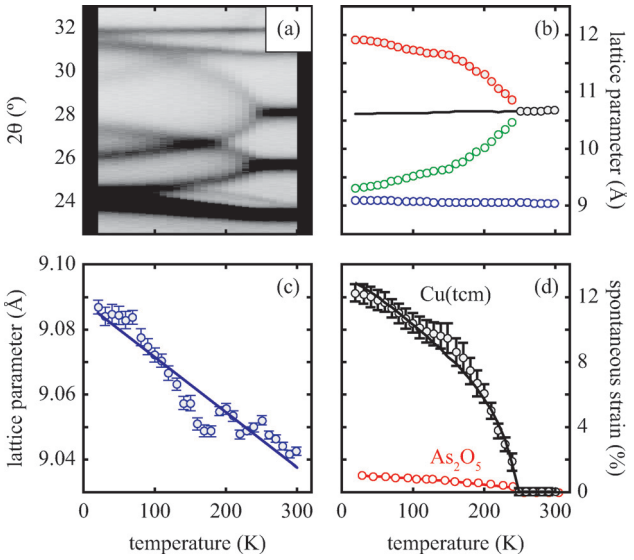

Fig. 4 (a) Thermal variation in the X-ray powder diffraction pattern of Cu(tcm), shown here over a 2θ range that illustrates the large splitting of certain peaks at T_f = 240 K. (b) The corresponding thermal variation in lattice parameters. The parameters *a* and *b* are given by green and red circles, respectively, for the orthorhombic phase and black circles for the tetragonal phase; the *c* parameter is given by blue circles for both phases. Uncertainties are smaller than the symbols. The black line represents the mean value $\frac{1}{2}(a + b)$ for α-Cu(tcm). (c) The approximately-linear thermal variation of the *c* lattice parameter, as shown in (b) but given here on an expanded scale. (d) Thermal variation of the spontaneous strain as defined in eqn (2); the corresponding fit of form $\kappa |T - T_f|^{\frac{1}{2}}$ is shown as a solid line. The strain observed for the "conventional" ferroelastic transition of As_2O_5 is shown in red, where the temperature scale has been shifted by 345 K in order to match transition temperatures.[30]

we obtained an approximate structural model for the low-temperature phase, from which Rietveld refinement was possible. The Rietveld fit obtained using data collected at 20 K is shown in Fig. 2(b). The quality of fit is satisfactory, though we note that severe anisotropic peak broadening associated with large lattice strains and also the experimental constraints of measuring diffraction data at 20 K have both degraded the fit relative to that achieved for data collected under ambient conditions. Because of the presence of anisotropic peak broadening, we have not explored the possibility of further symmetry lowering beyond *Fdd*2; nevertheless, any additional symmetry-lowering distortions—if present—must be very much weaker than the orthorhombic strain itself, which dominates the phase transition behaviour at T_f. Moreover, because the low-angle peak intensities are well accounted for by the Rietveld model, we can be confident that the transition is displacive (*i.e.*, the framework connectivity is maintained). The transition from $I4_1md$ to *Fdd*2 is a ferroelastic transition associated with softening of the Γ_3 zone-centre mode.[29] The corresponding spontaneous strain

$$\varepsilon = \frac{b-a}{a+b} \quad (2)$$

is expected on the basis of Landau theory to vary as $|T - T_f|^{\frac{1}{2}}$ near T_f (*i.e.*, the transition should be second order). Experimental values of ε determined from our lattice parameter data are shown in Fig. 4(d) and are consistent with this expected temperature dependence, indicating that this is a proper (*i.e.* strain-driven) ferroelastic transition.[13,30] A combination of spectroscopic measurements and lattice dynamical modelling would help determine the microscopic driving force for Γ_3 mode softening. Here we note only that this mode allows tilting of the tcm units about an axis parallel to *c*, which has the effect of reducing slightly the distance between tcm groups of one framework and Cu^+ centres of the other two interpenetrated frameworks. Consequently, at low temperatures there may be a small electrostatic driving force for symmetry lowering that is overcome by the increased vibrational entropy of the $I4_1md$ geometry only for temperatures above T_f.

The atomic coordinates and atomic displacement parameters determined from our Rietveld refinement for the low-temperature phase are given in Table 3, and the crystal structure itself is illustrated in Fig. 3(d). From this structural model it is clear that the framework connectivity is entirely preserved across T_f. The single most important difference between high- and low-temperature phases of Cu(tcm) is the framework angle θ: in the former it is identically equal to 90° whereas in the latter it is reduced to $\theta = 2\tan^{-1}\left(\frac{a}{b}\right) = 76°$ at 20 K. Noting the parallel to symmetry-breaking transitions in various well-known framework silicates such as cristobalite and quartz, we borrow from the terminology of that field and denote the high-temperature phase as β-Cu(tcm) and the low-temperature phase as α-Cu(tcm).

Access to variable-temperature diffraction data allows us to explore the mechanical flexibility of both α- and β-Cu(tcm) in terms of their linear coefficients of thermal expansion, and so to determine whether the intuitive picture developed in Fig. 1 does indeed hold in practice. For β-Cu(tcm) there are two independent coefficients of thermal expansion, corresponding to the behaviour parallel and perpendicular to the tetragonal *c* axis:

$$\alpha_a = \left(\frac{\mathrm{d}a}{a\,\mathrm{d}T}\right)_p \quad (3)$$

Table 3 Structural parameters for α-Cu(tcm) as determined by Rietveld refinement against powder X-ray diffraction data collected at 20 K. Space group: *Fdd*2. Lattice parameters: *a* = 9.297(5) Å, *b* = 11.891(5) Å, *c* = 9.093(5) Å. All displacement parameters were fixed at B_{iso} = 2 Å^2

Atom	*x*	*y*	*z*
Cu	0	0	0
C1	0	0	0.503(3)
C2	0	0	0.350(3)
C3	−0.075(4)	0.082(5)	0.579(3)
N1	0	0	0.229(3)
N2	−0.136(5)	0.149(6)	0.641(3)

Open Access Article. Published on 02 October 2014. Downloaded on 04/04/2016 18:20:24.
This article is licensed under a Creative Commons Attribution 3.0 Unported Licence.

$$\alpha_c = \left(\frac{\mathrm{d}c}{c\,\mathrm{d}T}\right)_p \quad (4)$$

Our data give α_a = +10.8(23) MK^{-1} and α_c =−21(4) MK^{-1},[31] which—although anomalous in sign and magnitude for conventional framework materials ($a \simeq 10$ MK^{-1})—are comparable to the values obtained for many MOFs.[32–36] In such systems the low energies of transverse vibrational modes tend to favour NTE, which then often drives anomalously large PTE in other crystal directions.[32] Within the low-temperature α-Cu(tcm) phase, the behaviour along *c* is essentially unchanged: here we find α_c = −13.6(11) MK^{-1} over the temperature range 20–240 K [Fig. 4(c)]. In contrast, the behaviour along the *a* and *b* axes is fundamentally different from that observed in β-Cu(tcm) because these are the axes affected by changes in the framework angle θ. Linear fits to our data over the same temperature range 20–240 K give α_a = +591(28) MK^{-1} and α_b = −407(28) MK^{-1}. There is clearly a drastic increase in thermal expansivity—and hence framework flexibility—on cooling below T_f, justifying our characterisation of the α/β-phase transition as a 'flexibility transition' in Cu(tcm).

The extraordinarily large coefficients of thermal expansion observed here for α-Cu(tcm) deserve further comment because they exceed even the threshold for so-called 'colossal' NTE and PTE ($|\alpha|$ = 100 MK^{-1}).[6] Examples of colossal thermal expansion remain extremely rare, even amongst MOFs. Until recently, 'FMOF-1' exhibited the strongest known thermal expansion behaviour: its coefficients of thermal expansion are α_a = +230 MK^{-1} and α_c = −170 MK^{-1}.[16] More extreme PTE has since been observed in the zinc terephthalate-based MOFs of ref. 9 for which α_b = +340(35) MK^{-1} over the temperature range 303–463 K.[31,37] Yet the response we see here for α-Cu(tcm) is larger again by some margin; in particular, the uniaxial NTE along *b* is so extreme that an aligned composite containing just 2.5% Cu(tcm) would be sufficient to counteract the PTE effect of conventional engineering materials. Moreover, the temperature range over which this NTE occurs (20–240 K)—perhaps problematic for some applications—is nonetheless relevant to industries such as aerospace.

But why is α-Cu(tcm) so very flexible? Empirically it is found that framework flexibility tends to scale inversely with metal–ligand interaction strength.[32,38,39] Here, the low charge densities of Cu$^+$ and of the terminal N atoms of the tcm$^-$ ion[40] will reduce any electrostatic contribution to the thermodynamic cost of framework flexing. Furthermore the combination of a closed-shell d^{10} configuration together with low Cu 3d–tcm π^* overlap will mean that (directional) covalent effects are also much smaller than in many other MOFs. Consequently, the mechanical properties of this system would be expected to be especially sensitive to low-energy interactions such as dispersion forces, which are well-known to drive extreme thermal expansion in other framework materials.[6] Quantum mechanical calculations would help understand more fully the origin of this extreme mechanical flexibility.[4,5,41]

Solvent-induced reorganisation

Exposure of a polycrystalline sample of Cu(tcm) to acetonitrile gave rise to a new phase with a powder diffraction profile quite distinct from that of either α- or β-Cu(tcm). TGA measurements of this phase revealed a mass loss of 19% at 400 K, which suggests the formulation [Cu(MeCN)(tcm)] (expected mass loss 21%) [Fig. 5(a)]. We found that single-crystal samples could in fact be obtained directly from acetonitrile solution, which allowed us to determine the crystal structure using single-crystal X-ray diffraction methods. Our structure solution is illustrated in Fig. 6(a), confirming the formulation [Cu(MeCN)(tcm)]; key structural parameters are given as ESI.† In this structure, the Cu$^+$ ions now have tetrahedral coordination, with one coordination site occupied by a MeCN group; the tcm$^-$ ion remains trigonal in its coordination. From a topological perspective, both Cu and tcm components are effectively three-coordinate, connecting to form (6,3) honeycomb layers (Schläfli symbol 6^3). These layers stack without interpenetration, in contrast to the related acetonitrile derivative [Ag(MeCN)(tcm)] reported elsewhere [Fig. 6(b–c)].[42]

Of greatest relevance to this study is the clear difference in connectivity between the structures of Cu(tcm) and [Cu(MeCN)(tcm)]. Generation of the latter by exposure of the former to acetonitrile must proceed by concerted cleavage and reconstruction of Cu–tcm bonds, which in itself demonstrates a remarkable coordinative flexibility of the original framework. The closed-shell d^{10} electronic configuration of Cu$^+$ facilitates bond cleavage, and allows the formation of network structures with coordination numbers between two and four.[43,44] Moreover, this interconversion process is reversible: powder samples of [Cu(MeCN)(tcm)]—themselves prepared by exposing Cu(tcm) to MeCN—revert to β-Cu(tcm) on heating at 200 °C for 3 h [Fig. 7]. This series of solid–solid transformations can be followed using infrared spectroscopy, with the acetonitrile-containing phase exhibiting an additional characteristic absorption at

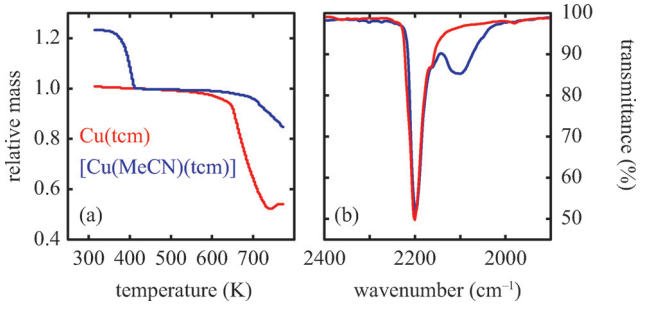

Fig. 5 (a) Thermogravimetric behaviour of Cu(tcm) and [Cu(MeCN)(tcm)]. The mass loss observed near 400 K for the latter corresponds to volatilisation of one molar equivalent of MeCN. Both TGA curves have been normalised to the mass measured at 420 K (b). High-frequency region of the infrared absorption spectra of Cu(tcm) and [Cu(MeCN)(tcm)] showing the emergence of an additional band in the latter, attributed to the nitrile C–N stretch. Colour scheme as in (a).

 This journal is © The Royal Society of Chemistry 2015

Open Access Article. Published on 02 October 2014. Downloaded on 04/04/2016 18:20:24.
This article is licensed under a Creative Commons Attribution 3.0 Unported Licence.

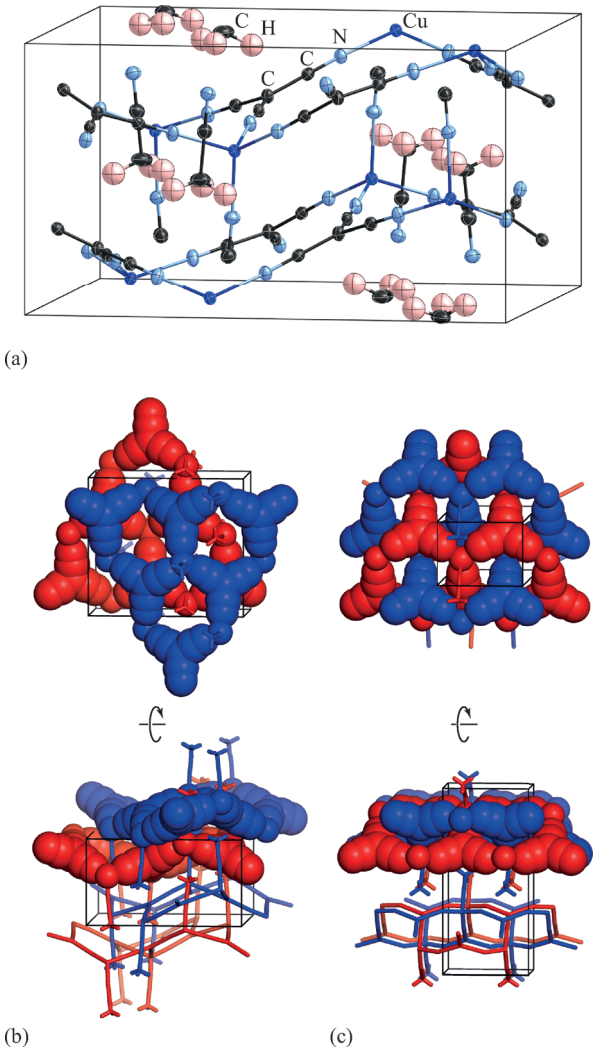

Fig. 6 (a) Representation of the crystal structure of [Cu(MeCN)(tcm)], viewed away from **a**, as determined using single-crystal X-ray diffraction measurements carried out at 100 K. Thermal ellipsoids are drawn at 50% probability level. Panels (b) and (c) show topological representations of, respectively, this same framework and that of [Ag(MeCN)(tcm)] as reported in ref. 42. Both structures are assembled from honeycomb (6,3) nets of connected Cu/Ag cations and tcm^- anions. In (b) these nets stack such that the MeCN ligands of one net interdigitate the hexagonal channels of the next. In (c) pairs of adjacent nets interweave, with the MeCN groups occupying the space between adjacent honeycomb pairs. The corresponding unit cells for both systems are shown in black; the Cu/Ag and tcm components of two adjacent honeycomb nets (but not the coordinated MeCN groups) are shown in space-filling representation.

2101 cm^{-1} associated with the nitrile C–N stretch [Fig. 5(b)]. Samples of Cu(tcm) exposed to moist air over extended periods show no structural transformation, so the binding of MeCN appears to be strongly selective even in the presence of competitive ligands such as H_2O. This observation suggests that, like the recently-reported CuCN-based systems of ref. 45, and quite separate from its extreme thermal expansion behaviour, Cu(tcm) may find application in acetonitrile sensing.

4. Conclusions

In summary, the 'wine-rack'-type framework material Cu(tcm) exhibits a ferroelastic transition at 240 K. This transition demarcates an order-of-magnitude change in elastic response, seen here most obviously in the 'colossal' PTE and NTE effects of α-Cu(tcm) that disappear in β-Cu(tcm). Indeed this anomalous thermal expansion behaviour establishes a new record within the field that means that Cu(tcm) may find application in the athermalisation of functional composites.

With respect to the ferroelastic transition itself, there are strong qualitative parallels to well-known tetragonal/orthorhombic transitions in oxide frameworks such as As_2O_5,[30] for which the elastic anomalies associated with ferroelasticity affect not only the thermal expansion, but also the lattice dynamics (*e.g.* mode softening, phonon lifetimes), microdomain formation, twin-wall motion, and susceptibility. While our study has been limited to determination of the thermal variation in lattice parameters, we anticipate that further investigation of elastic behaviour in Cu(tcm) at T_f may prove informative in establishing parallels between conventional and MOF-type framework materials.[14,46] In particular, the verification of softening of zone-centre acoustic phonons polarised along ⟨110⟩, and the use of microscopy techniques to characterise domain microstructure within the low-temperature ferroelastic phase will provide important experimental constraints on the phenomenology of what appears to be a canonical proper ferroelastic transition in a

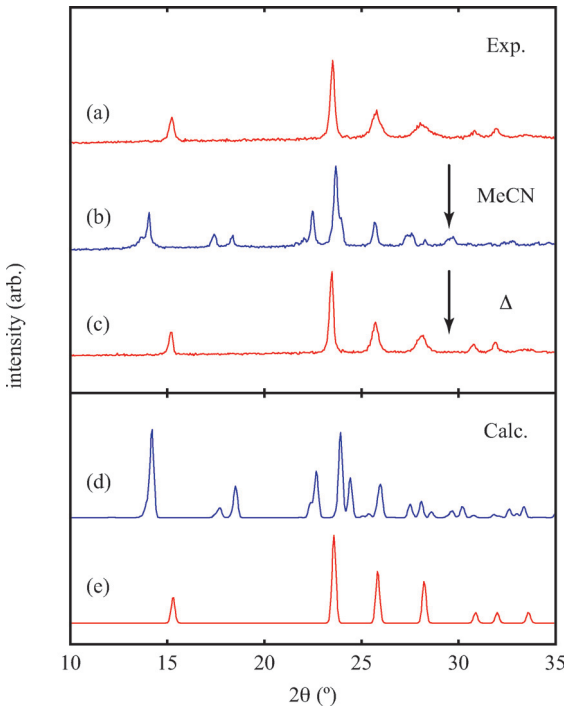

Fig. 7 (Top) Powder X-ray diffraction patterns of (a) as-prepared Cu(tcm), (b) the same sample after exposure to MeCN, and (c) after subsequent heating at 200 °C for 3 h. (Bottom) Calculated X-ray diffraction patterns of (d) [Cu(MeCN)(tcm)] and (e) Cu(tcm).

Open Access Article. Published on 02 October 2014. Downloaded on 04/04/2016 18:20:24.
This article is licensed under a Creative Commons Attribution 3.0 Unported Licence.

MOF. The most obvious difference between the ferroelastic behaviour of Cu(tcm) and that of "conventional" systems such as As_2O_5 is the very large strains realised within the ferroelastic phase [Fig. 4(d)], as implied by the colossal thermal expansion.

Finally, the coordinative flexibility of Cu(tcm) is found to affect not only elastic behaviour but also the ability of the framework to reorganise itself on exposure to a coordinating solvent. In this way, we have demonstrated proof-of-principle for application of Cu(tcm) as an acetonitrile sensor. Given the diversity of known Ag(tcm)·{guest} phases,[27,42] the possibility that Cu(tcm) may respond selectively to a variety of different solvents offers an attractive avenue for further research.

Acknowledgements

This research was supported financially by the EPSRC (grant EP/G004528/2) and the ERC (project 279705). The authors are grateful to Prof. C. J. Howard (Newcastle) for useful discussions.

References

1 S. Kitagawa and K. Uemura, *Chem. Soc. Rev.*, 2005, **34**, 109–119.
2 G. Férey and C. Serre, *Chem. Soc. Rev.*, 2009, **38**, 1380–1399.
3 C. Serre, C. Mellot-Draznieks, S. Surblé, N. Audebrand, Y. Filinchuk and G. Férey, *Science*, 2007, **315**, 1828–1831.
4 A. U. Ortiz, A. Boutin, A. H. Fuchs and F.-X. Coudert, *Phys. Rev. Lett.*, 2012, **109**, 195502.
5 A. U. Ortiz, A. Boutin, A. H. Fuchs and F.-X. Coudert, *J. Chem. Phys.*, 2013, **138**, 174703.
6 A. L. Goodwin, M. Calleja, M. J. Conterio, M. T. Dove, J. S. O. Evans, D. A. Keen, L. Peters and M. G. Tucker, *Science*, 2008, **319**, 794–797.
7 A. B. Cairns, A. L. Thompson, M. G. Tucker, J. Haines and A. L. Goodwin, *J. Am. Chem. Soc.*, 2012, **134**, 4454–4456.
8 A. B. Cairns, J. Catafesta, C. Levelut, J. Rouquette, A. van der Lee, L. Peters, A. L. Thompson, V. Dmitriev, J. Haines and A. L. Goodwin, *Nat. Mater.*, 2013, **12**, 212–216.
9 S. Henke, A. Schneemann and R. A. Fischer, *Adv. Funct. Mater.*, 2013, **23**, 5990–5996.
10 G. Thornton, B. C. Tofield and A. Hewat, *J. Solid State Chem.*, 1986, **61**, 301–307.
11 C. J. Howard, B. J. Kennedy and B. C. Chakoumakos, *J. Phys.: Condens. Matter*, 2000, **12**, 349–365.
12 J. F. Mitchell, D. N. Argyriou, C. D. Potter, D. G. Hinks, J. D. Jorgensen and S. D. Bader, *Phys. Rev. B*, 1996, **54**, 6172–6183.
13 E. K. H. Salje, *Phase Transitions in Ferroelastic and Co-elastic Crystals*, Cambridge University Press, Cambridge, 1993.
14 W. Li, Z. Zhang, E. G. Bithell, A. D. Batsanov, P. T. Barton, P. J. Saines, P. Jain, C. J. Howard, M. A. Carpenter and A. K. Cheetham, *Acta Mater.*, 2013, **61**, 4928–4938.
15 Z.-Y. Du, Y.-P. Zhao, W.-X. Zhang, H.-L. Zhou, C.-T. He, W. Xue, B.-Y. Wang and X.-M. Chen, *Chem. Commun.*, 2014, **50**, 1989–1991.
16 C. Yang, X. Wang and M. Omary, *Angew. Chem., Int. Ed.*, 2009, **48**, 1–6.
17 K. E. Bessler, L. A. d. P. Calzavara, V. M. Deflon and E. Niquet, *Acta Crystallogr., Sect. E*, 2001, **57**, m522–m533.
18 J. Cosier and A. M. Glazer, *J. Appl. Crystallogr.*, 1986, **19**, 105–107.
19 A. Altomare, G. Cascarano, C. Giacovazzo, A. Guagliardi, M. Burla, G. Polidori and M. Camalli, *J. Appl. Crystallogr.*, 1994, **27**, 435.
20 P. Betteridge, J. Carruthers, R. I. Cooper, K. Prout and D. J. Watkin, *J. Appl. Crystallogr.*, 2003, **36**, 1487.
21 R. I. Cooper, A. L. Thompson and D. J. Watkin, *J. Appl. Crystallogr.*, 2010, **43**, 1100–1107.
22 A. A. Coelho, *Coelho Software*, Brisbane.
23 P. W. Stephens, *J. Appl. Crystallogr.*, 1999, **32**, 281–289.
24 K. Larsson and L. Öhrström, *CrystEngComm.*, 2003, **5**, 222–225.
25 S. R. Batten and R. Robson, *Angew. Chem., Int. Ed.*, 1998, **37**, 1460–1494.
26 S. R. Batten, B. F. Hoskins and R. Robson, *Chem. – Eur. J.*, 2000, **6**, 150–161.
27 S. R. Batten, B. F. Hoskins and R. Robson, *New J. Chem.*, 1998, 173–175.
28 S. A. Hodgson, J. Adamson, S. J. Hunt, M. J. Cliffe, A. B. Cairns, A. L. Thompson, M. G. Tucker, N. P. Funnell and A. L. Goodwin, *Chem. Commun.*, 2014, **50**, 5264–5266.
29 H. T. Stokes and D. M. Hatch, *Isotropy subgroups of the 230 crystallographic space groups*, World Scientific, Singapore, 1988.
30 S. A. T. Redfern and E. Salje, *J. Phys. C: Solid State Phys.*, 1988, **21**, 277–285.
31 M. J. Cliffe and A. L. Goodwin, *J. Appl. Crystallogr.*, 2012, **45**, 1321–1329.
32 J. M. Ogborn, I. E. Collings, S. A. Moggach, A. L. Thompson and A. L. Goodwin, *Chem. Sci.*, 2012, **3**, 3011–3017.
33 Y. Wu, V. K. Peterson, E. Luks, T. A. Darwish and C. J. Kepert, *Angew. Chem., Int. Ed.*, 2014, **53**, 5175–5178.
34 D. Dubbeldam, K. S. Walton, D. E. Ellis and R. Q. Snurr, *Angew. Chem., Int. Ed.*, 2007, **46**, 4496–4499.
35 S. S. Han and W. A. Goddard III, *J. Phys. Chem. C*, 2007, **111**, 15185–15191.
36 W. Zhou, H. Wu, T. Yildirim, J. R. Simpson and A. R. Hight Walker, *Phys. Rev. B*, 2008, **78**, 054114.
37 These same systems undergo a first-order phase transition between 400 and 500 K, such that the authors report thermal expansion coefficients as extreme as $-380\ MK^{-1}$ and $+1161\ MK^{-1}$; however, these values hold over only very small temperature intervals immediately below the transition and so overstate the intrinsic response of the material.
38 J.-C. Tan, P. Jain and A. K. Cheetham, *Dalton Trans.*, 2012, **41**, 3949–3952.
39 S. Henke, W. Li and A. K. Cheetham, *Chem. Sci.*, 2014, **5**, 2392–2397.
40 D. A. Dixon, J. C. Calabrese and J. S. Miller, *J. Am. Chem. Soc.*, 1986, **108**, 2582–2588.

 This journal is © The Royal Society of Chemistry 2015

41 M. Calleja, A. L. Goodwin and M. T. Dove, *J. Phys.: Condens. Matter*, 2008, **20**, 255226.
42 B. F. Abrahams, S. R. Batten, B. F. Hoskins and R. Robson, *Inorg. Chem.*, 2003, **42**, 2654–2664.
43 S. J. Hibble, S. G. Eversfield, A. R. Cowley and A. M. Chippindale, *Angew. Chem., Int. Ed.*, 2004, **43**, 628–630.
44 A. M. Chippindale and S. J. Hibble, *J. Am. Chem. Soc.*, 2009, **131**, 12736–12744.
45 J.-H. Wang, M. Li and D. Li, *Chem. Sci.*, 2013, **4**, 1793–1801.
46 I. E. Collings, A. B. Cairns, A. L. Thompson, J. E. Parker, C. C. Tan, M. G. Tucker, J. Catafesta, C. Levelut, J. Haines, V. Dmitriev, P. Pattison and A. L. Goodwin, *J. Am. Chem. Soc.*, 2013, **135**, 7610–7620.

Open Access Article. Published on 02 October 2014. Downloaded on 04/04/2016 18:20:24.
This article is licensed under a Creative Commons Attribution 3.0 Unported Licence.



ChemComm

COMMUNICATION

View Article Online
View Journal | View Issue

Published on 07 July 2015. Downloaded by University of Oxford on 04/04/2016 18:19:59.

Cite this: *Chem. Commun.*, 2015, **51**, 12728

Received 5th June 2015,
Accepted 7th July 2015

DOI: 10.1039/c5cc04626b

www.rsc.org/chemcomm

Glass formation *via* structural fragmentation of a 2D coordination network†

D. Umeyama,[a] N. P. Funnell,[b] M. J. Cliffe,[b] J. A. Hill,[b] A. L. Goodwin,[b] Y. Hijikata,[c] T. Itakura,[d] T. Okubo,[e] S. Horike*[a] and S. Kitagawa*[af]

The structure of a glass obtained by the melt quenching of a two-dimensional (2D) coordination network was examined. X-ray analyses disclosed a 2D-to-0D structural transformation before and after glass formation. The mechanism is unique to coordination compounds, as it is characterized by labile and flexible coordination bonds.

Glasses are an important class of materials and can be formed by many routes. Of various routes to the glassy state, melt quenching is one of the most common methods to obtain glasses.[1] Many types of substances form glasses *via* melt quenching; there are several types of glasses classified according to their building units, including molecular (toluene), metallic (Au–Si), covalent (As_2Se_3), and open network glasses (SiO_2).[2] Recently we have reported a number of melting coordination polymers (CPs), and demonstrated the glass formation of one such melting CP by melt quenching.[3] CPs are a class of crystalline inorganic–organic hybrids that form extended networks *via* coordination bonds.[4] The immense number of possible combinations of metal ions and ligands results in rich structural and compositional diversity in CPs. This enables fine-tuning to give CPs that can melt. In addition to the aforementioned archetypal glasses, those from molten CPs can be classified as a new type of glass former that potentially inherits the useful properties of CPs.[5]

Although glasses do not have long range order, the local structures often resemble those of their crystalline counterparts; therefore molecular crystals form molecular glasses, and network crystals form network glasses.[6] In a previous study, we examined the structure of a vitreous CP and identified that the glass state had a network structure that was similar to its crystalline state.[3] Other extended coordination materials, including metal–organic frameworks (MOFs), also exhibit network structures in the vitreous states inherited from their parent crystals.[7] The network preservation of these materials in glass and crystalline state can be rationalized by considering the lattice enthalpies that must be comparable in both states.[8] However, this "preservation rule" might be expected to break down in cases where the lattice enthalpies between the two states are similar despite having very different structures.

In this communication, we report a study on a glass-forming CP, which exhibits a network-to-molecular transformation before and after glass formation. This kind of drastic fragmentation is not observed in conventional glass formers such as organic polymers and silica glasses.[6] The suggested molecular structure of the vitreous state, determined on the basis of X-ray absorption and pair distribution function (PDF) analyses, indicates that the chemical diversity of coordination species and flexibility in coordination geometry are responsible for the unique glass formation, which is accompanied by a dynamic rearrangement in a coordination sphere.

The glass-forming CP, $[Zn(H_2PO_4)_2(HTr)_2]_n$ (**1**; Tr: 1,2,4-triazolate), comprises octahedral (O_h) zinc ions surrounded by HTr and phosphate ligands in the crystalline state. Each HTr ligand bridges two zinc ions equatorially to build an extended two-dimensional (2D) network, with the phosphate ligands standing axially on the sheet (Fig. 1a).[9] Air cooling at ambient temperature from the molten state of **1** is sufficiently rapid to afford the vitreous state (**1′**), suppressing the recrystallization into **1** (Fig. 1b). **1′** exhibits a glass transition at 305 K (T_g), determined as described below using differential scanning calorimetry (DSC), and is thus stable as a glass at ambient temperature.

[a] *Department of Synthetic Chemistry and Biological Chemistry, Graduate School of Engineering, Kyoto University, Katsura, Nishikyo-ku, Kyoto 615-8510, Japan. E-mail: horike@sbchem.kyoto-u.ac.jp*
[b] *Inorganic Chemistry Laboratory, Department of Chemistry, University of Oxford, South Parks Road, Oxford OX1 3QR, UK*
[c] *Institute of Transformative Bio-Molecules (WPI-ITbM), Nagoya University, Chikusa-ku, Nagoya 464-8602, Japan*
[d] *DENSO CORPORATION, 1-1 Showa-cho, Kariya, Aichi 448-8661, Japan*
[e] *Department of Chemistry, School of Science and Engineering, Kinki University, Kowakae, Higashi-Osaka, Osaka 577-8502, Japan*
[f] *Institute for Integrated Cell-Material Sciences (WPI-iCeMS), Kyoto University, Yoshida, Sakyo-ku, Kyoto 606-8501, Japan. E-mail: kitagawa@icems.kyoto-u.ac.jp*

† Electronic supplementary information (ESI) available: Experimental details on $[Zn(H_2PO_4)_2(HTr)_2]_n$ synthesis, X-ray absorption spectra, X-ray total scattering, reverse Monte Carlo model construction and refinement, differential scanning calorimetry, and density functional theory calculations. See DOI: 10.1039/c5cc04626b

This journal is © The Royal Society of Chemistry 2015

Published on 07 July 2015. Downloaded by University of Oxford on 04/04/2016 18:19:59.

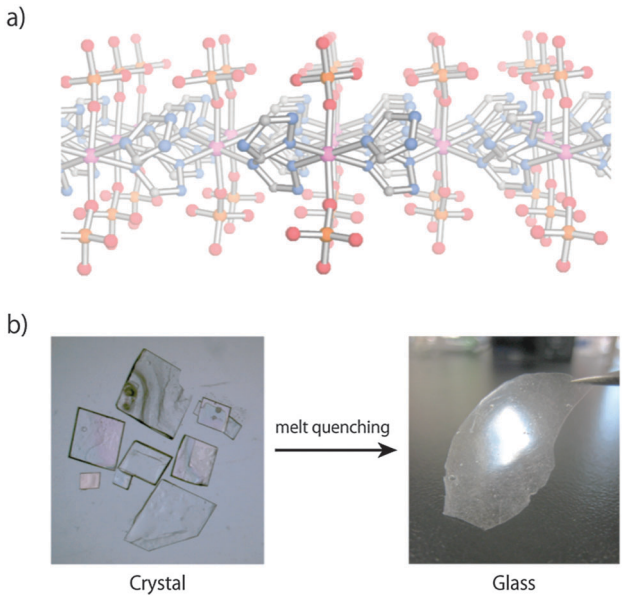

Fig. 1 (a) Crystal structure of **1**. The Zn, P, O, N, and C atoms are shown in purple, orange, red, blue, and gray, respectively. H atoms have been omitted for clarity. (b) Photographs of the crystals of **1** and the glassy flake of **1′**.

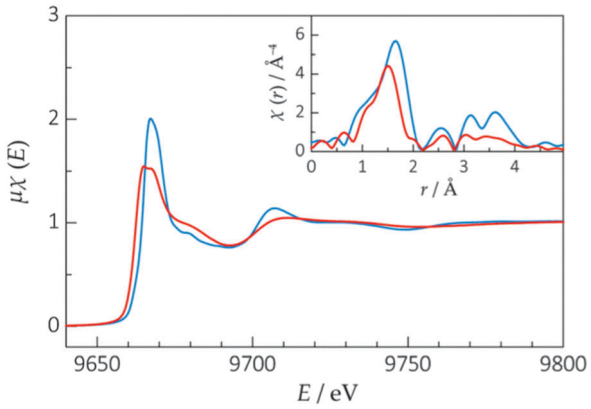

Fig. 2 XASs of **1** (blue) and **1′** (red) observed at the K edge of the zinc atoms at 298 K and the derived RDFs (inset).

The X-ray absorption spectra (XAS) of the K edge of the zinc ions of **1** and **1′** indicate that the arrangements around these zinc ions are distinct even at the nearest neighbors (Fig. 2). The sharp peak at the rising absorption edge—the so called "white-line"—of **1** becomes less intense in **1′**. The difference in the white-line intensities suggests a change in the site symmetries of the zinc ions (*i.e.*, how the orbitals are hybridized) because the intensities are subject to the selection rule of electron transitions ($\Delta l = \pm 1$). Besides an O_h arrangement, a zinc ion is also stable in a tetrahedral (T_d) arrangement. The T_d arrangement is well ascribed to the less intense white line of **1′** because the electronic transitions associated with X-ray absorption at the K edge of the T_d zinc ions have a stronger character of 1s → 3d transition ($\Delta l = +2$) than those of O_h.[10] The radial distribution function (RDF) around the zinc ions of **1′** deduced from its XAS is fitted well by a model in which the zinc ions are surrounded by

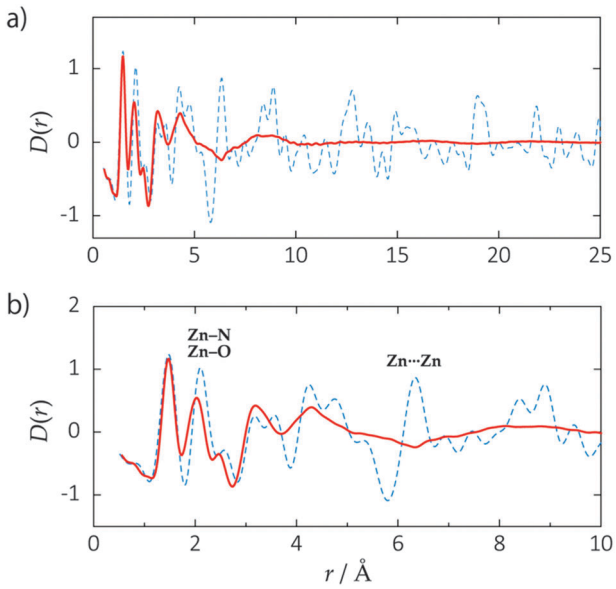

Fig. 3 (a) $D(r)$ of **1** (blue) and **1′** (red) at 298 K from 1 to 25 Å. (b) Comparison of the $D(r)$s of **1** (blue) and **1′** (red) in the range from 1 to 10 Å (298 K). Some of the assigned peaks of the $D(r)$ of **1** are indicated.

four atoms with a shorter bond distance than those of **1** (Fig. S1 and Table S1 in ESI†). Therefore, we postulate that the arrangement around the zinc ions has changed from O_h to T_d during the phase transition.

In order to probe the detailed structure of **1′**, we collected X-ray total scattering data using a PANalytical Empyrean diffractometer equipped with a Ag X-ray tube. The normalized and corrected X-ray structure factors $F(Q)$ and the corresponding pair distribution functions $D(r)$ are given in Fig. 3.[11] On the basis of the $D(r)$ of **1**, the single crystal structure of **1** was refined and thus some peaks of the $D(r)$ were assigned (Fig. S2 in ESI†). One of the remarkable features of the $D(r)$ of **1′** is that the atomic correlations are much diminished beyond 5 Å (Fig. 3a). The Zn–Zn correlation observed at 6.4 Å in the $D(r)$ of **1** has disappeared in that of **1′**, suggestive of the absence of an extended structure in **1′** (Fig. 3b). This is in striking contrast to the PDFs of the amorphous ZIFs, for which the Zn–Zn correlation is preserved.[12,7a] In addition, the peak for the coordination shell of the zinc ions (around 2 Å) has a lower intensity and occurs at shorter distance for **1′** than for **1**, consistent with the T_d arrangement of the zinc ions of **1′** suggested by the XAS spectrum.

The remarkably short correlation length evident from the PDF profile of **1′** suggests that the building unit of **1′** is likely a discrete molecule (0D).[13] Therefore, we built a molecular model for **1′** as shown in Fig. 4a (bottom). The model was obtained by changing the HTr molecules from bridging to monodentate ligands; thus the geometry becomes T_d while the chemical formula remains the same as **1**, $[Zn(H_2PO_4)_2(HTr)_2]$, except that it is no longer a constitutional repeating unit. Expecting that the vitreous **1′** is a condensed phase in which $[Zn(H_2PO_4)_2(HTr)_2]$ molecules pack randomly, we constructed a 25 × 25 × 25 Å^3 cubic amorphous cell with $P1$ symmetry filled with the fifty molecules by using the Amorphous Cell module implemented in

Published on 07 July 2015. Downloaded by University of Oxford on 04/04/2016 18:19:59.

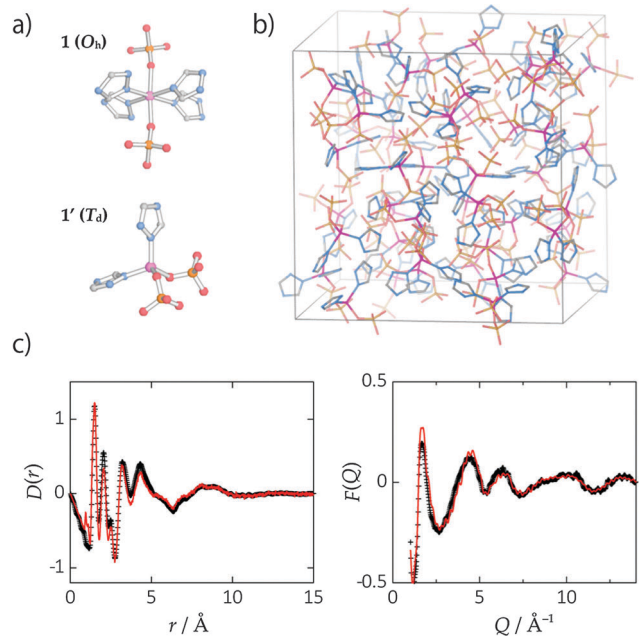

Fig. 4 (a) Arrangements around the zinc ions for **1** (top) and **1′** (bottom, postulated). (b) Amorphous cell that comprises 50 T_d models for **1′**. (c) Result of RMC refinement of the amorphous cell in real (left) and reciprocal spaces (right). Experimental data and fitting results are shown in black crosses and red lines, respectively.

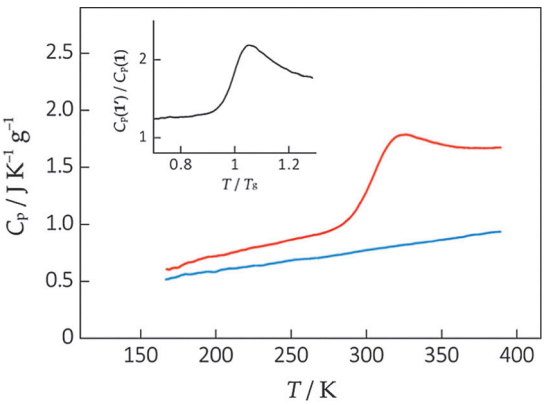

Fig. 5 Heat capacities of **1** (blue) and **1′** (red) calculated from DSC measurements. Inset shows the variation of the heat capacity through the glass transition for **1′**.

Accelrys Materials Studio 6.0.[14] The amorphous cell was relaxed *via* MD simulation using the Forcite module (Fig. 4b), and whose 2 × 2 × 2 super cell was settled as an initial model for a reverse Monte Carlo (RMC)[15] refinement. We used the program RMCProfile and refined the structure to fit the X-ray total scattering data in real and reciprocal space (Fig. 4c).[16] The refined structure maintained the initial MD constitution (Fig. S3 in ESI†), and thus we succeeded in suggesting a consistent structural model for **1′**.

Having established a viable structural model for **1′**, its physical properties are of interest. Heat capacity (C_p) is one of the most important thermodynamic parameters to characterize glasses, and we ascribe the behavior of the C_p of **1′** to its discrete molecular structure. As shown in Fig. 5, the glass transition of **1′** is superimposed on a gradually-rising background, indicating that the molecular rearrangements involved in the glass transition commence before the vibrational heat capacity is fully exited. This is a common characteristic for molecular glass formers, which have vibrational modes in infrared and Raman regions (*i.e.*, with high Einstein temperatures). While thermally amorphized ZIF-4, known to be a molecular network glass, also exhibits glass transitions on the slope of C_p, the jump of the C_p at the T_g ($\Delta C_p(T_g)$) of **1′** is more than four times larger ($\Delta C_p(T_g)$ = 0.70 J K^{-1} g^{-1}) than that of high density amorphous (HDA) ZIF-4 ($\Delta C_p(T_g)$ = 0.16 J K^{-1} g^{-1}).[7a] The small $\Delta C_p(T_g)$ of amorphous ZIF-4 is explained by its three dimensional bonding pattern, *cf.* vitreous GeO_2 (an inorganic network glass).[1] In contrast, the large $\Delta C_p(T_g)$ of **1′** is due to its discrete structure, as seen in other molecular glass formers including toluene and ethanol.[17] The normalized C_p value of **1′**, C_p(**1**)/C_p(**1′**), exceeds 2 around T_g (Fig. 5 inset). This supports the attribution of a discrete molecular structure in which the configurational heat capacity is larger than that of a network glass. The change in entropy across the glass transition was calculated as ΔS(**1′**) = 81 J K^{-1} mol^{-1} (280–325 K).

We performed density functional theory (DFT) calculations to understand the energetics of **1** and **1′**. According to the Gibbs free energies of the complex formation reactions ($\Delta_r G$) of the finite O_h and T_d models at 298 K (Fig. S4 and Scheme S1 in ESI†), the energy difference between the two configurations is only 54 kJ mol^{-1} ($\Delta_r G(O_h)$ = − 2616 kJ mol^{-1}, $\Delta_r G(T_d)$ = − 2562 kJ mol^{-1}). Considering that the T_d arrangement can form more hydrogen bonds (which are not included in the DFT calculation) than the O_h arrangement, the energy difference may be less than 54 kJ mol^{-1}, and thus the small free energy difference indicated by the DFT calculations also represents the validity of the T_d model. The bistability of zinc ion in the two arrangements, combined with electrical neutrality of the bridging ligand (HTr), appear to be the keys for enabling the fragmentation into 0D structure. The structural flexibility and compositional diversity of coordination compounds are of central importance for this unique behavior. Having a permanent dipole moment (5.61 Debye; indicated by the DFT calculation), the dielectric and optical properties of **1′** are of interest for applications as a functional glass.[18]

The disordered structures of glasses are most commonly characterized as continuous random networks (CRNs) in 3D and 2D systems,[19] or entangled strings in 1D systems (linear polymers).[20] In this study, we examined the structure and properties of a glass obtained by melt quenching of a 2D coordination network. The XAS and PDF analyses indicated a discrete (0D) structure for the glass state which was consistent in terms of composition, preferred coordination geometries for zinc ions, behavior in heat capacity, and energetics in DFT calculations. The RMC refinement of the amorphous cell of the 0D models visualized the glass structure in bulk, elucidating a unique glass formation from 2D materials. This mechanism of glass formation is characteristic to coordination compounds in the sense that it requires labile bonds and flexible rearrangements. Having performed a structure study for a glass from 2D coordination network, in addition to 1D[3] and 3D[7a] systems, we

 This journal is © The Royal Society of Chemistry 2015

would be able to understand an important design guide for preparing glass forming CPs. Our study provides a useful insight to developing novel functional glasses from CPs.

This work was supported by the PRESTO of the Japan Science and Technology Agency (JST), and a Grant-in-Aid for Scientific Research on the Innovative Areas: "Fusion Materials", Grant-in-Aid for Young Scientists (A), Grant-in-Aid for Challenging Exploratory Research from the Ministry of Education, Culture, Sports, Science and Technology, Japan. iCeMS is supported by the World Premier International Research Initiative (WPI) of MEXT, Japan. D.U. is grateful to JSPS Research Fellowships for Young Scientists. N.P.F, M.J.C, J.A.H. and A.L.G acknowledge financial support from the E.P.S.R.C. (EP/G004528/2) and the E.R.C. (Grant Ref: 279705)

Notes and references

1 C. A. Angell, *Science*, 1995, **267**, 1924.
2 C. A. Angell, *Pure Appl. Chem.*, 1991, **63**, 1387.
3 D. Umeyama, S. Horike, M. Inukai, T. Itakura and S. Kitagawa, *J. Am. Chem. Soc.*, 2015, **137**, 864.
4 (*a*) B. Moulton and M. J. Zaworotko, *Chem. Rev.*, 2001, **101**, 1629; (*b*) L. Carlucci, G. Ciani and D. M. Proserpio, *Coord. Chem. Rev.*, 2003, **246**, 247; (*c*) C. Janiak, *Dalton Trans.*, 2003, 2781.
5 (*a*) Y. Pei, M. Verdaguer, O. Kahn, J. Sletten and J. P. Renard, *J. Am. Chem. Soc.*, 1986, **108**, 7428; (*b*) H. Kitagawa, N. Onodera, T. Sonoyama, M. Yamamoto, T. Fukawa, T. Mitani, M. Seto and Y. Maeda, *J. Am. Chem. Soc.*, 1999, **121**, 10068; (*c*) H. Kishida, H. Matsuzaki, H. Okamoto, T. Manabe, M. Yamashita, Y. Taguchi and Y. Tokura, *Nature*, 2000, **405**, 929; (*d*) S. R. Batten and K. S. Murray, *Coord. Chem. Rev.*, 2003, **246**, 103; (*e*) Y. Nagao, M. Fujishima, R. Ikeda, S. Kanda and H. Kitagawa, *Inorg. Chem. Commun.*, 2003, **6**, 346; (*f*) S. Kitagawa, R. Kitaura and S. Noro, *Angew. Chem., Int. Ed.*, 2004, **43**, 2334; (*g*) M. Ballesteros-Rivas, A. Ota, E. Reinheimer, A. Prosvirin, J. Valdés-Martinez and K. R. Dunbar, *Angew. Chem.*, 2011, **123**, 9877.
6 G. N. Greaves and S. Sen, *Adv. Phys.*, 2007, **56**, 1.
7 (*a*) T. D. Bennett, J.-C. Tan, Y. Z. Yue, C. Ducati, N. Terril, H. H. M. Yeung, Z. Zhou, W. Chen, S. Henke, A. K. Cheetham and G. N. Greaves, *ARXIV*, 2014, arXiv:1409.3980; (*b*) T. S. Eike, E. Edengeiser, B. Mallick, M. Havenith and A.-V. Mudring, *Chem. – Eur. J.*, 2014, **20**, 5338.
8 A. B. Cairns and A. L. Goodwin, *Chem. Soc. Rev.*, 2013, **42**, 4881.
9 D. Umeyama, S. Horike, M. Inukai, T. Itakura and S. Kitagawa, *J. Am. Chem. Soc.*, 2012, **134**, 12780.
10 J. Rose, I. Moulin, A. Masion, P. M. Bertsch, M. R. Wiesner, J. Y. Bottero, F. Mosnier and C. Haehnel, *Langmuir*, 2001, **17**, 3658.
11 (*a*) D. A. Keen, *J. Appl. Crystallogr.*, 2001, **34**, 172; (*b*) The total scattering functions used here follow the formalisms given by ref. 11a.
12 (*a*) T. D. Bennett, A. L. Goodwin, M. T. Dove, D. A. Keen, M. G. Tucker, E. R. Barney, A. K. Soper, E. G. Bithell, J.-C. Tan and A. K. Cheetham, *Phys. Rev. Lett.*, 2010, **104**, 115503; (*b*) T. D. Bennett and A. K. Cheetham, *Acc. Chem. Res.*, 2014, **47**, 1555.
13 N. P. Funnell, M. T. Dove, A. L. Goodwin, S. Parsons and M. G. Tucker, *J. Phys.: Condens. Matter*, 2013, **25**, 454204.
14 Accelrys Software Inc, *Material Studio Modeling Environment, Release 6*, Accelrys Software Inc., San Diego, California, USA, 2011.
15 R. L. Mcgreevy and L. Pusztai, *Mol. Simul.*, 1988, **1**, 359.
16 M. G. Tucker, D. A. Keen, M. T. Dove, A. L. Goodwin and Q. Hui, *J. Phys.: Condens. Matter*, 2007, **19**, 335218.
17 C. Alba, L. E. Busse, D. J. List and C. A. Angell, *J. Chem. Phys.*, 1990, **92**, 617.
18 N. F. Borrelli and M. M. Layton, *J. Non-Cryst. Solids*, 1971, **6**, 197.
19 (*a*) M. G. Tucker, D. A. Keen, M. T. Dove and K. Trachenko, *J. Phys.: Condens. Matter*, 2005, **17**, S67; (*b*) P. Y. Huang, S. Kurasch, A. Srivastava, V. Skakalova, J. Kotakoski, A. V. Krasheninnikov, R. Hovden, Q. Mao, J. C. Meyer, J. Smet, D. A. Muller and U. Kaiser, *Nano Lett.*, 2012, **12**, 1081; (*c*) L. Lichtenstein, C. Büchner, B. Yang, S. Shaikhutdinov, M. Heyde, M. Sierka, R. Włodarczyk, J. Sauer and H.-J. Freund, *Angew. Chem., Int. Ed.*, 2012, **51**, 404.
20 (*a*) R. H. Colby, L. J. Fetters and W. W. Graessley, *Macromolecules*, 1987, **20**, 2226; (*b*) M. D. John and G. L. Ronald, *Structure and Rheology of Molten Polymers*, Carl Hanser Verlag GmbH & Co. KG, 2006.

Published on 07 July 2015. Downloaded by University of Oxford on 04/04/2016 18:19:59.

PCCP

PAPER

View Article Online
View Journal | View Issue

CrossMark click for updates

Cite this: *Phys. Chem. Chem. Phys.*, 2015, **17**, 11586

Defect-dependent colossal negative thermal expansion in UiO-66(Hf) metal–organic framework†

Matthew J. Cliffe,[a] Joshua A. Hill,[a] Claire A. Murray,[b] François-Xavier Coudert[c] and Andrew L. Goodwin*[a]

Received 5th March 2015,
Accepted 31st March 2015

DOI: 10.1039/c5cp01307k

www.rsc.org/pccp

Thermally-densified hafnium terephthalate UiO-66(Hf) is shown to exhibit the strongest isotropic negative thermal expansion (NTE) effect yet reported for a metal–organic framework (MOF). Incorporation of correlated vacancy defects within the framework affects both the extent of thermal densification and the magnitude of NTE observed in the densified product. We thus demonstrate that defect inclusion can be used to tune systematically the physical behaviour of a MOF.

Published on 02 April 2015. Downloaded by University of Oxford on 04/04/2016 18:20:41.

Introduction

It has long been recognised that defects and their correlations play a central role in determining the physical properties of many functional materials: the mass transport pathways of fast-ion conductors,[1,2] charge localisation in high-temperature superconductors,[3,4] and emergence of polar nanoregions in relaxor ferroelectrics[5] are just three examples. The recent discovery that correlated defects can be systematically introduced into the structures of some canonical metal–organic frameworks (MOFs)[6] suggests the possibility of establishing defect–property relationships in this broad family of materials long-favoured for its chemical versatility.[7–9] Perhaps the most obvious benefit of determining such relationships would be the ability to exploit defects and non-stoichiometry to develop MOFs with particularly attractive or otherwise-inaccessible physical properties.

The few recent studies of defective MOFs have focussed either on the nature of defect inclusion itself or on how defects influence chemical properties such as catalytic activity and guest sorption.[10–13] Here we ask a different question: namely, is it possible that defects can influence the physical properties of MOFs? In attempting to answer this question, we focus in this proof-of-principle study on the thermomechanical behaviour of the canonical hafnium terephthalate MOF UiO-66(Hf).[14] Our choice of this specific pairing of physical property and chemical system is motivated by the following considerations. First, the response of framework geometry to changes in temperature is at once both straightforwardly measured and strongly characteristic of the underlying elastic behaviour of the material in question.[15,16] Second, the empirical propensity for MOFs to exhibit anomalous mechanical effects such as thermal contraction (*i.e.* negative thermal expansion, NTE; ref. 17–19) has led to a general expectation that such properties will be especially sensitive to the existence and nature of structural defects.[9] And third, UiO-66(Hf) is the MOF for which there is arguably the greatest and best-understood chemical control over defect incorporation.[6,11,20,21]

The idealised structure of non-defective UiO-66(Hf) consists of a face-centred cubic array of oxyhydroxyhafnium(IV) clusters connected *via* terephthalate (benzene-1,4-dicarboxylate, bdc^{2-}) linkers [Fig. 1(a)].[14] The particular defects we study here are introduced by substituting formate for terephthalate during framework synthesis. As a monotopic (capping) ligand, formate reduces the connectivity of the framework. This, in turn, encourages vacancies of entire hafnium clusters. Formate content can be increased at least as far as the situation where, of the 12 carboxylate ligands of each hafnium cluster, four ligands are formates and eight are terephthalate carboxylates [Fig. 1(b)].[6,11] While this substitution results in substantive structural modification over the unit-cell (nanometre) length scale—indeed one in four hafnium clusters are vacant in this case—the actual coordination environment within the clusters is essentially indistinguishable in the defective and defect-free modifications.[6,22,23] In order to amplify the structural consequences of defect incorporation we exploit the high-temperature ligand elimination reaction known to occur in this system.[11,24,25] Whereas this step involves elimination of H_2O for defect-free UiO-66, the lability of non-bridging formate

[a] *Department of Chemistry, University of Oxford, Inorganic Chemistry Laboratory, South Parks Road, Oxford OX1 3QR, UK. E-mail: andrew.goodwin@chem.ox.ac.uk; Fax: +44 (0)1865 274690; Tel: +44 (0)1865 272137*
[b] *Diamond Light Source, Ltd, Harwell Science and Innovation Campus, Didcot, Oxfordshire, OX11 0DE, UK*
[c] *PSL Research University, Chimie ParisTech–CNRS, Institut de Recherche de Chimie Paris, 75005 Paris, France*

† Electronic supplementary information (ESI) available: Synthesis, experimental methods, and sample characterisation; X-ray powder diffraction refinement details. See DOI: 10.1039/c5cp01307k

 This journal is © the Owner Societies 2015

Published on 02 April 2015. Downloaded by University of Oxford on 04/04/2016 18:20:41.

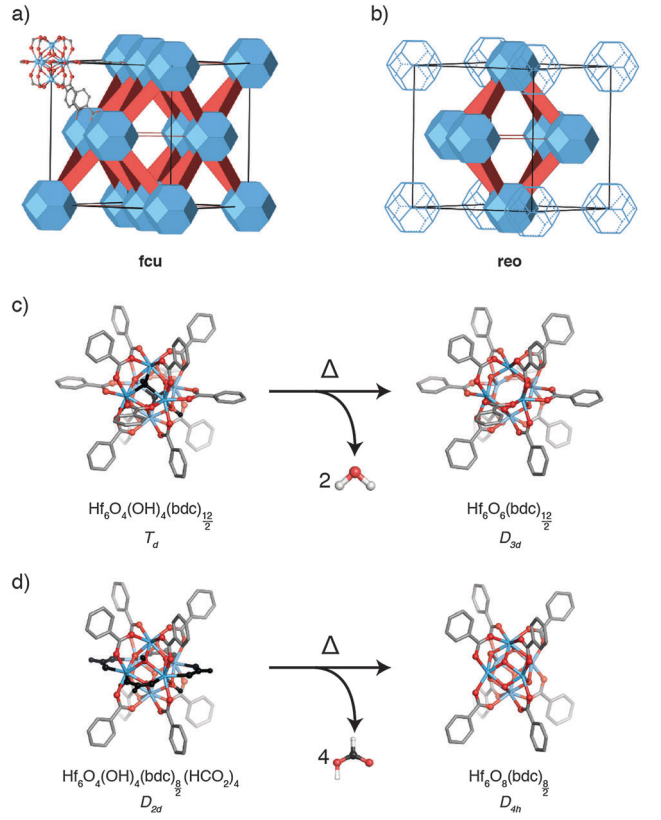

Fig. 1 The ideal non-defective UiO-66(Hf) consists of oxyhydroxyhafnium(IV) clusters connected *via* terephthalate linkers into a face-centred cubic **fcu** topology network. A unit cell is shown in panel (a), with the Hf clusters represented as blue truncated octahedra and linkers as red rectangles. The atomic-scale structure of a single cluster is shown in detail in the top-left of the panel. (b) At high concentrations, formic acid promotes the formation of nanodomains of the primitive **reo** topology, containing correlated linker and hafnium cluster absences. Absent hafnium clusters are shown in skeletal form. In spite of the differences in framework topology, the cluster coordination environments of **fcu** (c) and **reo** (d) UiO-66(Hf) are very similar.[6,23] After ligand elimination (right-hand panels of (c),(d)) the two cluster types are distinct in both coordination and symmetry. Atoms are coloured as follows: Hf, blue; O, red; and C, grey. Atoms lost during thermal elimination are coloured black.

ligands is such that it is formic acid that is eliminated in our defective UiO-66, resulting in markedly different cluster geometries for the two cases [Fig. 1(c,d)].[25,26]

Making use of *in situ* variable-temperature synchrotron X-ray diffraction measurements of a series of UiO-66(Hf) samples with a range of defect concentrations, we proceed to demonstrate the following. First, ligand elimination results in framework densification, the magnitude of which is dependent on defect concentration. Quantum mechanical calculations help interpret the microscopic origin of this volume reduction. Second, all densified-UiO-66(Hf) samples exhibit isotropic NTE behaviour that is many times stronger than that of any other MOF, and in one case even satisfies the condition of "colossal" NTE (its volumetric coefficient of thermal expansion $\alpha_V = \mathrm{d}V/V\mathrm{d}T \simeq -100\ \mathrm{MK}^{-1}$). This is the first report of colossal NTE in an isotropic MOF. Third, the magnitude of NTE can also be tuned systematically by defect concentration. Our paper concludes with a discussion of the likely mechanisms by which defect inclusion might influence elastic properties of this particular MOF, the challenges posed for understanding NTE in defective materials, and the implications for exploiting defect–property relationships in other MOF systems.

Results and discussion

Having used the method of ref. 6 to prepare a series of six UiO-66(Hf) samples with a range of defect concentrations, we sought first to establish that our samples included defects of the type discussed above. X-ray powder diffraction measurements revealed the existence of structured diffuse scattering in the form of broad superlattice reflections that are symmetry-forbidden in the defect-free system but are associated with nanodomains of correlated cluster vacancies in defective UiO-66 [Fig. 2(a)]. The ratio of the intensity of this diffuse scattering to that of the parent reflections is a measurable quantity that is sensitive to defect concentration. We find an approximately linear relationship between this ratio and the quantity of terephthalic acid used during synthesis, suggesting that our ensemble of defective UiO-66(Hf) samples spans a suitable range of defect concentrations [Fig. 2(a,b)].

The onset temperature of ligand elimination was determined using thermogravimetric analysis (TGA). The TGA traces of all our samples are qualitatively similar and can be interpreted on the basis of previous studies of this system:[11,25,27] each reveals three primary stages of mass loss, corresponding in turn to adsorbate volatilisation (~100 °C), ligand elimination

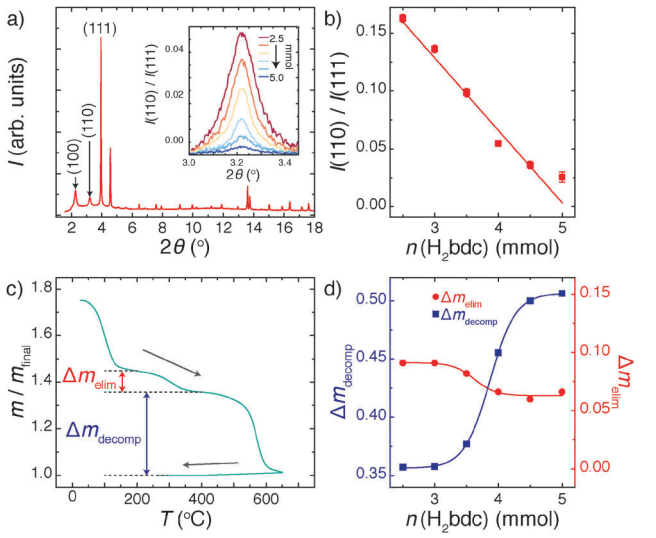

Fig. 2 (a) A diffraction pattern of the most defective sample of UiO-66(Hf). The structured diffuse scattering located at primitive superlattice positions is a signature of the presence of correlated defects in UiO-66(Hf). The most intense of these broad reflections are the (100) and (110). On increasing the quantity of H_2bdc in the reaction mixture, the concentration of defects decreases, and so the relative intensity of the primitive reflections decreases ((a) inset and (b)). (c) The TGA trace of UiO-66(Hf) shows three steps corresponding to, in turn, guest volatilisation, ligand elimination and framework decomposition. (d) The decrease in defect concentration is evident in the variation with bdc concentration of normalised mass losses both on ligand elimination (Δm_{elim}), and framework decomposition ($\Delta m_{\mathrm{decomp}}$). Fitted curves are included as guides to the eye.

Published on 02 April 2015. Downloaded by University of Oxford on 04/04/2016 18:20:41.

(250–350 °C) and framework decomposition (550–600 °C) [Fig. 2(c), ESI,† Fig. S1 and S2]. Qualitative trends in defect concentrations can be inferred from the relative mass losses associated with the second and third stages [Δm_{elim} and $\Delta m_{\mathrm{decomp}}$, respectively, in Fig. 2(c,d)]. Framework decomposition corresponds to the loss of terephthalate (leaving behind HfO_2) and so larger values of $\Delta m_{\mathrm{decomp}}$ are expected for the least defective examples, which should contain the highest relative concentrations of terephthalate. This is precisely what we observe [Fig. 2(d)]. Likewise the value of Δm_{elim} should decrease as the defect concentration is reduced (since H_2O is eliminated instead of the heavier HCOOH), and again this trend is observed in practice. So both X-ray diffraction and TGA measurements point to a systematic variation in defect concentration across our series of UiO-66(Hf) samples.

In order to determine the effect of defect concentration on thermomechanical behaviour, we measured variable-temperature X-ray powder diffraction patterns for all six samples. Because we were interested in determining the thermal expansivity of the phases produced by ligand elimination, we paid particular care to ensuring that our samples were heated sufficiently to drive this elimination step but not so far as to initiate framework decomposition. In practice this dictated an experimental protocol of heating each sample to a temperature of 340 °C and then measuring thermal expansivity on subsequent cooling to 100 °C. So the temperature range probed in these experiments corresponds to the first two stages observed in the TGA measurements described above.

For all samples the same qualitative behaviour was observed (although, as will form the focus of subsequent discussion, the magnitudes of these changes varied from sample to sample). On heating through the first stage of mass loss (*i.e.* up to 250 °C) the most noticeable changes to the diffraction pattern were in the relative intensities of reflections sensitive to solvent occupation within the framework pores. There was only a very small change (~0.1%) in the size of the unit cell within this regime. These observations are consistent with our interpretation of the TGA trace and with previous investigations.[11,25] In contrast, the ligand elimination process that occurs between 250 and 350 °C resulted in an order-of-magnitude larger decrease in the cubic unit cell parameter that has not previously been observed in defect-free samples [Fig. 3(a)]. The diffraction pattern of the densified framework formed at this higher temperature can still be accounted for by a model based on the ambient-temperature structure, adjusted for the change in lattice dimensions; however the scattering intensity in high-angle Bragg peaks was much reduced such that detailed structural refinement did not prove possible. On subsequent cooling from 340 to 100 °C all samples showed NTE [Fig. 3(a,b)]. The two processes of densification and NTE, together with their dependence on defect concentration, are discussed in turn below.

Thermal densification

In the absence of a diffraction-based structural model for the densified framework, we turned to quantum mechanical calculations to verify that the structural changes associated

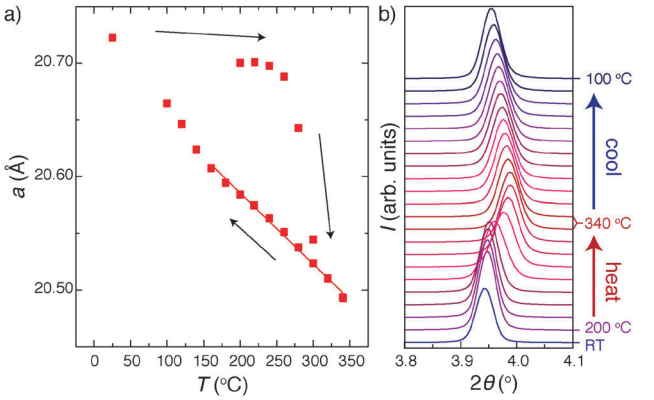

Fig. 3 (a) Evolution of the lattice parameter of the UiO-66(Hf) sample synthesised with the largest quantity of H_2bdc (5.0 mmol)—*i.e.* the lowest defect concentration—on heating from room temperature to 340 °C then cooling to 100 °C. A linear fit to the lattice parameter over the temperature range 340–160 °C is shown, for the determination of α_V. (b) The evolution of the most intense peak, the (111) reflection, throughout this process.

with formate elimination were consistent with the magnitude of volume collapse observed experimentally. From a computational viewpoint it would have been unfeasible to use *ab initio* methods to relax large atomistic configurations describing the nanodomain defect structure reported in ref. 6. Instead we focussed on an ordered defect structure corresponding to substitution of four equatorial carboxylate sites by formate on each hafnium cluster; this is the 'ordered-**reo**' model of ref. 6. For this model, ligand elimination corresponds to the chemical process

$$Hf_6O_4(OH)_4(bdc)_4(OOCH)_4 \rightarrow Hf_6O_8(bdc)_4 + 4HCOOH\uparrow.$$

In silico relaxation of structural models for the framework compositions represented on either side of this reaction equation suggested that a 1.0% change in lattice parameters is expected upon HCOOH elimination: a = 20.862 Å for $Hf_6O_4(OH)_4(bdc)_4(OOCH)_4$ and 20.652 Å for $Hf_6O_8(bdc)_4$.‡ In contrast, it is already known that elimination of water from defect-free UiO-66 does not result in any significant volume change.[26] By inspection of the relaxed structural model for $Hf_6O_8(bdc)_4$, we conclude that distortions of the Hf_6 octahedra are responsible for this framework densification. Elimination of HCOOH amplifies the tetragonal distortion of Hf_6 octahedra, reducing the effective octahedral volume by 4.2% and bending the cluster–bdc–cluster connection so as to couple local distortion to macroscopic volume contraction [ESI,† Fig. S4]. The relaxed structural models are available as crystallographic information files as part of the ESI.†

If, as this analysis would suggest, the process of framework densification depends on the presence of structural defects, then we should expect stronger densification in UiO-66(Hf) samples with larger defect concentrations. By heating our samples to

‡ The tendency for calculations to overestimate lattice parameters for organic and organic-containing materials is a well-known phenomenon and arises due to the difficulty of correctly accounting for dispersive interactions. It does not impact the analysis of structural and lattice parameter trends in families of materials of similar composition and porosity.[28]

 This journal is © the Owner Societies 2015

Published on 02 April 2015. Downloaded by University of Oxford on 04/04/2016 18:20:41.

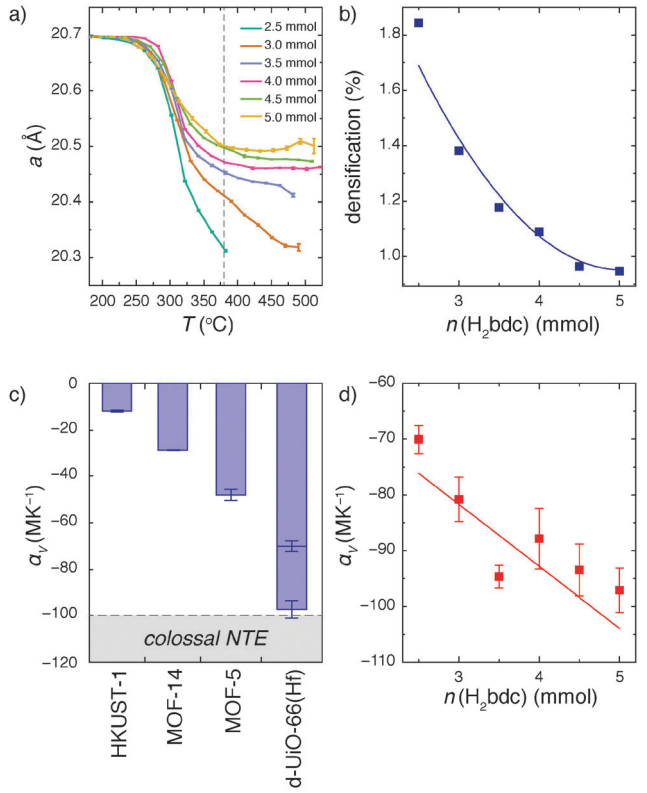

Fig. 4 (a) The evolution of the lattice parameter through the ligand elimination process for a series of samples with different defect concentrations. To correct for minor variations in the onset temperature of ligand elimination between sample, the curves are offset in temperature such that the maximum change in volume corresponds to 300 °C. (b) Composition dependence of the densification (percentage linear decrease) associated with ligand elimination, measured at 380 °C, highlighted in (a) by a dashed grey line. (c) Coefficients of thermal expansion for isotropic NTE MOFs. The two values given for densified-UiO-66(Hf) correspond to upper and lower defect concentrations.[17–19] (d) Variation in NTE behaviour as a function of decreasing defect concentration (increasing quantity of H_2bdc in the reaction mixture).

sufficiently-high temperatures to ensure complete densification (and working within the constraints of available synchrotron beam time), we found this expected property–defect relationship to be borne out in practice [Fig. 4(a,b)]. Our most defective samples showed densifications that were larger by ~1% (of the total lattice parameter) than for the least defective samples; this result is consistent not only with the results of our *ab initio* calculations but also with previous experimental reports.[26]

Negative thermal expansion

Perhaps the most intriguing physical property of densified-UiO-66(Hf) is its NTE response, which is evident in the increase of the cubic unit cell parameter on cooling from 340 °C [Fig. 3(a)] and in the anomalous thermal shifts of Bragg peaks in the raw diffraction data themselves [Fig. 3(b)]. While NTE is increasingly frequently observed amongst MOFs, there are two particular aspects of the behaviour we observe here that are especially attractive: on the one hand, the cubic crystal symmetry of defective UiO-66 means that its NTE is isotropic—*i.e.*, it occurs with constant magnitude in all crystal directions; and, on the other hand, the magnitude itself is really very large. Thermal expansion effects in different materials can be compared *via* the lattice expansivities

$$\alpha_V = \frac{1}{V}\left(\frac{\partial V}{\partial T}\right)_p, \quad (1)$$

with typical (positive) thermal expansion of engineering materials corresponding to values of α_V in the range 10–30 MK^{-1}.[29] Here, the lattice parameter data of Fig. 3(a) correspond to a thermal expansivity of $\alpha_V = -97(4)$ MK^{-1} over the temperature range 160–340 °C, which is comparable in magnitude to that of "colossal" thermal expansion materials ($|\alpha| \simeq 100$ MK^{-1}) such as $Ag_3[Co(CN)_6]$.[30] Although we observe an even more rapid increase in lattice parameter on further cooling from 160–100 °C, we cannot rule out the possibility that this feature may arise from re-uptake of guest molecules at these lower temperatures, and hence do not attach particular weight to that observation here. We have also carried out separate variable temperature diffraction measurements confirming the reversibility of the NTE behaviour [ESI,† Fig. S4].

Isotropic NTE behaviour of this magnitude is rare indeed. First discovered in ZrW_2O_8 in the late 1960s,[31] isotropic NTE is now known to occur in a handful of materials, such as ZrW_2O_8 itself and related substitutional variants,[31–33] the perovskite analogues ScF_3 and ReO_3,[34–36] the cuprite-structured oxides Ag_2O and Cu_2O,[37] the $Zn_xCd_{1-x}(CN)_2$ family and anhydrous Prussian Blue analogues,[38–41] and the three MOFs HKUST-1, MOF-5, and MOF-14.[17–19] Recent theoretical calculations suggest that isotropic NTE may occur in a wider range of MOF materials than currently experimentally reported and re-emphasise the important role of topology.[42] Of these various systems, single-network $Cd(CN)_2$ is the only colossal NTE material ($\alpha_V = -100.5(15)$ MK^{-1}).[41] Despite decades of theoretical and experimental studies there is only general consensus that low-energy transverse vibrational modes play at least some role in the NTE mechanisms for most of these materials. The details of NTE mechanisms remain controversial, with new studies frequently demanding reinterpretation of long-held assumptions as and when they appear.[17,43–45] Here we avoid speculating on a detailed NTE mechanism and focus instead on the measurement and defect dependence of the phenomenon. We note simply that, with its open framework structure of high-nuclearity clusters connected by long, light, and flexible organic linkers, densified-UiO-66(Hf) certainly shares many of the basic design features thought to favour low-energy NTE modes. Fig. 4(d) places the isotropic NTE behaviour of UiO-66(Hf) in the context of the three other MOFs known to show the effect.[17–19]

As anomalous as the thermal expansion behaviour of densified-UiO-66(Hf) is, our key interest is in the possibility that the magnitude of NTE might be sensitive to defect concentration. What sensitivity, if any, do we actually expect? An earlier study of the geometric contribution to NTE in molecular frameworks suggested that defects of the type thought to occur

Published on 02 April 2015. Downloaded by University of Oxford on 04/04/2016 18:20:41.

in UiO-66(Hf) should actually encourage NTE because they act to increase the relative contribution of NTE vibrational modes to the overall framework dynamics.[46] Likewise, even simple Maxwellian counting suggests that the balance of degrees of freedom and geometric constraints would be tipped increasingly in favour of the former (and hence NTE) as linkers are removed from a three-dimensional network.[47] Not taken into account in either analysis, however, is the observation we make here that defects are also linked to framework densification. Empirically, one finds that higher densities usually result in weaker NTE—this is exactly what is observed in zeolites, Prussian blues, and the $Zn_xCd_{1-x}(CN)_2$ family alike.[38,40,48] To complicate further this balance of competing effects, we remark that the ligand elimination process alters the point symmetry of the Hf_6 clusters in a way that may itself affect the dynamics—and hence the NTE—of defective UiO-66(Hf). The point symmetries of both defect-free and defective Hf_6 clusters (D_{3d} and D_{4h}, respectively) are incompatible with one another, as they are with the point symmetry of the crystallographic site on which they both sit (O_h) [Fig. 1(c,d)]. Consequently, the effective energy potential governing transverse vibrational motion—which, by analogy to better-understood NTE materials, is likely to be implicated in NTE—will not be constrained by symmetry and hence will vary from site to site throughout the defective lattice. Despite the differences in local symmetry between the **reo** nanodomains and **fcu** matrix, both phases retain their cubic symmetry on the unit cell level. The thermal expansion within each domain will therefore remain isotropic. Differences in thermal expansion between phases will lead to the development of thermal strains at the domain walls, which would in principle manifest as additional peak broadening on heating. The large strains produced by the densification precluded our measurement of this comparatively subtle effect. The effect of defect concentration on the average effective potential, its asymmetry, and its variance, collectively poses an interesting challenge for computational and theoretical methods of understanding NTE lattice dynamics in this system.

What we observe in practice is that our UiO-66(Hf) samples with higher defect concentrations actually show reduced NTE effects relative to defect-poor samples. The coefficients of thermal expansion determined from our variable-temperature X-ray powder diffraction measurements range systematically from $-70(2)$ to $-97(4)$ MK^{-1} as defect concentrations are reduced [Fig. 4(c)]. So any effect of increased flexibility arising from the reduced framework connectivity at high defect concentrations must be outweighed by considerations of densification and/or local symmetry. Whatever the microscopic origin for this defect dependence, we note that the chemical control over NTE behaviour we observe here would usually be associated with aliovalent substitution, as exploited in conventional solid-state NTE compounds (*e.g.* the $ZrV_xP_{2-x}O_7$ family[32]). That we can achieve similar control over the physical properties of MOFs through the use of defect chemistry is precisely the proof-of-principle needed to demonstrate that defects might be used as a design element in their own right when engineering MOFs with targeted properties.

Concluding remarks

One of the key motivations for exploring NTE behaviour in defective MOFs was always that NTE is very often diagnostic of other lattice-dynamical anomalies, such as pressure-induced amorphisation and/or mechanical softening. Consequently the variation in magnitude of NTE documented in this study implies that changes in defect concentrations are likely also to affect the mechanical stability of MOFs in high pressure environments and their resistance to amorphisation. We find that this relationship is likely to be entirely counterintuitive for defective UiOs (at the very least): reduced NTE nearly always translates to greater pressure stability, and so higher defect concentrations might now be expected actually to frustrate amorphisation rather than to encourage it. In turn this may provide a mechanism to improve the mechanical properties of MOFs, such as their machinability and durability under operating conditions. Whether this bizarre relationship of defect-driven toughening actually holds in practice remains to be shown, but what is clear even at this stage is that further studies of defect-property relationships in MOFs are set to challenge our collective intuition of the physical consequences of structural disorder.

While we have focussed heavily on the implications of variable NTE in the UiO-66 system, we note for completeness that the control over framework densification evident in Fig. 4(b) may highlight another means of exploiting defects in MOFs. It has recently been shown that densification of guest-containing MOFs through pressure or mechanical grinding can be an effective method of immobilising dangerous species (*e.g.* radioactive iodine).[49,50] Perhaps the incorporation of defects might simultaneously increase capacity for adsorption of these guest molecules while also trapping these molecules more efficiently as a result of an increased density change on framework collapse.

In summary, we have shown for the first time how the thermomechanical properties of a MOF can be systematically varied *via* controlled incorporation of defects. The thermomechanical properties we observe in defective UiO-66(Hf) are extremely unusual, and include the strongest isotropic NTE effect ever observed for a MOF. This property in itself may have application in counteracting the positive thermal expansion behaviour of other engineering materials. Yet the most important result remains a conceptual one: namely that defects might now realistically play a key role in the design of new classes of functional MOFs.

Methods

Preparation of defective UiO-66(Hf)

We synthesised defective UiO-66(Hf) using the method described for large scale synthesis in ref. 6. The most defective sample was synthesised as follows. $HfCl_4$ (3 mmol, 99.9% (metals basis, $<0.5\%$ Zr), Alfa Aesar) and terephthalic acid (2.5 mmol, Sigma Aldrich) were added to a 250 ml Schott bottle and dissolved in *N*,*N*-dimethylformamide (DMF) (40 ml, Sigma Aldrich). This mixture was sonicated until the metal and ligand had dissolved and then formic acid (20 ml, 95%, Sigma Aldrich)

 This journal is © the Owner Societies 2015

Published on 02 April 2015. Downloaded by University of Oxford on 04/04/2016 18:20:41.

was added. The bottle was sealed then placed in an oven at 120 °C for 24 h. The product was isolated by filtration, washed (DMF) and then heated at 60 °C with DMF for 3 days to ensure the removal any residual ligand. Further impurities were removed from the filtered product by Soxhlet extraction (ethanol). The purified product was then dried at 150° for 24 h *in vacuo*. Less defective samples were prepared using larger concentrations of terephthalic acid: 3.0, 4.0, 4.5 and 5.0 mmol. All samples were loaded in 0.5 mm quartz glass capillaries with Al_2O_3 as an internal temperature standard (*ca.* 50% by mass) and sealed with cotton wool.

Thermogravimetric analysis

Thermogravimetric analysis was carried using a Mettler Toledo TGA/DSC 1 System, heating from 30 °C to 650 °C at a rate of 20 °C min^{-1} before cooling to room temperature.

Variable-temperature synchrotron X-ray diffraction measurements

Variable temperature X-ray powder diffraction measurements were carried out on the I11 beamline at the Diamond Light Source (λ = 0.82562 Å) using a position-sensitive detector with a Cyberstar hot air blower.[51,52] Analysis of the data was carried out using Topas Academic version 4.1.[53] The purity of all samples was checked using a Rietveld fit to the reported structure for UiO-66(Zr),[54] with Hf substituted for Zr. The additional primitive peaks were fitted using a secondary Pawley phase with the same lattice parameter but with additional size broadening as described in ref. 6. Lattice parameters were determined using Pawley refinement in space group $Fm\bar{3}m$, omitting the low-angle region where the broad primitive reflections make an important contribution. The Pawley refinements were carried out using the previous temperature's refined parameters as the input for the next refinement.

Quantum mechanical calculations

All structures were fully relaxed by optimizing both atomic positions and unit cell parameters. We performed quantum mechanical calculations in the density functional theory approach with localized basis sets (CRYSTAL14 code[55]). We used the B3LYP hybrid exchange–correlation functional[56] and all-electron basis sets for all atoms,[25] except Hf for which we used a small relativistic effective core potential with 12 outer electrons considered explicitly.[57] Full methodological details can be found in ref. 6 and 57. The optimised structures are included as crystallographic information files as part of the ESI.†

Acknowledgements

M.J.C., J.A.H., and A.L.G. gratefully acknowledge financial support from the ERC (Grant No. 279705) and EPSRC (Grant No. EP/G004528/2). This work was performed using HPC resources from GENCI-IDRIS (grant x2015087069). We thank Diamond Light Source for access to beamline I11 (Proposal Number EE9940-1).

References

1 C. Tealdi, P. Mustarelli and M. S. Islam, *Adv. Funct. Mater.*, 2010, **20**, 3874–3880.
2 J. C. Ruiz-Morales, J. Canales-Vázquez, C. Savaniu, D. Marrero-López, W. Zhou and J. T. S. Irvine, *Nature*, 2006, **439**, 568–571.
3 E. S. Božin, S. J. Billinge, G. H. Kwei and H. Takagi, *Phys. Rev. B*, 1999, **59**, 4445–4454.
4 J. Bobroff, H. Alloul, S. Ouazi, P. Mendels, A. Mahajan, N. Blanchard, G. Collin, V. Guillen and J.-F. Marucco, *Phys. Rev. Lett.*, 2002, **89**, 157002.
5 M. Paściak, T. R. Welberry, J. Kulda, M. Kempa and J. Hlinka, *Phys. Rev. B*, 2012, **85**, 224109.
6 M. J. Cliffe, W. Wan, X. Zou, P. A. Chater, A. K. Kleppe, M. G. Tucker, H. Wilhelm, N. P. Funnell, F.-X. Coudert and A. L. Goodwin, *Nat. Commun.*, 2014, **5**, 4176.
7 S. Horike, S. Shimomura and S. Kitagawa, *Nat. Chem.*, 2009, **1**, 695–704.
8 R. Banerjee, A. Phan, B. Wang, C. Knobler, H. Furukawa, M. O'Keeffe and O. M. Yaghi, *Science*, 2008, **319**, 939–943.
9 A. B. Cairns and A. L. Goodwin, *Chem. Soc. Rev.*, 2013, **42**, 4881–4893.
10 J. Park, Z. U. Wang, L.-B. Sun, Y.-P. Chen and H.-C. Zhou, *J. Am. Chem. Soc.*, 2012, **134**, 20110–20116.
11 F. Vermoortele, B. Bueken, G. Le Bars, B. Van de Voorde, M. Vandichel, K. Houthoofd, A. Vimont, M. Daturi, M. Waroquier, V. Van Speybroeck, C. Kirschhock and D. E. De Vos, *J. Am. Chem. Soc.*, 2013, **135**, 11465–11468.
12 G. Barin, V. Krungleviciute, O. Gutov, J. T. Hupp, T. Yildirim and O. K. Farha, *Inorg. Chem.*, 2014, **53**, 6914–6919.
13 Z. Fang, J. P. Dürholt, M. Kauer, W. Zhang, C. Lochenie, B. Jee, B. Albada, N. Metzler-Nolte, A. Pöppl, B. Weber, M. Muhler, Y. Wang, R. Schmid and R. A. Fischer, *J. Am. Chem. Soc.*, 2014, **136**, 9627–9636.
14 S. Jakobsen, D. Gianolio, D. S. Wragg, M. H. Nilsen, H. Emerich, S. Bordiga, C. Lamberti, U. Olsbye, M. Tilset and K. P. Lillerud, *Phys. Rev. B*, 2012, **86**, 125429.
15 J. M. Ogborn, I. E. Collings, S. A. Moggach, A. L. Thompson and A. L. Goodwin, *Chem. Sci.*, 2012, **3**, 3011–3017.
16 I. E. Collings, M. G. Tucker, D. A. Keen and A. L. Goodwin, *CrystEngComm*, 2014, **16**, 3498–3506.
17 W. Zhou, H. Wu, T. Yildirim, J. R. Simpson and A. R. Hight Walker, *Phys. Rev. B*, 2008, **78**, 054114.
18 Y. Wu, A. Kobayashi, G. J. Halder, V. K. Peterson, K. W. Chapman, N. Lock, P. D. Southon and C. J. Kepert, *Angew. Chem., Int. Ed.*, 2008, **47**, 8929–8932.
19 Y. Wu, V. K. Peterson, E. Luks, T. A. Darwish and C. J. Kepert, *Angew. Chem., Int. Ed.*, 2014, **53**, 5175–5178.
20 H. Wu, Y. S. Chua, V. Krungleviciute, M. Tyagi, P. Chen, T. Yildirim and W. Zhou, *J. Am. Chem. Soc.*, 2013, **135**, 10525–10532.
21 M. J. Katz, Z. J. Brown, Y. J. Colón, P. W. Siu, K. A. Scheidt, R. Q. Snurr, J. T. Hupp and O. K. Farha, *Chem. Commun.*, 2013, **49**, 9449–9451.
22 S. Øien, D. Wragg, H. Reinsch, S. Svelle, S. Bordiga, C. Lamberti and K. P. Lillerud, *Cryst. Growth Des.*, 2014, **14**, 5370–5372.

Published on 02 April 2015. Downloaded by University of Oxford on 04/04/2016 18:20:41.

23 A. D. Wiersum, E. Soubeyrand-Lenoir, Q. Yang, B. Moulin, V. Guillerm, M. B. Yahia, S. Bourrelly, A. Vimont, S. Miller, C. Vagner, M. Daturi, G. Clet, C. Serre, G. Maurin and P. L. Llewellyn, *Chem. – Asian J.*, 2011, **6**, 3270–3280.
24 G. C. Shearer, S. Forselv, S. Chavan, S. Bordiga, K. Mathisen, M. Bjørgen, S. Svelle and K. P. Lillerud, *Top. Catal.*, 2013, **56**, 770–782.
25 L. Valenzano, B. Civalleri, S. Chavan, S. Bordiga, M. H. Nilsen, S. r. Jakobsen, K. P. Lillerud and C. Lamberti, *Chem. Mater.*, 2011, **23**, 1700–1718.
26 M. Vandichel, J. Hajek, F. Vermoortele, M. Waroquier, D. E. De Vos and V. Van Speybroeck, *CrystEngComm*, 2014, DOI: 10.1039/C4CE01672F.
27 G. C. Shearer, S. Chavan, J. Ethiraj, J. G. Vitillo, S. Svelle, U. Olsbye, C. Lamberti, S. Bordiga and K. P. Lillerud, *Chem. Mater.*, 2014, **26**, 4068–4071.
28 V. Haigis, Y. Belkhodja, F.-X. Coudert, R. Vuilleumier and A. Boutin, *J. Chem. Phys.*, 2014, **141**, 064703.
29 R. S. Krishnan, R. Srinivasan and S. Devanarayanan, *Thermal Expansion of Crystals*, Pergamon, Oxford, 1979.
30 A. L. Goodwin, M. Calleja, M. J. Conterio, M. T. Dove, J. S. O. Evans, D. A. Keen, L. Peters and M. G. Tucker, *Science*, 2008, **319**, 794–797.
31 C. Martinek and F. A. Hummel, *J. Am. Ceram. Soc.*, 1968, **51**, 227–228.
32 V. Korthuis, N. Khosrovani, A. W. Sleight, N. Roberts, R. Dupree and W. W. Warren Jr., *Chem. Mater.*, 1995, **7**, 412–417.
33 S. E. Tallentire, F. Child, I. Fall, L. Vella-Zarb, I. R. Evans, M. G. Tucker, D. A. Keen, C. Wilson and J. S. O. Evans, *J. Am. Chem. Soc.*, 2013, **135**, 12849–12856.
34 E. E. Rodriguez, A. Llobet, Th. Proffen, B. C. Melot, R. Seshadri, P. B. Littlewood and A. K. Cheetham, *J. Appl. Phys.*, 2009, **105**, 114901.
35 T. Chatterji, P. F. Henry, R. Mittal and S. Chaplot, *Phys. Rev. B*, 2008, **78**, 134105.
36 B. K. Greve, K. L. Martin, P. L. Lee, P. J. Chupas, K. W. Chapman and A. P. Wilkinson, *J. Am. Chem. Soc.*, 2010, **132**, 15496–15498.
37 W. Tiano, M. Dapiaggi and G. Artioli, *J. Appl. Crystallogr.*, 2003, **36**, 1461–1463.
38 A. L. Goodwin and C. J. Kepert, *Phys. Rev. B*, 2005, **71**, 140301.
39 A. L. Goodwin, K. W. Chapman and C. J. Kepert, *J. Am. Chem. Soc.*, 2005, **127**, 17980–17981.
40 K. W. Chapman, P. J. Chupas and C. J. Kepert, *J. Am. Chem. Soc.*, 2006, **128**, 7009–7014.
41 A. E. Phillips, A. L. Goodwin, G. J. Halder, P. D. Southon and C. J. Kepert, *Angew. Chem., Int. Ed.*, 2008, **47**, 1396–1399.
42 L. Bouëssel du Bourg, A. U. Ortiz, A. Boutin and F.-X. Coudert, *APL Mater.*, 2014, **2**, 124110.
43 N. Lock, Y. Wu, M. Christensen, L. J. Cameron, V. K. Peterson, A. J. Bridgeman, C. J. Kepert and B. B. Iversen, *J. Phys. Chem. C*, 2010, **114**, 16181–16186.
44 N. Lock, M. Christensen, Y. Wu, V. K. Peterson, M. K. Thomsen, R. O. Piltz, A. J. Ramirez-Cuesta, G. J. McIntyre, K. Norén, R. Kutteh, C. J. Kepert, G. J. Kearley and B. B. Iversen, *Dalton Trans.*, 2013, **42**, 1996–2007.
45 L. H. N. Rimmer, M. T. Dove, A. L. Goodwin and D. C. Palmer, *Phys. Chem. Chem. Phys.*, 2014, **16**, 21144–21152.
46 A. L. Goodwin, *Phys. Rev. B*, 2006, **74**, 134302.
47 M. F. Thorpe, *Encyclopedia of Complexity and Systems Science*, Springer, New York, 2009, pp. 6013–6024.
48 P. Lightfoot, D. A. Woodcock, M. J. Maple, L. A. Villaescusa and P. A. Wright, *J. Mater. Chem.*, 2001, **11**, 212–216.
49 T. D. Bennett, P. J. Saines, D. A. Keen, J.-C. Tan and A. K. Cheetham, *Chem. – Eur. J.*, 2013, **19**, 7049–7055.
50 D. F. Sava, M. A. Rodriguez, K. W. Chapman, P. J. Chupas, J. A. Greathouse, P. S. Crozier and T. M. Nenoff, *J. Am. Chem. Soc.*, 2011, **133**, 12398–12401.
51 S. P. Thompson, J. E. Parker, J. Potter, T. P. Hill, A. Birt, T. M. Cobb, F. Yuan and C. C. Tang, *Rev. Sci. Instrum.*, 2009, **80**, 075107.
52 S. P. Thompson, J. E. Parker, J. Marchal, J. Potter, A. Birt, F. Yuan, R. D. Fearn, A. R. Lennie, S. R. Street and C. C. Tang, *J. Synchrotron Radiat.*, 2011, **18**, 637–648.
53 A. Coelho, *TOPAS - Academic: General Profile and Structure Analysis Software for Powder Diffraction Data., Version 4.1*, Brisbane, Australia, 2007.
54 J. H. Cavka, S. Jakobsen, U. Olsbye, N. Guillou, C. Lamberti, S. Bordiga and K. P. Lillerud, *J. Am. Chem. Soc.*, 2008, **130**, 13850–13851.
55 R. Dovesi, R. Orlando, B. Civalleri, C. Roetti, V. R. Saunders and C. M. Zicovich-Wilson, *Z. Kristallogr.*, 2005, **220**, 571–573.
56 A. D. Becke, *J. Chem. Phys.*, 1993, **98**, 5648–5652.
57 A. U. Ortiz, A. Boutin, A. H. Fuchs and F.-X. Coudert, *J. Chem. Phys.*, 2013, **138**, 174703.

 This journal is © the Owner Societies 2015

Volume 45 | Number 10 | 14 March 2016 | Pages 4043–4440

Dalton Transactions

An international journal of inorganic chemistry

www.rsc.org/dalton

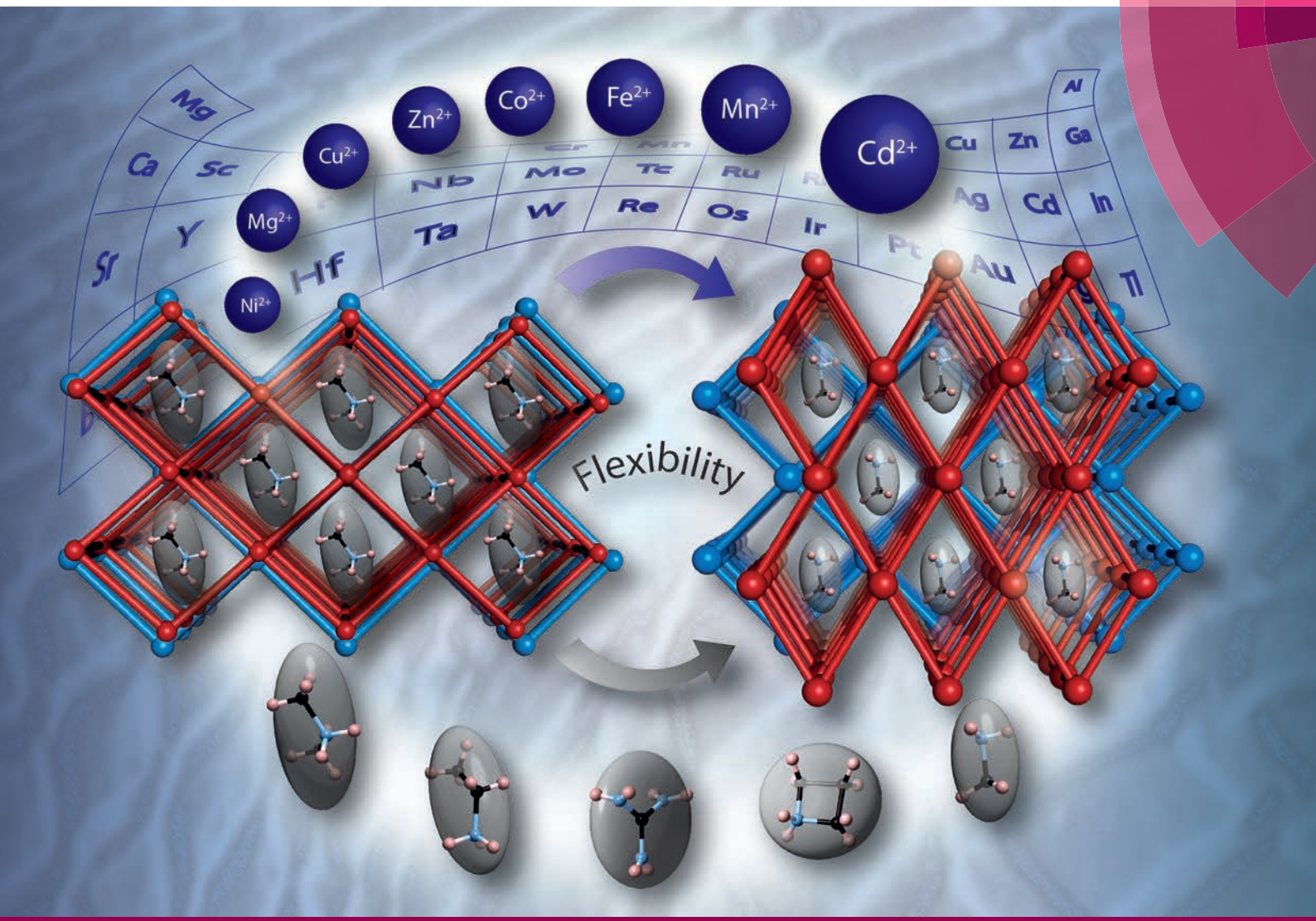

Themed issue: Flexibility and Disorder in Metal-Organic Frameworks

ISSN 1477-9226

ROYAL SOCIETY OF CHEMISTRY

PAPER
Andrew L. Goodwin *et al.*
Compositional dependence of anomalous thermal expansion in perovskite-like ABX_3 formates

175 YEARS

Dalton Transactions

PAPER

View Article Online
View Journal | View Issue

Cite this: *Dalton Trans.*, 2016, **45**, 4169

Compositional dependence of anomalous thermal expansion in perovskite-like ABX_3 formates†

Ines E. Collings,[a,b] Joshua A. Hill,[a] Andrew B. Cairns,[a] Richard I. Cooper,[a] Amber L. Thompson,[a] Julia E. Parker,[c] Chiu C. Tang[c] and Andrew L. Goodwin*[a]

Received 24th August 2015,
Accepted 7th October 2015

DOI: 10.1039/c5dt03263f

www.rsc.org/dalton

The compositional dependence of thermal expansion behaviour in 19 different perovskite-like metal–organic frameworks (MOFs) of composition $[A^{I}][M^{II}(HCOO)_3]$ (A = alkylammonium cation; M = octahedrally-coordinated divalent metal) is studied using variable-temperature X-ray powder diffraction measurements. While all systems show essentially the same type of thermomechanical response—irrespective of their particular structural details—the magnitude of this response is shown to be a function of A^{I} and M^{II} cation radii, as well as the molecular anisotropy of A^{I}. Flexibility is maximised for large M^{II} and small A^{I}, while the shape of A^{I} has implications for the direction of framework hingeing.

Published on 08 October 2015. Downloaded on 04/04/2016 18:18:19.

1. Introduction

The discovery that many metal–organic frameworks (MOFs) respond mechanically to external stimuli in extreme and counter-intuitive ways (*e.g.* negative thermal expansion (NTE),[1,2] negative compressibility,[3–5] breathing transitions,[6,7] and amorphisation[8,9]) has focussed attention within the field on establishing composition–property relationships. The hope—as in much of MOF science—is to develop design strategies that will allow the targeted synthesis of MOFs with specific and optimised physical properties.[10,11] Given the enormous structural and compositional diversity of this family, the task of establishing design rules has focussed on two separate areas: namely, determining in turn the roles of network *topology/geometry* and network *composition* in governing elastic response.

With regard to the former, it is now well established that certain network connectivities intrinsically favour counter-intuitive mechanical responses.[12–16] Perhaps the best known example is the wine-rack topology, which is associated with anomalous elastic behaviour across a large variety of chemically-distinct MOF families.[17–23] For a given network topology, changes in geometry (*e.g.*, network angles) can invert the type of anisotropy but the basic mechanical response remains the same.[24,25]

With regard to network composition, variation of the chemical makeup of MOFs with the same topology will usually influence only the magnitude of mechanical response.[20,26–28] For instance, nanoindentation studies of the perovskite-structured $[(CH_3)_2NH_2][M(HCOO)_3]$ family (M = Mn, Co, Ni, Zn) showed a strong relationship between ligand field stabilisation energy of the transition metal dication and the mechanical stiffness of the corresponding MOF.[29] In the related systems $[C(NH_2)_3][Mn(HCOO)_3]$ and $[(CH_2)_3NH_2][Mn(HCOO)_3]$, the hydrogen-bonding strength of the extra-framework alkylammonium cation was found to direct the stiffness and flexibility of the two structures.[28] In all cases, the fundamental mechanism of elastic response is unchanged by chemical substitution, with the degree of flexibility scaling inversely with strength of interaction.[4] Precisely the same conclusion has been reached in similar studies of inorganic frameworks. For example, an investigation of the thermal expansion response of Prussian Blue analogues and related lanthanide hexacyanocobaltates showed that cation size correlates with the magnitude of NTE.[30–32] Likewise, cation size also plays an important role in the magnitudes of thermal expansion behaviour in the family of frameworks related to $NaZr_2(PO_4)_3$.[33] Perhaps the only exceptions to these general rules are in instances where chemical substitution alters the nature of the dominant chemical interaction within a particular MOF.[17,34]

One particularly important way in which dense MOFs can differ from "conventional" ceramic frameworks is in their capacity to accommodate extra-framework ions that are molecular rather than monatomic in nature. The added complexity of cation *asphericity* is conceptually related to the symmetry-lowering effect of second-order Jahn–Teller instabilities and

[a]*Department of Chemistry, University of Oxford, Inorganic Chemistry Laboratory, South Parks Road, Oxford OX1 3QR, UK. E-mail: andrew.goodwin@chem.ox.ac.uk; Fax: +44 (0)1865 274690; Tel: +44 (0)1865 272137*
[b]*Laboratory of Crystallography, University of Bayreuth, D-95440 Bayreuth, Germany*
[c]*Diamond Light Source Ltd., Harwell Science and Innovation Campus, Didcot, Oxfordshire OX11 0DE, UK*

†Electronic supplementary information (ESI) available: Gua-Cd single-crystal X-ray diffraction, Rietveld fits, variable-temperature lattice parameters, XBU r and θ equations, and A-site cation size details. CCDC 1420162–1420165. For ESI and crystallographic data in CIF or other electronic format see DOI: 10.1039/C5DT03263F

Published on 08 October 2015. Downloaded on 04/04/2016 18:18:19.

may play a key role in the lattice dynamics of high-profile hybrid frameworks such as $[CH_3NH_3]PbI_3$.[35] Yet, to the best of our knowledge, there are no systematic studies of the relationship between counterion shape and mechanical response in MOF-type systems.

In this paper, we use thermal expansion measurements to explore the relationship between framework flexibility and chemical composition across 19 MOFs drawn from the widely-studied family of alkylammonium transition-metal ("ABX_3") formates. These compounds have the same general formula $[A^I][M^{II}(HCOO)_3]$ and are structurally related to the perovskites [Fig. 1]. The larger M···M separation in formates relative to perovskites (~6 Å *vs.* 4 Å) allows incorporation of molecular cations within the framework cavities. As in the perovskites there is scope for substitution on both the "twelve-coordinate" A-site and on the transition-metal B-site. While the cation charges on each of these sites are fixed at 1+ (A) and 2+ (B) in the formates (unlike perovskites), there is now an additional degree of freedom in terms of the molecular shape at the A-site.

Their relative structural simplicity makes these compounds ideal candidates for a composition/property study such as ours. But the broader family is also of significance from a functional materials viewpoint. ABX_3 formates exhibit a variety of useful properties, including ferroelectricity,[36–38,44,45] ferroelasticity,[39] and even multiferroic behaviour.[40–43] Composition/property studies of the ferroelectric response in the $A^I = NH_4^+$ or $(CH_3)_2NH_2^+$ members points to the different possible effects of substitution on the alkylammonium site and the transition-metal site.[36,45] Substitution at the A-site allows tuning of the ferroelectric polarisation,[46,47] whereas variation in transition-metal affects the ferroelectric transition temperature T_c.[36,38,45,48] In this context, framework flexibility may have important implications for A-site orientational ordering and/or mechanisms of accommodating the large strains induced during ferroelectric/paraelectric switching. So this study has the additional relevance beyond establishing composition–property relationships of exploring the role of flexibility in ferroelectric MOFs.

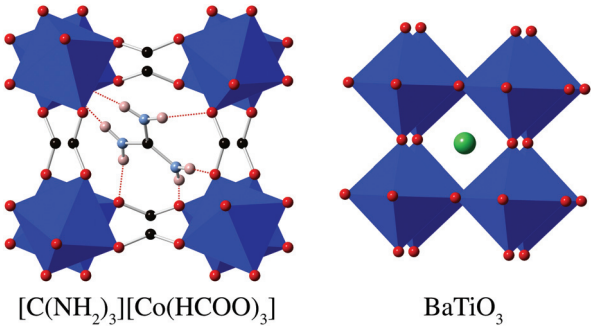

Fig. 1 ABX_3 frameworks of $[C(NH_2)_3][Co(HCOO)_3]$ and $BaTiO_3$. The hydrogen bonding in $[C(NH_2)_3][Co(HCOO)_3]$ is shown with dotted red lines. The Co^{2+} and Ti^{4+} coordination environments are represented by polyhedra.

Our paper is arranged as follows. We begin by summarising the synthesis and characterisation techniques used in our study. In the results section that follows, we report the thermal expansion properties of the various ABX_3 formates we study. Using the mechanical building unit (XBU) abstraction developed in ref. 4, we reduce the experimental lattice parameter data we measure to two characteristic values for each system: namely, the expansivities of the framework struts and of the intra-framework angles. By comparing the magnitudes of these two parameters as a function of framework composition, we are able to establish composition/flexibility relationships for this family.

2. Experimental methods

2.1. Sample preparation

The 19 structures we investigated share the composition $[A^I][M^{II}(HCOO)_3]$, where A^I = CH_3NH_3, $(CH_3)_2NH_2$, $CH_3CH_2NH_3$, $(CH_2)_3NH_2$, $C(NH_2)_3$ and M^{II} = Mg, Mn, Fe, Co, Ni, Cu, Zn, Cd [Fig. 2]. For simplicity, the $[CH_3NH_3][M(HCOO)_3]$ structures will be referred to as $MeNH_3$–M, where M is the metal cation. Likewise we refer to $[CH_3CH_2NH_3][M(HCOO)_3]$ as $EtNH_3$–M, $[(CH_3)_2NH_2][M(HCOO)_3]$ as Me_2NH_2–M, $[(CH_2)_3NH_2][M(HCOO)_3]$ as Aze–M (*i.e.*, Aze = azetidinium), and $[C(NH_2)_3][M(HCOO)_3]$ as Gua–M (*i.e.*, Gua = guanidinium).

Our general strategy for preparing $[A][M(HCOO)_3]$ samples was as follows. Methanolic solutions of HCOOH (0.5 M, 5 mL) and of the (usually) neutral A-site amine (0.5 M, 5 mL) were mixed at the bottom of a glass vial. Onto this solution methanol (2 mL) was carefully added, followed by a methanolic solution of the transition metal nitrate (0.1 M, 8 mL).[49] The tube was then sealed and kept undisturbed. Following precipitation of the product (often as single crystals), the solution was

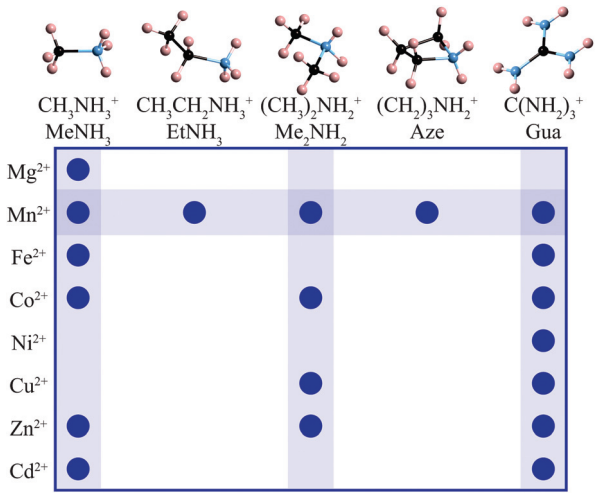

Fig. 2 Compositions of the various ABX_3 formates used in our study. For the structural representations of the different A-site cations given at the top of the table, N atoms are shown in blue, C atoms in black, and H atoms in pink. The shaded regions of the table show the four compositional studies possible in which one or other of the A and B components is kept constant.

This journal is © The Royal Society of Chemistry 2016

Published on 08 October 2015. Downloaded on 04/04/2016 18:18:19.

filtered off, and the sample was washed with methanol, dried in air, and ground. The precise species used in the methanolic amine preparation were: methylamine (Acros Organics, 2 M solution in methanol), dimethylamine (Sigma Aldrich, 2 M solution in methanol), ethylamine (Sigma Aldrich, 2 M solution in methanol), azetidine (Sigma Aldrich, 98%), and guanidine carbonate (Aldrich, 99%).

2.2. X-ray powder diffraction

Synchrotron X-ray powder diffraction data were collected using the I11 beamline[50] at the Diamond Light Source (λ = 0.82715 Å) for each of the 19 different ABX_3 compositions given above. Finely-ground powder samples were loaded into 0.5 mm diameter borosilicate capillaries and mounted on the diffractometer. The Cryostream Plus from Oxford Cryosystems was used to vary the temperature between 110 and 300 K, and diffraction patterns were collected using the Mythen2 position sensitive detector (PSD). For each sample, data collection started at 300 K, before cooling to 110 K at a rate of 5 K min^{-1}. To minimise the effects of beam damage, data were not collected continuously but rather at intervals of 10 K during this cooling process. Once the minimum temperature was achieved, the goniometer was translated to allow a fresh part of the sample to be illuminated during heating. The sample temperature was then increased to 300 K at a rate of 6 K min^{-1}, with data collected at intervals of 10 K. For all data collected, diffraction patterns were obtained using two separate measurements (5 s each) at different angular orientations offset by 0.25° that were subsequently merged.[51]

Structural models were determined from the powder diffraction patterns using Rietveld refinement as implemented in the TOPAS software (academic version 4.1).[52] For most of the systems studied, the corresponding crystal structures are already well known; the literature values were used as a starting model for Rietveld refinement.[36,37,49,53–56] To the best of our knowledge, the structures of $MeNH_3$–M (M = Mg, Fe, Co, Zn, Cd) have not been determined previously; we found these to be isostructural to $MeNH_3$–Mn and we used the known structure of this compound as a starting point for Rietveld refinement. In the case of Gua–Cd—which is also previously uncharacterised—we made use of both single-crystal X-ray diffraction‡ and our synchrotron X-ray powder diffraction measurements to determine a relevant structural model (see ESI† for further details).

Our Rietveld refinements made use of a number of chemically-informed restraints and constraints. Bonding restraints were applied to the metal–formate bonds, while rigid bodies were used to model the organic molecular units (*i.e.* the A-site cations and the formate ligands). The bond lengths and internal angles defining the rigid bodies were refined for the initial temperature point. After refinement of the ambient-temperature structure for all $[A][M(HCOO)_3]$ compounds, subsequent diffraction patterns were refined sequentially using the refinement model from the previous temperature as a starting model. In these sequential refinements, the free variables were: a polynomial background function, the lattice parameters, the atomic coordinates, a scale factor, and peak shape parameters. The molecular geometries of the formate anions and the A-site cations were modelled as rigid bodies with translational and rotational degrees of freedom. The Rietveld fits to the ambient and 110 K temperature points are given as ESI.†

3. Results and discussion

3.1. Thermal expansivities and XBU analysis

Our determination of the thermal expansion characteristics of ABX_3 formates is based on the interpretation of temperature-dependent lattice parameters extracted *via* Rietveld refinement of synchrotron X-ray powder diffraction data. While the various phases we study are isostructural in the sense that their topologies are identical, they adopt a variety of different space group symmetries. The various crystal phases included in our study are shown in Fig. 3. What is immediately clear is that direct comparison of lattice expansivities from one system to another is not physically meaningful, since the various structures involve different relationships between the perovskite lattice and the unit cell geometry.

Our solution to this problem is to interpret the lattice parameter changes for a given system in terms of two fundamental XBUs:[4] the framework strut length r and the intra-framework angle θ. For systems of sufficiently high symmetry (*e.g.* the rhombohedral structures of Me_2NH_2–Mn/Co/Zn and Gua–Cd) there is a one-to-one mapping between the lattice parameters and XBU coordinates r, θ. In other words, the elastic behaviour of the framework is completely described by the propensity for hingeing (changes in θ) and network deformation (changes in r). For lower-symmetry structures, there will be more than one crystallographically-distinct value of r and/or θ; we use an average value in order to facilitate comparison between different systems (see ESI† for further details). This means that the relationship between lattice parameters and r, θ is approximate rather than exact, but we find that in practice the degree of approximation is $\lesssim$10%, which is sufficient for our analysis.

We demonstrate this approach using $MeNH_3$–Mn as a representative example. This compound has the *Pnma* structure shown in the leftmost panel of Fig. 3. The relative changes in lattice parameters determined using Rietveld refinement against our experimental X-ray powder diffraction are shown in Fig. 4. These reveal that, on heating, the framework expands

‡Single-crystal X-ray diffraction data for Gua-Cd were collected using a Nonius KappaCCD diffractometer or an Oxford Diffraction (Agilent) SuperNova diffractometer fitted with an Oxford Cryosystems Cryostream 600 Series/700 Plus open flow nitrogen cooling device. DENZO/SCALEPACK[68] or CrysAlisPro were used for data collection and reduction as appropriate. In general, the structures were solved *ab initio* using SIR92[69] although coordinates from 150 K were used as a starting model for the other temperatures. All structures were refined with full-matrix least-squares on F^2 using CRYSTALS.[63,70] Hydrogen atoms were generally visible in the difference Fourier map and treated in the usual manner.[71] Full structural data have been submitted to the CCDC as numbers 1420162–1420165.

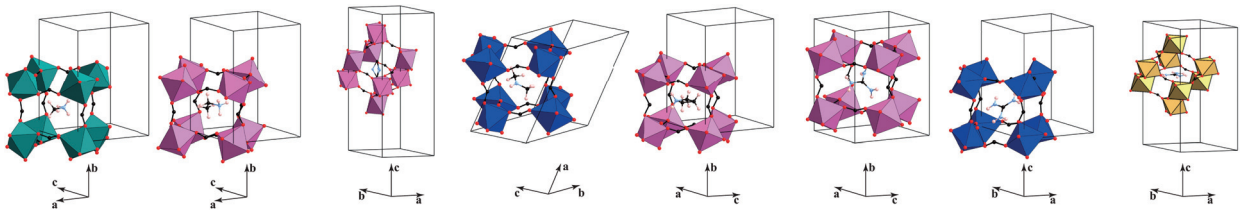

Fig. 3 Relationship between unit cell and perovskite-like cubic structural unit for each of the crystallographically-distinct phases in our study. In each case, the transition-metal coordination polyhedra are represented as filled octahedra. C atoms are shown in black, N atoms in blue, O atoms in red, and H atoms in pink.

Published on 08 October 2015. Downloaded on 04/04/2016 18:18:19.

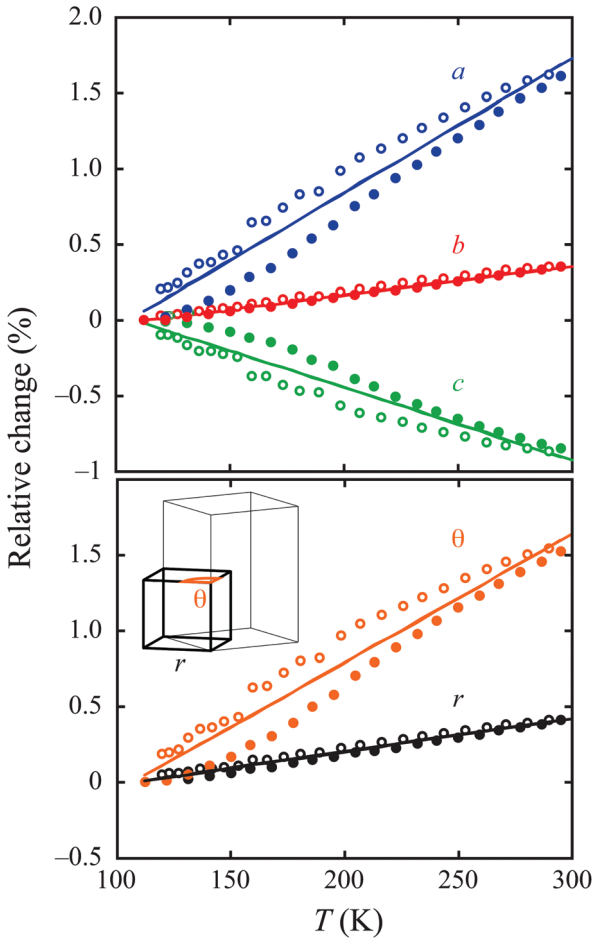

Fig. 4 Thermal expansion behaviour of $MeNH_3$–Mn, represented in terms of the temperature dependence of lattice parameters (top panel) and XBUs (bottom panel). Data collected during cooling are shown as open circles; those collected during heating are shown as filled circles. The discrepancy between cooling and heating runs likely reflects a combination of beam damage and thermal lag.

rapidly along the *a*-axis and contracts almost as rapidly along the *c*-axis; this collective behaviour corresponds to hingeing of the framework as discussed elsewhere.[3] The *b*-axis length is unaffected by framework hingeing, and its modest expansion with temperature reflects the intrinsic positive thermal expansion characteristic of M–formate–M linkages.[4] We quantify the magnitude of thermal response in terms of the coefficients of thermal expansion

$$\alpha = \frac{1}{\ell}\frac{\mathrm{d}\ell}{\mathrm{d}T}, \quad (1)$$

to give α_a = +88(3) MK^{-1}, α_b = +19.5(4) MK^{-1} and α_c = −49(2) MK^{-1}.[57]

For this particular structure, the projection from lattice parameter coordinates onto XBUs is given by the pair of equations

$$r = \frac{1}{3}\left(\frac{b}{2} + \sqrt{a^2 + c^2}\right), \quad (2)$$

$$\theta = 2\tan^{-1}\left(\frac{a}{c}\right). \quad (3)$$

The corresponding change in XBU magnitude with temperature is shown in the bottom panel of Fig. 4, from which it is clear that the thermomechanical response is dominated by hingeing (changes in θ) rather than network deformation. The XBU coefficients of thermal expansion are α_r = +21.8(6) MK^{-1} and α_θ = +84(3) MK^{-1}. XBU projection equations for the various crystal structures of Fig. 3 are given as ESI.†

The extent of approximation in reducing the three lattice degrees of freedom to the two XBU degrees of freedom can be assessed by calculating values of α for the XBU-derived lattice parameters

$$a_{\mathrm{XBU}} = \frac{2r\tan(\theta/2)}{\sqrt{1+\tan^2(\theta/2)}} \quad (4)$$

$$b_{\mathrm{XBU}} = 2r \quad (5)$$

$$c_{\mathrm{XBU}} = \frac{2r}{\sqrt{1+\tan^2(\theta/2)}} \quad (6)$$

obtained *via* inversion of eqn (2) and (3): we find $\alpha_{a_{\mathrm{XBU}}}$ = +87(3) MK^{-1}, $\alpha_{b_{\mathrm{XBU}}}$ = +21.8(6) MK^{-1} and $\alpha_{c_{\mathrm{XBU}}}$ = −50(2) MK^{-1}. These are all equal within error to the original lattice coefficients of thermal expansion.

This journal is © The Royal Society of Chemistry 2016

Published on 08 October 2015. Downloaded on 04/04/2016 18:18:19.

Table 1 Lattice and XBU coefficients of thermal expansion for the 110–300 K temperature range, given in units of MK^{-1}. For orthorhombic and hexagonal structures $\alpha_1 = \alpha_a$, $\alpha_2 = \alpha_b$, $\alpha_3 = \alpha_c$; for monoclinic structures the α_i index represents the principal coefficients of thermal expansion.[57] The expansivities for Aze–Mn given here were determined for the orthorhombic cell characteristic of the ambient-temperature phase; see ESI for the principal-axis expansivities of the low-temperature monoclinic phase

A^+	M^{2+}	Space group	α_1	α_2	α_3	α_r	α_θ
$MeNH_3$	Mg	*Pnma*	54.5(1.3)	22.1(5)	−20.0(5)	20.1(5)	46.0(1.1)
	Mn	*Pnma*	88(3)	19.5(4)	−49(2)	21.8(6)	84(3)
	Fe	*Pnma*	74(2)	14.7(4)	−25.1(1.2)	22.5(6)	61(2)
	Co	*Pnma*	68.7(1.3)	22.3(4)	−28.8(6)	21.6(4)	61.1(1.2)
	Zn	*Pnma*	69(3)	18.9(9)	−34.6(1.0)	18.9(1.2)	65(3)
	Cd	*Pnma*	102(7)	15.0(1.4)	−61(7)	21.5(7)	100(8)
$EtNH_3$	Mn[a]	$Pn2_1a$	44.2(4)	33.2(4)	4.14(13)	28.4(3)	23.88(15)
Me_2NH_2	Mn	$R\bar{3}c$	4.5(5)	4.5(5)	60.4(1.3)	25.9(6)	24.2(6)
	Co	$R\bar{3}c$	10.6(2)	10.6(2)	46.5(1.0)	24.2(5)	15.5(3)
	Cu	$C2/c$	−14.3(1.0)	45.7(1.7)	57(3)	31.7(1.6)	24.7(6)
	Zn	$R\bar{3}c$	8.3(9)	8.3(9)	36.4(4)	18.9(1.9)	12.2(1.2)
Aze	Mn	*Pnma*	104(8)	15.3(1.2)	−21(6)	31.6(1.1)	−78(9)
Gua	Mn	*Pnna*	42.2(6)	30.0(4)	−10.6(3)	19.2(3)	−32.2(5)
	Fe	*Pnna*	33.1(4)	31.6(3)	−1.5(2)	20.2(2)	−21.2(3)
	Co	*Pnna*	36.6(6)	25.8(5)	−6.7(2)	17.5(3)	−26.3(4)
	Ni	*Pnna*	27.1(8)	22.4(6)	3.59(16)	17.1(5)	−14.3(4)
	Cu	$Pn2_1a$	45.9(1.8)	21.4(9)	1.4(8)	22.0(1.1)	−27.2(7)
	Zn	*Pnna*	30.7(1.9)	21.9(9)	−5.3(6)	14.9(7)	−21.9(1.4)
	Cd	$R\bar{3}c$	−16.8(9)	−16.8(9)	106(3)	16.3(3)	−43.7(1.3)

[a] For this phase, values of α were calculated using cooling data only.

The ABX_3 lattice and XBU expansivities determined from our entire ensemble of X-ray diffraction data and corresponding Rietveld fits are summarised in Table 1; the raw lattice parameter data from which these values were derived are given as ESI.† While the magnitudes of the lattice expansivities vary over two orders of magnitude, we find essentially the same basic thermomechanical response for all ABX_3 structures. For example, nearly all of the orthorhombic structures exhibit large positive thermal expansion (PTE) along the *a*-axis (27–104 MK^{-1}), moderate PTE along the *b*-axis (14.7–33 MK^{-1}), and NTE along the *c*-axis (−61 to −1.5 MK^{-1}).

3.2. Effect of variation in M^{2+}

In order to investigate the effect of M^{2+} variation on the mechanics of $[A][M(HCOO)_3]$ frameworks, we compare our results for the $MeNH_3$–M and Gua–M families—these are the two systems for which we have the greatest diversity of M^{2+} substitution. Fig. 5 presents graphically the relevant data from Table 1, organised according to the (Shannon) radii of the M^{2+} ions.[58] Two results are immediately obvious from consideration of the dependence of XBU expansivity on ionic radius. The first is that the value of α_r is essentially composition-independent; the second is that the magnitude of α_θ increases linearly with increasing M^{2+} radius.

The magnitude of α_r reflects the effect of increased thermal motion on the M···M separation across connected M–formate–M links. Our Rietveld refinements do not allow us to comment with certainty on the temperature-dependence of the position, orientation, and/or thermal displacement of the formate anions in the various compounds in the way that has allowed detailed analysis of thermal expansion effects in other dense MOFs.[13] Nevertheless a likely origin of the composition-independence of α_r is the balance between two competing effects: on the one hand, larger M^{2+} ions would allow greater vibrational motion of bridging formates (*i.e.*, lower vibrational frequencies);[59–61] on the other hand, the increased M···M separation for larger ions means that formate displacements have less effect on this separation *in relative terms*. So while it is likely that the thermal motion of formate ions increases with increasing M^{2+} radius, the relative effect on *r* as an XBU remains roughly constant.

By contrast, the value of α_θ represents the degree of hingeing flexibility in a given framework. The increase in flexibility we observe with increasing cation size could arise from several effects. First, the strength of the metal–formate coordination bond will decrease as larger metal cations are used,[59–62] which in turn facilitates the movement of this bond. This causes an enhancement of the framework flexibility towards framework hingeing, especially as the neighbouring formate linkers are now further apart within the coordination sphere of the metal cation. In previous compositional dependent studies of Prussian Blue analogues, the strength of the coordination bonds was important for tuning the transverse vibrations of the M–ligand–M strut.[30] Second, the larger unit cells obtained with larger metal cations may allow greater structural freedom due to the increased distances between intermolecular contacts. These two factors mean that small metal cations, such as Ni^{2+}, will have (i) short and strong M–O bonds, restricting

Published on 08 October 2015. Downloaded on 04/04/2016 18:18:19.

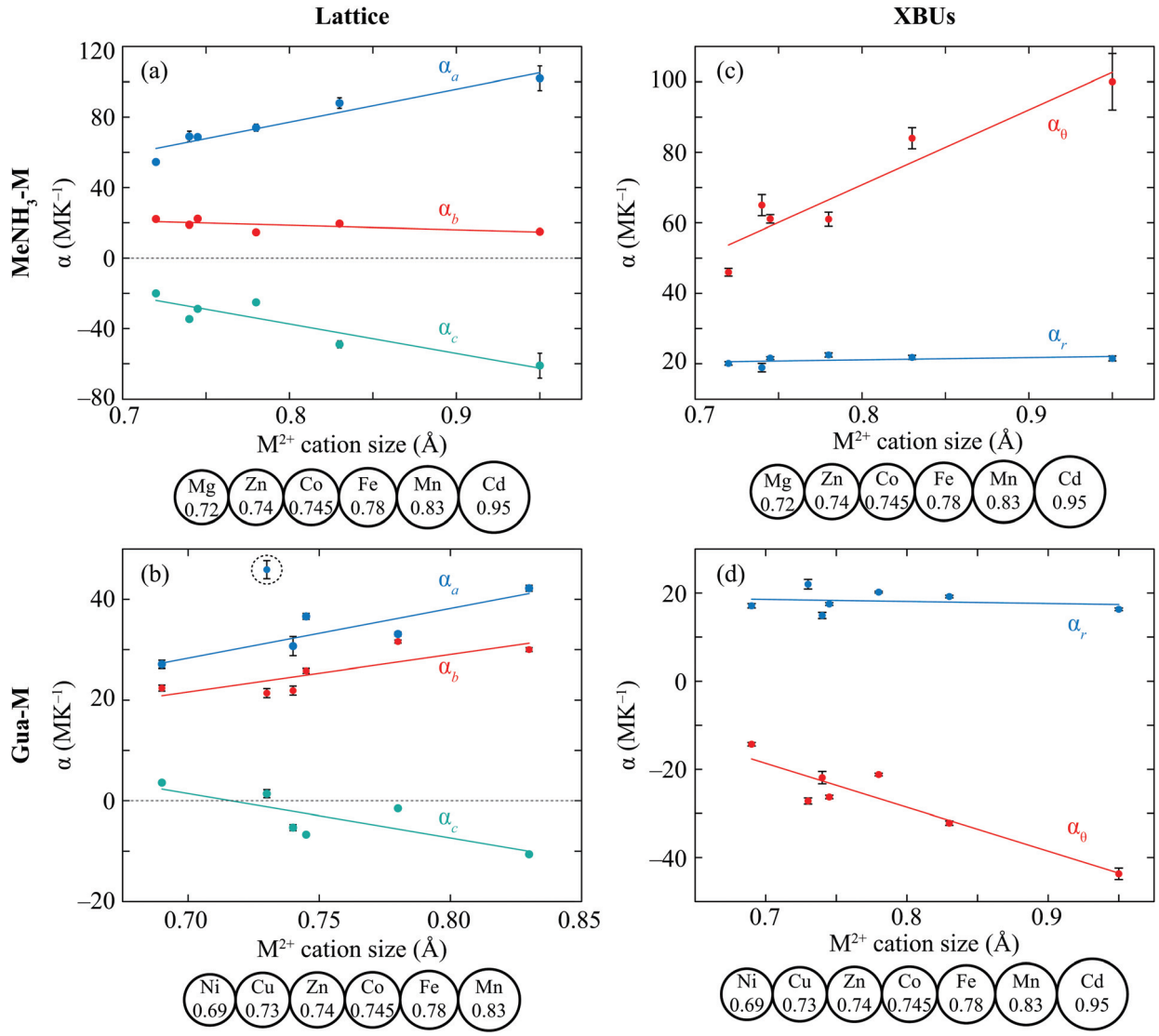

Fig. 5 Lattice expansivities as a function of metal cation size for (a) $MeNH_3$–M and (b) Gua–M families (only data for the orthorhombic members are shown). The dotted ellipse in (b) indicates the α_a value for Gua–Cu, which is not included in the linear fit shown here as a guide-to-the-eye. XBU expansivities calculated for complete (c) $MeNH_3$–M and (d) Gua–M families. Ionic radii are taken from ref. 58 for octahedrally coordinated (high-spin) M^{2+} cations.

M–formate movement, and (ii) a small unit cell, thus forming shorter contacts between formate linkers; both of these factors will result in a restriction of framework hingeing.

While the Mg^{2+} member in ABX_3 formates has been observed to behave slightly differently to the transition metal ABX_3 compounds, *i.e.* higher values of ferroelectric transition temperatures and certain vibrational frequencies,[38,48,59] here the reduced flexibility of $[MeNH_3][Mg(HCOO)_3]$ compared to other $[MeNH_3][M(HCOO)_3]$ can be simply explained by its ionic size. This is likely to be because the atomic displacements we observe upon heating can be correlated with the strength of M–O interaction which scales well with ionic size. In contrast, the ferroelectric transition and vibrational frequencies observed will in addition be dependent on the electronic dipoles in the structure and the mass of the metal cation, respectively.[38,48,59] However, we note that the nature of the M–O bonding as well as other subtle factors beyond size may contribute to the scatter in the linear dependence of α values with ionic radius observed in Fig. 5.

Although the values of α_r are essentially identical for both $MeNH_3$–M and Gua–M families (~20 MK^{-1}), the magnitudes of α_θ *and their sensitivity to cation radius* are substantially smaller for the latter family than for the former. We discuss this dependence on alkylammonium cation in more detail below, but note here that this difference has the consequence for Gua–M systems with small M^{2+} that $|\alpha_\theta| \sim |\alpha_r|$ and so the NTE effect that would ordinarily arise from framework hingeing can be masked by the network deformation (expansion in r). This is why Gua–Ni and Gua–Cu do not exhibit NTE along any crystal axis.

 This journal is © The Royal Society of Chemistry 2016

Published on 08 October 2015. Downloaded on 04/04/2016 18:18:19.

3.3. Effect of variation in A^+

Our results for the $MeNH_3$–M and Gua–M families show clearly that variation in A-site cation can affect the extent of framework hingeing observed. To investigate this in more detail, we consider the family of Mn-containing ABX_3 formates with A = $CH_3NH_3^+$, $CH_3CH_2NH_3^+$, $(CH_3)_2NH_2^+$, $(CH_2)_3NH_2^+$, and $C(NH_2)_3^+$. The sizes of the different A-site cations were estimated by fitting the atomic coordinates refined from the powder diffraction data to a shape tensor, L, using the program CRYSTALS.[63] This shape tensor represents an anisotropic ellipsoid that contains all atoms within the A-site cation.[64] The smallest, median, and largest components of this ellipsoid are shown in Table 2. We initially use the maximum effective length of the A-site cation (L_{max}) as our metric by which to compare the mechanical properties of our different systems. In a another study, a different method was used to calculate the sizes of the A-site cations mentioned here.[65] The two approaches are consistent with one another except that the order of the $Me_2NH_2^+$ and Gua^+ cations is reversed (see ESI† for further discussion).

Fig. 6 shows the XBU expansivities for the five Mn-containing formate frameworks, arranged according to the value of L_{max} for their A-site cation. As observed in the previous section, there is essentially no meaningful compositional dependence of α_r. By contrast, the magnitude of α_θ is much reduced for those systems with larger A-site cations. Our use of the absolute value of α_θ reflects the fact that its sign is not conserved amongst the various compounds we study, a point we will expand upon below. So, at face value our results suggest that bulkier A-site cations inhibit framework flexibility. This may be due simply to steric interactions between the A-site cation and the host framework, with bulkier cations preventing large changes in framework angles. From a chemical viewpoint it is likely that the different H-bonding strengths of the various A-site cations will also impact the framework flexibility;[28] however, our data do not allow us to probe changes in hydrogen-bond characteristics with any certainty. Even in these simplistic terms, and taken together with the results of the previous section, our analysis already suggests that the most flexible formate frameworks will be those with large M^{2+} but small A^+—precisely the combination that (rightly) identifies $MeNH_3$–Cd as the most flexible of the systems we study here [Table 1].

One of the key motivations for our study was to understand the relationship between A-cation *shape* and framework mechanics. There are a large number of metrics to quantify shape, but we constrain ourselves here (given that we have but five data points to compare) to the straightforward notion of *asphericity*.[66] The asphericity parameter

$$b = L_{med} - \frac{1}{2}(L_{min} + L_{max}) \quad (7)$$

takes into account both the size of an object and the anisotropy of the shape tensor $\mathbf{L}$. The parameter b assumes negative values for objects with prolate asphericity, positive values for oblate objects, and is zero for isotropic shapes. The various A-site cations we consider span a range of asphericities $-1 \lesssim b \lesssim 1$ Å^2 [Table 2]. Re-ordering the hingeing XBU expansivities according to these values, we find a clear distinction between prolate and oblate A-cations, for which $\alpha_\theta > 0$ and $\alpha_\theta < 0$, respectively.§ This switching in sign of anisotropic mechanical response as a consequence of cation asphericity is strongly reminiscent of the critical ratios that demarcate linear and area negative thermal expansion in a range of molecular

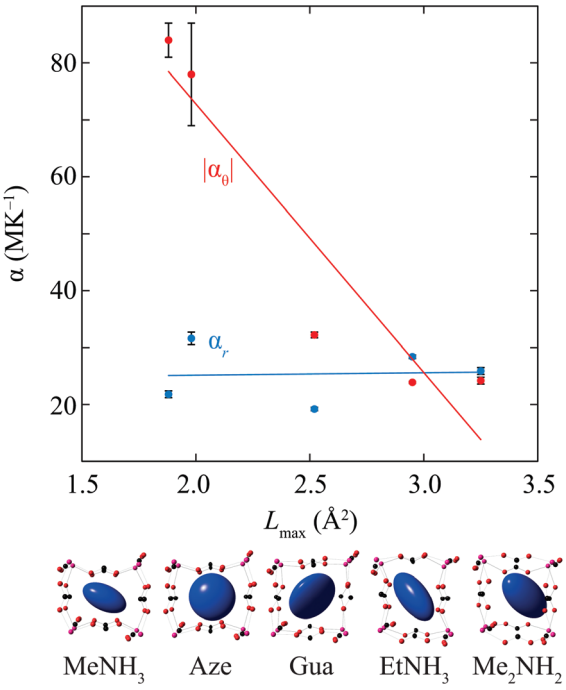

Fig. 6 XBU expansivities determined for $MeNH_3$–Mn, Aze–Mn, Gua–Mn, $EtNH_3$–Mn, and Me_2NH_2–Mn, given as a function of maximum effective A-site cation length. The cation shape tensor generated using CRYSTALS is represented for each compound below the graph.[63,64] The expansivities for Aze–Mn have an anomalously large uncertainty as a result of a low-temperature phase transition (see ESI† for further discussion).

Table 2 Computed principal axis effective lengths (given in units of Å^2) for each of the A-site cation centroids in the host manganese formate, calculated within CRYSTALS.[63,64] The asphericity b (also given in Å^2) is defined by eqn (7)

A^+	L_{min}	L_{med}	L_{max}	b
$MeNH_3$	0.54	0.57	1.88	−0.64
$EtNH_3$	0.65	0.88	2.95	−0.92
Me_2NH_2	0.71	1.21	3.25	−0.77
Aze	0.82	1.92	1.98	0.52
Gua	0.48	2.39	2.52	0.89

§ Note that in order for the sign of α_θ to have any physical meaning, we are careful to define the value of θ in a consistent way for all frameworks we study. In particular, it is given as the obtuse angle in the rhombic face of the perovskite-like cube. Hence $\alpha_\theta > 0$ implies that the cube geometry becomes more distorted with increasing temperature, and $\alpha_\theta < 0$ reflects a tendency to adopt an increasingly cubic geometry on heating.

Published on 08 October 2015. Downloaded on 04/04/2016 18:18:19.

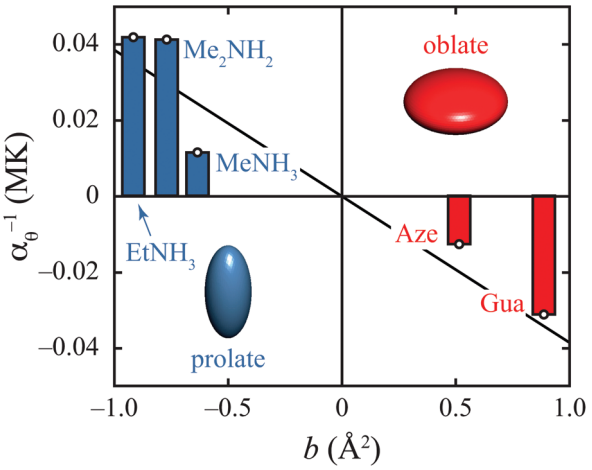

Fig. 7 Relationship between asphericity b and inverse XBU expansivity for the five Mn-containing ABX_3 formates in our study. The direction of framework flexing switches for prolate/oblate A-site cations; the extent of flexibility is largest for small, spherical cations ($b \rightarrow 0$).

framework materials.[24] As in those systems, the magnitude of hingeing response is actually larger for systems closer to the critical geometry (here, b = 0). Our data show an approximately-linear relationship between b and the inverse expansivity α_θ^{-1} [Fig. 7].

So, from a design perspective, our analysis suggests that it is not only the A-cation size that affects framework flexibility, but also its anisotropy. Hence we can explain why $EtNH_3$–Mn is less flexible than Aze–Mn, despite the fact that $EtNH_3^+$ is the smaller cation by ~25% (see ESI† for details). This relationship also explains why the qualitative ordering of Fig. 6 in terms of L_{max} is physically meaningful.

4. Concluding remarks

The relationships we establish between cation size and shape provide a set of straightforward structure–property rules which can be implemented as part of the strategic design of functional MOFs. The basis of these relationships is the correlation between cation size and M–formate bonding strength, which in turn affects the mechanical properties. In a computational study of the $[Me_2NH_2][M(HCOO)_3]$ family, it was shown that the calculated Bader charges on the metal cations exhibited the following order: Mn > Fe > Zn > Co > Ni.[62] This order was also suggested to represent the M–formate bonding strength, where Mn–formate exhibits the weakest bond (highest ionic component) and Ni–formate the strongest (greatest covalent component), and furthermore, the ordering is very similar to that of the metal cation size. There is a small discrepancy with the Zn and Co placement between the Bader charge and metal cation size sequences; however, as there is very little difference in the sizes (0.74 *vs.* 0.745 Å), the variation is not significant. This small discrepancy can be also seen in the coefficients of thermal expansion, which vary subtly in the order for these two metal cations [Fig. 5].

In a nanoindentation study of the $[Me_2NH_2][M(HCOO)_3]$ family, it was suggested that the metal ligand field stabilisation energy (LFSE) directs the resulting mechanical properties.[29] The LFSE order of Mn = Zn < Co < Ni was reproduced in the magnitudes of the Young's Moduli of these compounds.[29] This finding places compounds which contain either Mn^{2+}, Zn^{2+}, or Cd^{2+} on the same level of structural flexibility, which is not consistent with the thermal expansivity characteristics we measure here. Likewise, a Brillouin scattering study of related $[NH_4][Mn(HCOO)_3]$ and $[NH_4][Zn(HCOO)_3]$ structures indicated increased stiffness for M = Zn^{2+} than M = Mn^{2+}.[67] The thermal expansion data from this study and others[30] also show increased stiffness for Zn^{2+}-containing compounds compared to Mn^{2+}. This discrepancy could be due to the different experimental methods used: in the case of nanoindentation experiments, a uniaxial force is exerted upon the crystal, while upon temperature variation, an isotropic external stimulus is applied. One obvious and straightforward experiment would be to carry out a comparative nanoindentation study of Zn- and Cd-containing formate frameworks, since these species correspond to very different ionic radii but identical LFSEs.

A clear result of our study has been to show that the presence of A-site cations within the pores of the metal formate framework plays an important role in controlling the structural flexibility of the material. In particular, longer A-site cations cause a significant decrease in the framework hingeing observed. Thus these structures are not expected to give rise to anomalous mechanics, such as NTE. Instead their mechanics will be dominated by the behaviour of the M–linker–M units. In addition, the direction of framework hingeing can be switched by using differently-shaped A-site cations within the framework pores. In the case of oblate A-site cations, the framework hingeing is directed towards a convergence of framework angles (such as 90° for a 2D wine-rack) upon heating; whereas there is a divergence of framework angles in the case where prolate A-site cations are used. The framework hingeing direction could have implications for ferroelectric transitions arising from reorientation of extra-framework molecular ions. Stronger host–guest interactions might be expected for pore shapes which mimic the shape of the molecular ion. Thus ferroelectric ordering may be stabilised in cases where the pores vary (*i.e.* framework angle evolve) towards a shape that mimics that of the molecular ion.

In summary, our work has shown that metal cation size correlates well with expansivity magnitudes. For the octahedral cation site, cations with smaller radii give rise to stiffer frameworks, while the larger metal cations are associated with the more extreme framework flexibility. At the A-site, cation size is also found to affect framework flexibility, though in the opposite sense: framework hingeing is constrained when long A-site cations are present within the framework pore. Moreover, the type of asphericity of the A-site cation determines the direction of framework hingeing. This is most likely to be

 This journal is © The Royal Society of Chemistry 2016

observed only in dense MOFs, where the vibrational motion of the anisotropic A-site cation is of greater importance. The most readily applicable rule for rational mechanical design of MOFs involves that of the metal cations, where simple evaluation of its size within different oxidation states or coordination environments can provide a scale of flexibility within a series of isostructural frameworks.

Acknowledgements

The authors thank the EPSRC (grant no. EP/G004528/2) and ERC (grant no. 279705) for financial support. This work was carried out with the support of the Diamond Light Source.

Published on 08 October 2015. Downloaded on 04/04/2016 18:18:19.

References

1 W. Zhou, H. Wu, T. Yildirim, J. R. Simpson and A. R. Hight Walker, *Phys. Rev. B*, 2008, **78**, 054114.
2 Y. Wu, A. Kobayashi, G. J. Halder, V. K. Peterson, K. W. Chapman, N. Lock, P. D. Southon and C. J. Kepert, *Angew. Chem., Int. Ed.*, 2008, **120**, 9061–9064.
3 W. Li, M. R. Probert, M. Kosa, T. D. Bennett, A. Thirumurugan, R. P. Burwood, M. Parinello, J. A. K. Howard and A. K. Cheetham, *J. Am. Chem. Soc.*, 2012, **134**, 11940–11943.
4 J. M. Ogborn, I. E. Collings, S. A. Moggach, A. L. Thompson and A. L. Goodwin, *Chem. Sci.*, 2012, **3**, 3011–3017.
5 A. B. Cairns and A. L. Goodwin, *Phys. Chem. Chem. Phys.*, 2015, **17**, 20449–20465.
6 C. Serre, C. Mellot-Draznieks, S. Surblé, N. Audebrand, Y. Filinchuk and G. Férey, *Science*, 2007, **315**, 1828–1831.
7 G. Férey and C. Serre, *Chem. Soc. Rev.*, 2009, **38**, 1380–1399.
8 K. W. Chapman, G. J. Halder and P. J. Chupas, *J. Am. Chem. Soc.*, 2009, **131**, 17546–17547.
9 T. D. Bennett, A. L. Goodwin, M. T. Dove, D. A. Keen, M. G. Tucker, E. R. Barney, A. K. Soper, E. G. Bithell, J.-C. Tan and A. K. Cheetham, *Phys. Rev. Lett.*, 2010, **104**, 115503.
10 M. D. Allendorf, R. J. T. Houk, L. Andruszkiewicz, A. A. Talin, J. Pikarsky, A. Choudhury, K. A. Gall and P. J. Hesketh, *J. Am. Chem. Soc.*, 2008, **130**, 14404–14405.
11 P. Horcajada, C. Serre, G. Maurin, N. A. Ramsahye, F. Balas, M. Vallet-Regí, M. Sebban, F. Taulelle and G. Férey, *J. Am. Chem. Soc.*, 2008, **130**, 6774–6780.
12 L. Sarkisov, R. L. Martin, M. Haranczyk and B. Smit, *J. Am. Chem. Soc.*, 2014, **136**, 2228–2231.
13 I. E. Collings, A. B. Cairns, A. L. Thompson, J. E. Parker, C. C. Tang, M. G. Tucker, J. Catafesta, C. Levelut, J. Haines, V. Dmitriev, P. Pattison and A. L. Goodwin, *J. Am. Chem. Soc.*, 2013, **135**, 7610–7620.
14 L. Bouëssel du Bourg, A. U. Ortiz, A. Boutin and F.-X. Coudert, *APL Mater.*, 2014, **2**, 124110.
15 T. D. Bennett, J. Sotelo, J.-C. Tan and S. A. Moggach, *CrystEngComm*, 2015, **17**, 286–289.
16 A. U. Ortiz, A. Boutin, A. H. Fuchs and F.-X. Coudert, *J. Chem. Phys.*, 2013, **138**, 174703.
17 C. Nanthamathee, S. Ling, B. Slater and M. P. Attfield, *Chem. Mater.*, 2014, **27**, 85–95.
18 S. J. Hunt, M. J. Cliffe, J. A. Hill, A. B. Cairns, N. P. Funnell and A. L. Goodwin, *CrystEngComm*, 2015, **17**, 361–369.
19 W. Cai and A. Katrusiak, *Nat. Commun.*, 2014, **5**, 4337.
20 S. Henke, A. Schneemann and R. A. Fischer, *Adv. Funct. Mater.*, 2013, **23**, 5990–5996.
21 H.-L. Zhou, R.-B. Lin, C.-T. He, Y.-B. Zhang, N. Feng, Q. Wang, F. Deng, J.-P. Zhang and X.-M. Chen, *Nat. Commun.*, 2013, **4**, 1–8.
22 L. D. DeVries, P. M. Barron, E. P. Hurley, C. Hu and W. Choe, *J. Am. Chem. Soc.*, 2011, **133**, 14848–14851.
23 C. Yang, X. Wang and M. A. Omary, *Angew. Chem., Int. Ed.*, 2009, **48**, 2500–2505.
24 I. E. Collings, M. G. Tucker, D. A. Keen and A. L. Goodwin, *CrystEngComm*, 2014, **16**, 3498–3506.
25 S. Henke, W. Li and A. K. Cheetham, *Chem. Sci.*, 2014, **5**, 2392–2397.
26 D. Dubbeldam, K. S. Walton, D. E. Ellis and R. Q. Snurr, *Angew. Chem., Int. Ed.*, 2007, **46**, 4496–4499.
27 T. D. Bennett, J.-C. Tan, S. A. Moggach, R. Galvelis, C. Mellot-Draznieks, B. A. Reisner, A. Thirumurugan, D. R. Allan and A. K. Cheetham, *Chem. – Eur. J.*, 2010, **16**, 10684–10690.
28 W. Li, A. Thirumurugan, P. T. Barton, Z. Lin, S. Henke, H. H. M. Yeung, M. T. Wharmby, E. G. Bithell, C. J. Howard and A. K. Cheetham, *J. Am. Chem. Soc.*, 2014, **136**, 7801–7804.
29 J.-C. Tan, P. Jain and A. K. Cheetham, *Dalton Trans.*, 2012, **41**, 3949–3952.
30 K. W. Chapman, P. J. Chupas and C. J. Kepert, *J. Am. Chem. Soc.*, 2006, **128**, 7009–7014.
31 S. Adak, L. L. Daemen, M. Hartl, D. Williams, J. Summerhill and H. Nakotte, *J. Solid State Chem.*, 2011, **184**, 2854–2861.
32 S. G. Duyker, V. K. Peterson, G. J. Kearley, A. J. Ramirez-Cuesta and C. J. Kepert, *Angew. Chem., Int. Ed.*, 2013, **52**, 5266–5270.
33 V. I. Pet'kov and A. I. Orlova, *Inorg. Mater.*, 2003, **39**, 1013–1023.
34 F. Millange, N. Guillou, R. I. Walton, J.-M. Grenèche, I. Margiolaki and G. Férey, *Chem. Commun.*, 2008, 4732–4734.
35 J.-H. Lee, N. C. Bristowe, P. D. Bristowe and A. K. Cheetham, *Chem. Commun.*, 2015, **51**, 6434–6437.
36 P. Jain, V. Ramachandran, R. J. Clark, H. D. Zhou, B. H. Toby, N. S. Dalal, H. W. Kroto and A. K. Cheetham, *J. Am. Chem. Soc.*, 2009, **131**, 13625–13627.
37 M. Sánchez-Andújar, S. Presedo, S. Yáñez-Vilar, S. Castro-García, J. Shamir and M. A. Señarís Rodríguez, *Inorg. Chem.*, 2010, **49**, 1510–1516.
38 B. Pato-Doldán, M. Sánchez-Andújar, L. C. Gómez-Aguirre, S. Yáñez-Vilar, J. López-Beceiro, C. Gracia-Fernández, A. A. Haghighirad, F. Ritter, S. Castro-García and M. A. Señarís Rodríguez, *Phys. Chem. Chem. Phys.*, 2012, **14**, 8498–8501.

Published on 08 October 2015. Downloaded on 04/04/2016 18:18:19.

39 W. Li, Z. Zhang, E. G. Bithell, A. S. Batsanov, P. T. Barton, P. J. Saines, P. Jain, C. J. Howard, M. A. Carpenter and A. K. Cheetham, *Acta Mater.*, 2013, **61**, 4928–4938.
40 W. Wang, L.-Q. Yan, J.-Z. Cong, Y.-L. Zhao, F. Wang, S.-P. Shen, T. Zou, D. Zhang, S.-G. Wang, X.-F. Han and Y. Sun, *Sci. Rep.*, 2013, **3**, 2024.
41 A. Stroppa, P. Jain, P. Barone, M. Marsman, J. M. Perez-Mato, A. K. Cheetham, H. W. Kroto and S. Picozzi, *Angew. Chem., Int. Ed.*, 2011, **50**, 5847–5850.
42 A. Stroppa, P. Barone, P. Jain, J. M. Perez-Mato and S. Picozzi, *Adv. Mater.*, 2013, **25**, 2284–2290.
43 Y. Tian, A. Stroppa, Y. Chai, L. Yan, S. Wang, P. Barone, S. Picozzi and Y. Sun, *Sci. Rep.*, 2014, **4**, 6062.
44 G.-C. Xu, X.-M. Ma, L. Zhang, Z.-M. Wang and S. Gao, *J. Am. Chem. Soc.*, 2010, **132**, 9588–9590.
45 G.-C. Xu, W. Zhang, X.-M. Ma, Y.-H. Chen, L. Zhang, H.-L. Cai, Z.-M. Wang, R.-G. Xiong and S. Gao, *J. Am. Chem. Soc.*, 2011, **133**, 14948–14951.
46 D. Di Sante, A. Stroppa, P. Jain and S. Picozzi, *J. Am. Chem. Soc.*, 2013, **135**, 18126–18130.
47 R. Shang, G.-C. Xu, Z.-M. Wang and S. Gao, *Chem. – Eur. J.*, 2014, **20**, 1146–1158.
48 M Mączka, A. Pietraszko, B. Macalik and K. Hermanowicz, *Inorg. Chem.*, 2014, **53**, 787–794.
49 Z. Wang, B. Zhang, T. Otsuka, K. Inoue, H. Kobayashi and M. Kurmoo, *Dalton Trans.*, 2004, 2209–2216.
50 S. P. Thompson, J. E. Parker, J. Potter, T. P. Hill, A. Birt, T. M. Cobb, F. Yuan and C. C. Tang, *Rev. Sci. Instrum.*, 2009, **80**, 075107.
51 S. P. Thompson, J. E. Parker, J. Marchal, J. Potter, A. Birt, F. Yuan, R. D. Fearn, A. R. Lennie, S. R. Street and C. C. Tang, *J. Synchrotron Radiat.*, 2011, **18**, 637–648.
52 A. A. Coelho, *TOPAS-Academic, version 4.1 (computer software)*, Coelho Software, Brisbane, 2007.
53 K.-L. Hu, M. Kurmoo, Z. Wang and S. Gao, *Chem. – Eur. J.*, 2009, **15**, 12050–12064.
54 P. Jain, N. S. Dalal, B. H. Toby, H. W. Kroto and A. K. Cheetham, *J. Am. Chem. Soc.*, 2008, **130**, 10450–10451.
55 E. Sletten and L. H. Jensen, *Acta Crystallogr.*, 1973, **B29**, 1752–1756.
56 D. Kong, J. Zoñ, J. McBee and A. Clearfield, *Inorg. Chem.*, 2006, **45**, 977–986.
57 M. J. Cliffe and A. L. Goodwin, *J. Appl. Crystallogr.*, 2012, **45**, 1321–1329.
58 R. D. Shannon, *Acta Crystallogr.*, 1976, **A32**, 751–767.
59 M. Mączka, K. Szymborska-Małek, A. Ciupa and J. Hanuza, *Vib. Spectrosc.*, 2015, **77**, 17–24.
60 M. Mączka, M. Ptak and L. Macalik, *Vib. Spectrosc.*, 2014, **71**, 98–104.
61 M. Mączka, A. Gągor, B. Macalik, A. Pikul, M. Ptak and J. Hanuza, *Inorg. Chem.*, 2014, **53**, 457–467.
62 M. Kosa and D. T. Major, *CrystEngComm*, 2014, **17**, 295–298.
63 P. W. Betteridge, J. R. Carruthers, R. I. Cooper, K. Prout and D. J. Watkin, *J. Appl. Crystallogr.*, 2003, **36**, 1487.
64 R. I. Cooper, B. M. Foxman and L. Yang, *J. Appl. Crystallogr.*, 2004, **37**, 669–671.
65 G. Kieslich, S. Sun and A. K. Cheetham, *Chem. Sci.*, 2014, **5**, 4712–4715.
66 D. N. Theodorou and U. W. Suter, *Macromolecules*, 1985, **18**, 1206–1214.
67 M. Mączka, M. Ptak and S. Kojima, *Appl. Phys. Lett.*, 2014, **104**, 222903.
68 Z. Otwinowski and W. Minor, *Methods Enzymol.*, 1997, 276.
69 A. Altomare, G. Cascarano, C. Giacovazzo, A. Guagliardi, M. C. Burla, G. Polidori and M. Camalli, *J. Appl. Crystallogr.*, 1994, **27**, 435.
70 P. Parois, R. I. Cooper and A. L. Thompson, *Chem. Cent.*, 2015, **9**, 30.
71 R. I. Cooper, A. L. Thompson and D. J. Watkin, *J. Appl. Crystallogr.*, 2010, **43**, 1100–1107.

This journal is © The Royal Society of Chemistry 2016

Electronic Appendix

The contents of the Electronic Appendix contained on the enclosed CD are as follows:

- PDF of this Thesis
- Single crystal .cif and .fcf files for structures reported in Chapter 3
- Tables of structural refinement results, example refinement files (and data) relating to Chapter 5
- Single crystal .cif and .fcf files for structures relating to Chapter 5
- Single crystal .cif (modulated and approximant) and refinement files for Chapter 6
- FINDSYM output for compound **4** in Chapter 7
- Single crystal .cif and .fcf files, COPL output, and ISODISTORT files for Chapter 8.